

AD-A114 752

ATLANTIC RESEARCH CORP. ALEXANDRIA VA  
INTRASYSTEM ANALYSIS PROGRAM (IAP) MODEL IMPROVEMENT. (U)  
FEB 82 T E BALDWIN, W G DUFF, J J FOSTER  
F30602-79-C-0169

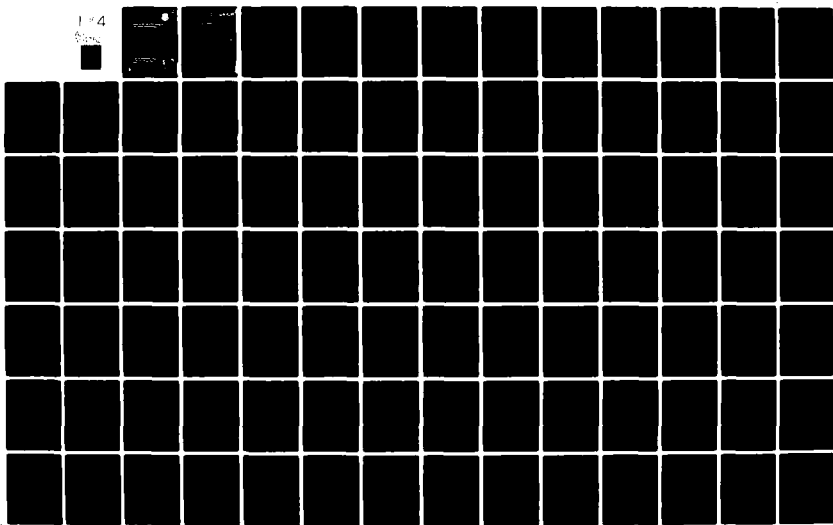
F/G 20/3

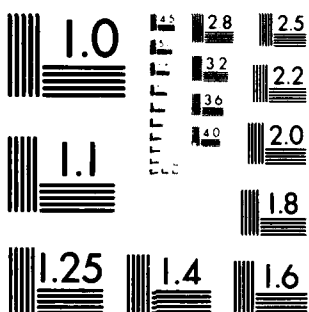
UNCLASSIFIED

RADC-TR-82-20

NL

1 x 4  
None



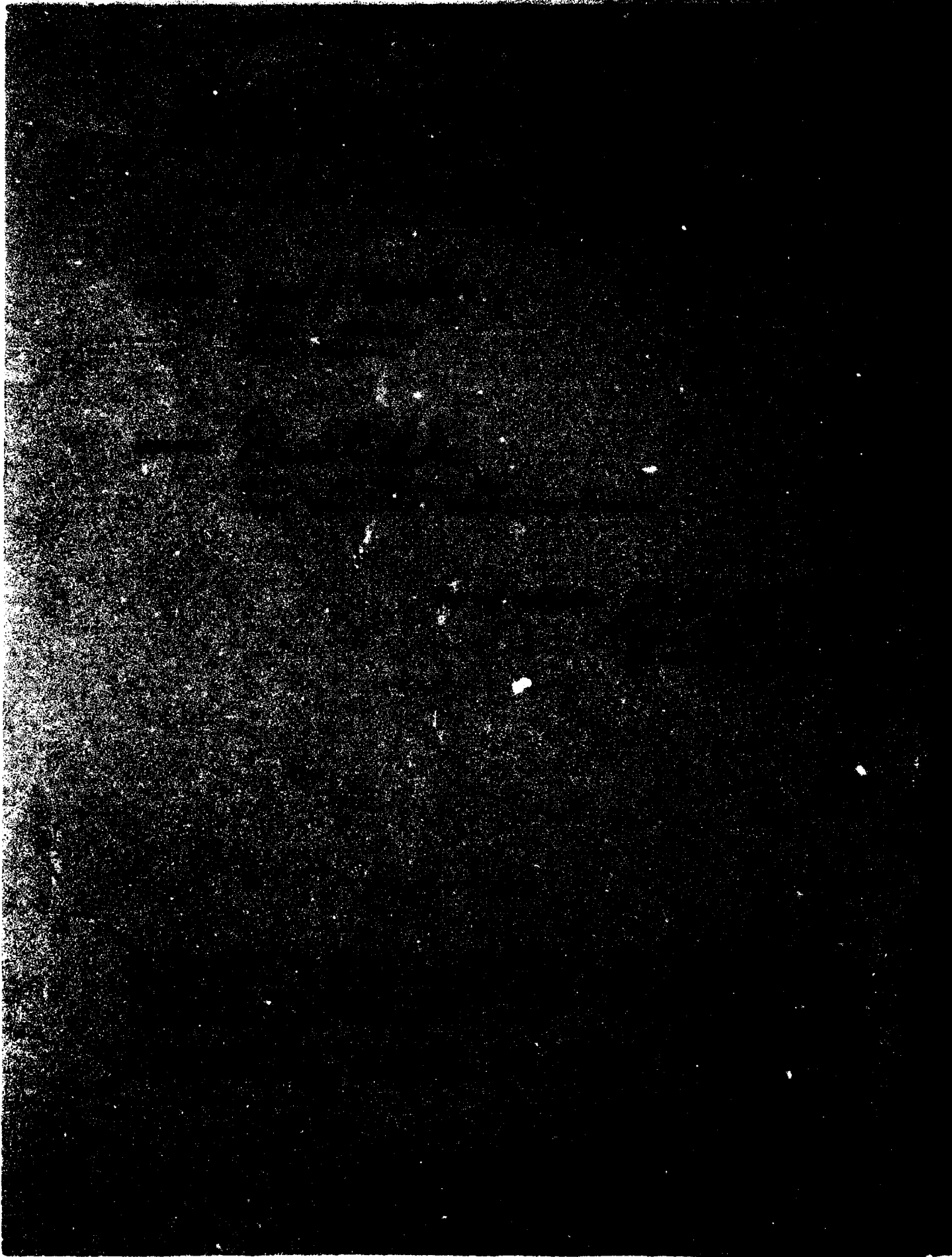


MICROCOPY RESOLUTION TEST CHART  
NATIONAL BUREAU OF STANDARDS 1963 A

# INTRODUCTION TO THE STUDY OF LAW IN THE UNITED STATES

人壽保險公司 保險代理人 代理人

## REFERENCES



## UNCLASSIFIED

SECURITY CLASSIFICATION OF THIS PAGE (When Data Entered)

REPORT DOCUMENTATION PAGE		READ INSTRUCTIONS BEFORE COMPLETING FORM
1. REPORT NUMBER RADC-TR-82-20	2. GOVT ACCESSION NO. AD-A114 752	3. RECIPIENT'S CATALOG NUMBER
4. TITLE (and Subtitle) INTRASYSTEM ANALYSIS PROGRAM (IAP) MODEL IMPROVEMENT	5. TYPE OF REPORT & PERIOD COVERED Final Technical Report Jun 79 - Dec 81	
	6. PERFORMING ORG. REPORT NUMBER N/A	
7. AUTHOR(s) Thomas E. Baldwin Richard G. Robinson Dr. William G. Duff Dr. Harvey K. Schumann James J. Foster Mildred K. Bartley	8. CONTRACT OR GRANT NUMBER(s) F30602-79-C-0169	
9. PERFORMING ORGANIZATION NAME AND ADDRESS Atlantic Research Corporation 5390 Cherokee Avenue Alexandria VA 22314	10. PROGRAM ELEMENT, PROJECT, TASK AREA & WORK UNIT NUMBERS 62702F 23380322	
11. CONTROLLING OFFICE NAME AND ADDRESS Rome Air Development Center (RBCT) Griffiss AFB NY 13441	12. REPORT DATE February 1982	
	13. NUMBER OF PAGES 366	
14. MONITORING AGENCY NAME & ADDRESS (if different from Controlling Office) Same	15. SECURITY CLASS. (of this report) UNCLASSIFIED	
	15a. DECLASSIFICATION/DOWNGRADING SCHEDULE N/A	
16. DISTRIBUTION STATEMENT (of this Report)  Approved for public release; distribution unlimited.		
17. DISTRIBUTION STATEMENT (of the abstract entered in Block 20, if different from Report) Same		
18. SUPPLEMENTARY NOTES RADC Project Engineer: Daniel J. Kenneally (RBCT)		
19. KEY WORDS (Continue on reverse side if necessary and identify by block number) Systems EMC Analysis, Intrasystem Analysis Code, Frequency Dep. Antenna Models, Nonlinear Receptor Models, Waveform Sensitive Receptors, Spectral Models, Intrasystem EMC Analysis Program, Antenna Matching Factor, Transmission Line Loss Factor, Antenna Directivity, Antenna Gain Pattern, Out-Of-Band Antenna Gain Models, Software Implementation		
20. ABSTRACT (Continue on reverse side if necessary and identify by block number) The Intrasystem Electromagnetic Compatibility Analysis Program (IEMCAP) is a systems level, computerized analysis program which may be used in analyzing electromagnetic compatibility (EMC) for aircraft, spacecraft or ground stations on both present and future systems. The objective of this effort was to increase the prediction capability of the IEMCAP. The defined tasks to obtain the new capability are the following: (1) development of a frequency dependent power gain antenna model for IEMCAP;		

UNCLASSIFIED

SECURITY CLASSIFICATION OF THIS PAGE(When Data Entered)

(2) modify IEMCAP to predict the electromagnetic (EM) interference for those devices whose compatibility is not related to average power; (3) implement within IEMCAP a mathematical model(s) to predict the degradation to receptors of EM energy, caused by spurious signal products generated at an emitter, a structural nonlinearity (i.e., in the transmission path), or in a victim receptor (i.e., signal harmonics, intermodulation, cross modulation, desensitization, gain compression/expansion and spurious responses); and (4) modification of the modeling procedure for a port's emission and/or susceptibility.

Upon completion of the above modeling effort, the developed models were to be coded and interfaced with the existing IEMCAP.

To interface the new models it was recognized and agreed that the order of priority for programming the new models should be (1) new port spectra model (Task 4), (2) nonlinear effects models (Task 3), (3) nonaverage power receptor models (Task 2) and (4) new antenna models (Task 1). As a result of the new user SPECT option associated with the new port spectra modeling, it was determined that a significant change was required in the narrowband integrated margin method used by IEMCAP. A significant effort was devoted to determining a technique that would be the most beneficial to the IEMCAP user so as not to compromise his data. An appropriate modification to the existing narrowband integrated margin model was made. The implementation of the modification to the narrowband integrated margin calculation involved modifying several existing subroutines in IEMCAP.

Accession For	
NTIS GRA&I	<input checked="" type="checkbox"/>
DTIC TAB	<input type="checkbox"/>
Unannounced	<input type="checkbox"/>
Justification	
By _____	
Distribution/ _____	
Availability Codes	
Avail and/or	
Dist	Special



UNCLASSIFIED

SECURITY CLASSIFICATION OF THIS PAGE(When Data Entered)

### Table of Contents

<u>Section</u>		<u>Page</u>
1.0	<b>Introduction</b>	1-1
2.0	<b>Frequency-Dependent Modeling of Antenna Gain</b>	2-1
2.1	Modeling the Impedance Matching Factor of Antennas	2-4
2.2	Power Transfer Characteristics of a Dipole Without Feed Circuitry	2-5
2.3	Measured Data of Resonant Antennas	2-69
2.4	Power Transfer Characteristics of a Dipole With A Matching Network	2-77
2.5	Impedance Matching Characteristics of Antennas Matched with Lumped Elements	2-79
2.6	Transmission Characteristics of Antennas Matched With Single-Stub Transmission Line Elements	2-89
2.7	Modeling the Impedance Matching Factor of an Antenna Having a Matching Network	2-106
2.8	Impedance Matching Factor of Slot Antennas	2-111
2.9	Impedance Matching Factor of Folded Dipoles	2-115
2.10	Impedance Matching Factor of Loop Antennas	2-117
2.11	Transmission Loss of Yagi-Uda Beam Antennas	2-120
2.12	Impedance Matching Factor of Frequency-Independent Antennas	2-121
2.13	Impedance Matching Factor of Helical Antennas	2-121
2.14	Impedance Matching Factor of Traveling Wave Antennas	2-124
2.15	Impedance Matching Factor of a Horn Antenna	2-125
2.16	Modeling Directive Gain Patterns of Antennas	2-128
2.16.1	Modeling the Directive Gain of Dipole Antennas	2-128
2.16.2	General Pattern Model for Medium-Gain	2-153
2.16.3	Directive Gain Models of Medium-Gain Antennas	2-163
2.16.4	Pattern Model for High-Gain Antennas	2-178
2.16.5	Directive Gain Model for a Loop Antenna	2-181
2.16.6	Directive Gain Model for a Planer Log-Spiral Antenna	2-182
2.16.7	Directive Gain Model for a Conical Log-Spiral Antenna	2-182

Table of Contents  
(Continued)

<u>Section</u>		<u>Page</u>
	2.17 Antenna Power Dissipation Factor	2-183
	2.18 Transmission Line Factor	2-185
	2.18.1 Attenuation Model for Coaxial Lines	2-185
	2.18.2 Attenuation in Waveguides	2-188
	2.19 Summary of Antenna Gain Model	2-191
	2.20 References	2-201
3.0	Non-Average Power Sensitive Receptor Modeling	3-1
	3.1 Total Energy - Deterministic Waveform	3-1
	3.2 Total Energy - Stochastic Waveform	3-13
	3.3 Peak Current/Voltage - Deterministic Waveform	3-15
	3.4 Peak Current - Stochastic Waveform	3-31
	3.5 Peak Current - Normal, Stationary Waveforms (Broadband Gaussian)	3-34
	3.6 Peak Current - Narrowband Gaussian	3-38
	3.7 Peak Current - Narrowband Gaussian Plus Sinusoid	3-39
	3.8 Rise Time - Bandwidth	3-41
	3.9 References	3-42
4.0	Nonlinear Interference Models	4-1
	4.1 The Modified Nonlinear Transfer Function Approach	4-1
	4.1.1 The Volterra Series	4-1
	4.1.2 The Nonlinear Transfer Function Approach	4-5
	4.1.3 The Modified Nonlinear Transfer Function Approach	4-13
	4.2 Desensitization	4-15
	4.3 Gain Compression and Gain Expansion	4-23
	4.4 Intermodulation	4-26
	4.4.1 Two-Signal, Third Order Receiver Intermodulation Products	4-27
	4.4.2 Second and Fifth Order, Two Signal Receiver Intermodulation Products	4-32
	4.4.3 Three Signal, Third Order Receiver Intermodulation Products	4-37
	4.4.4 Transmitter Intermodulation Products	4-39
	4.4.5 Structurally Generated Intermodulation Products	4-40

Table of Contents  
(Continued)

<u>Section</u>		<u>Page</u>
	4.5 Cross Modulation	4-43
	4.6 Spurious Responses	4-52
	4.7 References	4-59
5.0	New Model for Port Spectra	5-1
	5.1 Generation of Equipment Frequency Table	5-3
	5.1.1 Frequency Table Generation Routine (FTGEN)	5-7
	5.1.2 Frequency Range for Analysis	5-8
	5.2 Generation of Port Spectra Amplitudes	5-8
	5.2.1 Calculation of Port Spectra Levels	5-9
	5.3 References	5-14
6.0	Integration of the Four Tasks with the IEMCAP	6-1
	6.1 Modifications to IEMCAP Logic Flow	6-1
	6.1.1 Modifications to IDIPR	6-5
	6.1.2 Modifications to TART	6-8
	6.2 Interface of Antenna Out-of-Band Characteristics Models	6-11
	6.3 Interface of Nonaverage Power Sensitive Receptor Models	6-12
	6.3.1 Interface with IDIPR	6-12
	6.3.2 Interface with TART	6-13
	6.4 Interface of the Nonlinear Effects Models	6-13
	6.4.1 Interface with IDIPR	6-13
	6.4.2 Interface with TART	6-14
	6.5 Interface of Port Spectra Representation	6-14
	6.5.1 Interface with IDIPR	6-14
	6.5.2 Interface with TART	6-15

List of Illustrations

<u>Figure</u>		<u>Page</u>
2-1	Distribution of Power for General Antenna Gain Model	2-3
2-2	Conical and Cylindrical Antenna Shapes	2-5
2-3	Impedance Matching Factor of Ideal Conical Dipole ( $h/a=10^6$ )	2-8
2-4	Impedance Matching Factor of Ideal Conical Dipole ( $h/a=10^4$ )	2-8
2-5	Impedance Matching Factor of Ideal Conical Dipole ( $h/a=1,000$ )	2-9
2-6	Impedance Matching Factor of Ideal Conical Dipole ( $h/a=300$ )	2-9
2-7	Impedance Matching Factor of Ideal Conical Dipole ( $h/a=100$ )	2-10
2-8	Impedance Matching Factor of Ideal Conical Dipole ( $h/a=50$ )	2-10
2-9	Impedance Matching Factor of Ideal Conical Dipole ( $h/a=20$ )	2-11
2-10	Impedance Matching Factor of Ideal Conical Dipole ( $h/a=10$ )	2-11
2-11	Impedance Matching Factor of Ideal Conical Dipole ( $h/a=5$ )	2-12
2-12	Impedance Matching Factor of Ideal Conical Dipole ( $h/a=2$ )	2-12
2-13	Impedance Matching Factor of Ideal Cylindrical Dipole( $h/a=10^6$ )	2-13
2-14	Impedance Matching Factor of Ideal Cylindrical Dipole( $h/a=10^4$ )	2-13
2-15	Impedance Matching Factor of Ideal Cylindrical Dipole( $h/a=1,000$ )	2-14
2-16	Impedance Matching Factor of Ideal Cylindrical Dipole( $h/a=300$ )	2-14
2-17	Impedance Matching Factor of Ideal Cylindrical Dipole( $h/a=100$ )	2-15
2-18	Impedance Matching Factor of Ideal Cylindrical Dipole( $h/a=50$ )	2-15
2-19	Impedance Matching Factor of Ideal Cylindrical Dipole( $h/a=20$ )	2-16
2-20	Smith Chart of Ideal Conical Dipole ( $h/a=10^6$ )	2-16
2-21	Smith Chart of Ideal Conical Dipole ( $h/a=10^4$ )	2-17
2-22	Smith Chart of Ideal Conical Dipole ( $h/a=1,000$ )	2-17
2-23	Smith Chart of Ideal Conical Dipole ( $h/a=300$ )	2-18
2-24	Smith Chart of Ideal Conical Dipole ( $h/a=100$ )	2-18
2-25	Smith Chart of Ideal Conical Dipole ( $h/a=50$ )	2-19
2-26	Smith Chart of Ideal Conical Dipole ( $h/a=20$ )	2-19
2-27	Smith Chart of Ideal Conical Dipole ( $h/a=10$ )	2-20
2-28	Smith Chart of Ideal Cylindrical Dipole ( $h/a=10^6$ )	2-20
2-29	Smith Chart of Ideal Conical Dipole ( $h/a=2$ )	2-21
2-30	Smith Chart of Ideal Cylindrical Dipole ( $h/a=10^6$ )	2-21
2-31	Smith Chart of Ideal Cylindrical Dipole ( $h/a=10^4$ )	2-22
2-32	Smith Chart of Ideal Cylindrical Dipole ( $h/a=1,000$ )	2-22

**List of Illustrations**  
(Continued)

<u>Figure</u>		
2-33 Smith Chart of Ideal Cylindrical Dipole (h/a=300)	2-23	
2-34 Smith Chart of Ideal Cylindrical Dipole (h/a=100)	2-23	
2-35 Smith Chart of Ideal Cylindrical Dipole (h/a=50)	2-24	
2-36 Smith Chart of Ideal Cylindrical Dipole (h/a=20)	2-24	
2-37 Smith Chart of Ideal Cylindrical Dipole (h/a=10)	2-25	
2-38 Smith Chart of Ideal Cylindrical Dipole (h/a=5)	2-25	
2-39 Smith Chart of Ideal Cylindrical Dipole (h/a=2)	2-26	
2-40 Impedance Matching Factor of First Resonance of Conical Dipole (h/a=10 <sup>6</sup> )	2-28	
2-41 Impedance Matching Factor of First Resonance of Conical Dipole (h/a=10 <sup>4</sup> )	2-28	
2-42 Impedance Matching Factor of First Resonance of Conical Dipole (h/a=1,000)	2-29	
2-43 Impedance Matching Factor of First Resonance of Conical Dipole (h/a=300)	2-29	
2-44 Impedance Matching Factor of First Resonance of Conical Dipole (h/a=100)	2-30	
2-45 Impedance Matching Factor of First Resonance of Conical Dipole (h/a=50)	2-30	
2-46 Impedance Matching Factor of First Resonance of Conical Dipole (h/a=20)	2-31	
2-47 Impedance Matching Factor of First Resonance of Conical Dipole (h/a=10)	2-31	
2-48 Impedance Matching Factor of First Resonance of Conical Dipole (h/a=5)	2-32	
2-49 Impedance Matching Factor of First Resonance of Conical Dipole (h/a=2)	2-32	
2-50 Impedance Matching Factor of First Resonance of Cylindrical Dipole (h/a=10 <sup>6</sup> )	2-33	
2-51 Impedance Matching Factor of First Resonance of Cylindrical Dipole (h/a=10 <sup>4</sup> )	2-33	

**List of Illustrations  
(Continued)**

<u>Figure</u>	<u>Page</u>
2-52 Impedance Matching Factor of First Resonance of Cylindrical Dipole (h/a=1,000)	2-34
2-53 Impedance Matching Factor of First Resonance of Cylindrical Dipole (h/a=300)	2-34
2-54 Impedance Matching Factor of First Resonance of Cylindrical Dipole (h/a=100)	2-35
2-55 Impedance Matching Factor of First Resonance of Cylindrical Dipole (h/a=50)	2-35
2-56 Impedance Matching Factor of First Resonance of Cylindrical Dipole (h/a=20)	2-36
2-57 Impedance Matching Factor of First Resonance of Cylindrical Dipole (h/a=10)	2-36
2-58 Impedance Matching Factor of First Resonance of Cylindrical Dipole (h/a=5)	2-37
2-59 Impedance Matching Factor of First Resonance of Cylindrical Dipole (h/a=2)	2-37
2-60 Comparison Between Theoretical and Model Curves of Impedance Matching Factor at First Resonance(Conical, h/a=10 <sup>6</sup> )	2-39
2-61 Comparison Between Theoretical and Model Curves of Impedance Matching Factor at First Resonance(Cylindrical, h/a=10 <sup>6</sup> )	2-39
2-62 Comparison Between Theoretical and Model Curves of Impedance Matching Factor at First Resonance(Cylindrical, h/a=10 <sup>4</sup> )	2-40
2-63 Comparison Between Theoretical and Model Curves of Impedance Matching Factor at First Resonance(Cylindrical, h/a=100)	2-40
2-64 Comparison Between Theoretical Transmission Loss and the Model at First Resonance (Conical, h/a=10 <sup>6</sup> )	2-43
2-65 Comparison Between Theoretical Impedance Matching Factor and the Model at First Resonance (Conical, h/a=100)	2-43
2-66 Comparison Between Theoretical Impedance Matching Factor and the Model at First Resonance (Conical, h/a=10)	2-44
2-67 Comparison Between Theoretical Impedance Matching Factor and the Model at First Resonance (Cylindrical, h/a=10 <sup>6</sup> )	2-44

**List of Illustrations**  
(Continued)

<u>Figure</u>		<u>Page</u>
2-68	Comparison Between Theoretical Impedance Matching Factor and the Model at First Resonance (Cylindrical, $h/a=100$ )	2-45
2-69	Comparison Between Theoretical Impedance Matching Factor and the Model at First Resonance (Cylindrical, $h/a=20$ )	2-45
2-70	Comparison Between Theoretical Impedance Matching Factor and the Model at Second Resonance (Conical, $h/a=10^6$ )	2-47
2-71	Comparison Between Theoretical Impedance Matching Factor and the Model at Third Resonance (Conical, $h/a=10^6$ )	2-47
2-72	Comparison Between Theoretical Impedance Matching Factor and the Model at Fourth Resonance (Conical, $h/a=10^6$ )	2-48
2-73	Comparison Between Theoretical Impedance Matching Factor and the Model at Fifth Resonance (Conical, $h/a=10^6$ )	2-48
2-74	Comparison Between Theoretical Impedance Matching Factor and the Model at Sixth Resonance (Conical, $h/a=10^6$ )	2-49
2-75	Comparison Between Theoretical Impedance Matching Factor and the Model at Second Resonance (Conical, $h/a=1,000$ )	2-49
2-76	Comparison Between Theoretical Impedance Matching Factor and the Model at Sixth Resonance (Conical, $h/a=1,000$ )	2-50
2-77	Comparison Between Theoretical Impedance Matching Factor and the Model at Second Resonance (Conical, $h/a=100$ )	2-50
2-78	Comparison Between Theoretical Impedance Matching Factor and the Model at Third Resonance (Conical, $h/a=100$ )	2-51
2-79	Comparison Between Theoretical Impedance Matching Factor and the Model at Sixth Resonance (Conical, $h/a=100$ )	2-51
2-80	Comparison Between Theoretical Impedance Matching Factor and the Model at Second Resonance (Cylindrical, $h/a=10^6$ )	2-52
2-81	Comparison Between Theoretical Impedance Matching Factor and the Model at Third Resonance (Cylindrical, $h/a=10^6$ )	2-52
2-82	Comparison Between Theoretical Impedance Matching Factor and the Model at Sixth Resonance (Cylindrical, $h/a=10^6$ )	2-53
2-83	Comparison Between Theoretical Impedance Matching Factor and the Model at Second Resonance (Cylindrical, $h/a=1,000$ )	2-53

**List of Illustrations**  
(Continued)

<u>Figure</u>		<u>Page</u>
2-84	Comparison Between Theoretical Impedance Matching Factor and the Model at Third Resonance (Cylindrical, $h/a=1,000$ )	2-54
2-85	Comparison Between Theoretical Impedance Matching Factor and the Sixth Resonance (Cylindrical, $h/a=1,000$ )	2-54
2-86	Comparison Between Theoretical Impedance Matching Factor and the Model at First Six Resonance (Conical, $h/a=10^6$ )	2-56
2-87	Comparison Between Theoretical Impedance Matching Factor and the First Six Resonances (Cylindrical, $h/a=100$ )	2-56
2-88	Normalized Frequency Separation A Between Resonant Peaks Vs Q of First Resonance	2-58
2-89	3 dB Bandwidth of Resonant Peaks Vs. Resonant Frequency for Dipoles	2-59
2-90	Normalized Bandwidth of Resonant Peaks Vs. Normalized Resonant Frequency of Dipoles	2-61
2-91	Illustration of Normalized Bandwidth Spread	2-63
2-92	Q of Spread Resonant Peak Vs. Normalized Resonant Frequency	2-65
2-93	Depth of First Null of Impedance Mismatch Factor Vs. Q of First Resonance for Dipoles	2-68
2-94	Impedance Matching Factor of 6-Inch Monopole (from measured data)	2-70
2-95	Impedance Matching Factor of Dipole with Tunable Balun (from measured data)	2-70
2-96	Impedance Matching Factor of Dipole With Tunable Bazooka Balun (from measured data)	2-71
2-97	Impedance Matching Factor of Bowtie Dipole (from measured data)	2-71
2-98	Impedance Matching Factor of Biconical Dipole (from measured data)	2-72
2-99	Impedance Matching Factor of Duoconical Monopole (from measured data)	2-72
2-100	Impedance Matching Factor of a Sleeve Dipole (from measured data)	2-73
2-101	Impedance Matching Factor of a Sleeve Dipole (from measured data)	2-73

List of Illustrations  
(Continued)

<u>Figure</u>		<u>Page</u>
2-102	Impedance Matching Factor of a Sleeve Dipole (from measured data)	2-74
2-103	Impedance Matching Factor of Cylindrical Dipole ( $h/a=10^6$ ) Matched with LC Network for Resonance at $.1 h/\lambda$	2-81
2-104	Impedance Matching Factor of Cylindrical Dipole ( $h/a=10^6$ ) Matched with LL Network for Resonance at $.1 h/\lambda$	2-81
2-105	Impedance Matching Factor of Cylindrical Dipole ( $h/a=10^6$ ) Matched with LC Network for Resonance at $.15 h/\lambda$	2-82
2-106	Impedance Matching Factor of Cylindrical Dipole ( $h/a=10^6$ ) Matched with LL Network for Resonance at $.15 h/\lambda$	2-82
2-107	Impedance Matching Factor of Cylindrical Dipole ( $h/a=10^6$ ) Matched with LC Network for Resonance at $.20 h/\lambda$	2-83
2-108	Impedance Matching Factor of Cylindrical Dipole ( $h/a=10^6$ ) Matched with LL Network for Resonance at $.2 h/\lambda$	2-83
2-109	Impedance Matching Factor of Cylindrical Dipole ( $h/a=10^6$ ) Matched with LC Network for Resonance at $.23 h/\lambda$	2-84
2-110	Impedance Matching Factor of Cylindrical Dipole ( $h/a=10^6$ ) Matched with LL Network for Resonance at $.23 h/\lambda$	2-84
2-111	Impedance Matching Factor of Cylindrical Dipole ( $h/a=20$ ) Matched with LL Network for Resonance at $.1 h/\lambda$	2-85
2-112	Impedance Matching Factor of Cylindrical Dipole ( $h/a=20$ ) Matched with LL Network for Resonance at $.1 h/\lambda$	2-85
2-113	Impedance Matching Factor of Cylindrical Dipole ( $h/a=.15$ ) Matched with LC Network for Resonance at $.15 h/\lambda$	2-86
2-114	Impedance Matching Factor of Cylindrical Dipole ( $h/a=.20$ ) Matched with LL Network for Resonance at $.15 h/\lambda$	2-86
2-115	Impedance Matching Factor of Cylindrical Dipole ( $h/a=20$ ) Matched with LC Network for Resonance at $.2 h/\lambda$	2-87
2-116	Impedance Matching Factor of Cylindrical Dipole ( $h/a=20$ ) Matched with LL Network for Resonance at $.2 h/\lambda$	2-87
2-117	Comparison Between Theoretical Impedance Matching Factor and Model Points At Resonance of LC Matched Dipole For Resonance at $.15 f_1$	2-90

List of Illustrations  
(Continued)

<u>Figure</u>		
2-118 Diagram of Single-stub Match for an Antenna	2-91	
2-119 Impedance Matching Factor of Cylindrical ( $h/a=10^6$ ) Stud-Matched for Resonance at $.1 h/\lambda$	2-94	
2-120 Impedance Matching Factor of Cylindrical Dipole ( $h/a=10^6$ ) Stub-Matched for Resonance at $.1 h/\lambda$ with Stub Length Increased $\lambda/2$	2-94	
2-121 Impedance Matching Factor of Cylindrical Dipole ( $h/a=10^6$ ) Stub-Matched for Resonance at $.15 h/\lambda$	2-95	
2-122 Impedance Matching Factor of Cylindrical Dipole ( $h/a=10^6$ ) Stub-Matched for Resonance at $.2 h/\lambda$	2-95	
2-123 Impedance Matching Factor of Cylindrical Dipole ( $h/a=10^6$ ) Stub-Matched for Resonance at $.2 h/\lambda$ with Subt Length Increased $\lambda/2$	2-96	
2-124 Impedance Matching Factor of Cylindrical Dipole ( $h/a=10^6$ ) Stub-Matched for Resonance at $.2 h/\lambda$ with Series Length Increased $1\lambda$	2-96	
2-125 Impedance Matching Factor of Cylindrical Dipole ( $h/a=10^6$ ) Stub-Matched For Resonance at $.2 h/\lambda$ with Stub Length Increased $1\lambda$	2-97	
2-126 Impedance Matching Factor of Cylindrical Dipole ( $h/a=10^6$ ) Stub-Matched for Resonance at $.2 h/\lambda$ with Both Stub and Series Increased $1\lambda$	2-97	
2-127 Impedance Mathcing Factor of Cylindrical Dipole ( $h/a=20$ ) Stub-Matched for Resonance at $.1 h/\lambda$	2-98	
2-128 Impedance Matching Factor of Cylindrical Dipole ( $h/a=20$ ) for Resonance at $.15 h/\lambda$	2-98	
2-129 Impedance Matching Factor of Cylindrical Dipole ( $h/a=20$ ) Stub-Matched for Resonance at $.2 h/\lambda$	2-99	
2-130 Impedance Matching Factor of Cylindrical Dipole ( $h/a=20$ ) Stub-Matched for Resonance at $.2 h/\lambda$ with Series Section Increased $1\lambda$	2-99	

List of Illustrations  
(Continued)

<u>Figure</u>		
2-131 Impedance Matching Factor of Cylindrical Dipole ( $h/a=20$ ) Stub-Matched for Resonance at $.2 h/\lambda$ with Stub Length Increased $1\lambda$		2-100
2-132 Comparison of Model Points with Theoretical Impedance Matching Factor of Resonance Peak for Stub-Tuned Dipole shown in Figure 126		2-101
2-133 Resonance Peaks of Stub-Matched for Resonance at $.2 L/\lambda$ shown in Figure 121		2-103
2-134 Frequency Response Behavior of a Common UHF Aircraft Blade Antenna		2-104
2-135 Frequency Response Behavior of a Marker Beacon Antenna		2-105
2-136 Frequency Response of a Localizer Antenna		2-107
2-137 Frequency Response of HF Wire Antenna		2-108
2-138 Frequency Response of VLF/LF Trailing-wire Antenna		2-109
2-139 Suggested Models for Matched Antenna		2-112
2-140 Modified Universal Resonance Curves		2-113
2-141 Impedance Matching Factor of a Thin Slot Antenna ( $h/a=10^6$ ) Based on $Z_o=530$ ohms		2-114
2-142 Impedance Matching Factor of a Slot Antenna ( $h/a=20$ ) Based on $Z_o=530$ ohms		2-114
2-143 Impedance Matching Factor of a Folded Dipole with Thin Elements ( $h/a=10^6$ )(based on $Z_o=300$ ohms)		2-116
2-144 Impedance Matching Factor of a Folded Dipole with Fat Elements ( $h/a=20$ )(based on $Z_o=300$ ohms)		2-116
2-145 Impedance Matching Factor of First Resonance of Folded Dipole with Fat Elements ( $h/a=2$ )(based on $R_o=30$ ohms)		2-118
2-146 Impedance Matching Factor of a Folded Dipole in King [10], (based on measured data)		2-118
2-147 Impedance Matching Factor of a Folded Dipole Constructed of 300-ohm Twin-lead (based on measured data)		2-120

**List of Illustrations**  
**(Continued)**

<u>Figure</u>		<u>Page</u>
2-148	Impedance Matching Factor of a Log-periodic Antenna (from measured data)	2-122
2-149	Impedance Matching Factor of a Log-spiral Antenna (from measured data)	2-122
2-150	Impedance Matching Factor of a Rectangular Horn (from measured data)	2-126
2-151	Examples of Model Envelope Around Dipole Radiation Patterns	2-130
2-152	Geometry for Determining Radius of Envelope Circle	2-132
2-153	Radiation Pattern Function of Center-fed Dipole	2-135
2-154	Circular Envelope Curves of Pattern Model	2-137
2-155	Relationship Between $n_o$ for Model Circle Envelope Function and Electrical Length of Dipole = $n$ Half-wavelengths	2-138
2-156	Dipole Radiation Patterns Illustrating Model Envelope (Drawn on Linear Scale)	2-141
2-157	Dipole Radiation Patterns Illustrating Model Envelope (Drawn on Linear Scale)	2-143
2-158	Examples of Pattern Degradation Due to Fattening of Dipole Elements	2-152
2-159	Existing IEMCAP Model for Antenna Pattern	2-154
2-158	Proposed In-band Model for Pattern	2-154
2-161	Three-dimensional Illustration of Conic Gain Model of Antenna Pattern	2-156
2-162	General Three-Level Directive Gain Profile of Proposed Model	2-158
2-163	General Three-level Directive-gain Profile in Which Backlobe Gain Exceeds Sidelobe Gain	2-160
2-164	Spherical Trigonometric angles associated with Beam Pattern Model	2-161
2-165	Modeling Antenna Patterns of an Array of $n$ Isotropic Elements	2-164
2-165	Modeling Antenna Patterns of an Array of $n \cos\theta$ Elements	2-165
2-167	Three-dimensional Illustration of Directive Gain Model for a Linear Beam Antenna	2-168
2-168	Transition with Frequency of Pattern Model from Design Band to First Breakpoint	2-172

List of Illustrations  
(Continued)

<u>Figure</u>		
2-169 Example of Antenna Power Dissipation Factor for 1 MHz Antenna	2-186	
2-170 Attenuation rates of General-purpose Transmission Lines	2-187	
2-171 Attenuation Curves for Various Modes in a Typical Rectangular Waveguide	2-189	
3-1 General Receptor Model	3-2	
3-2 Measurement of energy Spectrum	3-5	
3-3 Rectangular Pulse Train (RECTPL)	3-18	
3-4 Mini-System B2 Input Deck	3-19	
3-5 Rectangular	3-20	
3-6 Plot of IEMCAP and Model $P_{BB}$	3-22	
3-7 Plot of $i_e(n)$ , IEMCAP Model, $ i_e $ and MIL-STD-461A Signal Port Spectra	3-24	
3-8 Normalized $i_e(n)$ , IEMCAP, $ i_e $ and MIL-STD-461 Signal Port Spectra	3-26	
4-1 Model of Weakly Nonlinear Circuit Used by the Nonlinear Transfer Function Approach	4-7	
4-2 Phasor Diagram of Response at Frequency $f_1$	4-14	
4-3 Phasor Diagram of 3rd Order Desensitization	3-17	
4-4 Limits for CS04	4-20	
4-5 Effect of Phase on Desensitization	4-22	
4-6 Voltage Gain Curves Illustrating (2) Compression and (b) Both Gain Expansion and Gain Compression	4-25	
4-7 Pulse Modulation of an AM Signal	4-44	
4-8 Pulse Modulation of AM Receivers	4-51	
4-9 3 Stage Superheterodyne Receiver	4-53	
4-10 Amplitude Needed to Generate Response Vs. Response Frequency	4-56	
5-1 Radar Rectangular Pulse	5-6	
5-2 RF EMTR Port Spectra	5-10	
5-3 Case Port Spectra	5-12	
5-4 RF RCPT Port Spectra	5-13	
6-1 IEMCAP Functional Flow	6-2	
6-2 IDIPR Section of IEMCAP Top Level Functional Flow	6-6	
6-3 TART Section of IEMCAP Top Level Functional Flow	6-9	

List of Tables

<u>Table</u>		
2-1      Calculated Quantities of Dipole Resonance Peaks	2-46	
2-2      Normalized Resonant Frequencies and Bandwidths	2-60	
2-3      Bandwidth Spread	2-64	
2-4      Two-Element Matching Networks for Antennas	2-80	
2-5      Reactance Values of Matching Network Elements at Resonance	2-88	
2-6      Electrical Length of Transmission Line Stub Elements Required for Matching Cylindrical Dipole Antennas to 50 ohms	2-93	
2-7      Breakpoint Parameter Table for Yagi Uda Antenna Model	2-170	
2-8      Frequency Transition Table for Yagi-Uda Antenna Model	2-173	
2-9      Model Parameters for Radar Antenna Patterns	2-179	
3-1      Definition of Variables	3-3	
3-2      Comparison of Peak Current Calculations	3-27	
3-3      Bandwidth Factor	3-28	
4-1      First and Second-Order Nonlinear Responses	4-11	
4-2      Default Models for CW Desensitization (No AGC)	4-19	
4-3      Third Order Intermodulation Equations	4-31	
4-4      Second Order Intermodulation Equations	4-34	
4-5      Fifth Order Intermodulation Equations	4-36	
4-6      Third Order, Three Signal Intermodulation Equations	4-38	
4-7      Intermod Default Models	4-41	
4-8      Structurally Generated Intermodulation Output Frequencies	4-42	
4-9      Summary of Equations for Cross Modulation	4-47	
4-10     Default Models for Spurious Responses	4-58	
5-1      Number of Model Frequencies	5-5	

## 1.0 INTRODUCTION

The Intrasystem Electromagnetic Compatibility Analysis Program (IEMCAP) is a systems level, computerized analysis program which may be used in analyzing electromagnetic compatibility (EMC) for aircraft, spacecraft or ground stations on both present and future systems. The IEMCAP improvement contract is sponsored by the Compatibility Branch (RADC/RBCT), Rome Air Development Center, Griffiss Air Force Base, New York, under contract number F30602-79-C-0169. The objective of this effort was to increase the prediction capability of the IEMCAP. The defined tasks to obtain the new capability are the following:

- (1) development of a frequency dependent power gain antenna model for IEMCAP;
- (2) modify IEMCAP to predict the electromagnetic (EM) interference for those devices whose compatibility is not related to average power;
- (3) implement within IEMCAP a mathematical model(s) to predict the degradation to receptors of EM energy, caused by spurious signal products generated at an emitter, a structural nonlinearity (i.e., in the transmission path), or in a victim receptor (i.e., signal harmonics, intermodulation, cross modulation, desensitization, gain compression/expansion and spurious responses); and
- (4) modification of the modeling procedure for a port's emission and/or susceptibility.

Upon completion of the above modeling effort, the developed models were to be coded and interfaced with the existing IEMCAP.

Performance of modern weapons systems is dependent upon the compatible functioning of electrical and electronic subsystems. A typical system includes numerous such subsystems with their associated interconnecting wires and, often, with large numbers of antennas for transmission and reception of required signals. The power and information signals occupy a wide range of the electromagnetic spectrum, resulting in the need for carefully designed control measures to confine them within the spatial, spectral, and temporal limits

necessary to avoid disruptive interference. Electromagnetic Compatibility (EMC) assurance is thus an integral and crucial part of subsystem and system design engineering. Computerized EMC analysis, as provided by the RADC Intra-system Electromagnetic Compatibility Program (IEMCAP) is a needed tool for establishing and maintaining cost-effective interference control throughout the lifetime of a weapon system.

IEMCAP is a link between equipment and subsystem EMC performance and total-system EMC characteristics. It provides the means for tailoring EMC requirements to the specific system, whether it be ground based, airborne, or a space/missile system. This is accomplished in IEMCAP by detailed modeling of the system elements and the various mechanisms of electromagnetic transfer to perform the following tasks:

- Provide a data base which can be continually maintained and updated to follow system design changes.
- Generate EMC specification limits tailored to the specific system.
- Evaluate the impact of granting waivers to the tailored specifications.
- Survey a system for incompatibilities.
- Assess the effect of design changes on system EMC.
- Provide comparative analysis results on which to base EMC tradeoff decisions.

The RADC model is an environmental model in that it is designed to predict interference in a population of receptors due to a population of emitters. The basic medium for modeling signals is the frequency domain.

IEMCAP incorporates state-of-the-art communications and EMC analysis math models into a routine which efficiently evaluates the spectra and the transfer modes of electromagnetic energy between generators and receptors within the system.

IEMCAP's combined capabilities provide a versatile framework which facilitates modification as the state-of-the-art progresses. This provides a flexibility in updating the program as new or improved mathematical models are developed, and it provides a program which may be easily

applied to a wide variety of EMC analysis and design problems by utilization of only the necessary modules for the specific problem.

The program is designed for use by an EMC systems engineer with a minimum of computer experience. The input data requirements, program control, and output formats are easily learned and engineering oriented. The input data is directly obtainable from system and subsystem operational specifications or measured data. For ease of use, all data input to IEMCAP is in free-field format. The entries may be placed anywhere on the punched cards.

The overall philosophy and basic analysis approach that had been designed into the IEMCAP was maintained in the improved modeling development effort on this contract. Each of the improved models and the associated impact on the IEMCAP is discussed below.

In the original IEMCAP, antennas were assumed to be frequency independent. Antenna gains were determined by preprogrammed equations for low-gain types and medium and high gain were represented by multilevel patterns, in which each level is specified by a gain and associated azimuth and elevation beamwidths. Provision was made for three discrete gain levels, which was assumed to be sufficient for representing most antennas. The development of the proposed antenna model (Task 1) on this effort was based largely on the results of theoretical antenna modeling. In many cases a heuristic approach had been applied based on the personal experience of the designer. There was a noticeable lack of empirical antenna data available, and a theoretical analysis would have been formidable. Further, antenna theory is generally based on ideal assumptions which lead to uncertain limitations in the results and must also be validated with measured data.

The problem of antenna modeling reduces to a tradeoff between generality and accuracy. The more general a model becomes, the less accurate it will tend to be in representing a wide variety of antennas. A specific antenna may be modeled reasonably accurately if empirical data describing all antenna characteristics to be modeled exist. If a model attempts to represent all antennas of a given type, there can easily be found samples of that class which do not agree with the model.

Because of the wide degree of variations in the design and construction of commercially available antennas of a given type or class, the assessment of a general model for the type must be made in a statistical sense. The accuracy of an antenna gain model will have a distribution which has, hopefully, an acceptably low variance. Since the models are used for EMC analyses, the mean values of gains should be adjusted toward the high side in order to provide worst-case or some degree of safety in the predictions. This arbitrary shift of the mean will increase the variance of the model error.

In consideration of the fact that the proposed antenna models have not been validated, it was recommended that the models not be implemented within IEMCAP. It was recommended that the proposed models be coded into a stand-alone computer program which can be exercised in a validation study using measurements of actual antennas. In some cases, the validation will result in adjustments of model parameters, while in other cases, the measurements may result in the need for redesign of certain models. Following some period of validation and refinement in which the models demonstrate an acceptable degree of accuracy, the entire model package can be implemented within IEMCAP by replacing subroutine GAIN.

The system model for IEMCAP employs the standard EMC approach of identifying all ports in the system having potential for undesired signal coupling. These ports are divided into arrays of emitter ports and of receptor ports having identifiable coupling paths.

All emitters in a system are characterized by emission spectra and all receptors are characterized by susceptibility spectra. All ports and coupling media are assumed to have linear characteristics. Emissions from the various emitter ports are assumed to be statistically independent so that

signals from several emitters impinging at a receptor port combine on an RMS or average power basis. Other waveform parameters that receptors may be sensitive to are total energy, peak current (or voltage) and rise time. For example, certain explosive devices are triggered by the burning away of a wire (resistive heating). This is a total energy susceptibility. Also many digital devices are susceptible to instantaneous waveform level ("peak" sensitivity). EMI margins for each of the above has been developed for the IEMCAP.

Each EMI margin for a particular waveform parameter is defined as the ratio of parameter value induced at the detector input to the interference threshold level for this parameter at the detector input. However, in all cases this computation is transferred to the receptor input port where actual measurements are more readily obtained.

An EMI margin of value greater than unity indicates interference. A value less than unity indicates either compatibility or interference. A minimization of the uncertainty, although the uncertainty is in accordance with the "worst case" philosophy of IEMCAP, has been considered in the choices of the margins actually included in IEMCAP.

A number of important system level EMI problems result from non-linear effects in emitters and receptors. At the present time, however, the IEMCAP considers only interference caused by power transferred linearly from emitter to receptor. To accurately predict all instances of possible EMI, it was necessary to expand IEMCAP to include interference due to the following nonlinear effects, which are recognized to cause system performance degradation:

- 1) Receiver Intermodulation
- 2) Spurious Responses
- 3) Cross Modulation
- 4) Desensitization
- 5) Gain Compression and Gain Expansion

This report documents the models developed to describe the effects enumerated above.

Several important aspects associated with representing a port's spectra were modified in the IEMCAP. IEMCAP is required to analyze a large number of ports with reasonable run times and reasonable computer core memory requirements. At the same time, it must quickly evaluate the coupling from any type of emitter port into any type of receptor port and use this result to perform the variety of tasks discussed above and be adaptable to future tasks. For specification generation, the spectra must be easily adjustable at the frequencies where incompatibilities are found as well as allow efficient incorporation of the adjustments for further adjustment. For trade-off and waiver analyses, the spectra and interference of modified ports must be efficiently compared to those from previous runs. Also, the spectra are stored on files and thus becomes readily available for future analyses.

Based on the above criteria, the IEMCAP was designed to use a sampled spectrum technique in which each spectrum amplitude is sampled at various frequencies across the range of interest. The new port spectra algorithm replacing the current "quantization" method in IEMCAP for modeling a port's spectra incorporates the following:

- 1) Generate Equipment Frequency Table
- 2) User Specified Frequency Range for Analysis  
(0 to 50 GHz and greater)
- 3) User defined port spectra of up to 90 frequency - amplitude points for required and/or nonrequired frequency ranges
- 4) Generate frequencies and amplitudes for prestored emitter and receptor models required by User's inputs currently required by IEMCAP
- 5) Generate frequencies and amplitudes for harmonic signals as directed by User inputs currently required by IEMCAP
- 6) Generate frequencies and amplitudes for any port's non-required spectra using prestored MIL-STDS (461A, 6181D and 704) and the corresponding system displacement factors.

Basically, the above criteria for the new port spectra model reduces to a requirement for generating all frequencies and corresponding amplitudes for defining the port spectra of an equipment. The generation of the equipment frequency table is accomplished by determining the required frequencies from prestored models, harmonics, nonrequired frequencies from appropriate MIL-STDS and user specified frequencies from IEMCAP input data. The port spectra amplitudes are computed from prestored emitter and receptor models, harmonics, user specified data and prestored military standards models.

It was recognized very early in the project that modification of a considerable portion of IEMCAP would be required. Since the modification of IEMCAP was so extensive, detailed flow diagrams were needed for interfacing the new models. No detailed flow diagrams existed for the IEMCAP and so considerable time and effort was devoted to developing the detailed flows before interfacing the new models could be accomplished.

To interface the new models it was recognized and agreed that the order of priority for programming the new models should be 1) new port spectra model (Task 4), 2) nonlinear effects models (Task 3), 3) nonaverage power receptor models (Task 2) and 4) new antenna models (Task 1). As a result of the new user SPECT option associated with the new port spectra modeling, it was determined that a significant change was required in the narrowband integrated margin method used by IEMCAP. The integrated EMI margin is an overall figure of merit representing the ratio of the power received by the receptor to susceptibility over the entire frequency range. The program as originally designed computes the margin per bandwidth at all spectrum sample frequencies (both emitter and receptor).

For narrowband emissions, the power received is independent of the receptor bandwidth, and the integral becomes a summation. For the case where a user specifies his narrowband spectra, the program performs the appropriate summation. If the narrowband spectra are represented by prestored models, then the narrowband components are computed as originally designed. A significant effort was devoted to determining a technique that would be the most beneficial to the IEMCAP user so as not to compromise his data. An appropriate modification to the existing IEMCAP narrowband integrated margin model was made. The implementation of the modification to the narrowband integrated margin calculation involved modifying several existing subroutines in IEMCAP.

A requirement on this effort was to minimize as much as possible the amount of increase in computer main memory required to run IEMCAP. The interfacing of the new models did in fact have an increasing effect on the main memory requirements. Considerable effort was devoted to this requirement and to offset the increased main memory requirement, it was agreed that the wire map portion of the data processing program (IDIPR) should be removed and established as an independent program. Making the wire map function a separate program accomplished 1) a reduction in the computer main memory storage requirements and 2) provides a user more flexibility in analyzing antenna-to-antenna coupling type problems.

The theoretical basis for each of the four tasks discussed above are separate and distinct but, the integration of these tasks into the existing IEMCAP code were not handled independently. This report provides complete and thorough information on the theory of the model development within each task (separate sections devoted to each task) and the integration of the developed models into the IEMCAP code is presented separately.

Section 2 presents the frequency dependent power gain antenna models for the IEMCAP. The antenna gain model calculates the power gain in dB of a specified type of antenna at a given frequency and arbitrary direction relative to the antenna axis. The model consists of four independent terms which add (in dB) to provide the antenna gain. Section 3 treats the modification of IEMCAP to predict the electromagnetic interference for devices in which the compatibility of the device is dependent upon parameters other than average power. Several models are developed for other waveform parameters that receptors may be sensitive to. These parameters are related to a susceptibility margin. The margins are numbers which indicate the level to which specified unwanted emissions cause unexceptable receptor performance.

Sections 4 and 5 present further modifications to the IEMCAP. Section 4 introduces the development of system level nonlinear models which expands the capabilities of IEMCAP to allow predictions of performance degradation for several nonlinear receptor effects. The models developed to describe nonlinear effects are based on a "modified" Volterra Series which is a hybrid technique combining aspects of both the Power Series and the Volterra

Series. Effects which can not be described by the Volterra approach, due to the nature of the nonlinearities involved, are based on empirical data. Section 5 presents a new model which replaces the current "quantization" method for modeling a port spectra. This new model provides the capability for a user to model the required and nonrequired portions of an emitter and receptor port spectra using the prestored models in IEMCAP.

The interfacing of the above models with the IEMCAP is presented in Section 6. Where applicable the new models where integrated into the existing IEMCAP. The overall philosophy of the IEMCAP has been maintained and emphasis placed on segmenting the program to keep down computer main memory requirements.

## 2.0

## FREQUENCY-DEPENDENT MODELING OF ANTENNA GAIN

It is desired to develop computer algorithms which provide the numerical value of power gain (relative to that of an isotrope) for a specified type of antenna at a specified frequency and spatial direction. The power gain model is intended for use in program IEMCAP, replacing the relatively simple frequency independent model that currently exists.

The words "antenna gain" immediately bring to mind the ideal of a three-dimensional radiation pattern of lobes and nulls describing the spatial radiation levels in azimuth and elevation from the antenna. Antenna theory books abound with antenna patterns that are derived for ideal, lossless antennas. Peak values associated with these patterns are generally relative to a lossless isotropic radiator. While radiation patterns are vitally important, they represent only one of the terms to be considered in the overall power gain model for antennas. In order to provide an absolute level of power gain, the model must account for several types of power losses associated with real antennas which directly subtract dB's from the ideal radiation pattern function for the antenna. In many cases these power losses dominate the performance of an antenna. Unfortunately, antenna textbooks seldom address this aspect.

The allocation of power delivered to an antenna system is diagrammed in Figures 2-1a and 2-1b. A conventional arrangement is assumed here, in which an rf power source delivers power through a transmission line or waveguide to the input terminals of the antenna. Since the antenna may generally have some kind of feed circuitry such as a balun, matching network, filter, multicoupler, etc., which is often an integral part of the antenna, particularly for commercially manufactured antennas, the antenna terminals are assumed here to be the input to the feed circuit/antenna combination. The transmission line or waveguide is generally lossy and reduces antenna power before it reaches the antenna terminals. The second loss of antenna power is the reflection of power back toward the source due to impedance mismatch between the transmission line and the antenna terminals. Power which is absorbed by the antenna may be further degraded by a) ohmic heating losses in the matching network and/or in dielectric materials associated with the antenna and by b) the effects of capacitive shunting between conductors and between conductors and ground in the base feed circuits, particularly at frequencies considerably higher than the design band frequencies.

The remaining power is that which is radiated into space, and it is this final power level which applies to the radiation pattern function for the antenna.

Consequently, the overall power gain function, alternately referred to as antenna gain, consists of four terms. The first term is the transmission line loss; the second is the impedance mismatch factor; the third is due to internal losses of the antenna, and the fourth term is the radiation pattern which gives the directive gain at specified angles in space.

When these terms are expressed as linear quantities, their product gives the total antenna gain. If expressed logarithmically as dB's their sum provides the total gain value.

For this study each of the terms is considered separately. This report describes the analysis effort and presents the results of the proposed models. The proposed models could be applied to active receiving antennas but require separate consideration of the parameters for the receiving and transmitting modes, since these antennas are non-reciprocal. The nonlinear aspects of active antennas are not considered in this study.

It should be noted that while the approach taken here is based on the behavior of a transmitting antenna, the law of reciprocity ensures that the same gain factors will apply when the antenna functions as a passive receiver.

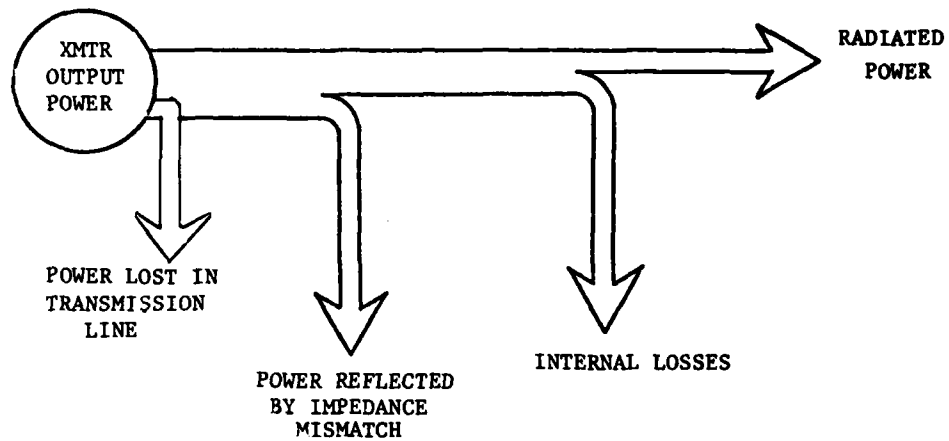


Figure 2-1a Power Losses Associated With Antenna Gain

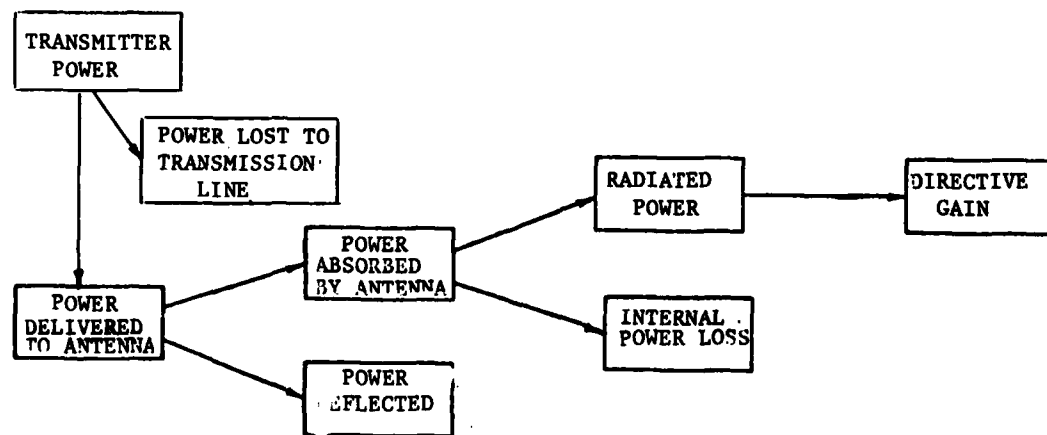


Figure 2-1b Distribution of Power for General Antenna Gain Model

## 2.1

Modeling the Impedance Matching Factor of Antennas

The power delivered to an antenna connected to a lossless transmission line of characteristic impedance  $Z_0$  at frequency  $f$  is determined from the input impedance  $Z_i$  of the antenna. First, the reflection coefficient  $r$  at the antenna terminals is given by

$$r = \frac{Z_i - Z_0}{Z_i + Z_0}$$

Since  $|r|$  represents the fraction of forward voltage or current in the line that is reflected at the antenna terminals due to impedance mismatch,  $|r|^2$  represents the fraction of incident power  $P_i$  reflected by the antenna load. Thus, the fraction of incident power delivered to the load or absorbed by the load (power radiated if the load is a lossless antenna) is

$$\frac{P}{P_i} = 1 - |r|^2$$

This ratio expressed in decibels is termed the impedance matching factor\*  $F_Z$ . That is,

$$F_Z = 10 \log \frac{P}{P_i} \\ = 10 \log(1 - |r|^2).$$

Note that when  $|r| = \frac{1}{\sqrt{2}} = .707$ , then  $\frac{P}{P_i} = \frac{1}{2}$ .

This corresponds to the half-power or -3 dB condition of the load.

The study analysis described here first considers dipole antennas without feed circuitry, and this is followed with analyses of the effects of matching networks on the power transfer characteristics of the dipoles over a wide range of frequencies. Finally, the impedance matching factors for other types of antennas are considered.

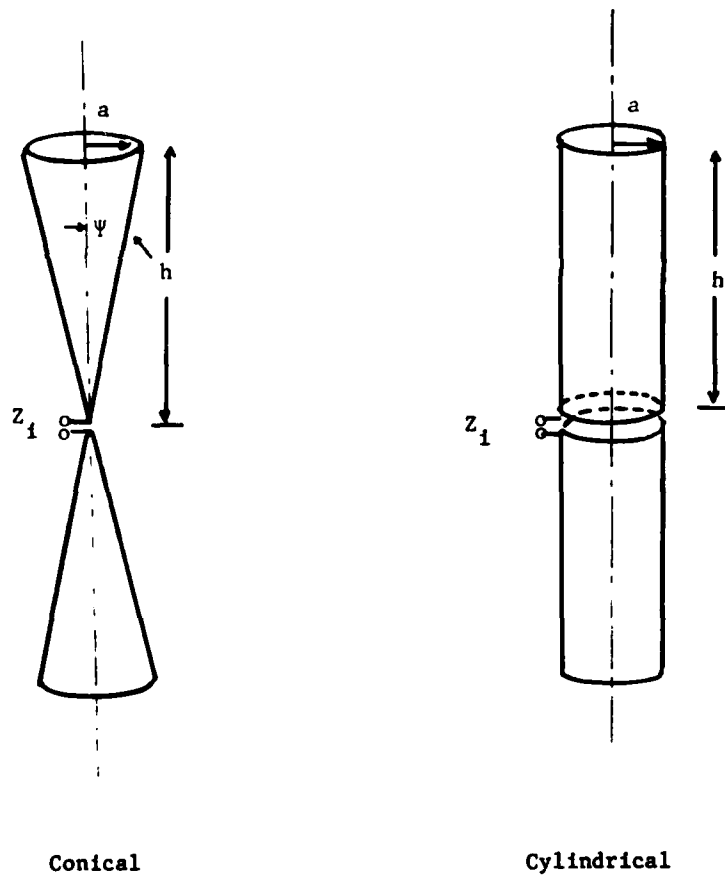
---

\* Since  $P \leq P_i$ , then  $F_Z \leq 0$ . Thus, the impedance matching factor as defined here is always a negative quantity.

## 2.2

Power Transfer Characteristics of a Dipole Without Feed Circuitry

Curves of the impedance matching factor for ideal dipoles over a wide range of frequencies have been computed using the analytical approximation developed by Schelkunoff [1a, Chap. X to 1b, pages 421-432] for the input impedance of ideal, lossless dipole antennas. Both the biconical and cylindrical dipoles, illustrated in Figure 2-2, were studied.



Conical

Cylindrical

Figure 2-2 Conical and Cylindrical Antenna Shapes

According to Schelkunoff's mode theory for dipole antennas, the input impedance  $Z_i$  is given by [1a, pages 453, 460, 461].

$$Z_i = K_a \frac{R_a \operatorname{sinh} + j[X_a - N] \operatorname{sinh} - (K_a - M) \operatorname{cosh}}{[(K_a + M) \operatorname{sinh} + (X_a + N) \operatorname{cosh}] - jR_a \operatorname{cosh}}$$

where  $R_a = 60(\gamma + \ln 2kh - Ci2kh)$   
 $+30(\gamma + \ln kh - 2Ci2kh + Ci4kh) \cos 2kh$   
 $+30(Si4kh - 2Si2kh) \sin 2kh$

$$X_a = 60Si2kh - 30(\gamma + \ln kh - Ci4kh) \sin 2kh$$
  
 $- 30Si4kh \cos 2kh$

$$Si x = \int_0^x \frac{\sin u}{u} du \quad (\text{sine integral})$$

$$Ci x = \int_{\infty}^x \frac{\cos u}{u} du \quad (\text{cosine integral})$$

Note:  $Cin x = \gamma + \ln x - Ci x = \int_0^x \frac{1 - \cos u}{u} du$

$$\gamma = 0.5772... \quad (\text{Euler's constant})$$

$$k = \frac{2\pi}{\lambda}$$

For the conical dipole:

$$K_a = 120 \ln \frac{2h}{a}$$

$$M = 0$$

$$N = 0$$

For the cylindrical dipole:

$$K_a = 120 (\ln \frac{2h}{a} - 1)$$

$$M = 60(\ln 2kh - Ci2kh + \gamma - 1 + \cos 2kh)$$

$$N = 60(Si 2kh - \sin 2kh)$$

The apparent limitations of the above expressions are that a) the conical angle is small such that  $\tan \psi \approx \psi = \frac{a}{h}$  [1a, pages 446, 454], and b) the length  $h \leq .75\lambda$  [1b, page 426].

The above expression for  $Z_1$  was evaluated in a minicomputer for conical and cylindrical dipoles of various  $h/a$  ratios over a frequency range corresponding to electrical lengths from  $h=0$  to  $h = 3.3\lambda$ . The resulting curves of  $F_Z$  based on  $Z_0 = 50$  ohms are presented in Figures 2-3 through 2-12 for the conical dipole, and Figures 2-13 through 2-19 for the cylindrical dipole. Also obtained from this study were plots of the complex input impedance or Smith Chart coordinates for the same dipole conditions. The concial case is shown in Figures 2-20 through 2-29, and the cylindrical case is presented in Figures 2-30 through 2-39.

For the Smith Chart plots, the horizontal line represents the real impedance axis with zero ohms (short circuit) at the left end, and infinite ohms (open circuit) at the right end. At the center is the characteristic impedance of the transmission line which was assumed to be 50 ohms for all calculations. The outer circle represents the reactance axis with inductance along the upper semicircle and capacitance along the lower semicircle. Thus complex inductive impedances plot within the upper semi-circular region and complex capacitive impedances in the lower semicircular region. The Smith Chart is actually a polar plot of complex reflection coefficient. The outer circle represents  $|r|= 1$ , and the center represents  $r = 0$ . The dashed circle represents  $|r|= .707$  or half-power level. Thus, all points within the dashed circle correspond to an impedance mismatch that reflects less than half the incident power, and all points outside indicate reflection of more than half the incident power.

The Smith Chart contours begin at the right edge where the impedance is highly capacitive. The impedance generally spirals inward in a clockwise direction with increasing frequency. All crossings of the contour with the real axis represent points where the impedance is resonant or anti-resonant. All crossings on the left side of the contour spiral are resonances where the impedance is real and relatively low. These points correspond to the resonant peaks in the curves of  $F_Z$ . All crossings on the right side of the contour spiral are antiresonance points where the impedance is real and relatively high. These points correspond to the nulls between the resonant peaks in the curves of  $F_Z$ .

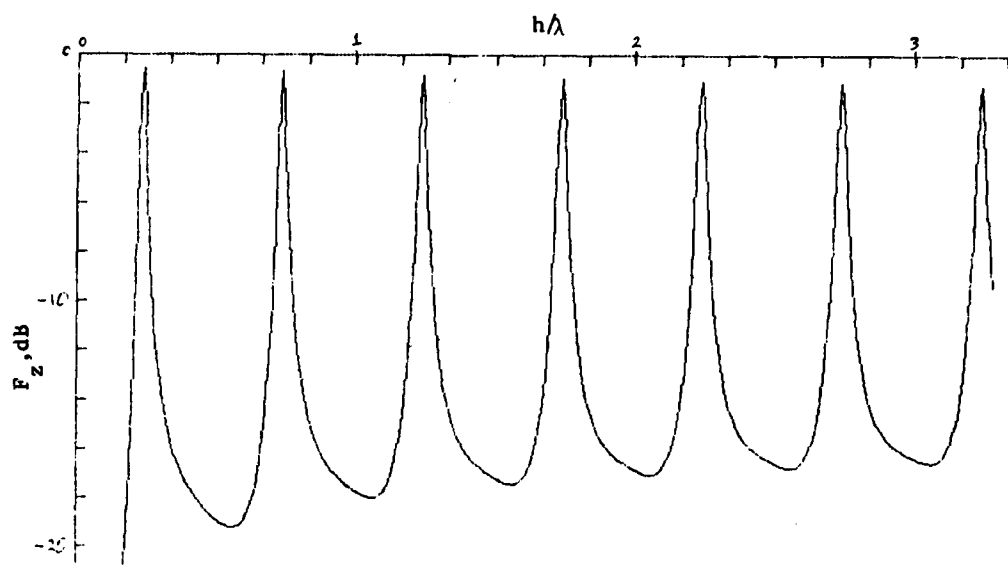


Figure 2-3 Impedance Matching Factor of Ideal Conical Dipole ( $h/a = 10^6$ )

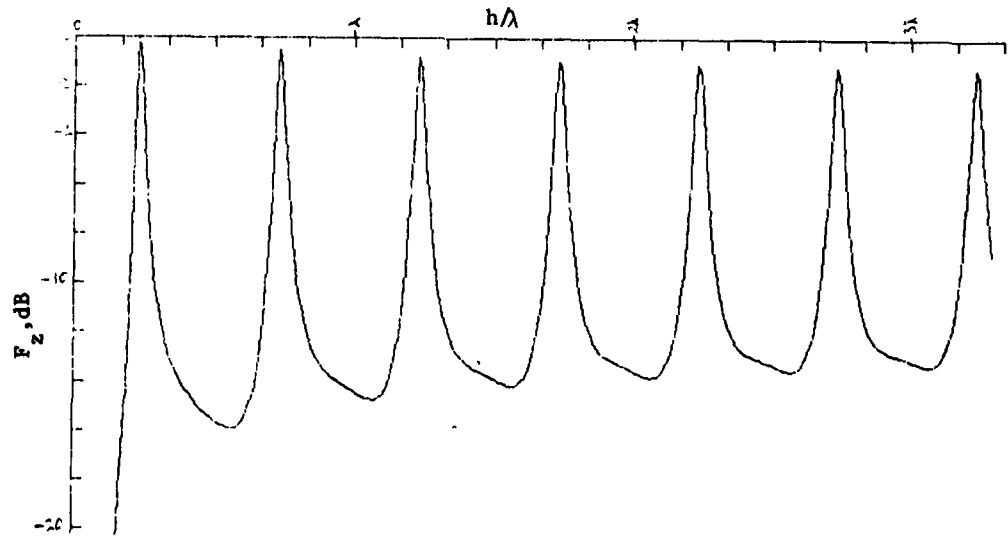


Figure 2-4 Impedance Matching Factor of Ideal Conical Dipole ( $h/a = 10^4$ )

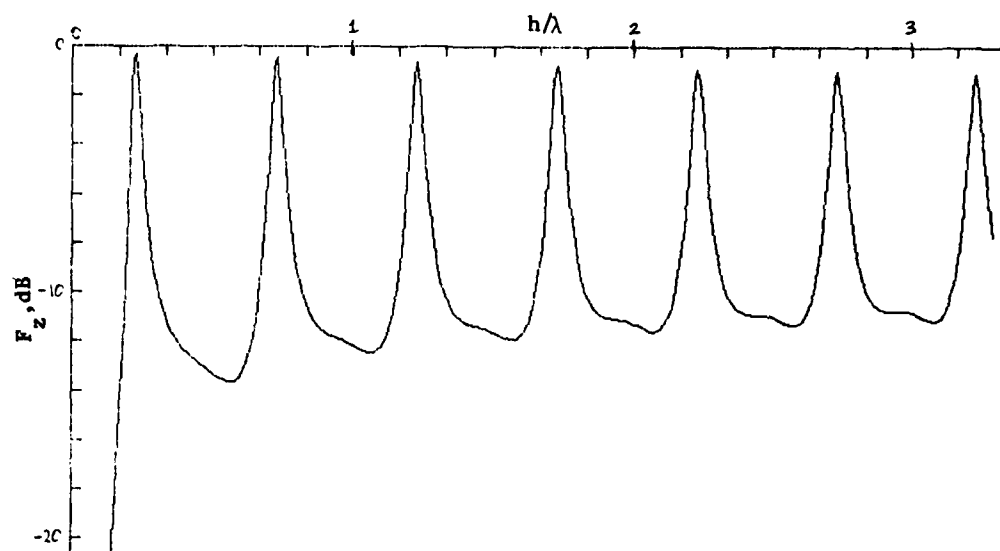


Figure 2-5 Impedance Matching Factor of Ideal Conical Dipole ( $h/a = 1,000$ )

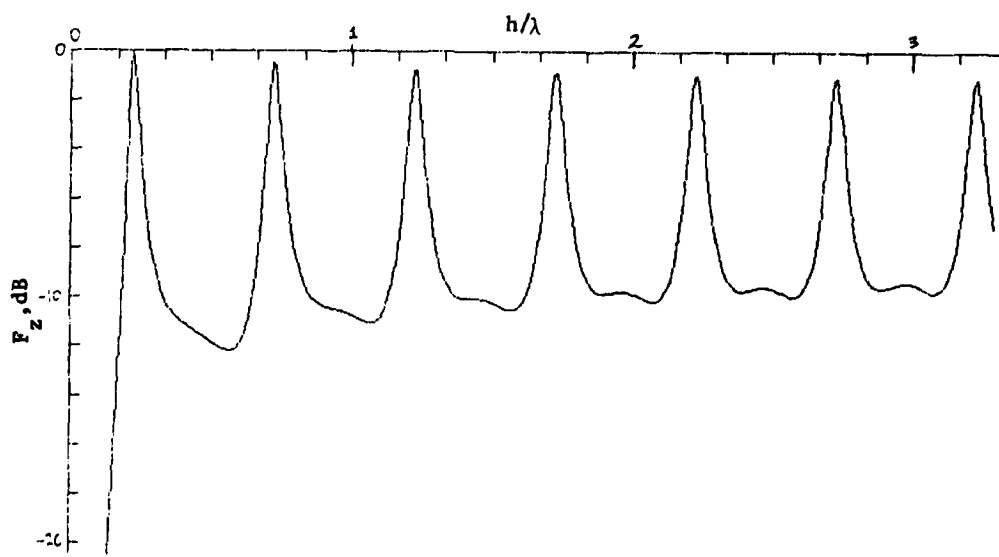


Figure 2-6 Impedance Matching Factor of Ideal Conical Dipole ( $h/a = 300$ )

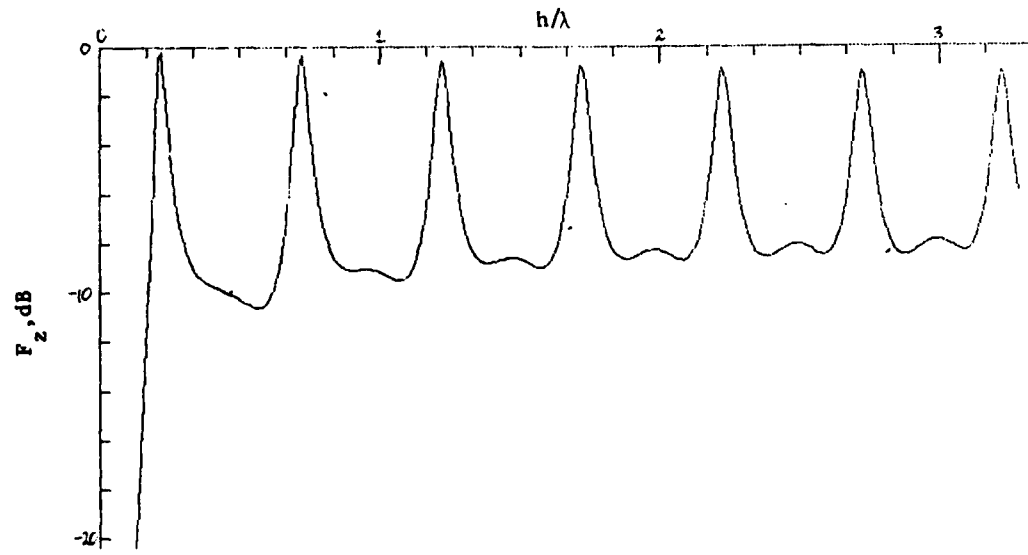


Figure 2-7 Impedance Matching Factor of Ideal Conical Dipole ( $h/a = 100$ )

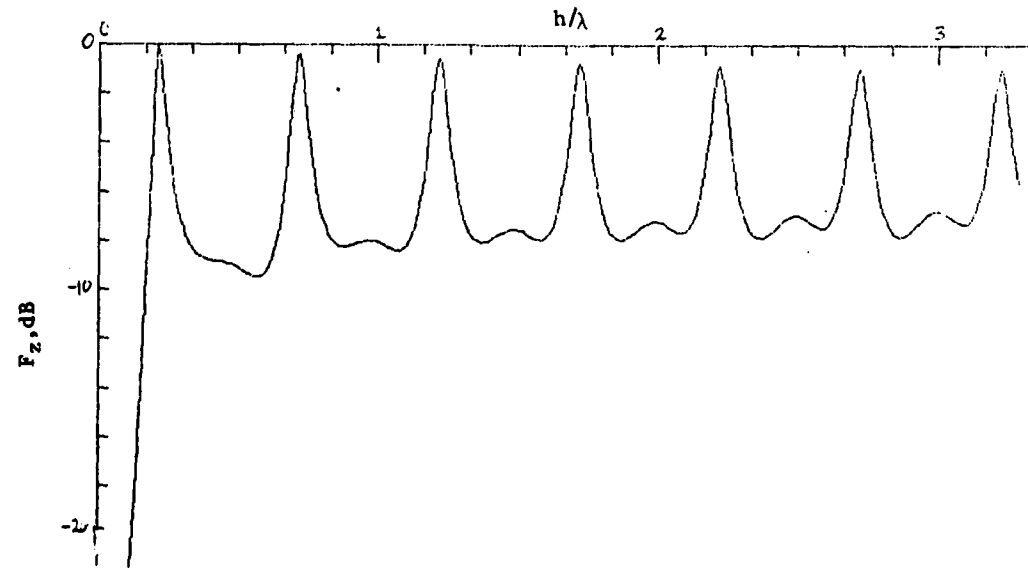


Figure 2-8 Impedance Matching Factor of Ideal Conical Dipole ( $h/a = 50$ )

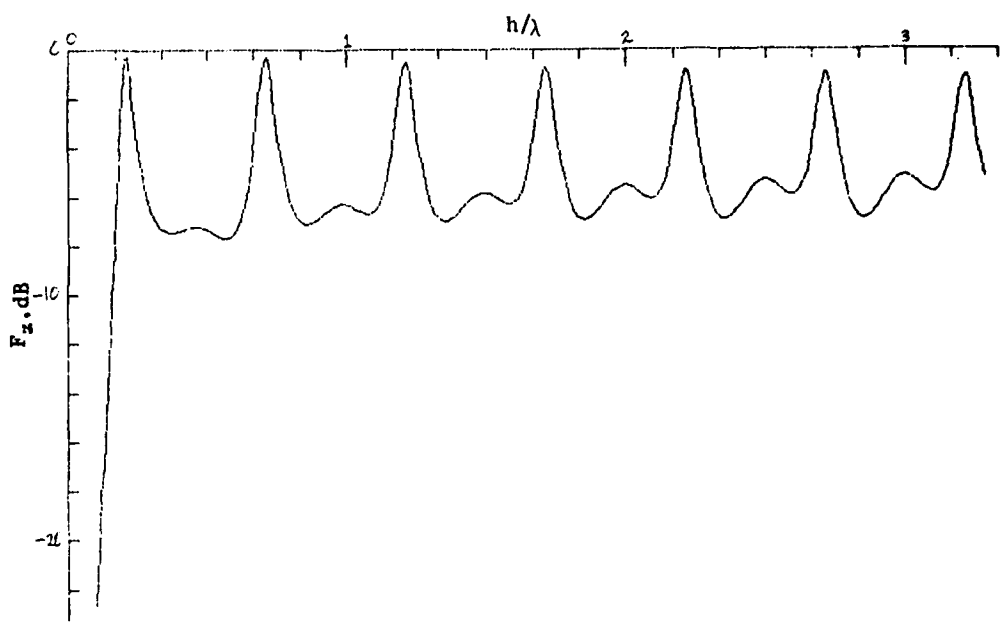


Figure 2-9 Impedance Matching Factor of Ideal Conical Dipole. ( $h/a = 20$ )

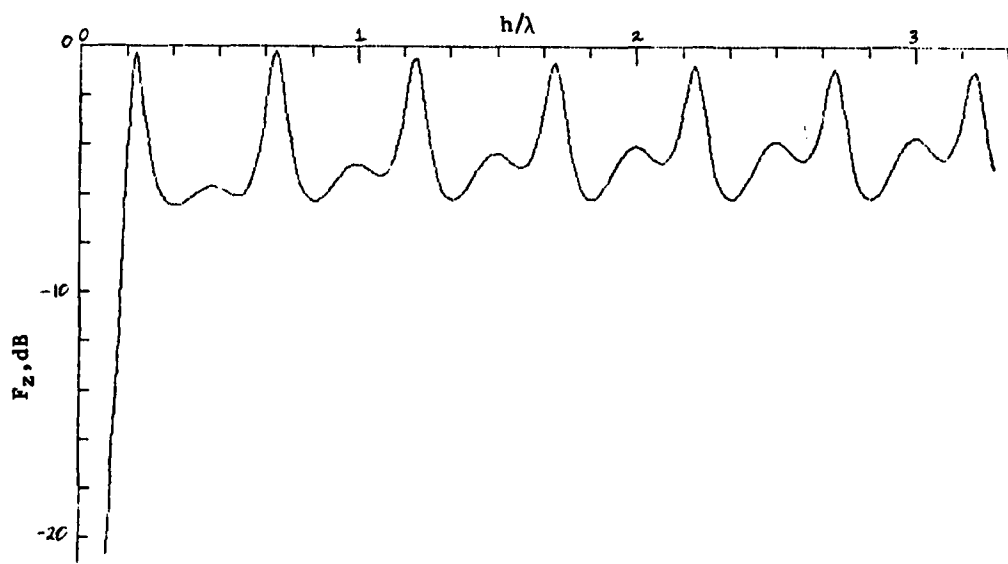


Figure 2-10 Impedance Matching Factor of Ideal Conical Dipole. ( $h/a = 10$ )

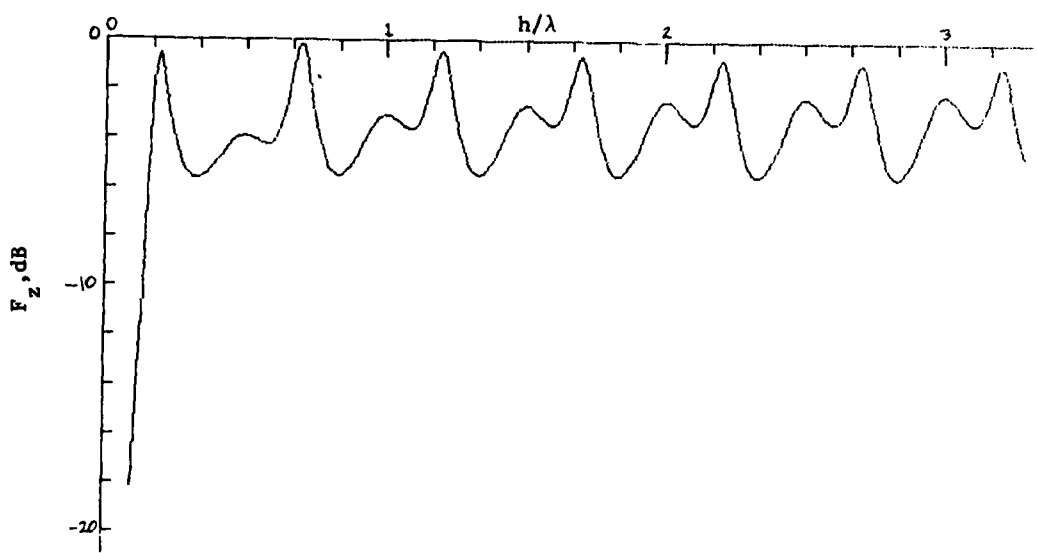


Figure 2-11 Impedance Matching Factor of Ideal Conical Dipole ( $h/a = 5$ )

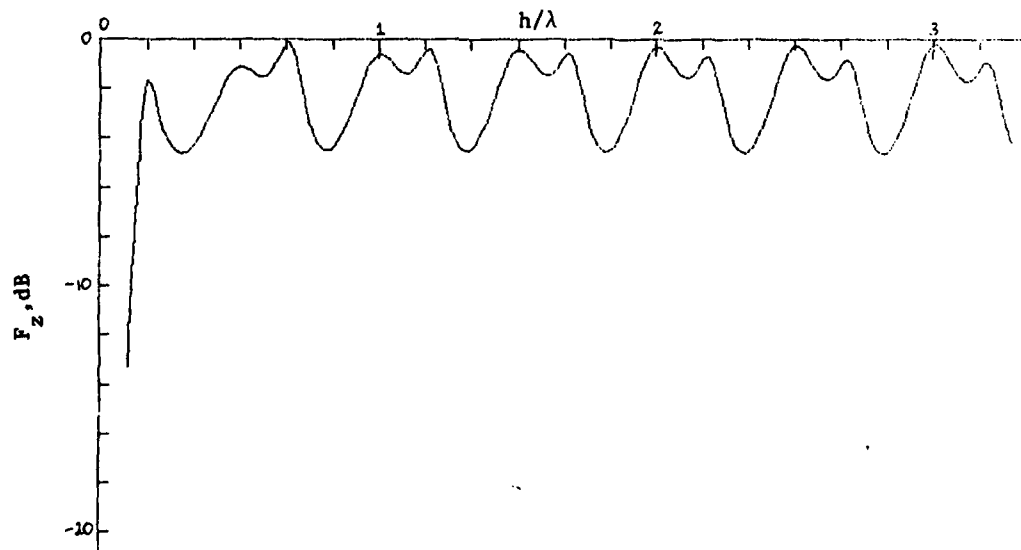


Figure 2-12 Impedance Matching Factor of Ideal Conical Dipole ( $h/a = 2$ )

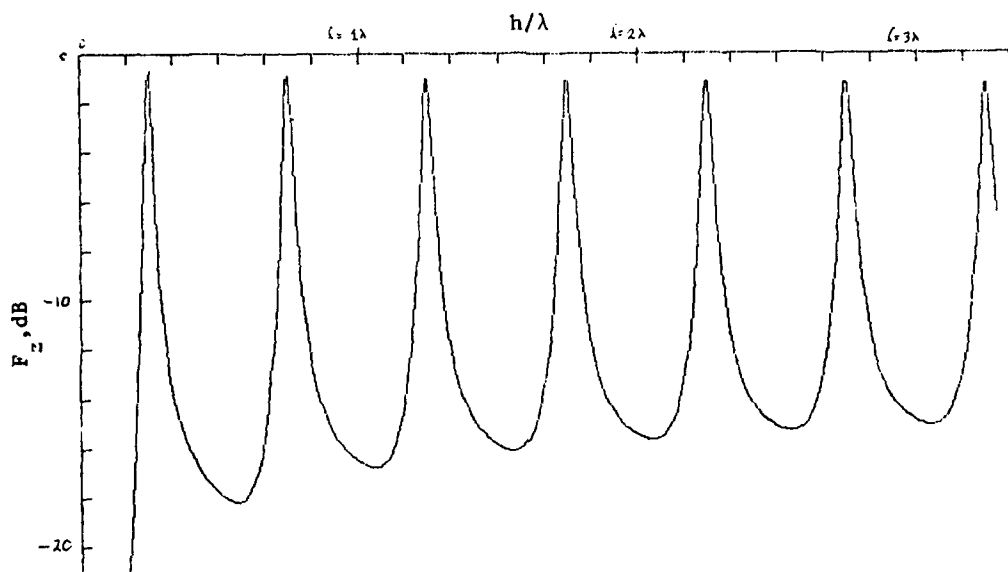


Figure 2-13 Impedance Matching Factor of Ideal Cylindrical Dipole ( $h/a = 10^6$ )

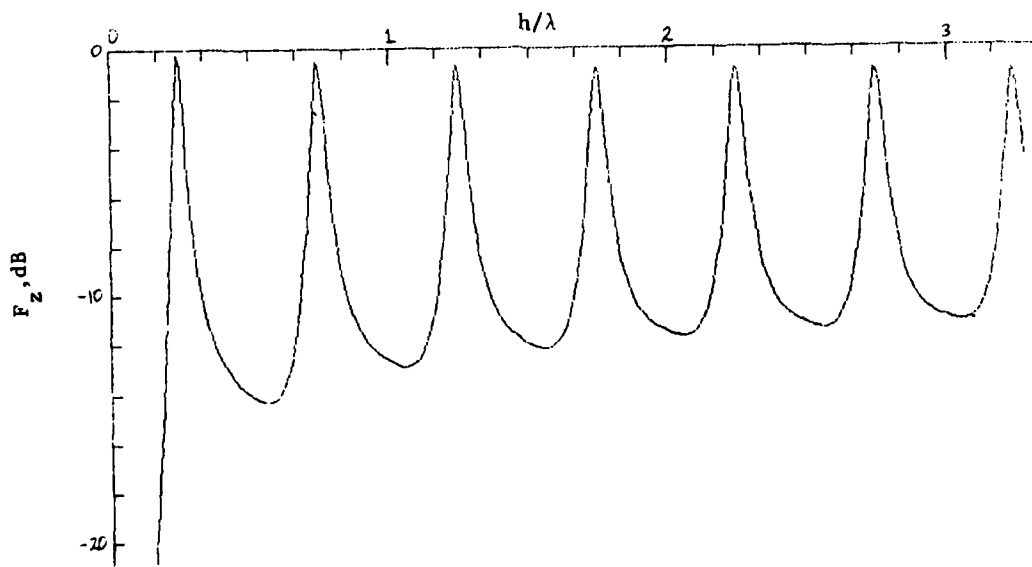


Figure 2-14 Impedance Matching Factor of Ideal Cylindrical Dipole ( $h/a = 10^4$ )

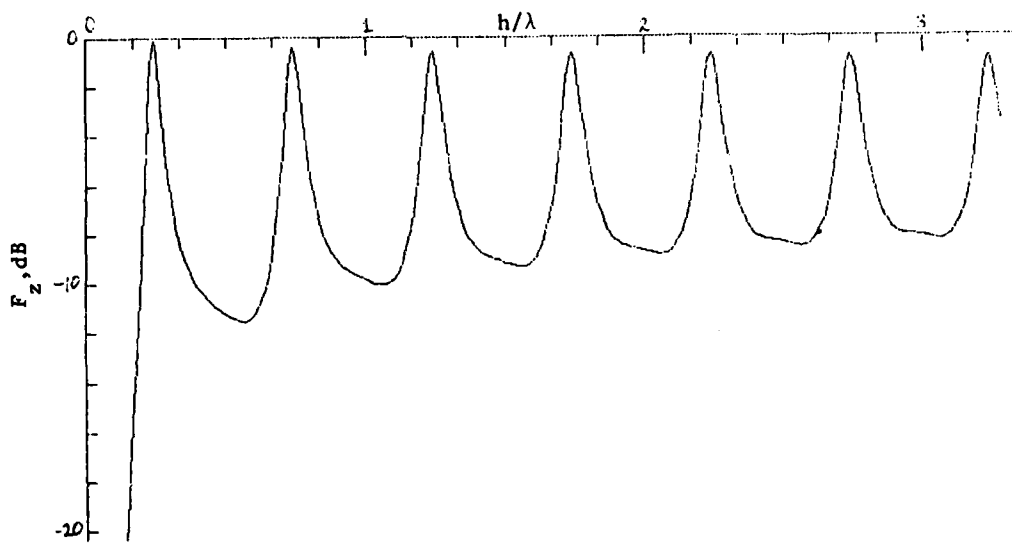


Figure 2-15 Impedance Matching Factor of Ideal Cylindrical Dipole ( $h/a = 1,000$ )

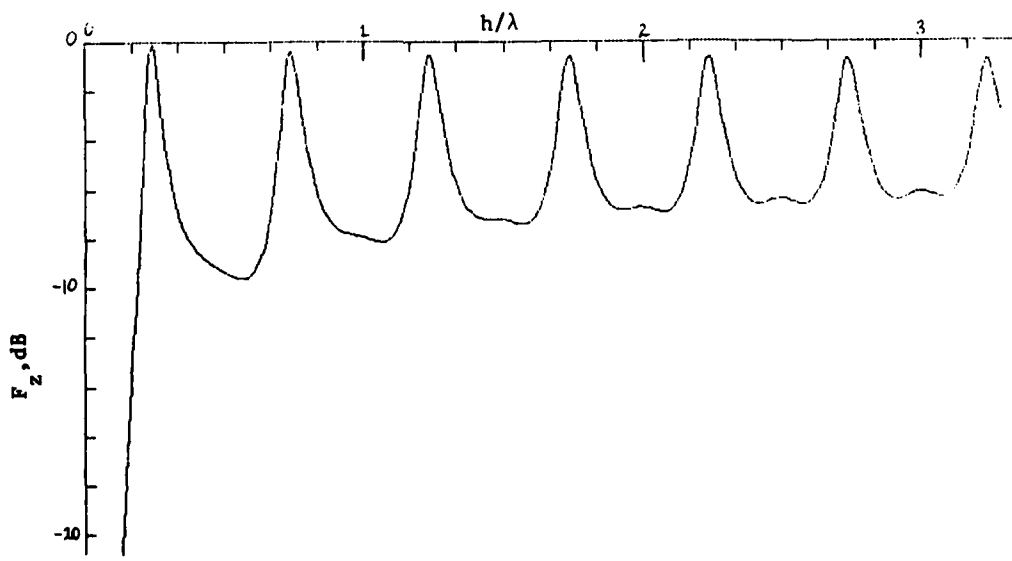


Figure 2-16 Impedance Matching Factor of Ideal Cylindrical Dipole ( $h/a = 300$ )

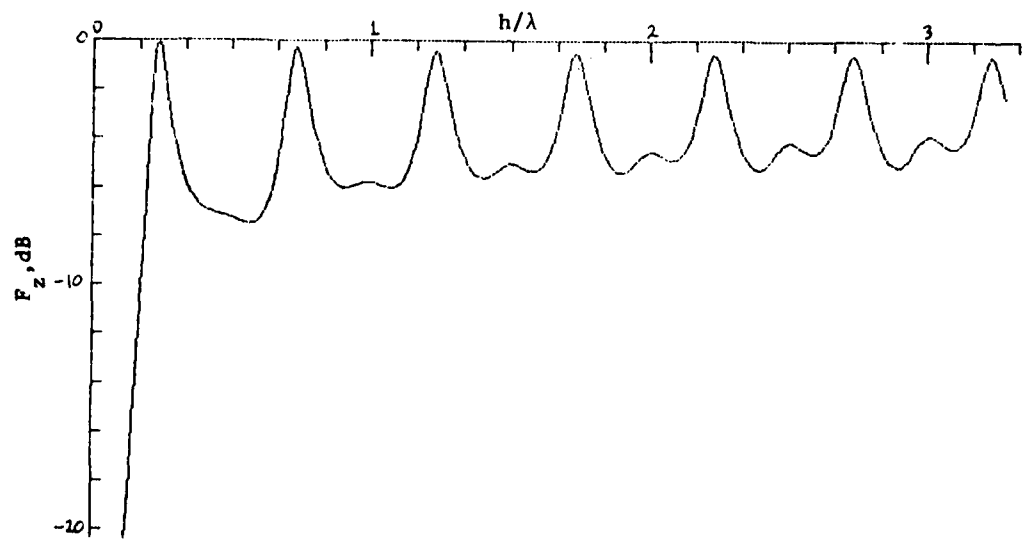


Figure 2-17 Impedance Matching Factor of Ideal Cylindrical Dipole ( $h/a = 100$ )

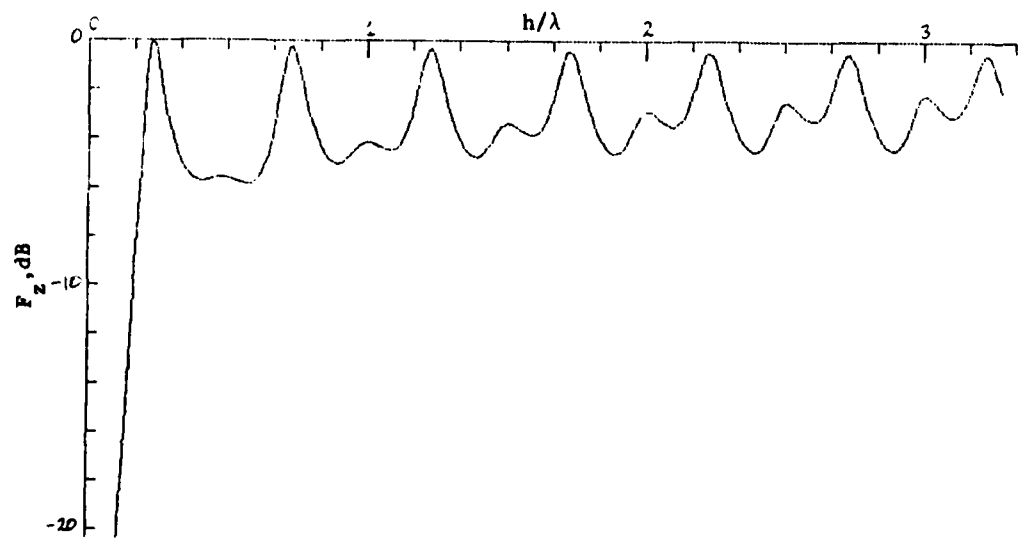


Figure 2-18 Impedance Matching Factor of Ideal Cylindrical Dipole ( $h/a = 50$ )

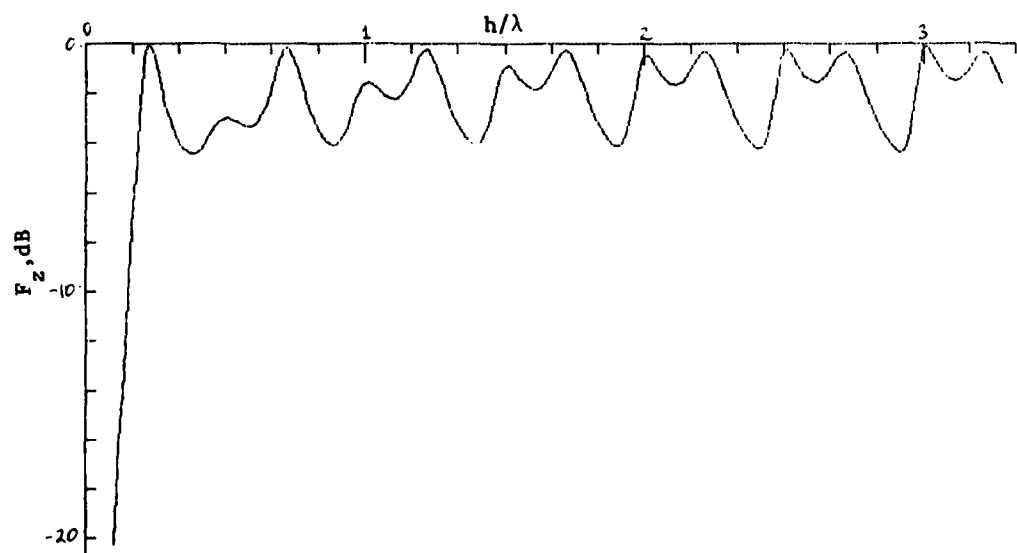


Figure 2-19 Impedance Matching Factor of Ideal Cylindrical Dipole (  $h/a = 20$  )

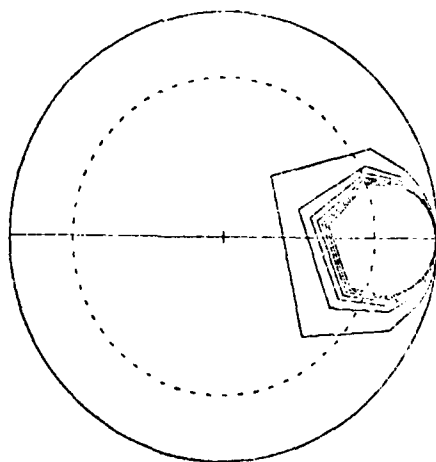


Figure 2-20 Smith Chart of Ideal Conical Dipole (  $h/a = 10^6$  )

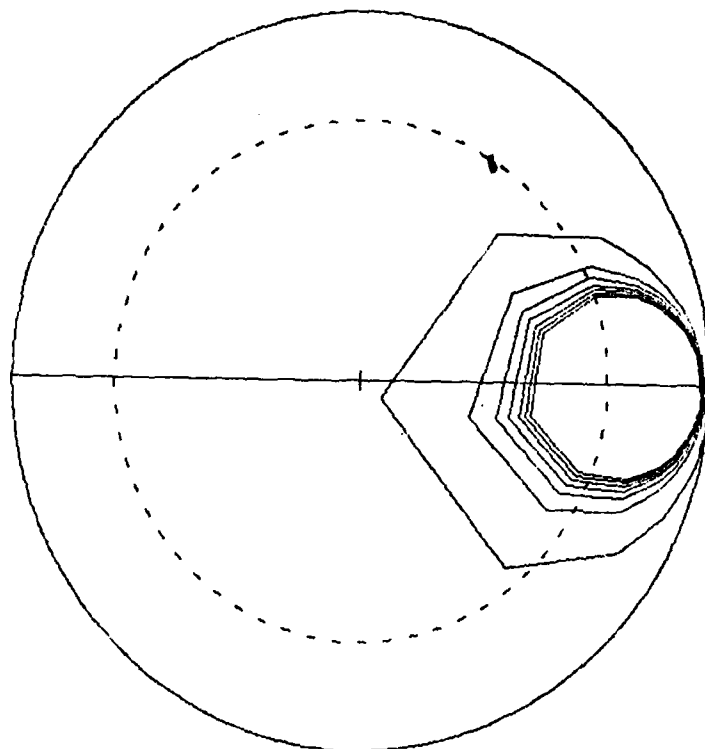


Figure 2-21 Smith Chart of Ideal Conical Dipole ( $h/a = 10^4$ )

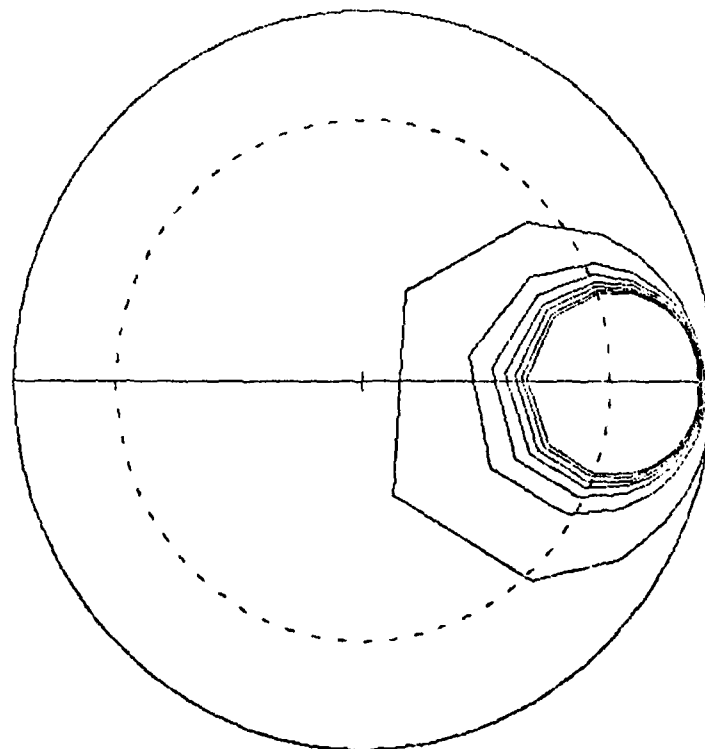


Figure 2-22 Smith Chart of Ideal Conical Dipole ( $h/a = 1,000$ )

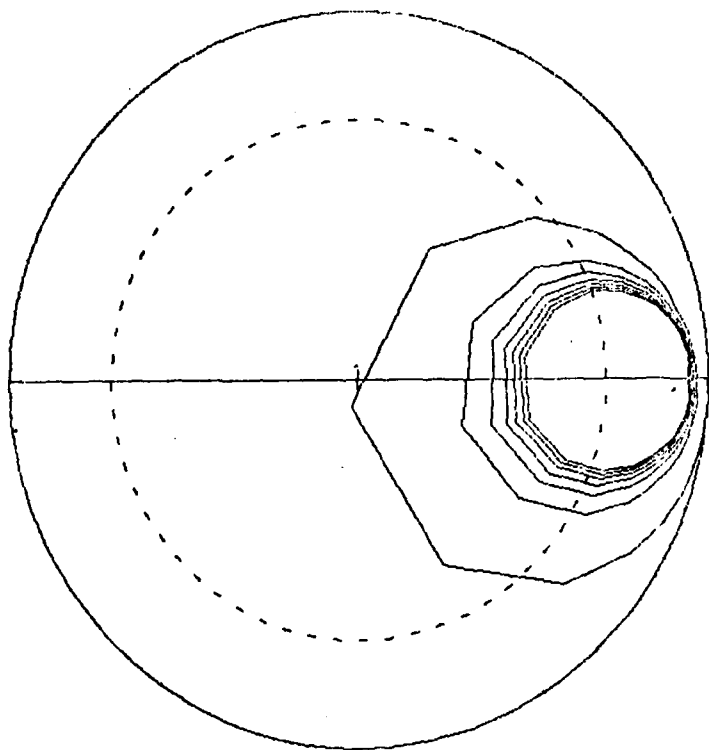


Figure 2-23 Smith Chart of Ideal Conical Dipole (  $h/a = 300$  )

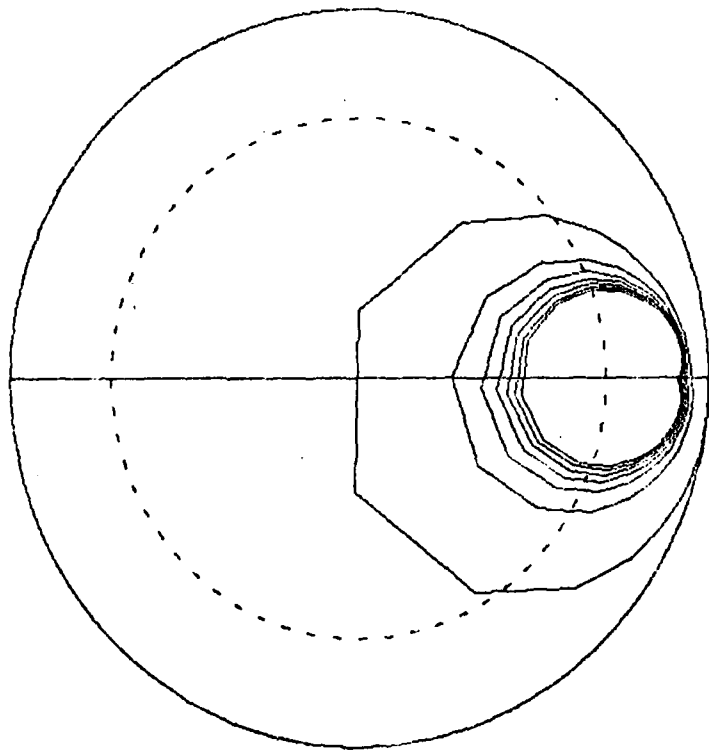


Figure 2-24 Smith Chart of Ideal Conical Dipole (  $h/a = 100$  )

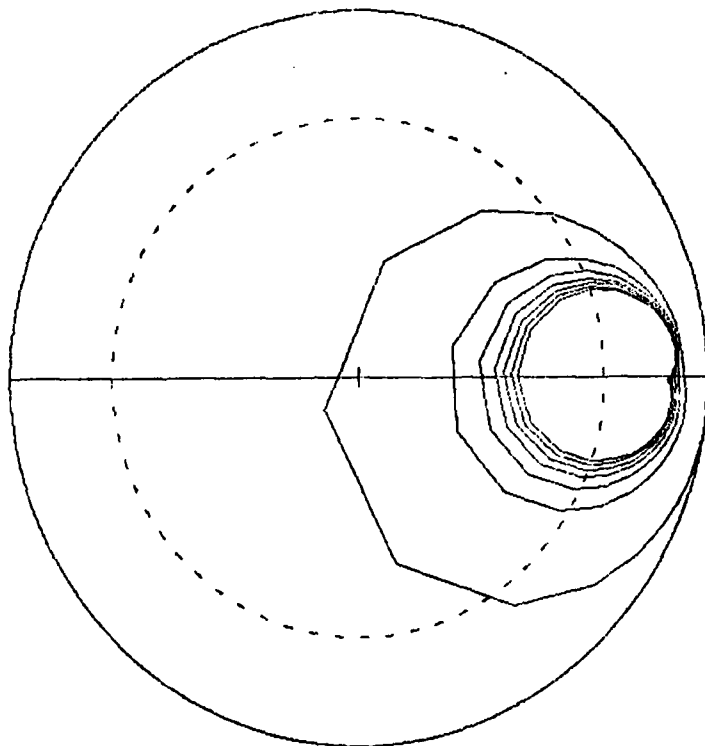


Figure 2-25 Smith Chart of Ideal Conical Dipole (  $h/a = 50$  )

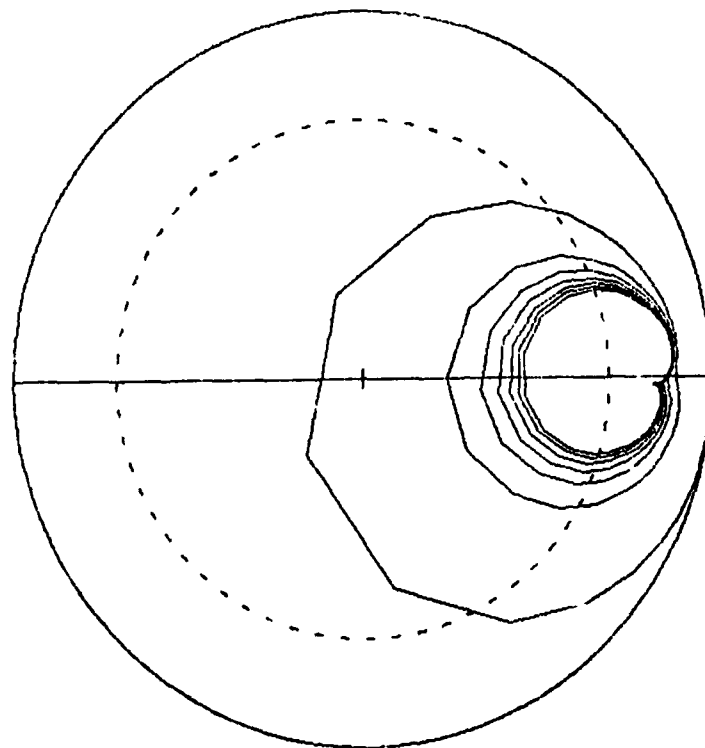


Figure 2-26 Smith Chart of Ideal Conical Dipole (  $h/a = 20$  )

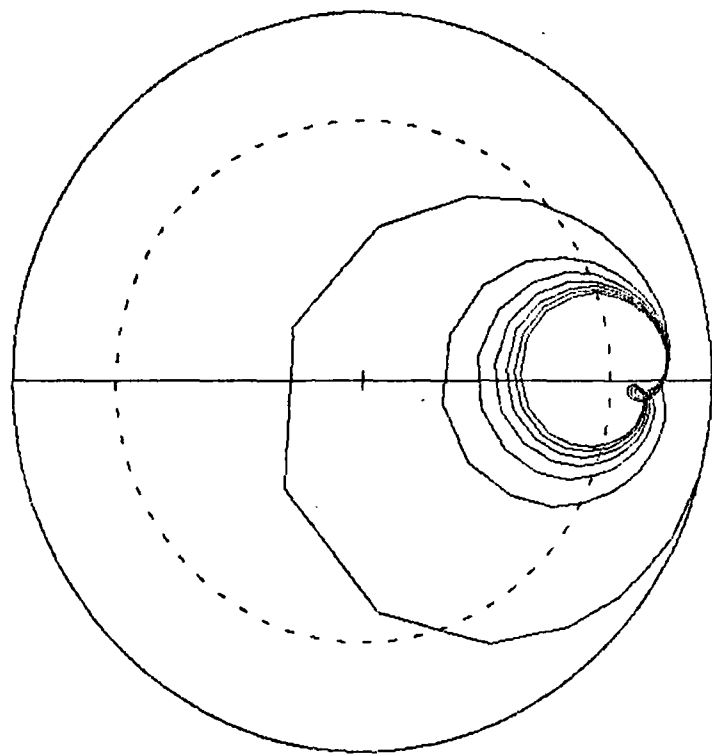


Figure 2-27 Smith Chart of Ideal Conical Dipole (  $h/a = 10$  )

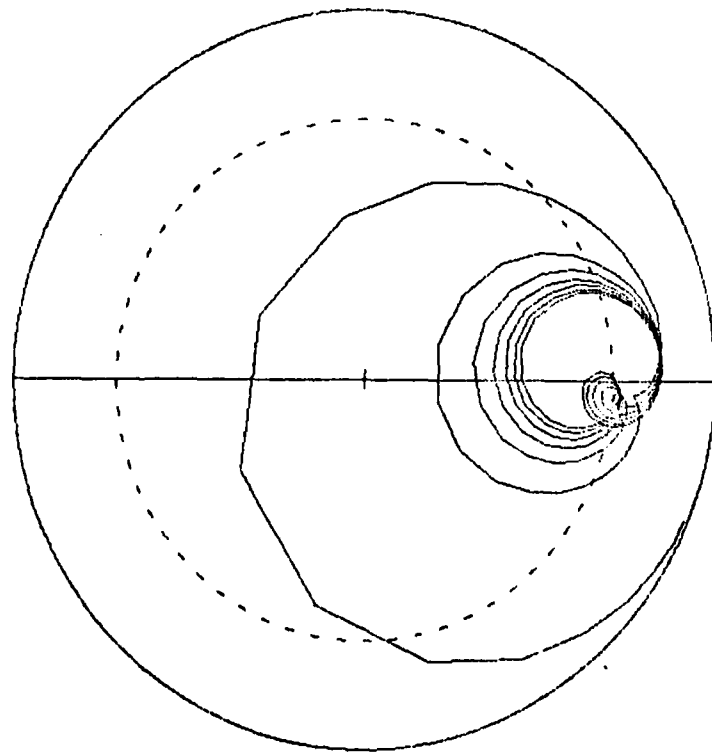


Figure 2-28 Smith Chart of Ideal Cylindrical Dipole (  $h/a = 5$  )

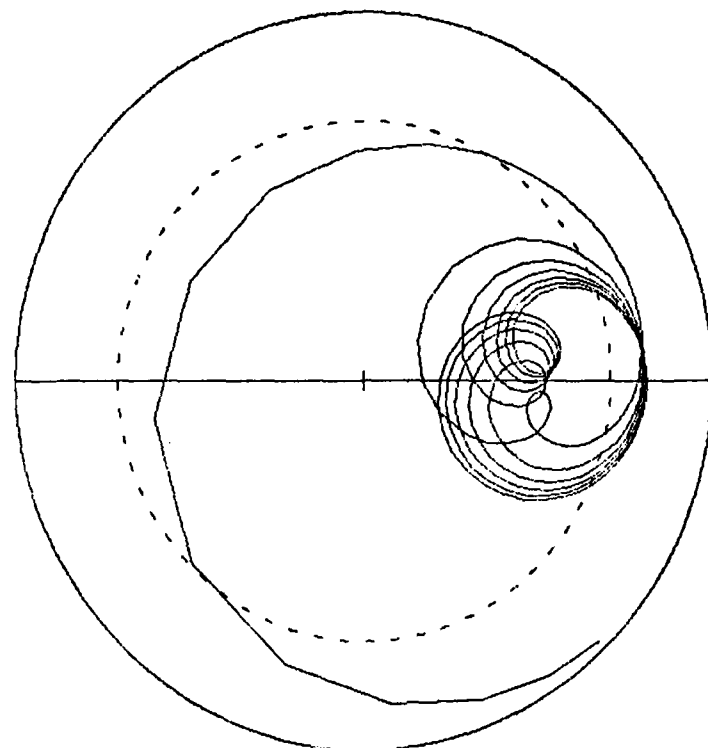


Figure 2-29 Smith Chart of Ideal Conical Dipole ( $h/a = 2$ )

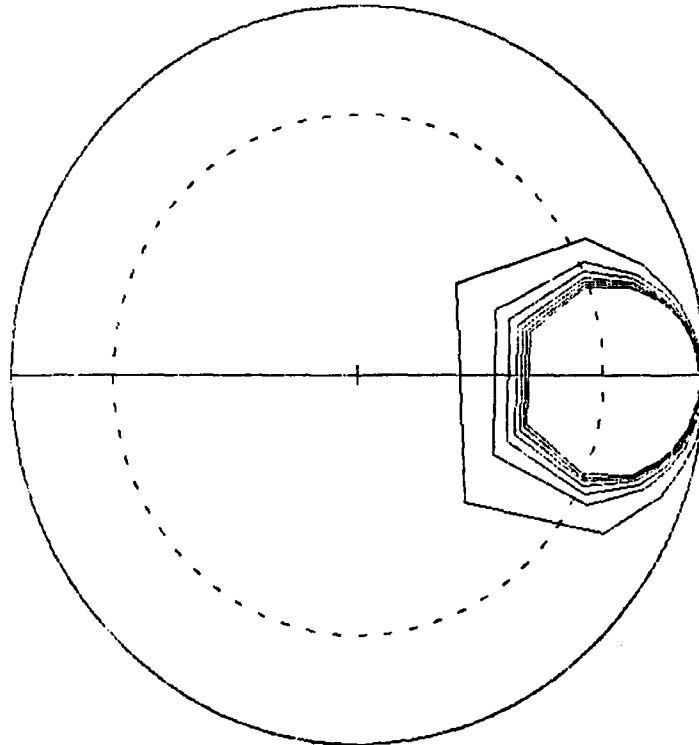


Figure 2-30 Smith Chart of Ideal Cylindrical Dipole ( $h/a = 10^6$ )

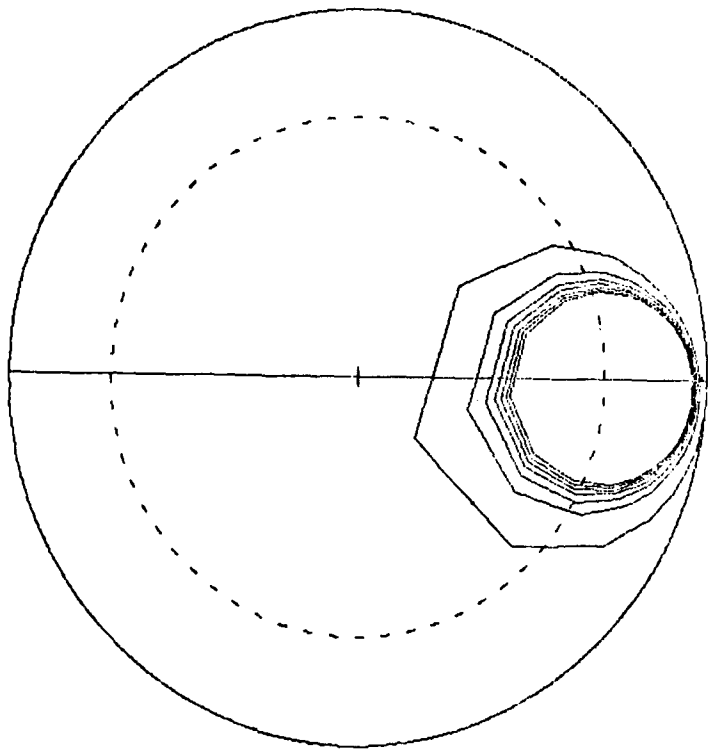


Figure 2-31 Smith Chart of Ideal Cylindrical Dipole ( $h/a = 10^4$ )

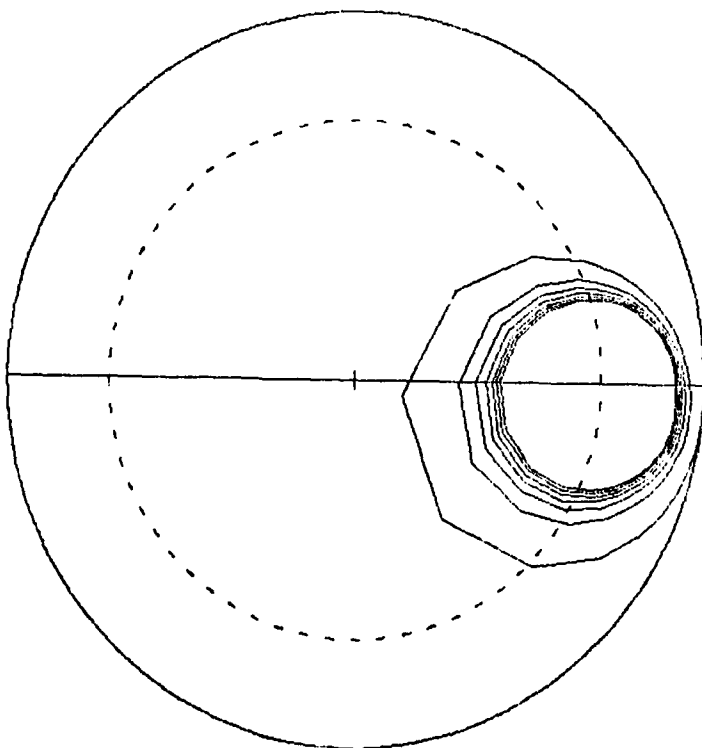


Figure 2-32 Smith Chart of Ideal Cylindrical Dipole ( $h/a = 1,000$ )

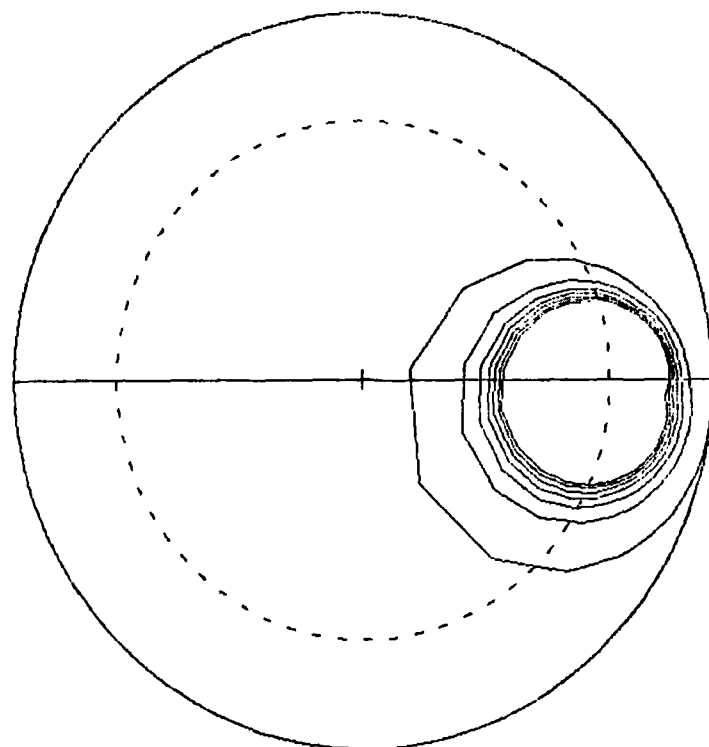


Figure 2-33 Smith Chart of Ideal Cylindrical Dipole ( $h/a = 300$ )

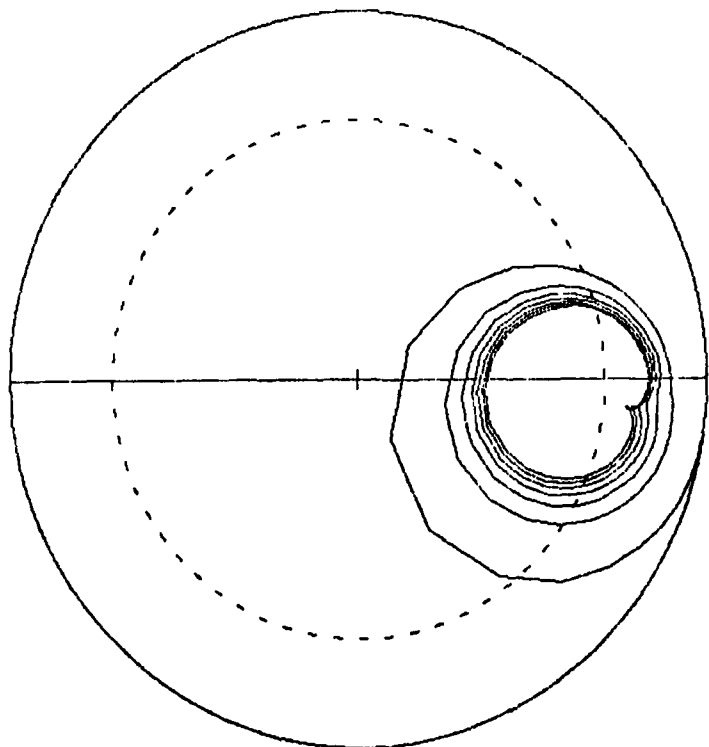


Figure 2-34 Smith Chart of Ideal Cylindrical Dipole ( $h/a = 100$ )

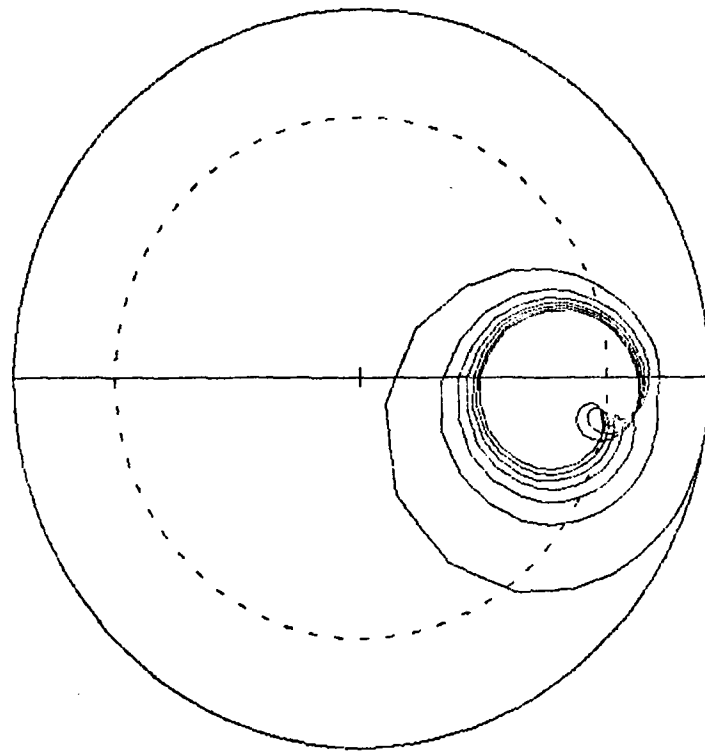


Figure 2-35 Smith Chart of Ideal Cylindrical Dipole ( $h/a = 50$ )

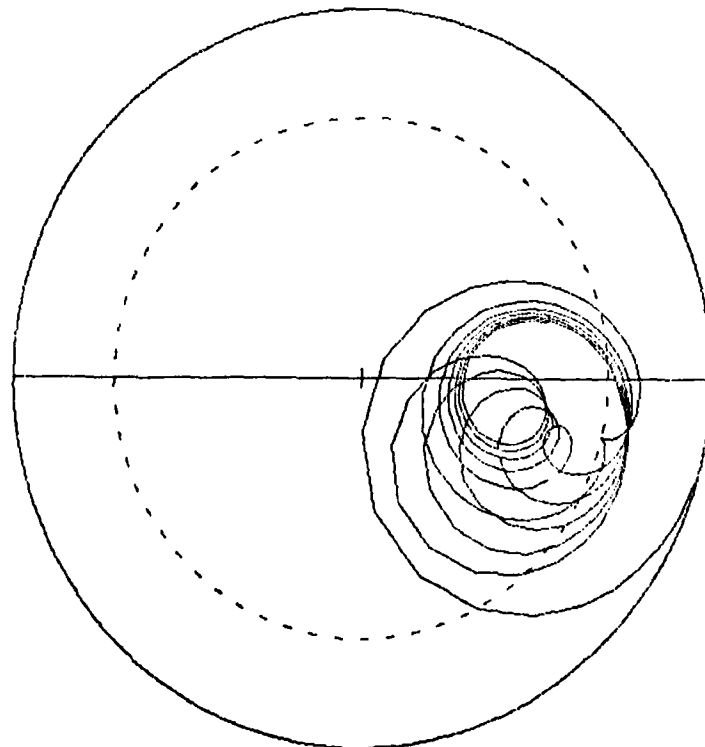


Figure 2-36 Smith Chart of Ideal Cylindrical Dipole ( $h/a = 20$ )

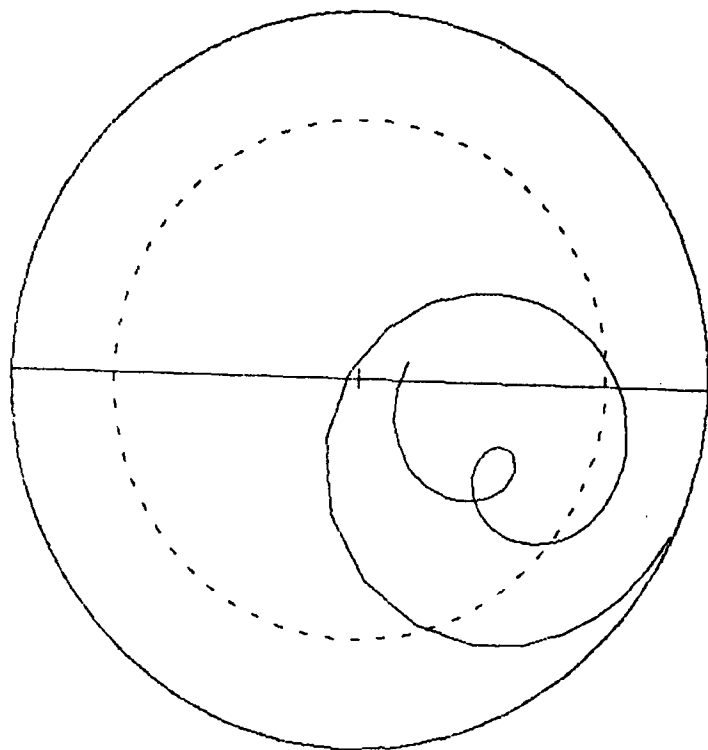


Figure 2-37 Smith Chart of Ideal Cylindrical Dipole (  $h/a = 10$  )

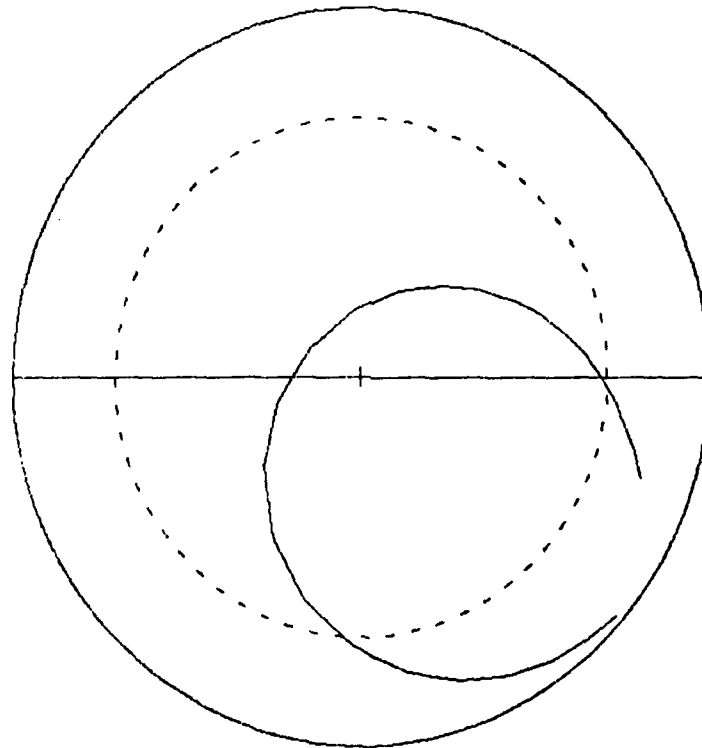


Figure 2-38 Smith Chart of Ideal Cylindrical Dipole (  $h/a = 5$  )

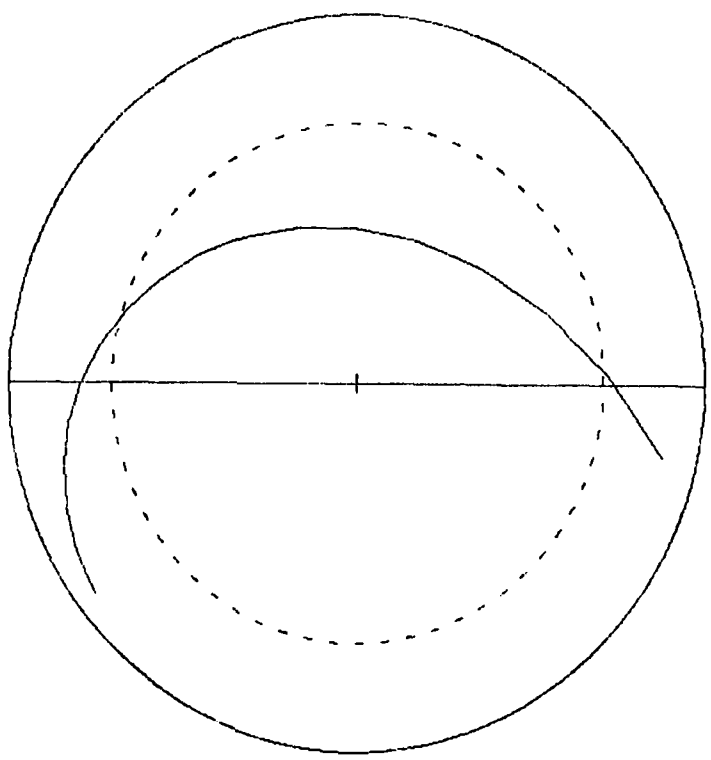


Figure 2-39 Smith Chart of Ideal Cylindrical Dipole ( $h/a = 2$ )

Since the calculations were performed at discrete frequencies the contours as shown consist of a series of straight-line segments connecting the data points. The computational increment has  $h/\lambda = .01$  or 1% electrical wavelength. Consequently, in many cases it is possible to measure the 3-dB bandwidth of a resonant peak by counting the number of line segments along the contour as it passes within the dashed circle.

Analyses were performed to model the common features of the transmission loss curves which will be significant for use in program IEMCAP. These features are the following:

1. Multiple occurrence of resonant peaks.
2. Selectivity of each resonant peak.
3. Nulls between resonant peaks.
4. Infinite fall-off below first resonant peak.

The shapes of the transmission loss curves in the vicinity of the first resonant peak were examined in detail in an attempt to find a simple algebraic expression which would model the curves with a reasonable degree of accuracy. Plots of the transmission loss on an expanded scale showing the first resonant peaks are presented in Figures 2-40 through 2-49 for the conical case, and Figures 2-50 through 2-59 for the cylindrical case. A natural choice for the model is the resonance function for a series RLC circuit. The universal resonance curve [2, page 143] can be expressed in the form

$$\frac{I}{I_r} = \frac{1}{\sqrt{1 + Q \left[ \left( \frac{f}{f_r} - \frac{f_r}{f} \right) \right]^2}}$$

where

- $I$  = input current at frequency  $f$
- $I_r$  = input current at resonance  $f = f_r$
- $Q$  = circuit  $Q$
- $f_r$  = resonant frequency

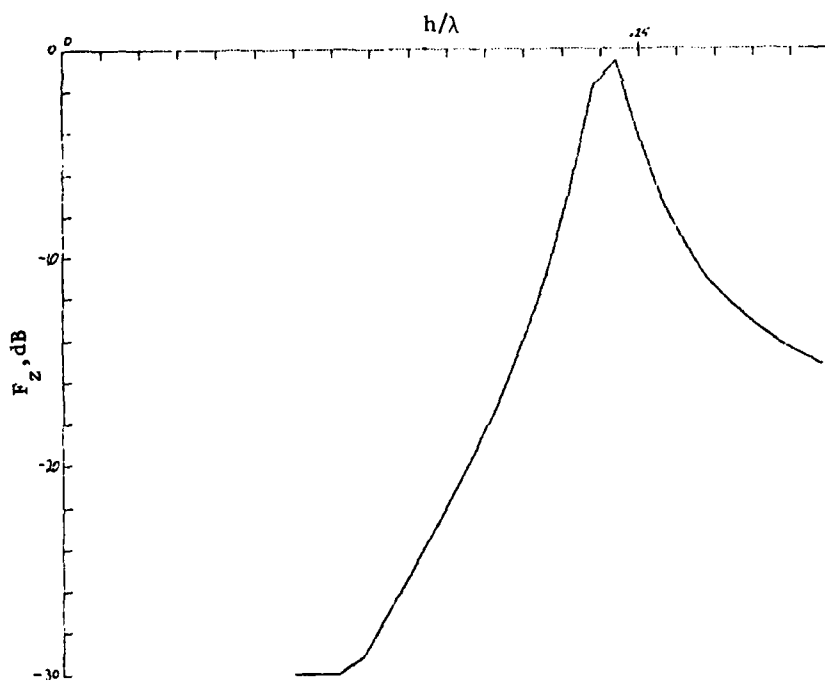


Figure 2-40 Impedance Matching Factor of First Resonance  
of Conical Dipole ( $h/a = 10^6$ )

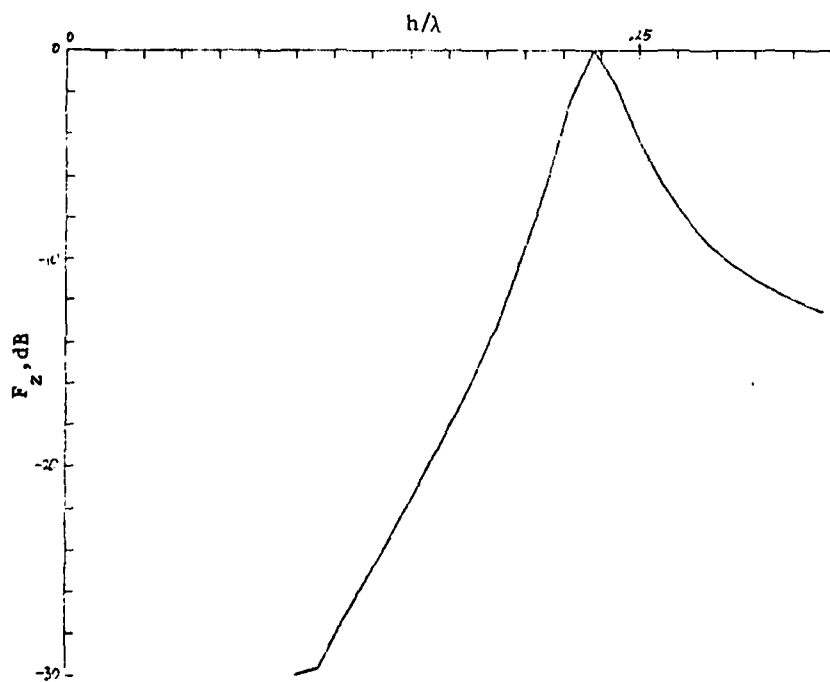


Figure 2-41 Impedance Matching Factor of First Resonance  
of Conical Dipole ( $h/a = 10^4$ )

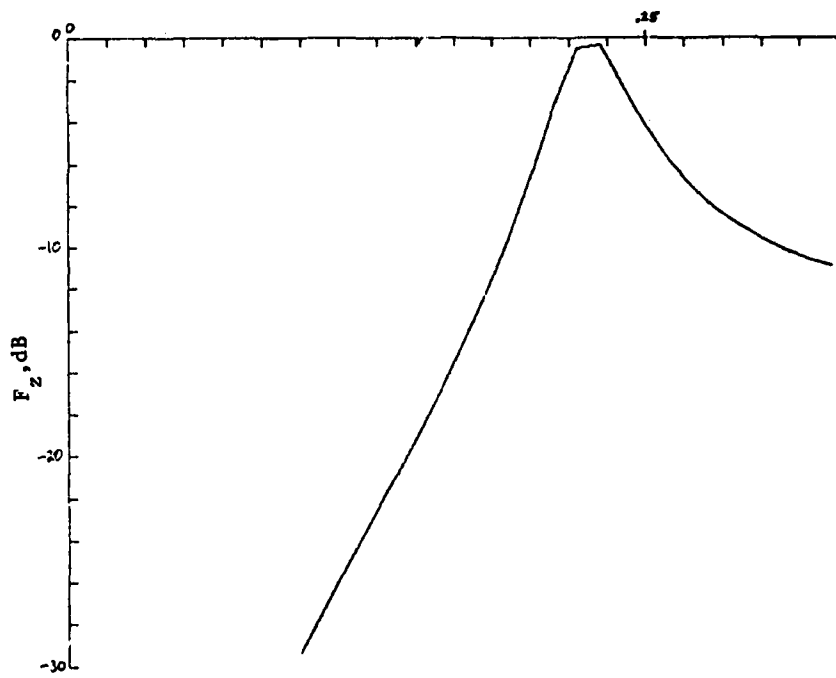


Figure 2-42 Impedance Matching Factor of First Resonance of Conical Dipole ( $h/a = 1,000$ )

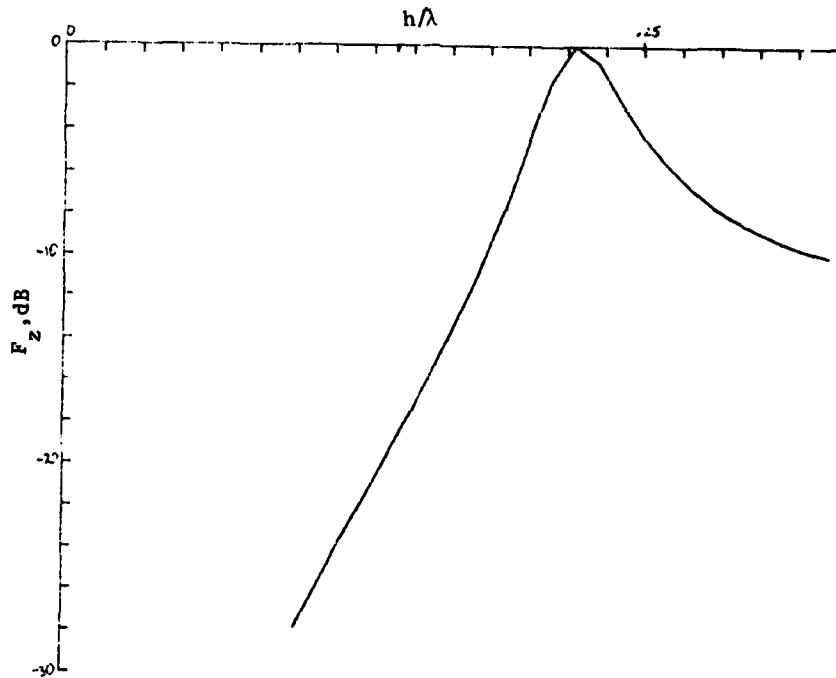


Figure 2-43 Impedance Matching Factor of First Resonance of Conical Dipole ( $h/a = 300$ )

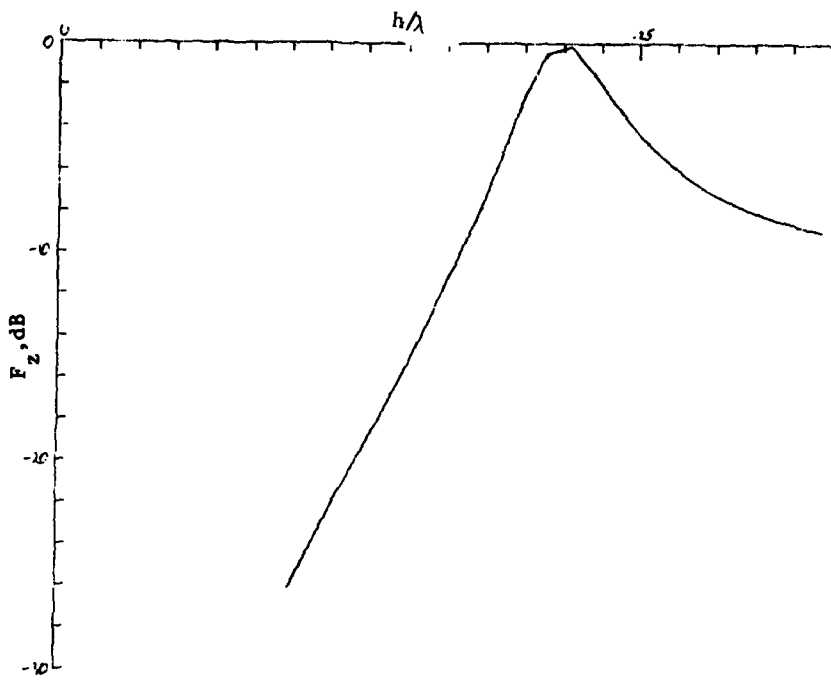


Figure 2-44 Impedance Matching Factor of First Resonance of Conical Dipole ( $h/a = 100$ )

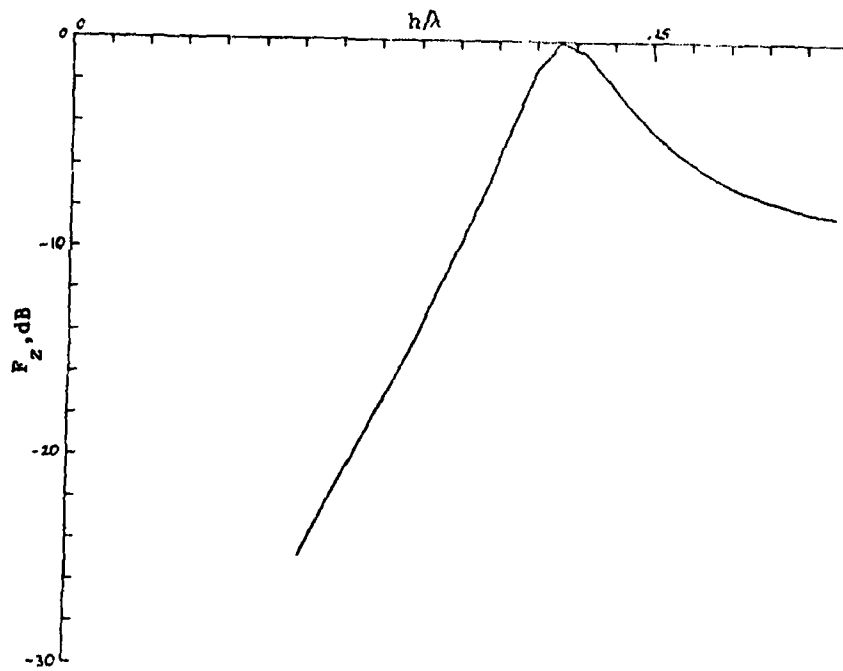


Figure 2-45 Impedance Matching Factor of First Resonance of Conical Dipole ( $h/a = 50$ )

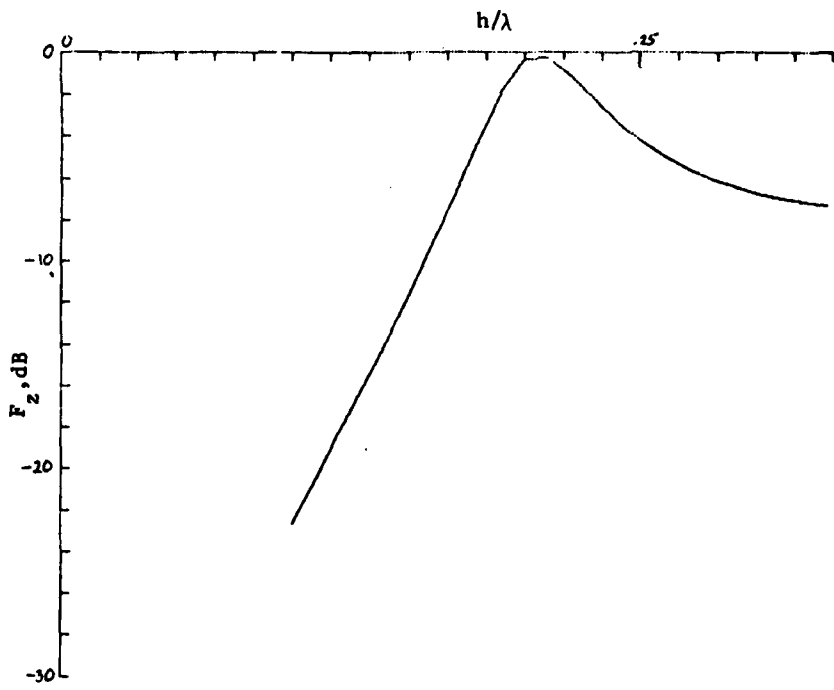


Figure 2-46 Impedance Matching Factor of First Resonance of Conical Dipole ( $h/a = 20$ )

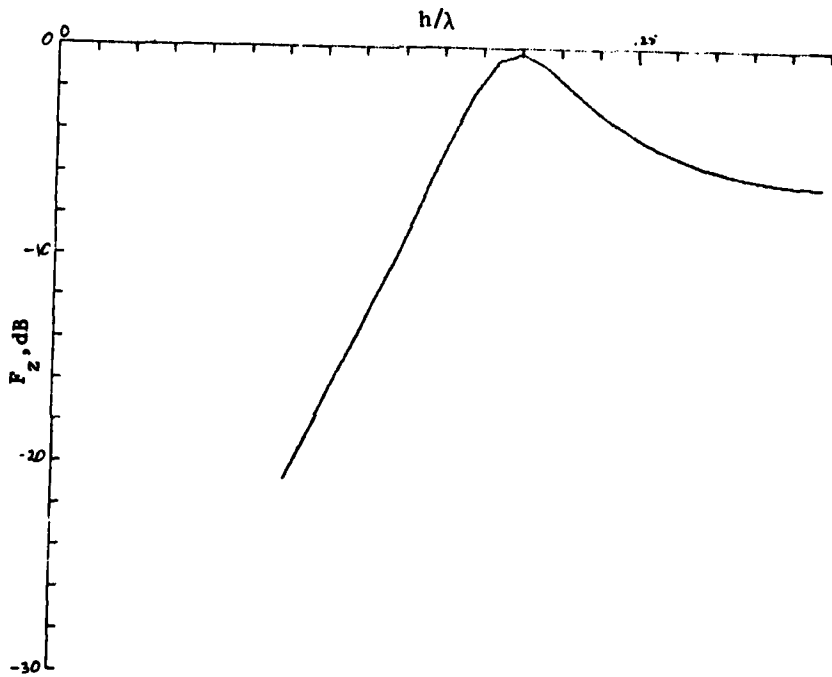


Figure 2-47 Impedance Matching Factor of First Resonance of Conical Dipole ( $h/a = 10$ )

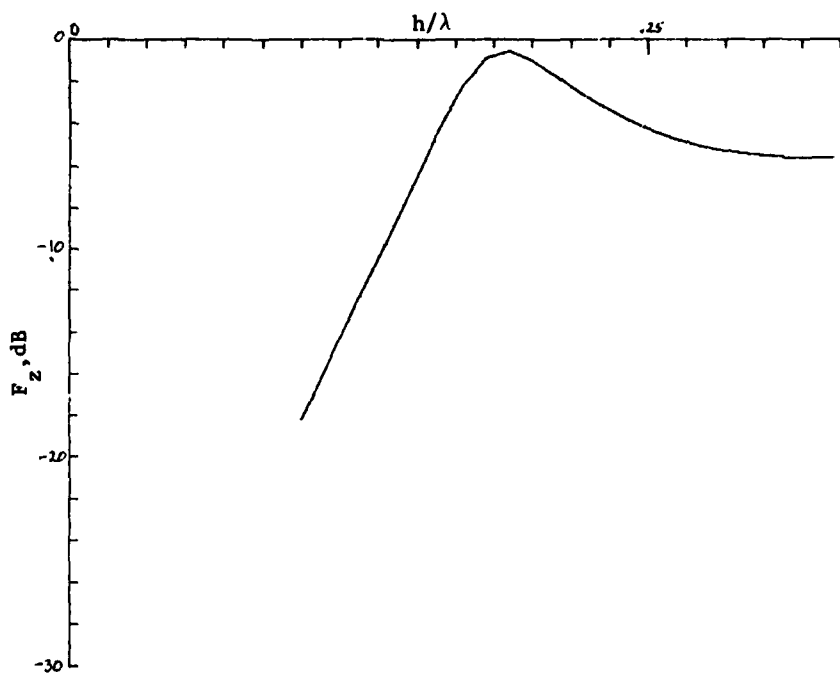


Figure 2-48 Impedance Matching Factor of First Resonance of Conical Dipole ( $h/a = 5$ )

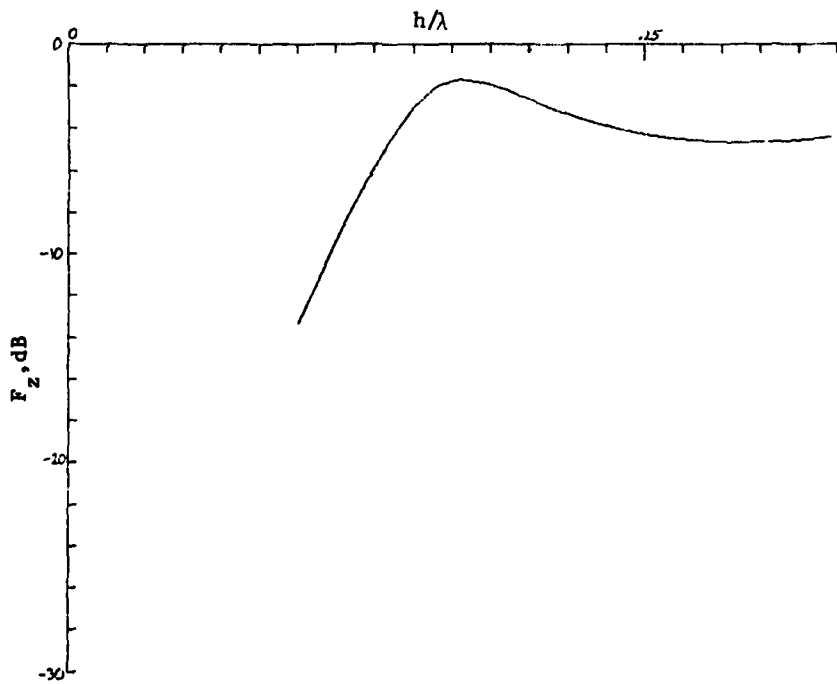


Figure 2-49 Impedance Matching Factor of First Resonance of Conical Dipole ( $h/a = 2$ )

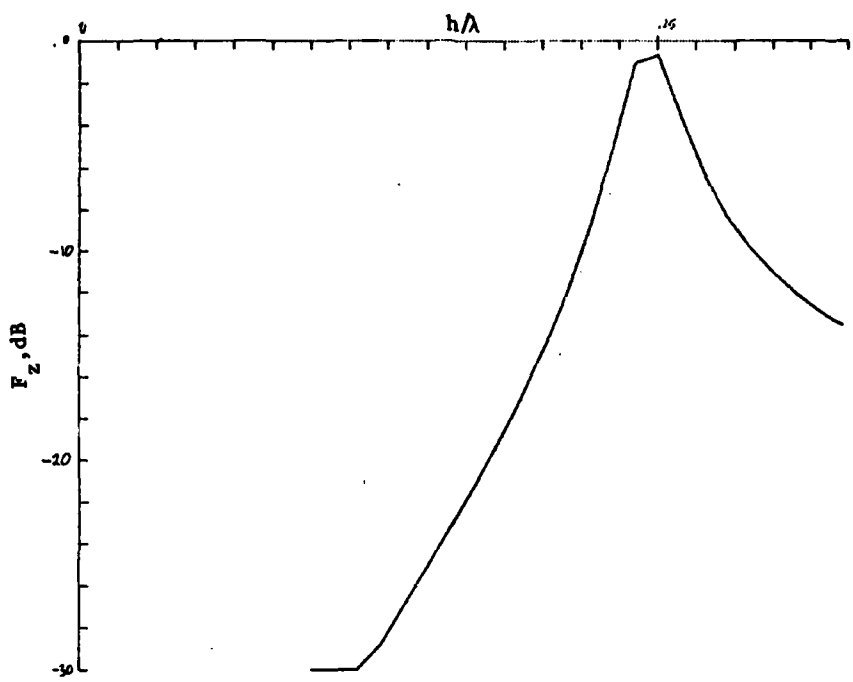


Figure 2-50 Impedance Matching Factor of First Resonance  
of Cylindrical Dipole ( $h/a = 10^6$ )

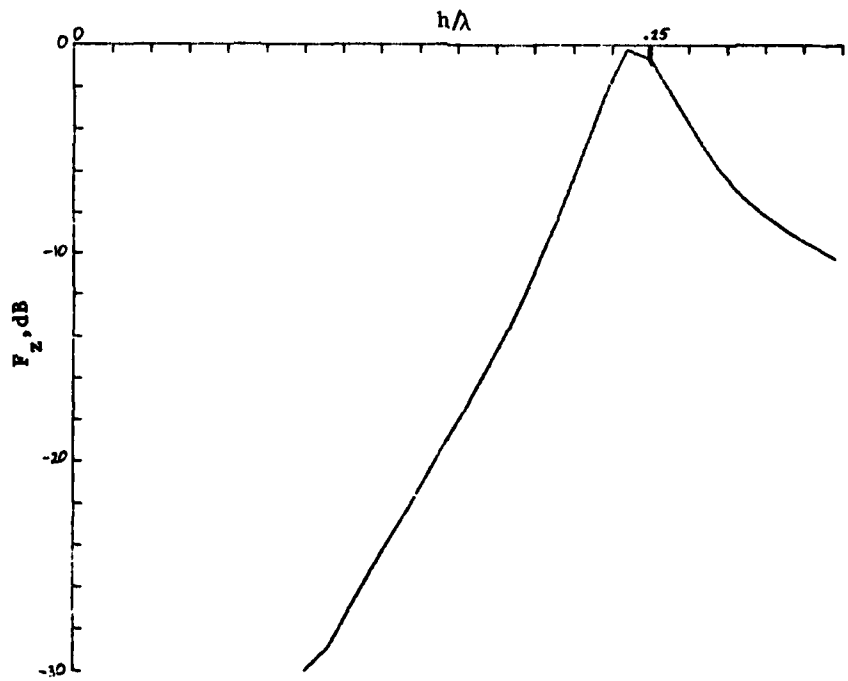


Figure 2-51 Impedance Matching Factor of First Resonance  
of Cylindrical Dipole ( $h/a = 10^4$ )

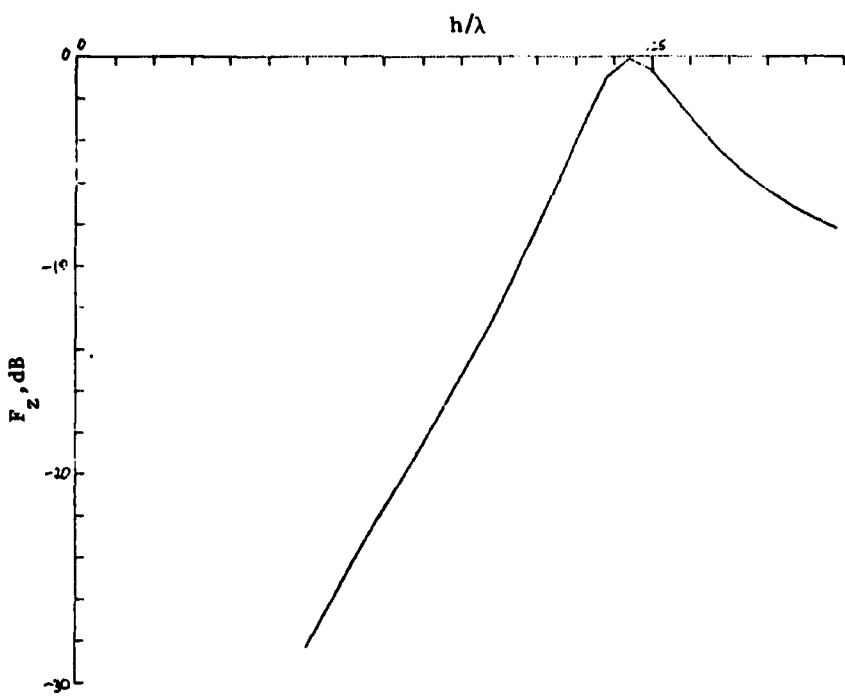


Figure 2-52 Impedance Matching Factor of First Resonance  
of Cylindrical Dipole ( $h/a = 1,000$ )

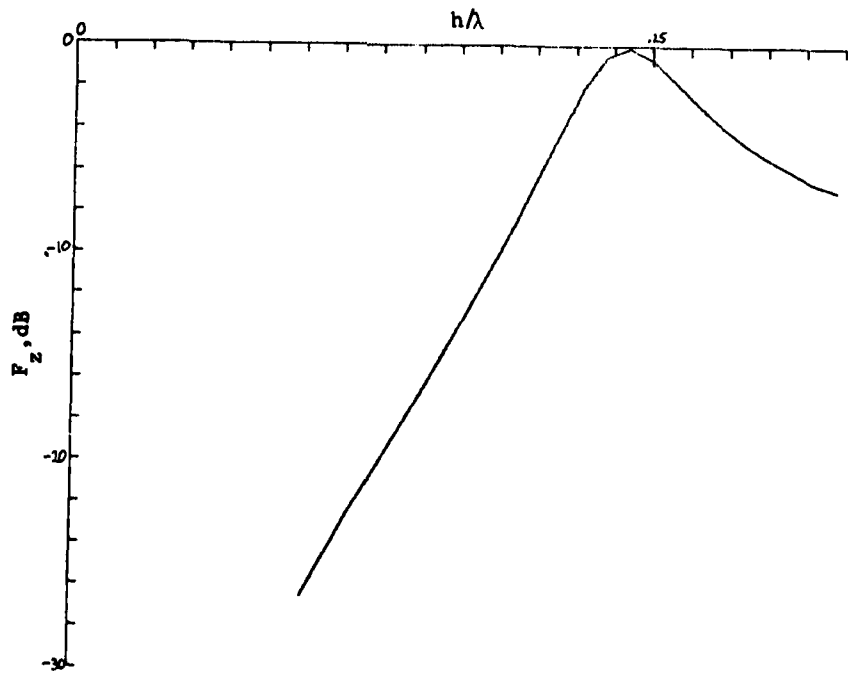


Figure 2-53 Impedance Matching Factor of First Resonance  
of Cylindrical Dipole ( $h/a = 300$ )

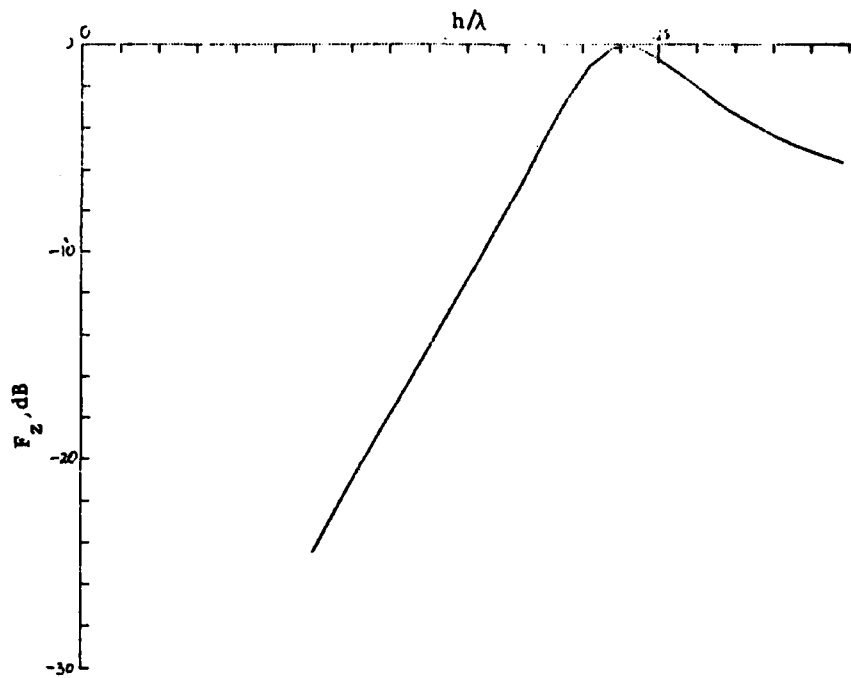


Figure 2-54 Impedance Matching Factor of First Resonance of Cylindrical Dipole ( $h/a = 100$ )

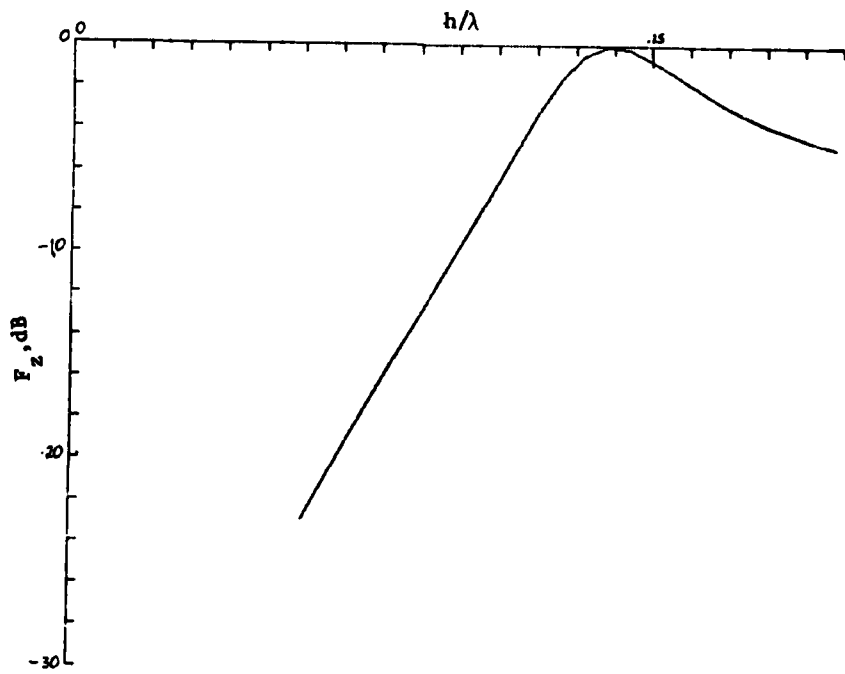


Figure 2-55 Impedance Matching Factor for First Resonance of Cylindrical Dipole ( $h/a = 50$ )

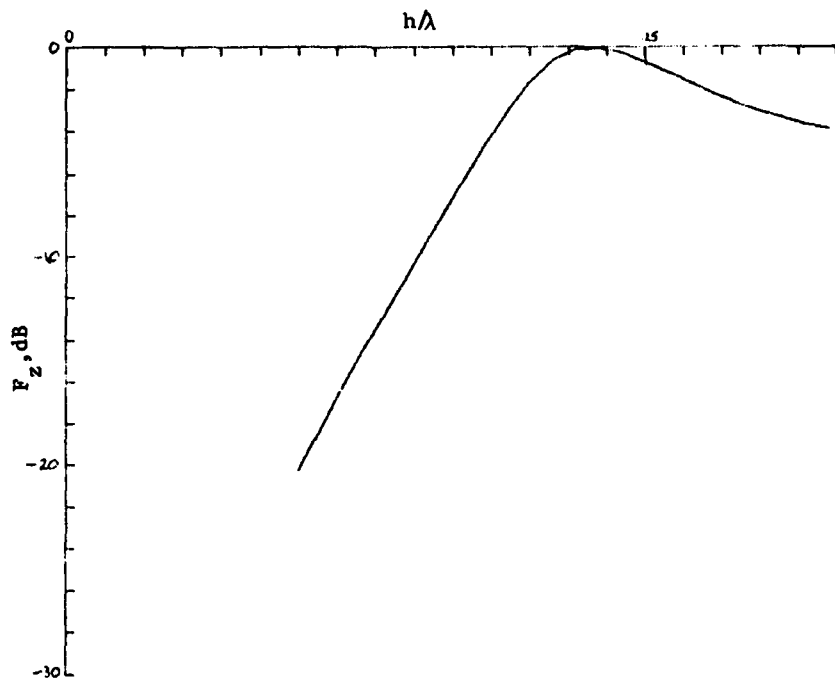


Figure 2-56 Impedance Matching Factor of First Resonance of Cylindrical Dipole ( $h/a = 20$ )

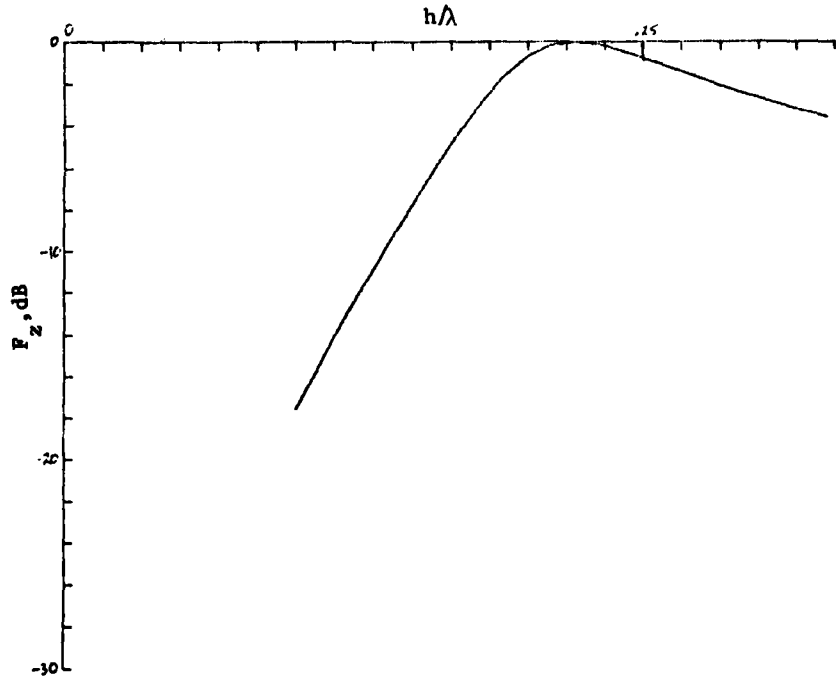


Figure 2-57 Impedance Matching Factor of First Resonance of Cylindrical Dipole ( $h/a = 10$ )

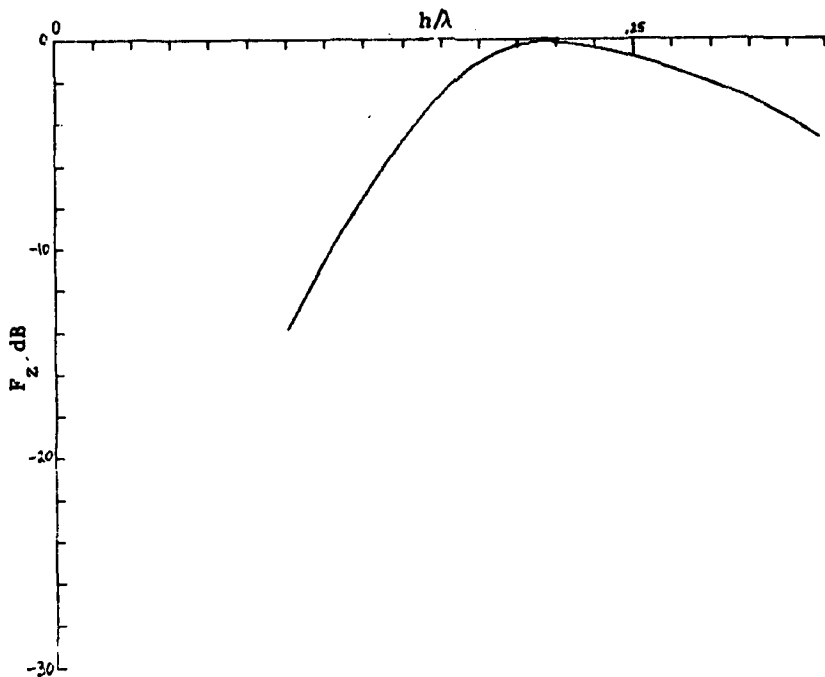


Figure 2-58 Impedance Matching Factor of First Resonance of Cylindrical Dipole ( $h/a = 5$ )

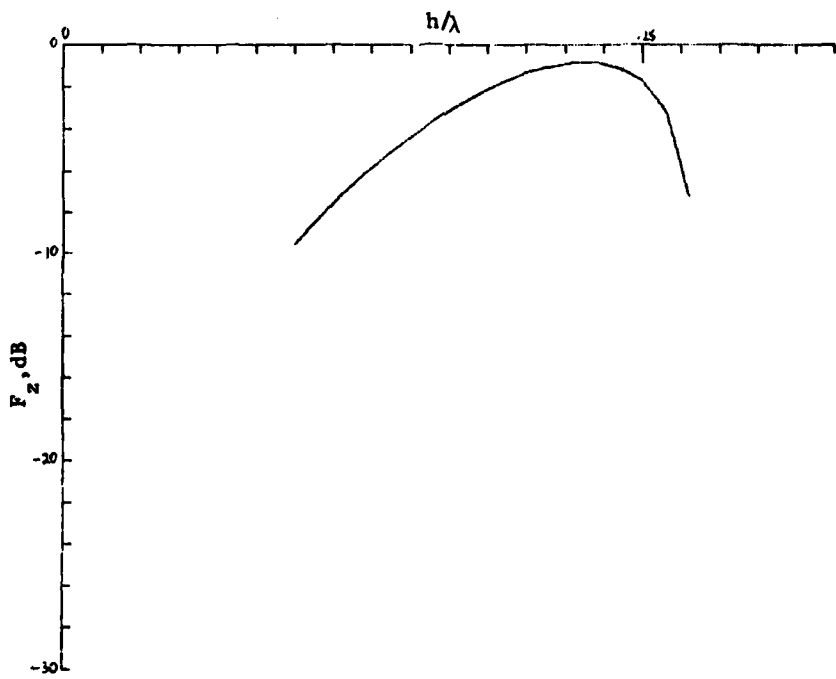


Figure 2-59 Impedance Matching Factor of First Resonance of Cylindrical Dipole ( $h/a = 2$ )

The power delivered to the circuit is  $I^2 R$ , if  $R$  is assumed to be constant with frequency, we have

$$\frac{P}{P_r} = \left| \frac{I^2 R}{I_r^2 R} \right| = \left| \frac{I^2}{I_r^2} \right| = \left| \frac{I}{I_r} \right|^2 = \frac{1}{1 + \left[ Q \left( \frac{f}{f_r} - \frac{f_r}{f} \right) \right]^2}$$

where  $P_r$  = power delivered to the circuit at resonance.

$$\text{When } \frac{P}{P_r} = \frac{1}{2}, \text{ we have } Q^2 \left( \frac{f}{f_r} - \frac{f_r}{f} \right)^2 = 1$$

from which the following relationships can be derived:

$$Q = \frac{f_r}{f_2 - f_1} \quad f_r = \sqrt{f_1 f_2}$$

where  $f_1$  = frequency below resonance at the one-half power level.

$f_2$  = frequency above resonance at the one-half power level.

Let the circuit bandwidth be defined as

$$\text{BW} = f_2 - f_1$$

so that

$$Q = \frac{f_r}{\text{BW}}$$

The  $Q$  and resonant frequency of each of the curves in Figures 2-40 through 2-58 were determined from the half power points associated with  $f_1$  and  $f_2$ . The curve in Figure 2-59 for cylindrical dipole with  $h/a = 2$  does not appear to be valid and was not included in this analysis. The theoretical antenna equations appear to be unreliable for excessively low values of  $h/a$ . The universal resonance function was then applied to four dipole curves presented in Figures 2-60 through 2-63. The universal resonance curve is shown superimposed on the theoretical transmission loss curve. The resonance value plotted is

$$F_Z = 10 \log \frac{P}{P_r}$$

$$= -10 \log \left[ 1 + Q^2 \left( \frac{f}{f_r} - \frac{f_r}{f} \right)^2 \right]$$

As can be seen in these figures, there is not good agreement since the universal resonance curve is above the dipole curve for frequencies below resonance and is below the dipole curve above resonance in all cases shown. This discrepancy is reasonable if one considers the antenna to behave as a series RLC circuit in which the  $R$  is approximately proportional to  $f^2$ .

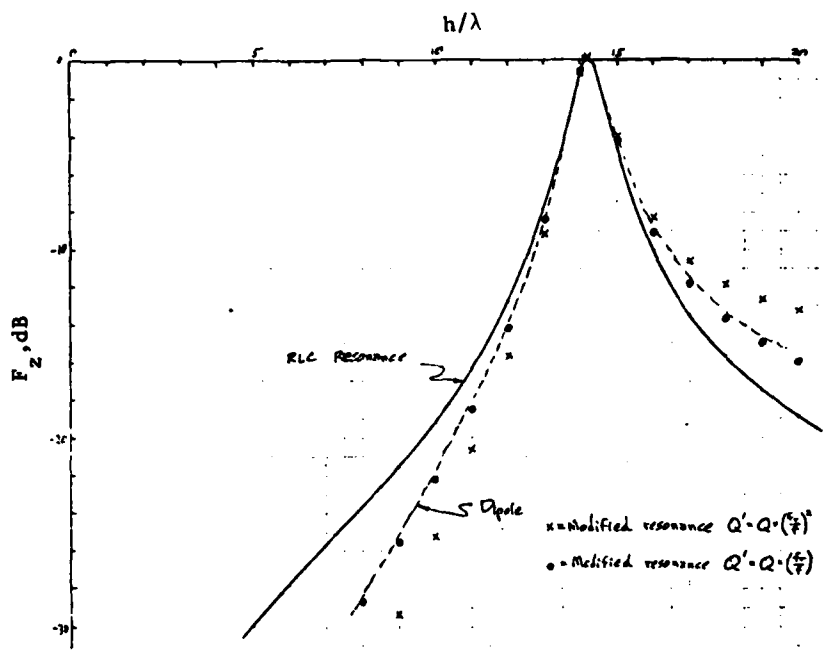


Figure 2-60 Comparison Between Theoretical and Model Curves of Impedance Matching Factor at First Resonance (Conical,  $h/a = 10^6$ )

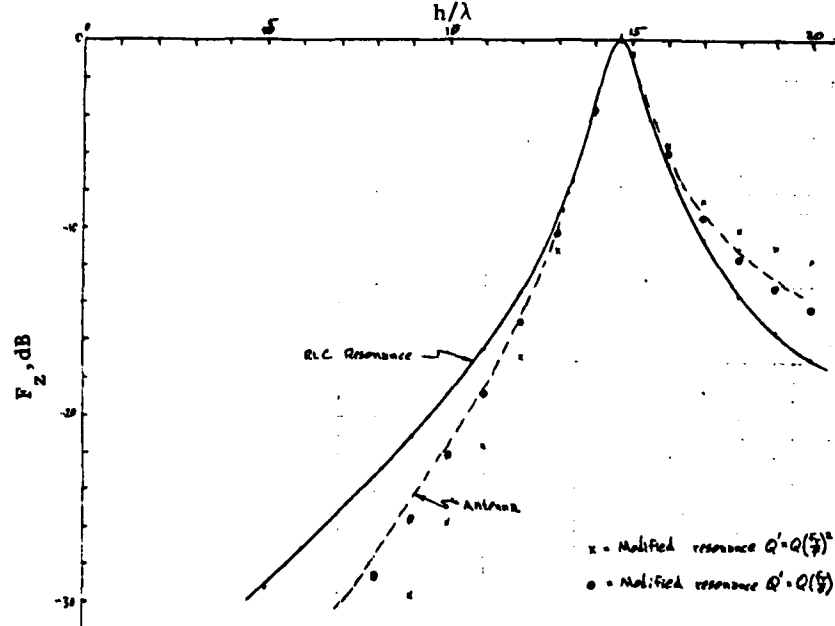


Figure 2-61 Comparison Between Theoretical and Model Curves of Impedance Matching Factor at First Resonance (Cylindrical,  $h/a = 10^6$ )

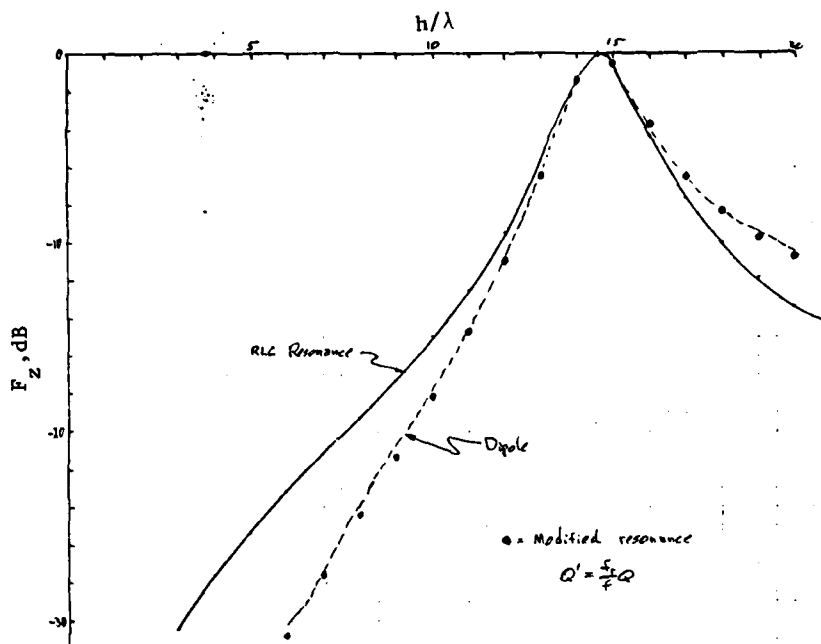


Figure 2-62 Comparison Between Theoretical and Model Curves of Impedance Matching Factor at First Resonance (Cylindrical,  $h/a = 10^4$ )

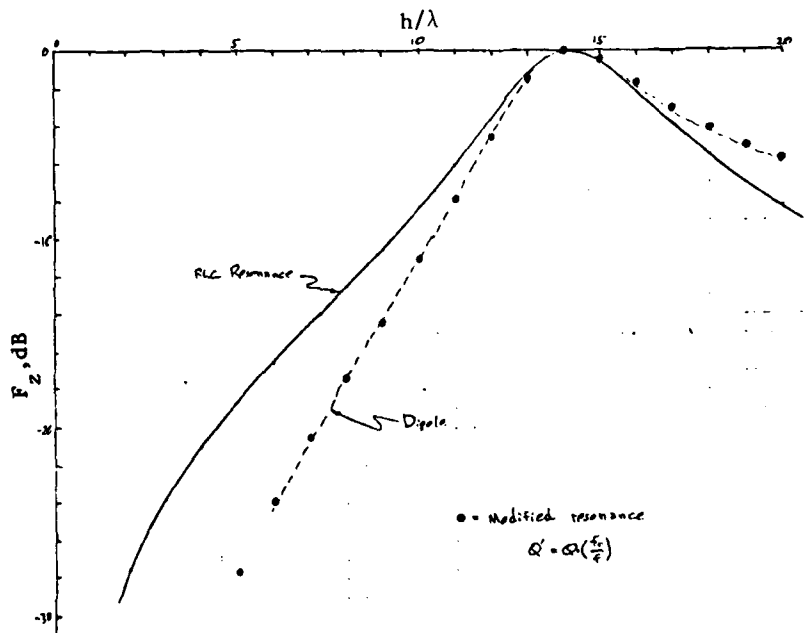


Figure 2-63 Comparison Between Theoretical and Model Curves of Impedance Matching Factor at First Resonance (Cylindrical,  $h/a = 100$ )

Accordingly, the  $Q$  of the antenna increases as frequency drops below resonance.

Since  $Q_r$  may be expressed as

$$Q = \frac{X}{R}$$

where  $X$  = inductive or capacitive reactance of a series RLC circuit,

let

$$Q' = \frac{X}{R'}$$

where

$$R' = \left(\frac{f}{f_r}\right)^2 R$$

Then,

$$Q' = \left(\frac{f_r}{f}\right)^2 Q$$

With  $Q$  replaced by  $Q'$  in the universal resonance function, we have the following modified resonance function.

$$\frac{P}{P_r} = \frac{1}{1 + \left[ \left( \frac{f_r}{f} \right)^2 Q \left( \frac{f}{f_r} - \frac{f_r}{f} \right) \right]^2}$$

The values from this function are shown plotted on Figures 2-60 and 2-61 and indicates over-correction. The correction is in the proper direction but is nearly double of that needed. A modification using

$$Q' = \frac{f_r}{f} Q$$

was then tried, and the results shown in Figures 2-60 through 2-63 appear to give excellent agreement. Thus, the modified universal resonance function found to model the selectivity of the first resonant peak of dipole impedance matching factor is

$$\begin{aligned} \frac{P}{P_r} &= \frac{1}{1 + \left[ \frac{f_r}{f} Q \left( \frac{f}{f_r} - \frac{f_r}{f} \right) \right]^2} \\ &= \frac{1}{1 + Q^2 \left[ 1 - \left( \frac{f_r}{f} \right)^2 \right]^2} \end{aligned}$$

This same function tested down to a dipole half-length  $h = \lambda/60$  for several high and low Q samples of first resonant peaks is shown in Figures 2-64 through 2-69. As can be seen, the function agrees well with the theoretical impedance matching curves down to levels less than -50 to -60 dB. It is reasonable to accept this function for modeling the impedance matching of a dipole down to DC (or a practical limit of 1 Hz).

Additional tests of this function for modeling resonant peaks of higher order were made for various high and low Q dipoles. The function was applied directly to each peak curve without shifting the frequency coordinate, but since the higher order resonant peaks generally drop below the 0 dB axis, the value of  $F_z$  given by the function was offset by the value of the resonant peak. That is, given  $f_r$ , Q and  $F_z[\max]_i$  = peak value of  $F_z$  at  $f=f_r$  for the  $i$ th resonant peak, the model curve computed for  $f_r$  and Q was shifted downward by  $F_z[\max]$ . It was found that the degree to which the empirical function fit a theoretical resonance curve was highly sensitive to the specific value of Q measured for the curve. Since Q is determined from estimates of the 3-dB bandwidth measured relative to the level of the resonant peak, it was found necessary to re-calculate the resonant peaks of  $F_z$  with a high degree of resolution. These data permitted an accurate determination of the peak value  $F_z[\max]$ , center frequency  $f_r$ , the Q, and bandwidth  $BW = f_2 - f_1$ . The results are presented in Table 2-1. The frequency scale is arbitrary: however, for convenience, it was scaled to one unit per  $h/\lambda = 1/60$  (each tic mark in the high resolution plots, e.g., Figures 2-40 to 2-69, or  $h/\lambda = 1/6$  per tic mark in low resolution plots, e.g., Figures 2-3 to 2-19).

Various samples of the model function plotted at high-order resonant peaks are presented in Figures 2-70 through 2-85. In general, the modeling is good at the peaks and at the upper parts of the selectivity skirts, but falls below the skirts in the lower regions. On the low-frequency side, the model agrees well down to a level (in dB) of one-half or two-thirds of the null depth, whereas on the high-frequency side the agreement is good only above the one-third to one-half null depth level. Some of this discrepancy in the lower skirt region can be overcome by using a model curve with a lower Q. As will be shown, however, the resonant peaks will, in fact, require modeling at wider bandwidths than shown.

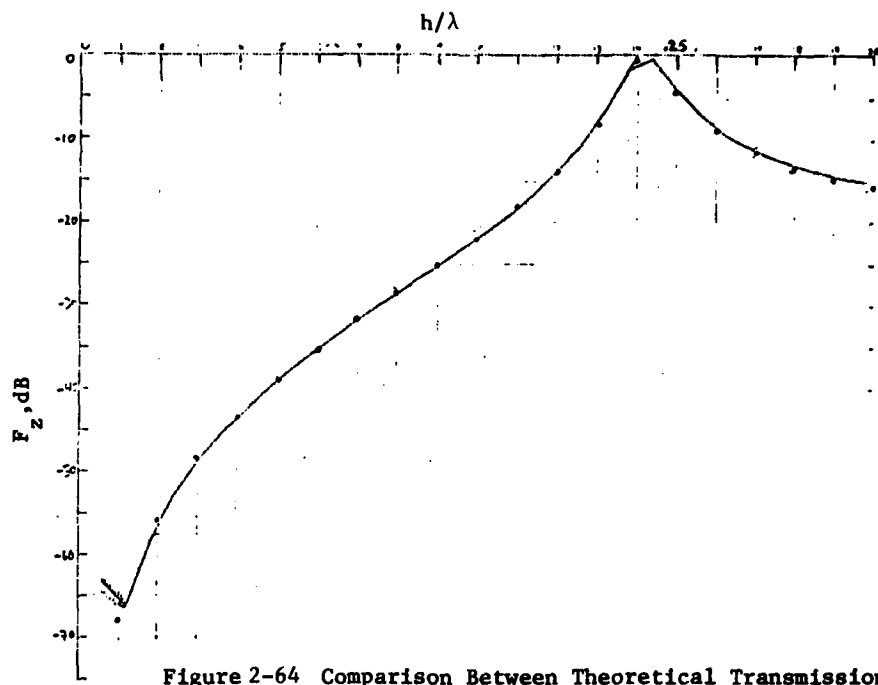


Figure 2-64 Comparison Between Theoretical Transmission Loss and the Model at First Resonance (Conical,  $h/a = 10^6$ ).

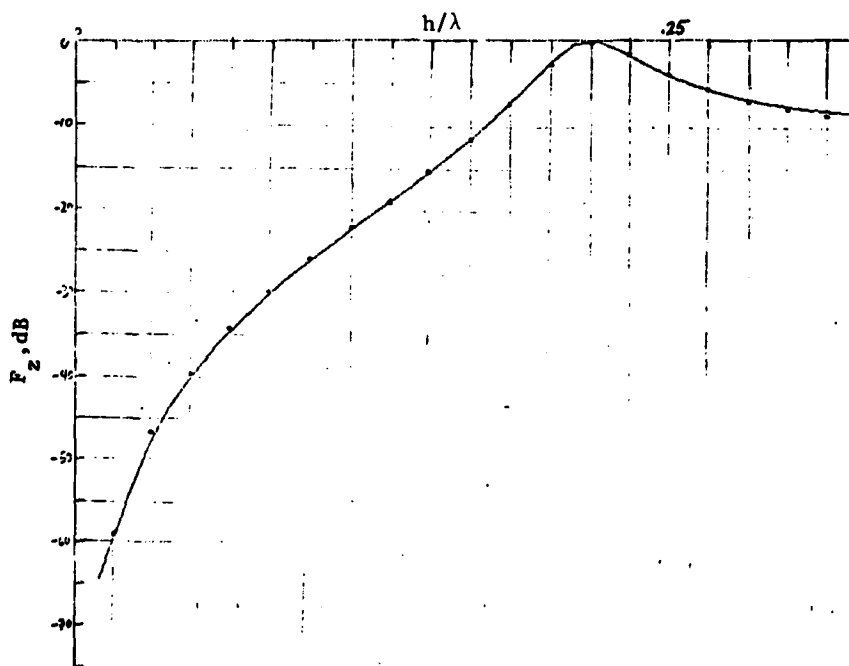


Figure 2-65 Comparison Between Theoretical Impedance Matching Factor and the Model at First Resonance (Conical,  $h/a = 100$ )

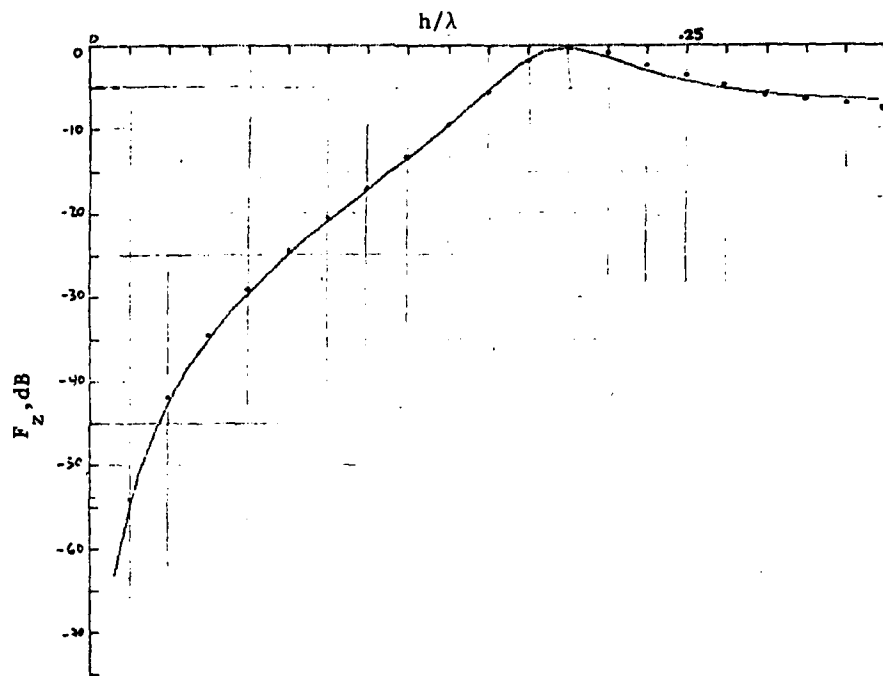


Figure 2-66 Comparison Between Theoretical Impedance Matching Factor and the Model at First Resonance (Conical,  $h/a = 10$ )

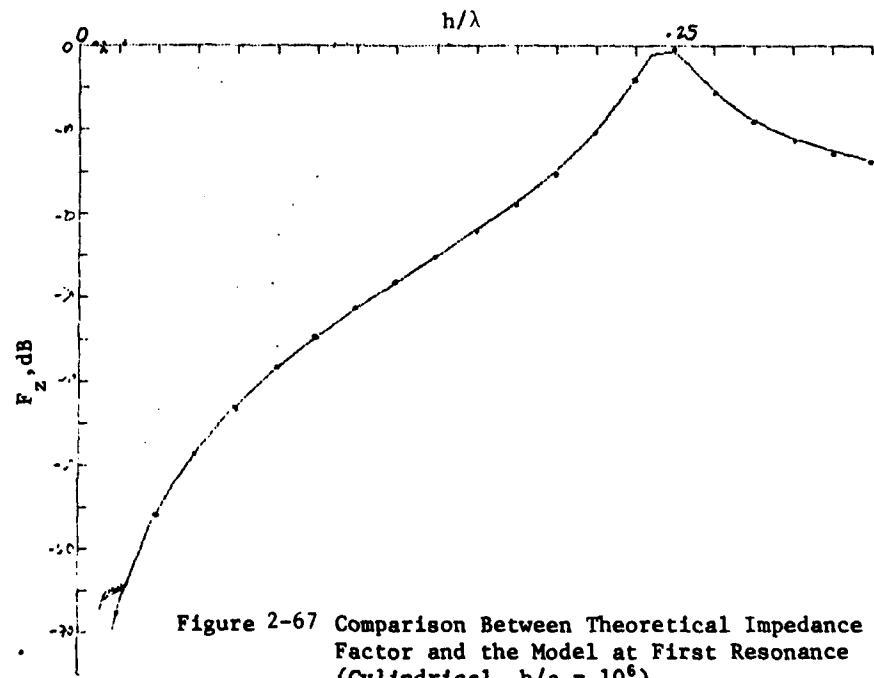


Figure 2-67 Comparison Between Theoretical Impedance Matching Factor and the Model at First Resonance (Cylindrical,  $h/a = 10^6$ )

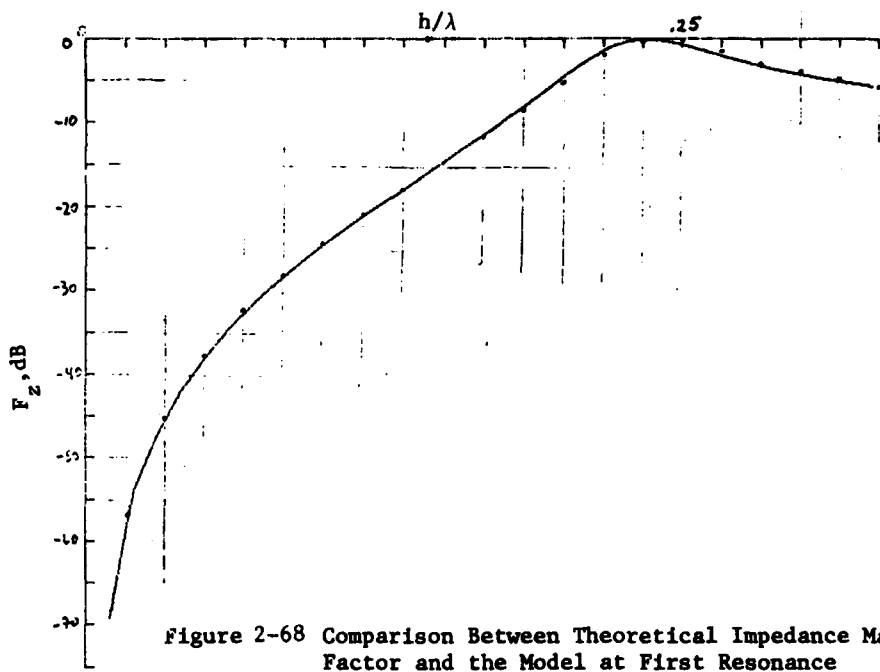


Figure 2-68 Comparison Between Theoretical Impedance Matching Factor and the Model at First Resonance (Cylindrical,  $h/a = 100$ )

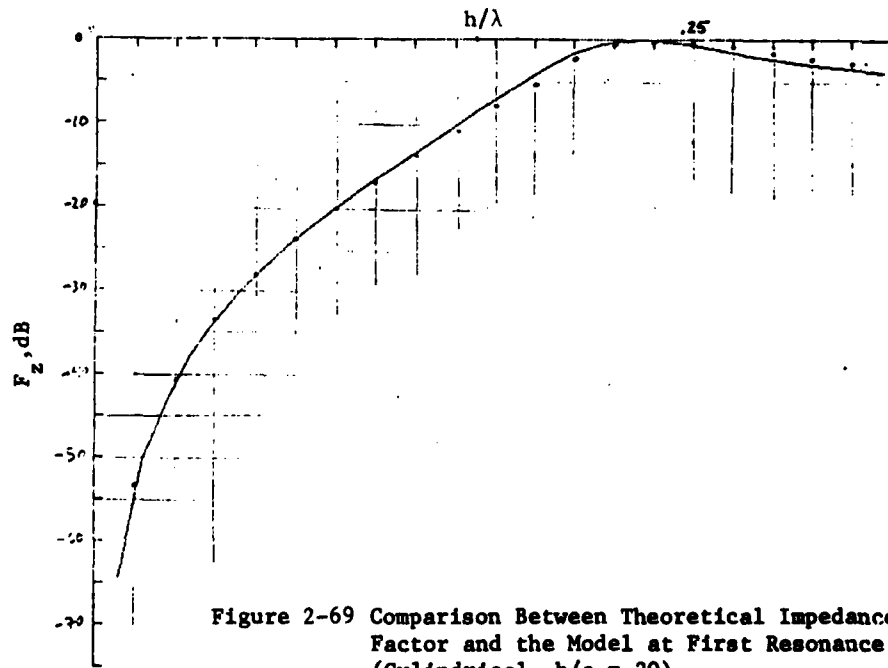


Figure 2-69 Comparison Between Theoretical Impedance Matching Factor and the Model at First Resonance (Cylindrical,  $h/a = 20$ )

Table 2-1  
Calculated Quantities of Dipole Resonant Peaks

Antenna	Peak No.	$f_r$	BW	Q	$F_z$ [max] (dB)
Conical ( $h/a=10^6$ )	1	14.21	1.174	12.10	-.06
	2	44.27	1.501	29.50	-.48
	3	74.29	1.640	45.31	-.71
	4	104.30	1.730	60.28	-.86
	5	134.31	1.798	74.71	-.98
	6	164.31	1.842	89.21	-1.07
Conical ( $h/a=1000$ )	1	13.60	1.97	6.89	.00
	2	43.70	2.59	16.89	-.38
	3	73.74	2.83	26.05	-.63
	4	103.76	2.98	34.79	-.79
	5	133.78	3.09	43.27	-.91
	6	163.79	3.17	51.59	-1.00
Conical ( $h/a=100$ )	1	13.12	2.55	5.15	-.02
	2	43.24	3.44	12.57	-.32
	3	73.29	3.77	19.42	-.57
	4	103.33	3.98	25.97	-.74
	5	133.35	4.12	32.35	-.86
	6	163.36	4.23	38.59	-.96
Conical ( $h/a=20$ )	1	12.55	3.23	3.89	-.12
	2	42.61	4.55	9.37	-.26
	3	72.67	5.04	14.42	-.51
	4	102.71	5.32	19.29	-.68
	5	132.73	5.52	24.03	-.81
	6	162.75	5.67	28.69	-.91
Cylindrical ( $h/a=10^6$ )	1	14.77	1.43	10.34	-.13
	2	44.74	1.86	24.03	-.50
	3	74.74	2.07	36.17	-.69
	4	104.73	2.20	47.61	-.81
	5	134.73	2.30	58.51	-.90
	6	164.73	2.39	69.03	-.97
Cylindrical ( $h/a=1000$ )	1	14.58	2.86	5.09	-.09
	2	44.49	3.91	11.38	-.39
	3	74.47	4.40	16.92	-.55
	4	104.45	4.73	22.07	-.65
	5	134.44	4.98	27.01	-.72
	6	164.43	5.18	31.77	-.77
Cylindrical ( $h/a=100$ )	1	14.45	4.30	3.36	-.05
	2	44.21	6.26	7.06	-.29
	3	74.09	7.28	10.18	-.41
	4	104.00	7.99	13.02	-.49
	5	133.91	8.56	15.65	-.55
	6	163.83	9.04	18.12	-.59

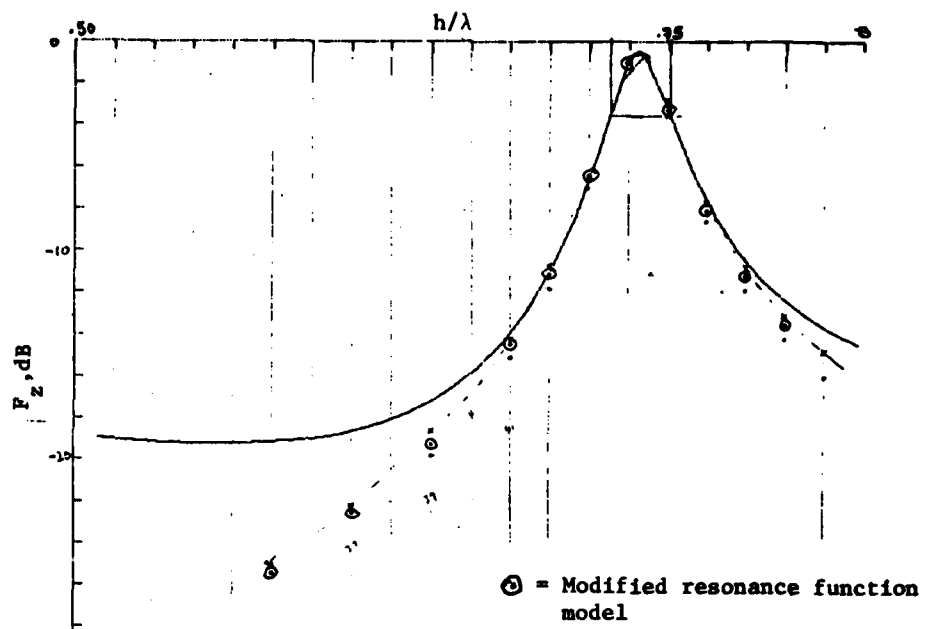


Figure 2-70 Comparison Between Theoretical Impedance Matching Factor and the Model at Second Resonance (Conical,  $h/a = 10^6$ )

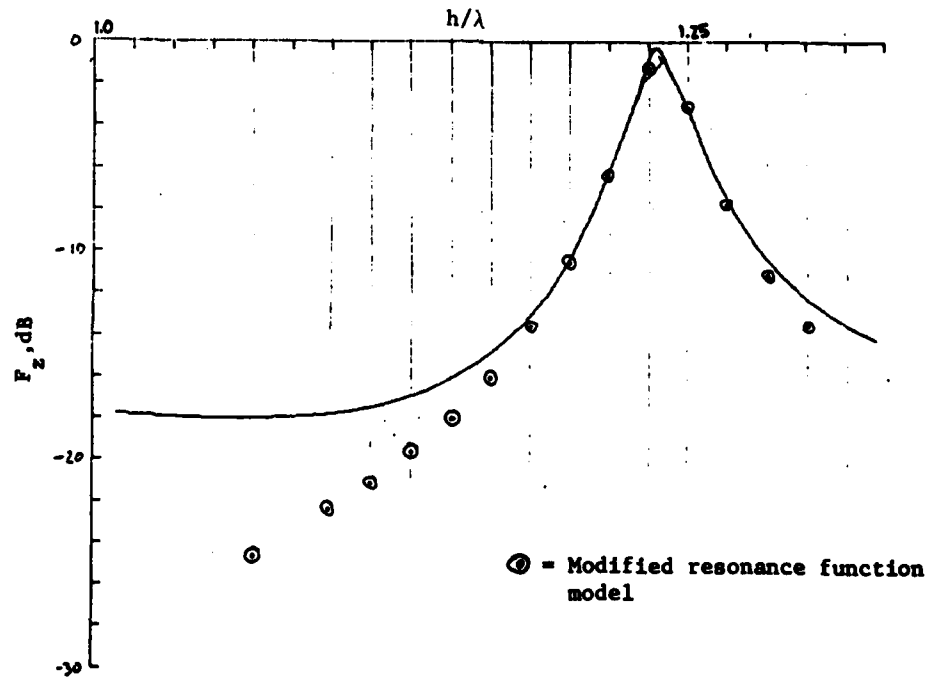


Figure 2-71 Comparison Between Theoretical Impedance Matching Factor and the Model at Third Resonance (Conical,  $h/a = 10^6$ )

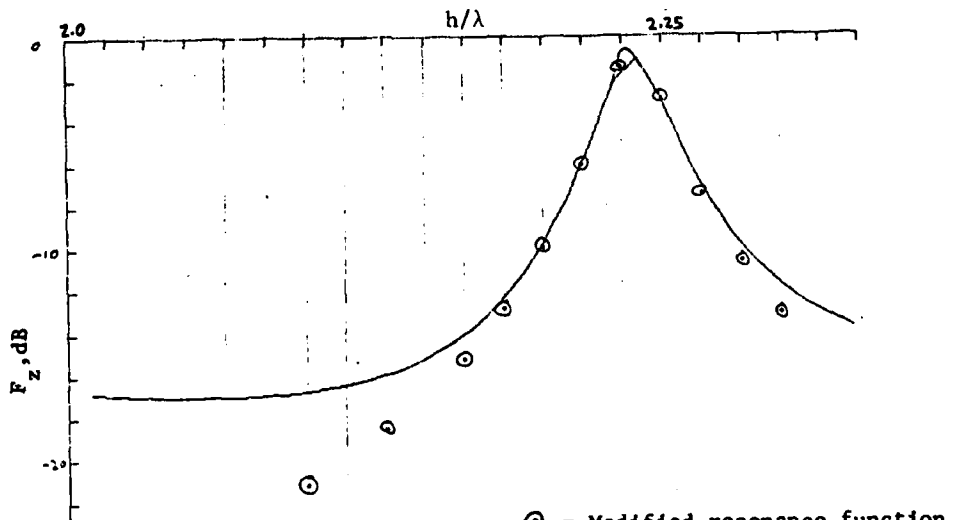
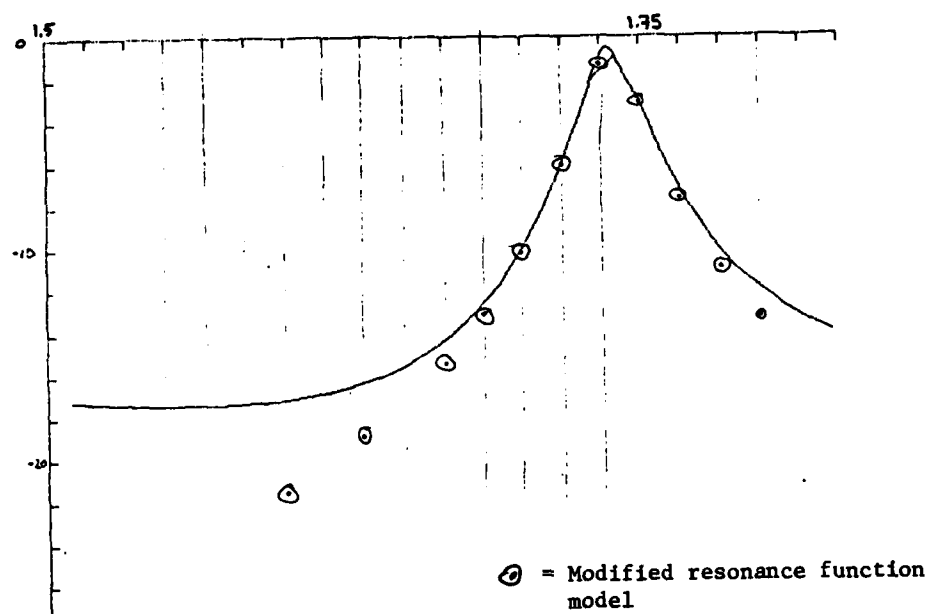
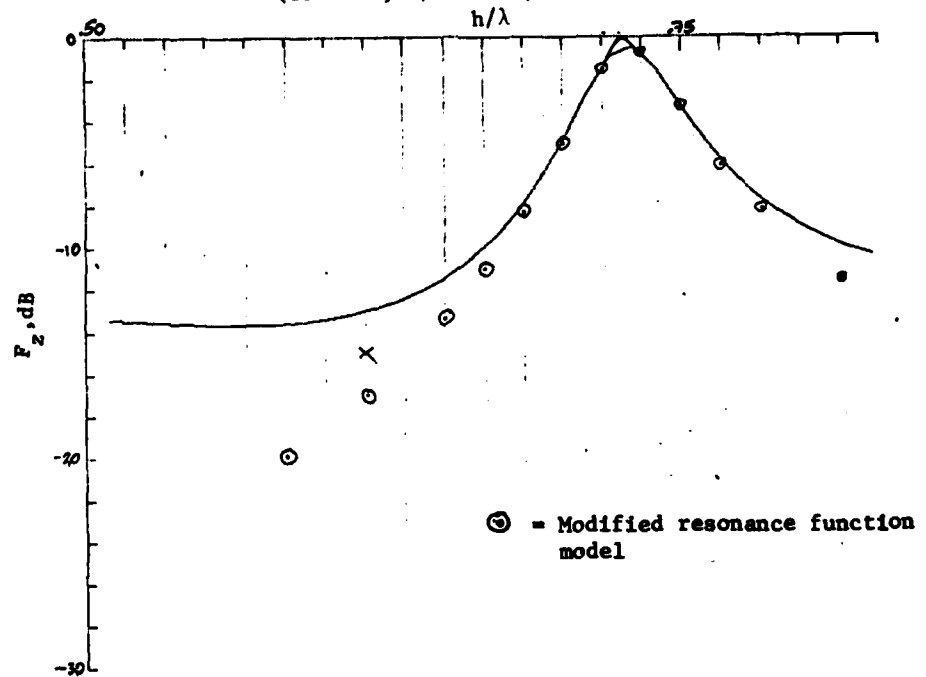
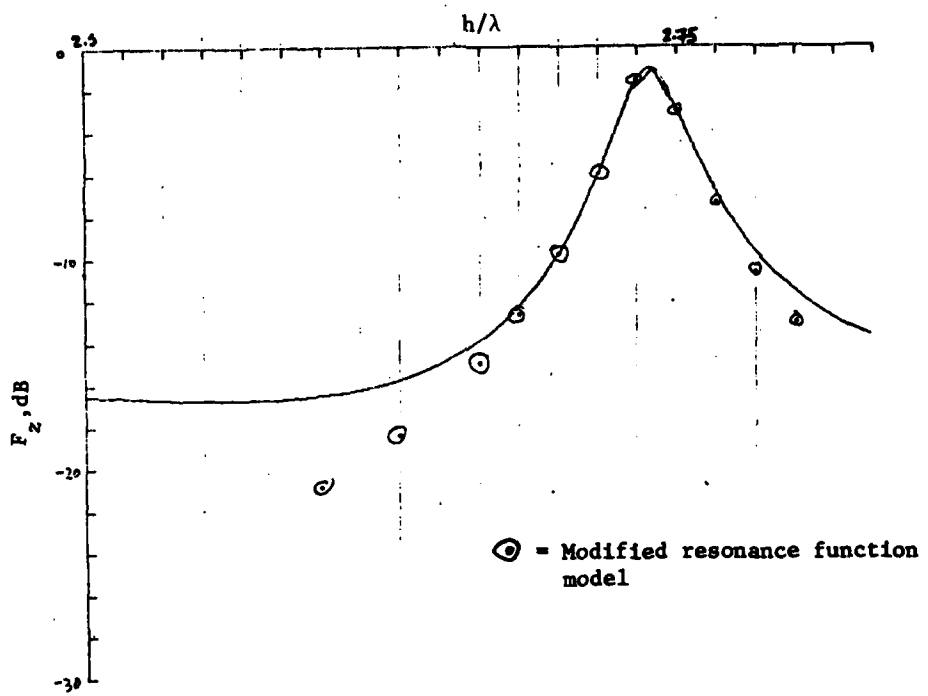


Figure 2-72 Comparison Between Theoretical Impedance Matching Factor and the Model at Fourth Resonance (Conical,  $h/a = 10^6$ )



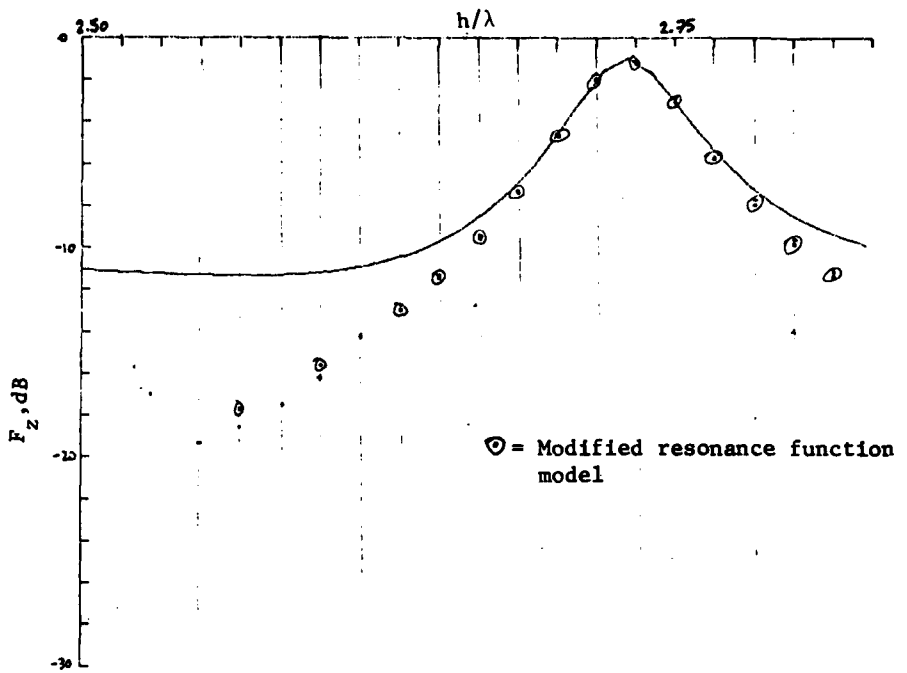


Figure 2-76 Comparison Between Theoretical Impedance Matching Factor and the Model at Sixth Resonance  
(Conical,  $h/a = 1,000$ )

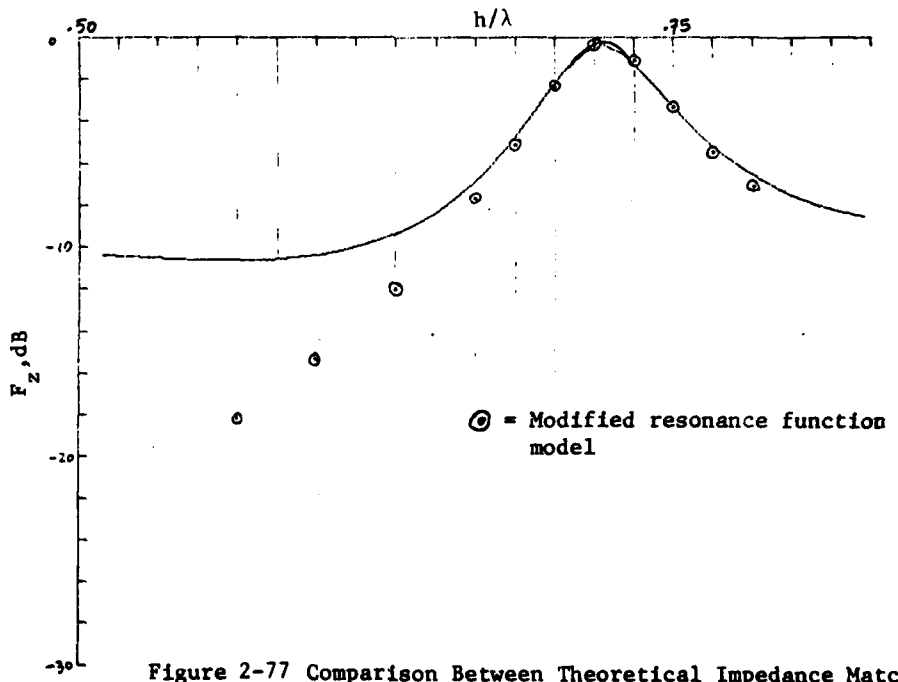


Figure 2-77 Comparison Between Theoretical Impedance Matching Factor and the Model at Second Resonance  
(Conical,  $h/a = 100$ )

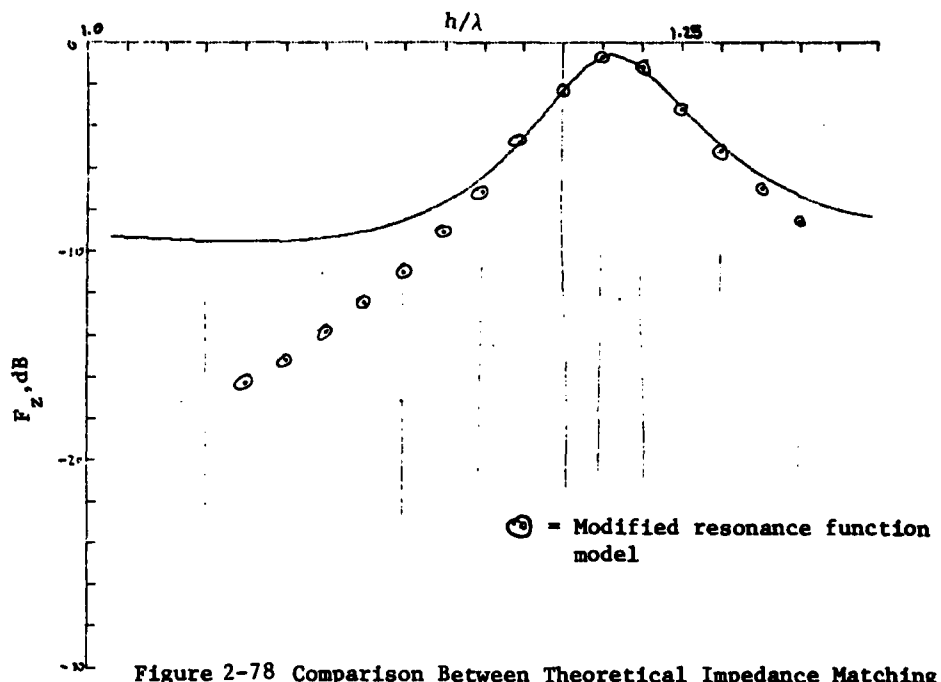


Figure 2-78 Comparison Between Theoretical Impedance Matching Factor and the Model at Third Resonance  
(Conical,  $h/a = 100$ )

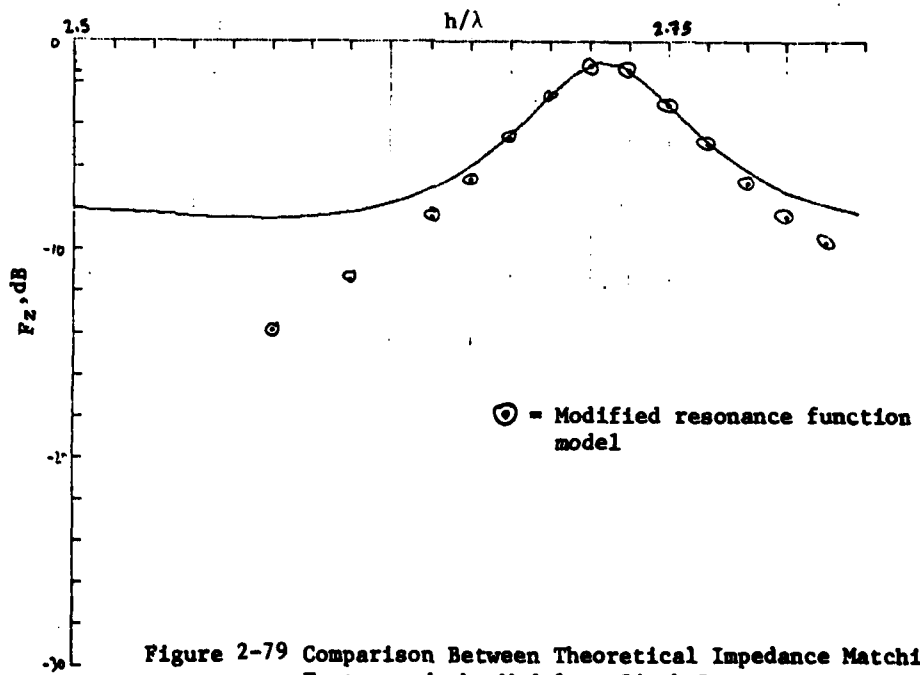


Figure 2-79 Comparison Between Theoretical Impedance Matching Factor and the Model at Sixth Resonance.  
(Conical,  $h/a = 100$ )

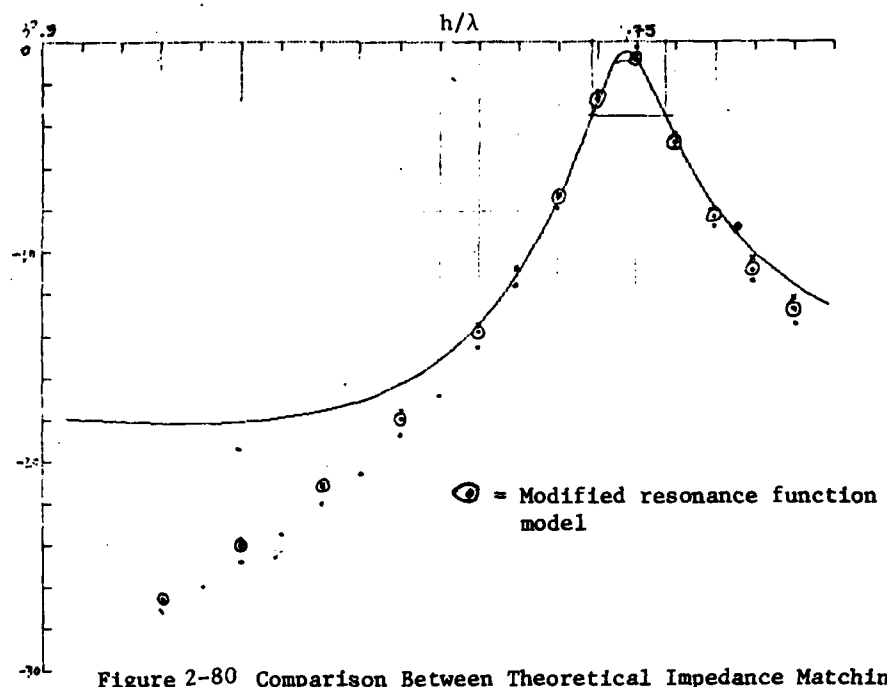


Figure 2-80 Comparison Between Theoretical Impedance Matching Factor and the Model at Second Resonance (Cylindrical,  $h/a = 10^6$ )

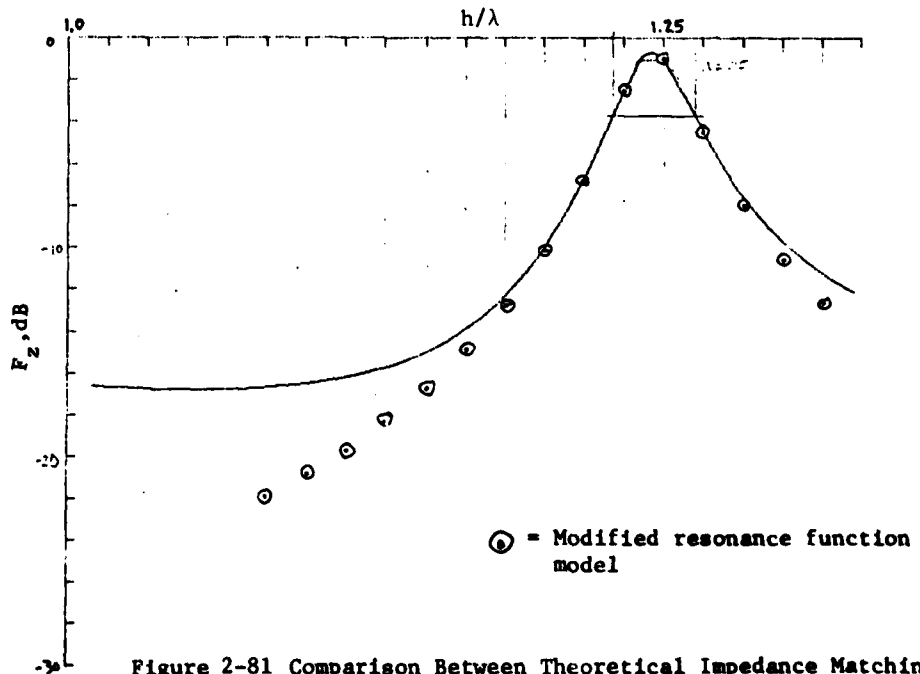
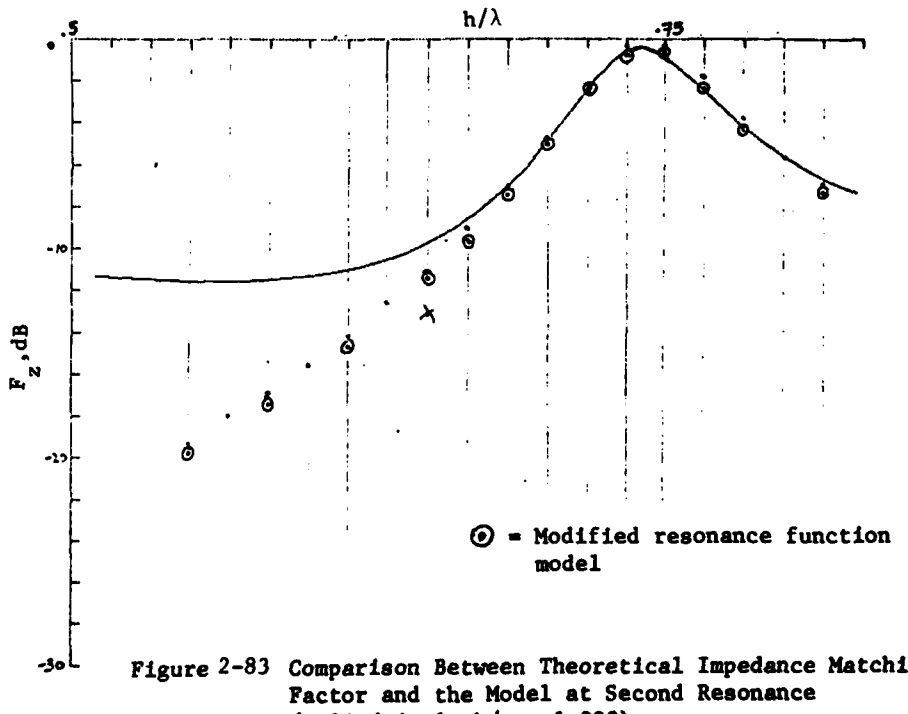
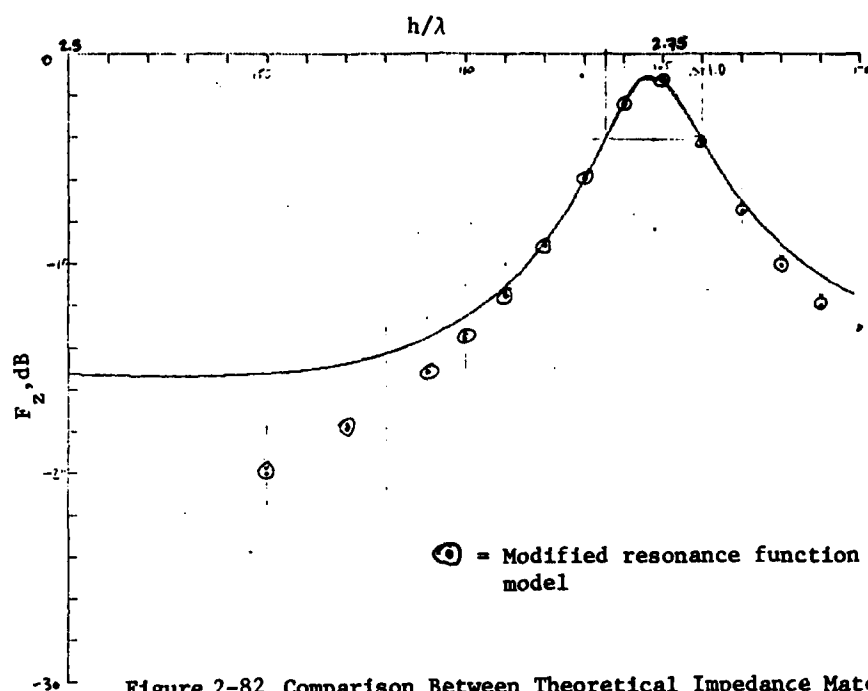
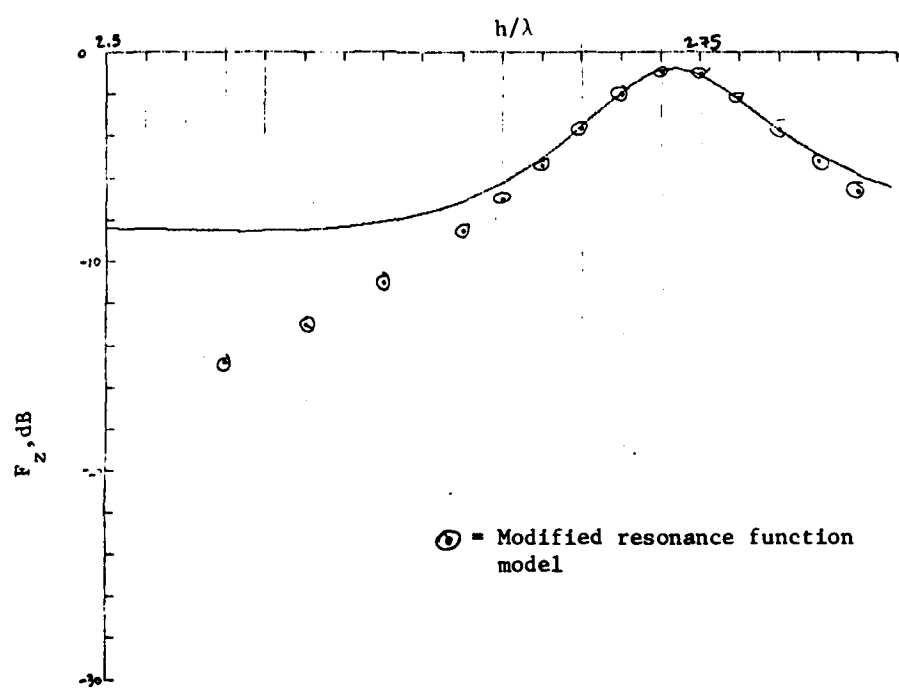
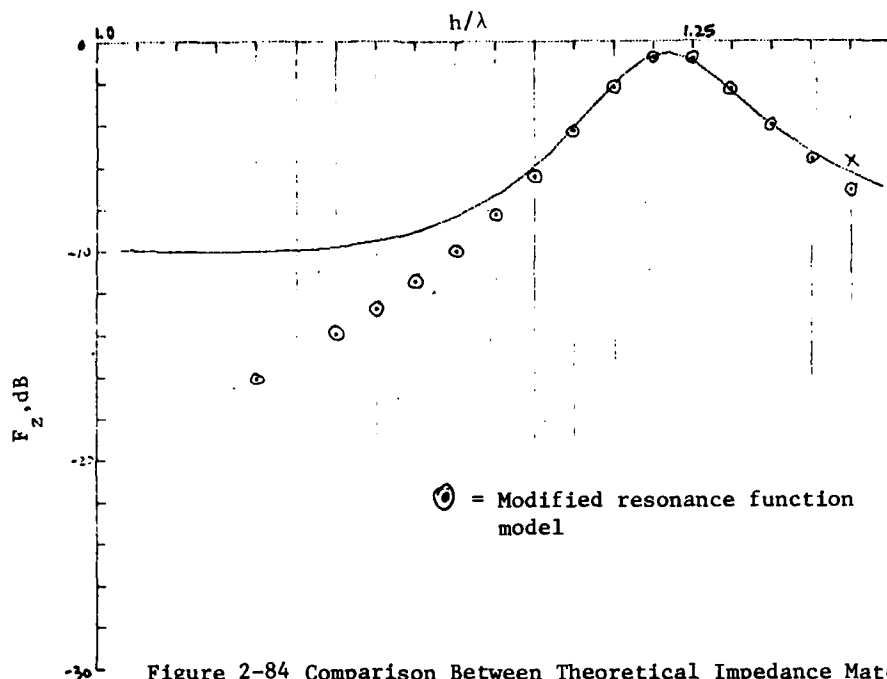


Figure 2-81 Comparison Between Theoretical Impedance Matching Factor and the Model at Third Resonance (Cylindrical,  $h/a = 10^6$ )





Composite plots of model curves for the first six resonant peaks are shown in Figure 2-86 for a high-Q dipole and in Figure 2-87 for a low-Q dipole. The most significant aspect seen in these figures is the inability of the model function to model the null regions well between resonant peaks. This must be handled with a separate function. It is noted that the first resonant peak is modeled best. In particular, the upper skirt of the first peak is modeled better than that of any higher order peak. It may be desirable to apply the model function to the higher peaks by shifting the origin of the model curve upward in frequency from the first peak. This could improve modeling of the upper skirt of each peak, but it appears that agreement with the lower skirt would suffer.

It has been demonstrated that the modified universal resonance function appears to provide a reasonable model for the first six resonant peaks of  $F_Z$  for an ideal dipole. The model function must be applied independently to each peak with a specific center frequency and bandwidth or Q. In order to accomplish this, it is necessary to determine apparent functional relationships between the resonant frequencies and bandwidths of higher order peaks given the center frequency and bandwidth of the first resonant peak for high and low Q dipole antennas. The data presented in Table 2-1 were examined in detail to develop these relationships.

a. Resonant Frequencies

Let  $f_n$  and  $Q_n$  ( $n=1,2,3\dots$ ) denote the resonant frequency and Q of the nth resonant peak, respectively. The differences between successive resonant frequencies for each antenna type given in Table 2-1 were calculated. These differences divided by  $f_1$  were found to be constant for the higher order resonances of each antenna. Consequently, an expression giving the nth resonant frequency in terms of the normalized frequency separation  $A = (f_i - f_{i-1})/f_1$  is

$$f_n = f_1[1 + (n-1)A],$$

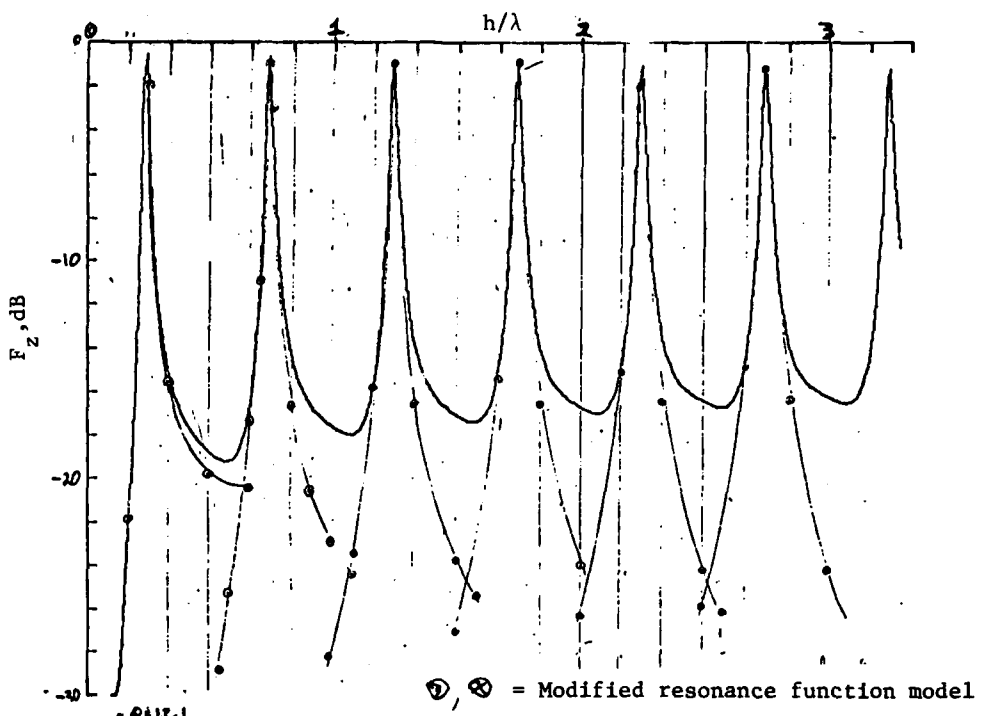


Figure 2-86 Comparison Between Theoretical Impedance Matching Factor and the Model at First Six Resonances (Conical,  $h/a = 10^6$ )

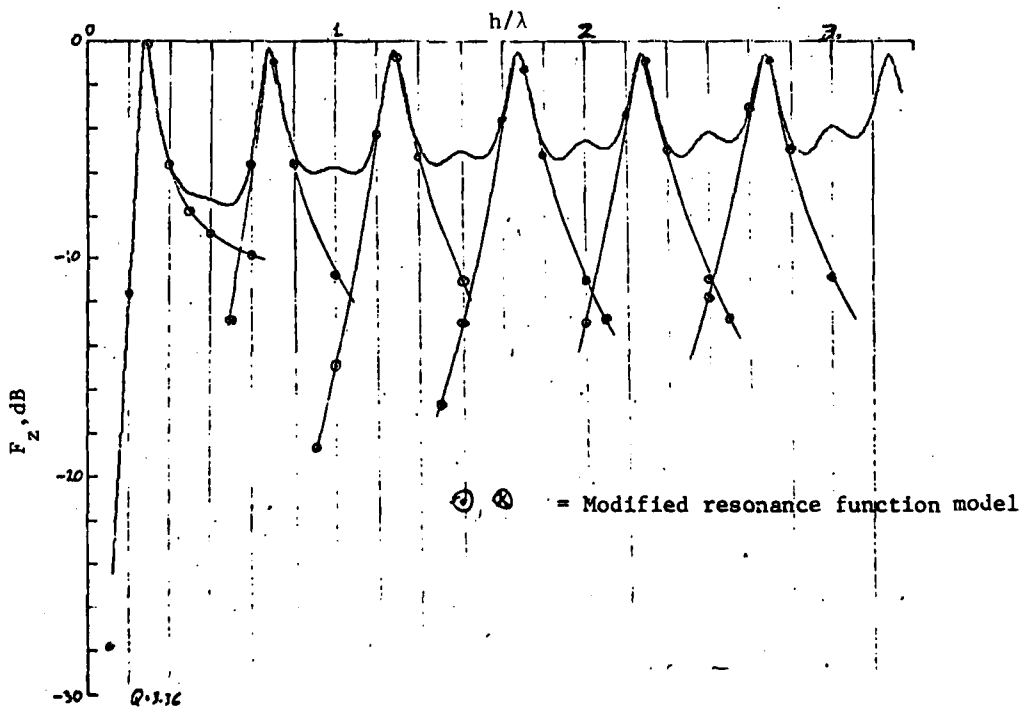


Figure 2-87 Comparison Between Theoretical Impedance Matching Factor and the Model at First Six Resonances (Cylindrical,  $h/a = 100$ )

<u>Antenna</u>	<u>Normalized Spacing, A</u>
CONICAL ( $10^6$ )	2.11
CONICAL (1,000)	2.21
CONICAL (100)	2.295
CONICAL (20)	2.395
CYLINDRICAL ( $10^6$ )	2.03
CYLINDRICAL (1,000)	2.05
CYLINDRICAL (100)	2.065

These values indicate that, in general, the relative spacing between resonant peaks is slightly more than twice the first resonant frequency. Since  $A$  decreases with increasing antenna  $Q$  (of the first resonance) for the conical and cylindrical dipoles considered separately,  $A$  was plotted against  $\log Q_1$  as shown in Figure 2-88. The values of  $A$  are significantly different for the two types of dipoles. The reason for this is unknown at this time, and it will be necessary to accept the spread in the values of  $A$  for a specified  $Q_1$ .

Lest it be assumed that for a given  $Q_1$ , the value of  $A$  can range from 2.00 to the value given by the conical curve in Figure 2-88. An empirical curve fit to the conical values results in the following:

$$A = 2.00 + 1.82Q_1^{-1.115}$$

#### b. Bandwidths of Resonant Peaks

The 3-dB bandwidths given in Table 2-1 are shown plotted in Figure 2-89. Although the bandwidth values exist through the points in order to describe the functional relationship. As can be seen, the resonant bandwidths increase nearly linearly with log frequency.

These same data normalized to  $f_1$  (first resonant frequency) for each antenna are listed in Table 2-2 and plotted in Figure 2-90. Since the curves appear to converge to a single point, it is possible to develop an expression to represent the curves given the bandwidth of the first resonance. This general function could be used for all monopole and dipole antennas since the only parameter required is the first resonant bandwidth. The independent variable is the center frequency of higher order resonances. As shown in (a) above, these frequencies cannot be predicted precisely for any given antenna,

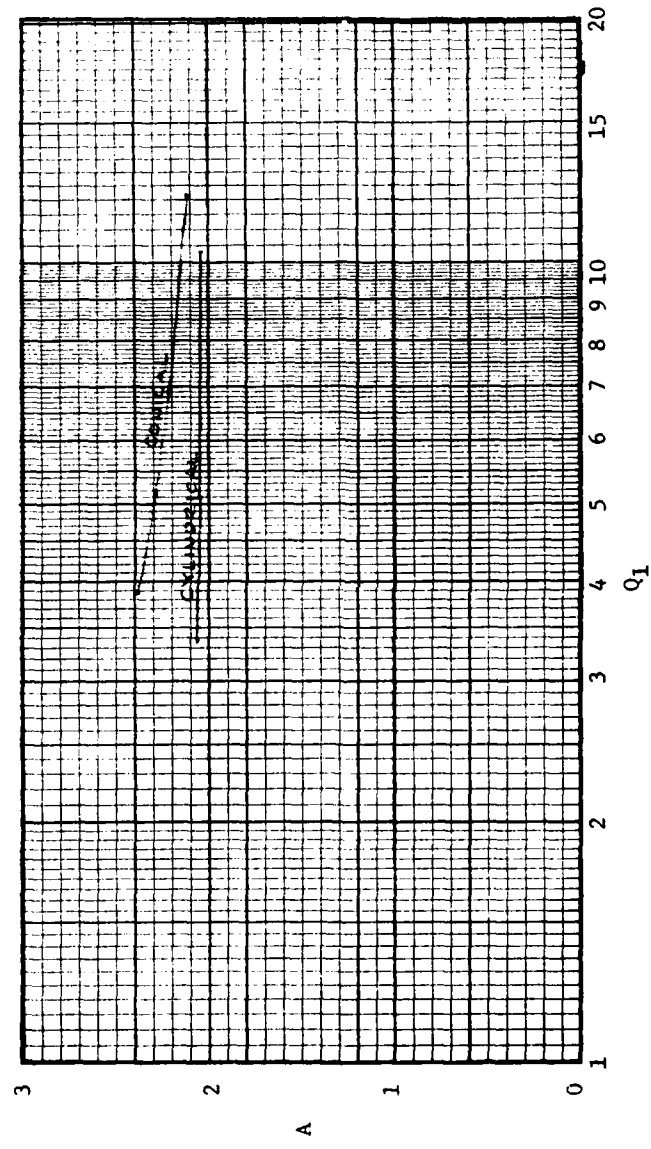


Figure 2-88 Normalized Frequency Separation A Between Resonant Peaks Vs Q  
Of First Resonance

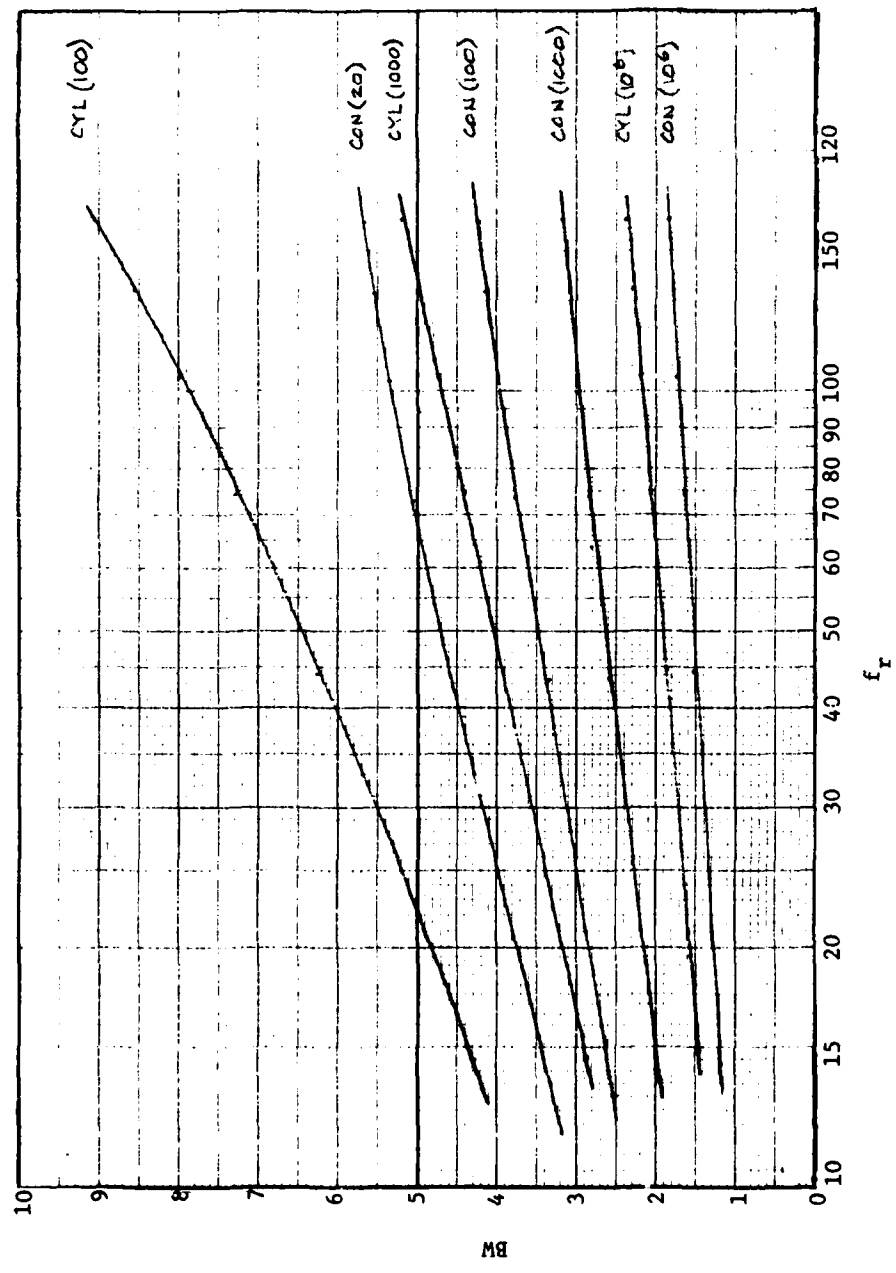


Figure 2-89 3 dB Bandwidth of Resonant Peaks Vs. Resonant Frequency for dipoles

Table 2-2  
Normalized Resonant Frequencies and Bandwidths

<u>Antenna</u>	<u>Peak No.</u>	$f_n/f_1$	$BW/f_1$
CON( $10^6$ )	1	1.00	.0826
	2	3.12	.1056
	3	5.23	.1154
	4	7.34	.1217
	5	9.45	.1265
	6	11.56	.1296
CON( $10^3$ )	1	1.00	.1449
	2	3.21	.1904
	3	5.42	.2081
	4	7.63	.2191
	5	9.84	.2272
	6	12.04	.2331
CON(100)	1	1.00	.1944
	2	3.30	.2622
	3	5.59	.2873
	4	7.88	.3034
	5	10.16	.3140
	6	12.45	.3224
CON(20)	1	1.00	.2574
	2	3.40	.3625
	3	5.79	.4016
	4	8.18	.4239
	5	10.58	.4398
	6	12.97	.4518
CYL( $10^6$ )	1	1.00	.0968
	2	3.03	.1259
	3	5.06	.1401
	4	7.09	.1490
	5	9.12	.1557
	6	11.15	.1618
CYL( $10^3$ )	1	1.00	.1962
	2	3.05	.2682
	3	5.11	.3018
	4	7.16	.3244
	5	9.22	.3416
	6	11.28	.3553
CYL(100)	1	1.00	.2976
	2	3.06	.4332
	3	5.13	.5038
	4	7.20	.5529
	5	9.27	.5924
	6	11.34	.6256

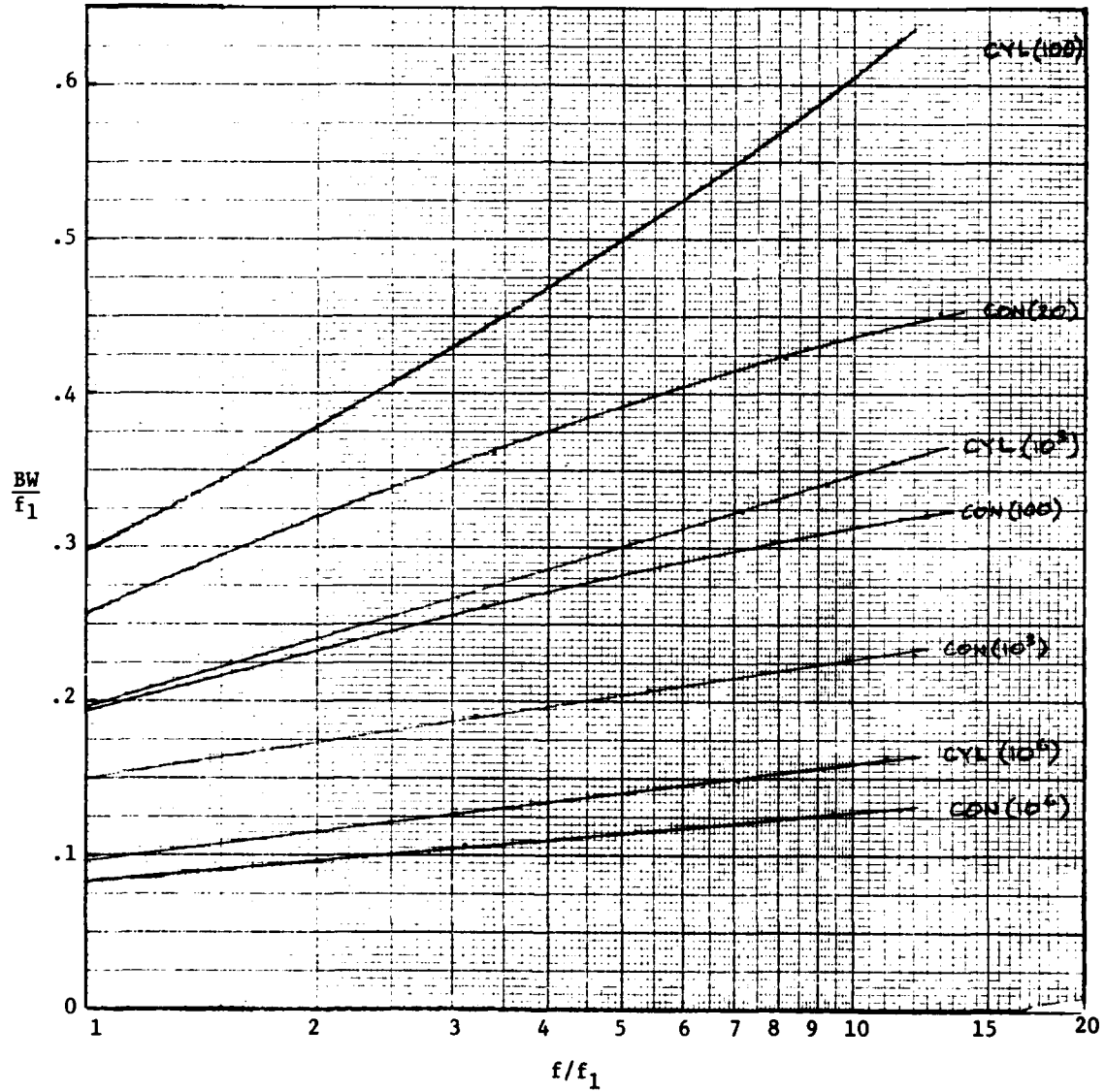


Figure 2-90 Normalized Bandwidth of Resonant Peaks Vs. Normalized Resonant Frequency of Dipoles

but have a range of values based on A ranging from 2.00 to the value given by the expression in (a). Modeling the higher order resonances while taking into account this spread in resonant frequencies is accomplished as follows. The bandwidth of any resonant peak must be increased by an amount equal to the spread of possible resonant frequencies for the peak. In this manner the modeled bandwidth contains the bandwidth of a resonant peak occurring at any frequency within the assumed range. Figure 2-91 illustrates this process. Curve A represents a resonant peak occurring at frequency  $f_a$  calculated with  $A = 2.00$ . Curve B represents the same resonant peak occurring at frequency  $f_b$  calculated with the upper limit of A. The 3-dB bandwidth BW is assumed the same for both peaks. Since the 3-dB level of the resonance curve can range between frequencies  $f_l$  and  $f_h$ , the bandwidth  $BW'$  of the model peak is set equal to this range. The resulting curve is therefore wider (of lower Q) than the theoretical curve but provides worst-case protection of the impedance matching factor for an IEMCAP analysis.

These calculations have been performed using the data in Tables 2-1 and 2-2 for the conical dipoles. The resulting values in Tables 2-3. The Q of each model peak has also been calculated and is shown plotted as a function of normalized resonant frequency in Figure 2-92. This figure, then, shows the family of curves to be used by the model to provide the Q of a resonant peak at any given normalized frequency for a specified Q of the first resonant peak.

An empirical expression has been developed to fit the curves in Figure 2-92. Each of the lines is assumed to be straight, and their slightly different slopes are assumed to be the same. The expression is of the form

$$y = mx+b$$

where

$$y = \log Q$$

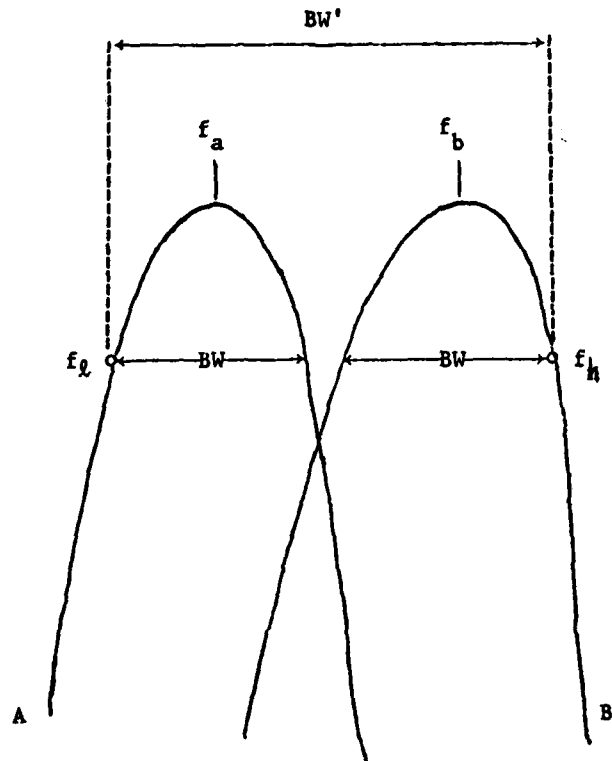
$$m = 0.115$$

$$x = \log \left( \frac{f_n}{f_1} \right)$$

$$b = \log Q_1.$$

The complete expression is

$$\log Q_n = 0.115 \log \left( \frac{f_n}{f_1} \right) + \log Q_1$$



$$\begin{aligned}
 f_a &= 2n-1 \\
 f_b &= 1+(n-1)(2+1.82Q_1^{-1.115}) \\
 f_l &= 1/2(-BW + \sqrt{BW^2 + 4f_a^2}) \\
 f_h &= 1/2(BW + \sqrt{BW^2 + 4f_b^2}) \\
 BW' &= BW + (f_b - f_a) \\
 f_r &= \sqrt{f_l f_h}
 \end{aligned}$$

Figure 2-91 Illustration of Normalized Bandwidth Spread

Table 2-3  
Bandwidth Spread\*

Antenna	Peak No	BW	$f_b - f_a$	BW'	$f_n$	$Q_n$ **
$CON(10^6)$ ( $Q_1 = 12.10$ )	2	.1056	.1129	.2185	3.055	13.98
	3	.1154	.2258	.3412	5.110	14.98
	4	.1217	.3388	.4605	7.166	15.56
	5	.1265	.4517	.5782	9.221	15.95
	6	.1296	.5646	.6942	11.277	16.24
$CON(10^3)$ ( $Q_1 = 6.89$ )	2	.1904	.2116	.4020	3.101	7.71
	3	.2081	.4231	.6312	5.203	8.24
	4	.2191	.6347	.8538	7.306	8.56
	5	.2272	.8463	1.0735	9.408	7.76
	6	.2331	1.0579	1.2910	11.511	8.92
$CON(100)$ ( $Q_1 = 5.15$ )	2	.2622	.2927	.5549	3.137	5.65
	3	.2873	.5854	.8727	5.277	6.05
	4	.3034	.8781	1.1815	7.417	6.28
	5	.3140	1.1708	1.4848	9.558	6.44
	6	.3224	1.4634	1.7858	11.699	6.55
$CON(20)$ ( $Q_1 = 3.89$ )	2	.3625	.4002	.7627	3.182	4.17
	3	.4016	.8004	1.2020	5.370	4.47
	4	.4239	1.2006	1.6245	7.560	4.65
	5	.4398	1.6008	2.0406	9.750	4.78
	6	.4518	2.001	2.4528	11.940	4.87

\* Values are normalized to  $f_1$ .

$$** Q_n = \frac{f_n}{BW'}$$

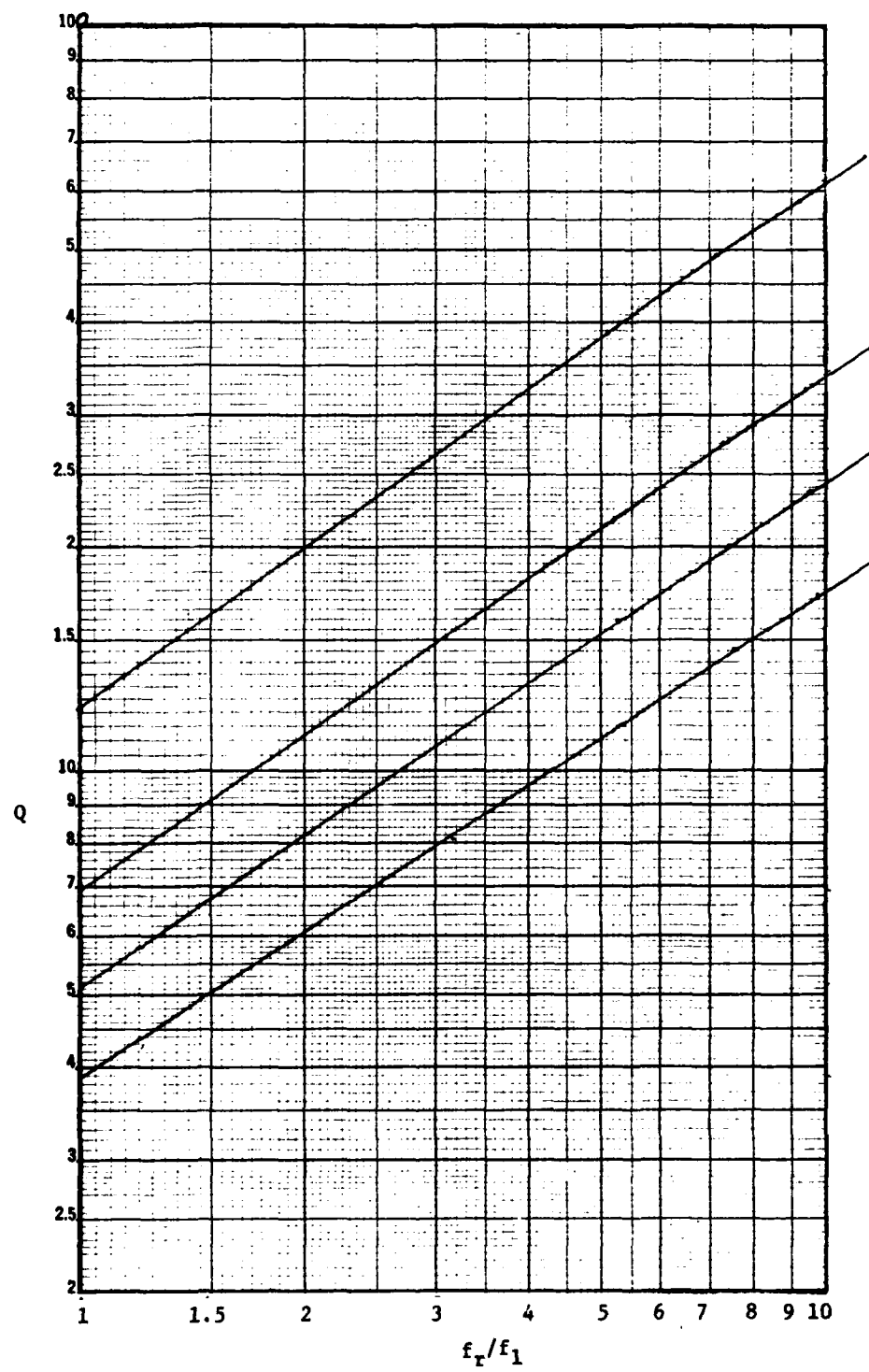


Figure 2-92 Q of Spread Resonant Peak Vs Normalized Resonant Frequency

The normalized frequencies at which the higher order resonances occur, given in Table 2-3, have also been generalized. The frequency differences between successive peaks have been calculated for each antenna case in Table 2-3 and are remarkably constant for each antenna. The average differences, corresponding to A described in Figure 2-88, are the following:

$Q_1$ of First Resonance	A
12.10	2.055
6.89	2.102
5.15	2.140
3.89	2.188

An empirical curve fit to these values is the following:

$$A = 2 + 0.8178 Q_1^{-1.083}$$

This expression is to be used in the model to provide the nth resonant frequency  $f_n$ .

$$f_n = f_1 [1 + (n-1)A]$$

Thus, for given values of  $f_1$  and  $Q_1$  of the first resonant peak of any simple monopole or dipole antenna, the resonance curves are defined by the above three expressions for resonant peaks of order n.

c. Decay of Resonant Peaks with Frequency

The theoretical curves of impedance mismatch factor as shown in Figures 2-3 through 2-19 generally indicate a rather slow decay or fall-off of the resonant peaks with frequency. This decay is too slight to be significant and is ignored in the model.

The Smith chart plots of these data (Figures 2-20 through 2-39) generally indicate that the impedance contour spirals inward toward an asymptotic point near the dashed circle or 3-dB loss level. Consequently, the peak decay would eventually drop to no more than about -3 dB, which is not a significant level for modeling this feature of the impedance mismatch factor. Further, measured data indicate very little decay of higher order resonances, as will be shown.

d. Null Depth

The minimum impedance mismatch factor occurring between resonant peaks is an important feature to be included in the model. Two aspects of null depth are evident. First, the depth of the first null (between first and second resonance) must be defined, and second, the decay of null depth with frequency should also be defined.

The depth of the first null is shown plotted against  $\log Q_1$  in Figure 2-93 for each case of the conical and cylindrical dipoles. As can be seen, the relationship is nearly linear. A curve fit to the cylindrical data line gives the following:

$$F_Z = 3.6 - 21.1 \log Q_1$$

The relationship of the higher order nulls is an exponential decay with log frequency. The theoretical values of null depth for the conical ( $h/a = 10^6$ ) dipole (Figure 2-3) were used to examine the null decay. An empirical fit to these data points gives the relationship

$$F_Z = -3 - 13.9 \left( \frac{h}{\lambda} \right) - 0.124$$

A more desirable form of this relationship is an exponential form given by

$$F_Z = -3 - 16.53 \epsilon^{-0.288(\log f/f')}$$

where  $f'$  = frequency at which  $h=\lambda/4$ , and the logarithm is base 10.

For the present, the expressions for null depth will be given in general form with unspecified constants. It appears, after examining measured antenna data, that the null depth is not as much as the theory predicts and the decay rate is considerably greater than that given above. Apparently, null depth is sensitive to several aspects of real antennas which were not accounted for in the theoretical model, e.g., losses, imperfections at the feed point, nonaxial directed currents, and nonrotationally symmetric currents.

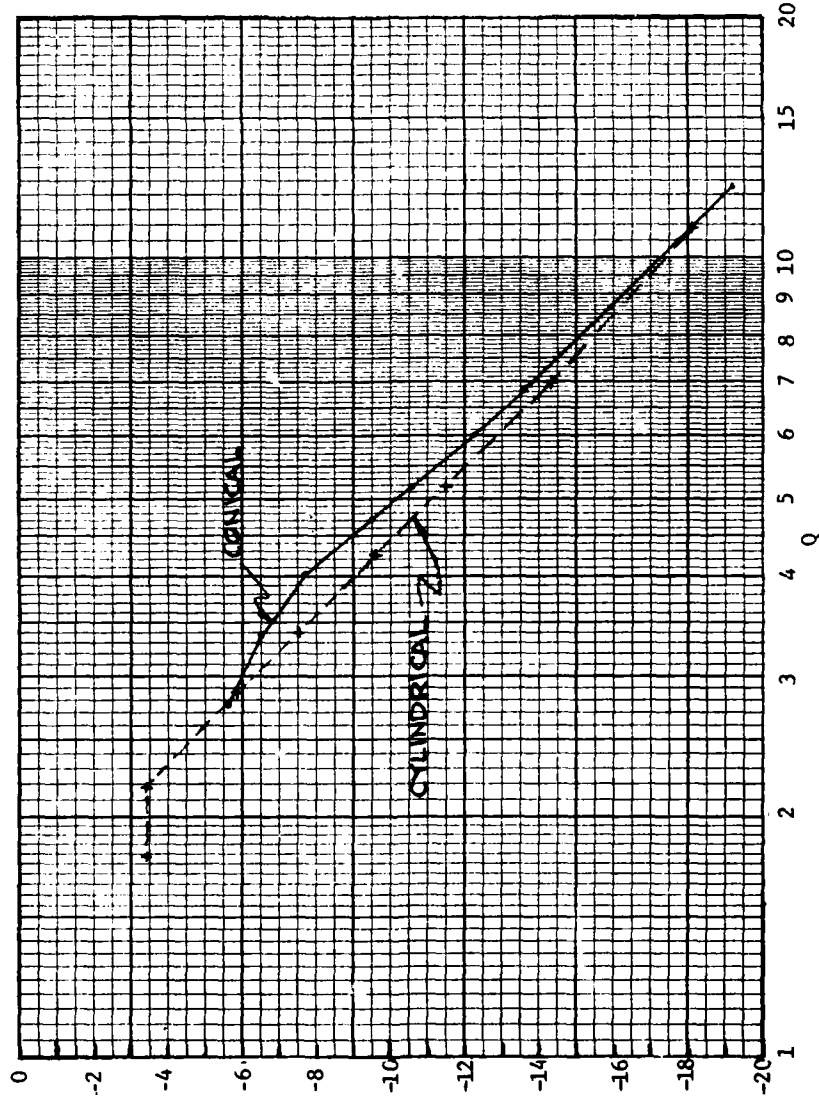


Figure 2-93 Depth of First Null of Impedance Mismatch Factor vs. Q of First Resonance for Dipoles

It is essential that the measured performance of antennas at out-of-band frequencies be studied during model development. Theoretical analyses of antennas generally do not predict performance characteristics very realistically, particularly at frequencies well outside the design band. The assumptions usually made in analyses minimize the error within the design band but often cause significant properties to be overlooked at frequencies out-of-band. The assumptions most commonly made are that the antenna is lossless, the current distribution is rotationally symmetric, and the current flow (in a linear antenna) is axial (the element is thin). The use of baluns with many antennas is commonplace: however, theoreticians seldom include baluns in their antenna models. Although a wide variety of balun designs exist for transforming an unbalanced line (e.g., coaxial cable) to a balanced line (e.g., dipole), they cannot be ignored as a part of the antenna. Wideband baluns, such as a transformer with primary and secondary windings, probably have the least effect on the out-of-band performance of antennas. Many baluns, however, are frequency selective and require tuning to the operating range of the antenna. These types of baluns are essentially transparent at frequencies in the design band, but they can have considerable effect on input impedance at frequencies outside the design band. Where a balun is used, it should be considered as being an integral part of the antenna and be included within the antenna terminals.

It should be clear that a balun is not principally a matching network for matching a reactive antenna impedance with 50 ohms. The majority of baluns transform 50-ohm unbalanced to 50-ohm balanced lines. Some baluns, however, do transform a 50-ohm impedance to some integral multiple of 50 ohms. The effects of matching networks are studied in the next section.

Unfortunately, measured out-of-band frequency data for antennas are very sparse in the technical journals. Figures 2-94 through 2-102 present curves of impedance matching factor derived from measured data for various types of single element resonant antennas. Several of the measurements were published, but most of the data were measured by ARC. The principal features to be derived from each of these results are described below.

AD-A114 752 ATLANTIC RESEARCH CORP. ALEXANDRIA VA  
INTRASYSTEM ANALYSIS PROGRAM (IAP) MODEL IMPROVEMENT. (U)  
FEB 82 T E BALDWIN, W G DUFF, J J FOSTER

F/6 20/3

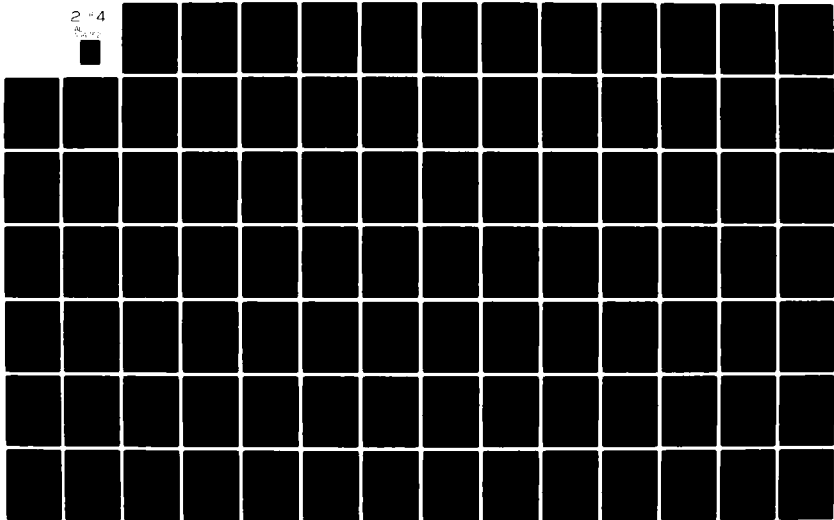
F30602-79-C-0169

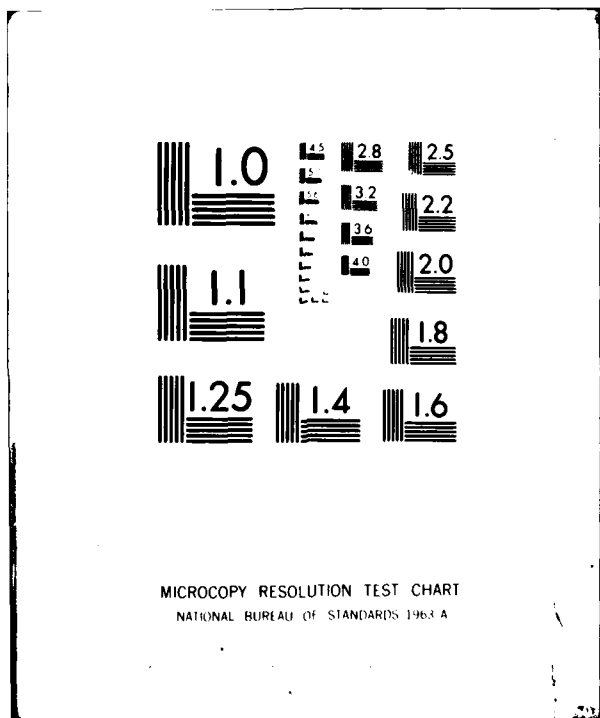
NL

UNCLASSIFIED

RADC-TR-82-20

2 4





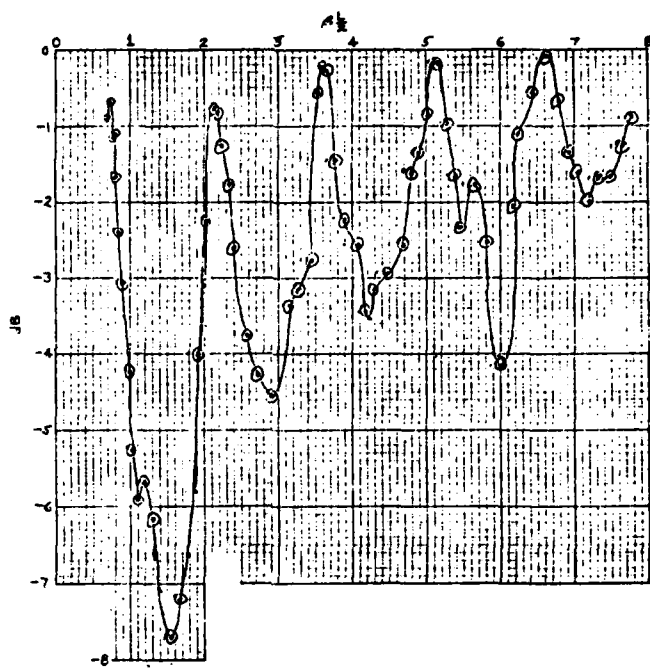


Figure 2-94 Impedance Matching Factor of 6-Inch Monopole  
(from measured data)

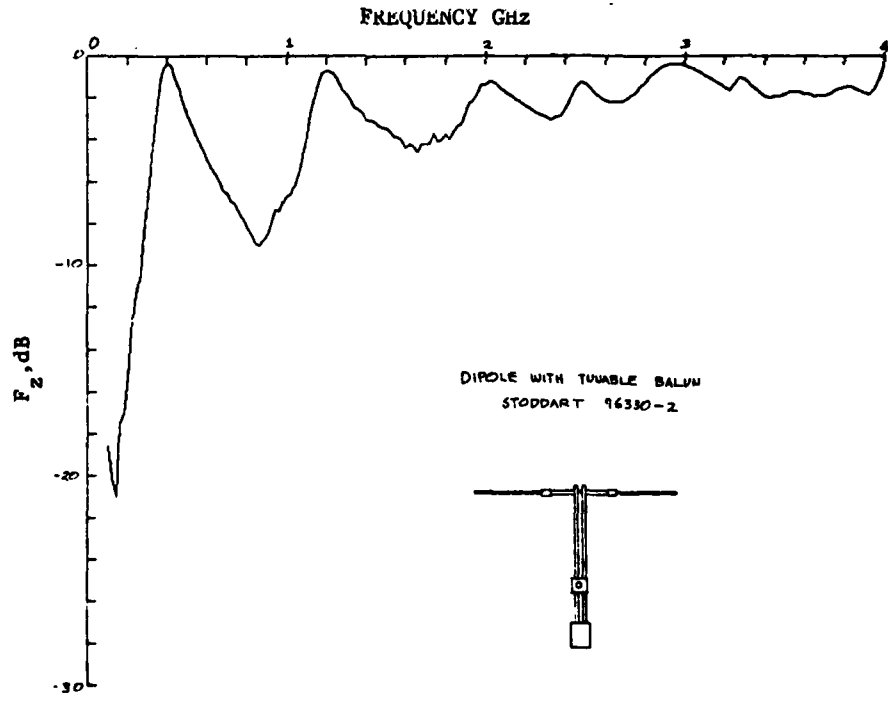


Figure 95 Impedance Matching Factor of Dipole with Tunable Balun  
(from measured data)

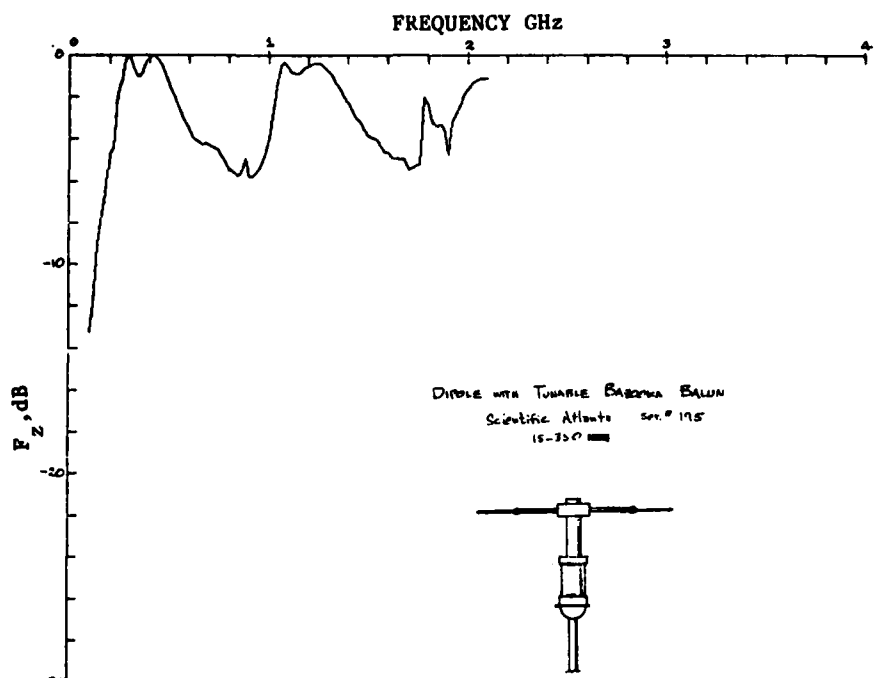


Figure 2-96 Impedance Matching Factor of Dipole With Tunable Bazooka Balun (from measured data)

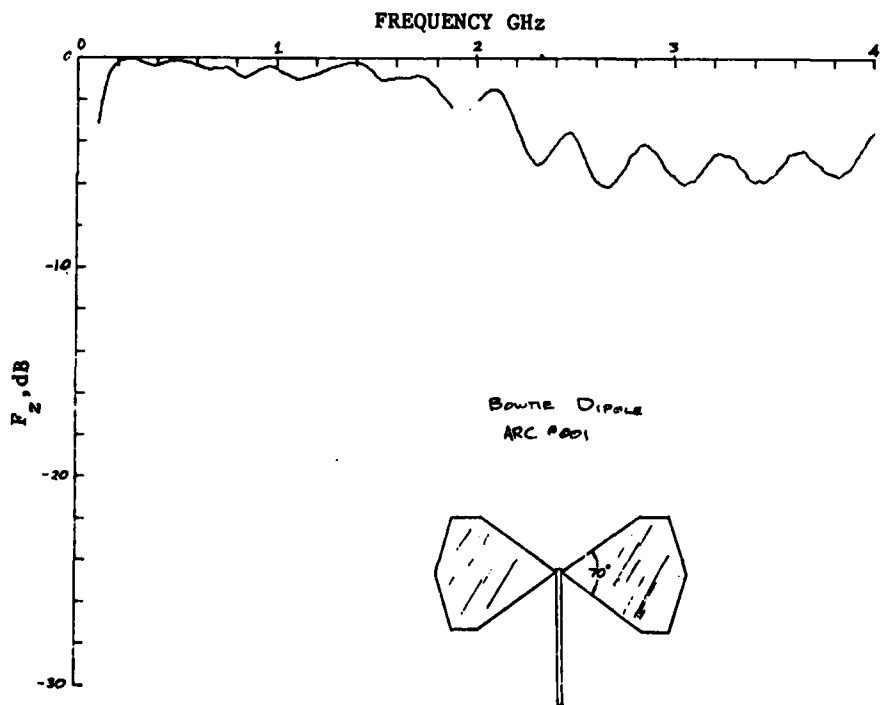


Figure 2-97 Impedance Matching Factor of Bowtie Dipole (from measured data)

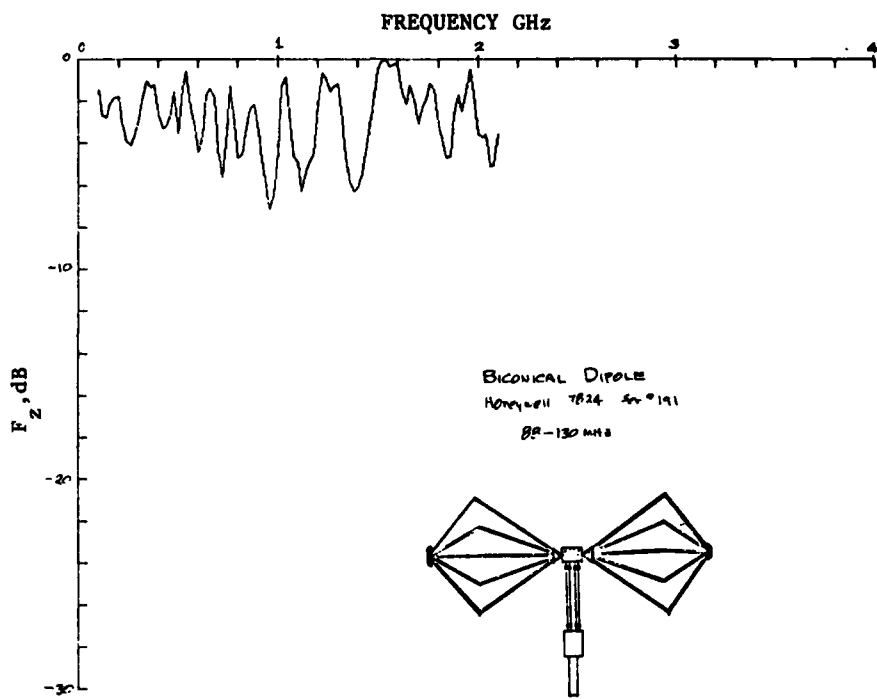


Figure 2-98 Impedance Matching Factor of Biconical Dipole  
(from measured data)

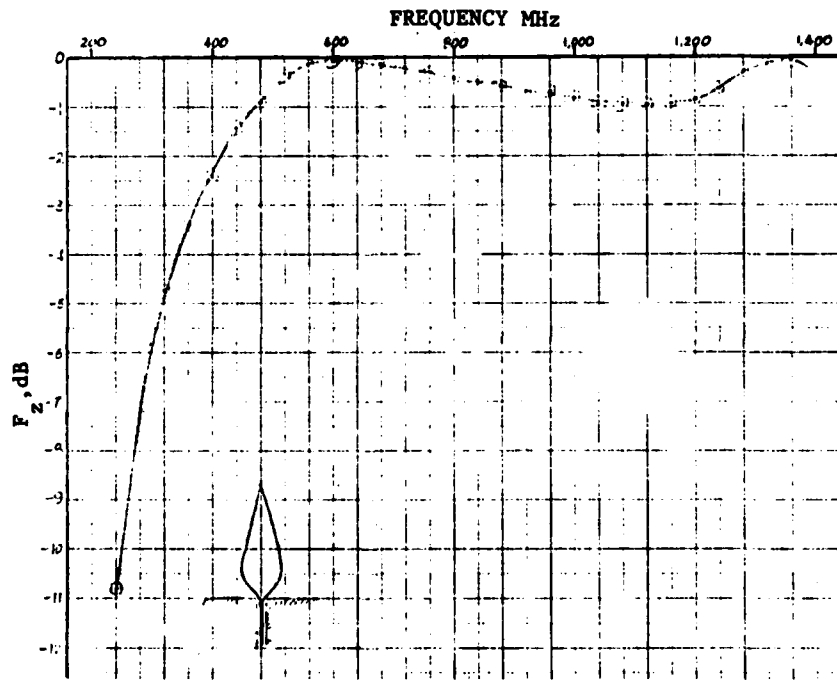


Figure 2-99 Impedance Matching Factor of a Duoconical Monopole  
(from measured data)

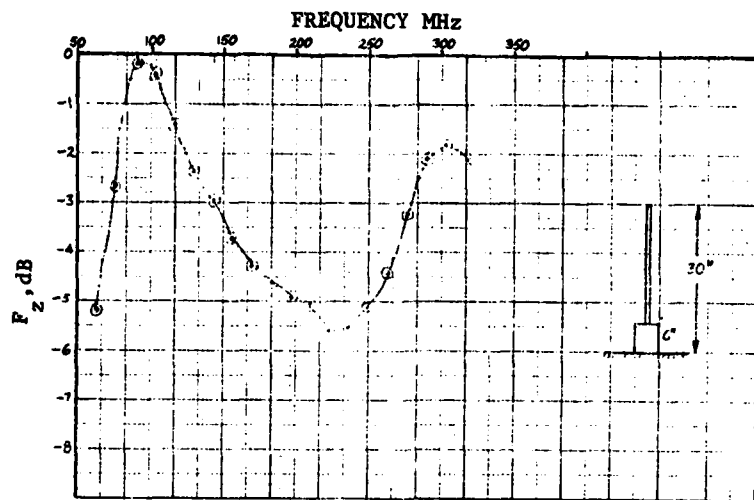


Figure 2-100 Impedance Matching Factor of a Sleeve Dipole  
(from measured data)

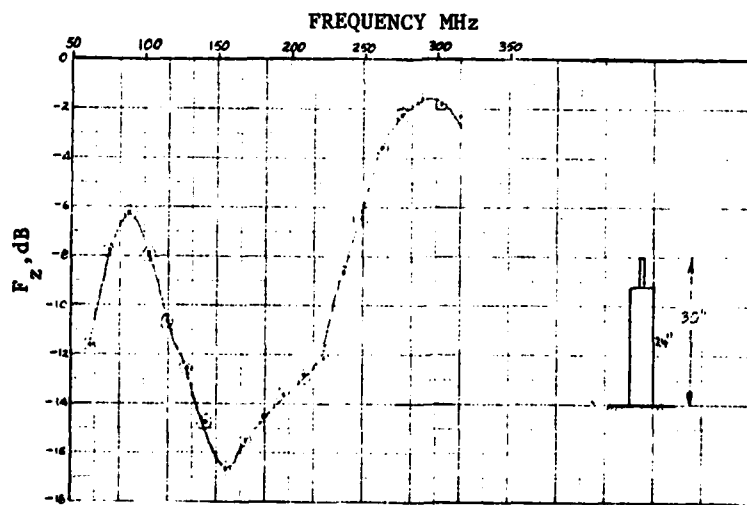
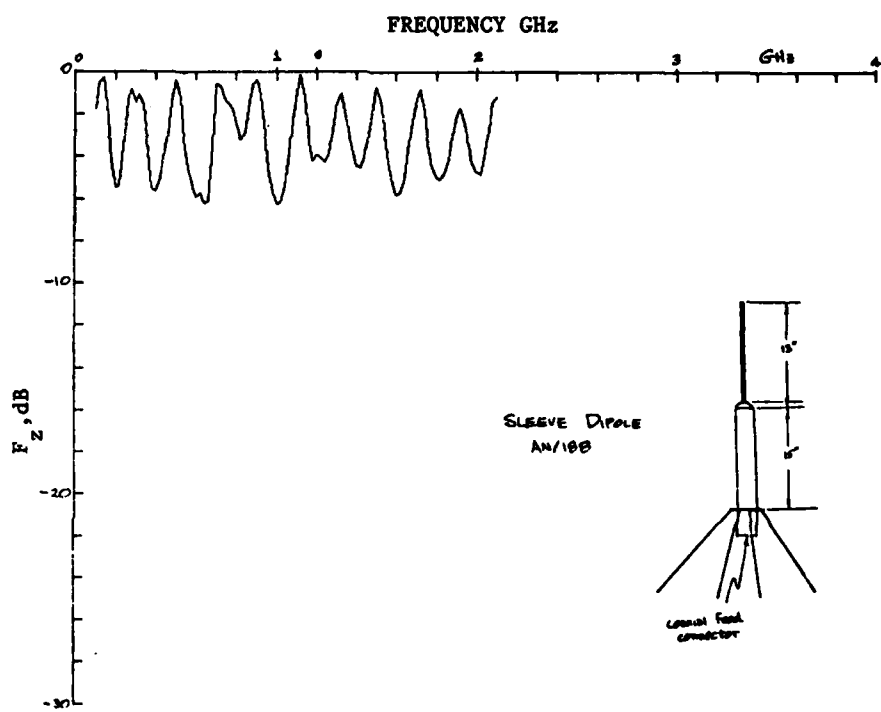


Figure 2-101 Impedance Matching Factor of a Sleeve Dipole  
(from measured data)



**Figure 2-102 Impedance Matching Factor of a Sleeve Dipole  
(from measured data)**

Figure 2-94 presents the impedance matching factor of a model cylindrical monopole 0.25" diameter and 6" high over a ground plane, giving an  $h/a$  ratio of 24. [3, pages 86, 87] Apparently, no feed circuitry or balun was required, as expected. The curve illustrates the predicted resonant peaks with a frequency spacing of about  $2.0f_1$ . Unfortunately, no data were taken below  $f_1$  to give a measure of  $Q_1$ . Comparing this curve with that of Figure 2-19 for a cylindrical dipole of  $h/a=20$ , the depth of the first null is nearly twice that predicted by the theory. The second, third and fourth nulls are that reasonably close to the theoretical depth of -4 dB. For the measured case, the resonant peaks rise with frequency, and secondary resonances appear as seen in the minor peak between the fourth and fifth resonant peak. It is suspected that the feed connection created some high frequency effects. In all, the antenna is not very lossy at any frequency shown above the first resonance to  $10f_1$ . The impedance matching factor tends to increase as the frequency increases.

Figure 2-95\* presents  $F_Z$  for a horizontal dipole having a tunable balun. The resonant frequency was set to 400 MHz. The second and third resonant peaks occur at the expected frequencies, but the behavior above the third peak is unpredictable. This is most likely due to the properties of the balun. Based on  $h/a$  ratio of 20 to 30 for this dipole, the depth of the first null is twice the theoretical value (see Figures 2-18 and 2-19). The depth of the second null agrees with theory. The  $Q$  of the second peak is nearly twice that of the first peak, which agrees with the theory.

Figure 2-96\* shows the  $F_Z$  curve of another small, horizontal dipole tuned for approximately 400 MHz. This dipole has a bazooka balun which is also tunable. The measurement, made only to  $5f_1$ , show the first and second resonant peaks. The behavior above the second peak is unpredictable. The null depths are deeper than theory would indicate, which is due probably to frequency selective properties of the balun.

---

\* Test antenna measured by ARC.

Figure 2-97\* presents  $F_Z$  of a broadband bow-tie (dipole) antenna having a broadband transformer-couple balun. Each element of the antenna is a flat piece of copper having the shape of the profile of a conical dipole with an apex angle of 70°. The design band was intended to be 180-600 MHz, but the curve indicates good impedance up to about 2 GHz. The shape of the  $F_Z$  curve for this antenna does not agree with the theory used and will require special considerations for modeling.

Figure 2-98\* presents the  $F_Z$  data for a commercial biconical dipole constructed of aluminum tubing in the form of a conical cage. The shape of the elements is more accurately described as being duoconical with the transition planes located about  $2/3 h$  from the center. This antenna contains a coiled-cable balun in the feed box. The design frequency range is 88-130 MHz. As can be seen  $F_Z$  is very erratic and does not appear to agree with theory. The cone angle is 70°. The maximum loss measured, however, was about 7 dB.

Figure 2-99 presents the results of an interesting study to design a broadband monopole. [4] The shape is duoconical with the transition plane at about  $.2\ell$  from the base. The transition corner was rounded to provide a smooth, teardrop shape. As can be seen, the antenna is remarkably good from 500 or 600 MHz to at least 1400 MHz. The shape of the curve does not agree with the results given for the conical or cylindrical types. This duoconical shape, however, is principally academic at this time, and does not appear to be used in practice.

Figure 2-100 and 2-101 show  $F_Z$  of two sleeve (monopole antennas, [5]) Both antennas have an overall height of 30 inches corresponding to the center conductor. The sleeves are 4 inches in diameter. The sleeve length is 6" for Figure 2-100 and 24" for Figure 2-101. In both cases it appears the first resonance occurs at  $\sim 2f_1$  as predicted for a monopole. The length of the sleeve apparently affects the relative amplitudes of the resonant peaks and the depth of the first null.

---

\* Test antenna measured by ARC.

Figure 2-102 illustrates  $F_Z$  for a commercially manufactured sleeve monopole. The overall height is 28 inches above a counter-poise. The height of the sleeve is 15 inches and is 3 inches in diameter. The curve shows a first resonant frequency at about 130 MHz. Higher order resonances, however, appear to occur at every odd multiple of 100 MHz all the way to 2100 MHz ( $f_{11}$ ). Thus, the higher order resonances are periodic based on a first resonant frequency of 100 MHz. The reason for the discrepancy between the 100 and 130 MHz resonance is not known. The null depths are erratic, but the maximum loss is less than 7 dB.

#### 2.4 Power Transfer Characteristics of a Dipole With a Matching Network

When a dipole or monopole operates at its natural resonant frequency, the terminal impedance is sufficiently close to the characteristic impedance of standard coaxial cables to permit the antenna to be connected directly to a cable with little loss due to reflected power. In many cases, however, a resonant type of antenna is required to operate at a frequency above or below its natural resonant frequency. As a result, the impedance of the antenna element is reactive and no longer matches the characteristic impedance of the transmission line. In order to minimize power transmission loss due to reflection at an impedance mismatch, a matching network is inserted into the line as close as possible to the antenna. A properly matched antenna prevents the reflection of power in either direction. For a transmitter, the network prevents power reflections back into the transmitter. For a receiving antenna, the matching network prevents power reflections back into space.

The function of a matching network may be viewed in different ways. The network is normally considered to be an impedance transformer that transforms the antenna or load impedance into the characteristic impedance of the connecting transmission line. It may also be viewed as a network which causes the antenna to appear to be resonant at the operating frequency and, thus, provide a non-reactive impedance which is adjusted to match the characteristic impedance of the transmission line. Consequently, matching networks are usually highly reactive and generally consist of low-loss inductances and/or capacitances. Since a matching network is resonant with its antenna at the matching frequency, currents and voltages within the network and

between the network cannot be avoided and are usually minimized with special construction techniques. Associated with a matched antenna is a Q of the circuit at the resonant or matched frequency. Thus, in general, the bandwidth and efficiency of a matched antenna is limited primarily by the properties of the matching network.

Because matching networks generally have a very significant effect on the frequency characteristics of the overall antenna impedance, any matching circuitry associated with an antenna should be considered as an integral part of the antenna. As with most commercially manufactured antennas that contain a matching circuit, the circuit is sealed within the antenna structure so that it is not possible to physically separate the network from the radiating elements of the antenna. The design and construction of such antennas is usually proprietary, and information relating to the individual components with the antenna structure is generally not available. The published specifications for the antennas which meet certain standard requirements are based on measurements of the terminal impedance of the total antenna/matching network/balun circuit. Consequently, the purpose of the present analysis is to determine characteristics of the transmission loss which appear to be common to a wide variety of matching conditions for purposes of modeling.

A very common design restraint for antennas is that they must be physically small. This is particularly true with aircraft antennas where the required dimensions of the antennas are often considerably less than one-half or one-fourth of a wavelength. This results in antenna elements which are electrically short and not capable of resonating at the required operating frequencies. Various techniques to lengthen the antenna electrically are usually applied, such as capacitive end loading or dielectric loading. Where these effects are insufficient to achieve natural resonance, the resulting impedance must be matched with appropriate circuitry to the standard characteristic impedance - e.g., 50 ohms - of transmission lines.

Consequently, matched antennas predominantly operate at frequencies below the natural resonant frequency of the antenna elements. As a result, the impedance of the antenna elements generally consists of a relatively small resistance and a large capacitive reactance. To match this impedance condition the matching network must contain at least one inductive reactance.

At radio frequencies reactive elements can be achieved either with lumped elements or with transmission line techniques (e.g., shorted stub, waveguide tuning techniques). In this report the frequency properties of dipole antennas matched by both methods are considered. Curves of the impedance matching factor for a wide range of frequencies outside the design range of the matched antenna are presented. The design frequency range of a matched antenna is the range over which the antenna (with its matching network) is designed to be reasonably well matched to the transmission line. All frequencies outside this range are considered to be out-of-band. Note that, in general, for a matched antenna, the natural resonant frequency of the antenna element is out-of-band.

## 2.5 Impedance Matching Characteristics of Antennas

### Matched with Lumped Elements

The simplest form of a matching network is an L-pad consisting of two reactive elements: one series and one shunt. Table 2-4 lists the six possible kinds of L-pads shown matching a capacitive load impedance  $Z_a = R_a + j X_a$ . The input impedance  $Z_{in}$  of the entire circuit is shown along with expressions giving values of the matching elements to provide  $Z_{in} = R_o$  at a resonant frequency corresponding to specified values of  $R_z$  and  $Z_a$  of resonance.

The transmission loss curves of dipole antennas for various matching conditions have been calculated. Schelkunoff's equations for the cylindrical dipole were used to provide the dipole impedance, and matching was modeled using Types I and II networks (shown in Table 2-4). A thin dipole ( $h/a=10^6$ ) and a fat dipole ( $h/a=20$ ) were studied for the matched frequencies corresponding to  $h/\lambda=0.1$ , 0.15, and 0.2, where the dipole has a natural resonance near  $h/\lambda=.25$ . The thin dipole was also studied at a matched length of  $h/\lambda=.23$ , which is slightly below the natural resonance of  $h/\lambda=0.246$ . The results are presented in Figures 2-103 through 2-116.

The numerical values used for each of the matching networks are listed in Table 2-5.

The lumped constants of the matching circuits were assumed to be ideal for this study.

Table 2-4 Two-Element Matching Networks For Antennas

I	<p><math>Z_a = R_a - jX_a</math> ASSUME <math>X_a</math> CAPACITIVE (<math>X_a &gt; 0</math>)</p>	$Z_{in} = \frac{R_a X_1}{R_a^2 + (X_a - X_1)^2}$ $+ j \left[ X_1 \frac{R_a^2 + X_a^2 - X_a X_1}{R_a^2 + (X_a - X_1)^2} + X_1 \right]$	$X_1 = \frac{X_a}{1 + \sqrt{\frac{R_a}{R_o}}}$	
II			$ X_1  = \frac{X_a}{\sqrt{\frac{R_a}{R_o}}}$	
III		$X_1, X_2 \begin{cases} > 0 \text{ IF INDUCTIVE} \\ < 0 \text{ IF CAPACITIVE} \end{cases}$		
IV			$X_1 = R_a \sqrt{\frac{R_o}{R_a}} - X_a$	
V		$Z_{in} = \frac{R_a X_2}{R_a^2 + (X_1 + X_2 - X_a)^2}$ $+ j X_2 \frac{R_a^2 + (X_1 - X_a)(X_1 + X_2 - X_a)}{R_a^2 + (X_1 + X_2 - X_a)^2}$		$ X_2  = \frac{R_o}{\sqrt{\frac{R_o}{R_a} - 1}}$
VI		$X_1, X_2 \begin{cases} > 0 \text{ IF INDUCTIVE} \\ < 0 \text{ IF CAPACITIVE} \end{cases}$	$X_1 = R_a \sqrt{\frac{R_o}{R_a}} - X_a$	

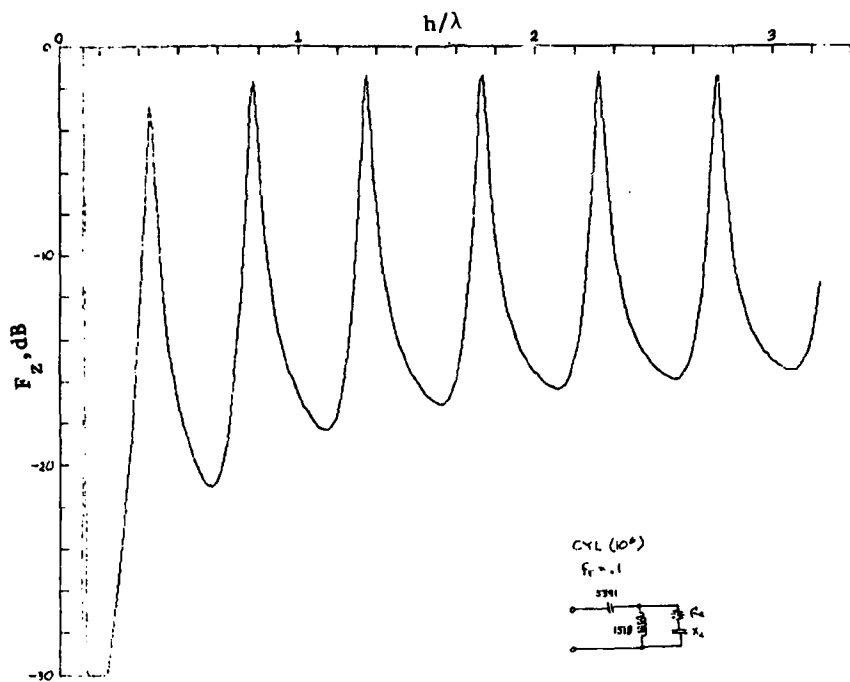


Figure 2-103 Impedance Matching Factor of Cylindrical Dipole  
( $h/a = 10^6$ ) Matched with LC Network for Resonance at  $.1 h/\lambda$

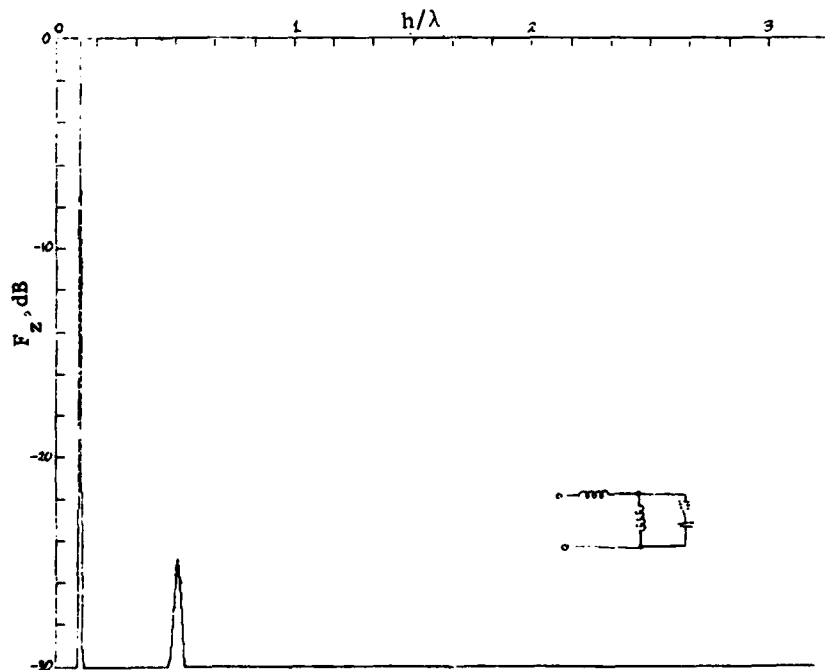


Figure 2-104 Impedance Matching Factor of Cylindrical Dipole  
( $h/a = 10^6$ ) Matched with LL Network for Resonance at  $.1 h/\lambda$

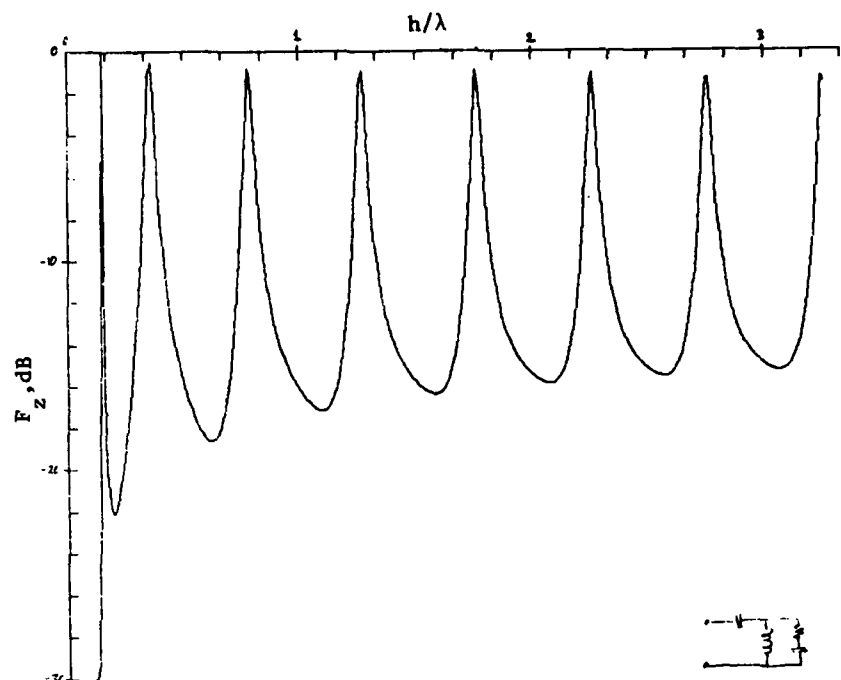


Figure 2-105 Impedance Matching Factor of Cylindrical Dipole  
( $h/a = 10^6$ ) Matched with LC Network for Resonance at  $.15 h/\lambda$

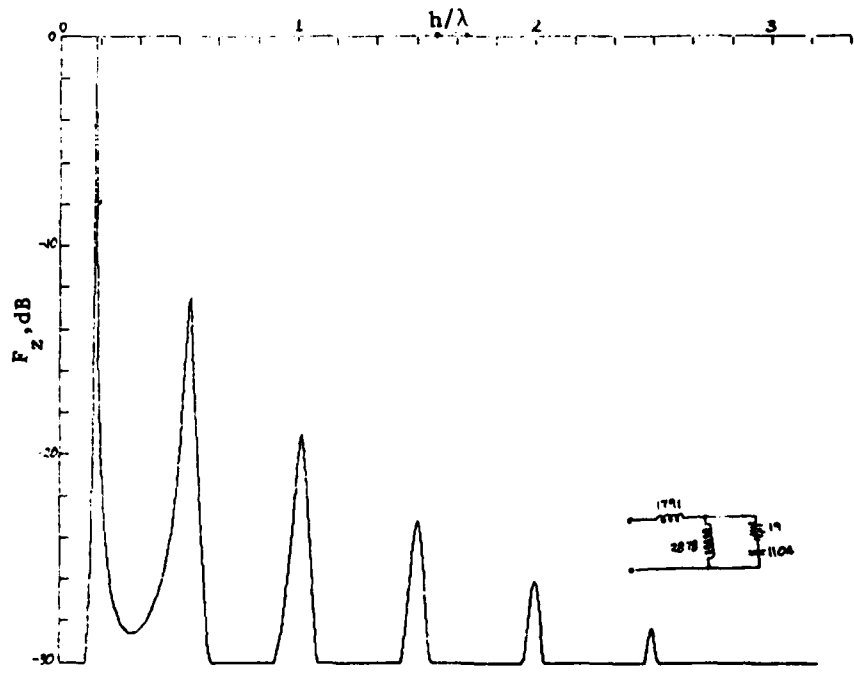


Figure 2-106 Impedance Matching Factor of Cylindrical Dipole  
( $h/a = 10^6$ ) Matched with LL Network for Resonance at  $.15 h/\lambda$

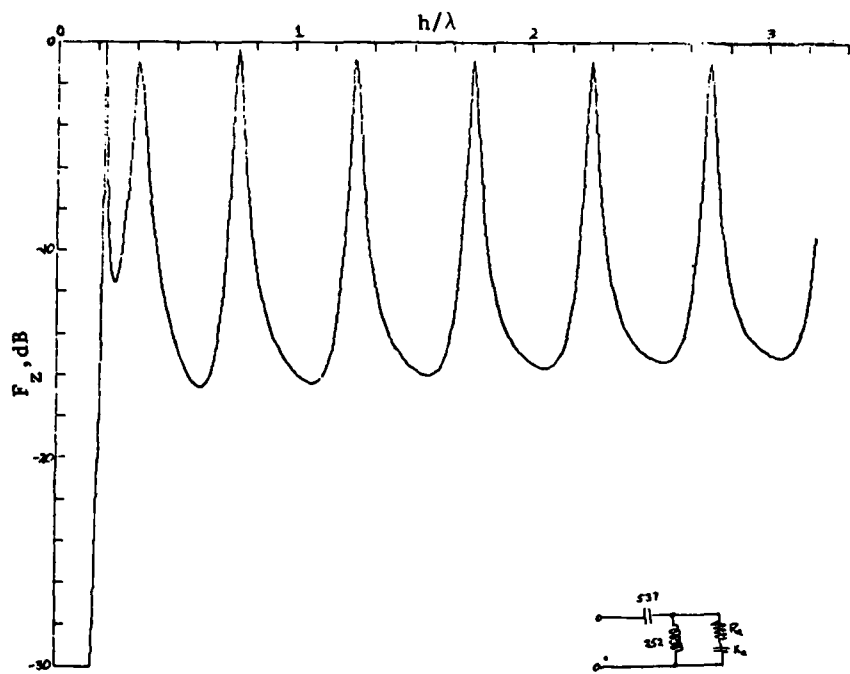


Figure 2-107 Impedance Matching Factor of Cylindrical Dipole  
( $h/a = 10^6$ ) Matched with LC Network for Resonance at  $.20 h/\lambda$

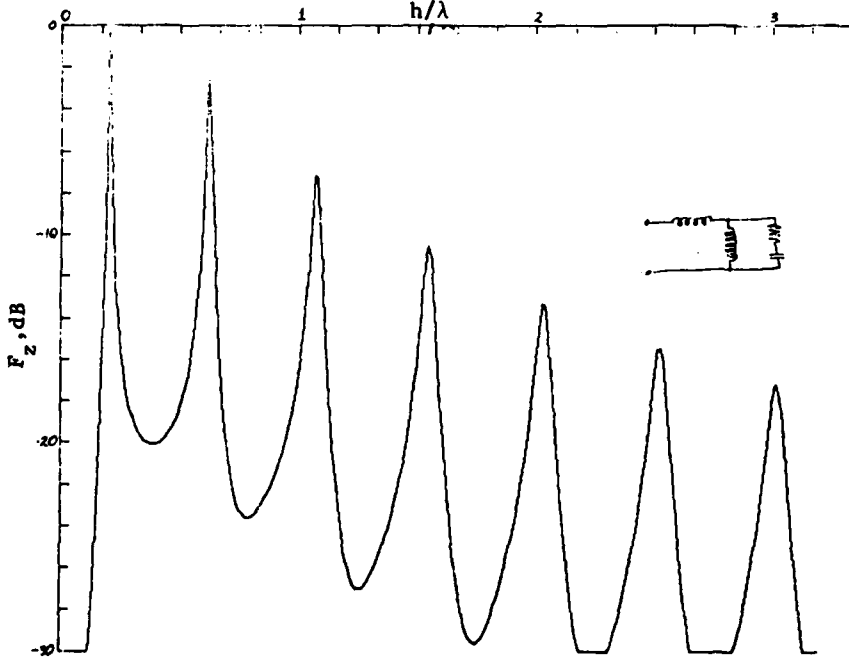


Figure 2-108 Impedance Matching Factor of Cylindrical Dipole  
( $h/a = 10^6$ ) Matched with LL Network for Resonance at  $.2 h/\lambda$

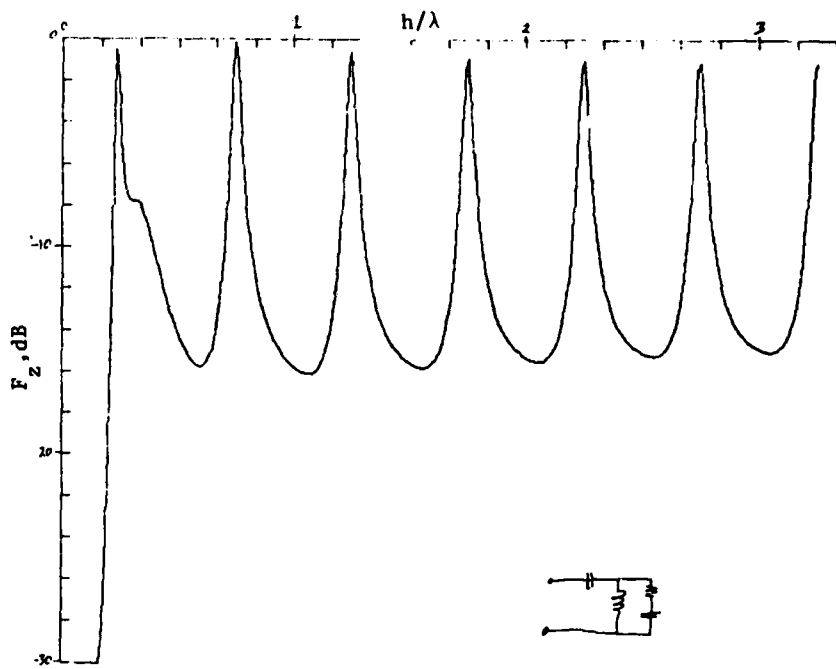


Figure 2-109 Impedance Matching Factor of Cylindrical Dipole ( $h/a = 10^6$ ) Matched with LC Network for Resonance at  $.23 h/\lambda$

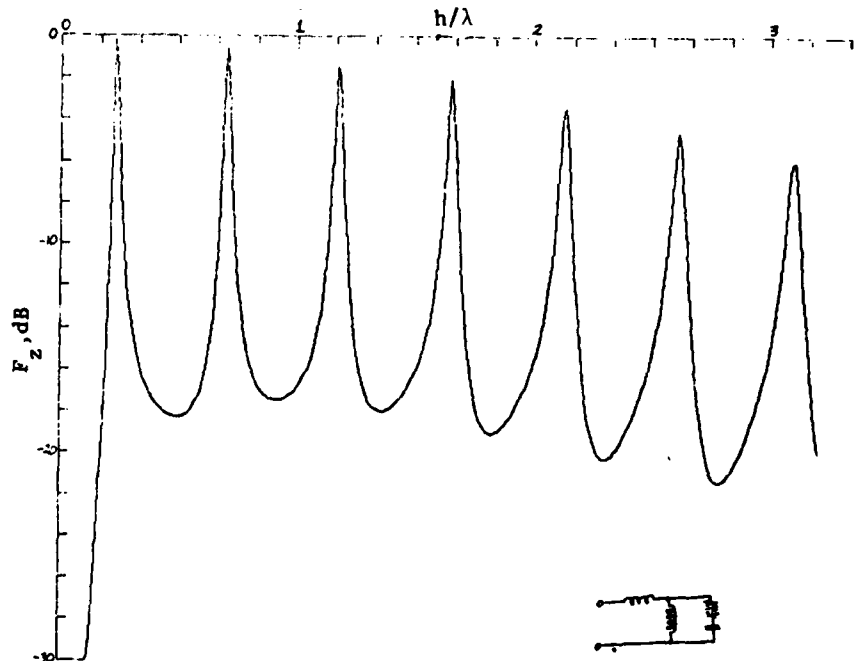


Figure 2-110 Impedance Matching Factor of Cylindrical Dipole ( $h/a = 10^6$ ) Matched with LL Network for Resonance at  $.23 h/\lambda$

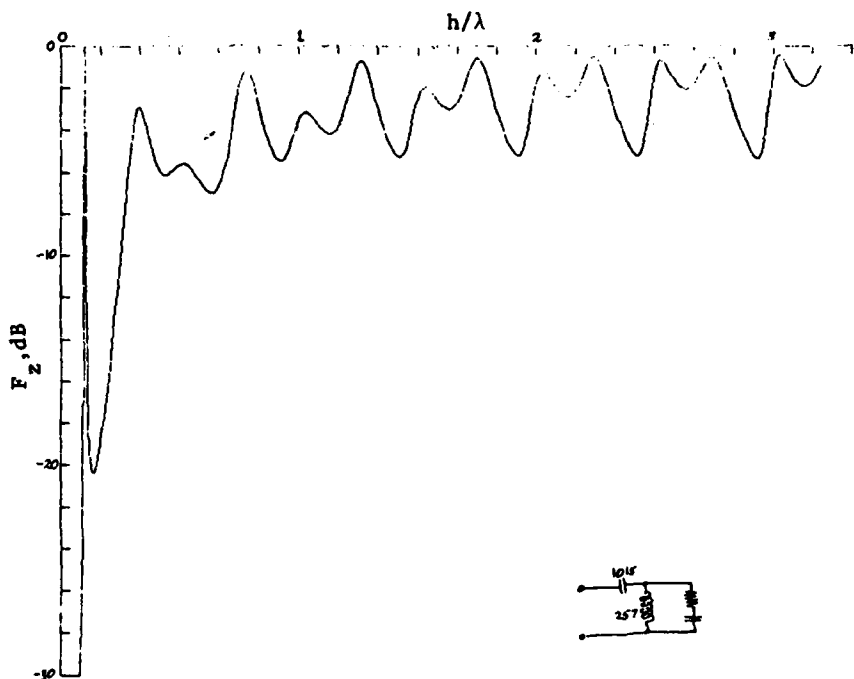


Figure 2-111 Impedance Matching Factor of Cylindrical Dipole  
( $h/a = 20$ ) Matched with LL Network for Resonance at  $.1 h/\lambda$

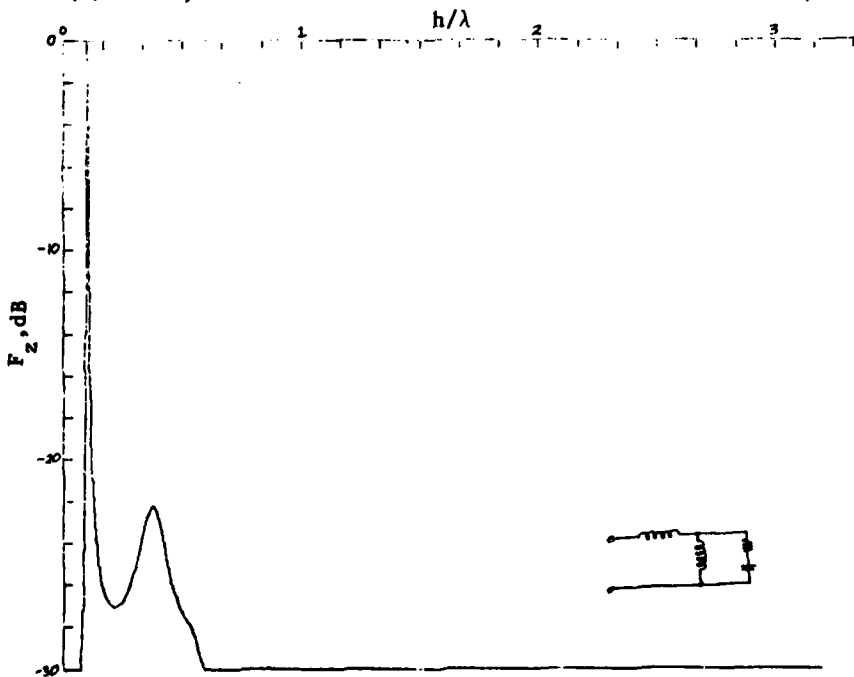


Figure 2-112 Impedance Matching Factor of Cylindrical Dipole  
( $h/a = 20$ ) Matched with LL Network for Resonance at  $.1 h/\lambda$

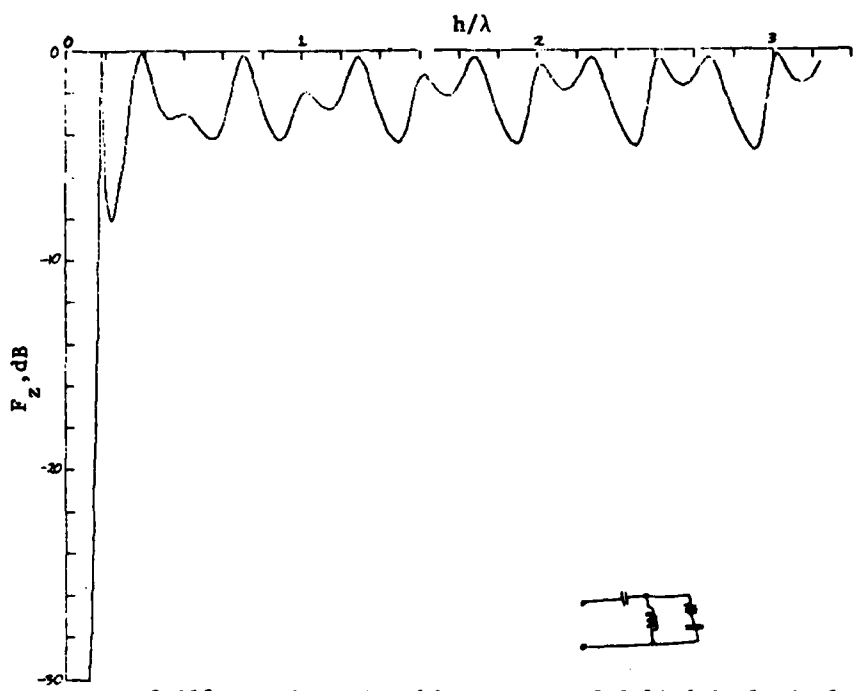


Figure 2-113 Impedance Matching Factor of Cylindrical Dipole  
( $h/a = .15$ ) Matched with LC Network for Resonance at  $.15 h/\lambda$

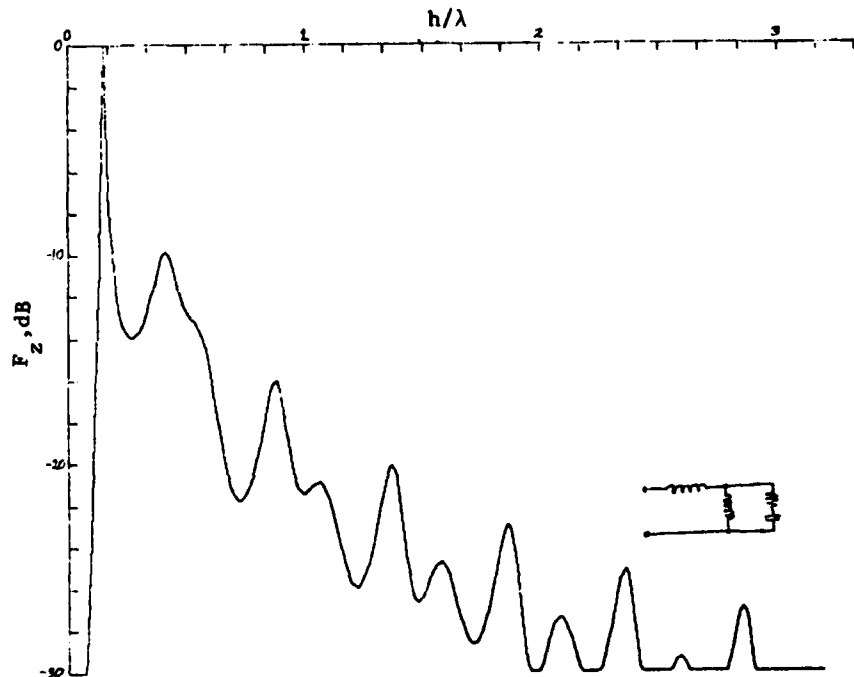


Figure 2-114 Impedance Matching Factor of Cylindrical Dipole  
( $h/a = .20$ ) Matched with LL Network for Resonance at  $.15 h/\lambda$

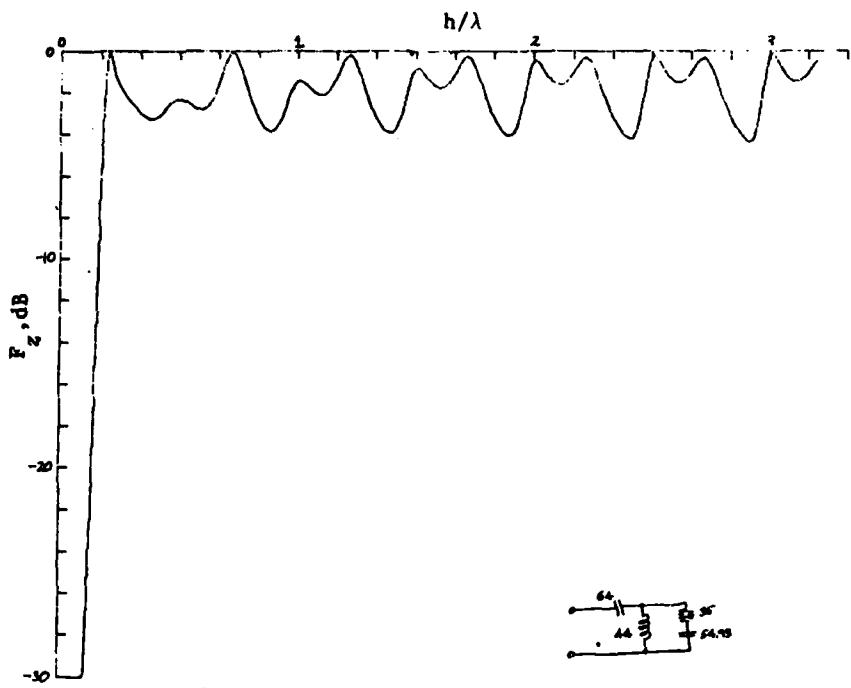


Figure 2-115 Impedance Matching Factor of Cylindrical Dipole  
( $h/a = 20$ ) Matched with LC Network for Resonance at  $.2 h/\lambda$

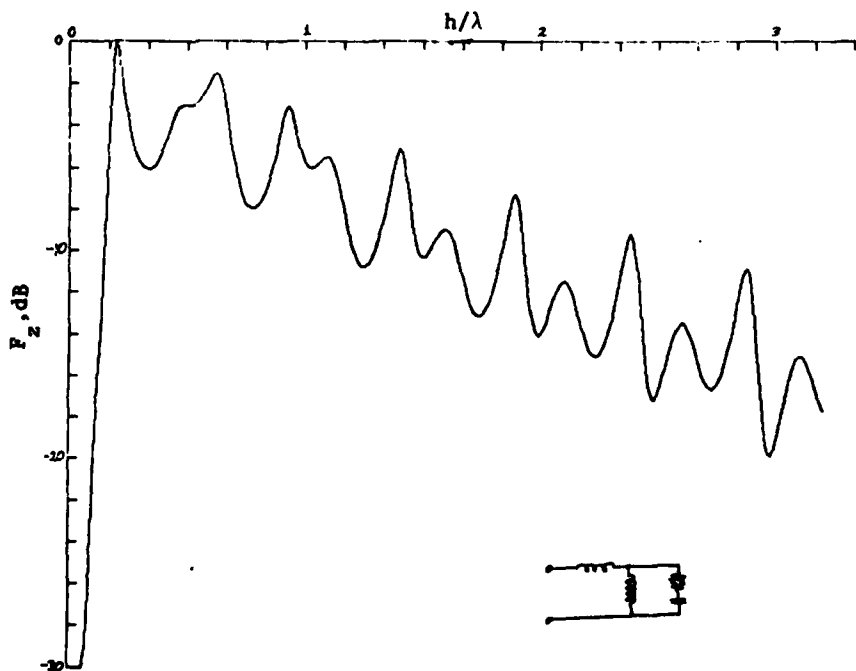


Figure 2-116 Impedance Matching Factor of Cylindrical Dipole  
( $h/a = 20$ ) Matched with LL Network for Resonance at  $.2 h/\lambda$

Table 2-5  
Reactance Values of Matching Network Elements at Resonance

Dipole: Cylindrical ( $h/a = 10^6$ )

<u>Resonant Length</u>	<u>Dipole Z At Resonance</u>	<u>Type I</u>		<u>Type II</u>	
		<u>XL</u>	<u>XC</u>	<u>X<sub>1</sub></u>	<u>X<sub>2</sub></u>
.10	7.68 - j2113	1518	5391	3475	5391
.15	19.0 - j1104	683	1791	2878	1791
.20	38.9 - j474	252	537	4018	537
.23	57.5 - j159	76.7	148	2197	148

Dipole: Cylindrical ( $h/a = 20$ )

<u>Resonant Length</u>	<u>Dipole Z At Resonance</u>	<u>Type I</u>		<u>Type II</u>	
		<u>XL</u>	<u>XC</u>	<u>X<sub>1</sub></u>	<u>X<sub>2</sub></u>
.10	5.74 - j344	257	1015	520	1015
.15	15.34 - j169	109	305	379	305
.20	35.0 - j54.93	44	64	336	65.6

The most notable finding seen with these curves is the fact that higher order resonances can still occur with a matched antenna. In particular, for Type I matching all higher order resonances of the dipole occur as though the matching network did not exist. The resonant frequencies are shifted slightly to higher frequencies but the peak values are essentially unaffected. When the matched resonant frequency is close to the first natural resonant frequency of the dipole the two resonant peaks converge into one, as seen in Figures 2-109, 2-110, 2-115 and 2-116. The resonant peaks which occur with Type II matching, however, attenuate with increasing frequency. The attenuation rate is higher for the dipoles that are matched at electrically shorter lengths. It is obvious that Types I and IV tend to become transparent to the circuit at higher frequencies, whereas the remaining types tend to block the antenna or shunt it out at increasing frequencies. In general, the type of matching circuit used in any given antenna is unknown.

These figures also indicate that the matched resonance selectivity curve is generally of relatively high Q. Figure 2-117 shows an expanded scale of the resonant peak given in Figure 2-105. The calculated Q of this peak is 61.6. Values of the modified resonance function applied to this curve are shown with the X's.

## 2.6 Transmission Characteristics of Antennas Matched With Single-Stub Transmission Line Elements

Single-stub matching involves locating a point on the transmission line at a distance  $L_1$  from the load impedance where the real part of the admittance looking toward the load is  $G_o = 1/R_o$ , where  $R_o$  is the characteristic impedance of the line. At this point a shorted transmission line stub of length  $L_2$  is connected in parallel to cancel the susceptance in the line. Beyond this point, then, the impedance looking toward the load is everywhere  $R_o$ . Thus, the load impedance is matched and no incident power is reflected. For this condition all incident power is absorbed by the load, except for ohmic losses in the  $L_1$  and  $L_2$  segments of the transmission line.

The physical arrangement of a single-stub match is illustrated in Figure 2-118. Let the reflection coefficient of the load impedance by  $r = |r| \angle \phi$

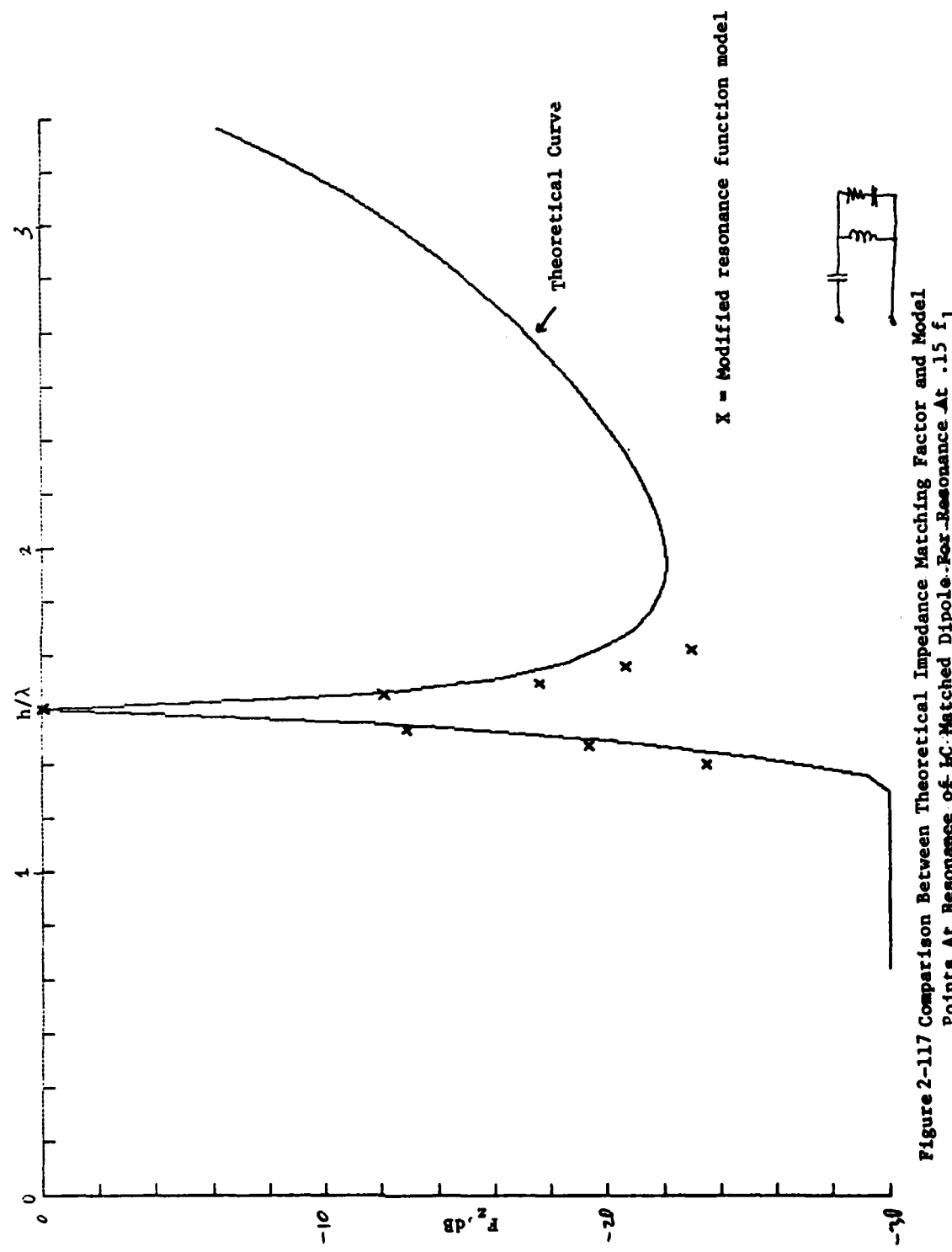


Figure 2-117 Comparison Between Theoretical Impedance Matching Factor and Model Points At Resonance of LC-Matched Dipole For Resonance At  $.15 f_1$

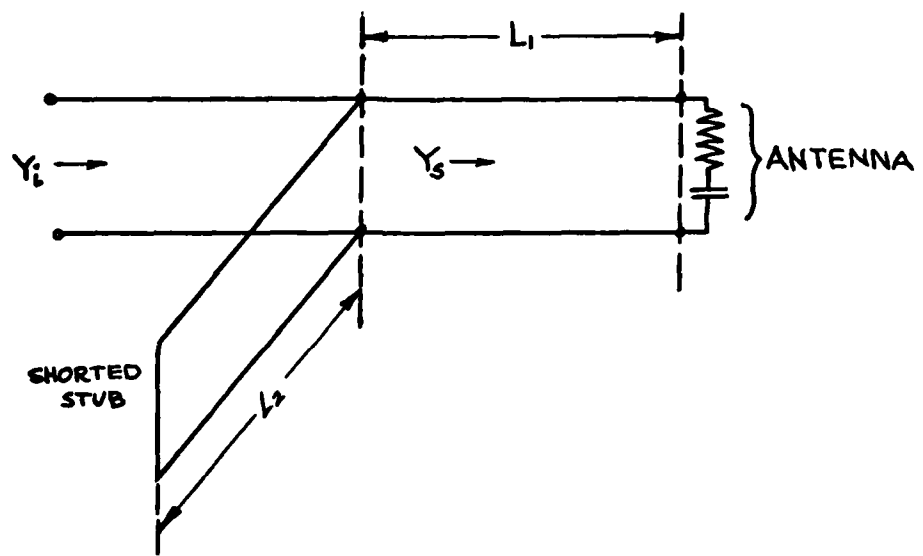


Figure 2-118 Diagram of Single-stub Match for an Antenna

as seen at the load. The admittance  $Y_s$  as seen looking toward the load at distance  $L_1$  from the load is given by [6, page 312]

$$Y_s = G \frac{1-|r| \frac{|\phi-2\beta L_1|}{\beta}}{1+|r| \frac{|\phi-2\beta L_1|}{\beta}} \quad (\beta = \frac{2\pi}{\lambda})$$

$$= G \frac{1-|r|^2 - j2|r| \sin(\phi-2\beta L_1)}{1+|r|^2 + 2|r| \cos(\phi-2\beta L_1)}$$

$$= G+jB.$$

The admittance looking into a shorted stub of length  $L_2$  is

$$Y_{SC} = -j G_o \cot \beta L_2.$$

The length  $L_1$  of the series section which gives  $G = G_o$  is

$$\frac{L_1}{\lambda} = \frac{1}{4\pi} \quad (\phi + \pi - \cos^{-1}|r|).$$

The length  $L_2$  of the shorted stub which provides

$$Y_{SC} = -B$$

is given by

$$\frac{L_2}{\lambda} = \frac{1}{2\pi} \tan^{-1} \left( \frac{\sqrt{1-|r|^2}}{2|r|} \right).$$

The frequency response of an antenna which is stub matched is expected to be different from that when matched with lumped constants, due to the manner in which the electrical effects of stub elements change with frequency. Note that transmission line elements possess the property of providing the same impedance effects when their lengths are increased by any integral multiple of one-half wavelength.

In order to study the frequency behavior of stub-tuned antennas, the impedance matching factor has been calculated for various matched conditions of electrically short cylindrical dipoles. Similar to the previous analysis for lumped constant matching, stub matching was examined for conditions of a thin dipole ( $h/a=10^5$ ) and fat dipole ( $h/a=20$ ) at natural resonant lengths of  $h/\lambda=.10, .15$  and  $.20$ . The impedances of the dipoles at these electrical lengths have been listed in Table 2-5. The electrical length required for the stub elements to match these impedances are given in Table 2-6.

**Table 2-6**  
**Electrical Length of Transmission Line**  
**Stub Elements Required for Matching Cylindrical**  
**Dipole Antennas to 50 ohms**

<u>Dipole Length/Radius</u>	<u>Dipole Length at Resonance</u>	<u><math>L_1/\lambda</math></u>	<u><math>L_2/\lambda</math></u>
$10^6$	$h/\lambda = .10$	.24476	.0014757
$10^6$	.15	.23836	.0044406
$10^6$	.20	.21877	.0147498
20	.10	.21928	.0077715
20	.15	.18006	.025245
20	.20	.072001	.100827

The resulting curves are presented in Figures 2-119 through 2-131. Many of these figures illustrate the effect of using transmission line elements increased by  $\lambda/2$  or  $\lambda$ . As can be seen, a stub match has a dominating effect on the antenna impedance over a wide range of frequencies. The design resonance peak tends to be extremely high Q. For example, the Q of the resonant peak in Figure 2-121 is 521, which is considerably higher than the Q reported earlier (61.6) resulting from a lumped constant match of the same antenna. In general, a stub match produces several random components in the fine-grain structure of these curves. The interaction of the stub matching circuit continues to create resonances at higher frequencies. Based on the assumption that specifications for only the first resonant peak will be known for any given antenna, it will not be possible to model reliably the structural details as shown.

As a matter of interest, the matched resonance peak of Figure 2-127 is shown on an expanded scale in Figure 2-132. The Q calculated for this peak is 171.3. Values of the modified resonance function for the Q value are shown by the X's.

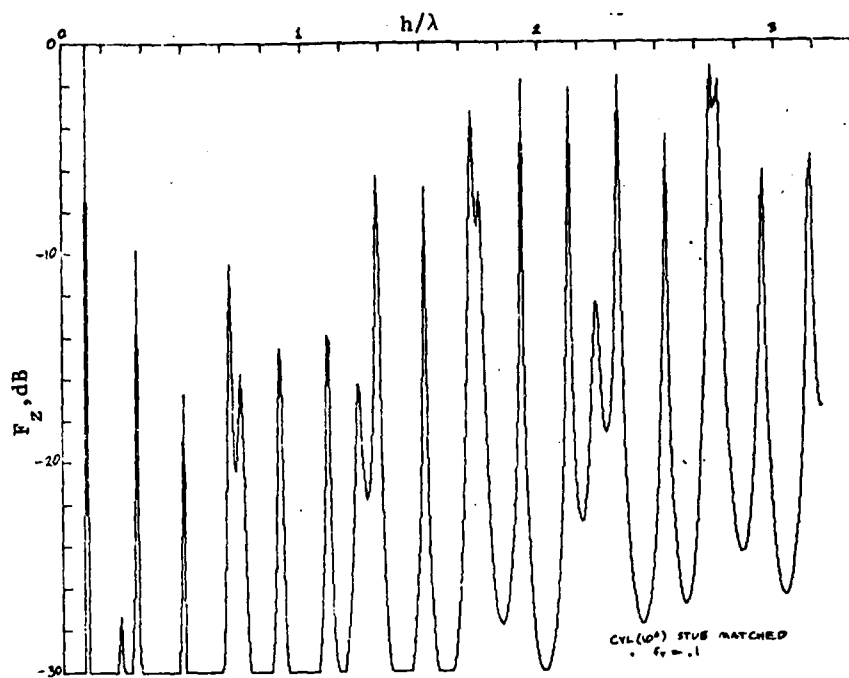


Figure 2-119 Impedance Matching Factor of Cylindrical ( $h/a = 10^6$ )  
Stub-Matched for Resonance at  $.1 h/\lambda$

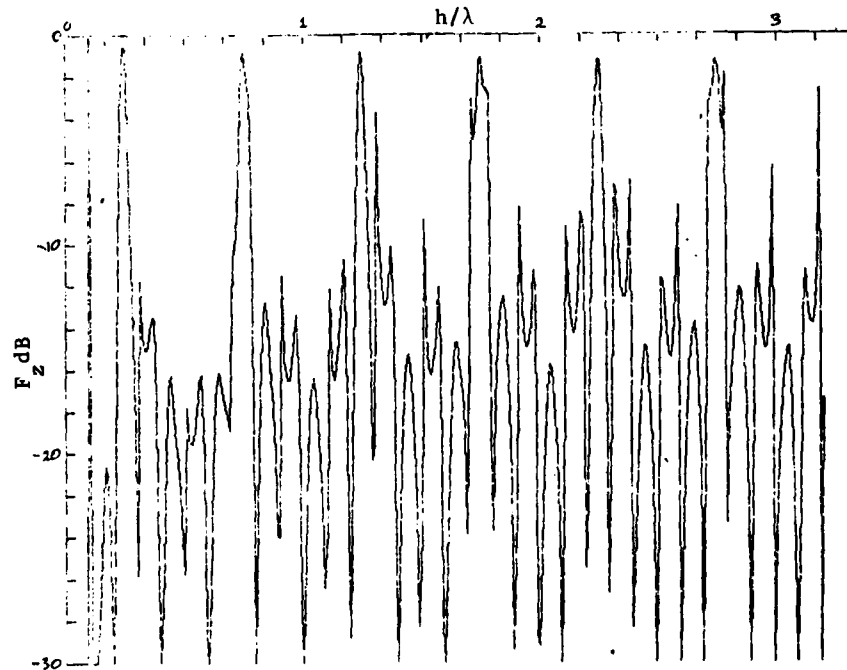


Figure 2-120 Impedance Matching Factor of Cylindrical Dipole  
( $h/a = 10^6$ ) Stub-Matched for Resonance at  $.1 h/\lambda$  with Stub  
Length Increased  $\lambda/2$

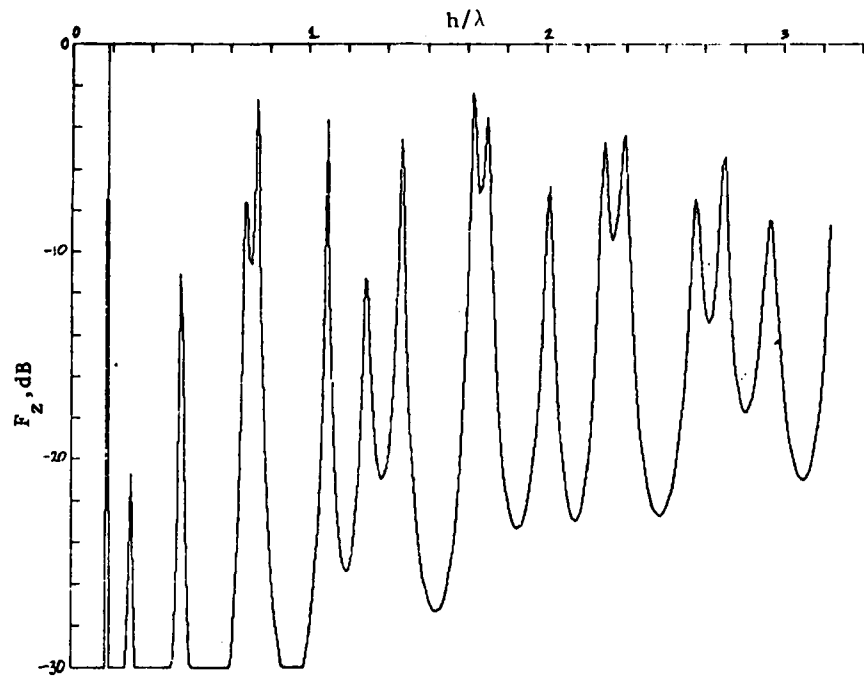


Figure 2-121 Impedance Matching Factor of Cylindrical Dipole  
( $h/a = 10^6$ ) Stub-Matched for Resonance at  $.15 h/\lambda$

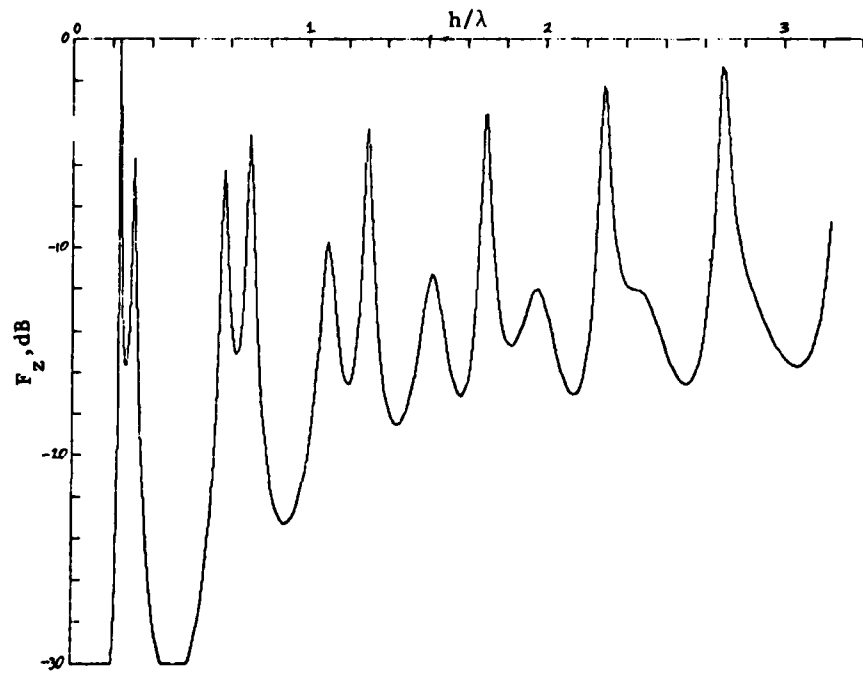


Figure 2-122 Impedance Matching Factor of Cylindrical Dipole  
( $h/a = 10^6$ ) Stub-Matched for Resonance at  $.2 h/\lambda$

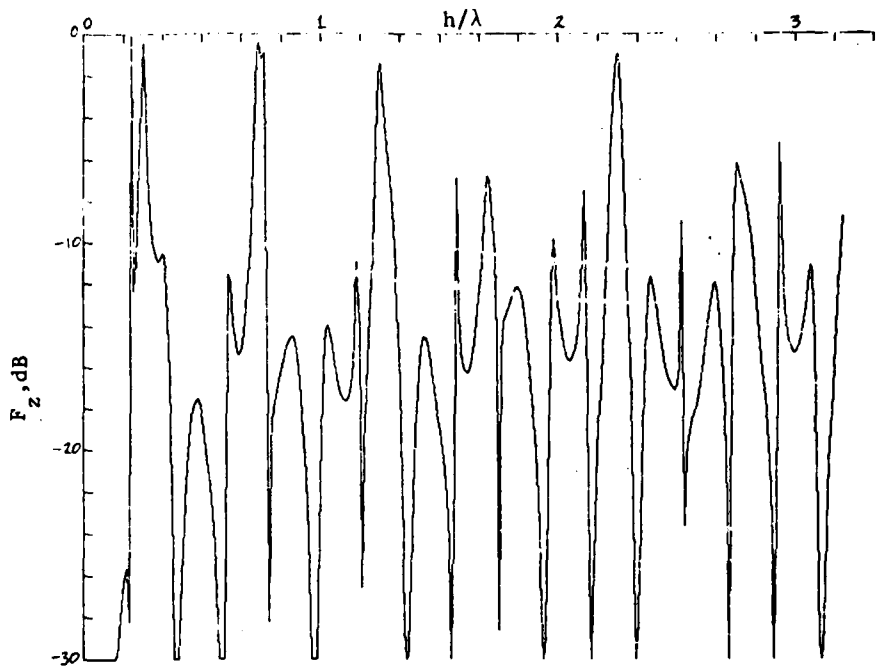


Figure 2-123 Impedance Matching Factor of Cylindrical Dipole  
( $h/a = 10^6$ ) Stub-Matched for Resonance at  $.2 h/\lambda$  with Stub Length  
Increased  $\lambda/2$

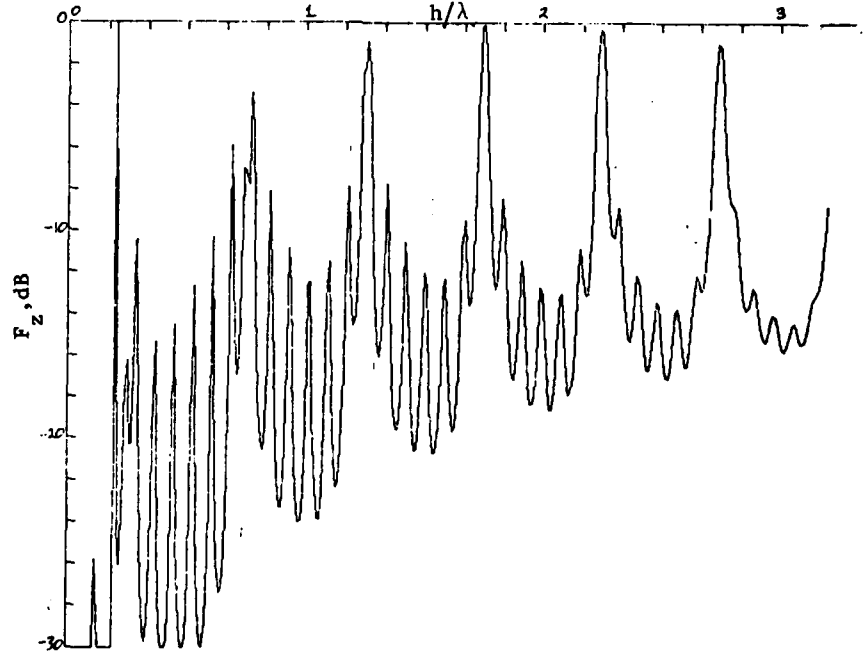


Figure 2-124 Impedance Matching Factor of Cylindrical Dipole  
( $h/a = 10^6$ ) Stub-Matched for Resonance at  $.2 h/\lambda$  with Series  
Length Increased  $1\lambda$

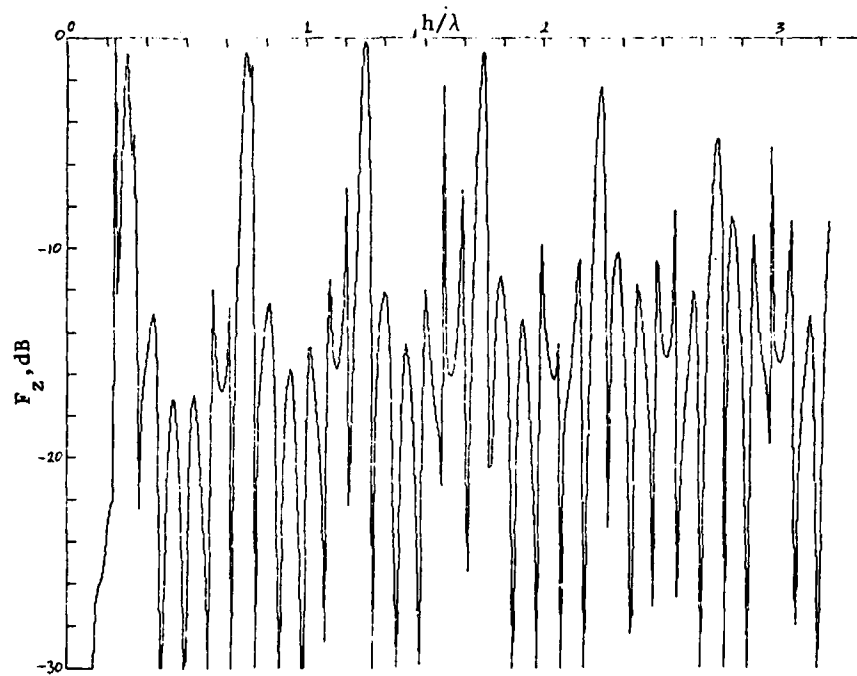


Figure 2-125 Impedance Matching Factor of Cylindrical Dipole  
( $h/a = 10^6$ ) Stub-Matched for Resonance at  $.2 h/\lambda$  with Stub Length Increased  $1\lambda$

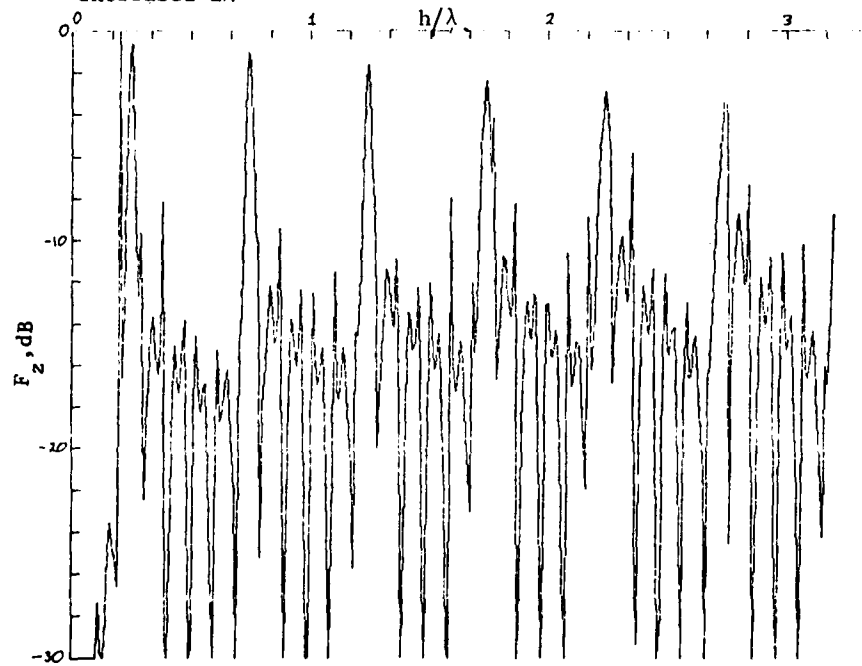


Figure 2-126 Impedance Matching Factor of Cylindrical Dipole  
( $h/a = 10^6$ ) Stub-Matched for Resonance at  $.2 h/\lambda$  with Both  
Stub and Series Section Increased  $1\lambda$

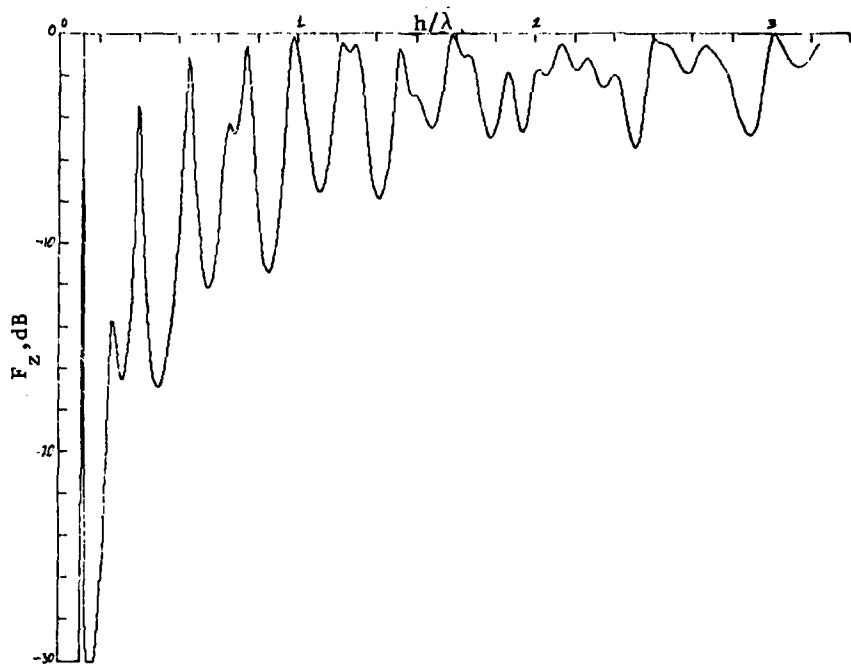


Figure 2-127 Impedance Matching Factor of Cylindrical Dipole  
( $h/a = 20$ ) Stub-Matched for Resonance at  $.1 h/\lambda$

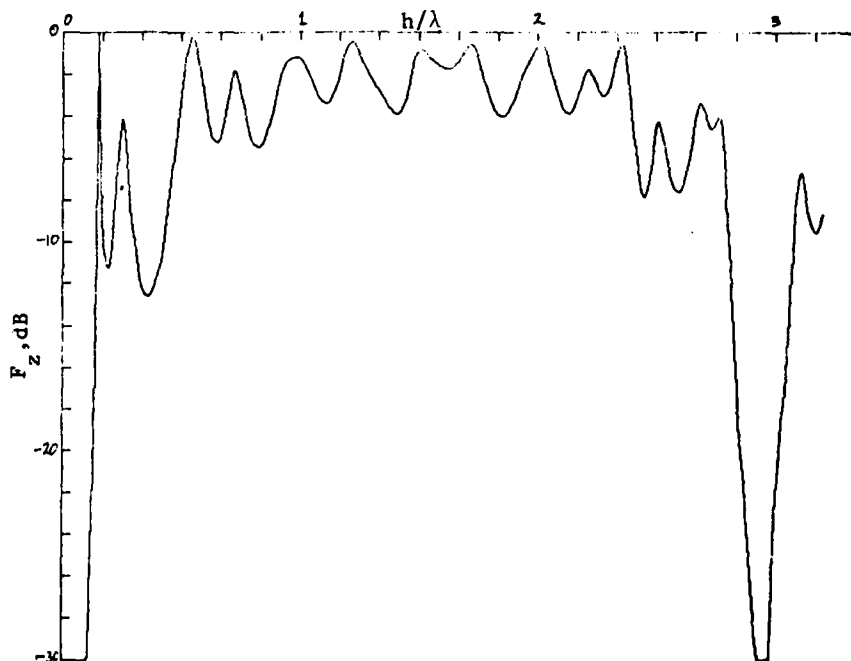


Figure 2-128 Impedance Matching Factor of Cylindrical Dipole  
( $h/a = 20$ ) Stub-Matched for Resonance at  $.15 h/\lambda$

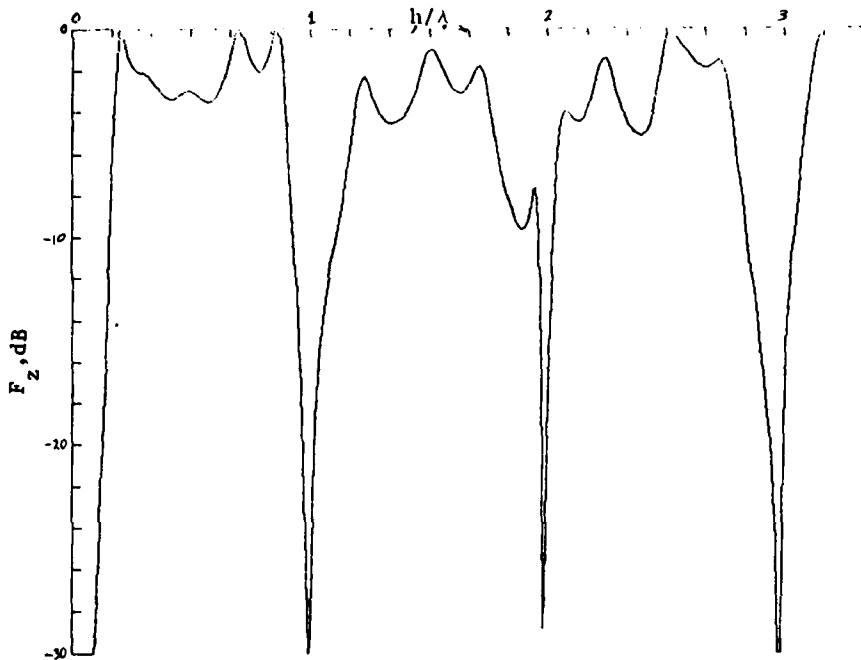


Figure 2-129 Impedance Matching Factor of Cylindrical Dipole  
( $h/a = 20$ ) Stub-Matched for Resonance at  $.2 h/\lambda$

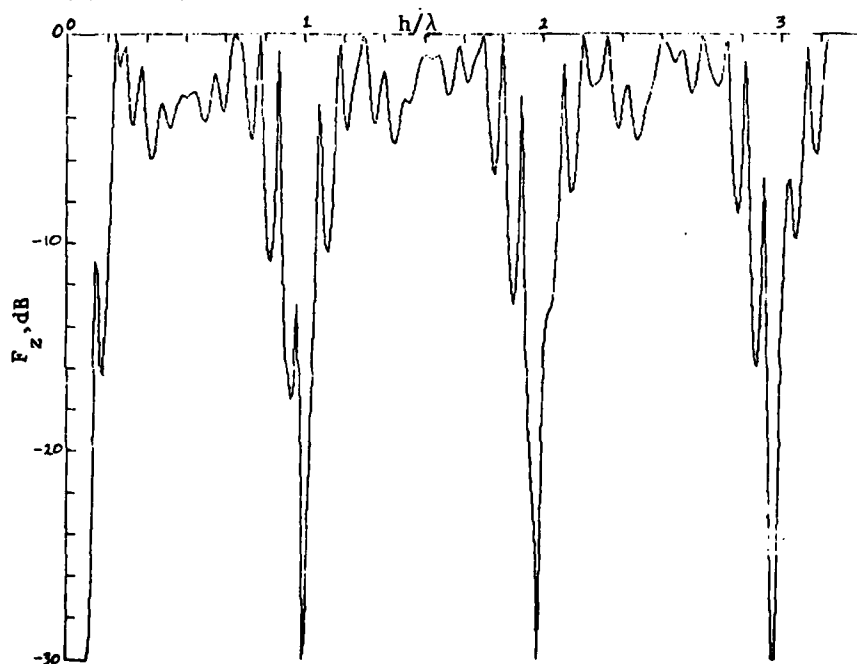


Figure 2-130 Impedance Matching Factor of Cylindrical Dipole  
( $h/a = 20$ ) Stub-Matched for Resonance at  $.2 h/\lambda$  with Series  
Section Increased  $1\lambda$

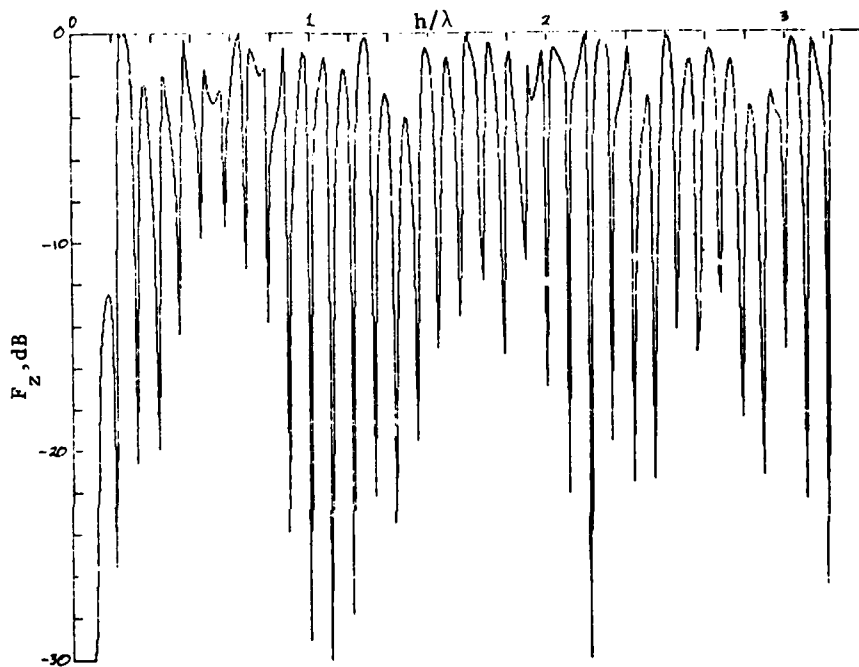


Figure 2-131 Impedance Matching Factor of Cylindrical Dipole  
( $h/a = 20$ ) Stub-Matched for Resonance at  $.2 h/\lambda$  with Stub  
Length Increased  $1\lambda$

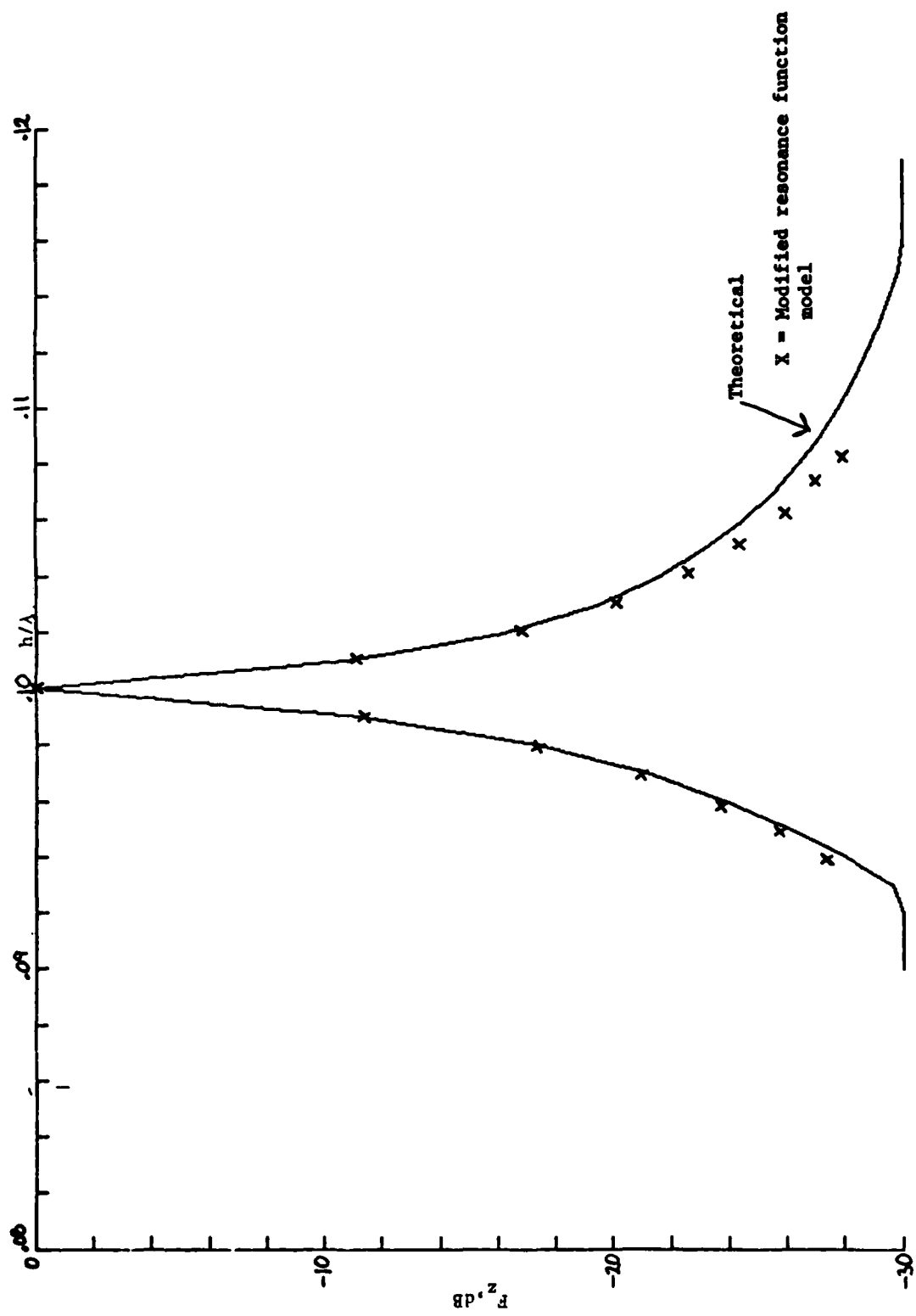


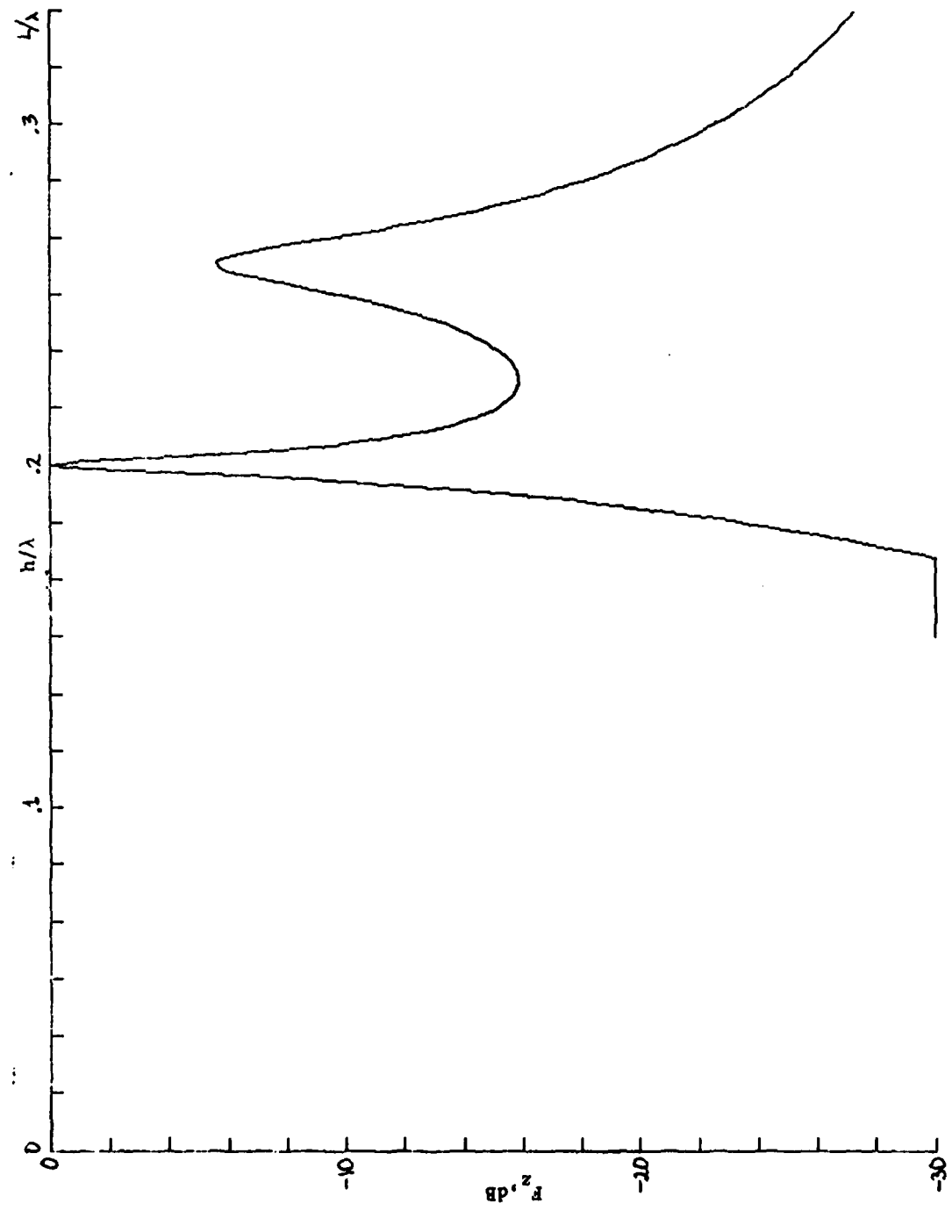
Figure 2-132 Comparison of Model Points with Theoretical Impedance Matching Factor of Resonant Peak for Stub-Tuned Dipole shown in Figure 126.

The first resonant peak of Figure 2-122 is shown on an expanded scale in Figure 2-133 illustrating that the matching resonance at  $.2 h/\lambda$  displaces the natural dipole resonance (at  $.25 h/\lambda$ ) slightly to the right.

The out-of-band responses of several types of aircraft antennas have been published [7,8]. Specific antenna structures were analyzed, and their electrical properties were modeled to permit theoretical calculations of the antenna response at frequencies outside the design band. The modeling of each antenna has been very thorough to account for the electrical properties of the antenna structure and any feed circuitry of the antenna. As shown, the equivalent circuits contain lumped elements and/or transmission line elements. These data which in part have been corroborated with measurements, provide some additional insight into the complicated nature of some real antennas that will undoubtedly require modeling in IEMCAP. All samples shown were analyzed as receiving antennas, thus, the resulting overall antenna effectiveness is represented by effective height, open-circuit voltage at the antenna terminals, or induced current.

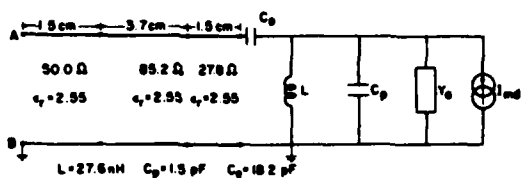
Figure 2-134 illustrates the effective height of a common UHF blade antenna for aircraft. The design band is 225-400 MHz. The different sections of the transmission lines and the end capacitances are for tuning purposes. The antenna is essentially a monopole represented by admittance  $Y_a$ , that is loaded capacitively by a conducting shroud which is dielectrically insulated from the active element. Unfortunately, the analysis does not extend above 400 MHz. The effective height of an antenna corresponds to the ability to receive a voltage from an incident field strength and compares to  $F_z$  for a transmitting antenna.

Figure 2-135 shows the open-circuit voltage of a marker beacon antenna which mounts flush on the underside of an aircraft. The antenna consists of a cavity shaped like a bowl with a capacitively loaded pickup inside. As can be seen, the antenna has a distinct resonance at 75 MHz. The input impedance curve for this antenna (not shown) does not indicate any other resonances below 250 MHz.

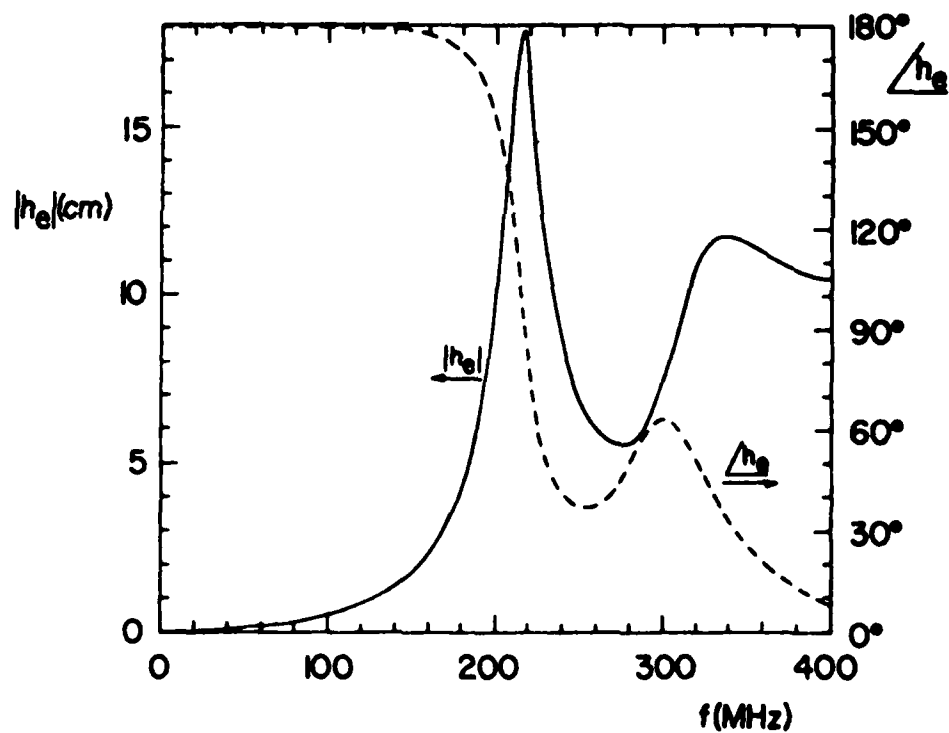


2-103

Figure 2-133 Resonance Peaks of Stub-Matched for Resonance at  $.2 L/\lambda$  shown in Figure 121

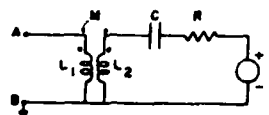


a. Equivalent Circuit



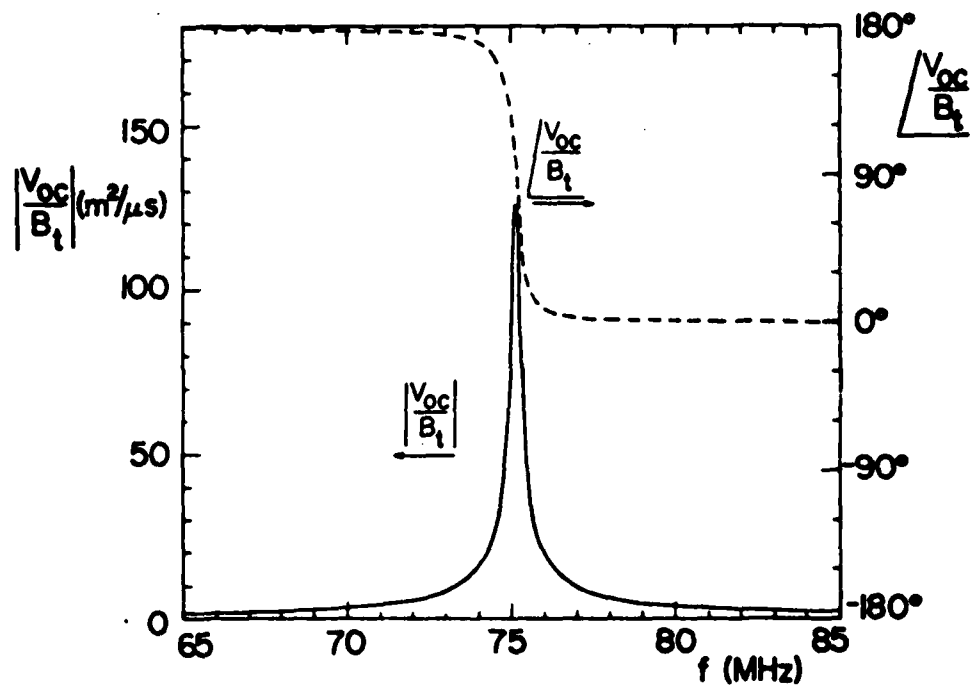
b. Effective Height

Figure 2-134 Frequency Response Behavior of a Common UHF Aircraft Blade Antenna



$L_1 = 35.7 \text{ mH}$ ,  $L_2 = 300 \text{ mH}$ ,  $M = 6.5 \text{ mH}$ ,  
 $R = 0.16 \Omega$ ,  $C = 48.9 \mu\text{F}$

a. Equivalent Circuit



B. Open-circuit Voltage At Antenna Terminals.

Figure 2-135 Frequency Response Behavior of a Marker Beacon Antenna

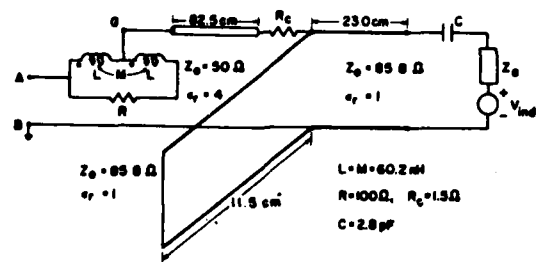
Figure 2-136 shows the open-circuit voltage of an aircraft localizer antenna which has an operating range of 108-112 MHz. This antenna contains two tuned loops, a coaxial cable balun, and a 100-ohm resistor with wires wrapped around the resistor.

Figure 2-137 illustrates the effective height of an HF fixed-wire antenna on an aircraft. The antenna is driven at the vertical stabilizer. The curve shows a resonance at 2.5-2.8 MHz, and a second resonance at 8.2 MHz ( $=3 \times 2.73$ ). It is presumed that this antenna is tunable at any one frequency, as shown in Figure 2-137.

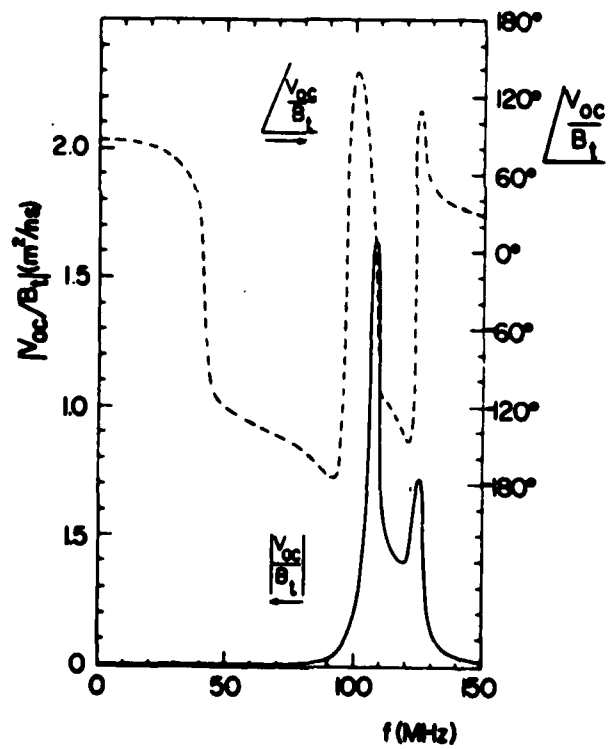
Figure 2-138 gives the induced current of a long dual-wire antenna trailing behind an aircraft. The antenna operates in the frequency range 17-60 kHz and is tuned by varying the wire lengths. At 17 kHz the wire length is about 5 miles. The lower, longer wire is grounded to the aircraft and serves as a counterpoise for the shorter upper wire which is driven against the aircraft at an "antenna gap." The curves shown in Figure 2-138 are for an antenna with wire lengths of 1.2 km and 7.2 km. The angle between the wires in the vertical plane is 6°. The first resonant peak is the natural first resonance of the long wire. Higher order resonances 18 kHz apart can be attributed to the combined length of the two wires. The peaks at 55 kHz, 180 kHz, 305 kHz and 430 kHz are due to resonances of the shorter wire.

## 2.7 Modeling the Impedance Matching Factor of an Antenna Having a Matching Network

In order to model an antenna having a matching network with sufficient accuracy to predict its unique characteristics of reflection losses at out-of-band frequencies, it is necessary to obtain detailed information concerning the physical and electrical structure of all components of the antenna. Antenna manufacturers, however, generally provide overall performance data applicable only to the design frequency range. Knowledge of the design and construction of the matching circuit, the balun, and of the antenna proper are seldom available. Consequently, it is assumed for the modeling that the only information available will be the specified frequency range of operation and an associated directive gain pattern. Where this

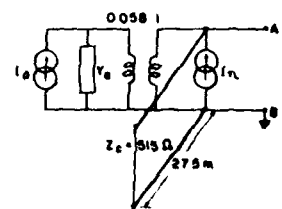


a. Equivalent Circuit

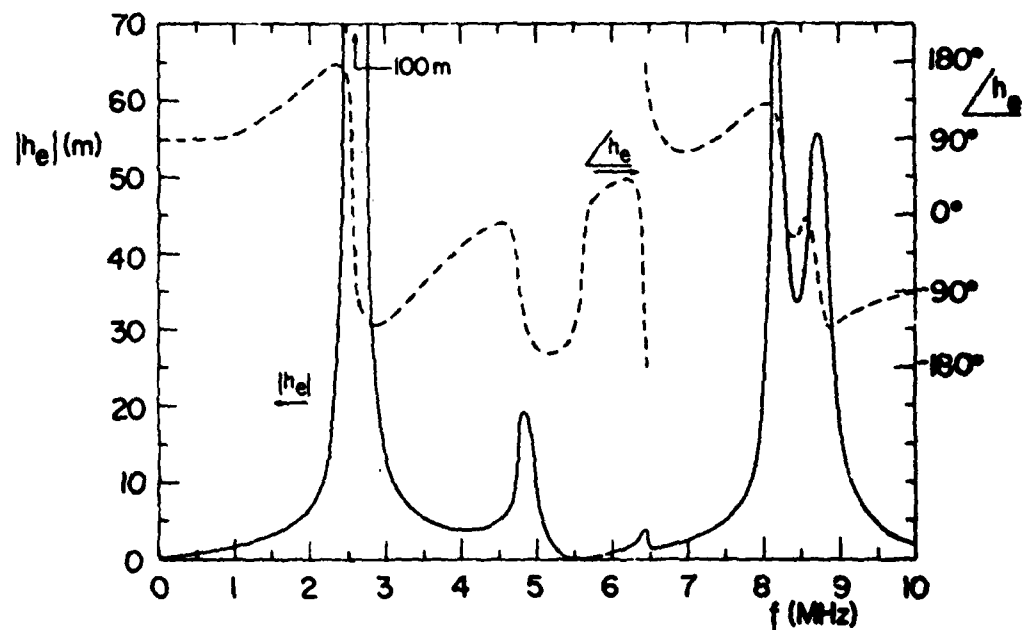


b. Open-circuit Voltage At Antenna Terminals.

Figure 2-136 Frequency Response of a Localizer Antenna

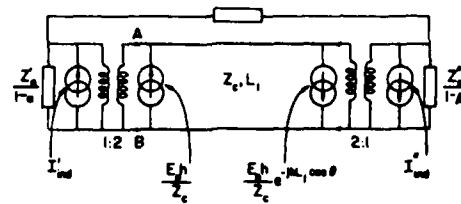


a. Equivalent Circuit

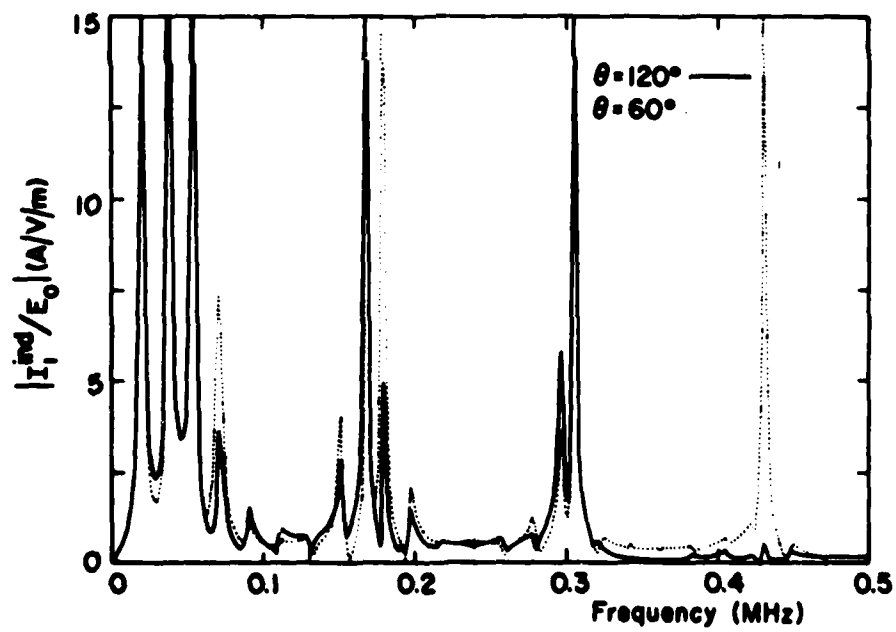


b. Effective Height

Figure 2-137 Frequency Response of HF Wire Antenna



a. Equivalent Circuit



b. Induced Current

Figure 2-138 Frequency Response of VLF/LF Trailing-wire Antenna

operating range is a resonant peak of a matched antenna, it is not possible to extrapolate further details of antenna performance without knowledge of the natural resonances of the antenna proper and of the type of matching circuit. There generally are too many unknown details to permit modeling the antenna with the desired degree of accuracy. Thus, it is necessary to look for characteristics which appear to be common to nearly all of the curves of impedance matching factor shown for matched antennas.

A noticeable feature seen with these curves is the degree to which the first resonant peak is isolated from other resonances. It appears that the specified operating bandwidth of a resonant antenna is generally the first resonance; that is, a significant resonant peak will rarely occur at a frequency below the specified operating design band of an antenna. Above the design band centered at  $f_r$ , there seldom appears to be another resonant peak below  $2f_r$ . This condition seems to hold true when the matched resonance at  $f_r$  is less than  $.8f_1$ , where  $f_1$  is the natural resonant frequency of the antenna proper. When  $f_r = f_1$  there is only one peak. However, for  $f_r$  in the approximate range there is only one peak. However, for  $f_r$  in the approximate range  $.8f_1$  to  $.9f_1$ , two resonant peaks appear, with the design resonance having greater amplitude. It is desirable to model the selectivity on both side of the specified resonance curve, since use is often made of this selectivity to isolate co-located systems operating on adjacent channels. It appears admissible to model the lower side according to the modified universal resonance function down to the limiting frequency of 1 Hz. For the upper side, it is proposed not to attempt to model the selectivity skirt of a second resonance. The upper skirt of the first resonance can be modeled down to some lower limiting level of  $F_Z$ . At some frequency, such as  $1.8f_1$ , the modeled level could jump to a high constant level, e.g., 0 dB. The level would remain at this value for all higher frequencies, except for a gradual decay rate to be considered in a later section.

It may be reasonable to model the upper skirt of the first resonance as follows. Model according to the modified universal resonance curve from  $f_1$  to a frequency  $f_2$  at which either of the following occurs first:

- a.  $f_2 = 1.8f_1$
- b.  $F_Z = -20.0$  dB.

This upper skirt would not be modeled if the Q of the operating range given by

$$Q = \frac{\sqrt{f_l f_u}}{f_u - f_l}$$

is less than 3. The model in this case would provide  $F_z = 0$  dB for  $f \geq f_1$ .

Three conditions of this possible model are illustrated in Figure 2-139. The modified universal resonance function is plotted for several values of Q in Figure 2-140 to indicate the model shapes for a given Q.

#### 2.8 Impedance matching factor of Slot Antennas

The electromagnetic properties of a slot in an infinite plane conductor are complementary to those of a thin, flat dipole of exactly the same dimensions as the slot. [9, page 196] The radiation patterns have identical shapes except that the electric and magnetic vectors are interchanged. The input impedance of a slot is related to that of the corresponding dipole as

$$Z_s = \frac{\eta^2}{4Z_d}$$

where  $\eta = 120\pi$  ohms, impedance of free space.

The impedance matching factor of a slot antenna was computed using the above expression and Schelkunoff's impedance equations for a dipole. If the input impedance of the complementary dipole is

$$Z_d = R_d + j X_d$$

then the input impedance of the slot is

$$Z_s = \frac{\eta^2}{4} \left( \frac{R_d}{R_d^2 + X_d^2} - j \frac{X_d}{R_d^2 + X_d^2} \right).$$

The impedance matching factor was determined by using  $Z_s$  to calculate the reflection coefficient based on a characteristic impedance of 330 ohms for the transmission line feeding the slot. [9, page 198]

The resulting curves of  $F_z$ , shown in Figures 2-141 and 2-142, are nearly identical with those for the complementary dipoles (Figures 2-13 and 2-19). The resonant frequencies occur at the same locations, but the null depths for the slot are slightly less than those of the dipole. Consequently,  $F_z$  of a slot antenna without feed circuitry may be obtained using the model of a resonant dipole of equivalent dimensions.

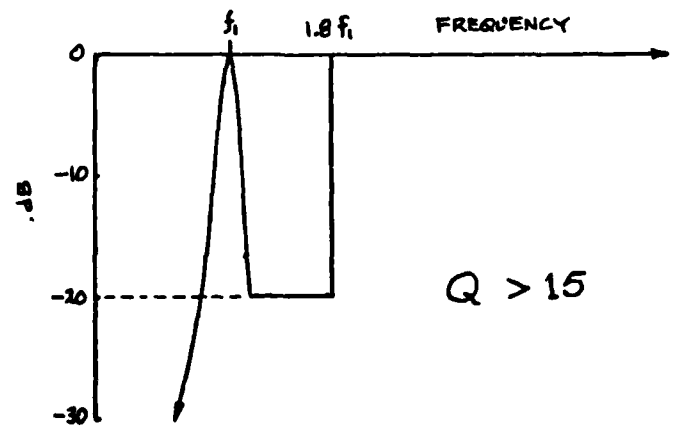
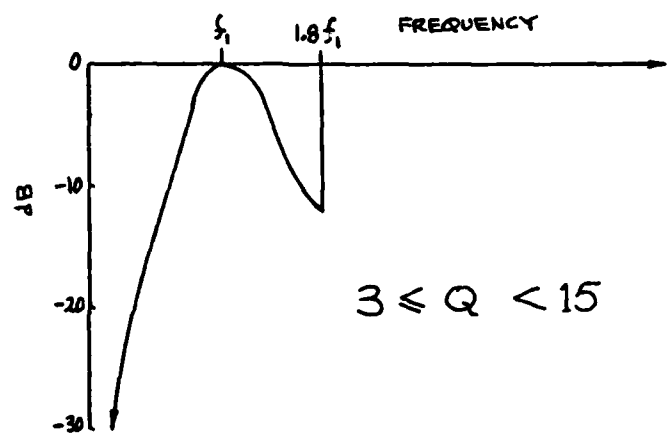
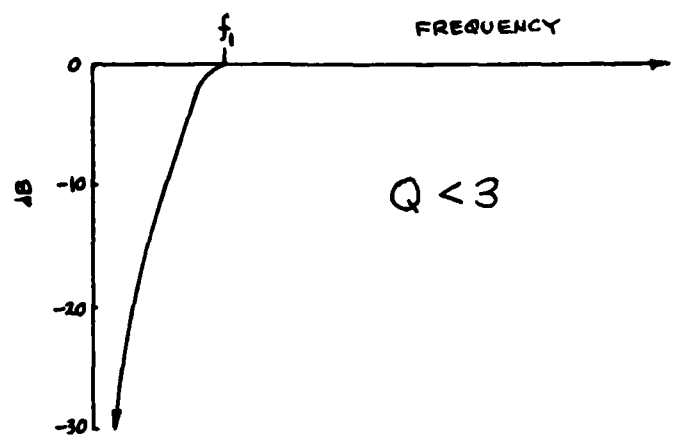


Figure 2-139 Suggested Models for Matched Antenna

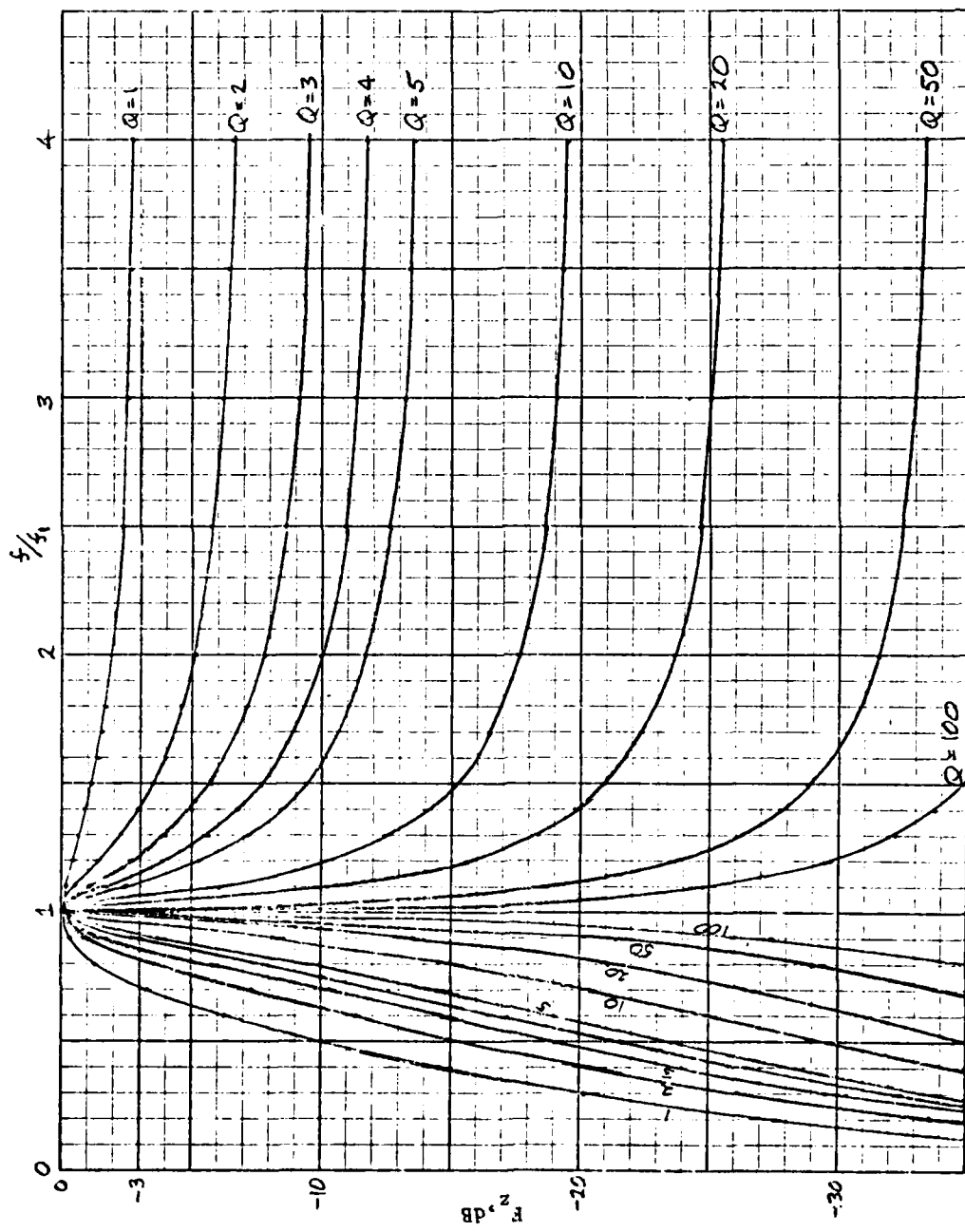


Figure 2-140 Modified Universal Resonance Curves

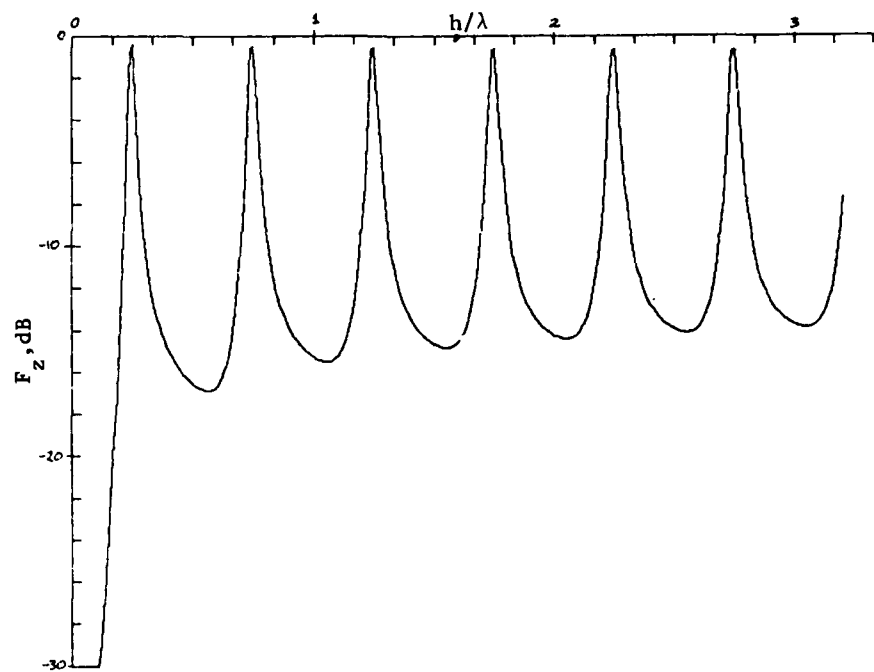


Figure 2-141 Impedance Matching Factor of a Thin Slot Antenna  
 $(h/a = 10^6)$  (Based on  $Z_0 = 530$  ohms)

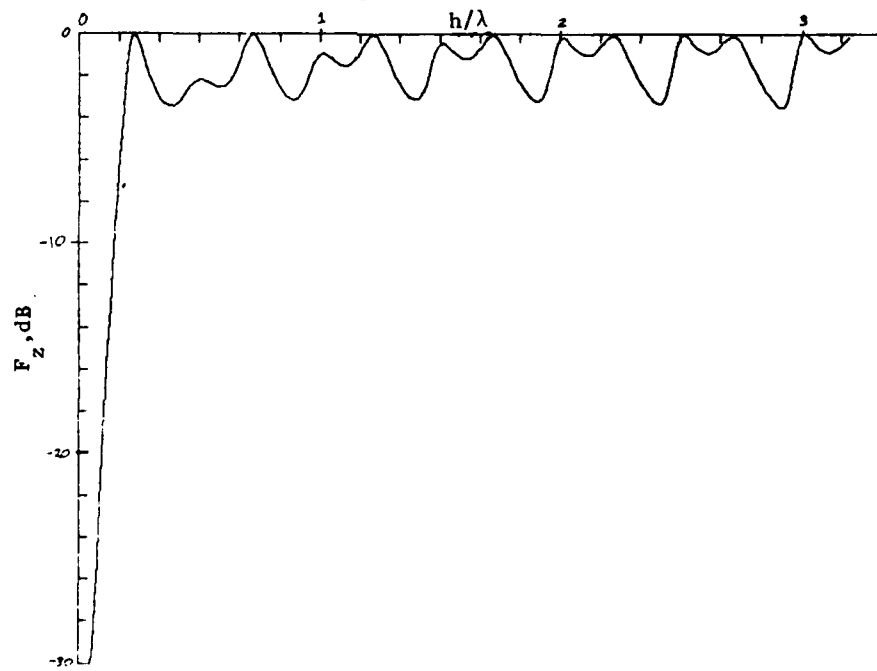


Figure 2-142 Impedance Matching Factor of a Slot Antenna  
 $(h/a = 20)$  (Based on  $Z_0 = 530$  ohms)

Impedance Matching Factor of Folded Dipoles

The impedance matching factor of a basic folded dipole was calculated at out-of-band frequencies. The dipole was assumed to have equal radii  $a$  for both arms, and an arm separation  $D$  to radius ratio of 10 was assumed.

Based on the existence of symmetrical and anti-symmetrical currents on the dipole arms [11, page 3-13], the input impedance of the folded dipole is

$$Z_f = \frac{4Z_a Z_s}{Z_a + 2Z_s}$$

where  $Z_s$  = input impedance of standard dipole

$Z_a$  = input impedance of a shorted transmission line  
 $= j Z_o \tan kh,$

$Z_o$  = characteristic impedance of balanced transmission line  
 consisting of dipole arms =  $276 \log(D/a)$  ohms  
 $= 276$  ohms.

Schelkunoff's equations were used to provide  $Z_s = R + jX$ . The expression for  $Z_f$  is

$$S_f = \frac{4R(Z_o \tan kh)^2}{4R^2 + (2X + Z_o \tan kh)^2} + j \frac{8(R^2 + X^2)Z_o \tan kh + 4X(Z_o \tan kh)^2}{4R^2 + (2X + Z_o \tan kh)^2}$$

The input impedance of the folded dipole was then used to calculate the reflection coefficient based on a characteristic impedance of 300 ohms for the feed transmission line.

Curves of  $Z_f$  were obtained for thin and fat cylindrical dipoles. The results are presented in Figures 2-143 and 2-144. Since these curves indicate periodic resonances at the same electrical lengths as the corresponding standard dipoles, the modeling of these curves may be done using the same principles as used for modeling standard resonant dipoles. It may not be practical to attempt modeling the deep nulls due to characteristic anti-resonances of folded dipoles. These nulls appear to be very sharp for calculations based on a fat cylindrical dipole, as seen in Figure 2-144. This example more closely resembles actual shapes of folded dipoles than does the extremely thin dipole case of Figure 2-143. The exact location of these nulls in frequency may be difficult to determine based on the data specified only for the first resonant peak. Even if both the first and second resonant peaks were specified, the null is not located exactly midway. For the example shown in Figure 2-144, the first and second peaks occur at  $h/\lambda = .23$  and  $.72$ , respectively, while the null occurs in  $h/\lambda = .50$ .

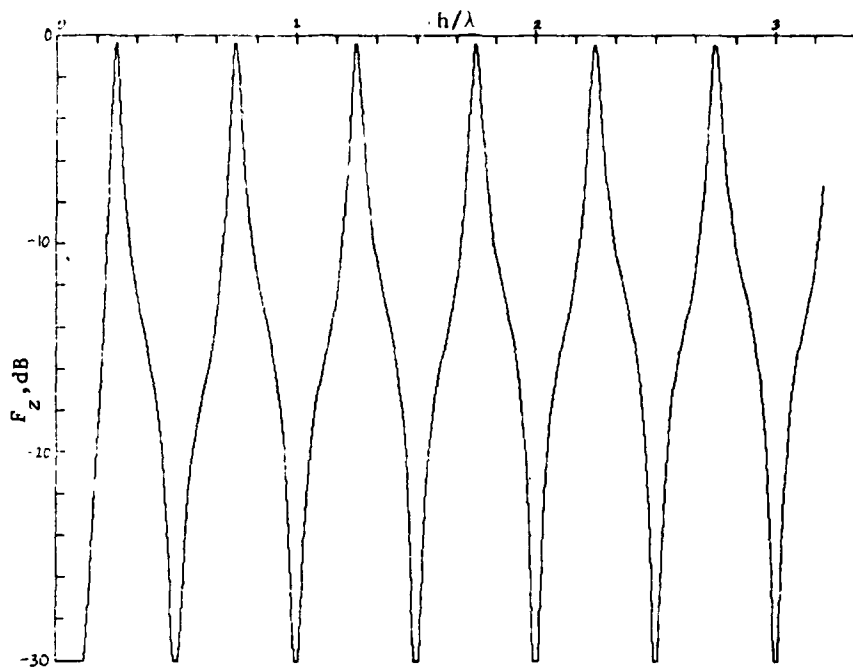


Figure 2-143 Impedance Matching Factor of a Folded Dipole with Thin Elements ( $h/a = 10^6$ ) (Based on  $Z_0 = 300$  ohms)

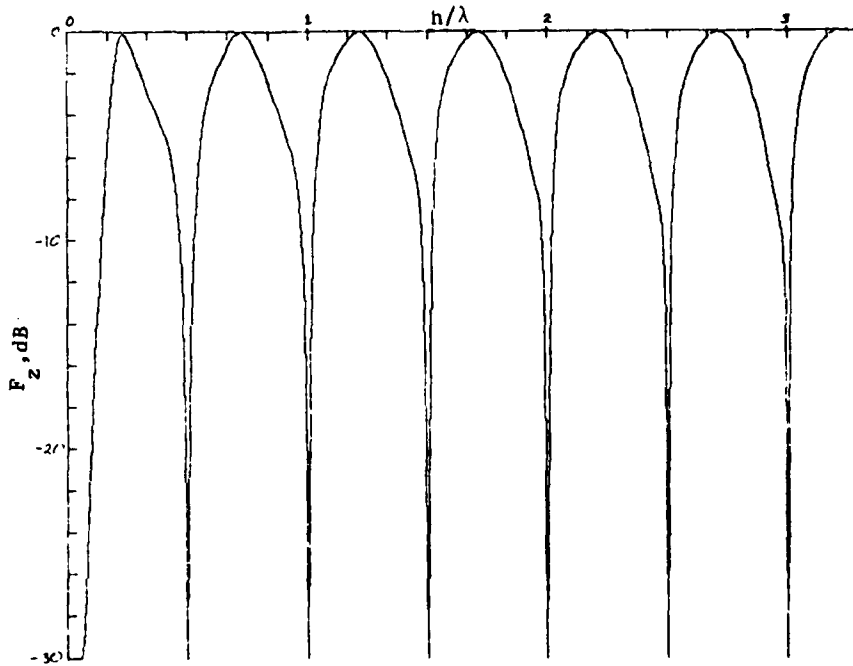


Figure 2-144 Impedance Matching Factor of a Folded Dipole with Fat Elements ( $h/a = 20$ ) (Based on  $Z_0 = 300$  ohms)

As a matter of interest, the first resonant peak and null of the example shown in Figure 2-144 are presented on an expanded scale in Figure 2-145. The relatively wide peak of the first resonance is indicative of the broadband nature of folded dipoles. One example of a resonant peak of a folded dipole based on measurements, given on page 341 of reference [10], is presented in Figure 2-146. The shape of this curve does not agree well with the theoretical shape of Figure 2-145.

Values of  $F_Z$  determined from input impedance measurements of a folded dipole constructed by ARC is shown in Figure 2-146. The dipole elements were made from 300-ohm twin lead taped to a lucite plastic board. A 4:1 transformer balun was attached at the feed point to permit the use of a 50-ohm BNC input connector. As can be seen, the resonances are not very regular, and the nulls are not well defined. The deepest null is -7.4 dB. The fatness ratio for each element of this dipole was about  $h/a = 600$ . For this antenna,  $f_1 = 110$  MHz.

If it is assumed that folded dipoles as found in practice always conform to analyses with a fat cylindrical dipole, the curve of Figure 2-144 represents the frequency performance to be modeled. Since it will generally not be possible to predict the nulls accurately, and since the resonant peaks are considerably broad, it is recommended that  $F_Z$  be modeled with a constant 0 dB level at all frequencies above the first resonance. Below resonance, the modified universal resonance curve can be applied based on a specified Q.

#### 2.10 Impedance Matching Factor of Loop Antennas

Loop antennas comprise a large group of antennas which have unique characteristics and appear with a wide variety of designs. Loops may be electrically small or large, tuned or untuned, shielded or unshielded, and have single or multiple turns of wire. However, let us consider the types of loops most commonly used in practice.

The loop antenna perhaps finds widest application as a receiver of low frequency signals - that is, LF and VLF. At these frequencies, with extremely long wavelengths, the loops are electrically small, and are not self-resonant. A tuning capacitor placed across the terminals of the loop permits

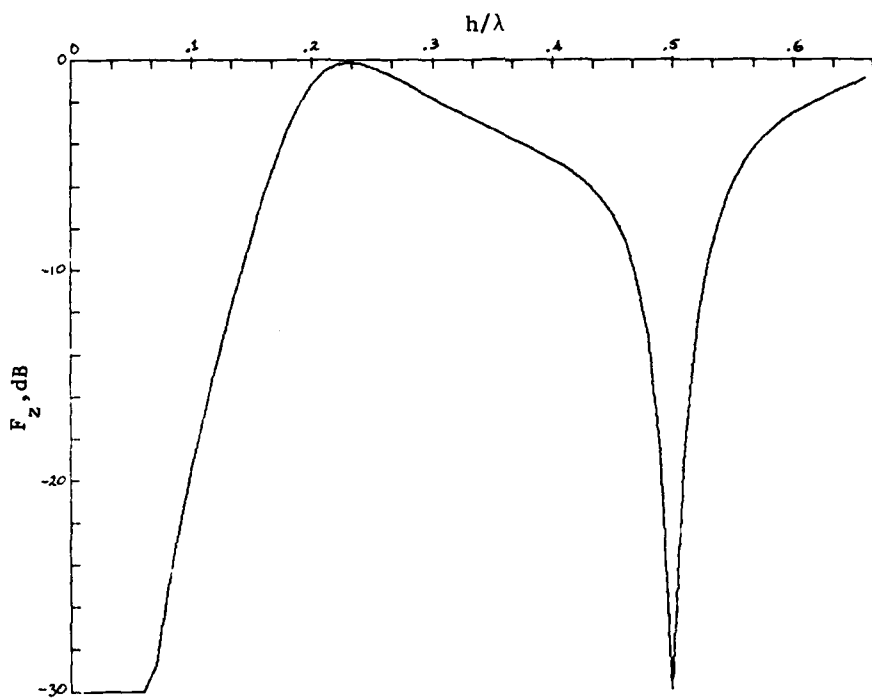


Figure 2-145 Impedance Matching Factor of First Resonance of Folded Dipole with Fat Elements ( $h/a = 20$ ) (Based on  $R_0 = 300$  ohms)

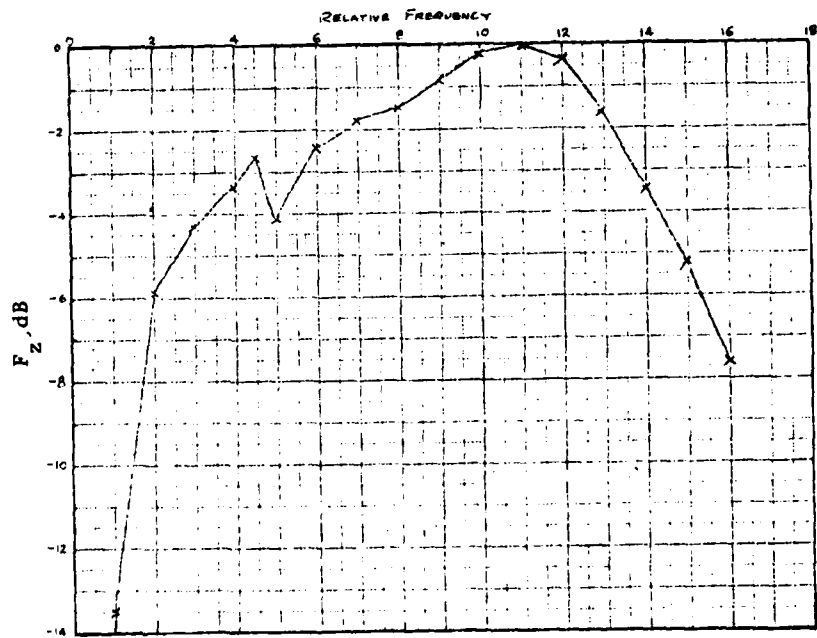
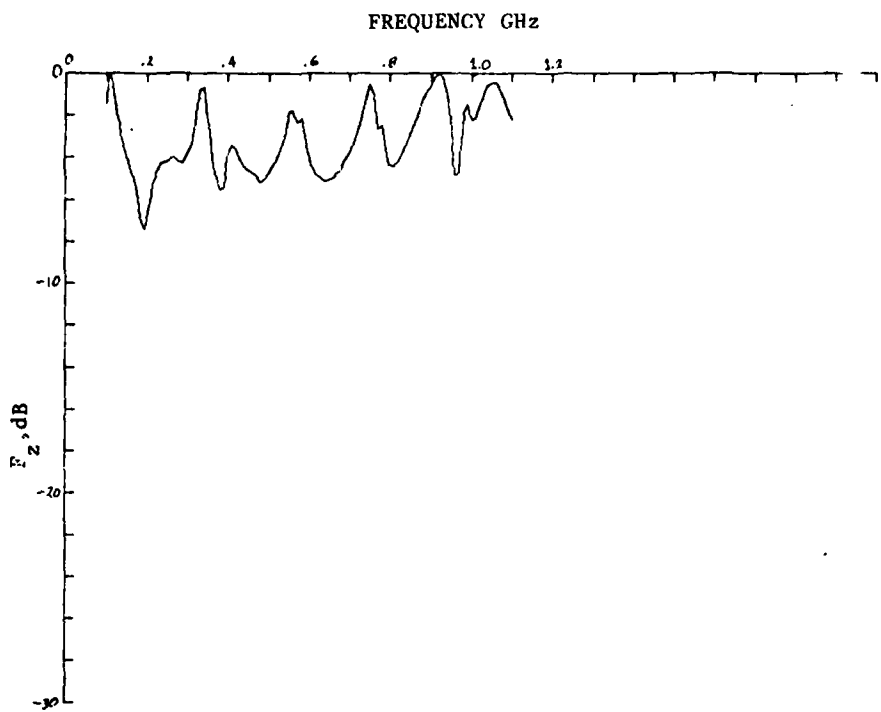


Figure 2-146 Impedance Matching Factor of a Folded Dipole in King [10] (Based on Measured Data)



**Figure 2-147 Impedance Matching Factor of a Folded Dipole  
Constructed of 300-ohm Twin-lead (Based on measured data)**

the loop inductance to be resonated against the capacitor to form a resonant tank circuit. The voltage across the capacitor is then monitored by a high impedance input to a receiver. An electrically small loop is generally very inefficient and is rarely used to transmit low frequency signals. A loop with an input tuning capacitor will have a distinct first resonance with good selectivity above and below this point. At sufficiently high frequencies the loop becomes electrically large where the physical length of the loop conductor is on the order of one-half wavelength or more. In this mode the loop behaves quite differently than it does when electrically small, and an endless sequence of high order resonances can occur as the frequency increases. These conditions will occur for the loop regardless of the number of turns or if it is shielded or not. If the loop has only a single turn its length is  $\pi \times$  diameter. If the loop has  $N$  turns, its length is  $N \times \pi \times$  diameter. This is the length that must be considered in determining its size relative to a wavelength. If  $N$  is unknown, the size of a loop cannot be determined from its diameter alone. If it is assumed that construction details of a loop are not available, it is suggested that modeling  $F_Z$  of an electrically small loop be done with the same model used for a matched dipole.

For the case of an electrically large loop which is designed to operate at a natural resonance without tuning elements, the  $F_Z$  may be described using the model for a resonant dipole without matching. It is expected that Alford loops, which operate at a circumference of one or two wavelengths [11, page 6-3], can be placed within this group. Alford loops, however, contain loading capacitances at the corners of the loop and, therefore, may not resonate at the higher modes as expected.

#### 2.11 Transmission Loss of Yagi-Uda Beam Antennas

The Yagi-Uda beam antenna is a parasitic endfire array of linear elements approximately one-half wavelength long. [9, page 231] It consists of one driven element, which is often a driven element, and a series of directors which are slightly shorter than the driven element. This kind of antenna is not frequency independent, for bandwidths of 2 percent ( $Q=50$ ) are typical. Consequently, the impedance matching factor for this antenna may be modeled as that of a resonant dipole without matching. It is expected that higher order resonances will occur at integral multiples of one-half wavelength based on the behavior of the driven element. If the driven element is a folded dipole, the absence of data describing the out-of-band performance of a Yagi-Uda array, the most suitable model for  $F_Z$  is difficult to determine.

## 2.12

Impedance matching Factor of Frequency-Independent Antennas

The class of frequency-independent antennas is considered here to consist of those antennas designed to have an operational frequency range of 3:1 or greater without the need for tuning. Examples of this class are log-periodic and log-spiral antennas. The useful operating range is so broadband that the concept of  $Q$  as applied to the power transmission loss curve is not valid. The range must be defined by lower and upper frequencies. The VSWR is considered to be acceptable over this entire range.

The impedance matching factor measured by ARC for a commercial log-periodic antenna is shown in Figure 2-148. The operating range of this antenna is 250-1100 MHz with a maximum VSWR of 2:1. As seen in the figure, however, the impedance is reasonably good up to at least 4 GHz with the maximum loss of 5 dB occurring near 1.5 GHz. Below the lower limit  $F_Z$  tends to increase rapidly.

An example of a logarithmic-spiral antenna is shown in Figure 2-149, also measured by ARC. The specified operating range of this antenna is 200-1000 MHz; however,  $F_Z$  is seen to remain less than 2 dB up to at least 4 GHz. Below 200 MHz  $F_Z$  tends to increase rapidly.

Based on these limited amount of data, it is apparent that frequency-independent antennas may be modeled using the modified universal resonance function (for some value of  $Q$ ) to simulate the lower cutoff, and to hold the loss at 0 dB for all frequencies above the lower frequency, except for a general decay due to ohmic loss. The selection of  $Q$  is somewhat arbitrary and is not necessarily determined from the operating frequencies of the antenna. The shapes of the curves in Figures 2-148 and 2-149 below the lower frequencies compared with the family of  $Q$ -curves in Figure 2-140 indicate that  $Q=1$  provides a reasonable fit. The curve for this  $Q$  falls to -10 dB at one-half the peak frequency.

## 2.13

Impedance Matching Factor of Helical Antennas

A helical antenna is constructed in the form of a monopole over a ground plane in which the monopole element is shaped as a helix. [9, page 187] Thus, it has a single radiating element which is fed at the base against the ground plane. The electrical properties of the helix are a function of its

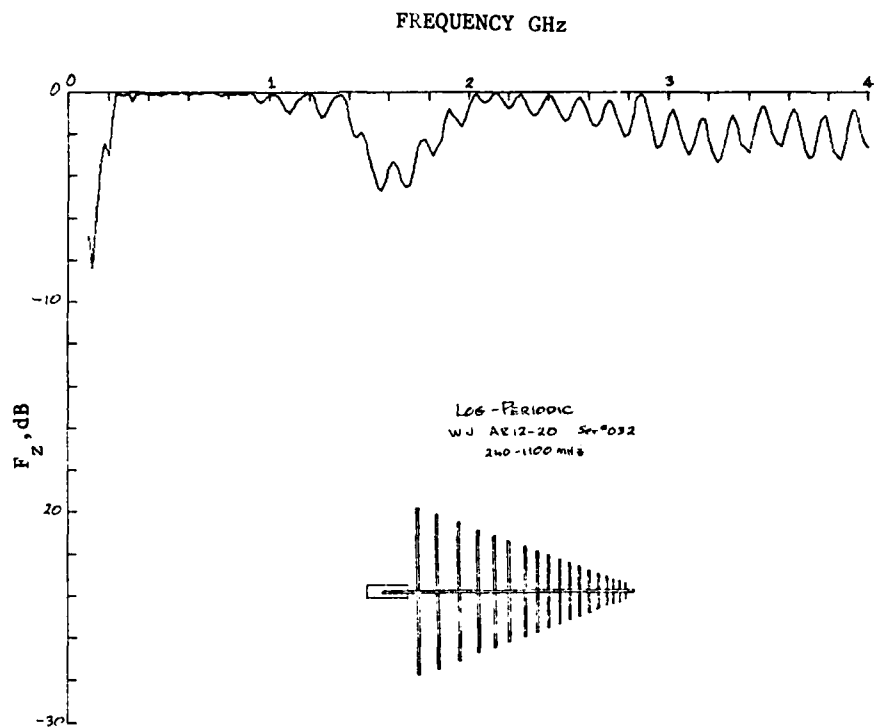


Figure 2-148 Impedance Matching Factor of a Log-periodic Antenna  
(from measured data)

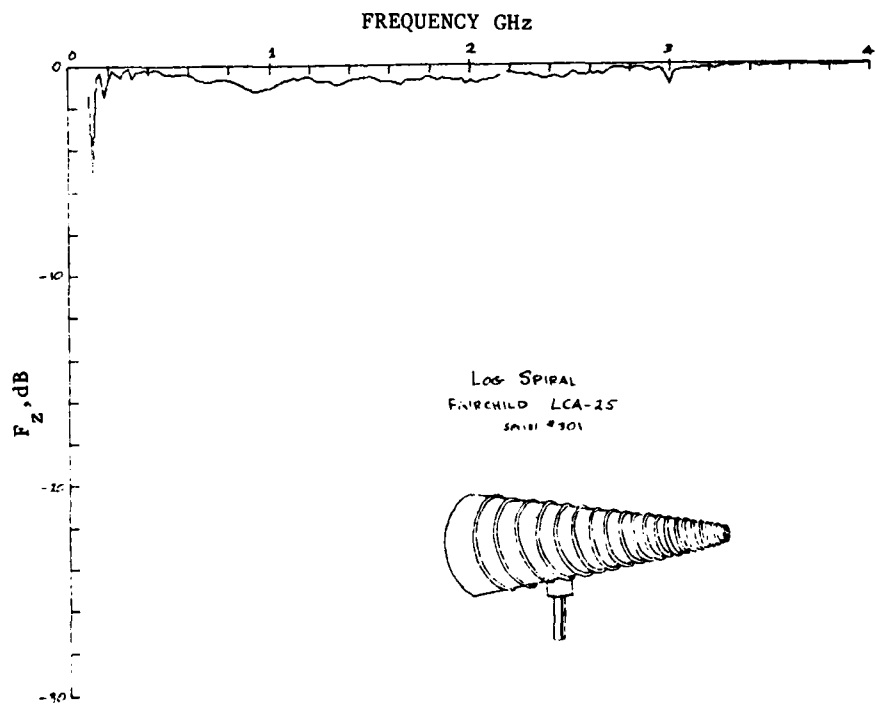


Figure 2-149 Impedance Matching Factor of a Log-spiral Antenna  
(from measured data)

Geometry, i.e., diameter and turn spacing. At low frequencies where the dimensions are very small compared with the wavelength, the helix behaves as a monopole with a small loop coaxial with the helix. For this mode the maximum radiation is in a plane perpendicular to the helix axis, and the radiation is minimum in the direction of the axis. When the diameter and spacing become appreciable fractions of a wavelength, another radiation mode occurs which concentrates the radiation in the axial direction. In practically all cases the helical antenna is designed to operate in this axial mode.

Helical antennas are not frequency-independent but do tend to be relatively broadband. Commercial models can have bandwidths that are 20% to 50% or more of the center frequency [12].

If the circumference of a helix of  $N$  turns is  $C$ , then the length  $L$  of the helix conductor is approximately  $NC$ . At a low frequency for which  $NC \approx \lambda/4$ , it is expected that the helix should behave as a monopole and exhibit resonance. This resonance is relatively broadband due to the diameter of the helix. There is expected to be selectivity on each side of this "normal" mode of resonance. When the frequency increases to where  $C \approx 0.7\lambda$ , the axial mode occurs, and the antenna becomes very efficient over a broad range of frequencies. [13, Ch. 7] Thus, if the axial mode begins at a frequency  $f_1$ , then the normal mode resonance should occur at approximately  $f_1/2.8N$ . For example, if a 6-turn helix has a lower frequency limit (axial mode) of 108 MHz, self-resonance is expected at about 6.4 MHz. Higher order resonances should occur at approximately  $6.4 + n \cdot 12.8$  MHz,  $n=1, 2, 3$ , etc. until the axial mode occurs. Thus, at frequencies below where the axial mode occurs, the terminal impedance of a helical antenna is highly sensitive to changes in frequency. In the axial mode, where  $3/4\lambda < C < 4/3\lambda$ , the terminal impedance is nearly constant with frequency. The dimensions of the helix are not critical in the axial mode. For frequencies above the design axial mode, it appears that the terminal impedance remains relatively stable, but the radiation pattern deteriorates from the desired beam shape and becomes multilobes in many directions. Consequently, in the absence of measurement data for helical antennas over a wide frequency range, a suggested model for the impedance matching factor is 0 dB level at all frequencies above the first natural resonance. The fall-off below this frequency can be modeled with the modified resonance function using an arbitrary value of  $Q=1$ .

Traveling wave antennas are non-resonant radiating systems that are normally large and constructed over the long wire antenna and the rhombic. These antennas can be designed to operate at VHF and UHF. [11, CH. 4] Traveling wave antennas are essentially transmission lines terminated in their characteristics impedance. Consequently, no energy is reflected and standing waves are not present on the conductors. It should be noted that one form of long wire antenna is without termination, where advantage is taken of the radiation from the resulting standing waves. Modeling the impedance matching factor for this standing wave type of wire antenna could use the model developed for a resonant dipole. However, an additional loss term at the low frequencies due to the height above ground should be added. This loss term is described below.

Traveling wave antennas are normally designed to operate within a frequency range where their electrical length is from one to ten or twelve wavelengths. Consequently, they are relatively broadband. Bandwidth limitations may be due more to degradation of the feed (matching and balun) network and the terminating resistor than of the radiating elements themselves. If the termination can be maintained at all frequencies there should be no lower frequency limits while an upper limit should arise eventually where other transmission modes begin to exist on the radiating wires. The terminating resistance for a rhombic must normally be non-inductive and have a resistance on the order of 700 to 800 ohms. The power to be dissipated in the terminal resistor varies from about 50 percent of the input power when the sides are of the order of two wavelengths to 1.5 percent for rhombics five wavelengths or more per side. Feed circuitry for rhombics is normally designed for a unique value of 600 ohms for the majority of applications.

Transmission loss terms arising from deterioration of the feed and termination elements at higher frequencies are considered in Section 2.0.

At the low frequencies below the design band, the feed circuit may deteriorate, but this condition is not assumed here. Instead, there appears to be a height factor which will tend to reduce radiation as the frequency decreases toward zero due to the cancelling effect of the ground reflection or image. This loss term is considered in Section 2.16.

As a result of the many uncertainties associated with this type of antenna at out-of-band frequencies, it is reasonable to accept a constant value of  $F_7=0$  dB at all frequencies for the model. As already mentioned, low and high frequency adjustments to account for degradation will be made in later sections.

2-15        Impedance Matching Factor of a Horn Antenna

Horn antennas generally consist of a rectangular or circular waveguide section having a flared opening at one end. The other end of the waveguide is either flanged for connection to a waveguide or is shorted to accommodate a probe for coupling with a coaxial line. It is principally the interaction between the coupling probe and the EM field inside the waveguide throat of the latter type of horn that determines the characteristics of input impedance with frequency.

Horns normally have a design operating range of about one octave. The upper and lower limits are distinctly determined by the dimensions of the waveguide. The lower limit is defined as the frequency for which the longer dimension of a rectangular waveguide is one-half wavelength. This is an absolute limit called the cutoff frequency. Theoretically, frequencies below this value will not be propagated in the guide. Within the design band there is a well defined mode of propagation of the electric and magnetic fields ( $TE_{10}$ ). The next higher order mode can occur when the larger guide dimension equals one wavelength. It is undesirable to operate a guide at frequencies which permit higher order modes, since they will not be properly coupled to the load. As a result, reflections and standing waves may be set up causing losses. Consequently, the design band of a horn ranges from the cutoff frequency to twice this frequency. [9, page 95]

Figure 2-150 shows the impedance matching factor measured for a commercial standard horn designed to operate from 1 to 2 GHz. As can be seen, the factor does not fall abruptly at 1 GHz, although, theoretically, propagation in the guide can't exist below 1 GHz. However, it is presumed the user will supply the frequency range below cutoff. Based on the curve shown, the simplest model is a straight line from  $(f/f_c, TLOSS)=(.8,0.0)$  to  $(.6,-20.)$  which is indicated by a dashed line. Theoretically, however, the attenuation in a waveguide operating below cutoff is not infinite. The loss (dB) per guide

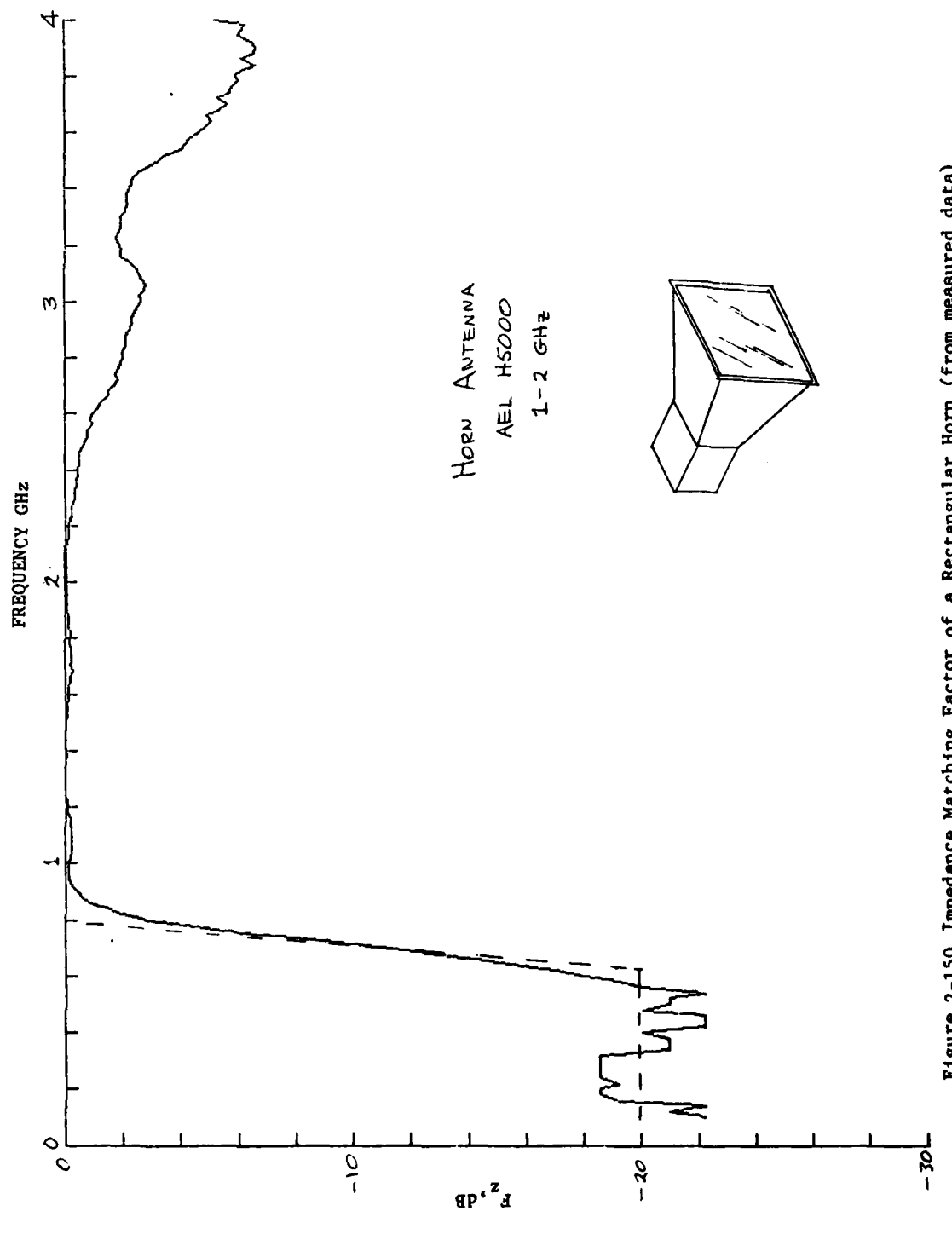


Figure 2-150 Impedance Matching Factor of a Rectangular Horn (from measured data)

length  $d$  is given by [14, page 23-6]

$$L = 54.4 \frac{d}{\lambda_c} \sqrt{1 - \left(\frac{\lambda_c}{\lambda}\right)^2}$$

where  $\lambda_c$  is the wavelength at cutoff. Note that at very low frequencies where  $\lambda \gg \lambda_c$ , limiting loss is independent of frequency and is

$$L = 54.4 \frac{d}{\lambda_c} \text{ dB.}$$

If we consider that the length of waveguide inside the horn is approximately  $d/\lambda_c = .5$ , then the limiting loss is  $L=27.2$  dB. Consequently, a limit of -20.0 is a reasonably safe level for modeling  $F_Z$  from  $f=0$  to  $f=.6f_c$ , as shown in Figure 2-150.

Above the design band there are too many uncertainties to allow prediction of the terminal impedance. It is expected that  $F_Z$  will vary considerably but may return to 0 dB over limited ranges of frequencies. Therefore, the model should provide a constant level at 0 dB for all frequencies above cutoff.

The input impedance characteristics of a horn antenna also apply to antennas which use the horn as a primary feed, such as radar antennas. The terminal characteristics are determined primarily by the nature of the feed point. However, radar antenna systems usually use waveguide to transfer power between the transmitter/receiver and the antenna. A large problem seen with out-of-band performance of a rotatable radar antenna is the existence of higher order modes in the guide. These modes are not generally predictable since they depend on dimensions of the waveguide sections, locations of discontinuities and fittings in the line (e.g., elbows, tees, reducers), and the angular position of the rotary joint.

Directive gain is the second term of the overall gain expression of an antenna. It accounts for the variations of radiation levels at different directions from the antenna and is given relative to the level that would be received if the antenna were an isotropic radiator. Internal power losses of the antenna are not considered in the directive gain term. Thus, the modeling of directive gains is based on lossless antennas.

As is currently done in IEMCAP, the models for low-gain antennas, such as dipoles, monopoles, loops, etc., are derived from theoretical expressions; whereas, for high-gain antennas the models are based on user input data such as mainbeam gain, sidelobe gain, and beamwidths which define the size and shape of the radiation pattern. In order to extend these models to out-of-band frequencies it will be necessary to rely heavily on available measured data and applicable theoretical analyses. Unfortunately, the field of antennas is lacking in both of these types of data at out-of-band frequencies.

#### 2.16.1 Modeling the Directive Gain of Dipole Antennas

The expression for the magnitude of the electric field of a symmetrical center-fed, thin linear antenna of length  $L=2h$  is [13, page 141].

$$|E| = \frac{60 I_0}{r} \left| \frac{\cos(\frac{kL}{2} \cos\theta) - \cos(\frac{kL}{2})}{\sin\theta} \right|$$

where  $I_0$  = peak value of sinusoidal current distribution on antenna  
 $r$  = distance from antenna (assumed to be far field)  
 $k$  =  $2\pi/\lambda$   
 $\theta$  = elevation angle in spherical coordinates, where antenna axis is aligned with Z-axis.

The expression in the absolute magnitude brackets describes the shape of the radiation pattern. Theoretically, this expression is valid over all frequencies - that is, for  $0 < L/\lambda < \infty$  - and provides a basis for modeling. This pattern function should not be used directly for the model for several reasons. The theoretical pattern for a dipole longer than one wavelength consists of multiple lobes with deep, sharp nulls between lobes. The angular positions of the nulls are highly sensitive to frequency and, in practice,

are easily affected by the local environment. Further, the "fatness" or diameter of real antennas tends to eliminate the nulls. Consequently, the null and lobing details defined by the pattern function are generally not reliable and should be eliminated from the model. A practical approach is to model the envelope of the pattern in a manner which preserves the most significant features. First, the nulls in the direction of the antenna axis should be included in the model. Second, the relatively high gain lobes near the antenna axis that occur at higher frequencies should also be included in the model.

A study of the shapes of the patterns over a wide range of frequencies suggests that they be enveloped with a circular arc tangent to the antenna axis plus a straight line parallel to the antenna axis. Two examples of this modeling are illustrated in Figure 2-151.

The first step is to determine the radius of the envelope circle. Let the antenna length be expressed as  $n$  half-wavelengths, where

$$n = 2 \frac{L}{\lambda} .$$

Then, the angle of maximum radiation, that is, the angle that the strongest lobe makes with the antenna axis, is given approximately by [9, page 180]

$$\cos \theta = \frac{n-1}{n} .$$

Figure 2-152 illustrates the geometry of a circle with center  $C$  on the Y-axis and tangent to the X-axis. The circle passes through point  $A$  where angle  $AOD = \theta$ . Let  $B$  bisect  $OA = S$ . By similar triangles angle  $OCB = \theta$ . If it is assumed that  $AD = 1$ , then from right triangle  $ODA$

$$\sin \theta = \frac{1}{S}$$

and from right triangle  $OBC$ , where  $OC = R$ ,

$$\sin \theta = \frac{S}{2R} .$$

Combining these, we have

$$\begin{aligned} R &= \frac{1}{2 \sin^2 \theta} \\ &= \frac{1}{2(1-\cos^2 \theta)} \end{aligned}$$

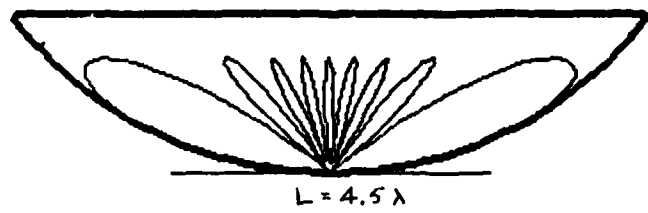
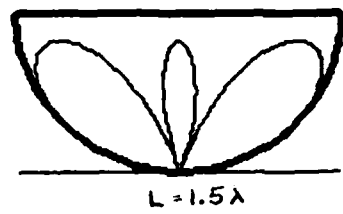


Figure 2-151 Examples of Model Envelope Around Dipole  
Radiation Patterns

Substituting  $\cos\theta$  from above into this expression and simplifying, we have

$$R = \frac{n^2}{2(2n-1)}.$$

This expression gives the approximate radius of a circle tangent to the antenna axis at the center of the antenna and passing through the peak of the maximum gain or outer lobes for an antenna of  $n$  half-wavelengths long. It is realized that this expression gives a slightly smaller radius than required since we want the circle to enclose the outer lobes, not pass through the center of them.

The equation of the tangent circle is in Polar form with the origin at 0 is

$$G_o(\theta) = 2R \sin\theta$$
$$= \frac{n^2}{2n-1} \sin\theta.$$

Next, it is necessary to fit this function to the theoretical pattern shapes for various values of  $n$  in order to determine an appropriate adjustment of  $n$  for the model.

Not only are we interested in the shape of the radiation pattern, we are also interested in the relative magnitude of it over all frequencies. The radiation pattern, given earlier, by

$$F(\theta) = \frac{\cos(\frac{kL}{2} \cos\theta) - \cos(\frac{kL}{2})}{\sin\theta}$$

does not, by itself, define the relative magnitudes of the patterns for a given antenna of length  $L$  radiating  $W$  watts of power at various frequencies. For example, the magnitude of the pattern envelope broadside to the antenna ( $\theta=90^\circ$ ) varies periodically from 1.0 (for odd  $n$ ) to 2.0 (for even  $n$ ). The variation of peak current  $I_o$  with frequency (or electrical length) for a constant level of radiated power  $W$  must also be considered since it affects pattern scaling. If we square the field strength expression, we have

$$|E|^2 = \left(\frac{60}{r}\right)^2 I_o^2 [F(\theta)]^2$$

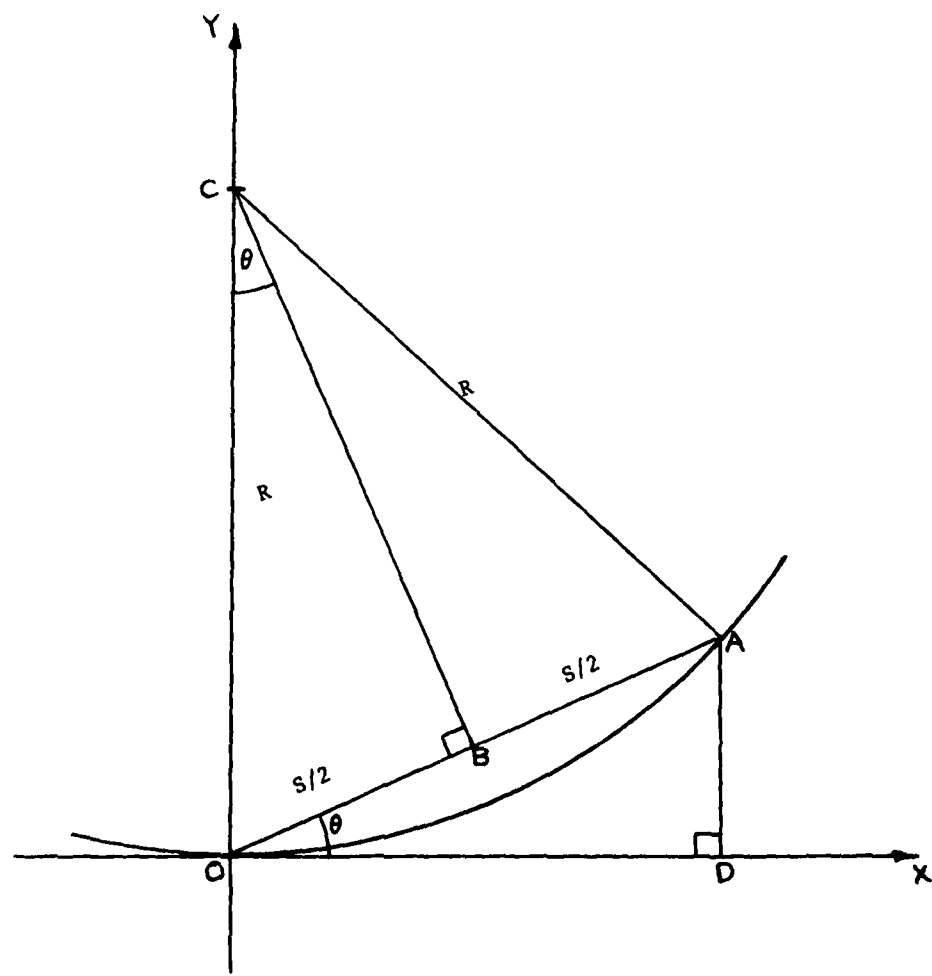


Figure 2-152 Geometry for Determining Radius of Envelope Circle

Multiply by  $\frac{R_o}{R} = 1$  where  $R_o$  = radiation resistance of antenna referenced to a current maximum (at  $I_o$ ).

$$\begin{aligned} |E|^2 &= \left(\frac{60}{r}\right)^2 \frac{I_o^2 R_o}{R_o} [F(\theta)]^2 \\ &= \left(\frac{60}{r}\right)^2 \frac{W}{R_o} [F(\theta)]^2 \\ |E| &= \frac{60\sqrt{W}}{r\sqrt{R_o}} |F(\theta)| \end{aligned}$$

The total power radiated from the antenna may be expressed as [13, page 147; 15, page 41]

$$W = I_o^2 R_o$$

That is, if the antenna were fed at a current peak with input current  $I_o$ , the input power would be given by the above expression. This is the same total power that would be radiated when the antenna is center-fed with an input current that results in a peak current of  $I_o$ . Consequently, the above field strength expression provides the absolute power density level in the direction  $\theta$  at a distance  $r$  for a total radiated power of  $W$  watts. For pattern modeling, variables  $W$  and  $r$  are assumed to be constant. The desired scaling factor is  $1/\sqrt{R_o}$  which varies with the electrical length of the antenna. This radiation resistance  $R_o$  is given by [15, page 40]

$$\begin{aligned} R_o(kL) &= \gamma + \ln(kL) - Ci(kL) + \frac{1}{2} \sin(kL) [Si(2kL) - 2Si(kL)] \\ &+ \frac{1}{2} \cos(kL) [\gamma + \ln(\frac{kL}{2}) + Ci(2kL) - 2Ci(kL)] \end{aligned}$$

(Note: A constant factor of 60 for this entire expression is omitted since it does not affect relative scaling with frequency.)

where  $\gamma$  = Euler's constant = 0.5772...

$Si$  = sine integral

$Ci$  = cosine integral

The gain pattern of the half-wave dipole is chosen for an absolute reference for all the patterns. Consequently, an absolute scaling factor  $K$  must be defined such that the peak value of the pattern of  $\theta=90^\circ$  for a half-wave dipole ( $kL=\pi$ ) is unity

$$|E| = \frac{K}{\sqrt{R_o(\pi)}} F\left(\frac{\pi}{2}\right) \\ = 1$$

For this case,  $F\left(\frac{\pi}{2}\right) = 1.0$  and  $\sqrt{R_o} = 1.10$ . Consequently,  $K = 1.10$ , and the scaled pattern function is

$$F'(\theta) = \frac{1.10}{\sqrt{R_o(kL)}} \left| \frac{\cos\left(\frac{kL}{2}\cos\theta\right) - \cos\left(\frac{kL}{2}\right)}{\sin\theta} \right|$$

Since multiple lobing does not occur for antenna lengths shorter than one wavelength ( $kL < 2\pi$ ), this region of modeling is treated separately. The model for all antenna lengths less than one wavelength is a unity circle, i.e.,  $G(\theta) = \sin\theta$ . This is the theoretical pattern of a very short dipole ( $kL \ll 2\pi$ ). The peak value of the scaled pattern for a one-wavelength dipole is 1.21 which is less than 1.7 dB above that of a half-wave dipole. Thus, a unity circle model is also applied to a full-wavelength antenna.

For antenna lengths greater than one wavelength multiple lobing occurs which tends to broaden the pattern along the antenna axis. A study of pattern behavior with increasing frequency (or  $kL$ ) reveals a periodic broadening with each wavelength. The pattern is broadest at odd multiples of one-half wavelength ( $n$  odd). Although the pattern generally becomes broader with increasing wavelengths, there is a relatively less broadening of the pattern between the odd multiples where even multiples or an integral number of wavelengths occur. In order to envelope the maximum excursions, the model parameters were developed from a detailed study of the scaled pattern at odd multiple half-wavelengths only ( $n$  odd).

The scaled pattern was calculated from  $\theta=2^\circ$  to the first peak for several odd values of  $n$  ranging from 3 to 61 and plotted on rectangular coordinates shown in Figure 2-153. This plot provides the shapes of the pattern boundaries which are to be modeled with a circular fit. These curves are similar to those shown in Figure 4-3 of Jasik [11, page 4-5].

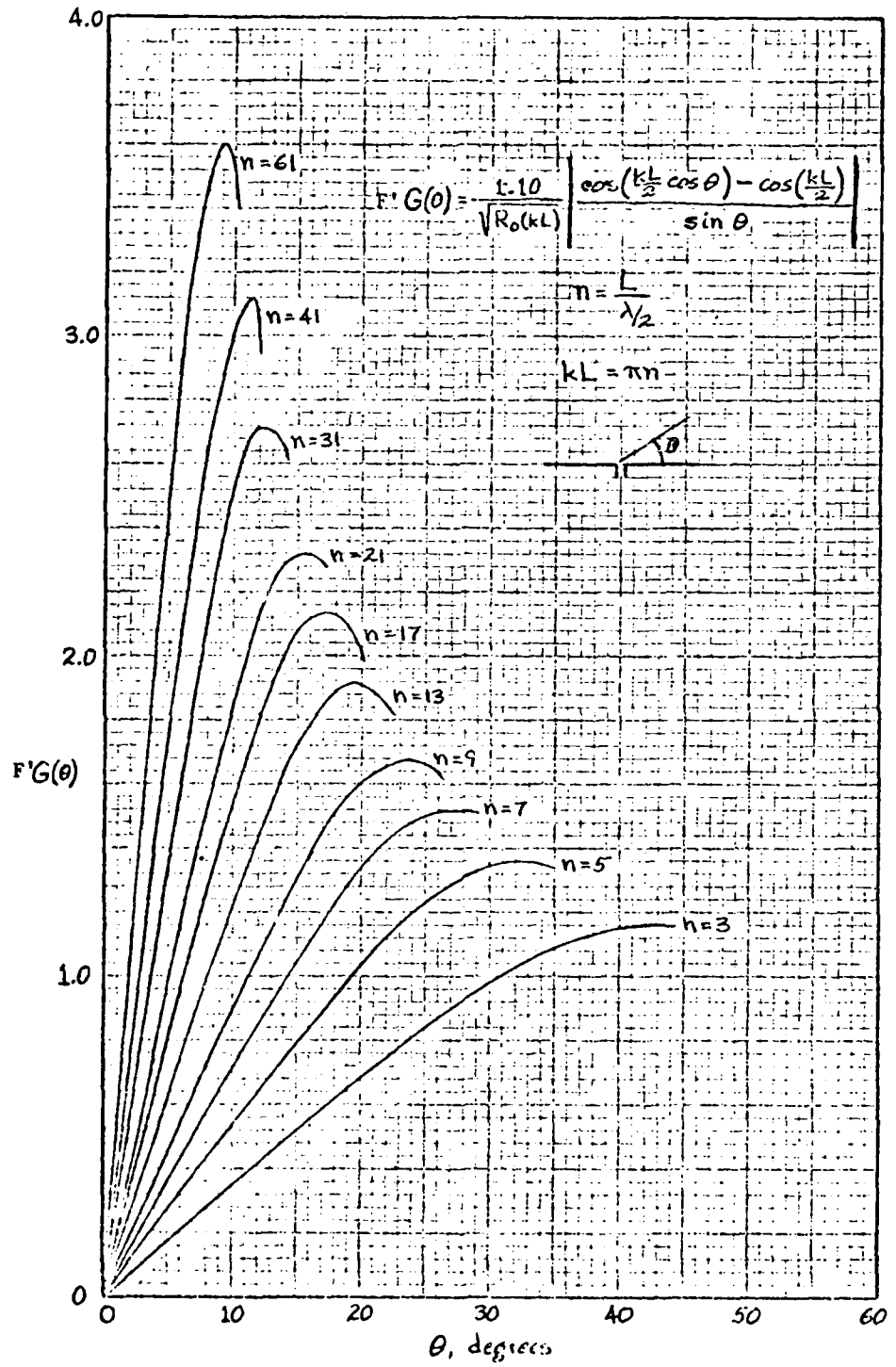


Figure 2-153 Radiation Pattern Function of Center-fed Dipole

The model function, given earlier,

$$G(\theta) = \frac{n_o^2}{2n_o - 1} \sin \theta$$

was plotted similarly for the values of  $n_o = n$  (results not presented here). A comparison between the two families of curves indicates good agreement if

$$n_o = n + .5$$

Using this definition for  $n_o$ , a new family of model curves was calculated and plotted as shown in Figure 2-154. The slopes of the model curves show excellent agreement with the slopes of the theoretical patterns in Figure 2-153.

Consequently, a new family of curves for these model values was calculated and plotted, as shown in Figure 2-154. The slopes of the model curves show excellent agreement with the slopes of the theoretical patterns in Figure 2-153

The relationship between  $n$  and  $n_o$  is presented in Figure 2-155. The solid line represents  $n_o = n$ , and the dashed line indicates the model relationship. As stated above, the value of  $n_o$  exceeds  $n$  by .5 for all  $n \geq 3$  ( $kL \geq 3K$ ). Since the amplitude of the model function becomes 1 for  $n_o = 1$ , the value of  $n_o$  is shown at a constant level of 1 for all  $n$  below 2. This corresponds to a unity circle for all model patterns in this region. Between  $n = 2$  and  $n = 3$  a straight line is drawn for the model function in order to provide model continuity. The equation of this line is

$$n_o = 2.5n - 4.$$

Further examination of the scaled patterns over a wide range of frequencies indicates that a straight-line envelope across the peaks of the lobes provides a reasonable containment of the pattern if located at a distance of 1 from the antenna axis. The unity circle is, therefore, tangent to the envelope line, and all larger radius circles are truncated at this line.

This essentially completes the definition of the proposed directive gain model for linear, center-fed antennas. There are three distinct regions of antenna electrical length for which the model is defined differently. These models are summarized below. The dipole length is expressed in terms of  $h - \frac{1}{2}L$ .

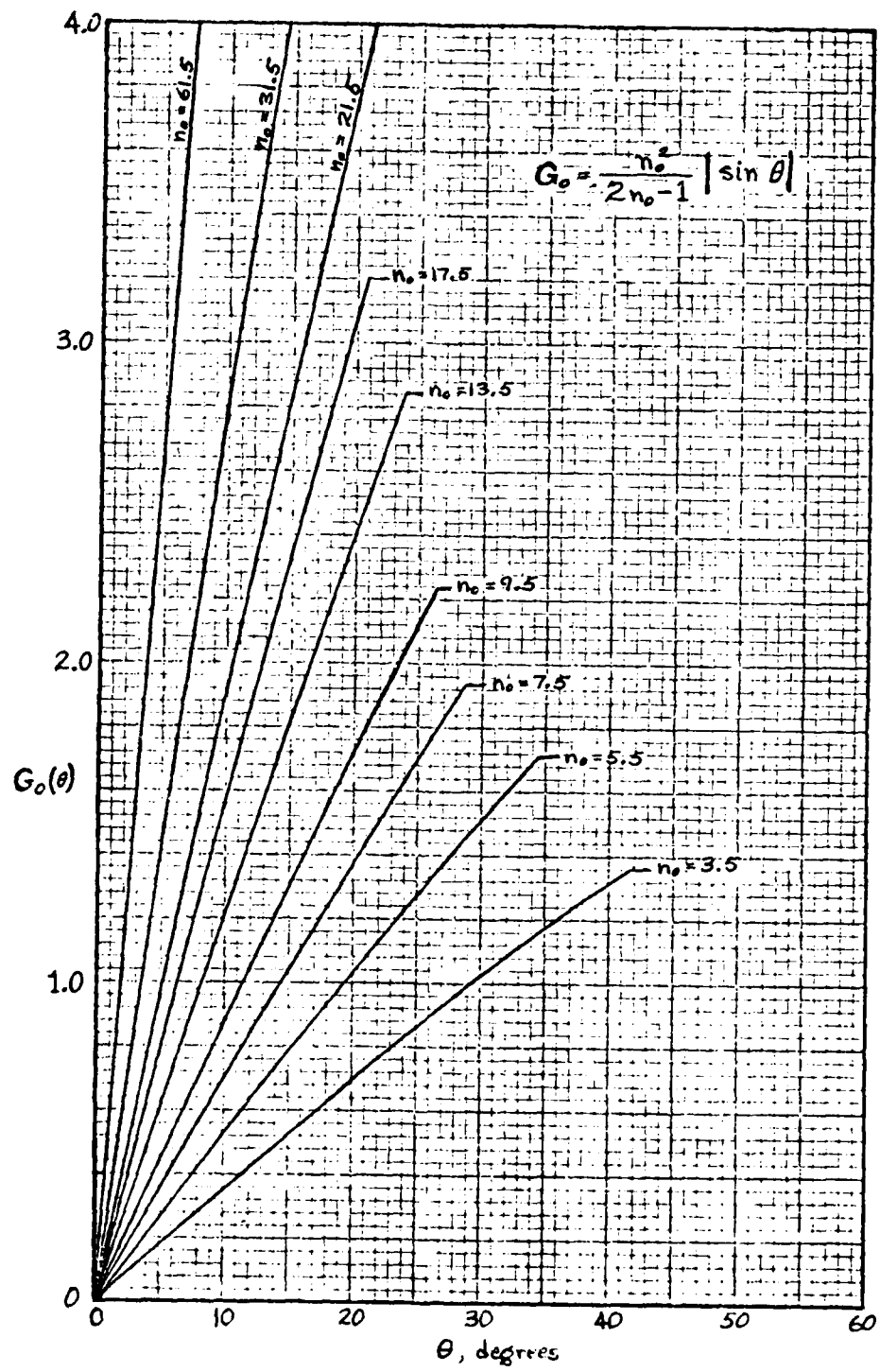


Figure 2-154 Circular Envelope Curves of Pattern Model

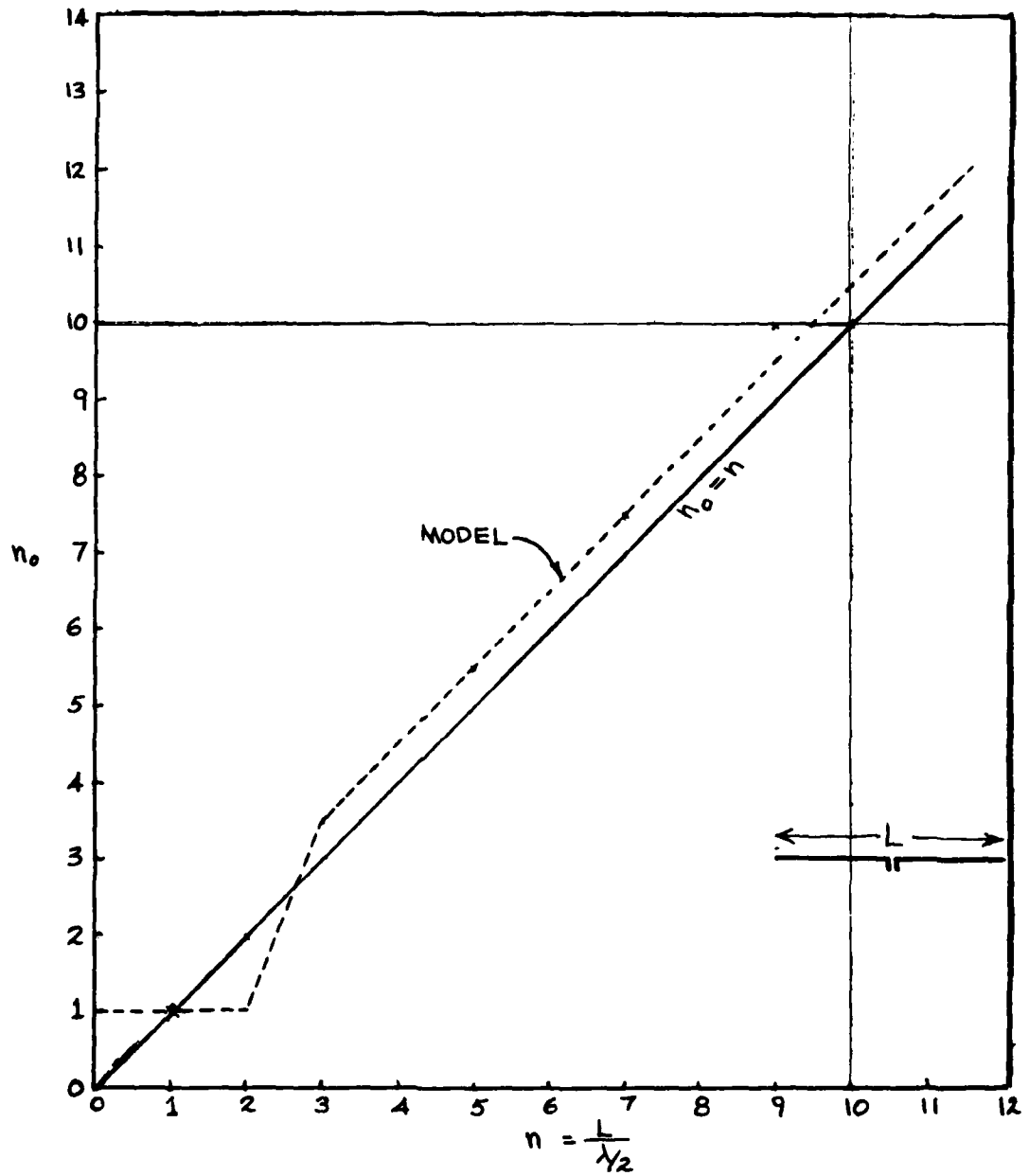


Figure 2-155 Relationship Between  $n_0$  for Model Circle Envelope  
Function and Electrical Length of Dipole =  $n$   
Half-wavelengths

Region I:  $0 < \frac{h}{\lambda} \leq .5$

$$G_1 = \sin\theta$$

If  $G < .1$ , then  $G = .1$

Region II:  $.5 \leq \frac{h}{\lambda} \leq .75$

$$G_2 = \frac{n_o^2}{2n_o - 1} \sin\theta$$

where  $n_o = 2.5n - 4$

$$= 10\left(\frac{h}{\lambda}\right) - 4$$

If  $G \sin\theta > 1$ , then  $G = \frac{1}{\sin\theta}$ ;  $0 \neq 0$

If  $G < .1$ , then  $G = .1$

Region III:  $.75 \leq \frac{h}{\lambda}$

$$G_3 = \frac{n_o^2}{2n_o - 1} \sin\theta$$

where  $n_o = n + .5$

$$= 10\left(\frac{h}{\lambda}\right) + .5$$

If  $G \sin\theta > 1$ , then  $G = \frac{1}{\sin\theta}$ ;  $0 \neq 0$

If  $G < .1$ , then  $G = .1$

For all three models a lower limit on the gain is placed arbitrarily at .1 or -20 dB. This is a practical limit for radiation in the axial direction, since real antennas with finite thickness seldom exhibit nulls deeper than -20 dB.

The above directivity gain model has been programmed on a minicomputer to be drawn superimposed on the theoretical scaled pattern function. A series of plots illustrating the features of the model for antenna lengths ranging from  $L/\lambda=.25$  to  $L/\lambda=10.1$  is presented in Figures 2-156 and 2-157. The patterns shown in Figure 2-156 are drawn on a linear polar scale, and those shown in Figure 2-157 are drawn on a logarithmic polar scale. The straight line seen at the bottom of each pattern represents the antenna wire. One half of the length of this line represents a scale of unity gain for the linear plots, and a scale of 20 dB for the logarithmic plots.

As expected, the model shows excellent enveloping of the outer lobes for odd half-wavelengths (1.5, 2.5, 3.5,...) but tends to appear excessively large for the integral wavelength cases (2.0, 3.0,...). It is possible to model these periodic variations; however, several factors should be considered. It is questionable whether the model should become sufficiently complicated to account for these second-order variations. The errors shown in the figures may appear excessive, however, there is evidence indicating that the radiation patterns of real dipoles having finite thickness exhibit a general lack of deep nulls and have a finite amount of radiation along the dipole axis. Figure 2-158 [11, page 3-8] illustrates pattern degradation as the dipole becomes fatter for various electrical lengths. The top row, for an infinitely thin dipole, shows the theoretical patterns. The remaining rows illustrate measured patterns for dipoles having the indicated length/diameter ratios.\* There is a striking degree of pattern degradation for the  $L = .625\lambda$  and  $L = 1.125\lambda$  cases. It is interesting to note that in some cases lobes disappear and in other cases new lobes are formed. Since these kinds of details are extremely difficult to predict with theory, the most practical solution may be to provide an envelope which will contain the majority of patterns for any given "fatness" ratio. It is felt that the proposed model provides a satisfactory compromise between minimal error and simplicity in view of the wide range of complex variations that can occur with actual patterns.

\* Note that  $L$  in Figure 2-158 is one-half the dipole length.

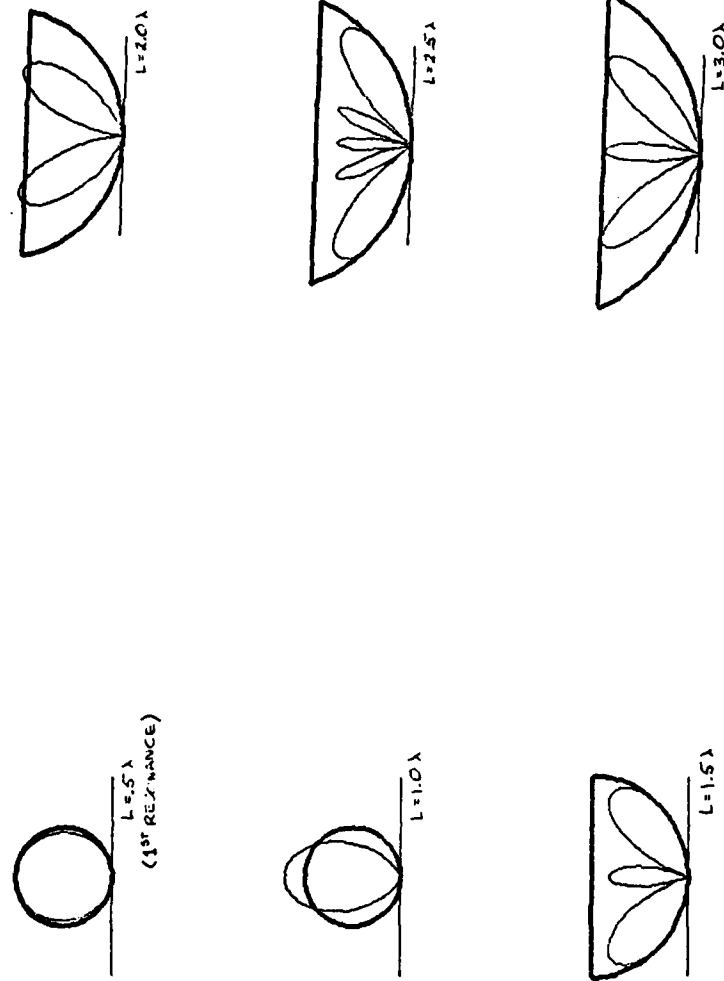


Figure 2-156 Dipole Radiation Patterns  
Illustrating Model Envelope (Drawn on  
Linear Scale)

Figure 2-156 Continued)

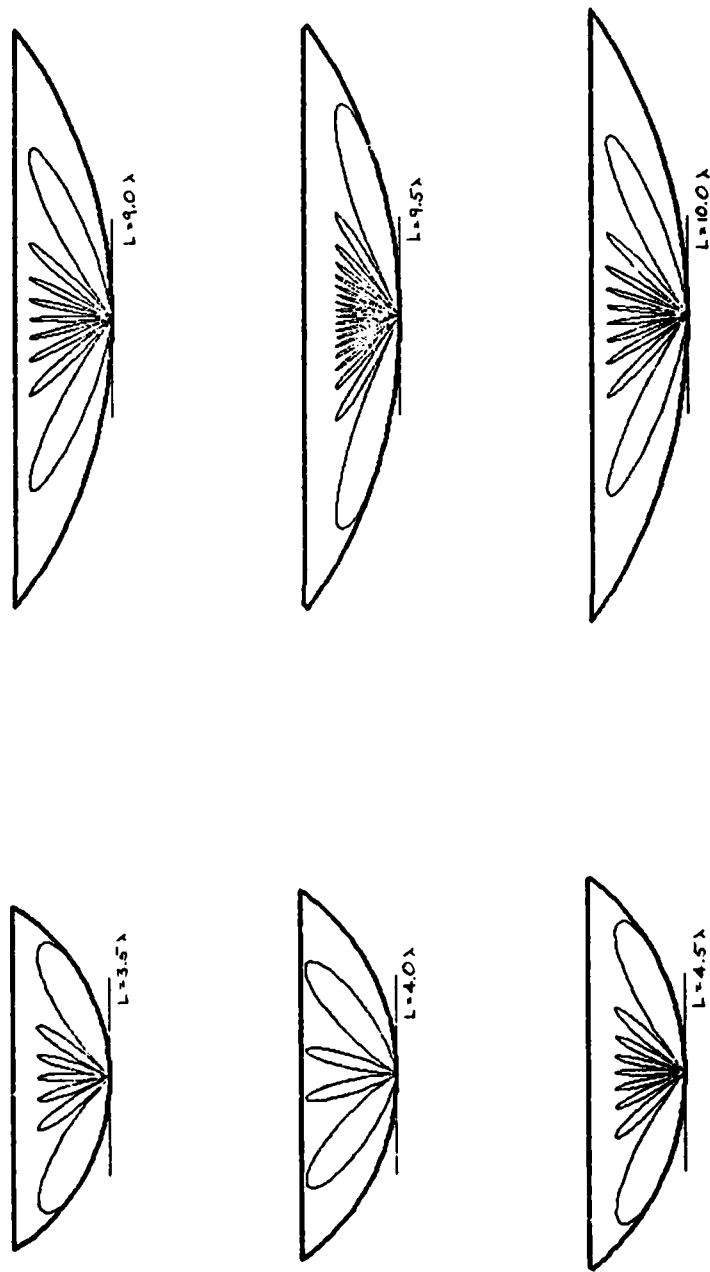
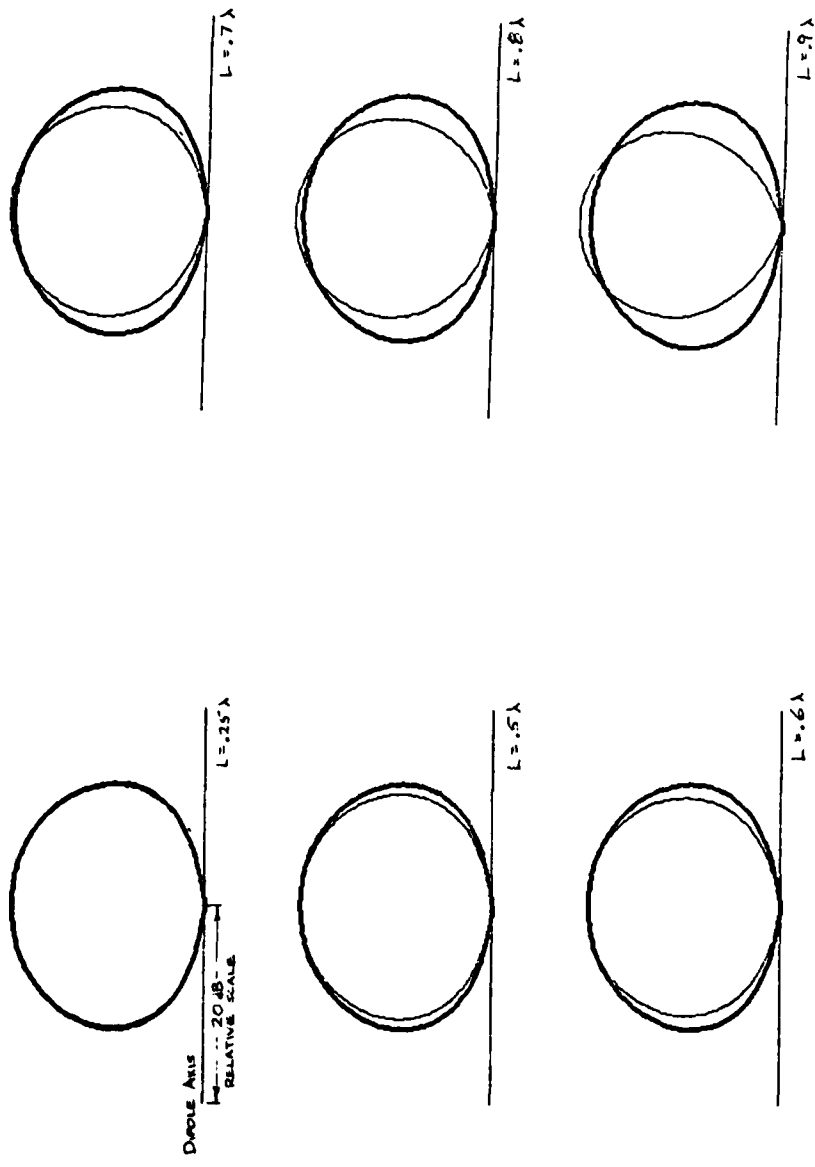


Figure 2-156 Continued

Figure 2-156 Continued



2-143

Figure 2-157 Dipole Radiation Patterns Illustrating Model Envelope (Drawn on Logarithmic Scale)

Figure 2-157 Continued

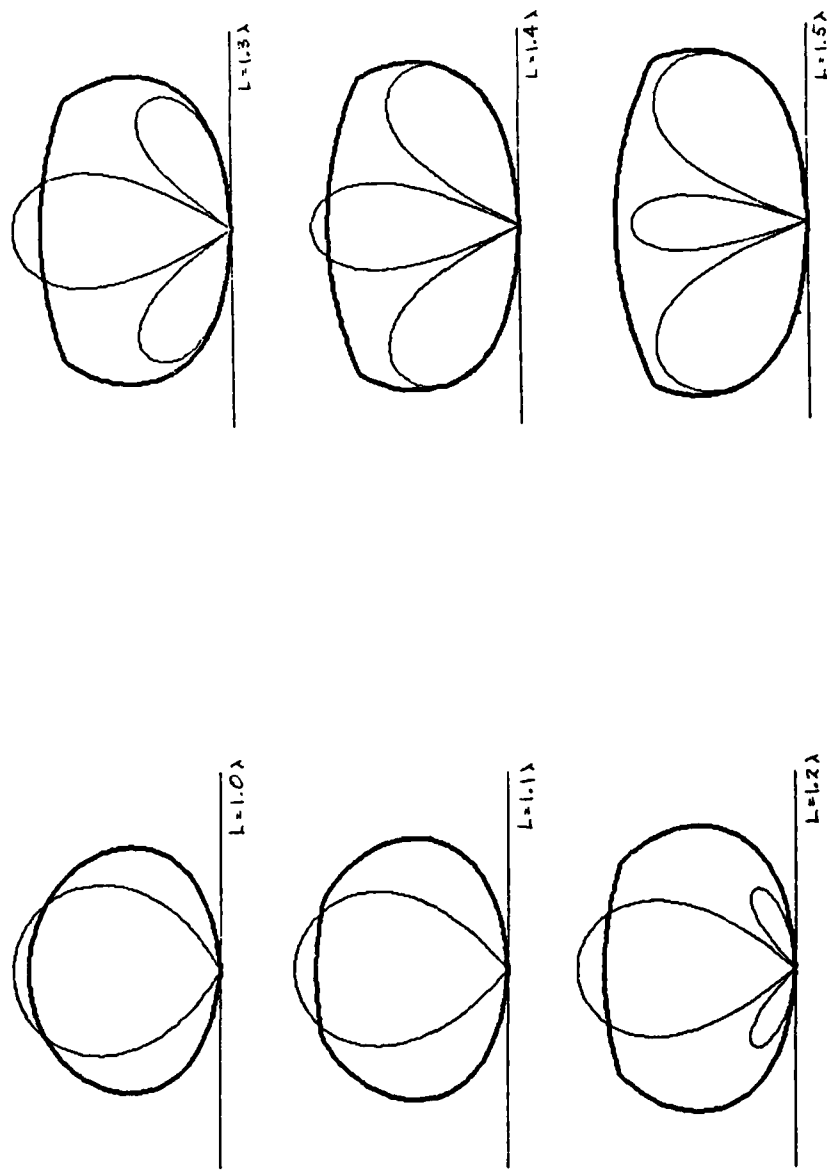


Figure 2-157 Continued

Figure 2-157 Continued

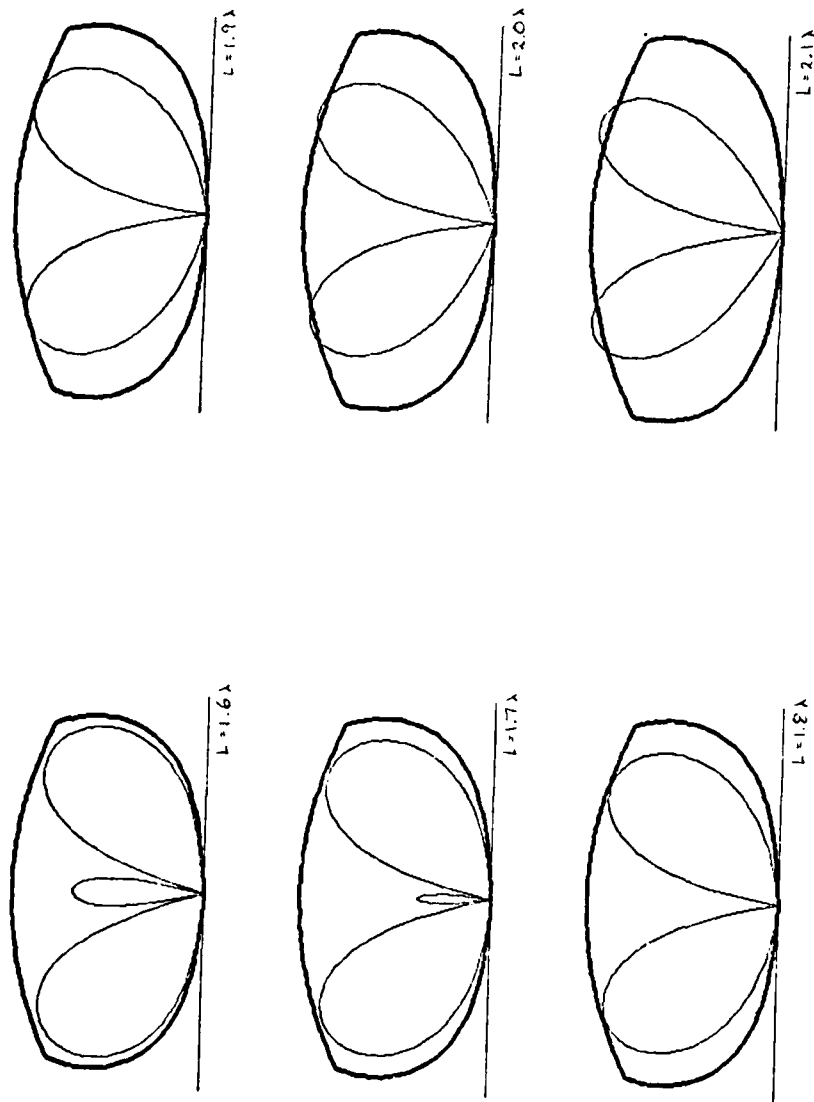


Figure 2-157 Continued

Figure 2-157 Continued

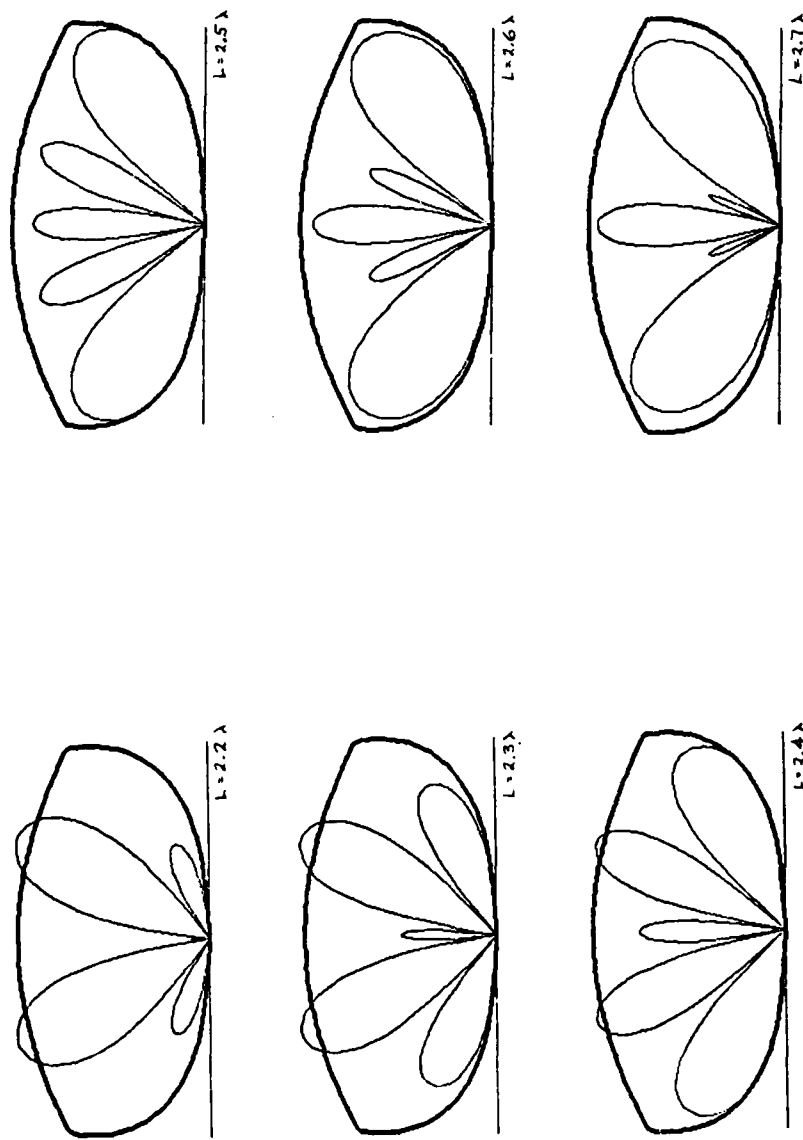


Figure 2-157 Continued

Figure 2-157 Continued

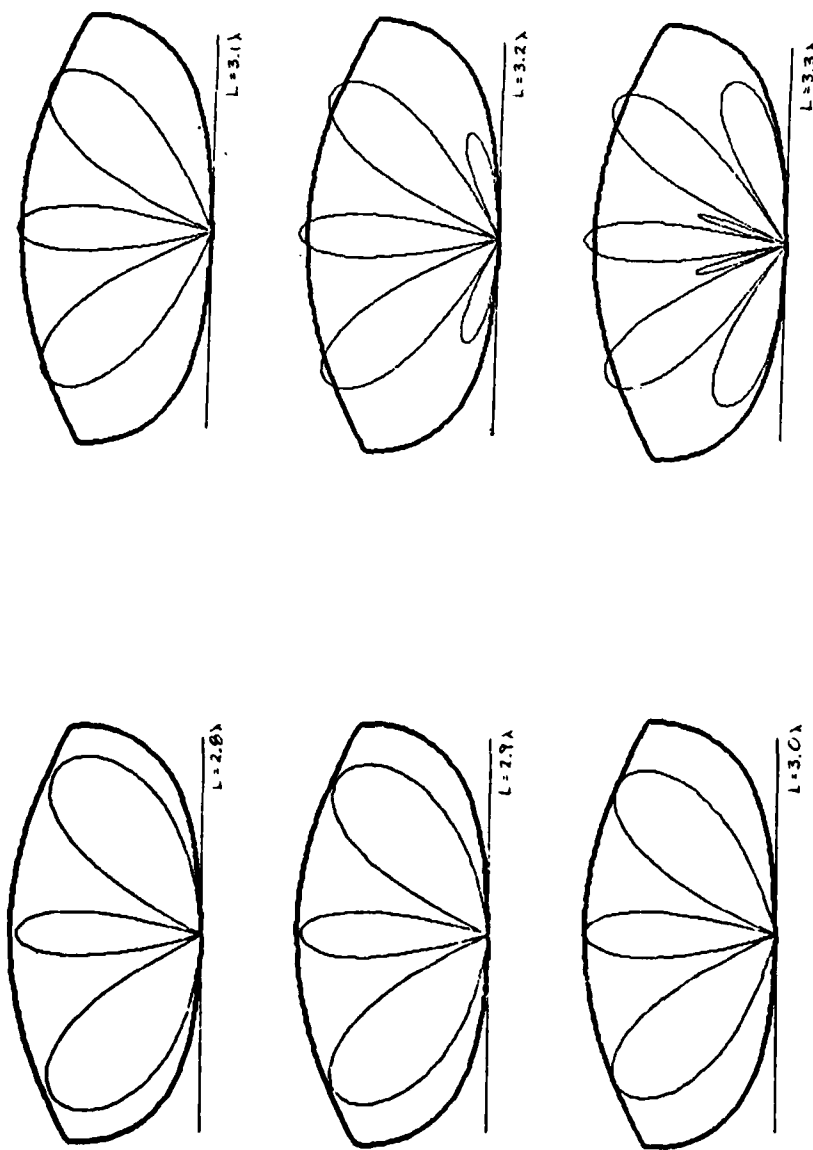


Figure 2-157

Continued

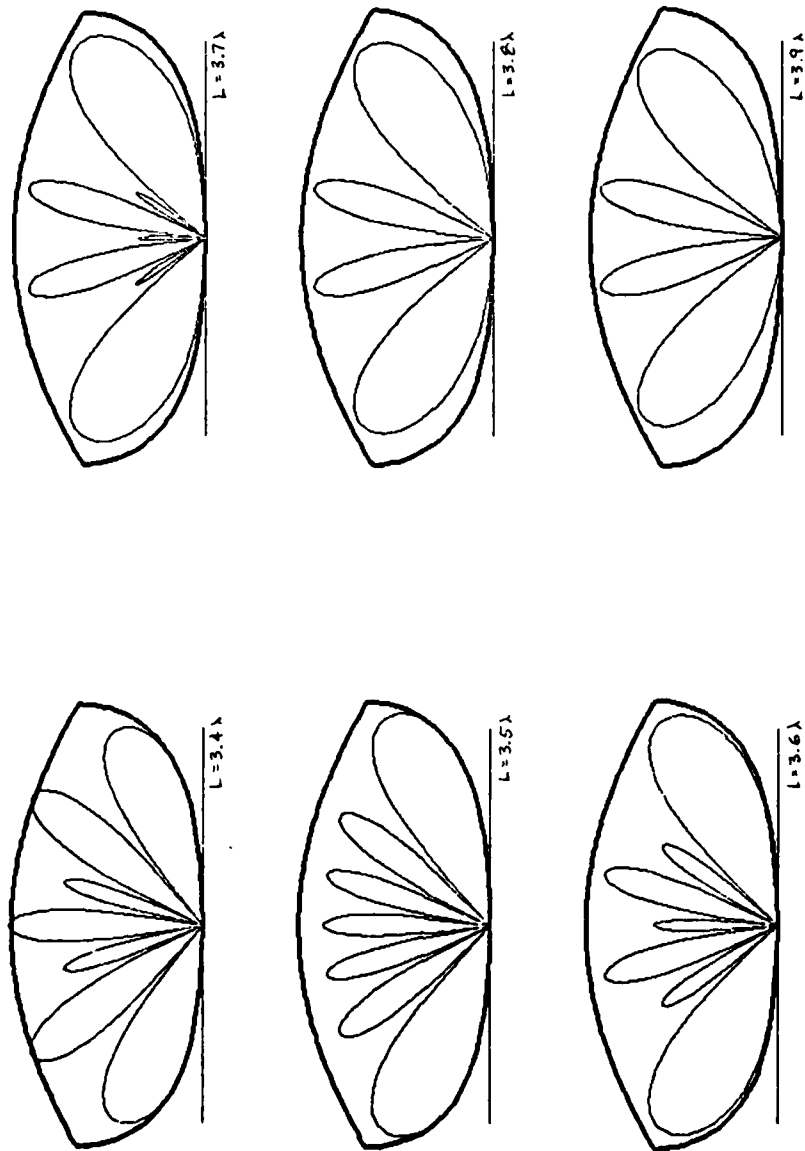


Figure 2-157 Continued

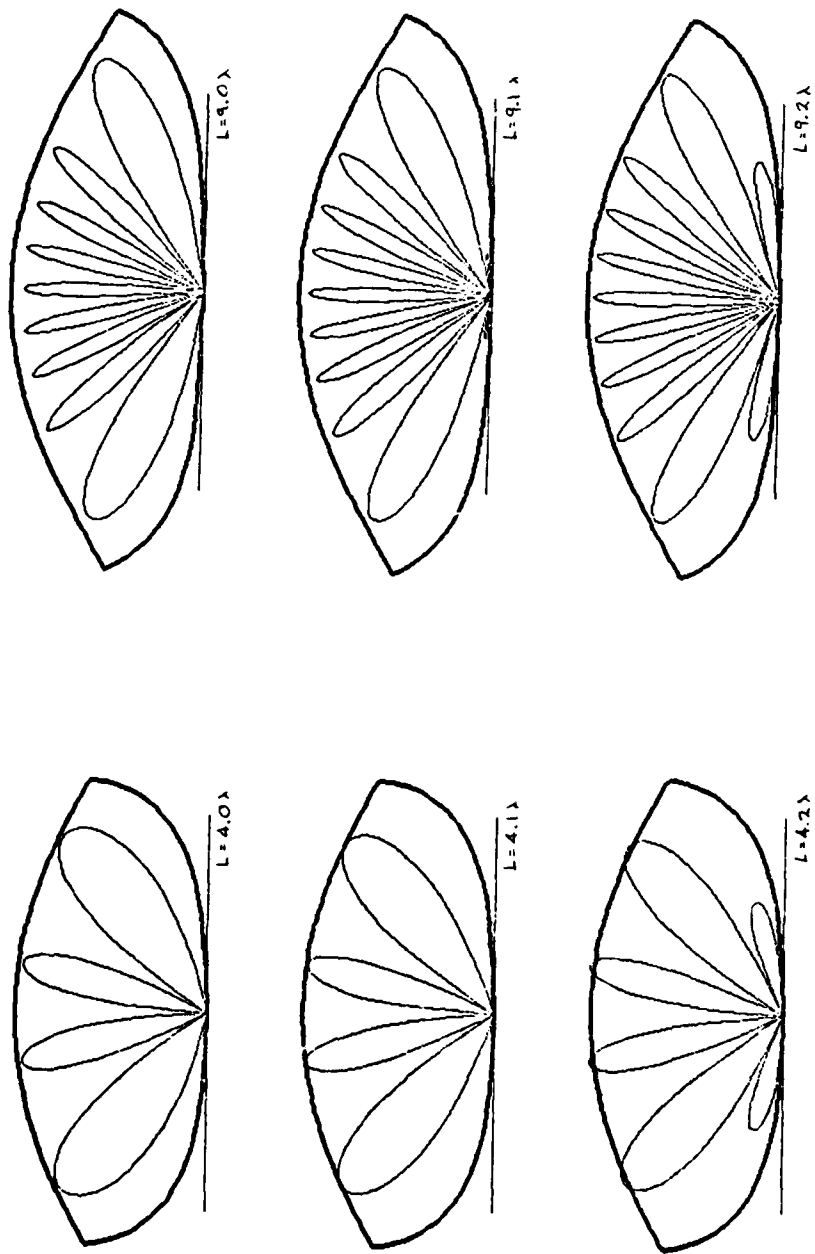
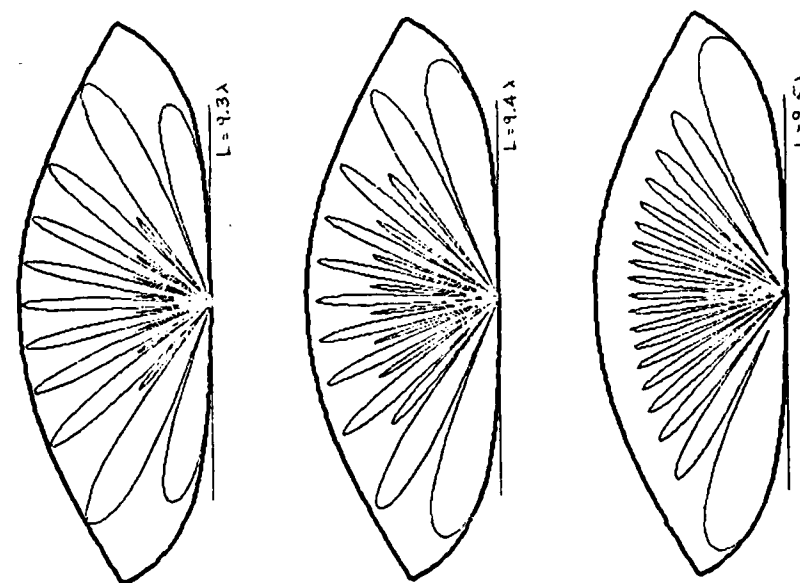
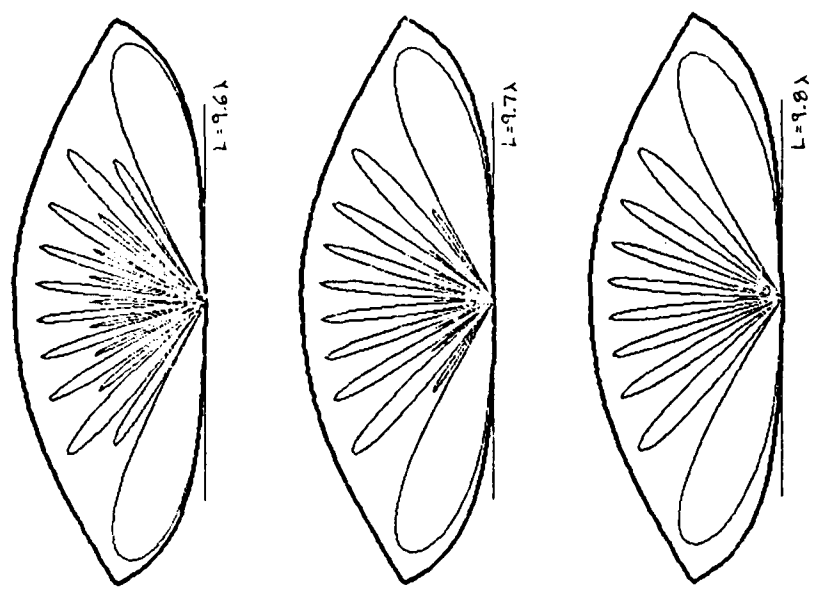


Figure 2-157 Continued

Figure 2-157 Continued



2-150

Figure 2-157 Continued

Figure 2-157 Continued

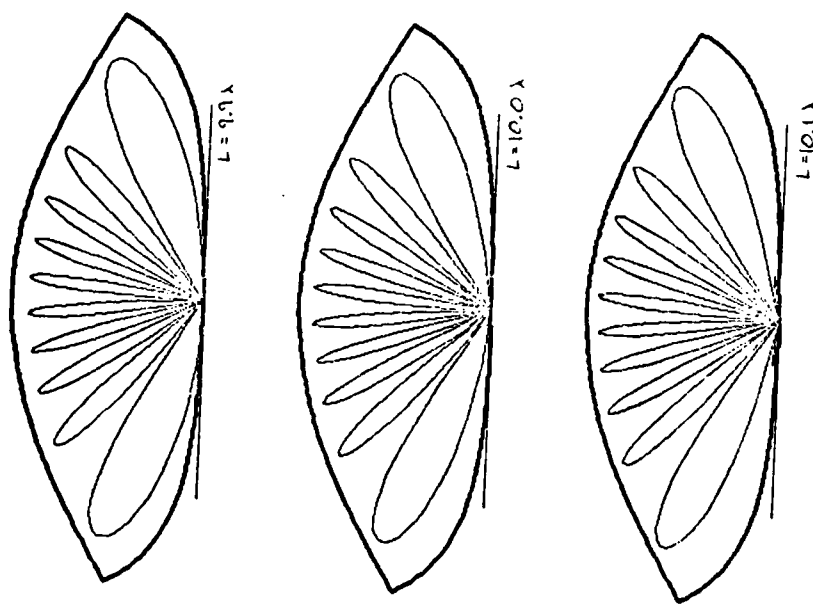


Figure 2-157 (Continued)

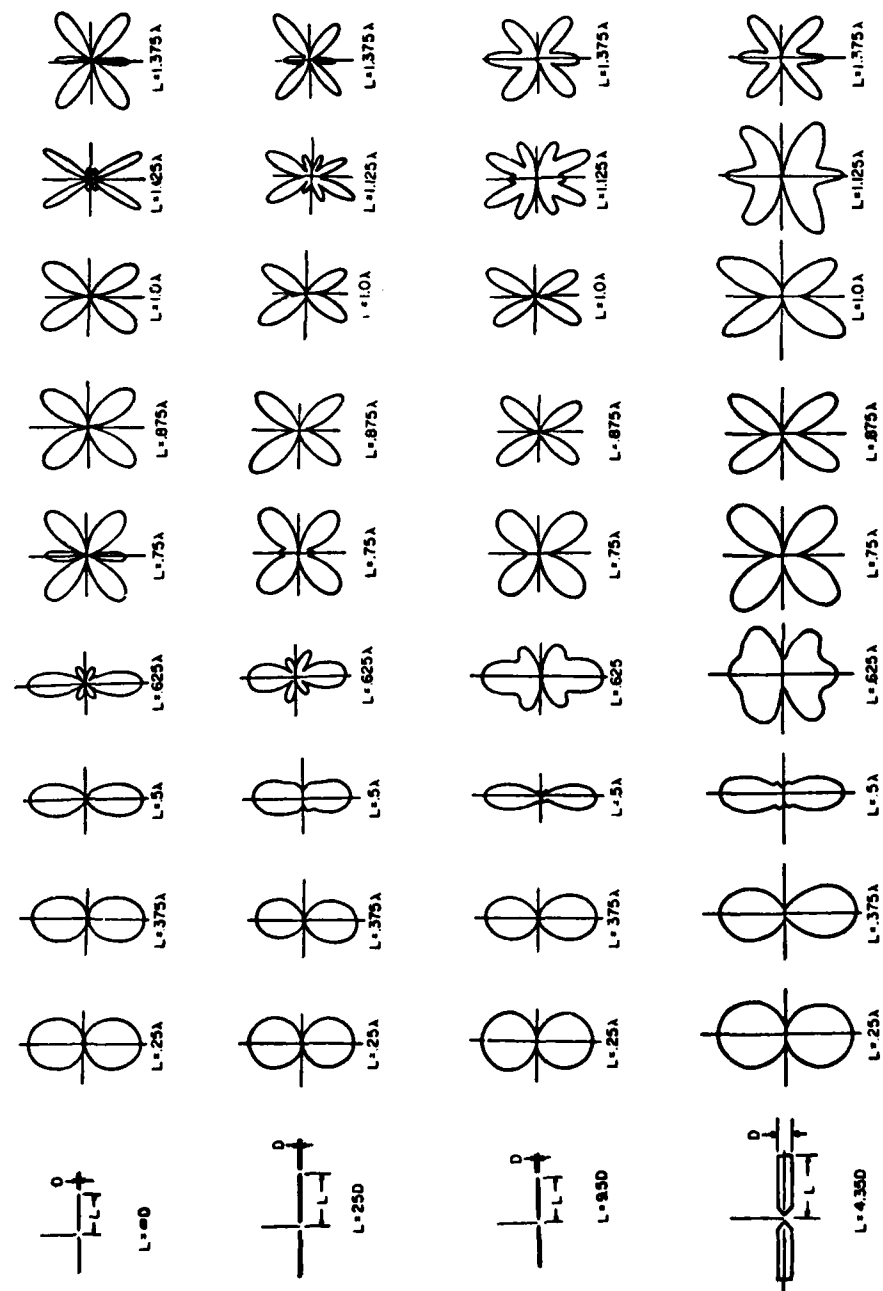


Figure 2-158 Examples of Pattern Degradation Due to Fattening of Dipole Elements

2.16.2 General Pattern Model for Medium-Gain and High Gain Antennas

The directive-gain patterns currently used in IEMCAP for medium-gain and high-gain antennas are defined by the following user-supplied sub-parameters entered on the ANT input card:

$G_{mB}$  = maximum gain  
 $\theta_B$  = 3 dB vertical half-beamwidth  
 $\phi_B$  = 3 dB azimuthal half-beamwidth  
 $G_{msL}$  = major side-lobe gain  
 $\phi_{B1}$  = side-lobe angle  
 $G_{B1}$  = back-lobe gain

These quantities define a three-level model with levels  $G_{mB}$ ,  $G_{msL}$  and  $G_{B1}$ . The user may specify a two-level model with levels  $G_{mB}$  and  $G_{B1}$  by setting  $G_{msL} = 0$  and  $\phi_{sl} = 0$ .

Figure 2-159 illustrates the existing three-level model in IEMCAP for a typical antenna pattern. A similar model defines the pattern in the orthogonal plane. The two orthogonal patterns generally differ only by the mainbeam half-beamwidths  $\theta_B$  and  $\phi_B$ .

The simplicity of the existing pattern model is desirable with regard to ease of coding (in subroutine GAIN), but the model provides several undesirable features. As can be seen in Figure 2-159, the model predicts gain values which may be considerably less than the actual values. Further, the gain is discontinuous at the angles  $\pm\theta_B$ ,  $\pm\phi_B$  and  $\pm\phi_{sl}$  because of rectangular profiles. Finally, while the user can specify separate orthogonal beamwidths for the main beam, only one side-lobe angle may be specified which defines a square contour of constant gain for the major side-lobes. That is, the model assumes that the side-lobe gains in both the horizontal and vertical planes are equal.

The proposed model for the in-band directive gain pattern is illustrated in Figure 2-160. This model is defined using the same antenna input parameters but improves upon the existing model by providing the following features. The transitions between constant-gain levels are defined by

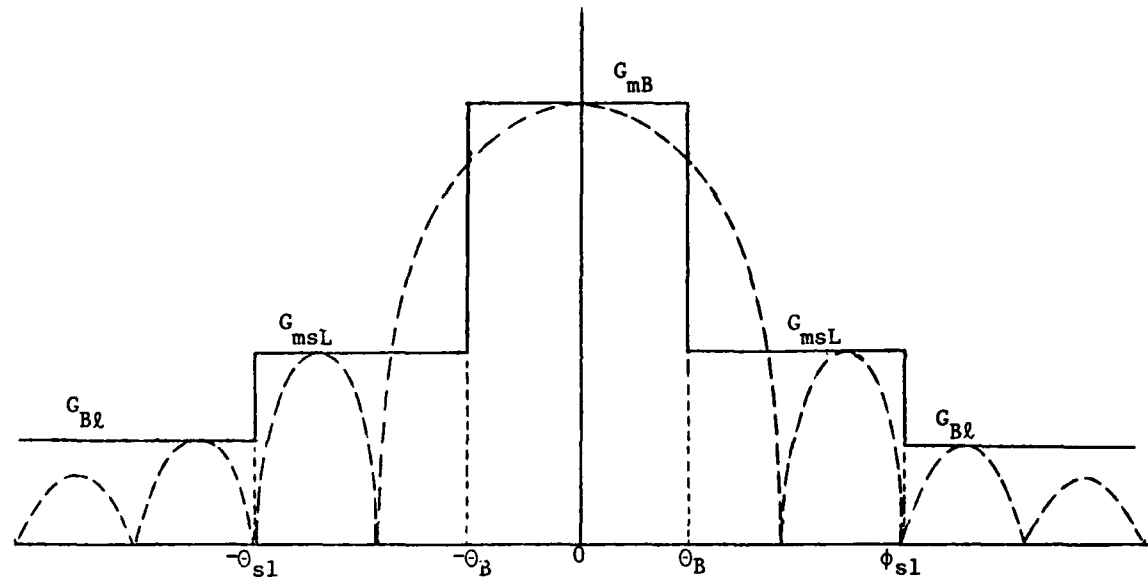


Figure 2-159 Existing IEMCAP model for antenna pattern.

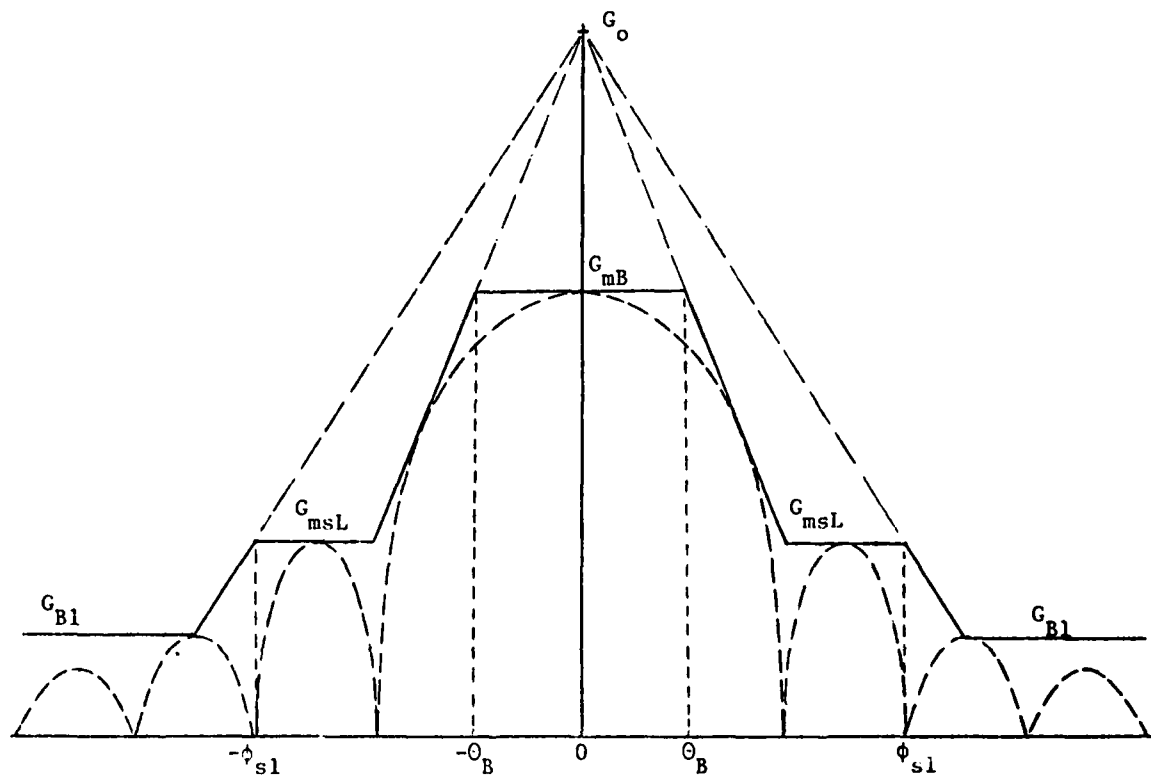


Figure 2-158 Proposed in-band model for pattern

finite, linear slopes (dB gain vs angle). The slopes are a function of the beamwidth and tend to enclose the actual pattern. It can be seen that the proposed model provides a continuous gain function at all angles.

In addition, the proposed model provides circular or elliptical contours of constant gain in order to more accurately represent the actual gain in directions off the principal planes.

As indicated in Figure 2-160, all sloping line segments converge to a common intercept point  $G_0$  on the gain axis. The value of  $G_0$  is relative to the mainbeam gain for a given frequency. For example, in the design band the mainbeam gain is  $G_{mB}$  and

$$G_0 = G_{mB} + \Delta$$

Values of  $\Delta$  for medium-gain antennas and for high-gain antennas have been determined empirically, as described in the respective sections for these antennas.

An isometric representation of the proposed pattern model in rectangular coordinates is illustrated in Figure 2-161. The horizontal axes are the azimuth and elevation angles. The vertical axis, which represents the antenna mainbeam axis, is the pattern directive gain. The profiles of directive gain for the two principle planes are indicated. This model effectively consists of a truncated cone or frustum to model the mainbeam, and a second frustum to model the major side-lobes. The base plane represents the back-lobe gain. Note that both cone models have a common vertex at  $G_0$ .

The three-dimensional gain model is fully defined by the azimuth and elevation gain profiles which are derived from user-input antenna parameters. The linear equations for the two sloping lines and the coordinates of the breakpoints at the lower ends of the sloping line segments are presented below.

It should be remarked here that  $\theta_{s1} = \phi_{s1}$  in the existing IEMCAP model. For the proposed model, a special case is permitted where  $\theta_{s1} \neq \phi_{s1}$ , which is described later.

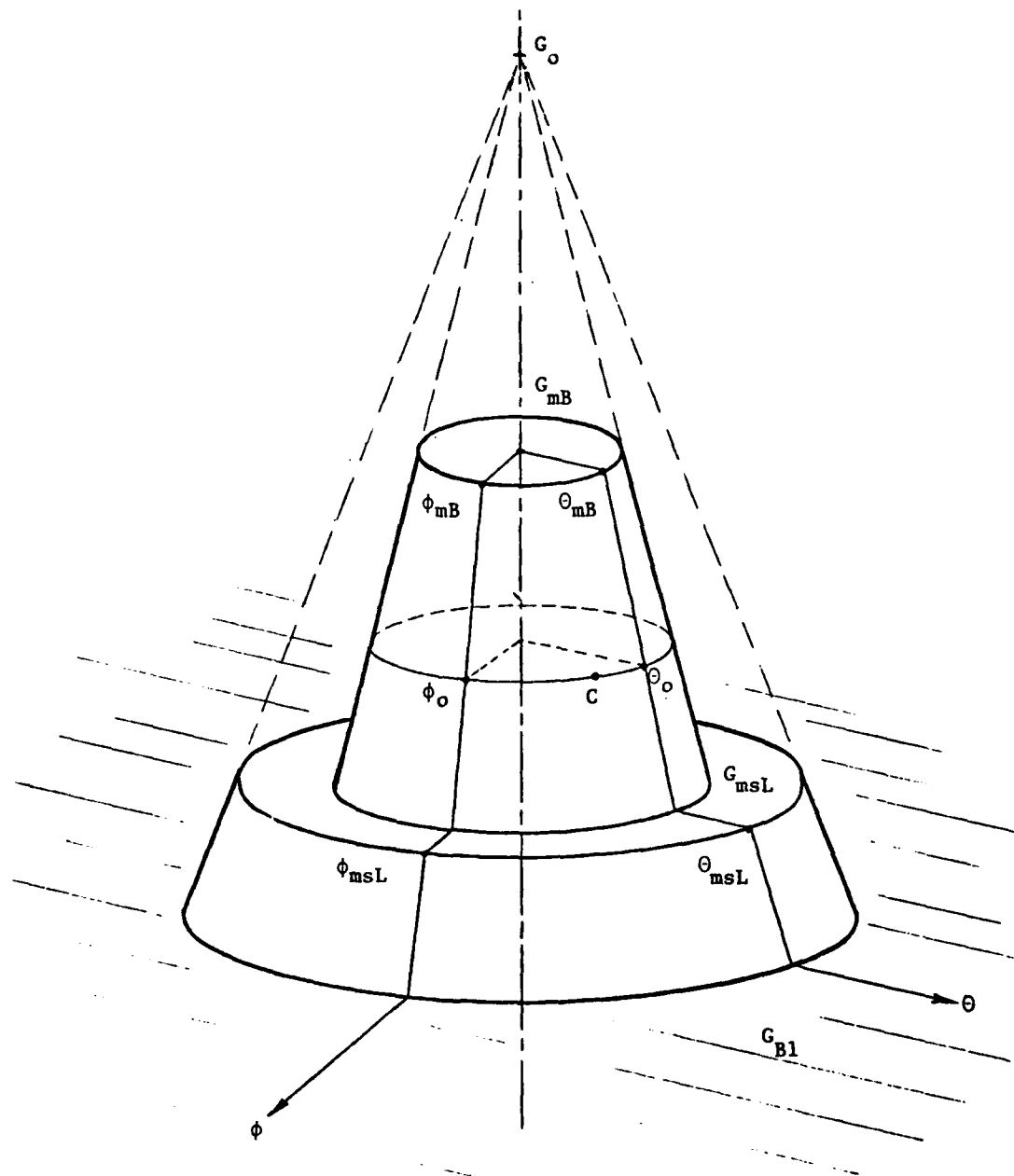


Figure 2-161 Three-dimensional illustration of conic gain model of antenna pattern

Figure 2-162 illustrates a general three-level gain profile with all breakpoints identified by the following variables:

$G_m$  = peak mainbeam gain  
 $G_s$  = major side-lobe gain  
 $G_b$  = back-lobe gain  
 $\beta_m$  = 3 dB half-beamwidth of mainbeam  
 $\beta_a$  = angle at which gain =  $G_s$   
 $\beta_s$  = side-lobe angle  
 $\beta_b$  = back-lobe angle

These variables are general and may assume values which are a function of frequency for a given antenna. Further, the general gain profile applies to either the azimuth or the elevation profile. For example, in the design band,  $G_m = G_{mB}$ ,  $G_s = G_{msL}$ ,  $\beta_m = \phi_B$  or  $\theta_B$ ,  $\beta_s = \phi_{sL}$ , etc. Figure 2-162 also illustrates the relationship

$$G_o = G_m + \Delta$$

Because of symmetry, only the positive half-plane is analyzed.

In general, the gain levels  $G_m$ ,  $G_s$ ,  $G_b$  and angles  $\beta_m$ ,  $\beta_s$  are specified for a given antenna. At out-of-band frequencies these quantities can be easily derived from expressions specified for a given type of antenna. However, angles  $\beta_a$ ,  $\beta_b$  and the equations of the two sloping segments which are not directly specified, must be derived using the specified quantities.

The following quantities are easily derived from similar triangles in Figure 2-162.

$$\beta_a = \beta_m \frac{G_m - G_s + \Delta}{\Delta}$$
$$\beta_b = \beta_s \frac{G_m - G_b + \Delta}{G_m - G_s + \Delta}$$

The equation of the mainbeam slope line is:

$$G(\beta) = G_m + \Delta - \beta \frac{\Delta}{\beta_m} \quad (\beta_m \leq |\beta| \leq \beta_a),$$

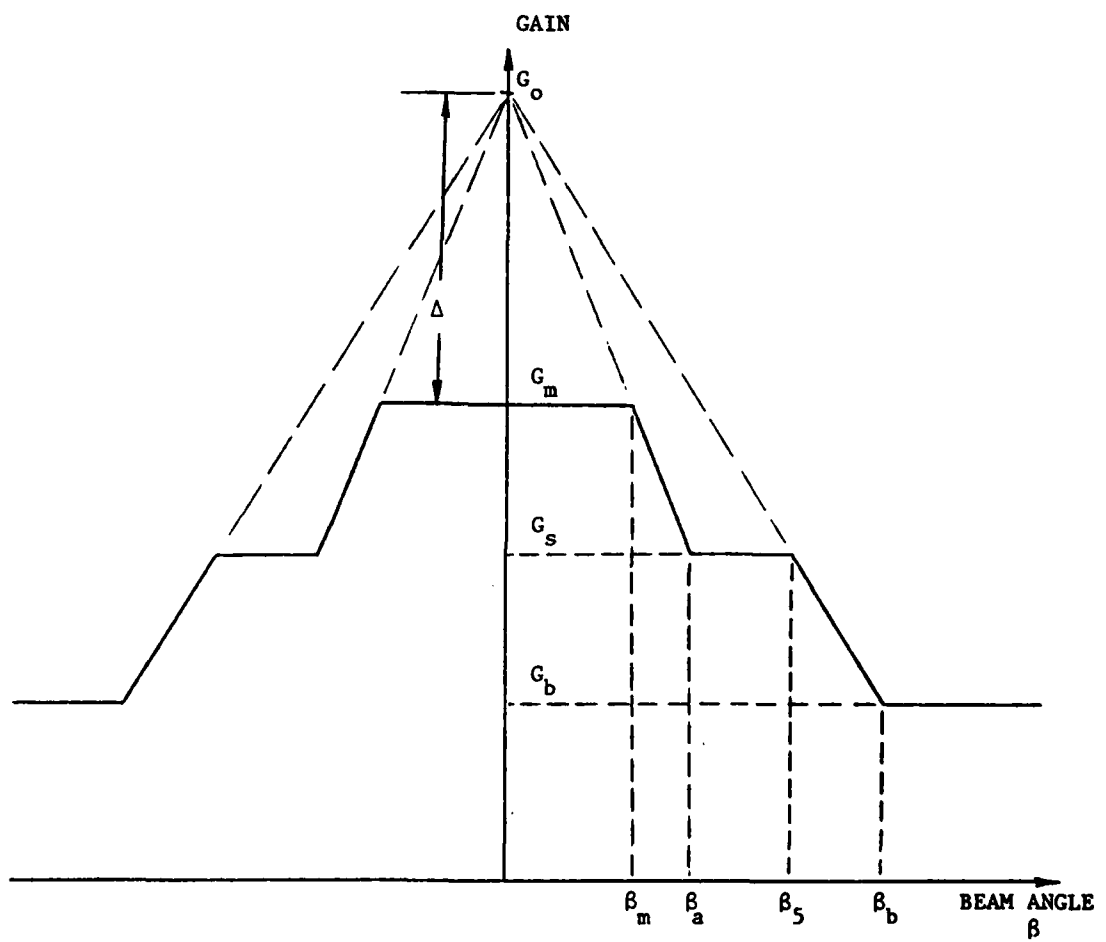


Figure 2-162 General three-level directive gain profile of proposed model

and the equation for the side-lobe slope is:

$$G(\beta) = G_m + \Delta - \beta \frac{G_m - G_s + \Delta}{\beta_s} \quad (\beta_s \leq |\beta| \leq \beta_b).$$

It has been assumed in the models described up to this point that the major side-lobe gain is greater than the back-lobe gain; that is,

$$G_{msL} > G_{BL}$$

In order to improve generality, the proposed model also permits the back-lobe gain level to exceed the side-lobe level, as illustrated in Figure 2-163. In this case, the side-lobe slope line extends to point  $G'_0$  such that the slope is the negative of that shown in Figure 2-162. Thus,

$$\begin{aligned} G'_0 &= G_s - (G_0 - G_s) \\ &= 2G_s - G_0 \\ &= 2G_s - G_m - \Delta \end{aligned}$$

That is,  $G_s$  is midway between  $G'_0$  and  $G_0$ . Then, for this case the back-lobe angle is given by

$$\beta_b = \beta_s \frac{G_m + G_b - 2G_s + \Delta}{G_m - G_s + \Delta} \quad (\beta_s \leq |\beta| \leq \beta_b),$$

and the equation of the side-lobe slope line is

$$G(\beta) = 2G_s - G_m + \Delta + \beta \frac{G_m - G_s + \Delta}{\beta_s}$$

The complete directive gain model is described in spherical coordinates. Figure 2-164 illustrates a sphere with center O and points A, B, C on the surface. The beam axis of the antenna lies along radius vector OA, thus point A represents the origin of the antenna beam angles  $\phi, \theta$ , where  $\phi$  is a horizontal azimuth angle and  $\theta$  is a vertical elevation angle. Points A and B lie on a great circle in a horizontal plane, passing through O, and points B and C lie on a great circle in a vertical plane passing through the poles P, P'. While point A corresponds to the antenna "look" angle, point C  $(\phi, \theta)$  corresponds to the direction of a coupling path for which the antenna gain is to be determined.

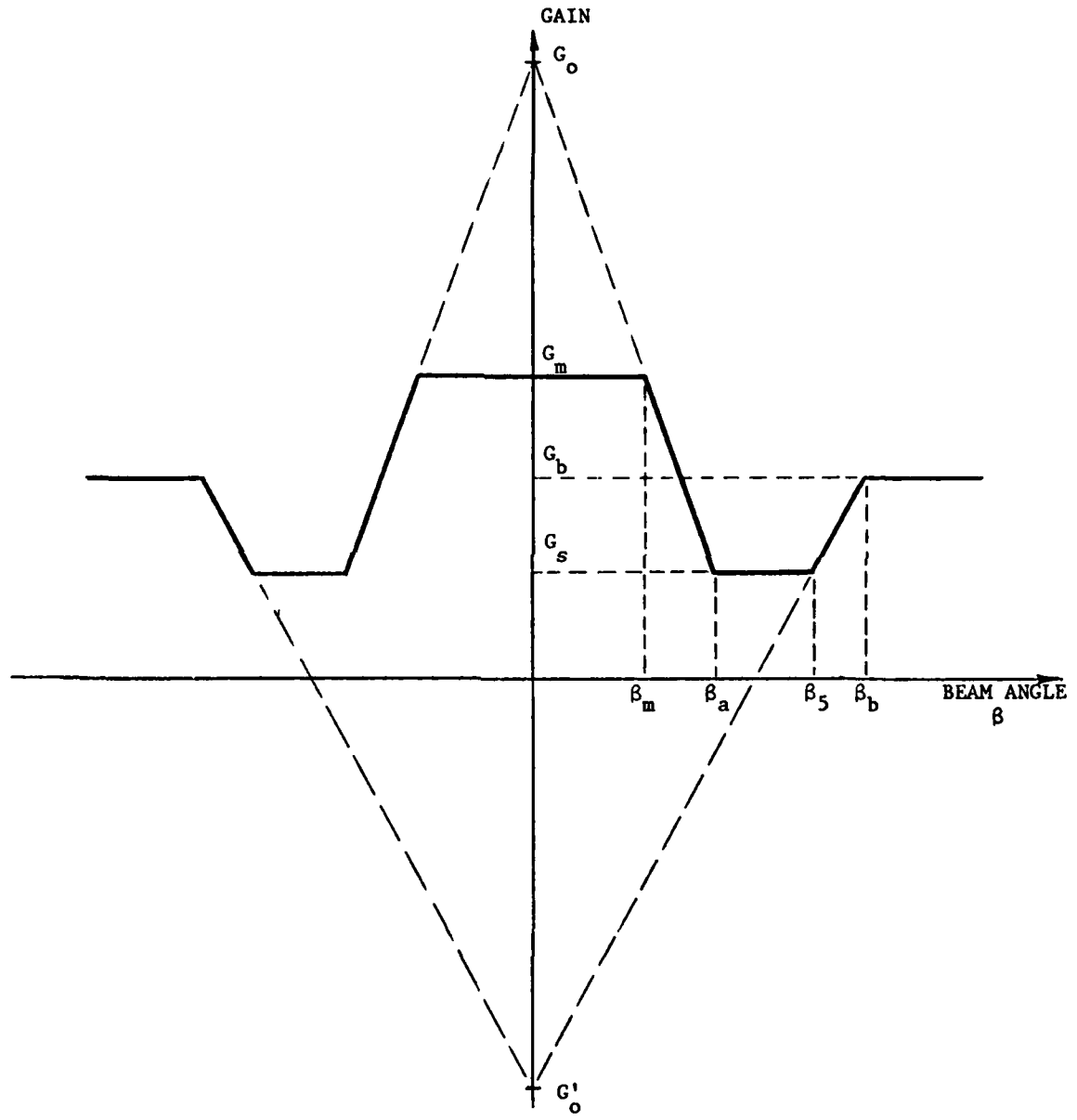


Figure 2-163 General three-level directive-gain profile in which backlobe gain exceeds sidelobe gain

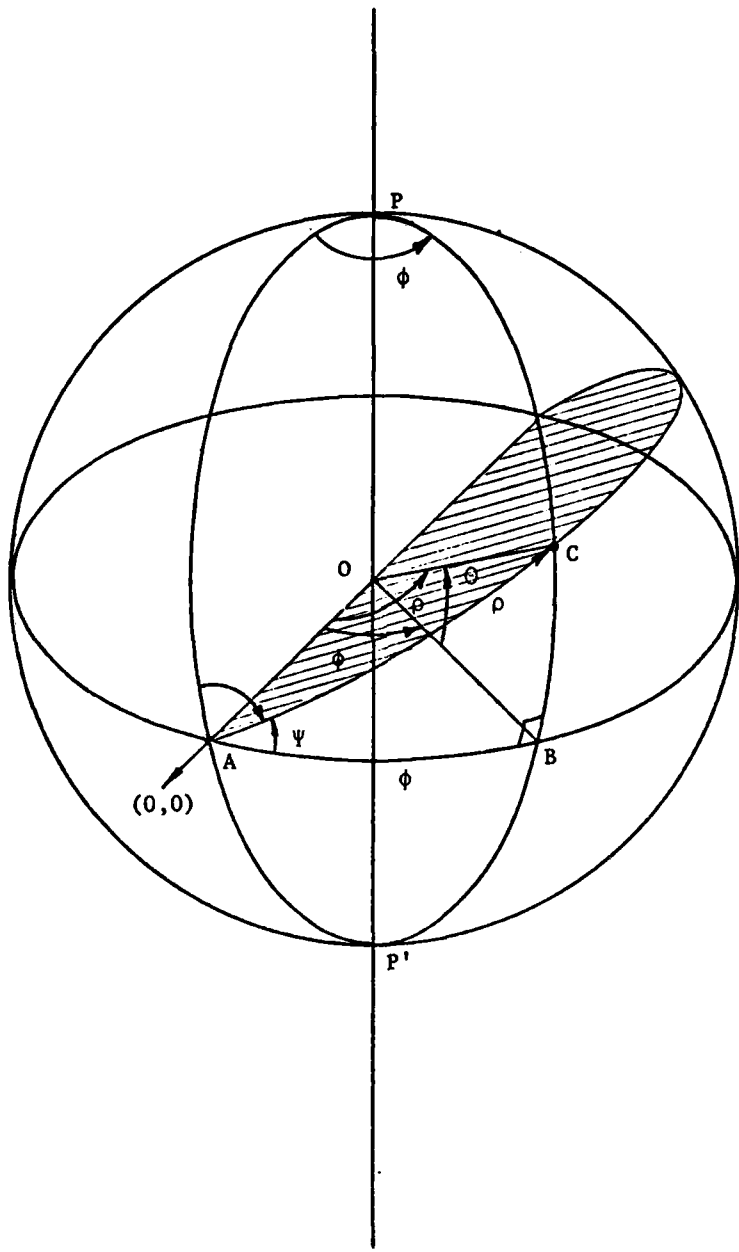


Figure 2-164 Spherical trigonometric angles associated with beam pattern model

The antenna gain pattern, which is specified by the azimuth and elevation profiles, as illustrated in Figure 2-160, is thus defined in the azimuth plane OAB and the elevation plane OPAP' of Figure 2-164. It is assumed that constant-gain contours in the model have a general elliptical shape in terms of  $\phi$  and  $\theta$ . Thus, for directions off the principal planes, the model gain is determined by calculating the elliptical gain contour passing through the given point. The ellipse contours are defined by polar coordinates  $(\rho, \psi)$  as shown in Figure 2-164. With the application of spherical trigonometry to right spherical triangle ABC, coordinates  $\rho, \psi$  relate to  $\phi, \theta$  by the following:

$$\cos \rho = \cos \phi \cos \theta$$

$$\tan \psi = \frac{\tan \theta}{\sin \phi}$$

The polar equation of an ellipse is usually expressed as a function of  $(r, \theta)$

$$r^2 = \frac{a^2 b^2}{a^2 \sin^2 \theta + b^2 \cos^2 \theta}$$

where  $a$  and  $b$  are the semi-axes. Substitution of the identities

$$\sin^2 \theta = \frac{1}{1 + \frac{1}{\tan^2 \theta}}, \quad \cos^2 \theta = \frac{1}{1 + \tan^2 \theta}$$

gives the alternate expression

$$r^2 = \frac{1 + \tan^2 \theta}{\frac{1}{a^2} + \frac{1}{b^2} \tan^2 \theta}$$

In terms of the spherical quantities  $(\rho, \psi)$ , this expression becomes

$$\rho^2 = \frac{1 + \tan^2 \psi}{\frac{1}{\phi_0^2} + \frac{1}{\theta_0^2} \tan^2 \psi}$$

where  $\phi_0$  and  $\theta_0$  are the semi-axes of the (spherical) ellipse.

It is desired to determine the gain profile in the plane OAC which is rotated by  $\psi$  from the principal azimuth plane OAB. The above expression can be used to calculate the beam angles  $\beta_m$ ,  $\beta_a$ ,  $\beta_s$ , and  $\beta_b$  for the profile by substituting the corresponding values for  $\phi_o$  and  $\theta_o$ . For example, by setting  $\phi_o = \theta_B$  and  $\theta_o = \theta_B$ , then  $\beta_m = \rho(\psi)$ . Also, with  $\phi_o = \phi_{s1}$  and  $\theta_o = \theta_{s1}$ , then  $\beta_s = \rho(\psi)$ . Values of  $\beta_a$  and  $\beta_b$  are given similarly by  $\rho(\psi)$  using values of  $\phi_o$  and  $\theta_o$  set equal to the respective azimuth and elevation beam angles  $\beta_a$ ,  $\beta_b$  calculated in the principle planes.

The value of gain at  $(\rho, \psi)$  is then given directly by the profile with  $\beta = \rho$ .

The directive-gain model is also applied to the out-of-band patterns of antennas. Since the model is fully defined by gain profile functions in the two principal planes, the out-of-band model is based on the profiles adjusted for out-of-band performance.

In general, the design band model will tend to deteriorate with out-of-band frequency. The mainbeam and side-lobe gains generally drop and the beamwidths increase until eventually the pattern degenerates into an isotropic pattern. All out-of-band effects are defined by frequency-dependent adjustments of the specified in-band parameters of gains and beam angles. The frequency functions are relative to  $f_L$  and  $f_U$  which define the lower and upper limits of the design band.

#### 2.16.3 Directive Gain Models of Medium-Gain Antennas

The directive gain of medium-gain antennas is considered to lie in the range from 10 dB to 20 dB or 25 dB. Examples of medium-gain antennas are the Yagi-Uda beam array, long-periodic, log-spiral, helical, corner reflector, and sectoral horn.

In order to apply the directive-gain pattern model to this class of antennas, the determination of the slope intercept point  $G_o$  was made as described below.

A series of directive-gain patterns for various beamwidths were calculated and plotted on rectangular coordinates of Gain (dB) vs angle with the mainbeam axis at  $0^\circ$ . These patterns represented those of a linear array of dipoles, such as a Yagi-Uda beam or a log-periodic antenna.

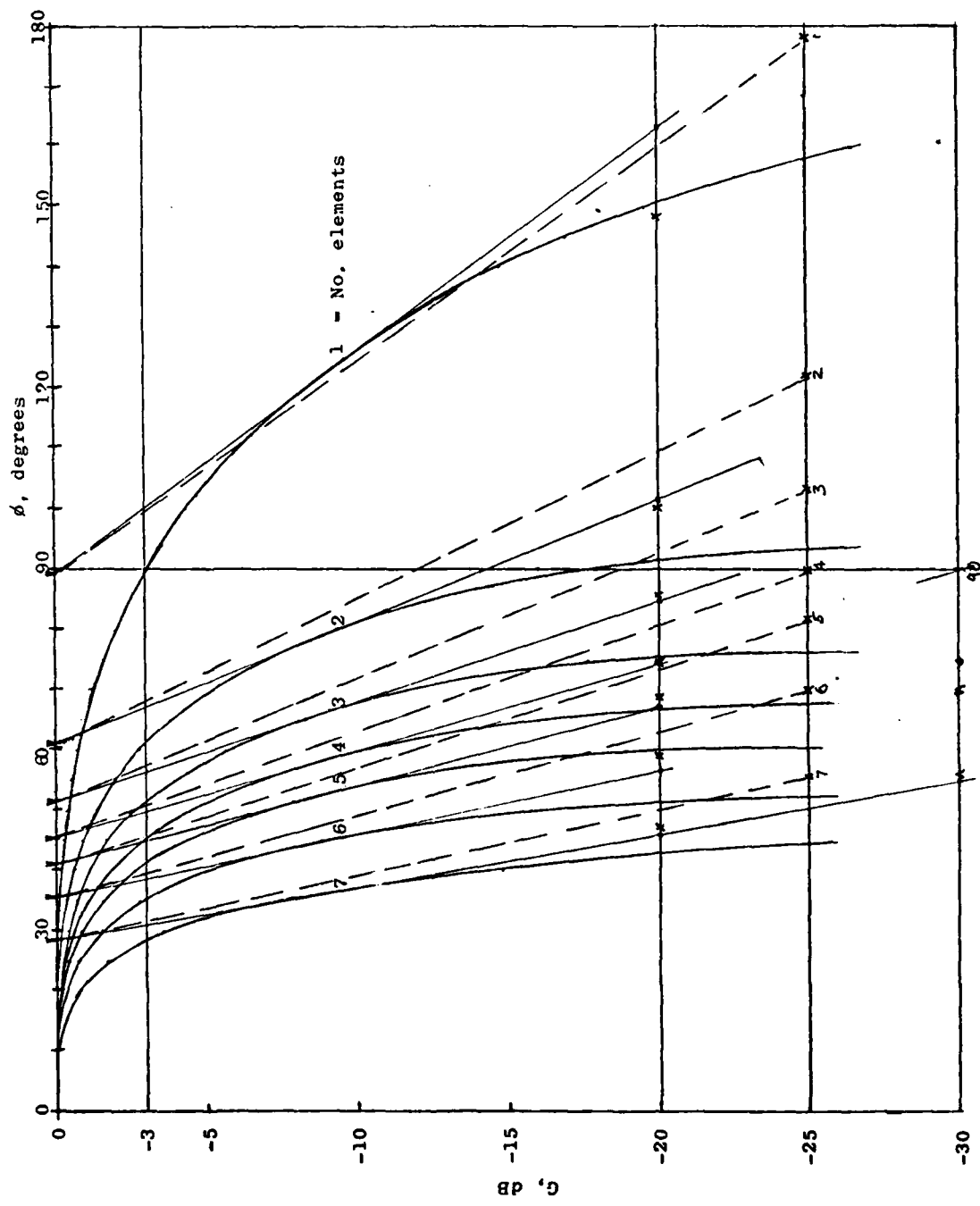


Figure 2-165 Modeling antenna patterns of an array of  $n$  isotropic elements

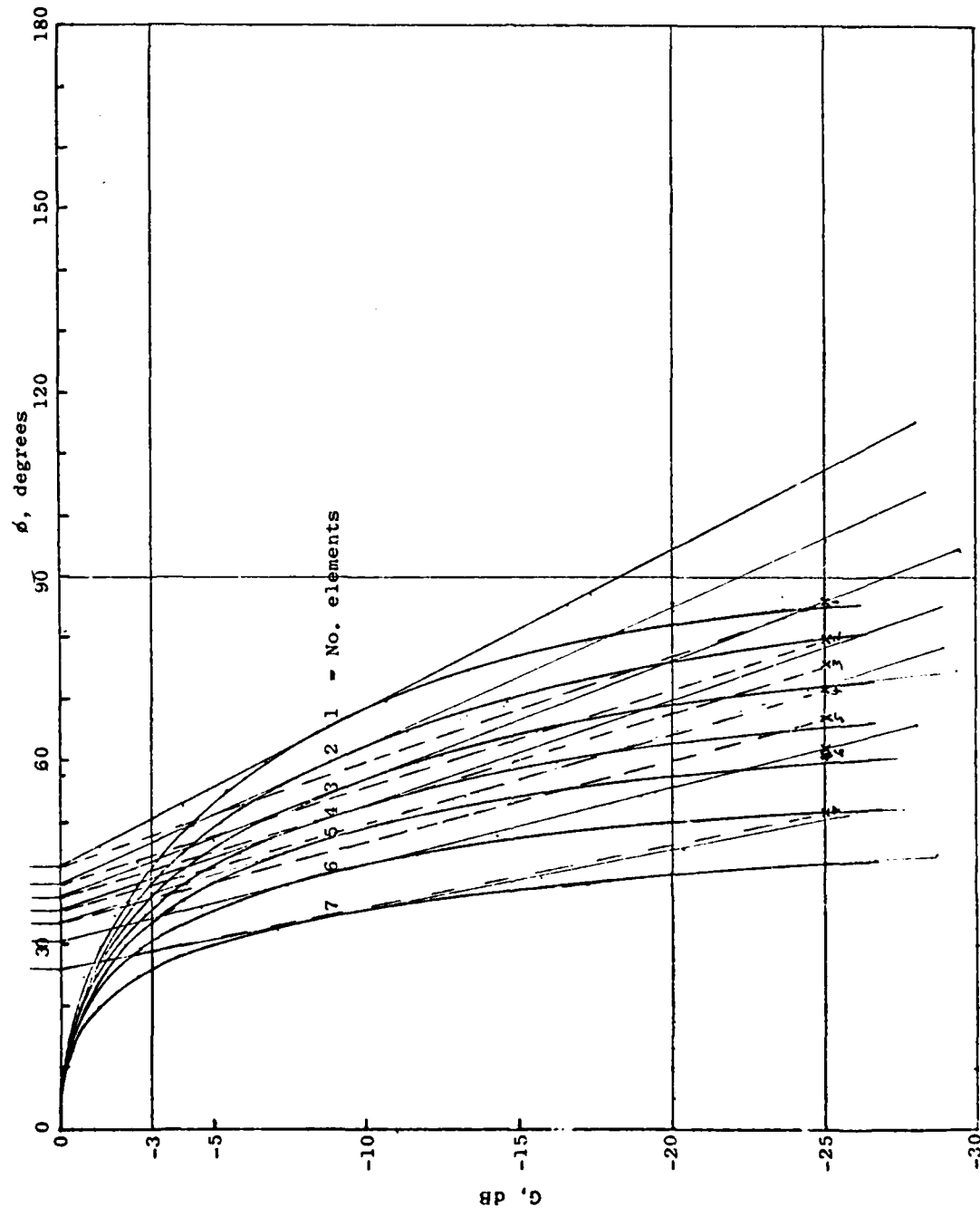


Figure 2-166 Modeling antenna patterns of an array of  $n \cos\theta$  elements

✓ AD-A114 752

ATLANTIC RESEARCH CORP ALEXANDRIA VA  
INTRASYSTEM ANALYSIS PROGRAM (IAP) MODEL IMPROVEMENT. (U)  
FEB 82 T E BALDWIN, W G DUFF, J J FOSTER F30602-79-C-0169

F/G 20/3

RADC-TR-82-20

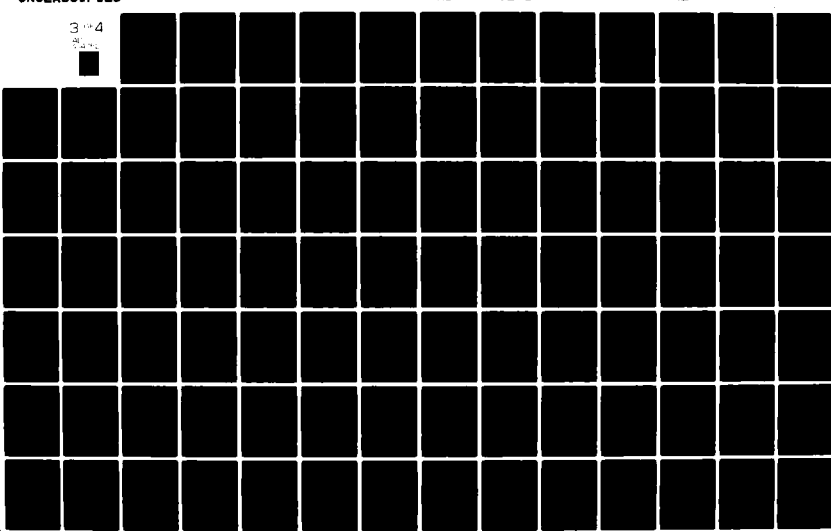
NL

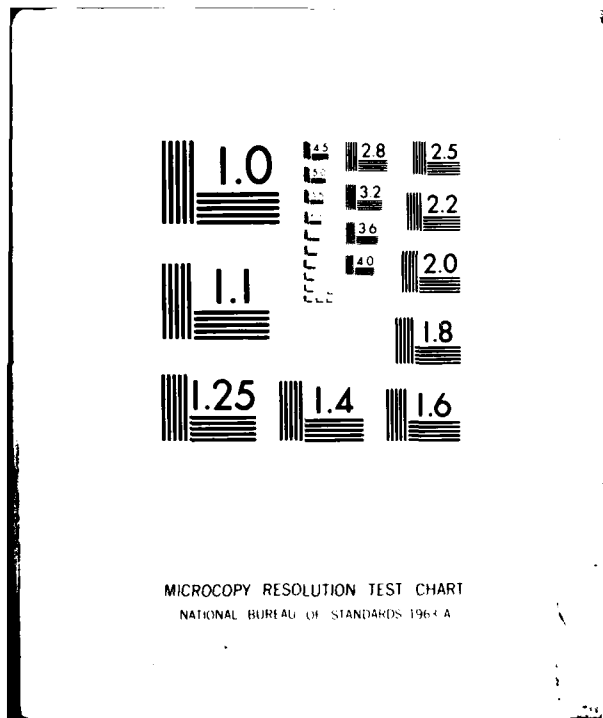
UNCLASSIFIED

3 1/4

2 1/4

1 1/4





The general expression for the pattern of an array of identical elements is [9, page 219].

$$E_A(\phi) = k_n \cdot E_e(\phi) \cdot E_a(\phi)$$

where

$E_A(\phi)$  = antenna pattern factor

$E_e(\phi)$  = element factor

$E_a(\phi)$  = array factor

$k_n$  = normalizing constant

That is, the pattern of the array is obtained by multiplying the pattern of single element by the pattern of the array as calculated for isotropic point-source elements. The array factor is given by

$$E_a(\phi) = \frac{\left| \sin \left[ n \left( \frac{\pi d \sin \phi}{\lambda} - \frac{\alpha}{2} \right) \right] \right|}{\left| n \sin \left[ \frac{\pi d \sin \phi}{\lambda} - \frac{\alpha}{2} \right] \right|}$$

where the array consists of  $n$  elements with equal spacing  $d$  and phase difference  $\alpha$  between adjacent elements.

For this study, two different element patterns were used. In the plane perpendicular to the elements (H-plane), the pattern of each element is isotropic -- that is,

$$E_{el}(\phi) = 1$$

In the plane containing the elements (E-plane) the element pattern is a figure 8 given by

$$E_{e2}(\phi) = |\cos \phi|$$

The resulting array patterns are presented in Figure 2-165 for the isotropic elements and Figure 2-166 for the  $\cos \phi$  elements. All curves are normalized to 0 dB peak by setting  $k_n = 1$ . The gain value shown was calculated by

$$G + 20 \log E_A(\phi).$$

The widest pattern in each figure is that of a cardioid ( $n=2$ ,  $d=\lambda/4$ ,  $\alpha=90^\circ$ ). For the remaining patterns  $d=.3\lambda$  and  $\alpha=108^\circ$ . In each figure the 3 dB beamwidth was determined and indicated on the  $\phi$ -axis. Straight lines were drawn through these points tangent to the corresponding pattern curve. It is apparent that the (negative) slopes of these lines tend to decrease proportionally with the 3 dB beamwidth, that is, they tend to converge to a point  $G_o$  on the  $G$  axis. The convergence point for the isotropic elements is approximately  $G_{mb}+30$  dB while that for the  $\cos\phi$  elements is about  $G_{mb}+20$  dB. Consequently, a practical compromise of  $G_o = G_{mb}+25$  dB or  $\Delta=25$ , was selected for both pattern families, as indicated by the dashed lines in both figures. This value of  $\Delta$  is applied to the modeling of all medium-gain antennas.

A feature which is common among medium-gain antennas which consist of linear, dipole elements lying in one plane, such as the Yagi-Uda beam or log-periodic antennas, is that there is relatively little radiation off the ends of the elements. Consequently, the major side-lobe gain of the E-plane patterns for these antennas tends to be relatively weak and is usually exceeded by the back-lobe gain. The major side-lobes for linear antenna arrays have peaks lying in the orthogonal plane (H-plane) where the individual elements radiate omnidirectionally.

Although the side-lobe cone segment of the proposed model is defined in terms of  $G_{msL}$ ,  $\phi_{s1}$ , and  $\theta_{s1}$ , only  $G_{msL}$  and  $\phi_{s1}$  are user input. The existing antenna model in IEMCAP assumes  $\theta_{s1} = \phi_{s1}$ . For the proposed model the value of  $\theta_{s1}$  will depend on the specified polarization. For circular polarization  $\theta_{s1} = \phi_{s1}$ , corresponding to circular contours of constant side-lobe gain. For horizontal or vertical polarization, the specified side-lobe angle  $\phi_{s1}$  is applied only to the H-plane pattern. For these cases it is assumed that no major side-lobes exist in the E-plane pattern which is, therefore, only a two-level profile.

An isometric view illustrating this special model is shown in Figure 2-167. As shown, the base of the mainbeam cone is tangent to the ellipse on the truncation plane of the side-lobe cone. For the E-plane profile the mainbeam slope extends from  $G_{mb}$  down to  $G_{B1}$  with a constant slope.

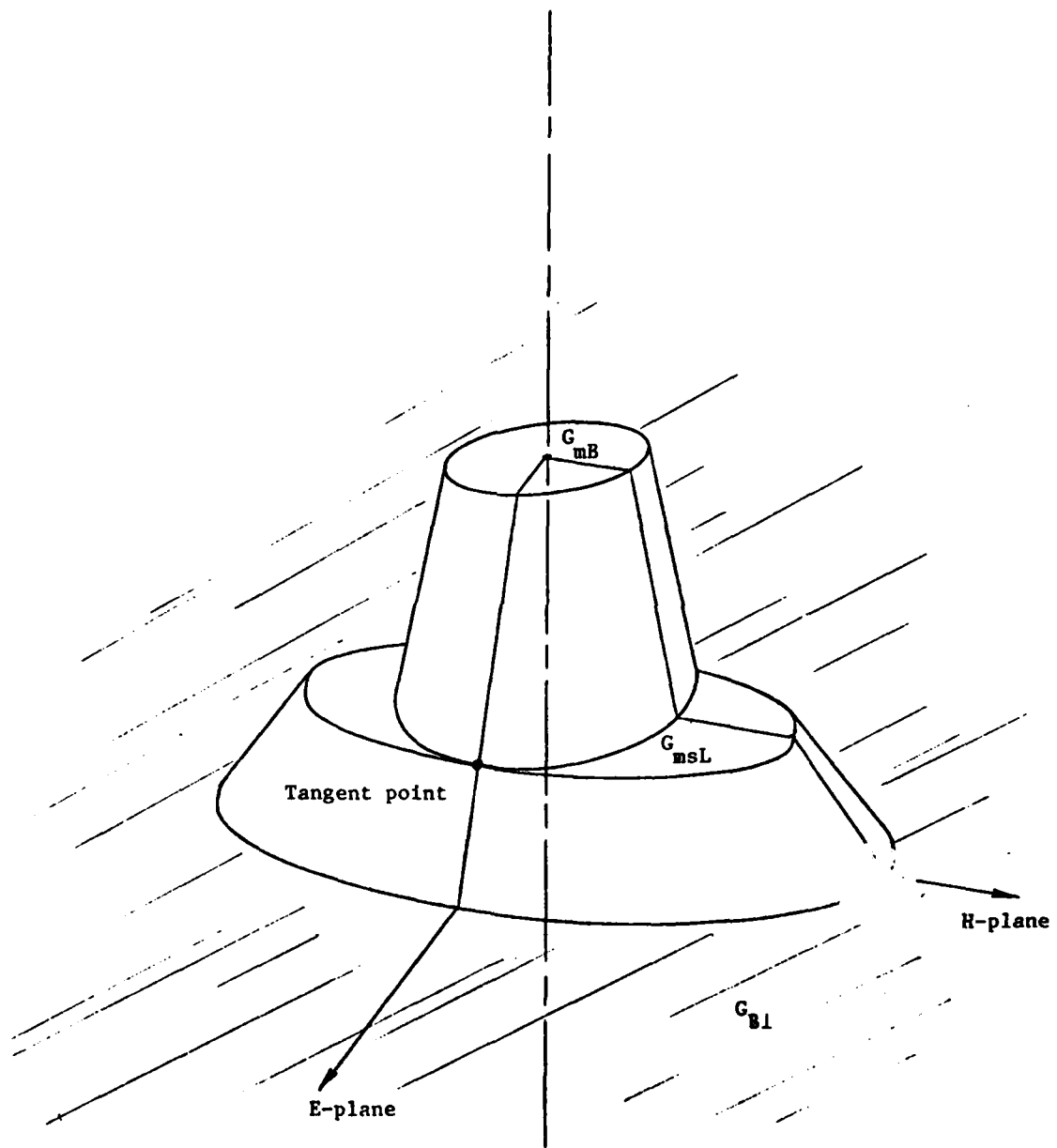


Figure 2-167 Three-dimensional illustration of directive gain model for a linear beam antenna

This slope line passes through the tangent point where the gain equals  $G_{msL}$ . The tangent point always lies in the E-plane profile which is the  $\phi$ -plane profile for a horizontally polarized antenna or the  $\theta$ -plane profile for a vertically polarized antenna.

The tangent point of this special model lies at the extremity of the semi-minor axis of the ellipse defining the side-lobe cone segment. The beam angle to this point is  $\beta_a = \beta_s$  as indicated in Figure 2-162 and given in section 2-16.2.

The out-of-band characteristics of typical medium-gain resonant antennas have been reported [16, page 5-24]; the mainbeam gain decreases 6 dB, the 3 dB-beamwidth doubles, and the major side-lobe vanish. These characteristics have been applied to the proposed antenna model.

The specific directive gain models which are proposed for various types of medium-gain antennas are described in the following sections. The first model described is for a Yagi-Uda beam array. This model is presented in detail and serves as an example for the remaining models which are defined in brief.

#### 2.16.3.1 Directive Gain Model for Yagi-Uda Beam Antenna

The Yagi-Uda beam antenna is considered to be an array of linear dipole elements in which only one is active. The remaining elements (reflector and directors) are parasitic of slightly different lengths than the active element. This tapering of element lengths along the beam array tends to increase the overall usable bandwidth of the antenna relative to the beamwidth of the active element alone. In many cases the active element is a folded dipole.

The directive gain model assumes two major effects at out-of-band frequencies. First, at frequencies  $\frac{1}{3} f_L$  and  $3f_U$  outside the design band, the gain and beamwidths degenerate into an isotropic pattern. Second, at frequencies above  $3f_U$ , the dipole pattern of the active element dominates and is superimposed on the isotropic pattern.

The proposed directive gain model is defined in Table 2-7. Each column defines the relative values of the parameters occurring at the

Table 2-7 Breakpoint Parameter Table for  
Yagi Uda Antenna Model

Para-meters	Breakpoint Frequencies						
	$< \frac{1}{3}f_L$	$\frac{1}{3}f_L$	$\frac{1}{2}f_L$	$f_L$ to $f_u$	$2f_u$	$3f_u$	$>3f_u$
$G_{mB}$	-	0 dB	$G_{mB} - 6$	$G_{mB}$	$G_{mB} - 6$	0 dB	-
$\phi_B, \theta_B$	-	-	$2\phi_B, 2\theta_B$	$\phi_B, \theta_B$	$2\phi_B, \theta_B$	-	-
$G_{msL}$	-	-	$G_{B1}$	$B_{msL}$	$G_{B1}$	-	-
$\phi_{s1}$	-	-	$\phi_{s1}$	$\phi_{s1}$	$\phi_{s1}$	-	-
$G_{B1}$	0 dB	0 dB	$G_{B1}$	$G_{B1}$	$G_{B1}$	0 dB	0 dB + Dipole

designate breakpoint frequency. The center column, which represents the design band  $f_L$  to  $f_U$ , lists the user input parameters for the antenna. All transitions of gain (in dB) and angles between breakpoints are linear with frequency.

The transition from  $f_U$  to  $2f_U$ , which is the same as that shown for  $f_L$  to  $\frac{1}{2}f_L$ , is illustrated in Figure 2-168a. The mainbeam gain drops 6 dB and the beamwidth doubles within the transition. Also, the major side-lobe gain (if any) decreases to the back-lobe gain level during the transition. The corner point ( $G_{msL}$ ,  $\phi_{sl}$ ) of the pattern drops linearly with frequency to ( $G_{B1}$ ,  $\phi_{sl}$ ). At the end of the first transition the major side-lobe has vanished. Further increase in the out-of-band frequency results in the pattern to transition linearly to the second breakpoint at  $3f_U$  (or  $\frac{1}{3}f_L$ ). This second transition is illustrated in Figure 2-168b in which both the main-beam gain and the back-lobe gain transition linearly with frequency to the 0 dB level. At the second out-of-band breakpoint the model patterns are defined by a constant 0 dB level which represents an isotropic radiator.

For frequencies above  $3f_U$  the model pattern is the superposition of a dipole pattern presented in Section 2.16.1 and a 0 dB isotropic radiator. This model is defined as the dipole model in which a gain value of less than 0 dB is set equal to 0 dB. The resonant frequency of the dipole may be defined as

$$f_o = \sqrt{f_L f_U}$$

Expressions for the various out-of-band transitions of the breakpoint parameters defined in Table 2-7 may be derived from one general expression. A linear transition of  $(f, a)$  from  $(f_1, a_1)$  to  $(f_2, a_2)$  is described by

$$a(f) = \frac{f - f_1}{f_2 - f_1} (a_2 - a_1) + a_1$$

The values of constants  $f_1$ ,  $f_2$ ,  $a_1$ , and  $a_2$  for each transition defined in Table 2-7 are enumerated in Table 2-8.

Since the Yagi-Uda antenna is an array of linear dipoles, the specified side-lobe angle  $\phi_{sl}$  is applied only to the H-plane pattern, as discussed in Section 2.16.3.

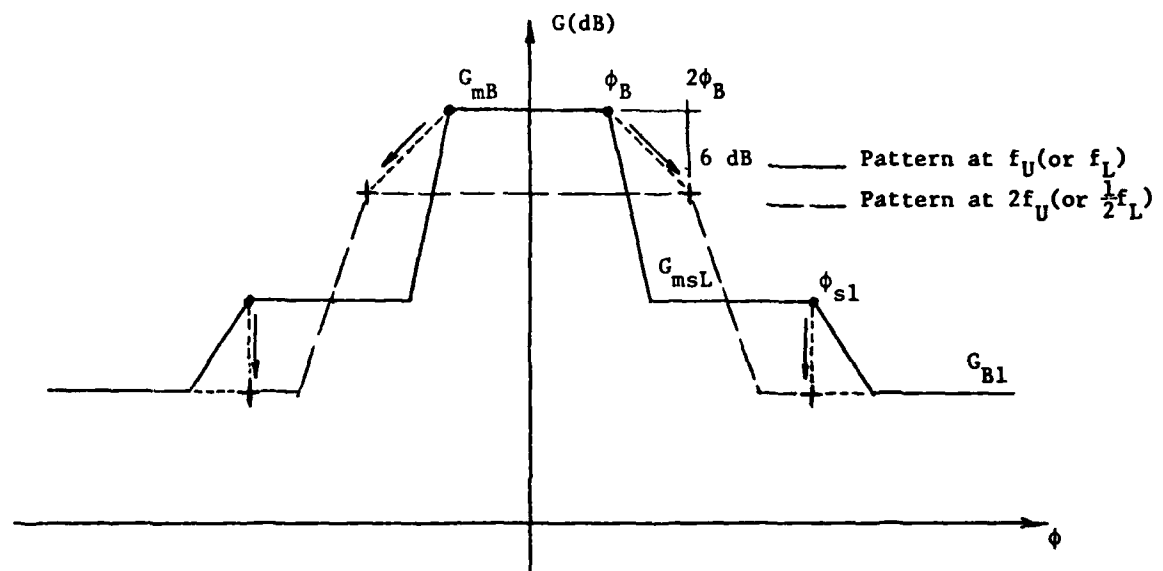


Figure 2-168a Transition with frequency of pattern model from design band to first breakpoint.

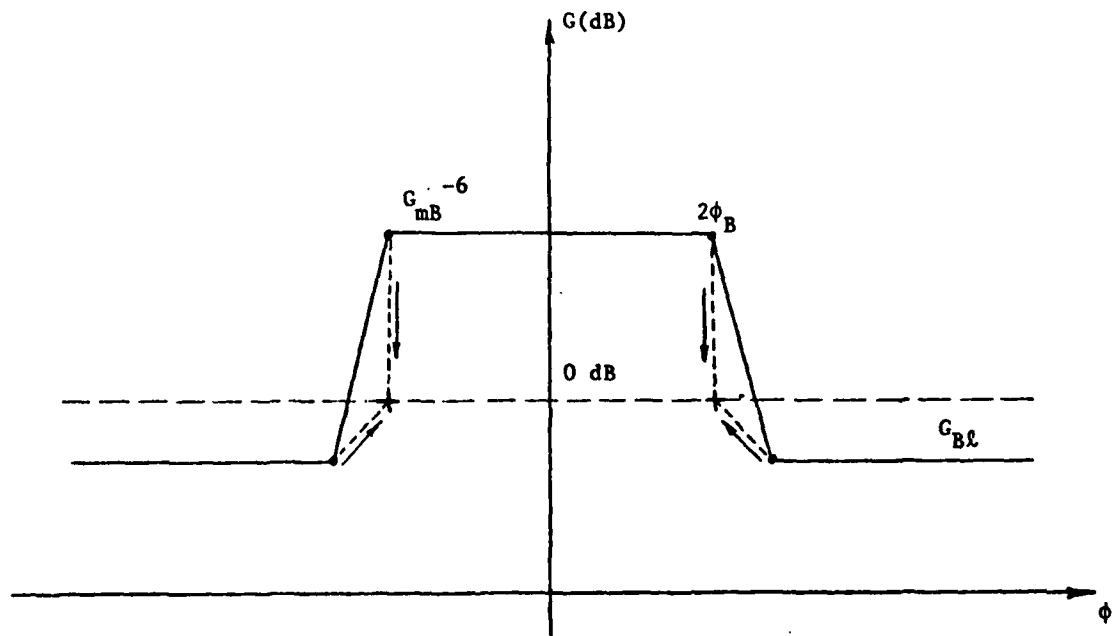


Figure 2-168b Transition with frequency of pattern model from first to second breakpoints

Table 2-8 Frequency Transition Table for Yagi-Uda Antenna Model

Transition	$f_1$	$f_2$	Parameter	$a_1$	$a_2$
$\frac{1}{3}f_L < f < \frac{1}{2}f_L$	$\frac{1}{3}f_L$	$\frac{1}{2}f_L$	Mainbeam Gain	0	$G_{mB}^{-6}$
			Backlobe Gain	0	$G_{B1}$
$\frac{1}{2}f_L < f < f_u$	$\frac{1}{2}f_L$	$f_u$	Mainbeam Gain	$G_{mB}^{-6}$	$G_{B1}$
			3 dB Beamwidths	$2\phi_B, 2\theta_B$	$\phi_B, \theta_B$
			Sidelobe Gain	$G_{B1}$	$G_{msL}$
$f_u < f < 2f_u$	$f_u$	$2f_u$	Mainbeam Gain	$G_{mB}$	$G_{mB}^{-6}$
			3 dB Beamwidths	$\phi_B, \theta_B$	$2\phi_B, 2\theta_B$
			Sidelobe Gain	$G_{msL}$	$G_{sl}$
$2f_u < f < 3f_u$	$2f_u$	$3f_u$	Mainbeam Gain	$G_{mB}^{-6}$	0
			Backlobe Gain	$G_{B1}$	0

#### 2.16.3.2 Directive Gain Model for Log-Periodic Antenna

The log-periodic antenna may be considered as an array of linear elements in which the phase center generally shifts position with frequency. Since the behavior of the log-periodic antenna is similar to that of a Yaga-Uda beam antenna, the proposed model for the log-periodic is the same as that given in Table 2-7, with the exception that the superposition of a dipole pattern above  $3f_u$  is omitted. It is felt that the alternating polarity of successive dipoles may tend to cancel signals received on several elements simultaneously at frequencies above the design band.

Although the design band may be relatively wide - e.g.,  $f_u/f_L = 10$  - the design gain and beamwidth of a log-periodic antenna are assumed to remain constant over the design band.

Since the log-periodic antenna is an array of linear dipoles, the specified sidelobe angle  $\phi_{s1}$  is applied only to the H-plane pattern, as described in Section 2.16.3.

#### 2.16.3.3 Directive Gain Model for a Helical Antenna

Helical antennas generally exhibit two modes of operation: a low-frequency mode, where it behaves like a monopole, and a high-frequency mode, which is end-fire of medium gain. This latter mode is the normal mode of operation and is assumed to be the mode for which the user specifies the input parameters. Thus, within the design band from  $f_L$  to  $f_u$  the radiation pattern is modeled as a medium-gain antenna. Major sidelobes may or may not be specified. Since the helix is symmetrical the field is circularly polarized and  $\phi_B = \theta_B$ ,  $\phi_{s1} = \theta_{s1}$ . The proposed model provides a transition of this pattern into an isotropic pattern outside the design band. At frequencies below the design band the isotropic pattern transitions into a figure-8 pattern of a dipole with the axis aligned with the helix axis. The proposed model is defined in the following table.

Para-meters	Breakpoint Frequencies					
	$<\frac{1}{2}f_L$	$\frac{1}{2}f_L$	$f_L$ to $f_u$	$2f_u$	$3f_u$	$>3f_u$
$G_{mB}$		0 dB	$G_{mB}$	$G_{mB}^{-6}$	0 dB	-
$\phi_B, \theta_B$	Isotropic + Dipole	$2\phi_B, 2\theta_B$	$\phi_B, \theta_B$	$2\phi_B, 2\theta_B$	$2\phi_B, 2\theta_B$	-
$G_{msL}$		0 dB	$G_{msL}$	0 dB	-	-
$\phi_{sl}$		$\phi_{sl}$	$\phi_{sl}$	$\phi_{sl}$	-	-
$G_{Bl}$		0 dB	$G_{Bl}$	0 dB	0 dB	0 dB

For frequencies less than  $\frac{1}{2}f_L$ , the model consists of the superposition of an isotropic pattern and a figure-8 pattern. The maximum gain of the figure-8 pattern remains fixed at  $1.0=0$  dB, while the isotropic pattern decreases linearly with frequency to  $-20$  dB at  $\frac{1}{16}f_L$ . The equation for the isotropic transition is given by

$$G_{iso}(f) = -20 \times \frac{8}{7} \left(1 - \frac{2f}{f_L}\right) \quad dB \quad \left(\frac{f_L}{16} \leq f \leq \frac{f_L}{2}\right)$$

The gain is the larger of the two patterns determined at any  $\phi, \theta$ .

#### 2.16.3.4 Directive Gain Model for a Corner Reflector

The mainbeam of a corner reflector antenna operating within the design band is of medium gain with little or no backlobe and sidelobes. This region is modeled by the user-defined conical model. Above the design band the beam tends to deteriorate as radiation begins to leak through the reflector, which is usually an open mesh. Since the feed element is usually some type of dipole, there will tend to be nulls along the dipole axis. Thus, the pattern does not transition into an isotropic pattern. Instead, the pattern above the design band is the superposition of the conical beam and that of a dipole, whichever provides the larger gain for a given  $\phi, \theta$ . At  $f_u$  when the mainbeam begins to deteriorate, the figure-8 dipole pattern develops in magnitude from

-20 dB to 0 dB at  $2f_u$ . From  $2f_u$  to  $4f_u$  the mainbeam vanishes and the maximum gain of the figure-8 pattern increases to 3 dB, which remains for all higher frequencies. The standard dipole pattern model is not applied here since the feed element often is a discone which is presumed not to experience increased gain with higher order resonances.

Below the design band the model transitions into an isotropic pattern. It is felt that at frequencies well below the design band the entire antenna assembly would tend to appear as a fat dipole and provide radiation in nearly all directions. The reflector would no longer be effective and would tend to carry induced currents in phase with the driven dipole.

The proposed model is summarized in the following table:

Parameters	Breakpoint Frequencies					
	$\frac{1}{4}f_L$	$\frac{1}{4}f_L$	$f_L$ to $f_u$	$2f_u$	$4f_u$	$>4f_u$
$G_{mB}$	-	0 dB	$G_{mB}$	$G_{mB}^{-\delta}$	$G_{B1}$	$G_{B1}$
$\phi_B, \theta_B$	-	$2\phi_B, 2\theta_B$	$\phi_B, \theta_B$	$2\phi_B, 2\theta_B$	$2\phi_B, 2\theta_B$	
$G_{msL}$	-	0 dB	$G_{msL}$	$G_{B1}$	-	
$\phi_{s1}$	-	$\phi_{s1}$	$\phi_{s1}$	$\phi_{s1}$	-	
$G_{B1}$	0 dB	0 dB	$G_{B1}$	$G_{B1}$	$G_{B1}$	Figure 8 (3 dB)

The maximum directive gain of the figure-8 pattern in the range  $f_u < f < 2f_u$  is given

$$G_{dip}(f) = 20 \left( \frac{f}{f_u} - 2 \right) \text{ dB}$$

The gain then increases to +3 dB in the range  $2f_u < f < 4f_u$ , as given by

$$G_{dip}(f) = 3 \left( \frac{1}{2} \frac{f}{f_u} - 1 \right) \text{ dB.}$$

### 2.16.3.5 Directive Gain Model for a Horn Antenna

The design band of a horn antenna usually ranges over one octave - i.e.,  $f_u \approx 2f_L$ . The lower cutoff frequency is usually just below  $f_L$ . Within the design band the user specifies the pattern parameters which are presumed to apply to midband. The 3-dB beamwidths are inversely proportional with frequency [9, page 194] and, therefore, the directivity increases with the square of the frequency. Consequently, the midband mainbeam gain  $G_{mB}$  should not present more than 3 dB error from the gains at  $f_L$  and  $f_u$ .

As the frequency increases above  $f_u$  the gain continues to increase. However, higher order modes can occur in an unpredictable manner which result in split beams and generally multilobing. While the directivity of individual beams may be considerably high, the beams tend to be narrow with unpredictable orientations.

The proposed model for horn antennas consists of the conical model for medium-gain antennas. The model remains constant for all frequencies below  $2f_u$ . In the range from  $2f_u$  to  $4f_u$  the mainbeam makes a transition which is linear with frequency that reduces the peak directive gain by 6 dB and doubles the beamwidth. The sidelobe and backlobe parameters remain fixed for all frequencies to account for higher frequency effects. The model does not change below  $f_L$ . The effect of waveguide cutoff is fully accounted for in the transmission loss term. The following table summarizes the directive gain model for a horn antenna.

Parameters	Breakpoint Frequencies				
	$< f_L$	$f_L$ to $f_u$	$2f_u$	$4f_u$	$> 4f_u$
$G_{mB}$	$G_{mB}$	$G_{mB}$	$G_{mB}$	$G_{mB} - 6$	$G_{mB} - 6$
$\phi_B, \theta_B$	$\phi_B, \theta_B$	$\phi_B, \theta_B$	$\phi_B, \theta_B$	$2\phi_B, 2\theta_B$	$2\phi_B, 2\theta_B$
$G_{msL}$	$G_{msL}$	$G_{msL}$	$G_{msL}$	$G_{msL}$	$G_{msL}$
$\phi_{s1}$	$\phi_{s1}$	$\phi_{s1}$	$\phi_{s1}$	$\phi_{s1}$	$\phi_{s1}$
$G_{B1}$	$G_{B1}$	$G_{B1}$	$G_{B1}$	$G_{B1}$	$G_{B1}$

#### 2.16.4 Pattern Model for High-Gain Antennas

The directive gain of a high-gain antenna operating within its design band is considered to be greater than 20 to 25 dB. Types of antennas within this classification are large arrays, such as phased arrays, and aperture antennas which are designed to produce a highly focused beam, such as large horn antennas, reflector antennas, and lens antennas. The predominant type of high-gain antenna is the reflector aperture type in which a parabolic dish reflects radiation from a primary feed antenna into a highly collimated beam. Radar antennas are the most common application of this type.

The proposed pattern model for high-gain antennas is the three-level conical model described in Section 2.16.2. For application to high-gain antennas, this model requires a different value of the slope intercept offset than used for the medium-gain antennas. In order to determine a practical value of  $\Delta$  a variety of theoretical radiation patterns have been studied. Table 2-9 lists 22 pattern shapes based on different types of aperture distributions of the primary radiation. [17, pages 268-333] For each type of secondary radiation pattern, the depth of the first major sidelobe was noted, and the position of the best model fit was determined. This fitting process consisted of adjusting the slope of a straight line passing through the point  $(G_{mB}, \phi_B)$  to given the best fit to the mainlobe along one side to the level of the first major sidelobe  $G_{msL}$ . The intercept of this line on the gain axis above  $G_{mB}$  is  $\Delta$ . In Table 2-9, the values of the theoretical sidelobe gain and  $\Delta$  are in dB relative to the mainbeam peak level of 0 dB. As seen in the Table, there is a relatively narrow spread in  $\Delta$  measured. The data exhibits a slight tendency for  $\Delta$  to increase with the depth of the major sidelobe; however, this relationship is not sufficiently distinct to justify the use of a functional relationship. For the proposed model, a value of  $\Delta = 17$  dB is selected as being the average of the  $\Delta$  values listed in Table 2-9. The selection of 17 dB is also weighted by the  $\Delta$  values of the more commonly used types of aperture distributions: cosine, cosine<sup>2</sup>, and cosine-on-pedestal. The model appears to provide a good fit to the theoretical mainlobe patterns representing practical types of aperture antennas. The model fit was performed on a graphic plot of dB gain vs  $\phi$  of normalized curves. Consequently, the model applies to any specified beamwidth which corresponds to linear scaling of the  $\phi$ -axis for the normalized curves.

Table 2-9 Model Parameters for Radar Antenna Patterns

<u>Illumination</u>	<u>First Sidelobe, dB</u>	<u>ΔdB</u>
1. Uniform	-13	+16
2. Cosine	-23	17.5
3. Cosine <sup>2</sup>	-31	18
4. Cosine <sup>3</sup>	-39	18
5. Parabolic	-21	18.5
6. Triangular	-26	17
7. Truncated Gaussian, n=1, 7, 20 dB Sidelobes	-21	16
8. Truncated Gaussian, n=2, 4, 30 dB Sidelobes	-35	17.5
9. Truncated Gaussian, n=2, 8, 40 dB Sidelobes	-37	15
10. Cosine-on-pedestal	-22	16
11. Taylor, n=2, 20 dB Sidelobes	-21	18
12. Taylor, n=4, 30 dB Sidelobes	-31	17.5
13. Taylor, n=6, 40 dB Sidelobes	-42	19
14. Hamming	-46	18
15. Uniform Circular	-18	17
16. Parabolic Circular	-25	18
17. Truncated Gaussian Circular, n=1, 1.7	-23	17
18. Truncated Gaussian Circular, n=2, 4	-34	18
19. Truncated Gaussian Circular, n=2, 8	-40	16
20. Taylor Circular, n=2	-22	16
21. Taylor Circular, n=4	-31	18
22. Taylor Circular, n=6	-42	17.5

The out-of-band characteristics of high-gain antennas have been reported [16, page 5-13]. These general results indicate that off the design frequency the mainbeam deteriorates by 8 dB, the 3-dB beamwidth triples, and the major sidelobes vanish. These characteristics are applied to the proposed model.

The proposed model for high-gain antennas is defined in the Breakpoint Parameter Table below.

Parameters	Breakpoint Frequencies					
	$<1f_L$	$1.f_L$	$f_L$ to $f_u$	$4f_u$	$10f_u$	$>10f_u$
$G_{mB}$	-	0	$G_{mB}$	$G_{mB}^{-8}$	0	-
$\phi_B, \theta_B$	-	$3\phi_B, 3\theta_B$	$\phi_B, \theta_B$	$3\phi_B, 3\theta_B$	$3\phi_B, 3\theta_B$	-
$G_{msL}$	-	0	$G_{msL}$	0	-	-
$\phi_{s1}$	-	$\phi_{s1}$	$\phi_{s1}$	$\phi_{s1}$		-
$G_{B1}$	0	0	$G_{B1}$	$G_{B1}$	0	0

### 2.16.5 Directive Gain Model for a Loop Antenna

An electrical small loop has a figure 8 pattern of a monopole aligned with the axis of the loop. Typically, the gain of a small loop is considerably less than that of an isotropic (0 dB) and tends to increase with frequency. The gain of a loop having a full-wave circumference is more than 3 dB. Higher frequencies can result in lobing in most any direction. Thus, the model for a loop should provide the figure 8 pattern of increasing size through the electrically-short region and degenerate into an isotropic at higher frequencies. The determination of the frequency at which a loop is no longer electrically small is presumed to be derived from the physical diameter  $d$  specified for the loop. Let  $f_o$  be the frequency at which the circumference of the loop is one wavelength. That is,

$$\lambda = \pi d \text{ meters.}$$

$$\text{Then } f_o = \frac{300}{\lambda} = \frac{300}{\pi d} \approx \frac{100}{d} \text{ MHz}$$

If the design frequency of a loop is  $f_1$  with an associated gain of  $G_1$ , then the gain of the loop is considered to increase to 0 dB at  $f_o$  due to radiation resistance, as follows:

$$G_{mB}(f) = G_1 \frac{f_o - f}{f_o - f_1}$$

Superimposed on the figure 8 pattern is an isotropic pattern which minimizes the null depth of the figure 8 pattern. The gain of the isotropic pattern is proposed to lie 10 dB below the peak gain of the figure 8 pattern at all frequencies below  $\frac{1}{2} f_o$ . From  $\frac{1}{2} f_o$  to  $f_o$  the isotropic gain level increases linearly to reduce the null depth. The gain of the isotropic pattern is proposed as

$$G_i(f) = G_{mB}(f) - 20 \left(1 - \frac{f}{f_o}\right) \quad \frac{f_o}{2} \leq f \leq f_o$$

Within the frequency range  $\frac{f_o}{2}$  to  $f_o$  the directive gain is equal to that of the figure 8 pattern or of the isotropic pattern, whichever is larger.

Above  $f_o$  the directive gain remains as 0 dB with an isotropic pattern.

### 2.16.6 Directive Gain Model for a Planer Log-Spiral Antenna

The planer log-spiral antenna is a low-gain, omnidirectional, circularly polarized, wideband antenna which typically has a design band pattern of a cardioid. The antenna generally contains an absorbing sheet behind the conducting plane to minimize back-lobe radiation.

The proposed model for this antenna is defined in the table below. The application of a two-level beam pattern as described by a frustum over a plane may be used here.

Parameters	Breakpoint Frequencies				
	$< \frac{1}{2} f_L$	$\frac{1}{2} f_L$	$f_L$ to $f_U$	$2f_U$	$> 2f_U$
$G_m^B$	---	0 dB	$G_m^B$	0 dB	---
$\phi_B, \theta_B$	---	$\phi_B, \theta_B$	$\phi_B, \theta_B$	$\phi_B, \theta_B$	---
$G_{msL}$	---	0 dB	$G_{msL}$	0 dB	---
$\phi_{s1}$	---	$\phi_{s1}$	$\phi_{s1}$	$\phi_{s1}$	---
$G_{B1}$	0 dB	0 dB	$G_{B1}$	0 dB	0 dB

The model permits the user to specify major side-lobe parameters, if desired.

### 2.16.7 Directive Gain Model for a Conical Log-Spiral Antenna

The conical log-spiral antenna is a broadband, low-gain antenna consisting of two balanced conductors wrapped in a spiral about a conical form. The conductors are closely spaced at the vertex where they are fed. The spacing increases logarithmically along the cone. The radiation pattern of this type of antenna is typically an omnidirectional figure 8 pattern with the nulls lying on the axis of the cone. The radiation is circularly polarized. The maximum gain is typically 0 dB to 3 dB relative

to an isotrope. Measured patterns indicate a filling in of the forward axial null.

The proposed model for the conical log-spiral antenna is a figure 8 pattern of 0 dB gain for all frequencies below the upper design frequency  $f_U$ . Superimposed on this is an isotropic pattern with a gain that increases linearly with frequency from -10 dB at the lower design frequency  $f_L$  to 0 dB at  $f_U$ . The gain in any direction is the larger of these two patterns. Above  $f_U$  the gain remains constant at 0 dB with an isotropic pattern.

#### 2.17 Antenna Power Dissipation Factor

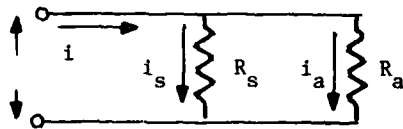
Antennas are generally designed to operate efficiently within their design frequency band. The shapes of the radiating elements, the physical arrangement of conductors in the feed circuits, and dielectric materials within the antenna are designed to provide acceptably low losses to the total power delivered to the antenna. An important consideration in the design are stray capacitances between adjacent conductors and between conductors and ground such as the antenna frame or case which encloses input feed circuitry. At design band frequencies the displacement currents flowing through stray capacitive circuits and the power dissipated in any dielectrics are designed to be a relatively small fraction of the total antenna current or power.

At frequencies considerably above the design band the stray capacitances offer less reactance and tend to short circuit the desired antenna circuit. This represents a flow of power that does not reach the radiating elements of the antenna. The by-passing effects of stray capacitances increases with frequency and generally become a dominating factor of antenna performance at sufficiently high frequencies. In addition, dielectric losses generally increase with frequency.

The proposed antenna model accounts for these power losses with a third term, called the Power Dissipation Factor  $F_D$ . This factor, then includes the effective loss of antenna power due to stray capacitances within the antenna feed circuits and ohmic losses due to imperfect dielectrics and

conductors within the antenna. Since high-gain antennas and horn antennas do not usually contain feed circuitry,  $F_D$  will be applied only to low-gain antennas and medium-gain antennas except horn antennas.

The modeling of  $F_D$  is accomplished by assuming a frequency dependent shunt resistor  $R_s$  in parallel with the antenna radiation resistance  $R_a$ , as shown below



The power efficiency of this circuit is

$$\eta = \frac{P_a}{P_t} = \frac{P_a}{P_s + P_a}$$

where  $P_a$  = power radiated =  $i_a^2 R_a$

$P_s$  = power loss =  $i_s^2 R_s$

$P_t$  = total power absorbed by antenna.

Since  $P_a = \frac{V^2}{R_a}$  and  $P_s = \frac{V^2}{R_s}$ ,

$$\eta = \frac{R_s}{R_s + R_a} = \frac{1}{1 + R_a/R_s}$$

Based on the inverse frequency dependence of capacitive reactance, let it be assumed that

$$R_s = \frac{1}{k_{of}}$$

Let the initializing constant  $k_o$  be established by the following conditions.

$$R_s = 10 R_a \text{ at } f = f_U$$

where  $f_U$  is the upper frequency limit of the antenna design band. Then,

$$k_o = \frac{1}{R_s f} = \frac{1}{10 R_a f_U}$$

With this constant substituted into  $R_s$  which is then substituted into the efficiency expression, we have

$$\eta = \frac{1}{1 + 0.1 \frac{f}{f_U}}$$

or  $\eta_{dB} = 10 \log \eta = -10 \log (1 + 0.1f/f_U)$ .

The efficiency at  $f=f_U = -0.4$  dB. This initial loss is removed from the above model to result in the following expression for the Power Dissipation Factor:

$$F_D (\text{dB}) = 0.4 - 10 \log (1 + 0.1 \frac{f}{f_U})$$

which applies only for  $f \geq f_U$ .

Several values of  $F_D$  are tabulated below.

$f/f_U$	$F_D$ (dB)
1	0.0
10	-2.6
100	-10.0
1000	-19.6

An example of this loss term applied to an antenna having an upper frequency limit of 1 MHz is shown in Figure 2-169.

### 2.18 Transmission Line Factor

The attenuation loss of the rf transmission line between the antenna terminal and the transmitter output port or receiver input port is included in the proposed antenna model as a fourth term called the Transmission Line Factor  $F_L$ . Two types of transmission lines are considered, coaxial cables and waveguides. Each type is treated separately below.

#### 2.18.1 Attenuation Model for Coaxial Lines

A wide variety of coaxial cables exist for rf applications. Figure 2-170 illustrates the attenuation curves of a number of general-purpose lines and cables [4, page 22-41]. Most of these are coaxial lines, but waveguide and microstrip are included for comparison. The various coaxial lines have a wide spread in attenuation rate at a given frequency; however, all the attenuation curves shown tend to increase approximately with  $\sqrt{f}$ .

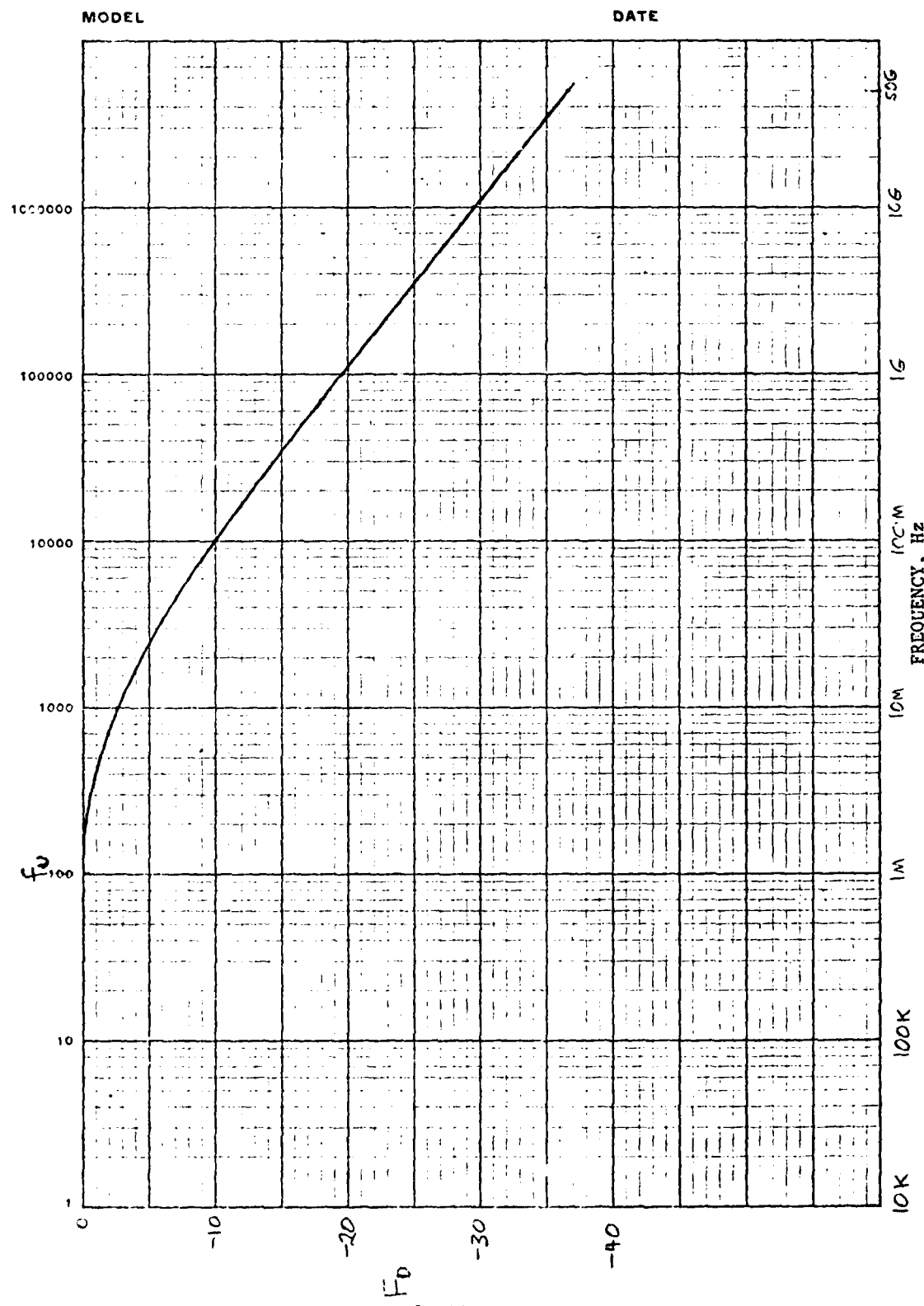


Figure 2-169 Example of Antenna Power Dissipation Factor for 1 MHz Antenna

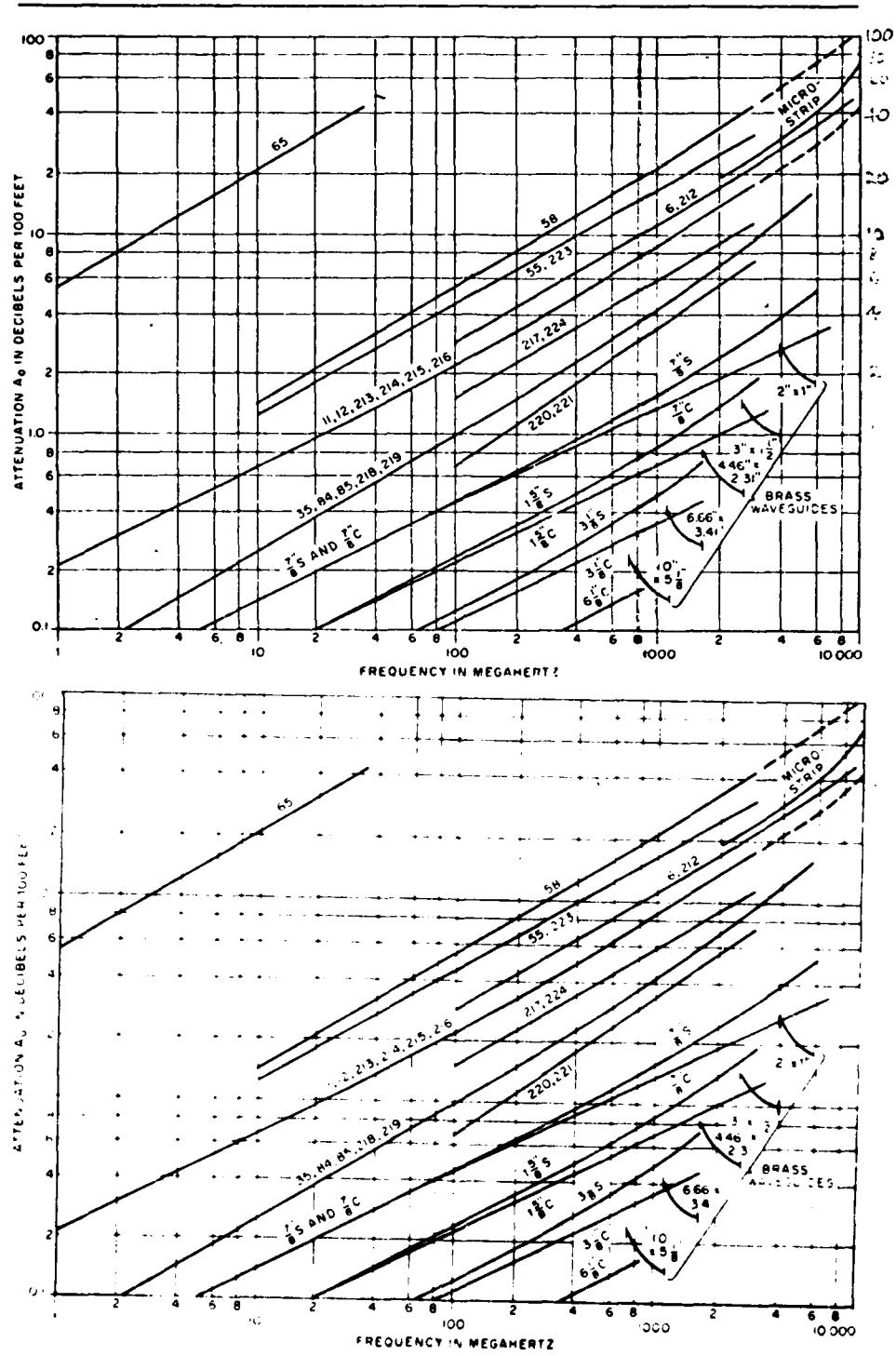


Figure 2-170 Attenuation rates of general-purpose transmission lines

The total attenuation  $T_L$  of a coaxial line of length  $L$  in feet is given by

$$T_L = \left(\frac{L}{100}\right) A \text{ (dB)}$$

where  $A$  is the attenuation rate of the line in dB/100 feet at frequency  $f$ . Let it be assumed that  $A$  varies with frequency as

$$A = k\sqrt{f}$$

where  $k$  is an initializing constant which allows the value of  $A = A_0$  to be defined for  $f = f_0$ . That is,

$$k = \frac{A_0}{\sqrt{f_0}}$$

and

$$A = A_0 \sqrt{\frac{f}{f_0}}$$

Substituting this function into the expression for the total line attenuation, we have

$$T_L = \left(\frac{L}{100}\right) A_0 \sqrt{\frac{f}{f_0}} \text{ (dB)}$$

for modeling the attenuation of a coaxial transmission line. A practical choice for  $f_0$  would be the center design frequency  $f_0 = \sqrt{f_L f_U}$  specified for the antenna. It is therefore required that the user specify the length  $L$  of the coaxial line and the attenuation rate  $A_0$  at  $f_0$ .

#### 2.18.2 Attenuation in Waveguides

The attenuation rates for waveguides are considerably less than those for most coaxial lines, as seen in Figure 2-170. The five waveguide samples indicated in this figure typically show attenuation rates decreasing with frequency. The reason for this, however, is due to the effect of cutoff frequency on the attenuation curve. Figure 2-171 presents the attenuation curves for several modes of propagation in a rectangular waveguide [8, page 132]. The lower frequency end of each curve is asymptotic to a cutoff frequency, and the higher frequency portion of each curve tends to increase with  $\sqrt{f}$ . In order

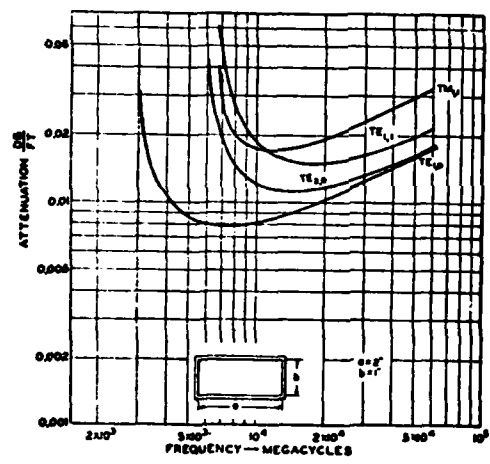


Figure 2-271 Attenuation curves for various modes in a typical rectangular waveguide

to prevent higher order modes from occurring, the waveguide should operate only within the frequency range which permits the  $TE_{10}$  to exist. As seen in Figure 2-171 this mode will be ensured if the frequency range extends from slightly above cutoff ( $3 \times 10^3$  MHz) to less than twice the cutoff frequency. In this region the slope of attenuation curve is negative and corresponds to the design band curves in Figure 2-170. Consequently, the design band attenuation rate of a waveguide is reasonably accurate over nearly a decade of frequency ranged above cutoff. As a result, the frequency dependent nature of waveguide attenuation does not appear to be significant and is not included in the proposed Transmission Line Factor. The user may indicate a waveguide transmission line, along with the total attenuation of the line. This loss becomes added to the antenna gain. Thus, the user should not include line losses in the specified antenna gains. The specification of a waveguide transmission line would also cause the model to apply the cutoff frequency model of the Impedance Matching Factor for a horn to the associated antenna, which may not be a horn.

## 2.19 SUMMARY OF ANTENNA GAIN MODEL

The antenna gain model calculates the power gain in dB of a specified type of antenna at a given frequency and arbitrary direction  $\phi, \theta$  relative to the antenna axis. The model consists of four independent terms which add (in dB) to give the resultant antenna gain.

$$G(f, \theta, \phi) = F_L + F_z + F_d + F_p$$

where

$F_L$  = Transmission line factor

$F_z$  = Impedance matching factor

$F_d$  = Power dissipation factor

$F_p$  = Directive gain pattern factor.

The inputs to the model consist of fixed and variable parameters listed in Table 2-10. Also shown in this table are the parameters which are not currently in IEMCAP and those required for each of the four terms of the model. The proposed model requires seven new input parameters which are not currently used in IEMCAP. The "look" angles  $\theta_o$  and  $\phi_o$  which define antenna orientation correspond to the mainbeam pointing direction of medium and high gain antennas, and the axis pointing direction of low-gain antennas.

The algorithms used for each of the four terms of the model are summarized below.

### Transmission Line Factor

The transmission line factor  $F_L$  represents the dB loss of power in the rf transmission line between the transmitter or receiver and the antenna. For a coaxial line,  $F_L$  is a function of frequency given by

$$F_L = -10 \log \left( \frac{L}{100} A_o \sqrt{\frac{f}{f_1}} \right)$$

where  $f_1 = \sqrt{f_L f_U}$ .

For a waveguide,  $F_L = 0$  if  $F_z$  = waveguide algorithm. Otherwise,  $F_L$  = waveguide algorithm for  $F_z$ .

TABLE 2-10. Input parameters required for proposed antenna gain model.

FIXED PARAMETERS		In IEMCAP?	F <sub>L</sub>	F <sub>Z</sub>	F <sub>d</sub>	F <sub>P</sub>
1. MODEL	Antenna type or model	YES				
2. QUAL	Qualifying condition of model	NO				
3. f <sub>L</sub>	Lower frequency limit of design band	NO	X	X	X	X
4. f <sub>U</sub>	Upper frequency limit of design band	NO	X	X	X	X
5. G <sub>mB</sub>	Mainbeam gain	YES				
6. θ <sub>B</sub>	3-dB vertical half-beamwidth*	YES				
7. φ <sub>B</sub>	3-dB azimuthal half-beamwidth*	YES				
8. G <sub>msL</sub>	Major sidelobe gain*	YES				
9. θ <sub>s1</sub>	Vertical sidelobe angle*	YES				
10. φ <sub>s1</sub>	Azimuthal sidelobe angle*	NO				
11. G <sub>B1</sub>	Backlobe gain*	YES				
12. POLAR	Polarization	YES				
13. θ <sub>O</sub>	Vertical "look" angle	YES				
14. φ <sub>O</sub>	Azimuthal "look" angle	YES				
15. l, d	Maximum dimension of antenna	YES				
16. LINE	Type of antenna feedline	NO	X			
17. L	Length of feedline	NO	X			
18. A <sub>O</sub>	Attenuation rate of feedline	NO	X			
*Applicable only to medium and high gain antennas						
VARIABLE PARAMETERS						
1. f	Frequency of gain calculation	YES	X	X	X	X
2. θ	Vertical "look" angle of coupling path	YES				
3. φ	Azimuthal "look" angle of coupling path	YES				

### Impedance Matching Factor

The impedance matching factor  $F_z$  represents the dB loss of power due to an impedance mismatch between the transmission line and the antenna terminals. Within the design band the antenna is assumed to be perfectly matched.  $F_z$  is calculated for a specified antenna model by one of three algorithms:

1. Resonant dipole algorithm
2. Matched dipole algorithm
3. Waveguide algorithm.

Each of these algorithms is presented below.

#### Resonant Dipole Algorithm for $F_z$

$$\text{First resonant frequency } f_1 = \sqrt{f_L f_U}$$

$$Q \text{ of first resonance } Q_1 = \frac{f_1}{f_U - f_L}$$

Resonant frequency of order  $n$ :

$$f_n = f_1 [1 + (n-1)A]$$

where  $A = 2 + 0.818 Q_1^{-1.083}$

Q of nth order resonance:

$$\log Q_n = 0.115 \log \left( \frac{f_n}{f_1} \right) + \log Q_1$$

The selectivity curve for the nth resonance is given by the modified universal resonance functions:

$$\text{MURF}_n(f) = \left( 1 + Q_n^2 \left[ 1 - \left( \frac{f_n}{f} \right)^2 \right]^2 \right)^{-1}$$

$$\text{Null level } N(f) = -3.0 - 16.53 e^{-0.288 \log \frac{f}{f_1}}$$

$$\text{For } f \leq f_1, F_z(f) = 10 \log \text{MURF}_1(f)$$

$$\text{For } f > f_1, F_z(f) = \max \begin{cases} 10 \log \text{MURF}_n(f) \\ N(f) \end{cases}$$

### Matched Dipole Algorithm for $F_z$

For  $Q_1 < 3$ ,

$$F_z(f) = \begin{cases} 10 \log \text{MURF}(f) & f \leq f_1 \\ 0 & f > f_1 \end{cases}$$

For  $3 \leq Q_1 \leq 15$ ,

$$F_z(f) = \begin{cases} 10 \log \text{MURF}(f) & f < 1.8f_1 \\ 0 & f > 1.8f_1 \end{cases}$$

For  $Q_1 > 15$ ,

$$F_z(f) = \begin{cases} 10 \log \text{MURF}(f) & f \leq f_1 \\ \text{MAX}(10 \log \text{MURF}(f), -20) & f < 1.8f_1 \\ 0 & f \geq 1.8f_1 \end{cases}$$

### Waveguide Algorithm for $F_z$

$$F_z(f) = \begin{cases} -20 & f \leq 0.6f_L \\ 100 \left( \frac{f}{f_L} \right) - 80 & 0.6f_L \leq f \leq 0.8f_L \\ 0 & f \geq 0.8f_L \end{cases}$$

### Power Dissipation Factor

The power dissipation factor  $F_d$  represents a power loss in the antenna due to stray capacitances, dielectric losses and other possible sources of antenna degradation which generally become noticeable at frequencies considerably above the design band. The model algorithm used for this term is

$$F_d(f) = \begin{cases} 0 & f \leq f_u \\ 0.4 - 10 \log \left( 1 + 0.1 \frac{f}{f_u} \right) & f > f_u \end{cases}$$

### Directive Gain Pattern Factor

The directive gain pattern factor  $F_p$  represents the antenna gain due to the radiation pattern in free space.

$F_p$  is calculated for a specified antenna model by one or more of three algorithms:

1. Dipole pattern algorithm
2. Medium-gain pattern algorithm
3. High-gain pattern algorithm

The first step for each antenna is to align the coordinate system with the antenna axis  $(\phi_0, \theta_0)$  by means of an Euler transformation and determine the relative direction  $(\phi, \theta)$  of the coupling path for which the gain is to be calculated.

Dipole Pattern Algorithm for  $F_p$

$$\text{Region I: } 0 < \frac{h}{\lambda} \leq .5 \quad \left( \begin{array}{l} h = \frac{l}{4} \text{ for monopole} \\ h = \frac{l}{2} \text{ for dipole} \end{array} \right)$$

$$G(\theta) = \max \left\{ \frac{|\sin \theta|}{.1} \right\}$$

$$\text{Region II: } .5 \leq \frac{h}{\lambda} \leq .75$$

$$G(\theta) = \frac{n_o^2}{2n_o - 1} |\sin \theta|$$

$$\text{where } n_o = 2.5n - 4 \quad (n = 4\frac{h}{\lambda}), \quad n_o = 10\frac{h}{\lambda} - 4$$

If  $G|\sin \theta| > 1$ , then  $G = \frac{1}{|\sin \theta|}, \theta \neq 0$ .

If  $G < .1$ , then  $G = .1$

$$\text{Region III: } .75 \leq \frac{h}{\lambda}$$

$$G(\theta) = \frac{n_o^2}{2n_o - 1} |\sin \theta|$$

where  $n_o = n + .5$

$$= 10\left(\frac{h}{\lambda}\right) + .5$$

If  $G|\sin \theta| > 1$ , then  $G = \frac{1}{|\sin \theta|}; \theta \neq 0$ .

If  $G < .1$ , then  $G = .1$

The resulting factor is

$$F_p(\theta) = 10 \log G(\theta)$$

### Medium-gain Pattern Algorithm for F<sub>p</sub>

The proposed directive-gain pattern model for medium-gain antennas is a general three-level gain pattern consisting of the mainbeam gain, major sidelobe gain, and backlobe gain. This pattern model is similar to the existing model in IEMCAP but has the advantage of providing continuous transitions between gain levels which are modeled by sections of cones.

At any given frequency the pattern model is fully defined by the gain profile in each of the two principal planes of azimuth ( $\phi$ -plane) and elevation ( $\theta$ -plane). Figure 2-162 shows an example of a gain profile showing various parameters required to define the profile. For cases in which the backlobe gain exceeds the sidelobe gain the profile has the general appearance illustrated in Figure 2-163.

The azimuth and elevation profiles for the design band are defined initially by user input quantities. The three gain levels are given by

$$G_m = G_{mB}$$

$$G_s = G_{msL}$$

$$G_b = G_{B1}$$

The beam angle breakpoints are given by

$$\text{Azimuth profile: } \beta_m = \phi_B$$

$$\beta_s = \phi_{s1}$$

$$\text{Elevation profile: } \beta_m = \theta_B$$

$$\beta_s = \theta_{s1}$$

$$\beta_a = \beta_m \frac{G_m - G_s + \Delta}{\Delta}$$

$$\beta_b = \beta_s \frac{G_m - G_b + \Delta}{G_m - G_s + \Delta} \quad (G_{msL} > G_{B1})$$

$$\beta_b = \beta_s \frac{G_m + G_b - 2G_s + \Delta}{G_m - G_s + \Delta} \quad (G_{msL} < G_{B1})$$

$$\Delta = 25 \text{ dB}$$

where the corresponding values of  $\beta_m$  and  $\beta_s$  are substituted for the azimuth and elevation profiles.

The out-of-band changes of directive gain with frequency are defined in terms of adjustments to the profile breakpoints as a function of frequencies relative to the design-band limits  $f_L$  and  $f_U$ . The out-of-band adjustments are presented in tables accompanying the discussions of the medium-gain antenna models.

In general, the breakpoint of a profile is defined by coordinates  $(G, \beta)$ . Each of these variables can be adjusted with frequency in which the transition between  $f_1$  and  $f_2$  is assumed to be linear with frequency. Accordingly, if  $x$  represents either  $G$  or  $\beta$  of a breakpoint, then the linear transition of  $x(f)$  from  $(x_1, f_1)$  to  $(x_2, f_2)$  is given by

$$x(f) = \frac{f-f_1}{f_2-f_1} (x_2-x_1) + x_1.$$

After the gain profiles in the two principal planes have been adjusted to the test frequency, the relative angular coordinates of the coupling path must be determined in polar form. The direction of the path at which the gain is to be calculated is given in rectangular form by  $(\phi_c, \theta_c)$ . The corresponding coordinates  $(\rho_c, \psi_c)$  in polar form are given by

$$\rho_c = \cos \phi_c \cos \theta_c$$

$$\psi_c = \frac{\tan \theta_c}{\sin \phi_c}$$

The plane containing both the antenna axis and the coupling path is rotated from the azimuth plane ( $\phi$ -plane) by angle  $\psi_c$ . The next step is to calculate the gain profile in this plane using values defining the breakpoints of the profiles in the principal planes as follows. The gain values remain unchanged. The beam angles of the breakpoints are calculated using a polar equation for an ellipse having semi-axes  $\phi_i$  and  $\theta_i$ , which represent the beam angles in the azimuth and elevation profiles of the  $i$ th breakpoint. The beam angle of this breakpoint at angle  $\psi_c$  is given by

$$\rho_i = \frac{1 + \tan^2 \psi_c}{\frac{1}{\phi_i^2} + \frac{1}{\theta_i^2} \tan^2 \psi_c}$$

The final step is to determine the directive gain from this profile for a beam angle  $\beta = \rho_c$ . The equations of the transition lines in the profiles are given below. The mainbeam-sidelobe transition line is given by

$$G_M(\beta) = G_m + \Delta - \beta \frac{\Delta}{\beta_m} \quad (\beta_b \leq |\beta| \leq \beta_a)$$

The sidelobe-backlobe transition line for the case  $G_s > G_b$  is

$$G_s(\beta) = G_m + \Delta - \beta \frac{G_m - G_s + \Delta}{\beta_s} \quad (\beta_s \leq |\beta| \leq \beta_b)$$

and for the case  $G_s < G_b$  is

$$G_s(\beta) = 2G_m - G_s + \Delta + \beta \frac{G_m - G_s + \Delta}{\beta_s}$$

The proposed model gives special consideration to the patterns of linear beam arrays, i.e., Yagi-Uda arrays and log-periodic antennas. Since the radiating elements are dipoles there is minimal radiation off the ends of the elements. If the array is horizontally polarized, the elevation profile is a three-level model. The azimuth profile, however is two-level consisting of only the mainbeam gain and backlobe gain. Similarly, if the array is vertically polarized, the azimuth profile is three-level and the elevation profile is two-level.

For some of the medium-gain antenna models the pattern degenerates into either an isotropic or dipole pattern at out-of-band frequencies. The second pattern must be computed and compared to the primary pattern. The resultant gain is determined from the larger of the two patterns at the given  $(\phi, \theta)$  direction.

#### High-gain Pattern Algorithm for $F_p$

The proposed directive-gain pattern model for high-gain antennas is identical to the general three-level model described for medium-gain antennas. The only exception is that the vertex offset for high-gain antennas is  $\Delta = 17$  dB.

Summary of Antenna Types

The various types of antennas which may be specified for the gain model are presented in Table 2-11. The third column defines the qualifying conditions of some of the antenna types. Columns four and five reference the specific algorithms for  $F_z$  and  $F_p$  applicable to each type. The other two gain terms  $F_L$  and  $F_d$  apply to all antenna types.

Table 2-11. Summary of Antenna Types and Applicable Model Algorithms for  $F_Z$  and  $F_p$ .

No.	Antenna Type	Qualifying Condition	$F_Z$	$F_p$
1	Monopole Dipole Sleeve Dipole Discone Slot	Resonant, no matching circuit	Res. Dip.	Dip
		Matched	Mat. Dip	
2	Folded Dipole	-	Mat. Dip $Q=1$	Dip
3	Loop	No tuning Circuit Tuning Circuit	Res. Dip Mat. Dip.	Dip + Isotropic
4	Corner Reflector	Resonant Matched	Res. Dip. Mat. Dip.	MG + Dip.
5	Yagi-Uda	Standard Dipole Feed Folded Dipole Feed	Res. Dip Mat. Dip. $Q=1$	MG + Dip
6	Log-periodic	-	Mat. Dip $Q=1$	MG
7	Helical	-	Mat. Dip $Q=1$	MG + Dip.
8	Spiral	Log-planer Conical	Mat. Dip. $Q=1$	MG Dip.+Isotropic
9	Horn	-	Horn	MG
10	Parabolic Reflector	Dipole or Slot Feed	Res. Dip.	HG
		Log-periodic Feed	Mat. Dip. $Q=1$	
		Horn Feed	Horn	
11	Phased Array	-	Mat. Dip.	HG
12	Traveling Wave Rhombic	-	0	MG

Abbreviations: Res. Dip. = resonant dipole  
Mat. Dip. = matched dipole

MG = medium gain  
HG = high gain

2.20            References

- 1a. Schelkunoff, S. A. "Electromagnetic Waves," D. Van Nostrand, 1944.
- 1b. Schelkunoff, S. A., and Friis, H. T., "Antennas Theory and Practice", John Wiley & Sons, Inc., 1966.
2. Everitt, W. L., and Anner, G. E., "Communication Engineering", McGraw-Hill Book Co., 1956.
3. Lind, W. R., "Out of Band Performance of Antennas", RADC-TR-65-43, May 1965, (University of Penna.).
4. Fukuzawa, K., and Sato, R., "The Characteristics of a Modified Duoconical Monopole with Curved Surface Transition", IEEE AP/B Poster A-6, 1979. (Dept. of Elec. Comm., Tohoku Univ., Sendai, 980 Japan.)
5. Norgorden, O., and Walters, A.W., "Experimentally Determined Characteristics of Cylindrical Sleeve Antennas", Jr. Am. Naval Engineers, May 1950, pg. 365-382.
6. Ryder, John D., "Networks, Lines and Fields", Prentice-Hall, Inc., 2nd Ed. 1955, pp. 312-316.
7. Lee, K. S. H., Liu, T. K., Marin, L., "EMP Response of Aircraft Antennas", IEEE Trans. EMC-20, No.1, Feb. 1978, pp. 94-99.
8. Marin, L., Costillo, J. P., Lee, K. S. H., "Broad-Band Analysis of VLF/LF Aircraft Wire Antennas", IEEE Trans., EMC., Vol. EMC-20, No. 1, Feb. 1978, pp. 141-145.
9. Blake, L. V., "Antennas", John Wiley & Sons, 1966.
10. King, R. W. P., "The Theory of Linear Antennas", Harvard University Press, 1956.
11. Jasik, H., "Antenna Engineering Handbook", McGraw-Hill Book Co., 1961.
12. "Telemetry and Special Purpose Antennas Catalog No. 300", Technical Appliance Corporation (TACO), Sherburne, N.Y.
13. Kraus, J. D., "Antennas", McGraw-Hill, 1950.
14. "Reference Data for Radio Engineers", ITT, 5th Ed., 1968.
15. Wolff, E. A., "Antenna Analysis", J. Wiley & Sons, 1966.
16. Jansky & Baily, "Interference Notebook," RADC-TR-66-1, 1966.
17. Barton, D. K.; Ward, H. R. "Handbook of Radar Measurement," Prentice-Hall, 1969.
18. Moreno, T., "Microwave Transmission Design Data," Dover, 1948.

### 3.0 NON-AVERAGE POWER SENSITIVE RECEPTOR MODELING

A detailed discussion of the waveform parameters total energy, peak current (and voltage) and rise time is given below. The discussion is in terms of EMI margins for each of these parameters that preserve the important features of the average power margin presently used in IEMCAP. In particular all margins are in terms of readily measurable quantities, such as power spectral density calculated at the receptor's input; applicable to both stochastic and deterministic waveforms; and adhere to a "worst case" philosophy. These margins are in terms of quantities that utilize both existing IEMCAP input data and additional input data that is realistic and easily obtainable on a given system.

In the following subsections example EMI margins are developed. The discussions consider total energy, peak waveform, and rise time margins. They are presented as candidates for possible inclusion within IEMCAP. They are discussed in terms of the general receptor model shown in Figure 3-1. Although this model explicitly considers current waveforms the extension to voltage waveforms is straightforward and, algorithms applicable to voltage waveforms can be developed.

Table 3-1 contains a listing of parameters and their corresponding definition used in this section.

#### 3.1 Total Energy - Deterministic Waveform

The total energy of a periodic waveform is infinite. Thus such a waveform will always cause interference to an energy sensitive receptor. However, in practice this interference can not occur unless the average power exceeds the average rate of energy dissipation (e.g., heat loss due to environmental cooling). Thus for periodic waveforms a total energy EMI criteria should actually be an appropriate power EMI criteria. The present IEMCAP average power EMI margins are directly applicable for this case.

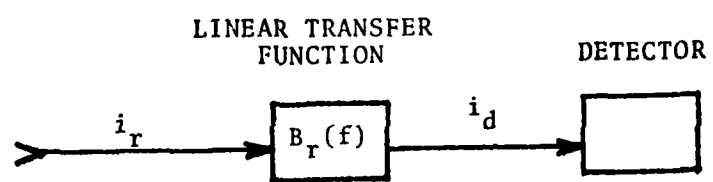


Figure 3-1. General Receptor Model

Table 3-1 Definition of Variables

$P_d$	= average power at input to detector (watts)
$P_r$	= average power at input to receptor (watts)
$E_d$	= total energy at input to detector (watt-sec)
$i_d(t)$	= detector input current (amp)
$i_r(t)$	= receptor input current (amp)
$i_r^{\uparrow}$	= peak value of $i_r(t)$ (amp)
$I_d(t)$	= Fourier transform of $i_d(t)$ (finite energy) (amps/Hz) { Phasor as defined by $i_d(t) = 2 \operatorname{Re}(I_d(f)e^{j\omega t})$ (amps) (sinusoid)
$I_r(f)$	= Fourier transform of $i_r(t)$ (finite energy) (amps/Hz) { Phasor as defined by $i_r(t) = 2 \operatorname{Re}(I_r(f)e^{j\omega t})$ (amps) (sinusoid)
$I_r^s(f)$	= level of $I_r(f)$ which induces the interference threshold (amps)
$K^P$	= detector interference threshold power level (watts)
$K^E$	= detector interference threshold energy level (watts-sec)
$K^{\beta}$	= detector interference threshold peak current level (amps)
$K^B$	= detector interference threshold bandwidth (Hz)
$G_r(f)$	= spectral power density at receptor input (watts/Hz) (Note: $G_r(f)$ is defined for negative $f$ .)
$B_r(f)$	= receptor input-to-detector linear current/Voltage transfer function (Dimensionless)
$ B_r(f) ^2$	= receptor input-to-detector energy transfer function
$\Delta_r(f)$	= time interval assigned to an energy sensitive (sec) receptor ( $\Delta_r(f)$ defines $ I_r^s(f) $ according to $K^E = 2\Delta_r(f) B_r(f) ^2 I_r^s(f) ^2$ )
$\Delta^2$	= duration of interference on receptor (sec)
$\sigma_d^2$	= variance of detector input waveform (watts)
$\sigma_r^2$	= variance of receptor input waveform $2 \int_{f_a}^{f_b} G_r(f) df$ (watts)
$\alpha$	= fraction of time that a stochastic waveform input must exceed $K$ to trigger interference peak at detector (dimensions)
$f_p$	= frequency for which $B_r(f)$ is maximum (Hz)
$f_o$	= center frequency of a narrowband Gaussian process (Hz)
$f_a, f_b$	= lower, upper frequencies defining common frequency band between interference and receptor (Hz)
$s$	= amplitude of the sinusoid in a narrowband (volts or amps) Gaussian - plus - sinusoid process
$\tau$	= pulse width of a pulse interfering waveform (sec)
$\beta$	= 3-dB point bandwidth of $B_r(f)$ (Hz)
$\beta_r^s$	= receptor input waveform bandwidth which induces the interference threshold bandwidth at the detector (Hz)
$\beta_r$	= portion of the receptor input waveform bandwidth within the passband of $B_r(f)$ (Hz)
$J_0(x)$	= modified Bessel function of zero order (Dimensionless)

For aperiodic waveforms, the total energy is defined as

$$E = \int_{t_1}^{t_2} f^2(t) dt$$

where  $(t_1, t_2)$  is the time interval of the waveform and it is understood that the reference of "1 ohm" is used. If  $f(t)$  satisfies the condition

$$\int_{-\infty}^{\infty} f^2(t) dt < \infty$$

it is said to have finite energy and is called an energy signal.

Recognizing that a nonperiodic function may be represented by the Fourier transform pair, we have

$$f(t) = \int_{-\infty}^{\infty} F(f) e^{j\omega t} df$$

and

$$F(f) = \int_{-\infty}^{\infty} f(t) e^{-j\omega t} dt.$$

Using the transform pair and the above relationship we can form the following

$$\int_{-\infty}^{\infty} f^2(t) dt = \int_{-\infty}^{\infty} f(t) \left[ \int_{-\infty}^{\infty} F(f) e^{j\omega t} df \right] dt$$

and by inversion of the order of integration, we have

$$\begin{aligned} \int_{-\infty}^{\infty} f^2(t) dt &= \int_{-\infty}^{\infty} F(f) \left[ \int_{-\infty}^{\infty} f(t) e^{j\omega t} dt \right] df \\ &= \int_{-\infty}^{\infty} F(f) F(-f) df. \end{aligned}$$

Note that

$$F(f) F(-f) = |F(f)|^2.$$

Then

$$\int_{-\infty}^{\infty} f^2(t) dt = \int_{-\infty}^{\infty} |F(f)|^2 df. \quad (3.1)$$

This result states that the total energy in a given nonperiodic time function is simply the area of the  $|F(f)|^2$  curve. The term  $|F(f)|^2$  is called the energy-density function and expresses the energy of  $f(t)$  as a function of frequency. Thus,  $|F(f)|^2$  has the units of watt-sec/Hz.

As an example, consider a signal having an arbitrary energy spectrum passed through an ideal bandpass filter with a narrow passband centered at frequency  $f_1$ . Assume the energy transfer function of the filter as unity for components lying in the filter passband and zero for other components (Figure 3-2).

The total energy of the output is

$$\begin{aligned} E_o &= \int_0^{\infty} |V_o(f)|^2 df \\ &= \int_{f_1 - \frac{W}{2}}^{f_1 + \frac{W}{2}} |V_i(f)|^2 df. \end{aligned}$$

For a sufficiently narrow filter bandpass (narrow enough so that the input spectrum is essentially constant over the band), the output can be approximated as

$$E_o \approx W |V_i(f_1)|^2.$$

Solving for  $|V_i(f_1)|^2$  gives

$$|V_i(f_1)|^2 \approx \frac{E_o}{W}.$$

From this expression it is evident that  $|V_i(f_1)|^2$  can be interpreted as the energy per unit bandwidth.

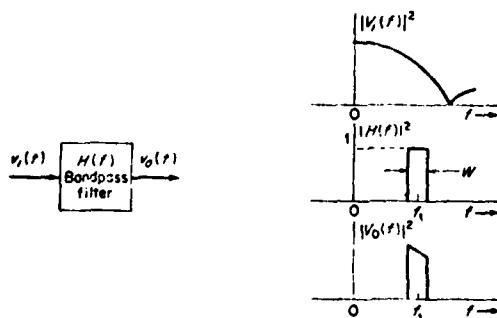
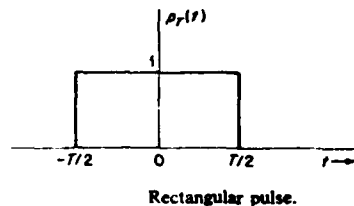


Figure 3-2 Measurement of energy spectrum

To determine the energy spectrum of an aperiodic function consider the rectangular pulse shown below.



This pulse can be expressed analytically as

$$\begin{aligned} p_T(t) &= 1 & -\frac{T}{2} < t < \frac{T}{2} \\ &= 0 & \text{otherwise.} \end{aligned}$$

The Fourier transform is obtained from

$$\begin{aligned} p_T(\omega) &= \int_{-\infty}^{\infty} p_T(t) e^{-j\omega t} dt \\ &= \int_{-T/2}^{T/2} e^{-j\omega t} dt = \frac{e^{-j\omega t}}{-j\omega} \Big|_{-T/2}^{T/2} \\ &= \frac{e^{+j\omega T/2} - e^{-j\omega T/2}}{j\omega}. \end{aligned}$$

Converting the exponentials to the equivalent trigonometric function leads to

$$p_T(\omega) = T \frac{\sin \omega T/2}{\omega T/2}.$$

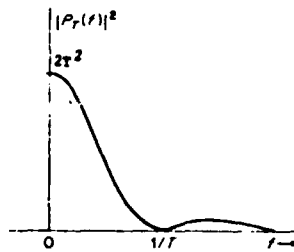
The energy spectrum of the pulse signal,  $p_T(t)$ , is

$$|p_T(\omega)|^2 = T^2 \left( \frac{\sin \omega T/2}{\omega T/2} \right)^2.$$

Changing from  $\omega$  to  $f = \omega/2\pi$  and converting to one-sided spectrum gives the energy spectrum as

$$\begin{aligned} |p_T(f)|^2 &= 2T^2 \left( \frac{\sin \pi T f}{\pi T f} \right)^2 = 2T^2 \text{sinc}^2(fT) & f \geq 0 \\ &= 0 & f < 0 \end{aligned}$$

The energy spectrum  $|P_T(f)|^2$ , of the rectangular pulse is shown below



Energy spectrum of rectangular pulse.

It is seen that the energy is concentrated in the low-frequency portion of the spectrum. The extent of this concentration can be found by computing the energy in the first loop (that is, for  $|f| < 1/T$ ) and comparing this to the total energy. The ratio, found by graphical integration, is 0.902. Thus, 90.2 percent of the energy in a rectangular pulse is contained in the band of frequencies below a frequency equal to the reciprocal of the pulse length. As a useful rule of thumb, it is often assumed that a pulse transmission system having a bandwidth equal to the reciprocal of the pulse width will perform satisfactorily. Actually, if high-fidelity reproduction of the pulse shape is required, a much greater bandwidth will be necessary. However, it can be seen that a system with this bandwidth will transmit most of the pulse energy.

Using equation (3-1) (See Figure 3-1), the total energy at the input to the detector (on a 1-ohm basis) is given by

$$E_d = \int_0^{\infty} |I_d(f)|^2 df \quad (\text{watt-sec})$$

where  $I_d(f)$  is the Fourier transform (one-sided) of the detector input waveform  $i_d(t)$ .

For a simple system with system function  $B_r(f)$ , the output (detector input) and input are related by

$$I_d(f) = B_r(f) I_r(f)$$

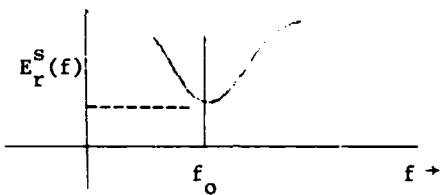
where  $I_r(f)$  is the Fourier transform of the receptor input waveform  $i_r(t)$ . Thus, the energy spectrum of the output is

$$\begin{aligned} |I_d(f)|^2 &= I_d(f) I_d^*(f) \\ &= [B_r(f)] [I_r(f)] [B_r^*(f) I_r^*(f)] \\ &= |B_r(f)|^2 |I_r(f)|^2 \end{aligned}$$

and

$$E_d = \int_0^{\infty} |B_r(f)|^2 |I_r(f)|^2 df.$$

In keeping with the IEMCAP definition of susceptibility and standard response an energy susceptibility is determined by the following. The energy susceptibility function may be represented as shown



As in the case of the power susceptibility curve, the energy susceptibility curve is a minimum at that frequency where the transfer function ( $B_r(f)$ ) is a maximum. The detector interference threshold energy level  $K^E$  can be related to the receptor input energy for a sinusoidal waveform if a time interval,  $\Delta_r(f)$ , is defined for the receptor. Thus, the susceptibility energy is

$$\begin{aligned} E_r^s(f) &= \Delta_r(f) |I_r^s(f)|^2 \\ &= \frac{K^E}{|B_r(f)|^2} \end{aligned}$$

or  $K^E = B_r(f) |I_r^s(f)|^2$

where  $E_r^s(f) =$  the CW energy at frequency  $f$  which generates the energy equal to the standard response energy level at the detector input (cooling included).

The total energy EMI margin for a deterministic, finite energy waveform becomes

$$\frac{E_d}{K^E} = \int_{f_b}^{f_a} \frac{|I_r(f)|^2}{E_r^s(f)} df.$$

where ( $f_a, f_b$ ) are the frequency limits for the energy susceptible devices. Note that the measurable quantities are transferred to the receptor input.

The energy received at the receptor from an emitter is given by the area under the received energy density function times the input impedance of the receptor. The result is

$$|I_t(f)|^2 t(f) b r_{ir}$$

where

$$|I_t(f)|^2 = \text{transmitted energy density } \frac{\text{watt-sec}}{\text{Hz}} \text{ (1 ohm)}$$

$b$  = bandwidth factor for the emitter (Hz)

$t(f)$  = transmission loss (dimensionless)

$r_{ir}$  = input impedance of the  $i$ th receptor (ohms)

This assumes  $|I_t(f)|^2$  is a constant over bandwidth  $b$ .

From the discrete equation notes<sup>(6)</sup>

$$|I_t(f)|^2 = (\sqrt{2}q)^2$$

$q$  = current spectral level (amps/Hz)

The broadband point energy EMI margin is then given by

$$epm_d(f) = \frac{(\sqrt{2}q)^2 t(f) b r_{ir}}{E_r^s(f)} .$$

Converting to decibels, the broadband point energy EMI margin for an aperiodic signal becomes

$$\begin{aligned} EPM_D(f) (\text{dB}) &= Q(\text{dB}\mu\text{A/MHz}) + T(f) (\text{dB}) \\ &\quad + B(\text{dBMHz}) + R_{IR} - \bar{E}_r^s(f) \\ &\quad - \bar{I}_r^s(f) (\text{dB}\mu\text{A}) \end{aligned}$$

where  $EPM_D(f) (\text{dB}) = 10 \log epm_d(f)$

$$Q(\text{dB}\mu\text{A/MHz}) = 20 \log (\sqrt{2}q/10^{-12})$$

$$T(f) (\text{dB}) = 10 \log t(f)$$

$$B(\text{dBMHz}) = 10 \log \left( \frac{b}{10^6} \right)$$

$$R_{IR} (\text{dB}) = 10 \log r_{ir}$$

$$\bar{E}_r^s(f) (\text{dB}) = 10 \log E_r^s(f) .$$

To determine the broadband integrated energy EMI margin, the derivation parallels that of the broadband integrated margin of the IEMCAP. Using Dr. Weiner's notation,<sup>(6)</sup> the derivation of the broadband integrated margin is presented below.

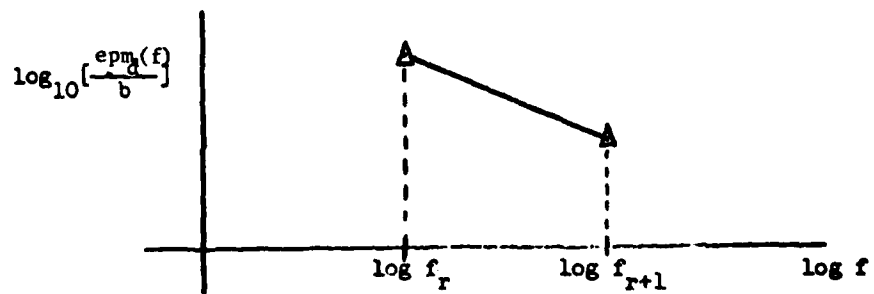
The point energy margins are converted to a margin density  
 $\frac{epm_d(f)}{b}$ .

Next, convert to a log-log scale and plot  $\frac{epm_d(f)}{b}$  vs.  $\log f$  and connect straight lines between the data points as shown below.



This curve represents the broadband margin density when plotted on a log-log scale. The broadband integrated EMI margin is obtained by finding the area under the curve.

To illustrate how this is done, focus attention on the  $r$ -th and  $(r+1)$ -st sample frequency as shown below.



The straight line connecting the points is of the form

$$\log_{10} \left[ \frac{epm_d(f)}{b} \right] = a \log_{10} \left( \frac{f}{f_r} \right) + C.$$

When  $f = f_r$ ,  $\log_{10}(f_r/f_r) = \log_{10}(1) = 0$  and

$$C = \log_{10} \left[ \frac{epm_d(f_r)}{b} \right]$$

Thus, C is the value of

$$\log_{10} \left[ \frac{epm_d(f)}{b} \right]$$

where  $f = f_r$  and a is the slope of the straight line. Letting  $f = f_{r+1}$  in the equation of the straight line, we have

$$\log_{10} \left[ \frac{epm_d(f_{r+1})}{b} \right] = a \log_{10} \left( \frac{f_{r+1}}{f_r} \right) + \log_{10} \left[ \frac{epm_d(f_r)}{b} \right].$$

Solving for the slope, yields

$$a = \frac{\log_{10} \left[ \frac{epm_d(f_{r+1})}{b} \right] - \log_{10} \left[ \frac{epm_d(f_r)}{b} \right]}{\log_{10} \left( \frac{f_{r+1}}{f_r} \right)}$$

For simplicity, let

$$g_r = \left[ \frac{epm_d(f_r)}{b} \right].$$

The slope is then given by

$$a = \frac{\log_{10} [g_{(r+1)} / g_r]}{\log_{10} (f_{r+1} / f_r)}.$$

Also, let

$$g_b(f) = \frac{e^{\mu_m(f)}}{b}.$$

The straight line can now be written as

$$\log_{10} [g_b(f)] = a \log_{10} \left( \frac{f}{f_r} \right) + \log_{10} [g_{r_b}].$$

Rearranging terms, we have

$$\log_{10} \left[ \frac{g_b(f)}{g_{r_b}} \right] = a \log_{10} \left( \frac{f}{f_r} \right) = \log_{10} \left[ \left( \frac{f}{f_r} \right)^a \right].$$

it follows that

$$\frac{g_b(f)}{g_{r_b}} = \left( \frac{f}{f_r} \right)^a$$

and

$$g_b(f) = g_{r_b} \left( \frac{f}{f_r} \right)^a.$$

This is the equation for the approximation to the margin density when the straight line on a log-log scale is converted to the corresponding curve on a linear scale. The area under the margin density in the frequency interval  $(f_r, f_{r+1})$  is given by

$$g_{12_r} = \int_{f_r}^{f_{r+1}} g_b(f) df = \int_{f_r}^{f_{r+1}} g_{r_b} \left( \frac{f}{f_r} \right)^a df$$

$$= \frac{g_{r_b}}{(f_r)^a} \cdot \frac{1}{a+1} (f)^{a+1} \Big|_{f_r}^{f_{r+1}}$$

$$\begin{aligned}
 &= \frac{g_{r_b}}{(f_r)^a} \frac{1}{a+1} [(f_{r+1})^{a+1} - (f_r)^{a+1}] \\
 &= \frac{g_{r_b}}{a+1} \left[ \frac{(f_{r+1})^{a+1}}{(f_r)^a} - f_r \right].
 \end{aligned}$$

To obtain the broadband integrated EMI margin over the entire frequency range of interest, it is necessary to sum the contributions from the area under each consecutive pair of sample frequencies. This is indicated by the following

$$= \sum_{r=1}^{n_c} g_{r_b} f_r$$

where  $n_c$  is the total number of sample frequencies due to the emitter and receptor in the frequency interval  $(f_a, f_b)$ .

From the above, the conclusion is that the same technique used in IEMCAP to obtain integrated margins is equally applicable to the total energy (aperiodic) integrated margin calculation.

### 3.2 Total Energy - Stochastic Waveform

As with periodic deterministic waveforms, a stationary stochastic waveform is of infinite duration and, thus has infinite energy. Therefore, the present IEMCAP average power EMI margin is then appropriate in order to predict whether dissipation (e.g., heat loss due to environmental cooling) exceeds energy buildup. The latter is necessary for interference to occur.

There may be instances where certain emitters may be considered sources of "Switched" stochastic waveforms in that an otherwise stationary process is turned-on and turned-off at known intervals. For example, consider a rotating reflector antenna that is emitting narrowband Gaussian noise within a receptor bandwidth. The total energy at the detector of the receptor can be determined from

$$E_d = \Delta P_d$$

where  $\Delta$  is the duration of interference on the receptor and where  $P_d$  is given by

$$P_d = \int_0^\infty G_r(f) |B_r(f)|^2 df.$$

As in the deterministic case, the detector interference threshold energy level is

$$K^E = |B_r(f)|^2 E_r^s(f).$$

It follows that the total energy EMI margin for "switched" stochastic waveforms is

$$\frac{E_d}{K^E} = \Delta \int_{f_a}^{f_b} \frac{G_r(f)}{E_r^s(f)} df$$

where  $(f_a, f_b)$  in the frequency limits for the energy susceptible device.

From the "Discrete Equation Notes," we can relate the above energy margin to the power spectral density function in the IEMCAP. A value of broadband emitter power spectral density is assigned to each sample frequency. The broadband power received at a receptor from an emitter is given by the area under the received power spectral density times the input impedance of the receptor. This may be defined as

$$G_r(f)(bw)r_{ir}$$

where  $G_r(f) = G_t(f) t(f)$

$G_t(f)$  = emitter power density at frequency  $f$  (watts/Hz)

$(bw)$  = FIM bandwidth (Hz)

and  $t(f)$  and  $r_{ir}$  are as defined previously.

The broadband energy point EMI margin (switched stochastic) is then given by

$$epm_s(f) = \frac{(\Delta)G_r(f)(bw)r_{ir}}{E_r^s(f)}$$

$$= \frac{(\Delta)G_t(f)t(f)(bw)}{E_r^s(f)}.$$

From IEMCAP we have

$$G_t(f) = q^2(bw).$$

Then  $epm_s(f) = \frac{(\Delta)q^2(bw)^2 t(f)}{E_r^s(f)}$

Converting to decibels, the broadband point energy EMI margin for the switched stationary signal becomes

$$\text{EMP}_s(f)(\text{dB}) = \bar{\Delta}(\text{dBsec}) + Q(\text{dB}\mu\text{A}/\text{MHz}) + \text{BW}(\text{dbMHz}) + T(f)(\text{dB}) \\ - \bar{\Delta}_r(f)(\text{dBsec}) - \bar{I}_r^s(f)(\text{dB}\mu\text{A})$$

where

$$\text{EMP}_s(f)(\text{dB}) = 10 \log \text{e}_{\text{PM}}(f)$$

$$\bar{\Delta}(\text{dBsec}) = 10 \log \Delta$$

$$Q(\text{dB}\mu\text{A}/\text{MHz}) = 20 \log \left( \frac{q}{10^{-12}} \right).$$

$$\text{BW}(\text{dbMHz}) = 20 \log \left( \frac{\text{bw}}{10^6} \right).$$

$$T(F)(\text{dB}) = 10 \log t(f)$$

$$\bar{\Delta}_r(f)(\text{dBsec}) = 10 \log \Delta_r(f)$$

$$\bar{I}_r^s(f)(\text{dB}\mu\text{A}) = 20 \log \left( \frac{I_r^s(f)}{10^{-6}} \right).$$

The integrated energy EMI margin for the switched stationary case is determined in the same manner as that presented in the deterministic total energy case.

### 3.3 Peak Current/Voltage - Deterministic Waveform

Some receptors (e.g., many digital devices) are sensitive to the peak value of a waveform (e.g., voltage or current). An upper bound to this peak can be given in terms of amplitude spectral density frequency domain data. This bound can be used to define a conservative estimate of a peak current (or voltage) EMI margin for deterministic waveforms in terms of receptor input quantities. The remainder of this section pertains to peak current but the peak voltage deviation can be performed in an analogous manner. Consider the detector current given by

$$i_d(t) = \int_{-\infty}^{\infty} I_r(f) B_r(f) e^{j\omega t} df.$$

Note that  $I_r(f)$  is a superposition of impulses for periodic (infinite-duration) waveforms and a continuous function for finite-energy (finite-duration) waveforms.

It follows that<sup>(1)</sup>

$$\left| i_d(t) \right| \leq \max \int_0^{\infty} |I_r(f)| |B_r(f)| df.$$

Also, the detector interference threshold peak current level  $K$  is given in terms of a CW receptor input level  $|I_r^s(f)|$  by

$$K = |B_r(f)| |I_r^s(f)|.$$

An interference margin may be defined by

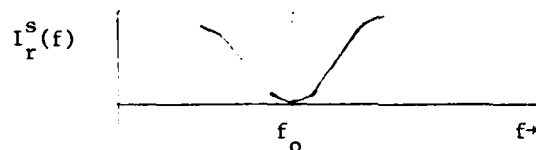
$$\frac{|i_d(t)|}{K} \leq \max \int_{f_a}^{f_b} \frac{|I_r(f)|}{|I_r^s(f)|} df$$

Where  $(f_a, f_b)$  is the frequency limit for the peak current susceptible device.

For IEMCAP a peak current EMI margin for deterministics waveforms (compatible with "worst case" philosophy) is defined by

$$\int_{f_a}^{f_b} \frac{|I_r(f)|}{|I_r^s(f)|} df.$$

Again, to conform with the IEMCAP definition of susceptibility and standard response a peak current susceptibility will be defined. The peak current susceptibility function may be represented as shown below.



As is the case of the power susceptibility curve, the peak current susceptibility curve is a minimum at that frequency where the transfer function  $B_r(f)$  is a maximum. The detector interference threshold peak current level  $K$  can be related to the receptor input peak current for a sinusoidal waveform by

$$K = |B_r(f)| I_r^s(f)$$

where  $I_r^s(f) =$  the peak CW input signal at frequency  $f$  needed to produce the standard response peak current level at the detector input.

To get an understanding of how "worst case" the above equation is, consider a rectangular pulse train as shown in Figure (3-3)<sup>(2)</sup> with parameters as defined in Figure (3-4).<sup>(3)</sup> Using this example, we will demonstrate how IEMCAP would make use of the above equation. Assume  $|I_r^s(f)| = 1$  and determine  $|I_r(f)|$ .

From Figure (3-5)<sup>(4)</sup>, the power density according to IEMCAP is:

$$\begin{aligned} P_{BB}(f) &= 2 A^2 \tau^2 f_B \\ &= 2 \times (0.1)^2 \times (1.25 \times 10^{-2}) \times 4 \times 10^3 \\ &= 1.25 \frac{\mu\text{watts}}{\text{Hz}} \quad 0 \leq f \leq f_m \\ &= 1.25 \times 10^{-6} \left( \frac{f_m}{f} \right)^2. \quad f > f_m \end{aligned}$$

$$\text{Bandwidth} = \frac{1}{2\tau} = \frac{1}{2 \times 1.25 \times 10^{-4}} = 4 \text{ kHz}$$

$$f_m = \frac{1}{\pi\tau} = \frac{1}{\pi \times 1.25 \times 10^{-4}} = 2.55 \text{ kHz}$$

The Fourier Series representation for the rectangular pulse train can be determined from

$$i(t) = \sum_{n=-\infty}^{\infty} a_n e^{j n \omega_0 t}$$

where

$$a_n = \frac{1}{T} \int_{t_i}^{t_1+T} i(t) e^{-j n \omega_0 t} dt$$

T = period of pulse train.

The coefficients are

$$a_n = \frac{a\tau}{T} \left[ \frac{\sin \frac{n\pi\tau}{T}}{\frac{n\pi\tau}{T}} \right] \exp \left[ -j \frac{2\pi n}{T} \left( \frac{\tau}{a} \right) \right]$$

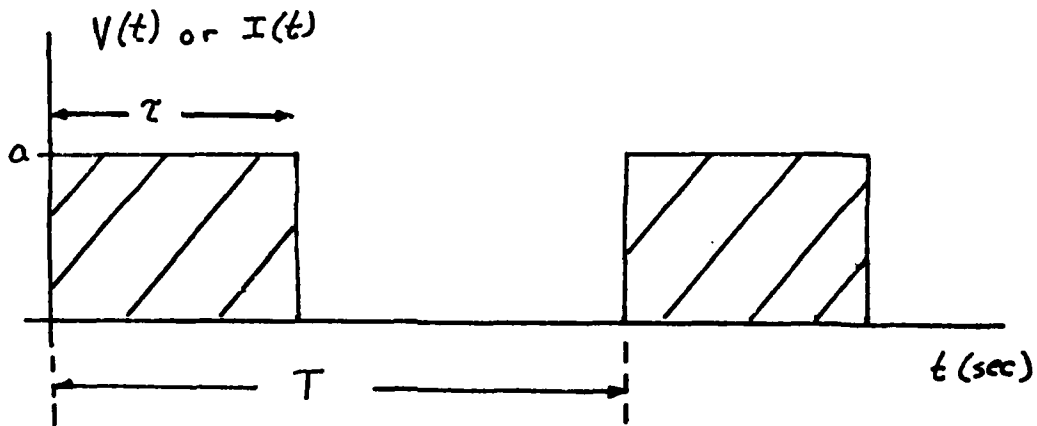
where  $\omega_0 = 2\pi/T$ .

Thus, the complete Fourier series expression for  $i(t)$  now becomes

$$i(t) = \sum_{n=-\infty}^{\infty} \frac{a\tau}{T} \left[ \frac{\sin n\pi\tau/T}{n\pi\tau/T} \right] \exp \left[ j \frac{a\pi n}{T} (t - \tau/2) \right]$$

or

$$i(t) = \frac{a\tau}{T} + \frac{2a\tau}{T} \frac{\sin n\pi\tau/T}{n\pi\tau/T} \cos \frac{2\pi n}{T} (t - \tau/2). \quad (3.2)$$



Required Input Parameters:

$a$  = volts/amps into designated load,  $R_L$

$\tau$  = pulse width (seconds)

$r_b$  = bit rate ( $r_b = \frac{1}{T}$ ) (Hertz)

$f_L$  = 30 Hz

$f_h = 3.18/\tau$  Hz

Frequency Table (Hz):

$f_L, .1f_h, .2f_h, .35f_h, .55f_h, f_h, f_h (1 \pm 10^{-P})$

Figure 3-3 Rectangular Pulse Train  
(RECTPL)

```

FREQ=30,50E6,1,90
POPT=CASE,17,0
  SOURCE=CASE,0,MILSPC,MILSPC
  RCEPT=CASE,0,MILSPC,MILSPC
PORT=4YDMC,WIRE,(B4,B12,F,GND,NONE,NOTEX),720,0,0,0,0,0
  PCEPT=CNTRL,0,30,1E3,RECTPL(1.5),.0333,AMPS,1E3
ECPT=B1,M461A,FIX,B1,NOTCLS,C,C,0
FREQ=30,50E6,1,90
PORT=CASE,0,0
  SOURCE=CASE,0,MILSPC,MILSPC
  RCEPT=CASE,0,MILSPC,MILSPC
PORT=T2QNT,WIRE,(B1,B1,A,UNBAL,GND,EX),11,0,0,0,0,0
  SOURCE=SIGNAL,0,30,4000,RECTPL(4E3,1.25E-4),.455,AMPS,4E3
PORT=T2LOW,WIRE,(B1,B2,A,UNBAL,GND,EX),280,0,0,0,0,0
  SOURCE=SIGNAL,0,30,4000,RECTPL(4E3,1.25E-4),.1,AMPS,4E3
EQPT=B2,M461A,FIX,B2,NOTCLS,0,0,0
FREQ=30,18E6,1,90
FOTBL=363.35E6
PORT=CASE,0,0
  SOURCE=CASE,0,MILSPC,MILSPC
  RCEPT=CASE,0,MILSPC,MILSPC
PORT=T2QNT,WIRE,(B1,B1,C,UNBAL,GND,EX),11,0,0,0,-53.6,0

RCEPT=RF,0,225E6,400E6,13.6,100E3,CW,0
PORT=T2LOW,WIRE,(B1,B2,0,UNBAL,GND,EX),280,0,0,0,0,0
  RCEPT=SIGNAL,0,30,4000,RECTPL(4E3,1.25E-4),.1,AMPS,4E3
EQPT=B4,M461A,FIX,B4,NOTCLS,0,0,0
FREQ=30,50E6,1,90
PORT=CASE,0,C
  SOURCE=CASE,0,MILSPC,MILSPC
  RCEPT=CASE,0,MILSPC,MILSPC
PORT=FLITE,WIRE,(B5,B13,0,GND,NONE,NOTEX),8,C,C,0,0,0
  RCEPT=POWER,0,115,400,3,1,M461A
EQPT=B5,M461A,FIX,B5,NOTCLS,0,0,0
FREQ=30,50E6,1,90
PORT=CASE,0,0
  SOURCE=CASE,0,MILSPC,MILSPC
  RCEPT=CASE,0,MILSPC,MILSPC
PORT=PNLIT,WIRE,(B9,B28,B,GND,GND,EX),.1,0,0,13,0,0
  SOURCE=POWER,0,5400,3,1,M461A
PORT=FLITE,WIRE,(B5,B13,A,GND,NONE,NOTEX),.1,0,0,0,0,0
  SOURCE=POWER,0,115,400,3,1,M461A

```

Figure 3-4 Mini-System B2 Input Deck

Rectangular Pulse  $P_{BB}(f) = 2A^2\tau^2f_B$  ;  $0 < f \leq f_M$  Watts/Hz

$$P_{BB}(f) = 2A^2\tau^2f_B \left(\frac{f_M}{f}\right)^2 ; f > f_M$$

where

$$\text{bandwidth} = \frac{1}{2\tau}$$

$f_B$  = bit rate

$A$  = peak current/voltage into 1 ohm

$$f_M = \frac{1}{\pi\tau}$$

$\tau$  = pulse width

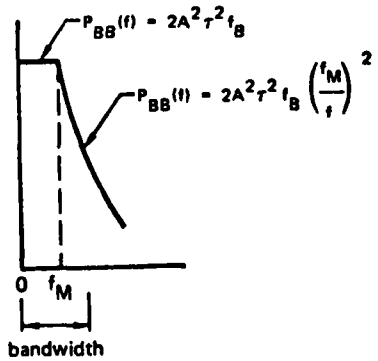


Figure 3-5. Rectangular

When a current  $i(t)$  flows through a one ohm resistor, the power dissipated is

$$P = \langle i^2(t) \rangle$$

$$\text{where } \langle i^2(t) \rangle = \frac{1}{T} \int_{-T/2}^{T/2} i^2(t) dt$$

for a periodic signal.

Hence, the power in a rectangular pulse train is given by

$$P\left(\frac{n}{T}\right) = \frac{2a^2\tau^2}{T^2} \left( \frac{\sin n\pi\tau/T}{n\pi\tau/T} \right)^2, \quad \frac{n}{T} > 0$$

To convert to a continuous spectrum, multiply  $P\left(\frac{n}{T}\right)$  by  $T$  and we have

$$P_{BB}(n) = \frac{2a^2\tau^2}{T} \left( \frac{\sin n\pi\tau/T}{n\pi\tau/T} \right)^2.$$

where  $P_{BB}(n)$  is the envelope of  $P(n\pi/T)$ .

Using the values for the above example:

$$P_{BB}(n) = \frac{2 \times (.1)^2 \times (1.25 \times 10^{-4})^2}{.25 \times 10^{-3}} \left( \frac{\frac{\sin \pi n \times 1.25 \times 10^{-4}}{2.5 \times 10^{-3}}}{\frac{\pi \times 1.25 \times 10^{-4} \times n}{2.5 \times 10^{-3}}} \right)^2$$

$$= 1.25 \times 10^{-6} \left( \frac{\sin 90n}{\frac{\pi}{2} n} \right)^2.$$

A plot of  $P_{BB}(n)$  is shown in Figure (3-6). Figure (3-6) also shows a plot of the IEMCAP model as determined from Figure (3-5) and the required frequency range as defined by Figure (3-3) and Figure (3-4). The required frequency range is a user input option.

To convert to a continuous current spectra, multiply  $i(t)$  by  $T$  to obtain

$$i_e\left(\frac{n}{T}\right) \left( \frac{\text{amps}}{\text{Hz}} \right) = 2a\tau \left( \frac{\sin \pi n\tau}{\pi n\tau} \right)$$

and with the above parameters

$$i_e(n) = 2 \times 1 \times 1.25 \times 10^{-4} \left( \frac{\sin 90n}{\frac{\pi}{2} n} \right)$$

$$= 25 \times 10^{-6} \left( \frac{\sin 90n}{\frac{\pi}{2} n} \right).$$

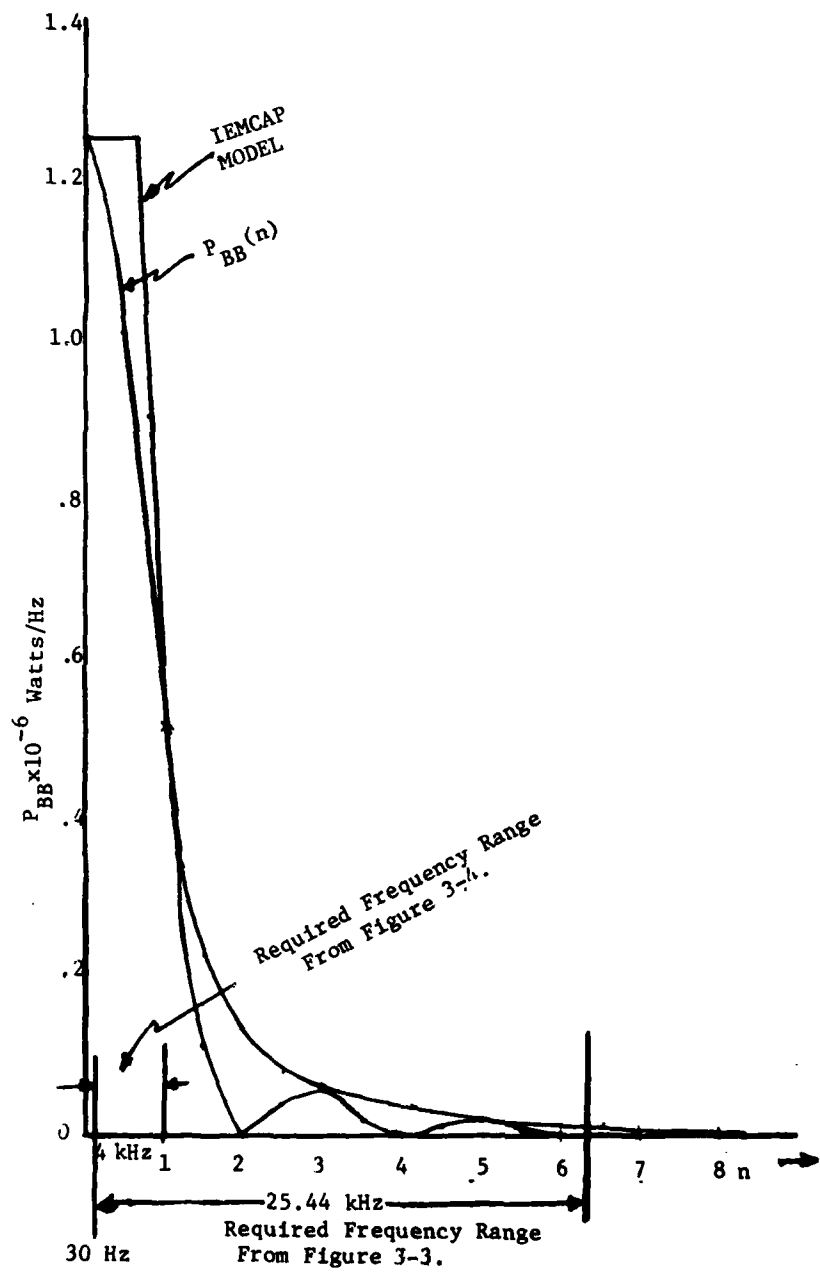


Figure 3-6 Plot of IEMCAP and Model  $P_{BB}$

The representation for  $i_e(n)$  is shown in Figure (3-7). From Figure (3-5), the IEMCAP model may be converted to current spectra by

$$\begin{aligned}
 I_r(f) \left( \frac{\text{amps}}{\text{Hz}} \right) &= \sqrt{\frac{2}{f_B} P_{BB}(f)} \quad 0 \leq f \leq f_m \\
 &= \sqrt{\frac{2 \times 1.25 \times 10^{-6}}{4 \times 10^3}} \\
 &= 25 \times 10^{-6} \frac{\text{amps}}{\text{Hz}} \\
 &= 25 \times 10^{-6} \left( \frac{f}{f_m} \right) \cdot \quad f > f_m
 \end{aligned}$$

$I_r(f)$  is shown in Figure (3-7) for the above example. Figure (3-7) also shows the MIL-STD-461A signal port spectra.

Using Figure 3-7, the effects of computing the peak current margin from equation (3-2) may be determined. Recognizing that  $i_e(n)$  is of the form

$$\frac{\sin x}{x}.$$

The integral (normalized to the peak value)

$$S_i(x) = \int_0^x \frac{\sin x}{x} dx$$

may be found in tabulated form in many different texts. (5)

Thus, the peak is defined by

$$i_{pe} = S_i(x) \quad (3.3)$$

where  $i_{pe}$  = peak current associated with  $i_e(n)$

The integral using the IEMCAP model is given by

$$i_{pe\text{IEMCAP}} = x_M (1 + \ln \frac{x}{x_m}) \quad (3.4)$$

where  $x_M$  = value of  $x$  corresponding to  $f_m$  of the model.

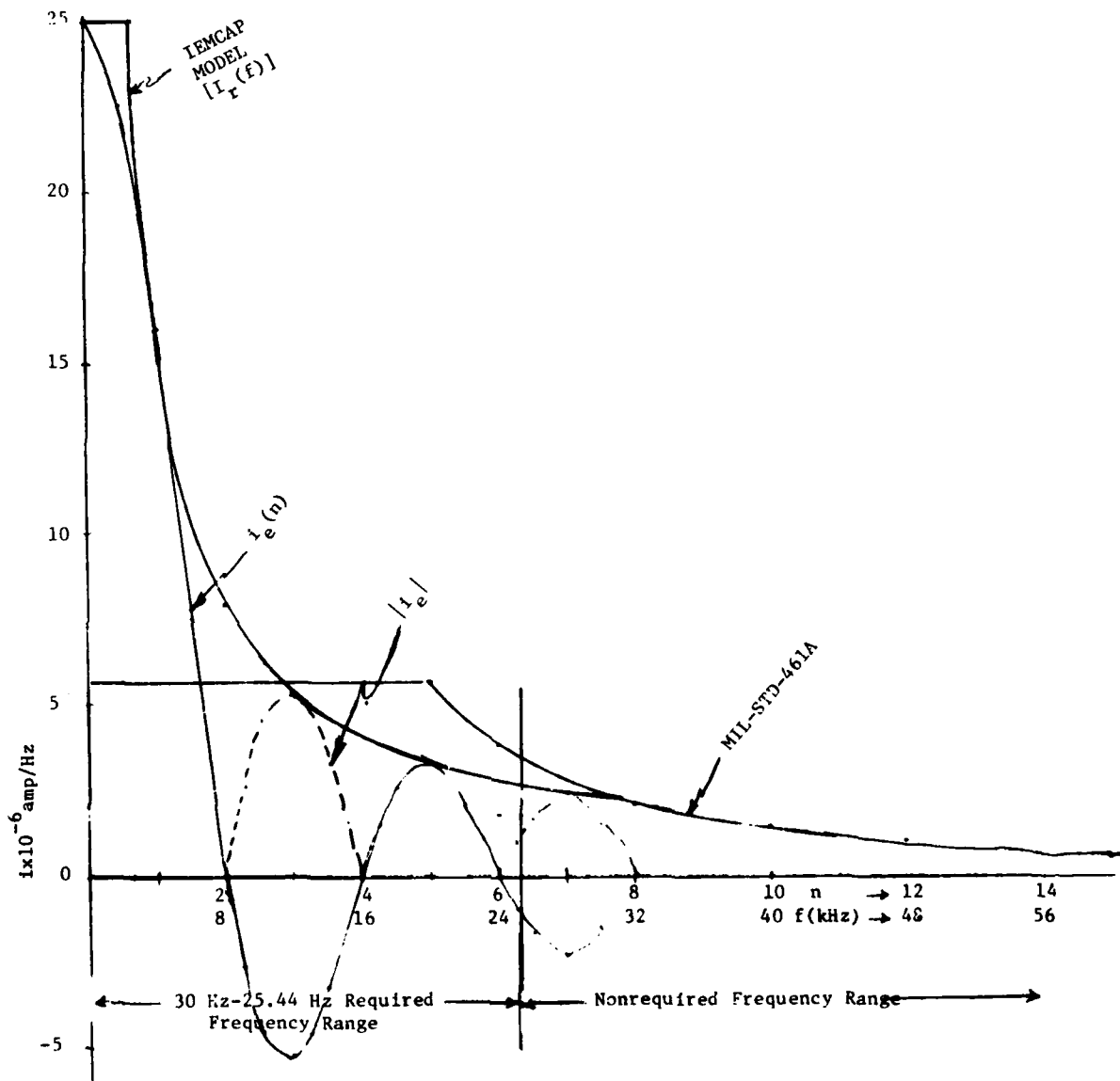


Figure 3-7 Plot of  $i_e(n)$ , IEMCAP Model,  $|i_e|$  and MIL-STD-461A  
Signal Port Spectra

The normalized models are shown in Figure (3-8) and the peak current calculation for equation (3-3) and (3-4) for various required frequency ranges are tabulated in Table 3-2. In Table 3-2, the column showing the ratio of the peak current ( $i_p / i_{p_{IEMCAP}}$ ) represents the factor by which the IEMCAP model over predicts the actual peak current for the above example. Thus, as shown in the table, the actual peak current for a rectangular pulse train may be over predicted by as much as a factor of two using the IEMCAP model.

In terms of the r.m.s. currents, (normalized to one microamp) the narrowband point EMI margin from IEMCAP is

$$m_p^N(f_\ell) = \frac{(\hat{I}/10^{-6})^2 t_{ij}(f_\ell)}{(\hat{I}_s/10^{-6})^2}$$

where  $t_{ij}(f_\ell)$  = power transfer function of coupling path between j-th emitter port and i-th receptor port

$\hat{I}_s$  = the receptor r.m.s. current equivalent to the power susceptibility level

$f_\ell$  =  $\ell$ -th sample frequency.

Converting to peak, we have

$$m_{pp}^N(f_\ell) = \frac{(\sqrt{2}\hat{I}/10^{-6})^2 t_{ij}(f_\ell)}{(I_r^s/10^{-6})^2}$$

where  $I_r^s$  = peak receptor current equivalent to the peak susceptibility level

and converting to dB,

$$m_{pp}^N(f_\ell)(dB) = T_{ij}(f_\ell)(dB) + I(dB\mu A) - I_s(dB\mu A)$$

where  $m_{pp}^N(f_\ell) = 20 \log m_{pp}^N(f_\ell)$

$$T_{ij}(f_\ell) = 10 \log t_{ij}(f_\ell)$$

$$I(dB\mu A) = 20 \log \frac{\sqrt{2}\hat{I}}{10^{-6}}$$

$$I_s(dB\mu A) = 20 \log \frac{I_r^s}{10^{-6}}$$

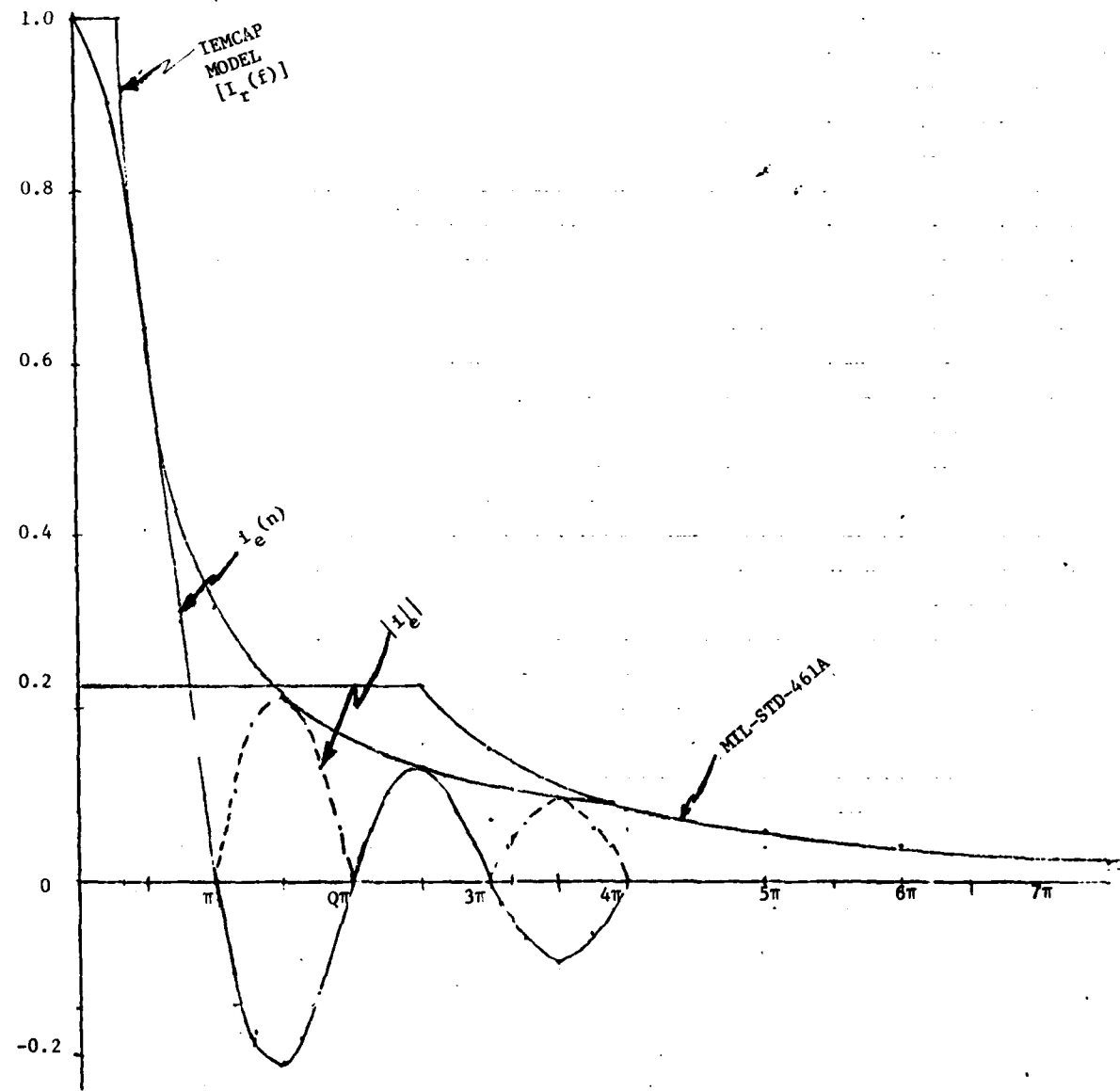


Figure 3-8. Normalized  $i_e(n)$ , IEMCAP,  $|i_e|$  and MIL-STD-461A Signal Port Spectra

Required Frequency Range (kHz)	X	$i_{p_e}$ (amp/Hz)	$i_{p_{IEMCAP}}$ (amp/Hz)	$\frac{i_{p_{IEMCAP}}}{i_{p_e}}$
4	1.57	1.36	1.45	1.07
8	3.14	1.85	2.14	1.17
12	4.71	1.61	2.55	1.58
16	6.28	1.42	2.84	2.00
20	7.85	1.56	3.06	1.96
24	9.42	1.67	3.24	1.94
28	11.0	1.58	3.40	2.15

Table 3-2 Comparison of Peak Current Calculations

The broadband emitter current spectral density is frequency quantized by the computer program. A value of broadband emitter current spectral density is assigned to each frequency. This value is the maximum value assumed by the current spectral density within the corresponding frequency interval associated with the frequency. To evaluate the broadband current point EMI margin at each sample frequency, we require the transfer function of the coupling path between an emitter and a receptor and a bandwidth factor,  $b$ . As defined for IEMCAP, the bandwidth factor,  $b$ , is assigned to each sample frequency. It is defined according to Table 3-3 of the User's Manual (Vol. II. p. 40) and is repeated below.

Table 3-3 Bandwidth Factor

EMITTER	RECEPTOR	BANDWIDTH
Required	Required	$\min(b_{emit}, b_{rec})$
Required	Non-required	$\min(b_{emit}, b_{std})$
Non-required	Required	$b_{rec}$
Non-required	Non-required	$b_{std}$

The standard bandwidth ( $b_{std}$ ) is associated with the EMC test instrument and is defined on page 30 of the IEMCAP User Manual. The broadband peak current spectral level margin is determined by

$$\frac{|i_d(t)|_{max}}{k} \leq \int_{f_a}^{f_a} \frac{|I_r(f)|}{|I_r^s(f)|} df = \frac{|I_r(f)|b}{|I_r^s(f)|}$$

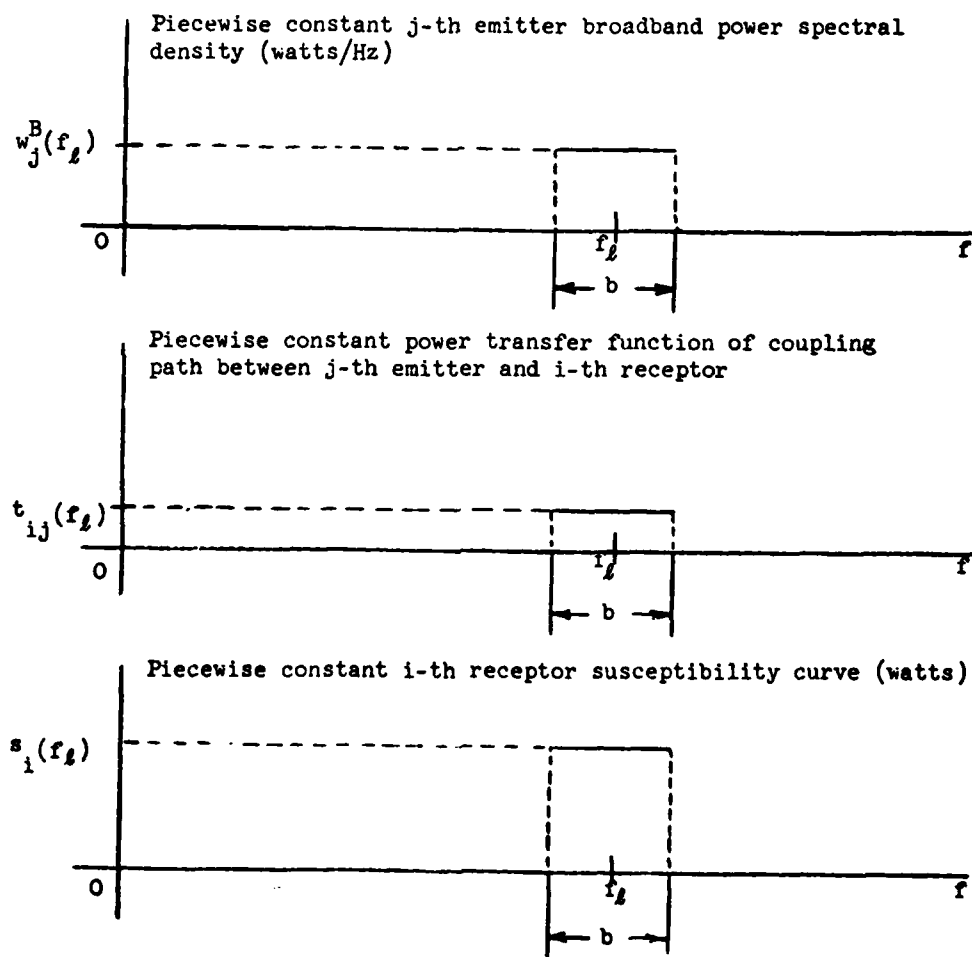
where it is assumed that  $|I_r(f)|$  and  $|I_r^s(f)|$  are constant over  $b$ . The received peak current is

$$|I_r(f)| = |I_t(f)| \sqrt{t_{ij}(f)}$$

where  $|I_t(f)|$  = peak current spectral level at the emitter.

$$\text{Thus } \frac{|I_r(f)|b}{|I_r^s(f)|} = \frac{|I_t(f)| \sqrt{t_{ij}(f)} b}{|I_r^s(f)|}$$

and, the peak current broadband point margin for deterministic signals is defined by



$$m_{PP}^B(f) = \frac{|I_t(f)| \sqrt{t_{ij}(f)} b}{|I_r^s(f)|}$$

From the IEMCAP notation the current spectral level is defined by

$$q = \frac{ip/\sqrt{2}}{(bw)}$$

where  $ip$  = peak current.

At the emitter

$$ip = |I_t(f)|(bw)$$

and

$$q = |I_t(f)|/\sqrt{2}.$$

It follows that

$$|I_t(f)| = \sqrt{2}q.$$

Therefore, the peak current broadband point margin may be expressed as

$$m_{PP}^B(f) = \frac{\sqrt{2}q \sqrt{t_{ij}(f)} b}{|I_r^s(f)|}.$$

Normalizing  $q$  by  $1\mu\text{A}/\text{MHz} = 10^{-12}\text{A}/\text{Hz}$

$$f_B \text{ by } 1 \text{ MHz} = 10^6 \text{ Hz}$$

$$b \text{ by } 1 \text{ MHz} = 10^6 \text{ Hz}$$

$$\hat{I}_s \text{ by } 1\mu\text{A} = 10^{-6} \text{ A},$$

we have

$$m_{PP}^B(f_\ell) = \frac{\left(\frac{\sqrt{2}q}{10^{-12}}\right)^2 \left(\frac{f_B}{10^6}\right) t_{ij}(f_\ell) \left(\frac{b}{10^6}\right)}{\left(\frac{I_r^s}{10^{-6}}\right)^2} \times \frac{10^{-24} \times 10^6 \times 10^6}{(10^{-6})^2}.$$

Converting to decibels, the broadband point EMI margin for a periodic signal becomes

$$M_{PP}^B(f_\ell)(\text{dB}) = Q(\text{dB}\mu\text{A}/\text{MHz} + F_B(\text{dBMHz}) + T_{ij}(f_\ell)(\text{dB}) + B(\text{dBMHz}) - I_s(\text{dB}\mu\text{A}))$$

$$\text{where } M_{PP}^B(f_\ell) = 10 \log m_{PP}^B(f_\ell)$$

$$Q(\text{dB}\mu\text{a}/\text{MHz}) = 20 \log \left( \frac{\sqrt{2}q}{10^{-12}} \right)$$

$$T_{ij}(f_\ell)\text{dB} = 10 \log t_{ij}(f_\ell)$$

$$B(\text{dBMHz}) = 20 \log \left( \frac{b}{10^6} \right)$$

$$I_s(\text{dB}\mu\text{A}) = 20 \log \left( \frac{I_r^s}{10^{-6}} \right)$$

## 3.4

Peak Current - Stochastic Waveform

The peak value of a stochastic waveform cannot be given precisely. Therefore, the peak waveform susceptibility of a receptor must include, along with  $K$ , an estimate of the fraction of time that a stochastic waveform peak at the detector input must exceed  $K$  in order for interference to occur. This estimate is denoted  $\alpha$ .

Let  $i_r(t)$  be a stationary stochastic process which is adequately described by first and second order statistics (means and autocorrelations). Then the same holds for  $i_d(t)$ . For simplicity also assume  $i_r(t)$  has zero mean. Then  $i_d(t)$  also has zero mean. The variance of  $i_d(t)$  is given by

$$\sigma_d^2 = \int_{-\infty}^{\infty} G_r(f) |B_r(f)|^2 df.$$

Now, from Chebyshev's inequality<sup>(1)</sup> the probability of  $i_d(t)$  exceeding  $K$  is bound by

$$p(|i_d(t)| > K) < \frac{\sigma_d^2}{K^2}.$$

Define the susceptibility margin as

$$\frac{p(|i_d(t)| > K)}{\alpha}$$

where  $\alpha$  is the probability ( $|i_d(t)| > K$ ) which should not be exceeded. Then from above

$$\frac{p(|i_d(t)| > K)}{\alpha} > \frac{\sigma_d^2/K^2}{\alpha}.$$

Therefore, an indication that a stochastic waveform is compatible, i.e. does not cause interference, is given by

$$\frac{\sigma_d^2/K^2}{\alpha} < 1.$$

We now consider the computation at the input to the receptor. The variance of  $i_r(t)$  is given by

$$\sigma_r^2 = \int_0^\infty G_r(f) df.$$

Then, using the following approximation for  $\sigma_d^2$ , we have

$$\sigma_d^2 < |B_r(f_p)|^2 \int_0^\infty G_r(f) df$$

where  $f_p$  is the frequency for which  $B_r(f)$  is maximum.

Thus,

$$\sigma_d^2 < |B_r(f_p)|^2 \sigma_r^2.$$

Dividing the inequality by  $K^2$ , we have

$$\frac{\sigma_d^2}{K^2} < \frac{|B_r(f_p)|^2}{K^2} \sigma_r^2$$

where  $K = |B_r(f_p)| |I_r^s(f_p)|$

and  $K^2 = |B_r(f_p)|^2 |I_r^s(f_p)|^2$ .

Substituting  $K^2$  into the above equation, it follows that

$$\frac{\sigma_r^2}{|I_r^s(f_p)|^2}$$

is an upper bound to

$$\frac{\sigma_d^2}{K^2}.$$

Therefore, the requirement for compatibility is the following

$$\frac{\sigma_r^2}{\alpha |I_r^s(f_p)|^2} < 1$$

and a peak current EMI margin for stationary stochastic processes is given by

$$m_{pp}^B(f) = \frac{\sigma_r^2}{\alpha |I_r^s(f_p)|^2}.$$

The current spectral level from IEMCAP for a stochastic waveform transmitted by the  $j$ -th emitter is given by

$$q = \left[ \frac{P_T / (bw)}{(bw)r_{je}} \right]^{1/2}.$$

This expression is only for Gaussian noise.

Following the identical steps outlined above for the peak current deterministic interference margin, the broadband point EMI margin for a stochastic signal can be determined. From IEMCAP, the variance of  $i_r(t)$  is

$$\sigma_r^2 = \int_{f_a}^{f_b} \omega_1(f) t_{ij}(f) df$$

where  $\sigma_r^2$  is the variance due to frequency components in the interval  $(f_a, f_b)$ ;  $\omega_1(f)$  is the power spectral density and  $t_{ij}(f)$  is the power transfer function of the coupling path between the  $j$ -th emitter port and the  $i$ -th receptor port.

It follows that

$$\begin{aligned} \sigma_r^2 &= \omega_1(f) t_{ij}(f) b \\ &= q^2(bw) t_{ij}(f) b \end{aligned}$$

where  $\omega_1(f) = \frac{P_T/(bw)}{r_{je}} = q^2(bw)$ .

Thus,

$$M_{PP}^B(f) = \frac{q^2(bw) t_{ij}(f) b}{\alpha |I_r^s(f_p)|^2}$$

which is the broadband point EMI margin for a stochastic signal. Converting to decibels, the broadband point EMI margin for a stochastic signal becomes.

$$\begin{aligned} M_{PP}^B(f_L)(dB) &= Q(dB\mu A/MHz) + BW(dBMHz) \\ &\quad + T_{ij}(f_L)(dB) + B(dBMHz) - I_s(dB\mu A) - \bar{\alpha}(dB) \end{aligned}$$

where

$$BW(dBMHz) = 10 \log\left(\frac{bw}{10^6}\right)$$

$$\bar{\alpha}(dB) = 10 \log(\alpha)$$

and

$bw$  = field intensity meter (FIM) bandwidth ,

To determine the broadband integrated peak EMI margin, the derivation parallels that of the broadband integrated margin of the IEMCAP. Using Dr. Weiner's notation,<sup>(6)</sup> the derivation of the broadband integrated peak margin is presented below.

The point peak margins are converted to a margin density

$$\frac{B_{pp}(f)}{b}.$$

Next, convert to a log-log scale and plot  $[B_{pp}(f)/b]$  vs.  $\log f$  and connect straight lines between the data points as shown for the energy density calculation above. Thus, the same technique used in IEMCAP to obtain integrated margins is used to obtain the peak current integrated margin.

### 3.5 Peak Current - Normal, Stationary Waveforms (Broadband Gaussian)

A peak current EMI margin applicable to normal, zero-mean, stationary waveforms is defined by

$$\begin{aligned} snim_{pc} &= \frac{p[(i_d(f) > K)]}{\alpha} \\ &= \frac{\sqrt{2}}{\alpha} \int_K^{\infty} \frac{1}{\sigma_d \sqrt{\pi}} e^{-\frac{x^2}{2\sigma_d^2}} dx \end{aligned}$$

where  $snim_{pc}$  = stationary normal interference margin for peak current with all the parameters as defined previously. For compatibility

$$snim_{pc} < 1.$$

From the previous derivation

$$\begin{aligned} \sigma_d^2 &< |B_r(f_p)|^2 \sigma_r^2 \\ \text{and} \quad \sigma_d &< |B_r(f_p)| \sigma_r \end{aligned}$$

where  $f_p$  is the frequency at which  $B_r(f)$  is maximum.

It follows that

$$\begin{aligned} \frac{\sqrt{2}}{\alpha} \int_K^{\infty} \frac{1}{\sigma_d \sqrt{\pi}} e^{-\frac{x^2}{2\sigma_d^2}} dx &< \\ \frac{\sqrt{2}}{\alpha} \int_K^{\infty} \frac{1}{|B_r(f_p)| \sigma_r \sqrt{\pi}} e^{-\frac{2|B_r(f_p)|^2 \sigma_r^2}{x^2}} dx. \end{aligned}$$

The right-hand side of the above inequality is also a suitable susceptibility margin.

Making a change of variable of integration.

Let

$$y = \frac{x}{|B_r(f_p)|}.$$

Then

$$dy = \frac{dx}{|B_r(f_p)|}.$$

Substituting the limits for x, we have

when

$$x = K$$

$$y = \frac{K}{|B_r(f_p)|}$$

and from

$$K = |B_r(f_p)| |I_r^s(f_p)|$$

$$y = |I_r^s(f_p)|.$$

Next when

$$x = \infty$$

$$y = \infty.$$

Substituting the above into the right-hand side of the inequality, we have

$$\sqrt{\frac{2}{\alpha}} \int_{|I_r^s(f_p)|}^{\infty} \frac{1}{|B_r(f_p)| \sigma_r \sqrt{\pi}} e^{-\frac{y^2 |B_r(f_p)|^2}{2|B_r(f_p)|^2 \sigma_r^2}} dy |B_r(f_p)|$$

Thus, after a change of variable of integration this margin becomes

$$\sqrt{\frac{2}{\alpha}} \int_{|I_r^s(f_p)|}^{\infty} \frac{1}{\sigma_r \sqrt{\pi}} e^{-\frac{x^2}{2\sigma_r^2}} dx.$$

Further, let

$$u = \frac{x}{\sqrt{2} \sigma_r}$$

$$du = \frac{dx}{\sqrt{2} \sigma_r}.$$

Substitution of x limits of integration, we have for the lower limit

$$u = \frac{|I_r^s(f_p)|}{\sqrt{2} \sigma_r}$$

and the upper limit

$$u = \infty.$$

Then, the above margin becomes

$$\frac{\sqrt{2}}{\alpha} \int_{\frac{|I_r^s(f_p)|}{\sqrt{2}\sigma_r}}^{\infty} \frac{1}{\sigma_r \sqrt{\pi}} e^{-\frac{u^2}{2\sigma_r^2}} du \sqrt{2\sigma_r}$$

or

$$\frac{2}{\alpha \sqrt{\pi}} \int_{\frac{|I_r^s(f_p)|}{\sqrt{2}\sigma_r}}^{\infty} e^{-u^2} du$$

which becomes

$$\frac{2}{\alpha \sqrt{\pi}} \int_{\frac{|I_r^s(f_p)|}{\sqrt{2}\sigma_r}}^{\infty} \frac{e^{-u^2}}{|I_r^s(f_p)|} du = \frac{\operatorname{erfc}\left(\frac{2|I_r^s(f_p)|}{\sqrt{2}\sigma_r}\right)}{\alpha}$$

where<sup>(7)</sup>

$$\operatorname{erfc}(u) = \frac{2}{\sqrt{\pi}} \int_u^{\infty} e^{-t^2} dt$$

is the complementary error function.

Hence, the peak current EMI margin for a normal zero mean, stationary waveform is given by

$$\operatorname{snim}_{pc} = \frac{\operatorname{erfc}\left(\frac{|I_r^s(f_p)|}{\sqrt{2}\sigma_r}\right)}{\alpha}$$

To determine the argument for the complementary error function, we have

$$\sigma_r^2 = \int_0^{\infty} G_r(f) df.$$

For an equivalent point margin

$$\sigma_r^2 = \int_b^{\infty} G_r(f) df = G_r(f)b$$

where  $b$  is as defined in Section 3.3 and  $G_r(f)$  is constant over the frequency interval.

From IEMCAP we have for a Gaussian stochastic process

$$G_r(f) = (q)^2(bw)t(f).$$

Hence,  $\sigma_r^2 = 2(q)^2(bw)t(f)b.$

Then, the argument of erfc may be determined by taking the square root of the above and multiplying by  $1/\sqrt{2}$  to obtain

$$\left[ \frac{1}{\sqrt{2}} \left( \frac{|I_r^s(f_p)|}{(2q^2(bw)t(f)b)^{1/2}} \right) \right].$$

Given the above a value for the erfc may be computed and the peak current point margin for a normal, zero-mean, stationary waveform ( $snim_{pc}$ ) determined. Converting to dB, we have

$$SNIM_{PC}(dB) = 10 \log snim_{pc}.$$

The integrated EMI margin for a normal, zero-mean, stationary waveform may be determined by the same method as presented in Section 3.1. This method requires that the point margins be converted to a margin density defined by

$$\frac{snim_{pc}(f)}{b}.$$

Then, convert to a log-log scale and plot  $(snim_{pc}(f)/b)$  versus  $\log f$  and connect straight lines between the data points.

## 3.6

Peak Current - Narrowband Gaussian

A peak current EMI margin applicable to narrowband Gaussian waveforms expressed by

$$i_r(t) = x_r(t) \cos(2\pi f_o t) + y_r(t) \sin(2\pi f_o t)$$

where  $x_r(t)$  and  $y_r(t)$  are stationary, normal, independent zero-mean processes with identical autocorrelations can be derived in a manner similar to the derivation for peak current susceptibility margin applicable to normal, zero mean, stationary waveforms described in Section 3.5. The result is (Rayleigh statistics<sup>(1)</sup>)

$$\frac{1}{\alpha} \int_{-\infty}^{\infty} \frac{x}{\sigma_r^2} e^{\frac{-x^2}{2\sigma_r^2}} dx.$$

This integral may be evaluated as follows:

$$\frac{1}{\alpha} \left[ -e^{\frac{-x^2}{2\sigma_r^2}} \right]_{-\infty}^{\infty} |I_r^s(f_o)|.$$

Then, we have

$$- \frac{|I_r^s(f_o)|^2}{2\sigma_r^2}.$$

As previously determined, (Section 3.5) the exponent is determined by noting that the received power is

$$\sigma_r^2 = 2(q)^2 (bw) t(f) b$$

where all variables are as defined previously.

The ratio of the above (signal-to-interference) at the input is

$$\frac{|I_r^s(f_o)|^2}{4(q)^2 (bw) t(f) b}.$$

Given the above, the exponential above may be evaluated and the peak current point margin for a narrowband Gaussian process determined. Converting to dB, we have

$$NBG_{PC}(\text{dB}) = 10 \log nbg_{pc}.$$

The integrated EMI margin for a narrowband Gaussian waveform may be determined by the same method as presented in Section 3.1. This method requires that the point margins be converted to a margin density defined by

$$\frac{nbg_{pc}(f)}{b}.$$

Then, convert to a log-log scale and plot  $(nbg_{pc}(f)/b)$  versus  $\log f$  and connect straight lines between the data points.

### 3.7 Peak Current - Narrowband Gaussian Plus Sinusoid

For the case where a sinusoidal signal is also present in the narrowband Gaussian waveforms, we have

$$i_r(t) = (x_r(t) + s) \cos(2\pi f_o t) + y_r(t) \sin(2\pi f_o t)$$

where a sinusoid of amplitude  $s$  has been added to the waveform of Section 3.6. The corresponding susceptibility margin becomes (Rician statistics<sup>(1)</sup>)

$$\frac{1}{\alpha} \int_{-\infty}^{\infty} \frac{x}{\sigma_r^2} e^{-\frac{(x^2+s^2)}{2\sigma_r^2}} J_0\left(\frac{xs}{\sigma_r^2}\right) dx$$

$$|I_r^s(f_o)|$$

where  $J_0(x)$  is the modified Bessel function of order zero.

Define  $z$  as the signal-to-interference power ratio at the input.

Thus,

$$z = \frac{s^2}{2\sigma_r^2}.$$

Then the integral above becomes

$$\frac{1}{\alpha} \int_{-\infty}^{\infty} \frac{x}{\sigma_r^2} e^{-\frac{x^2-z}{2\sigma_r^2}} J_0\left(\frac{x\sqrt{2z}}{\sigma_r^2}\right) dx.$$

$$|I_r^s(f_o)|$$

In general,  $J_0(y)$  may be shown to be  $\frac{y^2}{4}$

$$J_0(y) = 1 + \frac{y^2}{4} + \dots \approx e^{\frac{y^2}{4}}$$

when  $y \ll 1$

Using this approximation, the above integral becomes

$$\frac{1}{\alpha} \int_{-\infty}^{\infty} \frac{x^2}{\sigma_r^2} e^{\frac{-x^2}{2\sigma_r^2}} J_0\left(\frac{x}{\sigma_r}\sqrt{2z}\right) dx \approx$$

$$|I_r^s(f_o)|$$

$$\frac{1}{\alpha} \int_{-\infty}^{\infty} \frac{x^2}{\sigma_r^2} e^{\frac{-x^2}{2\sigma_r^2}} dx$$

$$|I_r^s(f_o)|$$

for  $z \ll 1$ . This is the Rayleigh density function and the interference margin may be determined as discussed in Section 3.6.

When  $z \gg 1$ , the modified Bessel function of zero order may be shown to be

$$J_0(y) \approx \frac{e^y}{\sqrt{2\pi y}}$$

Under this condition, the integral above becomes<sup>(8)</sup>

$$\frac{1}{\alpha} \int_{-\infty}^{\infty} \frac{x}{\sigma_r^2} e^{\frac{-(x^2+s^2)}{2\sigma_r^2}} J_0\left(\frac{xs}{\sigma_r^2}\right) dx \approx$$

$$|I_r^s(f_o)|$$

$$\frac{1}{\alpha} \int_{-\infty}^{\infty} \frac{1}{\sqrt{2\pi} \sigma_r} e^{\frac{-(x-s)^2}{2\sigma_r^2}} dx$$

$$|I_r^s(f_o)|$$

which is observed to be the Gaussian or normal density function. Thus, the interference margin may be determined as discussed in Section 3.5.

### 3.8 Risetime - Bandwidth

If a receptor's susceptibility is a function of the "rise time" of a waveform, then it will be sensitive to bandwidth. The relationship between rise time and bandwidth of systems is

$$T_r B = k$$

where

$T_r$  = rise time of receptor

$B$  = bandwidth

and  $k$  is a proportionality constant for the receptor. Using this relationship, the susceptibility of a receptor to the rise time of a given waveform may be determined. Thus, a bandwidth susceptibility margin for both deterministic and stochastic waveforms is given by

$$\frac{\beta_r}{\beta_r^s}$$

where  $\beta_r$  is the portion of the receptor input waveform bandwidth within the passband of  $B_r(f)$ , and  $\beta_r^s$  is the receptor input waveform bandwidth which induces the interference threshold bandwidth at the detector.

where  $\beta_r$  is the portion of the receptor input waveform bandwidth within the passband of  $B_r(f)$ , and  $\beta_r^s$  is the receptor input waveform bandwidth which induces the interference threshold bandwidth at the detector.

## 3.9

References

1. Papoulis, A., "The Fourier Integral and its Application," New York, McGraw Hill, 1962.
2. Paul, Dr. Clayton R. and Weiner, Dr. Donald D., "A Summary of Required Input Parameters for Emitter Models in IEMCAP," RADC-TR-78-140, Final Technical Report, June 1978.
3. Intrasystem Electromagnetic Compatibility Analysis Program (IEMCAP) F-15 Validation - Validation and Sensitivity Study; RADC-TR-77-290, Part I (of two), Final Technical Report, September 1977.
4. Intrasystem Electromagnetic Compatibility Analysis Program, Volume I - User's Manual Engineering Section; RADC-TR-74-342, Final Report, December 1974, (A008526).
5. Goldman, S. A., "Frequency Analysis, Modulation and Noise," McGraw Hill, New York, 1948 pps. 76-79.
6. Weiner, Dr. Donald D., "Discrete System Equations," IEMCAP Course Notes, RADC/RBCTI, Griffiss AFB, NY, 1978.
7. Handbook of Mathematical Function with Formulas, Graphs and Mathematical Tables, US Department of Commerce, NBS Applied Mathematics Series 55, p. 297, June 1964.
8. Skin, S. and Jones, J. J., "Modern Communication Principles - With Application to Digital Signaling," McGraw Hill Book Co., 1967, pg. 139.

## 4.0 NONLINEAR INTERFERENCE MODELS

This section will provide detailed mathematical derivations of all the models implemented in NONLIN. Since the basis of these derivations is the modified nonlinear transfer function, it will be discussed in great detail in section 4.1, with particular emphasis on its derivation from the more general Volterra series. After the general form of the nonlinear approach is developed, it will be used to derive the model used in NONLIN to describe desensitization. This model will then be used to examine the limitations and approximations of the nonlinear transfer function approach, as well as the relationship of this approach to the Volterra analysis. The remainder of Section 4 will then be devoted to the derivation of the remaining models implemented in NONLIN, with particular emphasis on the assumptions used to obtain the models in a form suitable for a system level analysis.

### 4.1 The Modified Nonlinear Transfer Function Approach

#### 4.1.1 The Volterra Series

The theory of functionals and functional expansions was first proposed by Vito Volterra in 1930 (Volterra, Reference 6). He established a working definition of a functional by noting that, just as a function operates on a set of variables to produce a new set of variables, a functional operates on a set of functions to produce a new set of functions. Using this definition, Volterra observed that an arbitrary functional could be expanded in what is now called a Volterra Series, in a manner similar to the power series expansion of a function. He showed that every homogeneous functional of degree  $n$ , acting on an arbitrary function,  $x(t)$ , could be written

$$F_n[x(t)] = \int_a^b \cdots \int_a^b k_n(\zeta_1, \zeta_2, \zeta_3 \cdots \zeta_n) x(\zeta_1) \cdots (\zeta_n) d\zeta_1 d\zeta_2 \cdots d\zeta_n \quad (4.1)$$

where  $[a, b]$  is the interval appropriate for the problem being considered.

Observing that 4.1 holds, the Volterra series expansion of any arbitrary functional,  $G[x(t)]$ , may be written:

$$\begin{aligned} G[x(t)] &= \sum_{n=0}^{\infty} F_n[x(t)] \\ &= k_0 + \int_a^b k_1(\zeta) x(\zeta) d\zeta \\ &\quad + \int_a^b \int_a^b k_2(\zeta_1, \zeta_2) x(\zeta_1) x(\zeta_2) d\zeta_1 d\zeta_2 + \dots \end{aligned} \quad (4.2)$$

The first important application of this Volterra series expansion to the analysis of nonlinear circuits was by (Wiener, Reference 7) in 1942, who related the output of a system,  $y(t)$ , to the input,  $x(t)$ , by a Volterra series of the form

$$y(t) = \sum_{n=1}^{\infty} y_n(t) \quad (4.3)$$

where the  $y_n$  are given by

$$y_1(t) = \int_{-\infty}^{\infty} h(\tau) x(t-\tau) d\tau \quad (4.4)$$

$$y_2(t) = \int_{-\infty}^{\infty} \int_{-\infty}^{\infty} h_2(\tau_1, \tau_2) x(t-\tau_1) x(t-\tau_2) d\tau_1 d\tau_2 \quad (4.5)$$

$$\text{and } y_n(t) = \int_{-\infty}^{\infty} \dots \int_{-\infty}^{\infty} h_n(\tau_1 \dots \tau_n) x(t-\tau_1) \dots x(t-\tau_n) d\tau_1 \dots d\tau_n \quad (4.6)$$

The simplification of equation 4.3 will provide the theoretical basis for our discussion of nonlinear interference effects.

In analyzing this equation, Fourier transforms will be performed on various terms in the expansion, resulting in time and frequency domain representations of the input/output relationship.

Begin by noting that  $h_n(\tau_1 \dots \tau_n)$  has been defined (Signatron, Reference 8) as the nonlinear impulse response of order  $n$ , and that the Fourier transform of  $h_n$

$$H_n(f_1 \dots f_n) = \int_{-\infty}^{\infty} \dots \int_{-\infty}^{\infty} h_n(\tau_1 \dots \tau_n) \cdot \exp\{-j2\pi(f_1\tau_1 + \dots + f_n\tau_n)\} d\tau_1 \dots d\tau_n \quad (4.7)$$

is defined as the nonlinear transfer function of order  $n$ . It is apparent that the inverse Fourier transform

$$h_n(\tau_1 \dots \tau_n) = \int_{-\infty}^{\infty} \dots \int_{-\infty}^{\infty} H_n(f_1, \dots, f_n) \exp\{j2\pi(f_1\tau_1 + \dots + f_n\tau_n)\} df_1 \dots df_n \quad (4.8)$$

will allow expression of equation 4.3 in terms of these  $H_n(f)$ . Therefore, if equation 4.8 is substituted into equation 4.3, and the convolutions over  $\tau_k$  are performed,  $y(t)$  is found to be

$$y(t) = \sum_{n=1}^{\infty} \int_{-\infty}^{\infty} \dots \int_{-\infty}^{\infty} H_n(f_1, \dots, f_n) X(f_1) X(f_2) \dots X(f_n) \exp\{j2\pi(f_1 + f_2 + \dots + f_n)t\} df_1 \dots df_n \quad (4.9)$$

The convolutions over  $\tau_k$  with  $e^{j2\pi f_k \tau_k}$  have produced  $X[f_k]$ , which is Fourier transform of the input signal and also the frequency domain input signal spectrum.

By noting that the frequency spectrum of  $y(t)$ ,  $Y(f)$ , is given by the Fourier transform of  $y(t)$ ,

$$Y(f) = \int_{-\infty}^{\infty} \sum_{n=1}^{\infty} \int_{-\infty}^{\infty} \int_{-\infty}^{\infty} H_n(f_1, \dots, f_n) X_1(f_1) \dots X_n(f_n) \exp\{j2\pi(f_1 + \dots + f_n)t\} df_1 \dots df_n \exp\{-j2\pi ft\} dt \quad (4.10)$$

equation 4.3 may also be expressed in terms of the output frequency spectrum

$$Y(f) = \sum_{n=1}^{\infty} \int_{-\infty}^{\infty} \dots \int_{-\infty}^{\infty} H_n(f_1, \dots, f_n) X_1(f_1) \dots X_n(f_n) \int_{-\infty}^{\infty} \exp\{-j2\pi(f - f_1 - f_2 - \dots - f_n)t\} dt df_1 \dots df_n \quad (4.11)$$

Since the unit impulse is defined by the Fourier transform relation

$$\delta(f - f_1 - f_2 - \dots - f_n) = \int_{-\infty}^{\infty} \exp\{-j2\pi(f - f_1 - f_2 - \dots - f_n)t\} dt \quad (4.12)$$

equation 4.11 may also be expressed in terms of the input/output frequency domain spectral relationships.

$$Y(f) = \sum_{n=1}^{\infty} \int_{-\infty}^{\infty} \dots \int_{-\infty}^{\infty} H_n(f_1 \dots f_n) X_1(f_1) \dots X_n(f_n) \delta(f - f_1 - \dots - f_n) df_1 \dots df_n \quad (4.13)$$

Equations 4.3, 4.9 and 4.13 are the relationships which will be used to develop models which describe system degradation due to equipment nonlinearities. They are the time and frequency domain Volterra series which relate system output to various order inputs.

Earlier in this section, functional series expansions were defined in a way which was analogous to the definition of a power series. To illustrate the application of the Volterra series to a specific problem, the exact relationship between the Volterra and power series will now be derived. It will, in fact, be shown that the power series, representing a nonlinear system with no memory, is a special case of the more general Volterra analysis.

A nonlinear system with no memory will have nonlinear impulse responses and transfer functions given by [Signatron, Reference 8]

$$h_n(\tau_1, \tau_2, \dots, \tau_n) = a_n \delta(\tau_1) \delta(\tau_2) \dots \delta(\tau_n) \quad (4.14)$$

$$H_n(f_1, f_2, \dots, f_n) = A_n, \text{ a constant} \quad (4.15)$$

By equation 4.8, note that  $a_n$  must be identically equal to  $A_n$  for all  $n$ . Equation 4.3 may thus be rewritten by substituting equation 4.14 for  $h_n$

$$y(t) = \sum_{n=1}^{\infty} \int_{-\infty}^{\infty} \dots \int_{-\infty}^{\infty} a_n \delta(\tau_1) \delta(\tau_2) \dots \delta(\tau_n) x(t-\tau_1) x(t-\tau_2) \dots x(t-\tau_n) d\tau_1 \dots d\tau_n \quad (4.16)$$

Using the sampling property of the delta function,  $\delta[\cdot]$ , to evaluate 4.16 yields the result

$$\begin{aligned} y(t) &= a_1 x^1(t) + a_2 x^2(t) + \dots \\ &= \sum_{n=1}^{\infty} a_n x^n(t) \end{aligned} \quad (4.17)$$

Similarly, substituting equation 4.15 into equation 4.9 yields

$$y(t) = \sum_{n=1}^{\infty} \int_{-\infty}^{\infty} \dots \int a_n X(f_1) X(f_2) \dots X(f_n) \exp\{j2\pi(f_1 + f_2 + \dots + f_n)t\} df_1 \dots df_n \quad (4.18)$$

which by definition of multidimensional Fourier Transforms reduces to

$$y(t) = \sum_{n=1}^{\infty} a_n x^n(t) \quad (4.19)$$

Equations 4.17 and 4.19 establish that the Volterra series does reduce to the power series for a zero memory system, as claimed, which helps explain why the classical power series yields accurate results in cases with zero memory nonlinearities.

A similar analysis of equations 4.3, 4.9 and 4.13 for sinusoidal inputs will be used in the following sections to develop the models implemented in NONLIN to describe system level nonlinear effects.

#### 4.1.2 The Nonlinear Transfer Function Approach

At this point in the discussion, it becomes useful to introduce several assumptions and a change in notation which will facilitate the mathematical manipulations used to simplify equation 4.3.

The first simplification is that the system in question is only "mildly" nonlinear. "Mildly" nonlinear is, of course, an arbitrarily defined concept, but will be utilized here to describe a nonlinear system which is characterized by only the first few terms of equation 4.3. The number of terms which must be retained is determined by the rate of convergence of equation 4.3. Thus, if only terms of degree  $n \leq N$  are retained, input signals will be limited in amplitude to those which allow convergence of equation 4.3 within the first  $N$  terms.

The second assumption made in this section is that inputs to the system of interest are sinusoidal. This appears to be a severe restriction, placing limitations on the applicability of equation 4.3 to phenomena which are not sinusoidal [e.g., Gaussian noise, etc.].

It has been shown, however, that equation 4.3 is valid for completely arbitrary inputs (Spina reference 4) and the equations derived using sinusoidal inputs have also been validated for arbitrary mild nonlinearities. This restriction is thus a legitimate approximation, which is valid for the types of inputs to be discussed in the sections which follow, and leads to the equations from which the models in NONLIN are derived.

Using these two assumptions, evaluation of equation 4.3 is straightforward, but cumbersome. Therefore, as the equation is simplified, the notational changes mentioned previously will be introduced to simplify bookkeeping and computational chores.

The first step in the derivation of the nonlinear transfer function series is to limit system nonlinearities so that terms of degree  $n > N$  contribute negligibly to the response,  $y(t)$ . Equation 4.3 is thus written

$$y(t) = y_1(t) + y_2(t) + \dots + y_N(t) = \sum_{n=1}^N y_n(t) \quad (4.20)$$

This situation, where the system is represented as  $N$  independent blocks, each having the common input  $x(t)$ , is depicted pictorially in Figure 4-1.

The nonlinear transfer function approach is thus seen to represent the total response of a nonlinear circuit as the sum of  $N$  individual responses. The first order response is characterized by the first order linear transfer function  $H_1(f_1)$ , the second order response is characterized by the second order nonlinear transfer function  $H_2(f_1, f_2)$ , and higher order responses are characterized by similar higher order transfer functions.

#### 4.1.2.1 Sinusoidal Steady-State Response of a Weakly Nonlinear System

This section closely follows the discussion in [Spina, Reference 4] and the reader is referred to Chapter 4 of that reference for a complete mathematical derivation of the results presented here.

To evaluate equation 4.20, the second simplifying assumption will be utilized, and the input to the system will be represented as the sum of  $Q$  sinusoids

$$x(t) = \sum_{q=1}^Q E_q \cos(2\pi f_q t) \quad (4.21)$$

where  $E_q$  is complex. If we let  $E_q^* = E_{-q}$ ,  $E_0 = 0$  and  $f_q = f_{-q}$  and note that

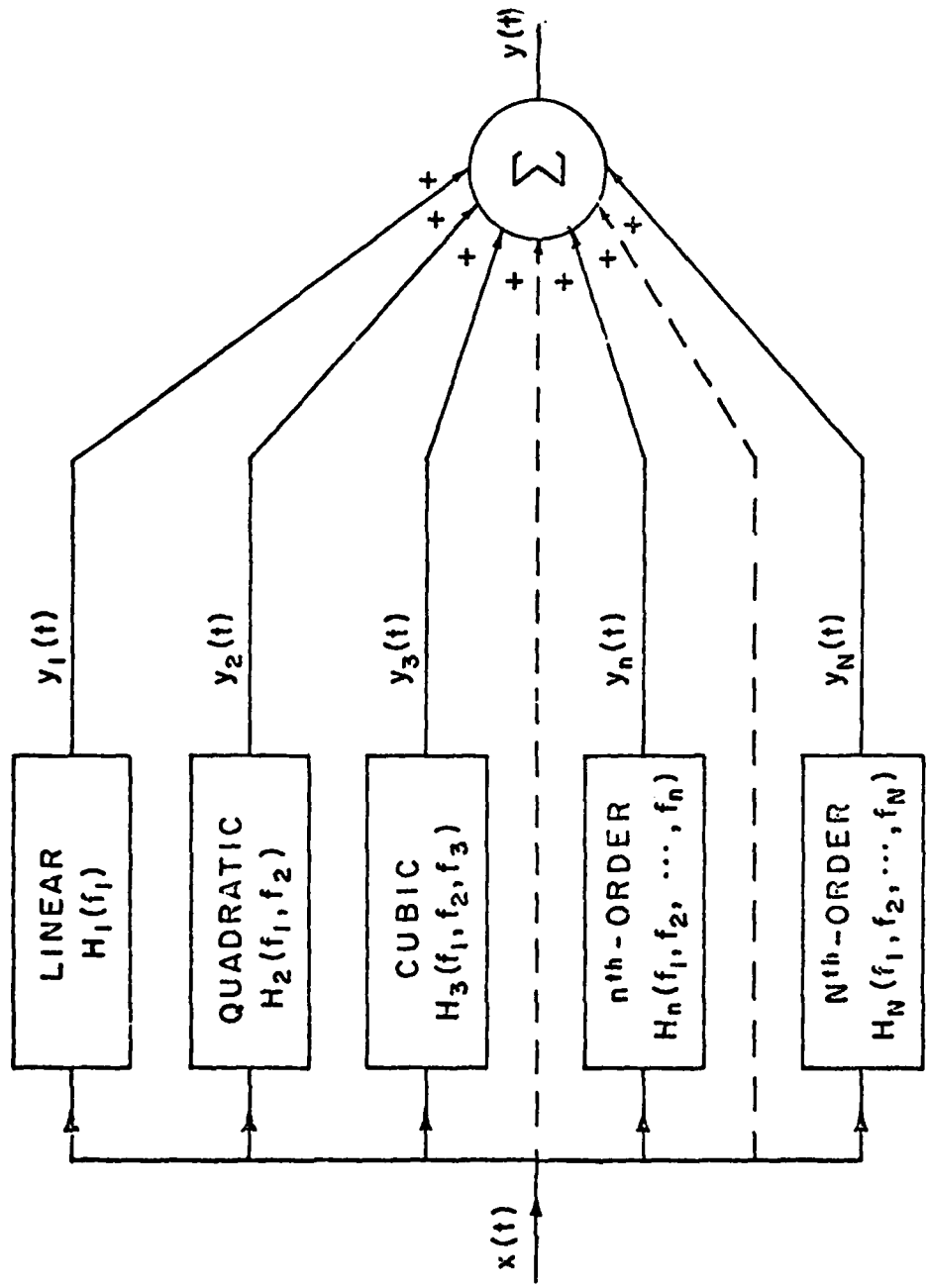


Figure 4-1 Model of weakly nonlinear circuit used by the nonlinear transfer function approach

$$\cos \xi = \frac{e^{j\xi} + e^{-j\xi}}{2} \quad (4.22)$$

then  $x[t]$  may be written in the complex plane as

$$x(t) = \frac{1}{2} \sum_{q=-Q}^Q E_q \exp(j2\pi f_q t) \quad (4.23)$$

Utilizing this form for the system input, and using equation 3.3 to obtain the form of the  $n^{\text{th}}$  order response term yields the result.

$$y_n(t) = \frac{1}{2^n} \sum_{q_1=-Q}^Q \cdots \sum_{q_n=-Q}^Q E_{q_1} \cdots E_{q_n} H_n(f_{q_1} \cdots f_{q_n}) \exp\{j2\pi(f_{q_1} + \cdots + f_{q_n})t\} \quad (4.24)$$

This result is stated without proof, but is a result which shows that the application of a sum of  $Q$  sinusoids to a mildly nonlinear system yields additional output frequencies generated by the  $n^{\text{th}}$  order portion of the circuit. These additional output frequencies consist of all possible combinations of the input frequencies  $f_{-Q}, \dots, f_Q$ , taken  $n$  at a time. At this point, a notational change is made and the vector  $\bar{m}$  is introduced to describe a particular frequency mix

$$\bar{m} = (m_{-Q}, \dots, m_{-1}, m_1, \dots, m_Q) \quad (4.25)$$

This vector will represent all possible frequency mixes, since an individual  $m$ , say  $m_k$ , is defined as the number of times  $f_k$  appears in a particular frequency mix. The response frequency described by the  $\bar{m}$  vector is thus

$$f_{\bar{m}} = \sum_{\substack{k=-Q \\ k \neq 0}}^Q m_k f_k = (m_1 - m_{-1})f_1 + \dots + (m_Q - m_{-Q})f_Q \quad (4.26)$$

For an  $n^{\text{th}}$  order portion of the response, the  $m_k$ 's are constrained such that

$$\sum_{\substack{k=-Q \\ k \neq 0}}^Q m_k = n \quad (4.27)$$

This, therefore, restricts the possible frequency mixes which may appear in equation 4.24, while at the same time quantizing all possible mixes.

Now, given a particular vector  $\bar{m}$ , a well known result from combinatorial analysis states that the number of ways the indices  $q_1 \dots q_n$  can be partitioned such that  $\bar{m}$  describes the output frequency (i.e.,  $f_{-Q}$  appears  $m_{-Q}$  times, etc.) is given by

$$(n; \bar{m}) = \frac{n!}{(m_{-Q}!) \dots (m_{-1}!) (m_1!) \dots (m_Q!)} \quad (4.28)$$

The general term in equation 4.24 is then seen to be

$$y_n(t) = \frac{1}{2^n} (\bar{E}_Q^*)^{m_{-Q}} \dots (\bar{E}_1^*)^{m_{-1}} (\bar{E}_1)^{m_1} \dots (\bar{E}_Q)^{m_Q}$$

$$H_n \underbrace{(f_{-Q}, \dots, f_{-Q})}_{m_{-Q} \text{ times}}, \underbrace{\dots, f_{-1}, \dots, f_{-1}}_{m_{-1} \text{ times}}, \underbrace{\dots, f_Q, \dots, f_Q}_{m_Q \text{ times}}$$

$$\exp \{j2\pi[(m_1 - m_{-1})f_1 + \dots + (m_Q - m_{-Q})f_Q]t\} \quad (4.29)$$

Combining identical terms derived from equation 4.29 yields

$$y_n(t) = \sum_{\bar{m}} y_n(t; \bar{m}) \quad (4.30)$$

which is the equivalent of equation 4.20 given the following assumptions

$$1) \quad \sum_{\bar{m}} = \sum_{m_{-Q}=0}^n \dots \sum_{m_{-1}=0}^n \sum_{m_1=0}^n \dots \sum_{m_Q=0}^n \quad (4.31)$$

2) Equation 4.27 is satisfied

$$3) \quad y_n(t; \bar{m}) = \frac{(n; \bar{m})}{2^n} (\bar{E}_Q^*)^{m_{-Q}} \dots (\bar{E}_1^*)^{m_{-1}} (\bar{E}_1)^{m_1} \dots (\bar{E}_Q)^{m_Q}$$

$$H_n \underbrace{(f_{-Q}, \dots, f_{-Q})}_{m_{-Q} \text{ times}}, \underbrace{\dots, f_Q, \dots, f_Q}_{m_Q \text{ times}} \exp \{j2\pi f_{\bar{m}} t\} \quad (4.33)$$

Equation 4.30, subject to the constraints 1, 2, and 3 above, is the input/output relationship used in the nonlinear transfer function approach. One further simplification will be needed to obtain equation .30 in a form which will be useful for implementation in NONLIN.

#### 4.1.2.2 Two-Tone Sinusoidal Response of a Weakly Nonlinear System

Combinatorial analysis yields the result that, if the excitation of equation 4.30 consists of  $Q$  sinusoids, the summation in 4.30 extends over

$$M = \frac{(2Q+n-1)!}{n!(2Q-1)!} \quad (4.34)$$

distinct  $\bar{m}$  vectors. Therefore for a two-tone input, (i.e.,  $Q=2$ ),

$$M = \frac{(4+n-1)!}{n!(6)} \quad (4.35)$$

Then  $y_1(t)$  contains  $\frac{(4!)!}{6}$  frequency mixes,  $y_2(t)$  contains 10 mixes,  $y_3(t)$  contains 20 mixes, and so on.

Consider, then, a system where terms with  $n>3$  contribute negligibly to the output. There will then be 34 different frequency mixes arising from an input of the form

$$x(t) = \bar{E}_1 \cos 2\pi f_1 t + \bar{E}_2 \cos 2\pi f_2 t \quad (4.36)$$

which may be re-written in the form of equation 3.23;

$$x(t) = \frac{1}{2} \{ \bar{E}_2 * e^{-j2\pi f_2 t} + \bar{E}_1 * e^{-j2\pi f_1 t} + \bar{E}_1 * e^{j2\pi f_1 t} + \bar{E}_2 * e^{j2\pi f_2 t} \} \quad (4.37)$$

Substituting equation 4.37 into equation 4.30 yields Table 4-1, which gives the 34 responses which must be summed to obtain  $y_n(t)$ .

Each of these 34 frequency mixes represents a different nonlinear response; harmonic generation, intermodulation, desensitization, etc., as seen in the table. These 34 responses will be utilized in the next section to illustrate the final modification of equation 4.30, leading to the series which describes system level nonlinear behavior.

Table 4-1  
FIRST AND SECOND-ORDER NONLINEAR RESPONSES

Combination No.	Combination		Frequency of Response	Amplitude of Response	Type of Response
	$m_1$	$m_2$			
$n = 1$					
1	1	0	0	$\frac{1}{2} E_1 H_1(\epsilon_1)$	
2	0	1	0	$\frac{1}{2} E_2 H_1(\epsilon_2)$	
3	0	0	1	$\frac{1}{2} E_1^* H_1(-\epsilon_1)$	
4	0	0	0	$\frac{1}{2} E_2 H_1(-\epsilon_2)$	
$n = 2$					
1	1	1	0	$\frac{1}{2} E_1 E_2 H_2(\epsilon_1, \epsilon_2)$	
2	0	1	1	$\frac{1}{2} E_1 E_2^* H_2(\epsilon_2, -\epsilon_1)$	
3	0	0	1	$\frac{1}{2} E_1^* E_2 H_2(-\epsilon_1, -\epsilon_2)$	Second-Order Intermodulation
4	1	0	0	$\frac{1}{2} E_1 E_2^* H_2(\epsilon_1, -\epsilon_2)$	
5	1	0	1	$\frac{1}{2}  E_1 ^2 H_2(\epsilon_1, -\epsilon_1)$	D.C. Fixed Bias Offset
6	0	1	0	$\frac{1}{2}  E_2 ^2 H_2(\epsilon_2, -\epsilon_2)$	
7	2	0	0	$\frac{1}{4} E_1^2 H_2(\epsilon_1, \epsilon_1)$	
8	0	2	0	$\frac{1}{4} E_2^2 H_2(\epsilon_2, \epsilon_2)$	
9	0	0	2	$\frac{1}{4} E_1^* E_2^2 H_2(-\epsilon_1, -\epsilon_1)$	Second Harmonic
10	0	0	0	$\frac{1}{4} E_2^* E_2^2 H_2(-\epsilon_2, -\epsilon_2)$	

Table 4-1. Continued  
THIRD-ORDER NONLINEAR RESPONSES.

Combination No.	Combination				Frequency of Response	Amplitude of Response	Type of Response
	$m_1$	$m_2$	$m_{-1}$	$m_{-2}$			
1	1	1	1	0	$f_1 + f_2 - f_1 = f_2$	$\frac{3}{4} E_1 2^* H_3 (f_1, f_2, -f_1)$	
2	0	1	1	1	$f_2 - f_1 - f_2 = -f_1$	$\frac{3}{4} E_1 E_2 H_3 (f_2, f_1, -f_2)$	
3	1	0	1	1	$f_1 - f_1 - f_2 = -f_2$	$\frac{3}{4} E_1 2^* E_2 H_3 (f_1, -f_1, -f_2)$	Third-Order Desensitization
4	1	1	0	1	$f_1 + f_2 - f_2 = f_1$	$\frac{3}{4} E_1 E_2 H_3 (f_1, f_2, -f_2)$	
5	2	1	0	0	$2f_1 + f_2$	$\frac{3}{4} E_1 E_2 H_3 (f_1, f_1, f_2)$	
6	0	2	1	0	$2f_2 - f_1$	$\frac{3}{8} E_1 E_2 H_3 (f_2, f_2, -f_1)$	Third-Order Intermodulation
7	0	0	2	1	$-2f_1 - f_2$	$\frac{3}{8} E_1 E_2^* H_3 (-f_1, -f_1, -f_2)$	
8	1	0	0	2	$f_1 - 2f_2$	$\frac{3}{8} E_1 E_2^* H_3 (f_1, -f_2, -f_2)$	
9	2	0	1	0	$2f_1 - f_1 = f_1$	$\frac{3}{8} E_1 E_1 2^* H_3 (f_1, f_1, -f_1)$	
10	0	2	0	1	$2f_2 - f_2 = f_2$	$\frac{3}{8} E_2 E_2 H_3 (f_2, f_2, -f_2)$	Third-Order Compression
11	1	0	2	0	$f_1 - 2f_1 - f_1 = f_1$	$\frac{3}{8} E_1 E_2 H_3 (f_1, -f_1, -f_1)$	
12	0	1	0	2	$f_2 - 2f_2 = -f_2$	$\frac{3}{8} E_2 E_2^* H_3 (f_2, -f_2, -f_2)$	
13	2	0	0	1	$2f_1 - f_2$	$\frac{3}{8} E_1 E_2 H_3 (f_1, f_1, -f_2)$	
14	1	2	0	0	$f_1 + 2f_2$	$\frac{3}{8} E_1 E_2 H_3 (f_1, f_2, f_2)$	Third-Order Intermodulation
15	0	1	2	0	$f_2 - 2f_1$	$\frac{3}{8} E_2 E_2^* H_3 (f_2, -f_1, -f_1)$	
16	0	0	1	2	$-f_1 - 2f_2$	$\frac{3}{8} E_1 E_2 H_3 (-f_1, -f_2, -f_2)$	
17.	3	0	0	0	$3f_1$	$\frac{1}{8} E_1 H_3 (f_1, f_1, f_1)$	
18	0	3	0	0	$3f_2$	$\frac{1}{8} E_2 H_3 (f_2, f_2, f_2)$	Third Harmonic
19	0	0	3	0	$-3f_1$	$\frac{1}{8} E_1^* H_3 (-f_1, -f_1, -f_1)$	
20	0	0	0	3	$-3f_2$	$\frac{1}{8} E_2^* H_3 (-f_2, -f_2, -f_2)$	

## 4.1.3

The Modified Nonlinear Transfer Function Approach

As a prelude to the final simplification to equation 4.30, consider the fact that the nonlinear transfer functions are, in general, complex functions which may be written

$$H_n(f_1, f_2 \dots f_n) = |H_n(f_1, f_2 \dots f_n)| e^{j\phi_n(f_1, f_2 \dots)} \quad (4.38)$$

where  $\phi_n$  is an arbitrary phase in the complex plane.

Consider, also, that the 34 responses in Table 4-1 occur at considerably fewer than 34 frequencies. The total response at each frequency is thus found by adding all individual responses at that frequency in the complex plane. This process can be illustrated for a particular case if the total  $n \leq 3$  response at frequency  $f_1$  is considered. The responses which must be summed to obtain the total response may be obtained from Table 4-1, and are: for  $n=1$  the 1st response and for  $n=3$ , the 4th and 9th responses. Combining these in the complex plane results in Figure 4-2, which is a phasor diagram showing how the responses are added vectorially to obtain the total response at  $f_1$ ,  $y(t, f_1)$ .

The final simplification of equation 4.30 will involve limiting the phase of the nonlinear transfer functions to either 0 or  $\pi$ . This is equivalent to considering the nonlinear transfer functions to be real functions, as opposed to the complex functions of the Volterra analysis. These functions will be called modified nonlinear transfer functions, due to their derivation from the complex Volterra functions, and are the functions used to describe system nonlinearities, where phase information is generally unavailable. The effect of limiting the transfer function in this manner will be examined in detail as models describing each of the individual effects are developed. The first effect to be considered is desensitization, which is examined in the next section.

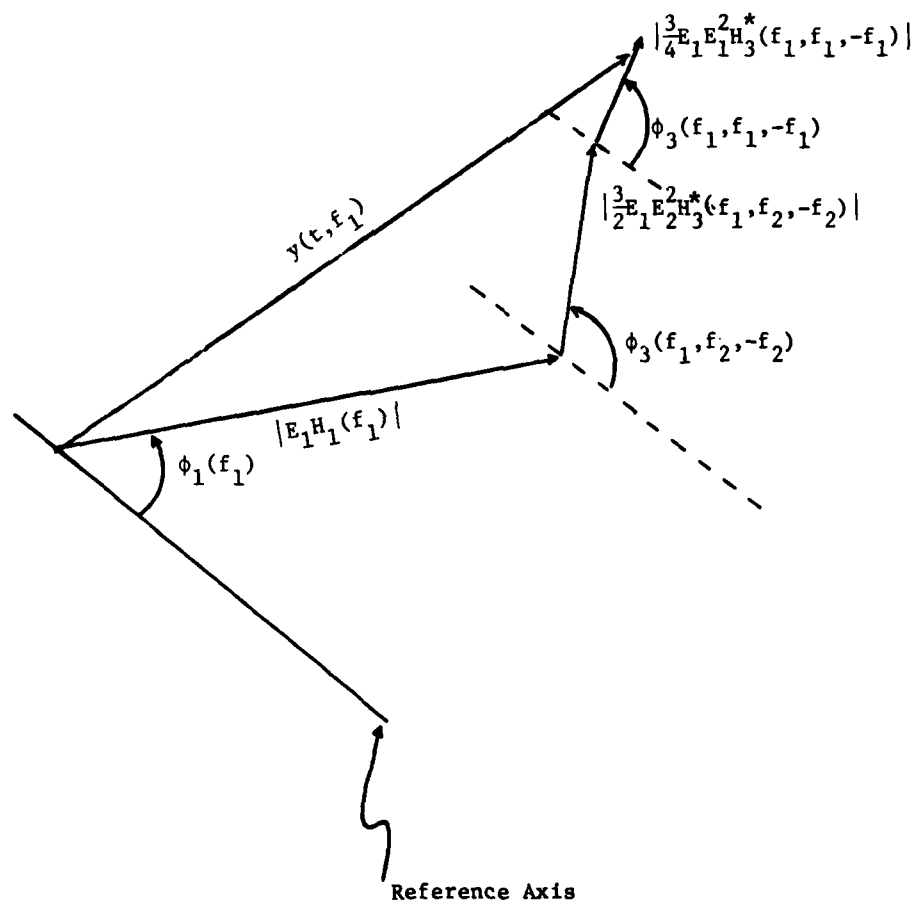


Figure 4-2 Phasor Diagram of Response at Frequency  $f_1$

## 4.2

Desensitization

Desensitization occurs when an interfering signal enters a receiver with sufficient magnitude to cause the receiver amplifiers to operate nonlinearly. This results in the response to the desired signal being "desensitized" due to the nonlinear operation of the amplifier. Desensitization can be a serious problem in a complex electromagnetic environment because its effects are cumulative; i.e., all signals entering the receiver RF passband contribute to desensitization, and the resulting nonlinear operation may cause system degradation even if individual interfering signals cause no problems.

To consider the effects of a third order desensitization, assume that the system of interest is only mildly nonlinear, and that terms of order  $n > 3$  need not be considered. Assume also that inputs to the system are voltages, one of which is the desired signal and modulation:

$$s_i(t) = S[1+s(t)] \cos \omega_s t \quad (4.39)$$

while the other is an interfering unmodulated carrier.

$$I_i(t) = I \cos \omega_i t \quad (4.40)$$

Assuming that noise is negligible, the total input to the system is simply the sum of the two signals  $s_i(t) + I_i(t)$ . This is a two-tone cosinusoidal input of the form seen in Section 4.1.2.2, and therefore the input/output voltage relationship may be derived from Table 4-1. Because of the presence of  $s(t)$ , it is assumed the system behaves quasistatically. Similar assumptions will be made in the discussion of other nonlinear phenomena.

$$v_o(t) = [1+s(t)] \text{SH}_1(f_s) \cos \omega_s t + \frac{3}{2} I^2 \text{SH}_3(f_s, f_i, -f_i) [1+s(t)] \cos \omega_s t \quad (4.41)$$

In equation 4.41, it can be seen that the cosine term involving  $\omega_i$  has been eliminated. This arises from the factor of 1/2 in the second term of equation 4.41. The equation is actually of the form

$$v_o(t) = [1+s(t)] \text{SH}_1(f_s) \cos \omega_s t + 3SI^2 \text{H}_3(f_s, f_i, -f_i) [1+s(t)] \cos \omega_s t \cos^2 \omega_i t \quad (4.42)$$

However, since  $\cos^2 \omega_i t = \frac{1}{2} + \frac{1}{2} \cos 2\omega_i t$ , and since terms involving  $\cos 2\omega_i t$  are eliminated due to receiver selectivity, equation 4.41 correctly describes the input/output relationship.

Now, collecting similar terms in equation 4.41 yields

$$v_o(t) = S[H_1(f_s) + \frac{3}{2}I^2H_3(f_s, f_i, -f_i)] \cdot [1+s(t)] \cos \omega_s t \quad (4.43)$$

This equation represents the transfer functions as complex functions with arbitrary phase. This relationship is depicted graphically in Figure 4-3. To obtain equation 4.43 in a form useful for a system level analysis requires that these arbitrary phase angles be specified. This specification will eliminate phase considerations, and involves two assumptions.

- 1) The linear (desired) portion of the response is entirely positive real. (i.e.,  $\phi_1=0$ )
- 2) The phase angle of  $H_3$  will be limited to values of 0 or  $\pi$ .

If equation 4.43 is to represent desensitization, however, the actual system output will be less than the linear portion of the response. This leads to the requirement that  $\phi_3$  should be approximated by  $\pi$ , which is equivalent to the statement that  $H_3$ , which is actually of the form  $|H_3(f_s, f_i, -f_i)| e^{j\phi_3}$  is an entirely real, negative quantity, due to the fact that  $e^{+j\pi} = -1$ . Equation 4.43 may be rewritten using this requirement

$$v_o(t) = S[H_1(f_s) - \frac{3}{2}I^2H_3(f_s, f_i, -f_i)] [1+s(t)] \cos \omega_s t \quad (4.44)$$

Using equation 4.44, the effects of desensitization may be expressed as:

$$\frac{\Delta S_o}{S_o} = \frac{S_o(\text{volts}) - S'_o(\text{volts})^*}{S_o(\text{volts})} \quad (4.45)$$

where  $S_o(\text{volts})$  = desired signal output without interference

$S'_o(\text{volts})$  = desired signal output with interference

$$\frac{\Delta S_o}{S_o} = \frac{3}{2} \frac{I^2 H_3(f_s, f_i, -f_i)}{H_1(f_s)} \quad (4.46)$$

\* Since  $\frac{\Delta S_o}{S_o} \text{ dB} = 0$  corresponds to total desensitization,  $\frac{\Delta S_o}{S_o} \text{ dB} \leq 0$ .

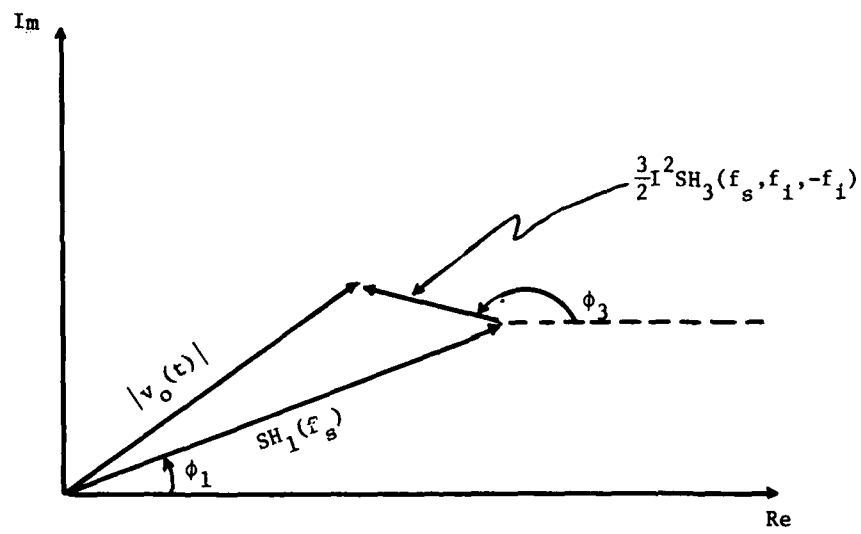


Figure 4-3 Phasor Diagram of 3rd Order Desensitization

$$\frac{\Delta S_o}{S_o} dB = 20 \log I^2 + 20 \log \left| \frac{3}{2} \frac{H_3(f_s, f_i, -f_i)}{H_1 f_s} \right| \quad (4.47a)$$

$$= 2P_I dBW + F(f_s, f_i) dBW \text{ where } F(f_s, f_i) = -20 \log \frac{H_1}{3H_3} \quad (4.47b)$$

$$= 2P_I dBm + F(f_s, f_i) dBm$$

where  $P_I$  dBm = interfering signal power in dBm

$F(f_s, f_i)$  = function that represents device characteristics with

$$F(f_s, f_i) dBm = F(f_s, f_i) dBW - 60 dB.$$

In equations 4.47a and 4.47b, the impedance is assumed to be normalized to 1 ohm. The power,  $P_I$  in equation 4.47b is assumed to be the average interfering signal power. These same assumptions will be utilized as models to describe the remaining nonlinear effects are developed.

Equation 4.47b may be equated to an interference margin by expressing  $\frac{\Delta S_o}{S_o}$  in terms of a reference level. This level will be assumed to be -20 dB [the minimum desensitization] and the interference margin will be the amount by which  $\frac{\Delta S_o}{S_o}$  exceeds -20 dB. Expressen mathematically:

$$\text{Interference Margin} = \frac{\Delta S_o}{S_o} + 20 dB \quad (4.48)$$

In order to use equation 4.48 to calculate the effects of desensitization, it is first necessary to evaluate the function  $F(f_s, f_i)$ .

If the change in signal level  $\Delta S_o / S_o^*$  is known for some reference interfering signal level ( $P_I^*$ ) this may be substituted into equation 4.48 and  $F(f_s, f_i)$  be calculated. Thus,

$$F(f_s, f_i) = -2P_I^*(f_I) dBm + \left[ \frac{\Delta S_o}{S_o} \right]^* dB \quad (4.49)$$

Once  $F(f_s, f_i)$  has been evaluated for these specific conditions, the value may be substituted into equation 4.48 to give an expression for  $F(f_s, f_i)$  for other interfering signal levels.

$$\frac{\Delta S_o}{S_o} dB = 2P_I dBm - 2P_I^*(f_I) dBm + \left[ \frac{\Delta S_o}{S_o} \right]^* dB \quad (4.50)$$

If the CS04 limits of MIL-STD-461 are used for the reference interfering signal level and  $\frac{\Delta S_o}{S_o}$  is assumed to be -20 dB, default models given in Table 4.2 result. A graph of the CS04 limit may be seen in Figure 4.4.

AD-A114 752 ATLANTIC RESEARCH CORP ALEXANDRIA VA  
INTRASYSTEM ANALYSIS PROGRAM (IAP) MODEL IMPROVEMENT. (U)  
FEB 82 T E BALDWIN, W G DUFF, J J FOSTER

F/6 20/3

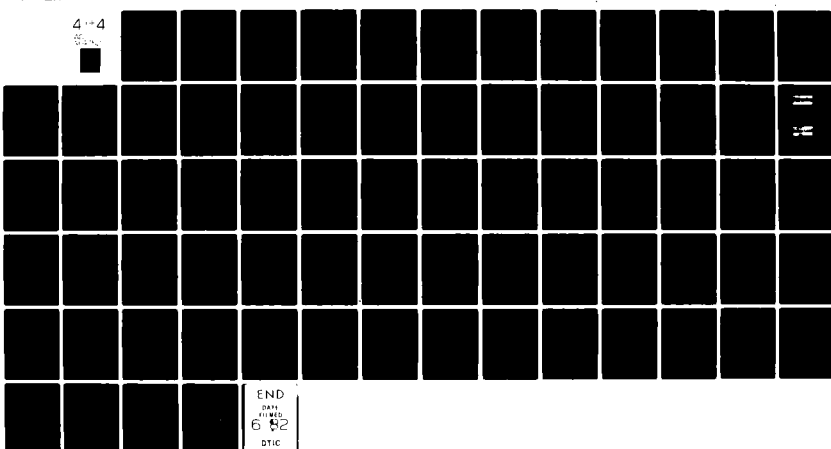
F30602-79-C-0169

UNCLASSIFIED

RADC-TR-82-20

NL

4 x 4  
52



END  
DATE  
6 1982  
DTIC

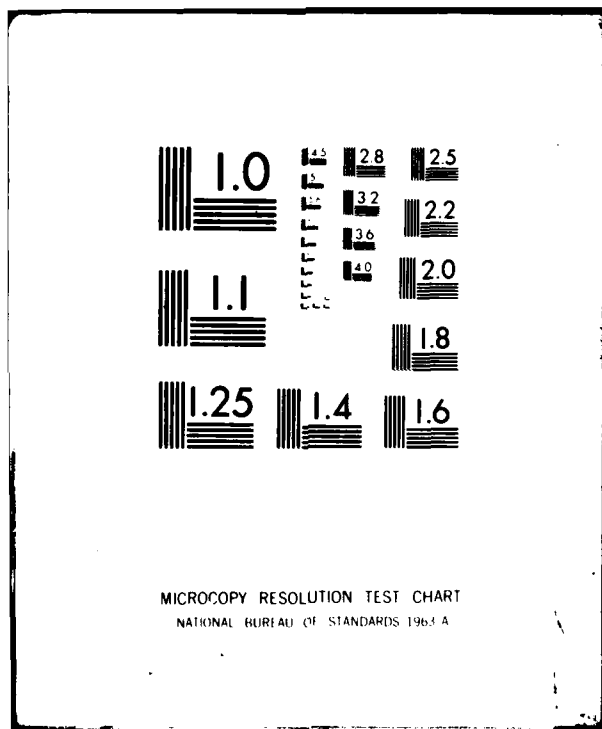


Table 4-2 Default Models for CW Desensitization  
(No AGC)

Amplifiers

For interfering signal frequencies outside of the amplifier pass band; MIL-STD-461 specifies a limit of 0 dBm. Therefore for

$$f_I < f_L \text{ or } f_I > f_H$$

where  $f_L$  = lowest operating frequency of amplifier

$f_H$  = highest operating frequency of amplifier

$$P_I^* \text{ dBm} = 0 \text{ dBm}$$

$$\left[ \frac{\Delta S_o}{S_o} \right]_* \text{ dB} = -20 \text{ dB}$$

$$\therefore \left[ \frac{\Delta S_o}{S_o} \right] \text{ dB} = 2P_I \text{ dBm} - 20 \text{ dB}$$

Receivers

For interfering signals within the receiver 80-dB bandwidth the default models are:

$$f_o - \frac{W}{2} \leq f_I \leq f_o + \frac{W}{2}$$

where  $f_o$  = receiver tuned frequency

$W$  = receiver 80-dB bandwidth

$$P_I^*(f_I) \text{ dBm} = P_R \text{ dBm} + \frac{160}{W} [f - f_o]$$

where  $P_R$  dBm = receiver sensitivity

$$\left[ \frac{\Delta S_o}{S_o} \right]^* \text{ dB} = -20 \text{ dB}$$

$$\therefore \left[ \frac{\Delta S_o}{S_o} \right] \text{ dB} = 2P_I \text{ dBm} - 2P_R \text{ dBm} - \frac{320}{W} [f - f_o] - 20 \text{ dB}$$

For interfering signals outside of the receiver 80-dB bandwidth but within the overall tuning range of the receiver, models are:

$$f_L \leq f_I \leq f_o - \frac{W}{2} \text{ or } f_o + \frac{W}{2} \leq f_I \leq f_H$$

where  $f_L$  = lowest operating frequency of receiver

$f_H$  = highest operating frequency of receiver

$$P_I^*(f_I) \text{ dBm} = P_R \text{ dBm} + 80 \text{ dB}$$

$$\left[ \frac{\Delta S_o}{S_o} \right]^* \text{ dB} = -20 \text{ dB}$$

$$\therefore \left[ \frac{\Delta S_o}{S_o} \right] \text{ dB} = 2P_I \text{ dBm} - 2P_R \text{ dBm} - 180 \text{ dB}$$

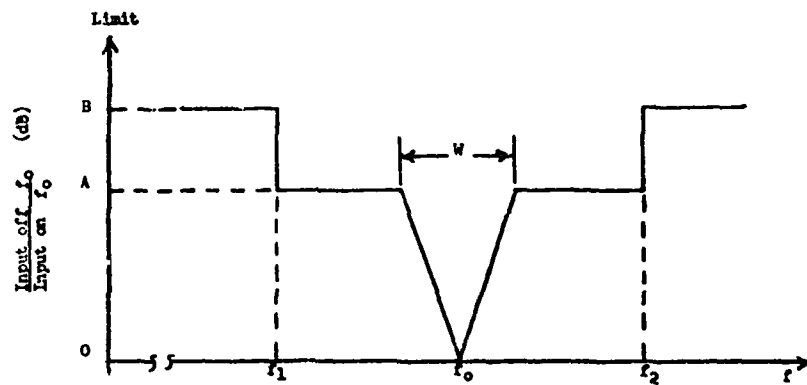
For interfering signals outside of the overall tuning range of the receiver the models are:

$$f_I < f_L \text{ or } f_I > f_H$$

$$P_I^* \text{ dBm} = 0 \text{ dBm}$$

$$\left[ \frac{\Delta S_o}{S_o} \right]^* \text{ dB} = -20 \text{ dB}$$

$$\therefore \left[ \frac{\Delta S_o}{S_o} \right] \text{ dB} = 2P_I \text{ dBm} - 20 \text{ dB}$$



$f_0$  = Receiver tuned frequency or band center for amplifiers.

$f_1$  = Lowest tunable frequency of receiver band in use or the lowest frequency of amplifier passband.

$f_2$  = Highest tunable frequency of receiver band in use or the highest frequency of amplifier passband.

W = Bandwidth between the 80 dB points of the receiver selectivity curve as defined in the test sample's technical requirements or the control plan.

Limits:

1. The limit at A is 80 dB above the input level required to produce the standard reference output. (This limit shall not be used for amplifiers)

2. The limit at B shall be set as follows:

a. Receivers: 0 dBm applied directly to the receiver input terminals.

b. Amplifiers: The limit shall be as specified in the test sample's technical requirement or control plan. If no limit is defined in the above documents, the 0 dBm value shall be used.

Figure 4-4 Limits for CS04

The preceding equations are for signals below the automatic gain control threshold ( $P_{AGC}$ ), and for interfering signal power less than the saturation power level corresponding to the desired signal level and the frequency separation between the input signals. When the desired signal is above  $P_{AGC}$ , the gain is reduced proportional to the increase in the desired signal so that the output remains constant. The gain reduction may be represented by

$$\Delta G \text{ dB} = k(P_D - P_{AGC})$$

$k$  = gain reduction fraction assumed to be 1 if all AGC is applied prior to the nonlinearity

$P_D$  = desired signal level in dBm

$P_{AGC}$  = AGC threshold in dBm

The resulting equation for  $\Delta S_o / S_o$  will be

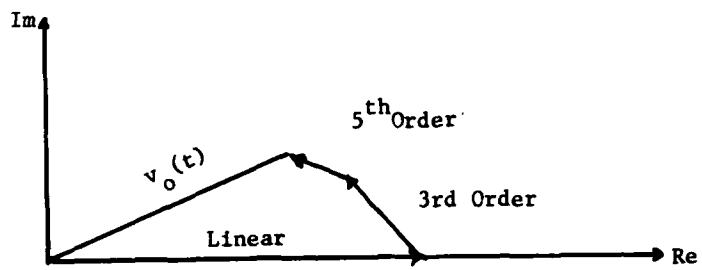
$$\frac{\Delta S_o}{S_o} \text{ dB} = 2P_I \text{ dBm} - 2(P_D - P_{AGC}) + F(f_s, f_i) \text{ dBm} \quad (4.51)$$

Equations 4.50 and 4.51 are valid if only terms of order  $N \leq 3$  must be considered to represent the transfer function of the nonlinear device. However, for any more than slight desensitization, higher order terms must be considered. Higher order terms could be added, but a series to represent the required circuitry is slowly converging and computation of the coefficients is, in general, not practical. The effects of considering only third order desensitization may be examined by considering Figure 4-5, which shows the effect of phase angle on desensitization. This figure shows that higher order terms and phase must be considered to accurately predict large desensitization. In fact it has been shown that the equations given above are valid only for desensitization of approximately 1 dB (Spina Ref. 4).

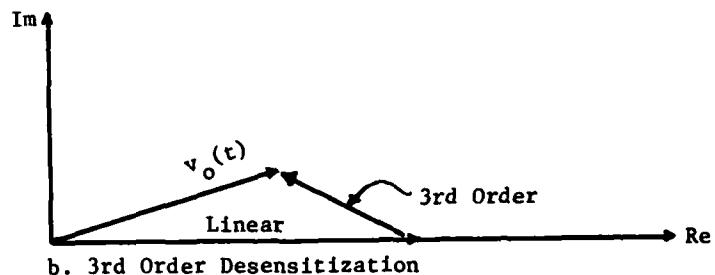
One might also represent the device as an ideal limiter, that is, constant gain for input signals below a saturation threshold, and complete saturation thereafter. By using a Fourier series (which allows more rapid convergence) and numerical integration to obtain the coefficients, the input-output relation can be computed.<sup>5</sup> The resulting desensitization ( $S'_o / S_o$ ) would be:

$$D = \frac{2}{\pi} \text{ arc sin } \left( \frac{I_{SAT}}{I} \right) \quad \text{for } I \geq I_{SAT} \quad (4.52)$$

<sup>5</sup> IIT Research Institute, 3rd Order Intermodulation Study, RADC-TR-67-344, Rome Air Development Center, Griffiss Air Force Base, July 1967.



a. Actual Desensitization (High order, arbitrary phase)



b. 3rd Order Desensitization

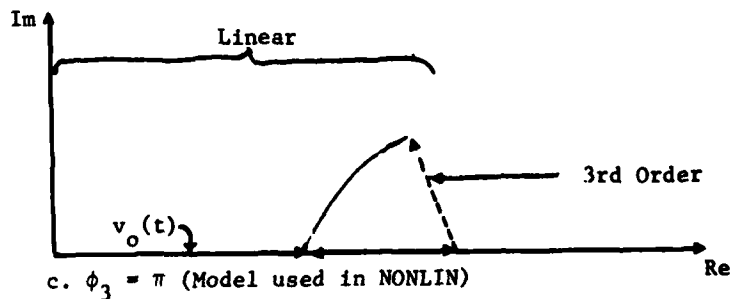


Figure 4-5 Effect of Phase on Desensitization

where

$I_{SAT}$  = saturation threshold in volts

$I$  = interfering signal level in volts

This equation describes the desensitization of desired signal as a function of interfering signal level.

The desensitization may be expressed in dB as:

$$D \text{ dB} = 20 \log \left[ \frac{2}{\pi} \arcsin \left[ \log^{-1} \left( \frac{P_{SAT} - P_I}{20} \right) \right] \right] \quad (4.53)$$

where

$P_{SAT}$  = saturation power in dBm

$P_I$  = interfering signal power in dBm.

This discussion of desensitization is of limited use for IEMCAP, however, due to the lack of accuracy inherent in the approximations involved. The model is merely included for reference, and as an illustration of the difficulty of obtaining accurate results for strongly nonlinear systems.

#### 4.3 Gain Compression and Gain Expansion

The phenomenon of gain compression/expansion is very similar to that of desensitization. It, too, is a third order effect which saturates the receiver amplifier stages and causes nonlinear operation. However, while desensitization is caused by an interfering signal, gain compression/expansion is caused by the desired signal, which may be of sufficient magnitude to cause nonlinear amplifier operation.

The equations describing gain compression/expansion are very similar to those presented in the last section. From Table 4-1, note that compression/expansion is obtained from  $n=1$ , combination 1, and from  $n=3$ , combination 9. It will be assumed that the desired signal is equivalent to equation 4.39, and that the other assumptions are as described in Section 4.2. The input/output equation may then be written

$$v_o(t) = S H_1(f_s) [1+s(t)] \cos \omega_s t \pm \frac{3}{4} S^3 H_3(f_s, -f_s, f_s) [1+s(t)] \cos \omega_s t \quad (4.54)$$

which may be written

$$v_o(t) = S [H_1(f_s) \pm \frac{3}{4} S^2 H_3(f_s, -f_s, f_s)] [1+s(t)] \cos \omega_s t \quad (4.55)$$

In equation 4.55, the (+) and (-) arise from phase considerations similar to those presented in Section 4.2, and refer to gain expansion and compression respectively. This corresponds to considering gain expansion to have a phase of  $\phi_3 = 0$  and gain compression to have a phase of  $\phi_3 = \pi$ . This situation, described by equation 4.55, where the voltage gain is not linear, but varies with desired signal power, may be seen in Figure 4-6.

At this point it becomes advantageous to consider only gain compression, since the discussion of gain expansion will be exactly the same, except for the (+) sign. This will simplify the discussion while the results obtained will be easily adapted to describe expansion effects.

Consider, as in Section 4.2, the ratio

$$\frac{\Delta S_o}{S_o} = \frac{S_o(\text{volts}) - S'_o(\text{volts})}{S_o(\text{volts})} \quad (4.56)$$

$$= \frac{3}{4} S^2 \frac{H_3(f_s, f_s, -f_s)}{H_1(f_s)} \quad (4.57)$$

and

$$\frac{\Delta S_o}{S_o} \text{ dB} = 20 \log S^2 + 20 \log \left| \frac{3}{2} \frac{H_3(f_s, f_s, -f_s)}{H_1(f_s)} \right| \quad (4.58a)$$

$$= 2P_s \text{ dBm} + F(f_s) \text{ dBm} \quad (4.58b)$$

An interference margin may be developed, as was done in Section 4.2. Again utilizing a reference value of -20dB, the interference margin may be written:

$$\text{Interference Margin} = \frac{\Delta S_o}{S_o} + 20 \text{ dB} \quad (4.59)$$

The value of the function,  $F(f_s)$ , may be evaluated by the same means as in Section 4.2. Let  $(P^*)$  be a reference input power which produces a gain compression of  $(\frac{\Delta S_o}{S_o})^*$ . Then equation 4.59 may be evaluated for  $F(f_s)$ , and the result substituted back into equation 4.59. This leads to the expression:

$$\frac{\Delta S_o}{S_o} \text{ dB} = 2P_s \text{ dBm} + \left[ \frac{\Delta S_o}{S_o} \right]^* \text{ dB} - 2P^* \text{ dBm} \quad (4.60)$$

Given empirical data for various input signal powers,  $P_s^*$ , default models for  $F(f_s)$  may be formulated.

It is possible to include the effects of Automatic Gain Control in equation 4.60 by noting that the modification needed to describe AGC in equation 4.60 is very similar to that found in equation 4.51. Performing this modification results in

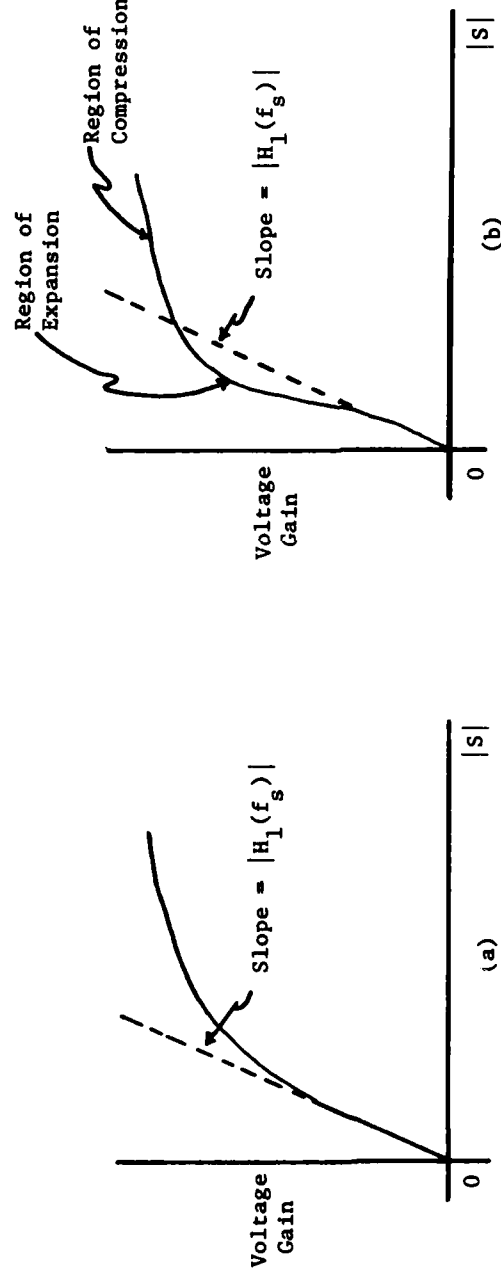


Figure 4-6 Voltage gain curves illustrating (a) gain compression and  
 (b) both gain expansion and gain compression

$$\frac{\Delta S_o}{S_o} \text{ dB} = 2P_s \text{ dBm} - 2(P_D - P_{AGC}) + F(f) \text{ dBm} \quad (4.61)$$

which is the equation used to describe "small signal" gain compression/expansion in a receiver with automatic gain control.

#### 4.4 Intermodulation

In this section, models used to describe nonlinear intermodulation effects will be discussed. Intermodulation is the process occurring when two or more signals mix in a nonlinear device to produce an output at a frequency which causes performance degradation. Effects which will be discussed in this section are second, third and fifth order, two-signal intermodulation products, and three signal, third order intermodulation products. These effects will be considered for three cases:

- 1) Intermodulation products generated in a receiver.
- 2) Intermodulation products generated in a transmitter.
- 3) Intermodulation products generated in a nonlinear metallic junction.

These will be considered separately because there are several simplifications which make the examination of transmitter and receiver intermods much less involved than an examination of products generated in a metallic structure. The discussion of two-signal, third order intermodulation will be quite detailed, while the equations describing higher order effects will be extrapolated from the third order, for although a rigorous mathematical derivation of these effects has been performed, to repeat it here would merely lend complexity to the discussion without offering any additional insight. The models used to describe transmitter intermodulation products will be developed following the Volterra analysis of receiver intermods. Following the development of the effects described above, the models utilized to describe structurally generated intermods will be presented. These equations will be based on empirical data, since structures cannot be considered mildly nonlinear, which prohibits description of their effects by a Volterra analysis.

#### 4.4.1 Two-Signal, Third Order Receiver Intermodulation Products

The assumptions used in the analysis of third order intermodulation are the same as those used in the desensitization and gain compression/expansion analyses with the exception of the representation used for the interfering signal. In this section, it is assumed that there are two interfering signal components,  $I_1(t)$  and  $I_2(t)$ , present at the input of the nonlinear device. The first interfering signal component is assumed to be an unmodulated carrier and the second is amplitude modulated. The total interfering signal is thus represented by

$$I_i(t) = I_1 \cos \omega_1 t + I_2(1+i(t)) \cos \omega_2 t \quad (4.62)$$

For this discussion of third order intermodulation the terms in the nonlinear transfer function expansion which must be considered are of the form:

$$v_o(t) = S_i(t) + 3S_i(t)I_i^2(t) + I_i^3(t) \quad (4.63)$$

The nonlinear transfer functions have not yet been included in equation 4.63, although they are an inherent part of the Volterra analysis. They will be included following several simplifying assumptions. This will serve to simplify the notation considerably, with no loss of generality. The assumptions are:

- 1) As has been discussed previously, the  $S_i(t)I_i^2(t)$  term contributes to desensitization.
- 2) The signal at  $f_1$  is assumed to be nearer the center of the receiver passband than the signal at  $f_2$ .
- 3) Of the possible third order responses:
  - a)  $2f_1 + f_2$
  - b)  $2f_1 - f_2$
  - c)  $2f_2 + f_1$
  - d)  $2f_2 - f_1$

the response, (b), at  $2f_1 - f_2$  is assumed to be the major interfering signal component. It is assumed that the others will be sufficiently attenuated by RF selectivity to be insignificant since they fall farther from the center of the RF passband than does (b).

Given assumption 1, equation 4.63 may be rewritten

$$v_o(t) = S_1(t) + I_1^3(t) \quad (4.64)$$

But  $I_1^3(t)$  may be expanded using the binomial theorem:

$$I_1^3(t) = I_1^3(t) + 3I_1^2(t)I_2(t) + 3I_1(t)I_2^2(t) + I_2^3(t) \quad (4.65)$$

Now, making use of assumptions 2 and 3 leads to the input/output relationship

$$v_o(t) = S_1(t) + 3I_1^2(t)I_2(t) \quad (4.66)$$

Given that the interfering signal is represented by equation 4.62, equation 4.66 may be written

$$v_o(t) = S_1(t) + 3[I_1^2 \cos^2 \omega_1 t I_2[1+i(t)] \cos \omega_2 t] \quad (4.67)$$

Making use of the relationship

$$\cos a \cos b = \frac{1}{2} [\cos(a+b) + \cos(a-b)] \quad (4.68)$$

leads to one term in equation 4.67 at the interfering frequency  $(2f_1 - f_2)$ :

$$v_o(t) = S_1(t) + \frac{3}{4} I_1^2 I_2[1+i(t)] \cos(2\omega_1 - \omega_2)t \quad (4.69)$$

If the appropriate nonlinear transfer functions are now added to the input/output relationship, and if  $S_1(t)$  is again assumed to be a modulated carrier, equation 4.69 becomes:

$$v_o(t) = S_1(f_s)[1+s(t)] \cos \omega_s t + \frac{3}{4} I_1^2 I_2 H_3(f_1, f_1, -f_2)[1+i(t)] \cos(2\omega_1 - \omega_2)t \quad (4.70)$$

The second term in equation 4.70 is the third order intermodulation term.<sup>6</sup> Higher order terms may also be calculated from the relationships in foot note 6, which will lead to the equations presented in future sections which describe these high order intermodulation effects.

<sup>6</sup> A general expression for the contribution of an nth degree term to a particular two signal intermodulation product is given by:

$$\frac{n!}{2^{n-1} (\alpha-n\alpha)!(\beta-n\alpha)! n_\alpha! n_\beta!} I_1^\alpha I_2^\beta \cos[(\alpha-2n_\alpha)\omega_1 t + (\beta-2n_\beta)\omega_2 t]$$

For this case,  $\alpha+\beta = n$ , and  $n_\alpha$  and  $n_\beta$  are zero/positive integers such that  $n_\alpha \leq 1/2 \alpha$  and  $n_\beta \leq 1/2 \beta$ . If consideration is limited to contributions of nth degree terms to nth order effects,  $n_\alpha$  and  $n_\beta$  are zero and the above equation reduces to

$$\frac{n! I_1^\alpha I_2^\beta}{2^{n-1} \alpha! \beta!} \cos(\alpha\omega_1 \pm \beta\omega_2)t.$$

This equation is developed from a combinatorial analysis in Reference 11.

Returning to equation 4.70, it may be seen that the amplitude of the third order intermodulation carrier is given by

$$IMV_o(t) = \frac{3}{4} I_1^2 I_2 H_3(f_1, f_1, -f_2) \quad (4.71)$$

while the intermodulation output power in dBm is given by

$$P_{IM} = 2P_1 \text{ dBm} + P_2 \text{ dBm} + 20 \log \frac{3}{\sqrt{2}} + H_3(f_1, f_1, -f_2) \text{ dB} \quad (4.72)$$

For receivers, it is convenient to express the results in terms of an equivalent input power level (i.e., in terms of the desired signal level  $P_D$ ) that is required to produce the same effects in the receiver as the intermodulation product. The output for the desired signal may be found from equation 4.70, and is just the magnitude of the desired signal carrier.

$$\text{Desired signal output power (dBm)} = P_D \text{ dBm} + H_1(f_s) \text{ dB} \quad (4.73)$$

If this desired output power is assumed equal to the intermodulation output power, equations 4.72 and 4.73 may be equated, resulting in

$$P_L \text{ dBm} = 2P_1 \text{ dBm} + P_2 \text{ dBm} + 20 \log \frac{3}{\sqrt{2}} + H_3(f_1, f_1, -f_2) \text{ dB} - H_1(f_s) \text{ dB} \quad (4.74)$$

$$= 2P_1 + P_2 + IMF(f_s, f_1, f_2) \text{ dBm} \quad (4.75)$$

where

$$IMF(f_s, f_1, f_2) = \text{The intermodulation functional} = -20 \log \frac{\sqrt{2}}{3} \frac{H_1}{H_3} \text{ dBW.}$$

With reference to equation 4.74, the equivalent input signal for intermodulation is a function of the power levels of the two interfering signals, the nonlinearity factor ( $20 \log \frac{3}{\sqrt{2}} = k_3$ ), and the transfer functionals. The problem becomes how to evaluate the intermodulation functional [ $20 \log \frac{3}{\sqrt{2}} + H_3(f_1, f_1, -f_2) - H_1(f_s)$ ] for a particular receiver. As was the case with desensitization, it will be convenient to use specific data to evaluate the functional for a particular set of input conditions.

Intermodulation measurements made in accordance with MIL-STD 461 or MIL-STD-449C are performed in a manner such that the equivalent intermodulation signal is equal to the receiver sensitivity,  $P_R$ , (i.e.,  $P_D = P_R$ ) and the two interfering signals are equal in amplitude. If this is the case, and if  $P_3^*(f_1, f_2)$  is defined as the power required for the signals at  $f_1$  and  $f_2$  to produce a standard response, then

$$IMF(f_s, f_1, f_2) = P_R - 3P_3^*(f_1, f_2) \quad (4.76)$$

Substituting equation 4.76 into equation 4.75 yields the result

$$P_{IM} \text{ dBm} = 2P_1 \text{ dBm} + P_2 \text{ dBm} + P_R \text{ dBm} - 3P_3^*(f_1, f_2) \text{ dBm} \quad (4.77)$$

Equation 4.77 applies to intermodulation situations where the two signals producing the intermodulation do not saturate the receiver front end, and the resulting intermodulation does not exceed the receiver automatic gain control threshold. The next problem is to define what happens to the intermodulation product as the input signals are changed to levels which result in conditions other than those for which the spectrum signature measurements were performed.

As the input power for one or both of the intermodulation signals or the desired signal is increased, the resulting signal exceeds the receiver automatic gain control threshold, the receiver AGC is activated, and the receiver RF gain is reduced. For this situation, equation 4.77 must be modified to account for the gain change ( $\Delta G$ ) resulting from the AGC as shown below.

$$P_{IM} \text{ dBm} = 2P_1 \text{ dBm} + P_2 \text{ dBm} + P_R \text{ dBm} - 3P_3^*(f_1, f_2) \text{ dBm} + \Delta \text{GdB} \quad (4.78)$$

In addition, as either of the interfering signals is increased, a saturation level,  $P_{SAT}(f)$  is reached such that additional increases in the interfering signal do not result in increases in the equivalent intermodulation input power. For this condition, the equivalent intermodulation input power may be represented as shown below:

a) for  $P_1(f_1) > P_{SAT}(f_1)$ ;

$$P_{IM} \text{ dBm} = 2P_{SAT}(f_1) \text{ dBm} + P_2 \text{ dBm} + P_R \text{ dBm} - 3P_3^*(f_1, f_2) \text{ dBm} \quad (4.79)$$

b) for  $P_2(f_2) > P_{SAT}(f_2)$ ;

$$P_{IM} \text{ dBm} = 2P_1 \text{ dBm} + P_{SAT}(f_2) \text{ dBm} + P_R \text{ dBm} - 3P_3^*(f_1, f_2) \text{ dBm} \quad (4.80)$$

Table 4-3 summarizes the third order intermodulation equations for the various conditions of interest.

Default models based on MIL-STD-461 may also be developed, due to the assumptions used to arrive at equation 4.77. The (CS03) limit of MIL-STD-461 specifies that no intermodulation responses shall be observed when either interfering signal is 66 dB above the level necessary to produce the standard response,  $P_R$ . This leads to the requirement:

$$P_3^*(f_1, f_2) = P_R \text{ dBm} + 66 \text{ dB} \quad (4.81)$$

Table 4-3 Third Order Intermodulation Equations

<u>Case</u>	<u>Condition</u>	<u>Equation</u>
I	$P_1, P_2 < P_{SAT}$	$P_{IM} = 2P_1 + P_2 +$
	$P_{IM} < P_{AGC}$	$IMF(f_1, f_2)$
II	$P_1, P_2 < P_{SAT}$	$P_{IM} = 2P_1 + P_2 +$
	$P_{IM} > P_{AGC}$	$IMF(f_1, f_2) + \Delta G$
III	$P_1 > P_{SAT}$	$P_{IM} = 2P_{SAT} + P_2 +$
	$P_2 < P_{SAT}$	$IMF(f_1, f_2)$
IV	$P_1 < P_{SAT}$	$P_{IM} = 2P_1 + P_{SAT} +$
	$P_2 > P_{SAT}$	$IMF(f_1, f_2)$

where  $IMF(f_1, f_2) = P_R - 3P_3(f_1, f_2)$

Substituting equation 4.81 into equation 4.77 leads to the third order MIL-STD-461 default model:

$$P_{IM} \text{dBm} = 2P_1 \text{dBm} + P_2 \text{dBm} - 2P_R \text{dBm} - 198 \text{ dB} \quad (4.82)$$

Equation 4.82 may be related to the IEMCAP Interference margins by noting that

$$\text{Interference margin} = P_{IM} \text{dBm} - P_R \text{dBm} \quad (4.83)$$

This will lead to the requirement that

$$\text{Interference margin} = 2P_1 \text{dBm} + P_2 \text{dBm} - 3P_R \text{dBm} - 198 \text{ dB} \quad (4.84)$$

which is the default model utilized within NONLIN.

#### 4.4.2 Second and Fifth Order, Two Signal Receiver

##### Intermodulation Products

As a continuation of the analysis presented in the previous section, consider a second order intermodulation product occurring at frequency  $f_1 + f_2$ . Extrapolating from equation 4.64 yields the input/output relationship:

$$v_o(t) = S_i(t) + I_1^2(t) \quad (4.85)$$

Given the assumptions of the previous section regarding signal representations leads to equation 4.85 being rewritten as:

$$\begin{aligned} v_o(t) = & S_i(t) + [1+i(t)] I_1 I_2 [H_2(f_1, f_2) \cos(\omega_1 + \omega_2)t \\ & + H_2(f_1, -f_2) \cos(\omega_1 - \omega_2)t] \end{aligned} \quad (4.86)$$

Of course, only one of the frequencies,  $f_1 + f_2$  or  $f_1 - f_2$  will fall into the receiver passband, so equation 4.86 will reduce to either of two equations, corresponding to the (+) and (-) below:

$$\begin{aligned} v_o(t) = & S H_1(f_s) [1+s(t)] \cos \omega_s t \\ & + I_1 I_2 H_2(f_1, \pm f_2) [1+i(t)] \cos(\omega_1 \pm \omega_2)t \end{aligned} \quad (4.87)$$

From equation 4.87, a representation for the intermodulation output power similar to equation 4.72 may be given:

$$P_{IM} \text{dBm} = P_1 \text{dBm} + P_2 \text{dBm} + H_2(f_1, \pm f_2) \text{dB} \quad (4.88)$$

If equation 4.88 is presented in terms of an equivalent input power, a relationship analogous to equation 4.74 may also be found:

$$P_{IM} \text{ dBm} = P_1 \text{ dBm} + P_2 \text{ dBm} + H_2(f_1, +f_2) \text{ dB} - H_1(f_s) \text{ dB} + 20 \log 2 \quad (4.89)$$

$$= P_1 \text{ dBm} + P_2 \text{ dBm} + IMF(f_1, f_2) \text{ dBm} \quad (4.90)$$

To evaluate the IMF, again assume that the interfering signal powers are equal to each other and to  $P_2^*(f_1, f_2)$ , the power required to create a standard response. If this is the case, and if  $P_R$ , the receiver sensitivity, is the standard response, the IMF is given by

$$IMF(f_1, f_2) = P_R - 2P_2^*(f_1, f_2) \quad (4.91)$$

and equation 4.90 becomes

$$P_{IM} \text{ dBm} = P_1 \text{ dBm} + P_2 \text{ dBm} + P_R \text{ dBm} - 2P_2^*(f_1, f_2) \text{ dBm} \quad (4.92)$$

In a manner analogous to that presented in Section 4.4.1, equation 4.91 may be modified to account for the effects of automatic gain control and receiver saturation. If these modifications are performed, the equations in Table 4-4 result.

If the (CS03) limit of MIL-STD-461 is again applied, the second order intermodulation default model results:

$$P_{IM} \text{ dBm} = P_1 + P_2 - P_R \text{ dBm} - 132 \text{ dB} \quad (4.93)$$

The interference margin as determined by the criterion described in Section 3.4.1 is

$$\text{Interference margin} = P_1 \text{ dBm} + P_2 \text{ dBm} - 2P_R \text{ dBm} - 132 \text{ dB.} \quad (4.94)$$

To examine the effects of fifth order intermodulation, it will be useful to refer to footnote 6 to obtain the 5th order contribution to the fifth order effect. This fifth order effect is assumed to be the only significant response. The fifth order term is:

$$\frac{5}{8} H_5(f_1, f_1, f_1, -f_2, -f_2) I_1^3 I_2^2 [1+i(t)]^2 \cos(3\omega_1 - 2\omega_2)t \quad (4.95)$$

From this, it is a simple matter to obtain the intermodulation carrier amplitude and the intermodulation output power. These are:

$$IM v_o(t) = \frac{5}{8} H_5(f_1, f_1, f_1, -f_2, -f_2) I_1^3 I_2^2 \quad (4.96)$$

Table 4-4 Second Order Intermodulation Equations

<u>Case</u>	<u>Condition</u>	<u>Equation</u>
I	$P_1, P_2 < P_{SAT}$	$P_{IM} = P_1 + P_2 + IMF(f_1, f_2)$
	$P_{IM} < P_{AGC}$	
II	$P_1, P_2 < P_{SAT}$	$P_{IM} = P_1 + P_2 +$
	$P_{IM} > P_{AGC}$	$IMF(f_1, f_2) + \Delta G$
III	$P_1 > P_{SAT}$	$P_{IM} = P_{SAT} + P_2 + IMF(f_1, f_2)$
	$P_2 < P_{SAT}$	
IV	$P_1 < P_{SAT}$	$P_{IM} = P_1 + P_{SAT} + IMF(f_1, f_2)$
	$P_2 > P_{SAT}$	

where  $IMF(f_1, f_2) \approx P_R - 2P_2 * (f_1, f_2)$

and

$$P_D^{\text{dBm}} = 3P_1^{\text{dBm}} + 2P_2^{\text{dBm}} + 20 \log \left(\frac{5}{8}\right) + 20 \log 4 \sqrt{2} + H_5(f_1, f_1, f_1, -f_2, -f_2) \text{ dB} \quad (4.97)$$

Using the assumption regarding standard responses presented previously yields

$$P_{IM}^{\text{dBm}} = 3P_1^{\text{dBm}} + 2P_2^{\text{dBm}} + 20 \log \left(\frac{5}{8}\right) + 20 \log 4 \sqrt{2} + H_5(f_1, f_1, f_1, -f_2, -f_2) \text{ dB} - H_1(f_s) \text{ dB} \quad (4.98)$$

while evaluation of the IMF leads to

$$IMF(f) = P_R^{\text{dBm}} - 5P_5^*(f_1, f_2). \quad (4.99)$$

Substituting equation 4.98 into 4.98 the equivalent intermodulation power may be obtained

$$P_{IM}^{\text{dBm}} = 3P_1^{\text{dBm}} + 2P_2^{\text{dBm}} + P_R^{\text{dBm}} - 5P_5^*(f_1, f_2) \quad (4.100)$$

Equation 4.100 may be modified to account for the effects of AGC and saturation.

The modifications are very similar to those performed to obtain Tables 4-3 and 4-4, and these changes lead to the results presented in Table 4-5.

The default model based on MIL-STD-461 is again derived from the relationship in equation 4.81, and is found to be

$$P_{IM}^{\text{dBm}} = 3P_1^{\text{dBm}} + 2P_2^{\text{dBm}} - 4P_R^{\text{dBm}} - 330 \text{ dB} \quad (4.101)$$

From equation 4.101, and the assumptions stated previously, the interference margin is found to be:

$$\text{Interference margin} = 3P_1^{\text{dBm}} + 2P_2^{\text{dBm}} - 5P_R^{\text{dBm}} - 330 \text{ dB}$$

Table 4-5 Fifth Order Intermodulation Equations

<u>Case</u>	<u>Condition</u>	<u>Equation</u>
I	$P_1, P_2 < P_{SAT}$	$P_{IM} = 3P_1 + 2P_2$
	$P_{IM} < P_{AGC}$	$+ IMF(f_1, f_2)$
II	$P_1, P_2 < P_{SAT}$	$P_{IM} = 3P_1 + 2P_2$
	$P_{IM} > P_{AGC}$	$+ IMF(f_1, f_2) + \Delta G$
III	$P_1 > P_{SAT}$	$P_{IM} = 3P_{SAT} + 2P_2$
	$P_2 < P_{SAT}$	$+ IMF(f_1, f_2)$
IV	$P_1 < P_{SAT}$	$P_{IM} = 3P_1 + 2P_{SAT}$
	$P_2 > P_{SAT}$	$+ IMF(f_1, f_2)$

where  $IMF(f_1, f_2) = P_R - 5P_5(f_1, f_2)$

## 4.4.3

Three Signal, Third Order Receiver Intermodulation Products

Equations similar to those in previous sections may be developed for third order, three signal intermods, where the output will be at frequencies of the form:

$$f_{IM} = f_1 + f_2 + f_3 \quad (4.102)$$

Due to RF selectivity, however, all three input signals must be approximately equal, or they will be attenuated and cause no degradation. Because of this, and because  $f_{IM}$  must also fall in the RF passband, equation 4.102 will be constrained to frequency mixes such that two of the three frequencies will be positive. For the purpose of the following mathematical discussion, the intermodulation frequency will be represented by:

$$f_{IM} = f_1 + f_2 - f_3 \quad (4.103)$$

Based on an analysis similar to that presented in Section 4.4.1, the input/output relationship may then be expressed by:

$$v_o(t) = \frac{3}{2} I_1 I_2 I_3 H_3(f_1, +f_2, -f_3) \cos(\omega_1 + \omega_2 - \omega_3)t \quad (4.104)$$

From this, it is possible to find the intermodulation output power

$$P_{IM} \text{dBm} = P_1 \text{dBm} + P_2 \text{dBm} + P_3 \text{dBm} + 20 \log(12 + H_3(f_1, +f_2, -f_3)) \text{dB} \quad (4.105)$$

Equating the intermodulation output power and the equivalent desired power leads to a result similar to equation 4.74.

$$P_{IM} \text{dBm} = P_1 \text{dBm} + P_2 \text{dBm} + P_3 \text{dBm} + 20 \log(12 + H_3(f_1, +f_2, -f_3)) \text{dB} - H_1(f_s) \quad (4.106)$$

$$= P_1 \text{dBm} + P_2 \text{dBm} + P_3 \text{dBm} + IMF(f_1, f_2, f_3) \quad (4.107)$$

It will again be useful to evaluate the IMF in terms of specific data, as was done in Sections 4.4.1 and 4.4.2. Given the assumptions of those two sections, the IMF may be written

$$IMF(f_1, f_2, f_3) = P_R - 3P_3(f_1, +f_2, -f_3) \quad (4.108)$$

which transforms equation 3.107 to

$$P_{IM} \text{dBm} = P_1 \text{dBm} + P_2 \text{dBm} + P_3 \text{dBm} + P_R \text{dBm} - 3P_3(f_1, +f_2, -f_3) \text{dBm} \quad (4.109)$$

The results of incorporating AGC and saturation effects into equation 4.109 leads to the equations in Table 4-6.

Table 4-6 Third Order, Three Signal Intermodulation Equations

<u>Case</u>	<u>Condition</u>	<u>Equation</u>
I	$P_1, P_2, P_3 < P_{SAT}$	$P_{IM} = P_1 + P_2 + P_3$
	$P_{IM} < P_{AGC}$	$+ IMF(f_1, f_2, f_3)$
II	$P_1, P_2, P_3 < P_{SAT}$	$P_{IM} = P_1 + P_2 + P_3$
	$P_{IM} > P_{AGC}$	$+ IMF(f_1, f_2, f_3) + \Delta G$
III	$P_1 > P_{SAT}$	$P_{IM} = P_{SAT} + P_2 + P_3$
	$P_2, P_3 < P_{SAT}$	$+ IMF(f_1, f_2, f_3)$
IV	$P_1, P_2 > P_{SAT}$	$P_{IM} = 2P_{SAT} + P_3$
	$P_3 < P_{SAT}$	$+ IMF(f_1, f_2, f_3)$

where  $IMF(f_1, f_2, f_3) = P_R - 3P_3(f_1, +f_2, -f_3)$

There are no MIL-STD-461 limits for three signal intermodulation products. For the purpose of developing default models, however, it will be assumed that the three interfering signal powers are each equal to  $P_3^*(f_1, +f_2, -f_3)$ , which in turn is the power 66 dB above the power  $P_r$  which causes the standard response.

$$P_{IM} \text{ dBm} = P_1 \text{ dBm} + P_2 \text{ dBm} + P_3 \text{ dBm} - 2P_r \text{ dBm} - 198 \text{ dB} \quad (4.110)$$

This is the default model which will be utilized by NONLIN, which has been extrapolated from the (CS03) requirements of MIL-STD-461. Again, it is possible to express equation 4.110 in the form of an interference margin as:

$$\text{Interference margin} = P_1 \text{ dBm} + P_2 \text{ dBm} + P_3 \text{ dBm} - 3P_r \text{ dBm} - 198 \text{ dB} \quad (4.111)$$

#### 4.4.4. Transmitter Intermodulation Products

In addition to the intermodulation products generated in receivers discussed in previous sections, products may also be generated in the nonlinear portions of transmitters. Due to the nature of transmitter nonlinearities, however, Volterra techniques are not the appropriate analytical tool for use in the study of transmitter intermods. Instead, the intermodulation output power, which propagates from one of the interfering transmitters to the affected receiver is of the form (See Reference 15)

$$P_{IM} \text{ dBm} = P_{LOW} \text{ dBm} - A \text{ dB} - B \log \Delta f\% \quad (4.112)$$

where

$P_{LOW}$  = the lowest interfering signal power

$\Delta f\%$  = the average percent difference of incoming transmitter frequencies from the mixing transmitter frequency

A, B = constants which must be determined for each transmitter and each product.

Based on equation 4.112, default models may be formulated for use in NONLIN. These models are:

- Third order, two signal or three signal

- 1) If  $\Delta f\% \leq 1\%$ : A=10, B=0

$$P_{IM} = P_I \text{ dBm} - 10 \text{ dB}$$

- 2) If  $\Delta f\% > 1\%$ : A=10, B=30

$$P_{IM} = P_I \text{ dBm} - 30 \log \Delta f\% - 10 \text{ dB}$$

- Fifth order, two signal

- 1) If  $\Delta f\% < 1\%$ :  $A=30, B=0$

$$P_{IM} = P_I \text{dBm} - 30 \text{ dB}$$

- 2) If  $\Delta f\% > 1\%$ :  $A=30, B=30$

$$P_{IM} = P_I \text{dBm} - 30 \log \Delta f\% - 30 \text{ dB}$$

- Second order, two signal

Due to the nature of transmitter nonlinearities, second order, two signal intermodulation products are insignificant. This may be seen by considering the intermodulation output frequency

$$f_{IM} = f_1 + f_2 \quad (4.113)$$

It is obvious that at least one of the frequencies  $f_1, f_2$  or  $f_{IM}$  will always be outside the transmitter operating band, which will cause the power at the out-of-band frequency to be attenuated to such an extent that the product is insignificant and causes no system degradation.

For reference, the default models for all receiver and transmitter intermodulation products are presented in Table 4-7.

#### 4.4.5 Structurally Generated Intermodulation Products

In addition to the receiver and transmitter intermodulation products discussed in the last three sections, it is possible for products to be generated in the nonlinear metallic junction between two structures. An example of this effect would be the generation of intermods at an interface between a rusted piece of metal and an unrusty piece. Since this problem often occurs at such an interface, it has been traditionally referred to as the "rusty bolt" problem. Major intermods generated at this type of junction will be second and third order, two-signal intermods, and three signal, third order intermods.

As stated previously, the highly nonlinear nature of this type of junction precludes a Volterra analysis. For this reason, the models used to describe structurally generated products are entirely empirical in nature, and may be described by the equation

$$P_{IM} \text{dBm} = P_{LOW} \text{dBm} - A \text{ dB} - B \log (\Delta f\%) \quad (4.114)$$

Table 4-7 Intermod Default Models

<u>Order</u>	<u>Receiver</u>	<u>Transmitter*</u>
2(2 sig)	$P_{IM} = P_1 + P_2 - P_R - 132 \text{ dB}$	-
3(2 sig)	$P_{IM} = 2P_1 + P_2 - 2P_R - 198 \text{ dB}$	$P_{IM} = P_I - 10 \text{ dB}$ or $P_{IM} = P_I - 10 \text{ dB}$ $-30 \log \Delta f(\%)$
3(3 sig)	$P_{IM} = P_1 + P_2 + P_3 - 2P_R - 198 \text{ dB}$	Same as above
5(2 sig)	$P_{IM} = 3P_1 + 2P_2 - 4P_R - 330 \text{ dB}$	$P_{IM} = P_I - 30 \text{ dB}$ or $P_{IM} = P_I - 30 \text{ dB}$ $-30 \log \Delta f(\%)$

\* The first equation for each order corresponds to  $\Delta f(\%) < 1\%$ .  
The second is for  $\Delta f(\%) > 1\%$ .

As was the case in previous sections,  $P_{LOW}$  will be the lowest power incident on the junction, and A and B will be constants which must be determined for various orders of intermodulation for each junction.

Utilization of equation 4.114 necessitates determination of all intermodulation frequencies which could cause degradation. For this reason, the frequency simplifications of previous sections may not be utilized, and many more frequency combinations must be considered. These are enumerated in Table 4-8.

Table 4-8 Structurally Generated Intermodulation  
Output Frequencies

<u>Order</u>	<u>Frequencies</u>	<u>Number</u>
2(2 signal)	$\pm f_1 \pm f_2$	4
3(2 signal)	$\pm 2f_1 \pm f_2$	8
	$\pm 2f_2 \pm f_1$	
3(3 signal)	$\pm f_1 \pm f_2 \pm f_3$	8

A default model based on equation .114 has been developed for structurally generated intermodulation products and is

$$P_{IM} \text{dBm} = P_{LOW} \text{dBm} - 10 \text{ dB} \quad (4.115)$$

In equation 4.115, it is assumed that the junction is very wideband, eliminating the frequency dependent term (i.e.,  $B=0$ ). It is also assumed that since the products are all low order, the default model will be the same for all orders and frequencies.

## 4.5

Cross Modulation

Cross modulation is the term used to describe degradation caused by the transfer of modulation from an interfering signal to the desired signal. Cross modulation is similar to desensitization (discussed earlier) in several ways which will bear on the following discussion. The similarities are:

- 1) Cross modulation is treated as a third order effect
- 2) Cross modulation may be considered a nonlinear phenomenon which occurs at intervals corresponding to increased interfering signal levels. This situation is depicted in Figure 4-7, where the desired signal is an unmodulated CW and the interfering signal is a pulse modulated CW.

Based on the preceding similarities, the discussion of cross modulation will closely follow that of desensitization except for the representation of the interfering signal, which is assumed to be an amplitude modulated carrier, with modulation such that  $i(t)$  is less than one.

$$I_i(t) = I[1+i(t)] \cos \omega_i t \quad (4.116)$$

Then, referring to Section 4.2, one may obtain the input/output relationship

$$v_o(t) = S_i(t) + 3S_i(t)I_i^2(t) \quad (4.117)$$

Expanding the expression  $I_i^2(t)$ ,

$$I_i^2(t) = I^2[1+2i(t)+i^2(t)][\frac{1}{2} + \frac{1}{2} \cos 2\omega_i t] \quad (4.118)$$

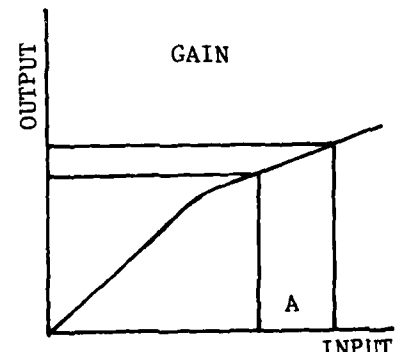
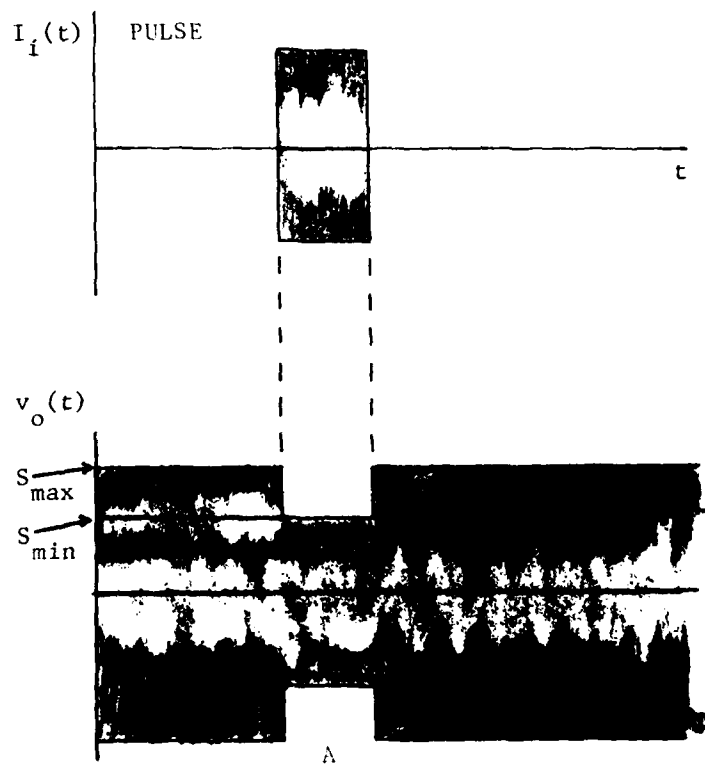
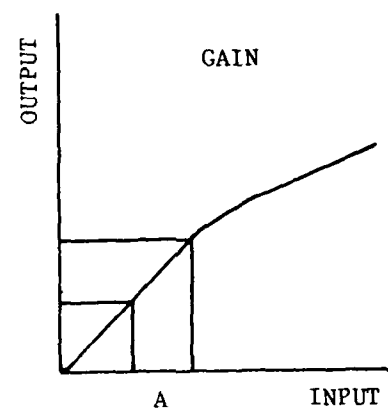
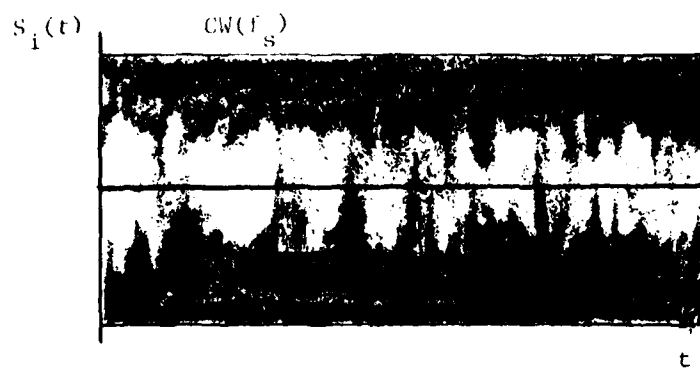


Figure 4-7 Pulse Modulation of an AM Signal

Again, as in the case of the desensitization analysis, terms involving  $\cos 2\omega_i t$  will be removed by filtering. Therefore, the significant terms in the output are

$$v_o(t) = S[H_1(f_s) + \frac{3}{2}I^2H_3(f_s, -f_i, f_i)[1+2i(t)]][1+s(t)]\cos \omega_s t \quad (4.119)$$

In equation 4.119, the term involving  $i^2(t)$  is second order and is insignificant with respect to the remainder of the expression. Now, carrying out the multiplications in equation 4.119, and eliminating terms with second order modulation, the relation in equation 3.119 may be written

$$v_o(t) = S[[H_1(f_s) + \frac{3}{2}H_3(f_s, f_i, -f_i)I^2][1+s(t)] + H_3(f_s, f_i, -f_i)[3I^2i(t)]]\cos \omega_s t \quad (4.120)$$

which may be written

$$v_o(t) = S[H_1(f_s) + \frac{3}{2}H_3(f_s, f_i, -f_i)I^2] \cdot \frac{[1+s(t) + \frac{\frac{3}{2}H_3(f_s, f_i, -f_i)I^2}{H_1(f_s) + \frac{3}{2}H_3(f_s, f_i, -f_i)I^2} 2i(t)]\cos \omega_s t}{H_1(f_s) + \frac{3}{2}H_3(f_s, f_i, -f_i)I^2} \quad (4.121)$$

Equation 4.121 is the expression for an amplitude modulated signal where the modulation consists of a combination of the desired and interfering signal modulations,  $s(t)$  and  $i(t)$ . If the modulation component resulting from the interfering signal modulation is restricted so that the maximum amplitude of the modulation signal is less than or equal to the amplitude of the carrier, overmodulation is avoided.<sup>7</sup> In this case, the nonlinearity should not cause significant distortion of the modulation.

7. In order to avoid overmodulation, it is necessary that:

$$m_s + \left| \frac{\frac{3}{2}I^2H_3(f_s, f_i, -f_i)}{H_1(f_s) + \frac{3}{2}I^2H_3(f_s, f_i, -f_i)} \right| 2m_i \leq 1,$$

where  $m_s$  and  $m_i$  represent the maximum values of  $s(t)$  and  $i(t)$ .

One measure of the effect of cross modulation is provided by the ratio of the sideband component resulting from the desired signal to the sideband component resulting from the interfering signal. The resulting ratio which is termed the "cross modulation ratio" (CMR), is expressed in terms of  $m_s$  and  $m_i$  (the maximum values of  $s(t)$  and  $i(t)$  as:

$$CMR = \frac{[H_1(f_s) + 3/2I^2H_3(f_s, f_i - f_i)]m_s}{[3/2I^2H_3(f_s, f_i, -f_i)]2m_i} \quad (4.122)$$

Expressing the ratio in terms of  $m_s$  and  $m_i$  provides an effective measure when similar modulation is present on both the desired and interfering signals. If the types of modulation on the two signals are significantly different, it may be desirable to use some other measure of the amplitudes (such as the RMS levels).

If the desired and interfering signals are limited to "small signal" conditions such that

$$H_1(f_s) \gg 3/2I^2H_3(f_s, f_i, -f_i), \quad (4.123)$$

The cross modulation ratio may then be written:

$$CMR \approx \frac{H_1(f_s)m_s}{3I^2H_3(f_s, f_i, -f_i)m_i} \quad (4.124)$$

or

$$CMR \text{ dB} = -2P_I \text{ dBm} + H_1(f_s) \text{ dB} - H_3(f_s, f_i, -f_i) \text{ dB} - 20 \log \frac{2m_s}{3m_i} \quad (4.125)$$

where  $P_I$  = interfering signal power in dBm

Equation 4.125 assumes that the major cross modulation is of third order origin and results in an amplitude modulation effect. If both the desired and interfering signals have the same modulation characteristics (i.e.,  $m_s = m_i$ ), the last three terms of equation 4.125 are functions of the gain, selectivity, and nonlinear characteristics of the device under consideration. For convenience, these terms may be represented by a single functional,  $CMF(f_i)$ , which is referred to as the cross modulation function. Thus

$$CMR \text{ dB} = -2P_I \text{ dBm} + CMF(f_i, f_s) \text{ dBm} \quad (4.126)$$

Equation 4.126 is valid for desired signals below the automatic gain control threshold ( $P_{AGC}$ ) and for interfering signal powers less than the saturation power level corresponding to the desired signal level and the frequency separation between the input signals. When the desired signal is above  $P_{AGC}$ , the gain is reduced proportional to the increase in the desired signal so that the output remains constant. The gain reduction may be represented by

$$\Delta G \text{ dB} = k(P_D - P_{AGC})$$

$k$  = gain reduction fraction (=1 since all AGC occurs prior to nonlinearity)

$P_D$  = desired signal level in dBm

$P_{AGC}$  = AGC threshold in dBm

The resulting equation for the cross modulation ratio will be

$$CMR \text{ dB} = -2P_I \text{ dBm} - 2(P_D - P_{AGC}) + CMF(f_I) \text{ dBm} \quad (4.127)$$

When the interfering signal becomes large, the nonlinear device will saturate. Beyond this level, if the desired signal is constant, changes in the interfering signal level do not produce corresponding changes in the signal-to-interference ratio. As a first approximation of the signal-to-interference ratio for  $P_I$  greater than the saturation level,  $P_{SAT}$ , the saturation level may be substituted for the interfering signal level. Therefore

$$CMR \text{ dB} = -2P_{SAT} + 2(P_{AGC} - P_D) + CMF(f_s, f_i) \quad (4.128)$$

The equations for cross modulation effects are summarized in Table 4.9.

Table 4-9 Summary of Equations for Cross Modulation

<u>Case</u>	<u>Conditions</u>	<u>Equation</u>
I	$P_I < P_{SAT}$ , $P_D < P_{AGC}$	$CMR = -2P_I + CMF(f_s, f_i)$
II	$P_I < P_{SAT}$ , $P_D \geq P_{AGC}$	$CMR = -2P_I + 2(P_{AGC} - P_D) + CMF(f_s, f_i)$
III	$P_I \geq P_{SAT}$ , $P_D \geq P_{AGC}$	$CMR = -2P_{SAT} + 2(P_{AGC} - P_D) + CMF(f_s, f_i)$
IV	$P_I \geq P_{SAT}$ , $P_D < P_{AGC}$	$CMR = -2P_{SAT} + CMF(f_s, f_i)$

In order to use the equations for cross modulation, it is necessary to specify a value for the cross modulation functional. If the cross modulation effects are specified for a given interfering signal level,  $P_I^*(f_I)$  dBm, the cross modulation functional may be evaluated as follows:

$$CMF(f_I) \text{ dB} = 2P_I^*(f_I) \text{ dBm} + CMR \text{ dB} \quad (4.129)$$

where  $CMR \text{ dB} = \text{cross modulation ratio resulting from reference interfering signal.}$

The limits for conducted susceptibility resulting from cross modulation are specified in MIL-STD-461 (CS05). If these limits are used the following default models shown below result.

From MIL-STD-461, the interfering signal power will be 66 dB above some standard reference, assumed to be the receiver sensitivity, so

$$P_I^*(f_I) \text{ dBm} = P_R \text{ dBm} + 66 \text{ dB} \quad (4.130)$$

and

$$CMR \text{ dB} = 0 \quad (4.131)$$

Then the CMF may be written

$$CMF \text{ dB} = 2P_R \text{ dBm} + 132 \text{ dB} \quad (4.132a)$$

and the default model is

$$CMR \text{ dB} = -2P_I \text{ dBm} + 2P_R \text{ dBm} + 132 \text{ dB} \quad (4.132b)$$

It is possible to define an interference margin for cross modulation in much the same manner as the desensitization interference margin was defined. The interference margin will be defined as the amount by which the CMR exceeds a reference of -20 dB, the minimum observable cross modulation. Equation 4.132b may then be written using this criterion.

$$\text{Interference Margin} = CMR \text{ dB} + 20 \text{ dB} \quad (4.133)$$

The equations just presented describe modulation of a desired AM signal by an interfering AM signal. Expressions similar to those in Table 4-9 will be derived for other types of cross modulation.

For interfering signals other than full carrier, double sideband AM, another approach is used to evaluate the cross modulation signal-to-interference ratio. This approach still correlates cross modulation with desensitization, but from a different point of view. Large signals entering a receiver cause desensitization, that is, gain reduction to the desired signal. If the bandwidth of the RF stages of a receiver is large enough, the gain reduction will follow the amplitude variations of the interfering signal and in this manner impart the unwanted modulation to the desired transmission.

Using this hypothesis, a modulation index, analogous to the AM modulation index, can be computed from the desensitization information. The expression for modulation index of an AM signal in terms of maximum and minimum instantaneous signal amplitude is

$$m_i = \frac{S_{\max} - S_{\min}}{S_{\max} + S_{\min}} = \frac{\Delta S_o / S_o}{2 - \Delta S_o / S_o} \quad (4.134)$$

where  $\frac{\Delta S_o}{S_o}$  is defined in Section .2, and:

$$\begin{aligned} m_i &= \text{modulation index} \\ S_{\max} &= \text{maximum instantaneous signal amplitude} \\ S_{\min} &= \text{minimum instantaneous signal amplitude} \end{aligned}$$

Since the CW signal now has modulation on it, the signal-to-interference ratio is the ratio of the carrier amplitude to the sideband amplitude.

$$S/I = 20 \log(m_i) \quad (4.135)$$

Suppose instead of CW carrier, the desired signal has been amplitude modulated, then the sideband-to-sideband ratio would be

$$S/I = 20 \log \left( \frac{m_s}{m_i} \right) \quad (4.136)$$

where

$$\begin{aligned} m_s &= \text{desired signal modulation index} \\ m_i &= \text{equivalent interfering signal modulation index.} \end{aligned}$$

Equation 4.136 is the cross modulation signal-to-interference model chosen for single sideband interference to AM receivers, when  $m_i$  is computed by equation 4.134. The desired signal modulation index for AM signals is proportional to the total power in the modulation sidebands. Actually, the fraction of total power in the sidebands equals  $m_s/2$ . Equation 4.136 can be modified to describe single sideband interference to a single sideband receiver if one considers that for this type of desired signal, all the power is contained in the information sidebands. Equation 4.137 expresses the cross modulation signal-to-interference ratio for SSB interference to SSB receivers.

$$S/I = 20 \log (2/m_i) \quad (4.137)$$

Equation 4.137 could also model pulse interference to AM receivers except that the interference appearing at the audio output of the receiver is proportional to the average power because, normally, the pulse bandwidth is considerably larger than the receiver last IF passband. A bandwidth correction factor is needed, also. The signal-to-interference ratio from cross modulation due to pulse interference is

$$S/I = 20 \log \left( \frac{m_s}{m_i} \right) - 10 \log (\tau f_r) - 10 \log (\tau \Delta f_3) \quad (4.138)$$

where

$\tau$  = pulse width (seconds)

$f_r$  = pulse repetition frequency (pps)

$\Delta f_3$  = receiver overall 3-dB bandwidth.

This can be seen if we examine the relationship of  $S/I_{peak}$ , given by equation 4.136, to  $S/I_{avg}$ , the desired ratio for pulse modulation of AM receivers.  $S/I_{avg}$  will equal  $S/I_{peak}$  minus the correction factors described above, since the factors affect the interference power, which is in the denominator of equation 4.136. Therefore

$$S/I_{avg} = 20 \log \frac{m_s}{m_i} - 20 \log \frac{\tau}{T} - 10 \log \frac{\Delta f_3}{f_r} \quad (4.139a)$$

But since

$$20 \log \frac{\tau}{T} = 20 \log \tau f_r \quad (4.139b)$$

and

$$10 \log \frac{\Delta f_3}{f_r} = 10 \log \Delta f_3 \tau - 10 \log \tau f_r \quad (4.140)$$

$S/I_{avg}$  is then seen to be the expression given by equation 4.138. This situation, where the interfering pulse width is much greater than the receiver bandwidth, is seen in Figure 4-8.

By applying the same rationale that was employed to arrive at equation 4.137, from the expression of single sideband interference to an AM receiver, an expression of pulse interference to single sideband receivers is given by equation 4.141.

$$S/I = 20 \log (2/m_i) - 10 \log (\tau f_r) - 10 \log (\tau \Delta f_3) \quad (4.141)$$

By applying the same logic used to obtain the form of the interference margin in Equation 4.133, all of the signal to interference ratios in this section may be expressed as interference margins using the relationship:

$$\text{Interference Margin} = \frac{S}{I} \text{ dB} + 20 \text{ dB} \quad (4.142)$$

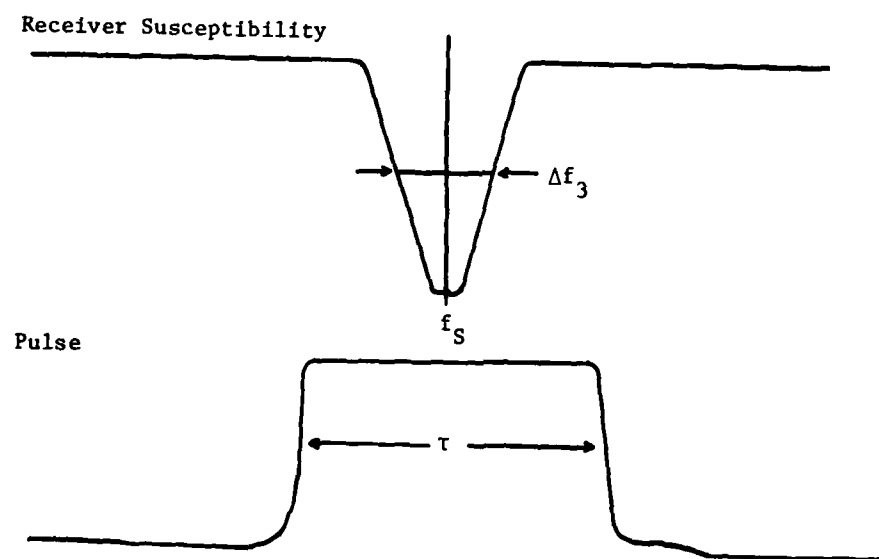


Figure 4-8 Pulse Modulation of AM Receivers

This section has presented equations describing third order cross modulation of many signal types. Three notable signal combinations were excluded from consideration, however, based on the reasons given below:

- 1) FM cross modulation is not considered since the frequency information in an FM signal is not adversely affected by cross modulation amplitude variations. In addition, since most FM receivers have some sort of amplitude limiting, the cross modulation fluctuations would be undetected.
- 2) Pulse modulation of pulse signals is deemed insignificant since cross modulation between pulses depends on their simultaneous occurrence. Considering typical pulse duty cycles, this simultaneous occurrence is highly unlikely, and was not considered in this analysis.
- 3) Cross modulation of pulse signals is deemed insignificant because it does not usually result in degradation of these types of receptors.

#### 4.6

#### Spurious Responses

A spurious response in a superheterodyne receiver arises when an interfering signal, (or one of its harmonics) enters a nonlinear mixer and combines with the local oscillator frequency of the mixer (or one of its harmonics) to produce a "spurious" output which falls into the receiver IF passband. This can be a serious problem due to the large amplitude of the local oscillator signal which can mix with even small interfering amplitudes to produce system degradation. A diagram of a typical superhetrodyne receiver, with three stages of nonlinear mixing may be seen in Figure 4-9. For the first mixer in Figure 4-9, assume the interfering signal (or one of it's harmonics, denoted by  $q$ ) passes through RF preselection and amplification with sufficient amplitude to enter mixer number one. When mixed with the first LO frequency (or one of it's harmonics, denoted by  $p$ ), the output frequency will occur at

$$f_{\text{OUT}} = p f_{\text{LO}} + q f_{\text{SPUR}} \quad (4.143)$$

In order to produce degradation,  $f_{\text{OUT}}$  must be within the first IF passband of the receiver. This will encompass a range of frequencies denoted by

$$f_{\text{OUT}} = f_{\text{IF1}} + \Delta f_{\text{IF1}} \quad (4.144)$$

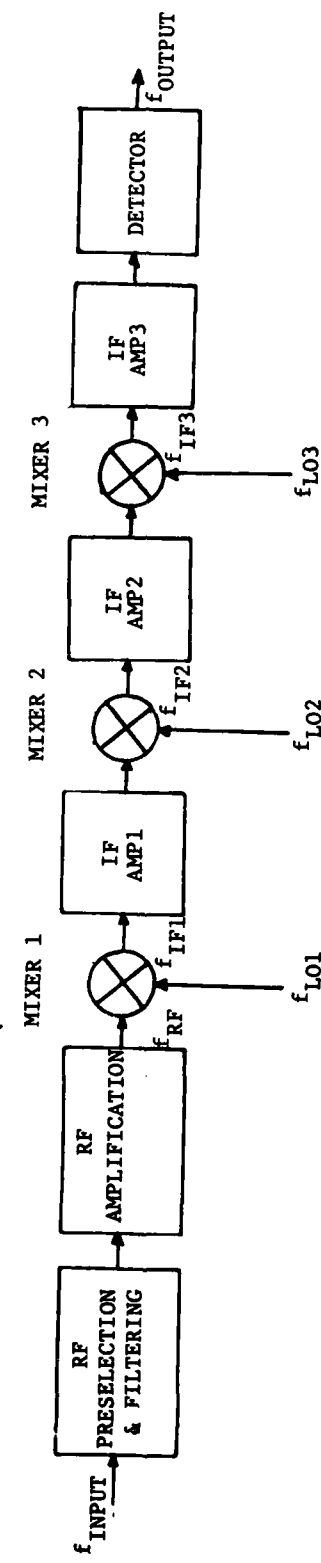


Figure 4-9. 3 Stage Superheterodyne Receiver

Therefore, degradation will occur for a range of interfering frequencies such that

$$f_{SPUR} = \frac{p_1 f_{LO1} + (f_{IF1} + \Delta f_{IF1})}{q_1} \quad (4.145)$$

Now, given that equation 4.145 holds at each mixer, the requirement that  $f_{SPUR}$  causes interference in a triple conversion receiver leads to the requirement that

$$f_{SPUR} = \frac{p_1 f_{LO1}}{q_1} \pm \frac{p_2 f_{LO2}}{q_1 q_2} \pm \frac{p_3 f_{LO3} + (f_{IF3} + \Delta f_{IF3})}{q_1 q_2 q_3} \quad (4.146)$$

where the final output must be within the final IF output passband.

From equations 4.145 and 4.146, it is obvious that the interfering signal need not be near the center of the receiver RF passband to cause degradation and may, in fact, be greatly attenuated prior to mixing with the large amplitude local oscillator frequency. This leads to two observations regarding spurious responses.

- 1) Since the spurious response frequency need not be in the RF passband, it will be the only nonadjacent channel effect considered in NONLIN. This will introduce an additional null at each interfering frequency.
- 2) Due to the large signal nature of local oscillator signal (typically  $\sim 1$  volt compared with an RF input to the mixer with amplitude on the order of 1mV), the modified Volterra analysis presented previously is not applicable to the study of spurious responses.

As a result of these observations, the algorithms used to describe spurious response interference will be considerably different from the algorithms used in the Volterra analysis. These differences will now be examined in more detail.

Assumption (1) states that the spurious responses need not be an adjacent channel effect. If the interfering signal is nonadjacent channel, however, it is assumed that the RF attenuation is such that only first mixer generated responses will cause degradation. The second and third stages will be assumed to provide only direct IF feed through (i.e., normal mixing).

These two observations, coupled with the large signal local oscillator (allowing large values for  $p_1$ ) will lead to nonadjacent channel spurious responses being quantified by

1st mixer:  $p_1$  = user defined range  
 $q_1$  = user defined or  $q_1 = 1$  default  
2nd mixer:  $p_2 = q_2 = 1$   
3rd mixer:  $p_3 = q_3 = 1$

If the interfering signal is adjacent channel it will experience considerably less RF attenuation than a nonadjacent channel signal. Therefore,  $p_1$  and  $q_1$  will be allowed to take on a range of values determined by the user. As may be seen in Figure 4.10, however, higher order mixes require very high input signal levels to cause degradation. It is thus deemed advisable to limit the second and third mixers to values of  $p$  and  $q$  which are equal. As seen from Figure 4.10, this will result in an output near the IF frequency, which will pass relatively unattenuated to the next receiver stage. Using the above assumptions yields the adjacent channel response quantization.

1st mixer:  $p_1$  = user defined range  
 $q_1$  = user defined range  
2nd mixer:  $p_2 = q_2 = 1, 2, 3$   
3rd mixer:  $p_3 = q_3 = 1, 2, 3$ .

Observation (2) will now be used to describe the response at the frequencies given above.

Because of the large signal nature of the local oscillator, an alternative to the Volterra analysis is needed to describe system degradation due to spurious responses. NONLIN will describe spurious responses in terms of piecewise linear response curves. For  $q = 1$  these response curves will be of the form

$$P_{SR} \text{ dBm} = I \log p + J \quad (4.147)$$

In general,  $I$  and  $J$  must be determined for each particular receiver under consideration. In fact, it is often necessary to consider that the power needed to produce a response will have a different linear relationship in different receiver frequency intervals. This will necessitate determination of other values for  $I$  and  $J$  for additional frequency intervals in the receiver passband.

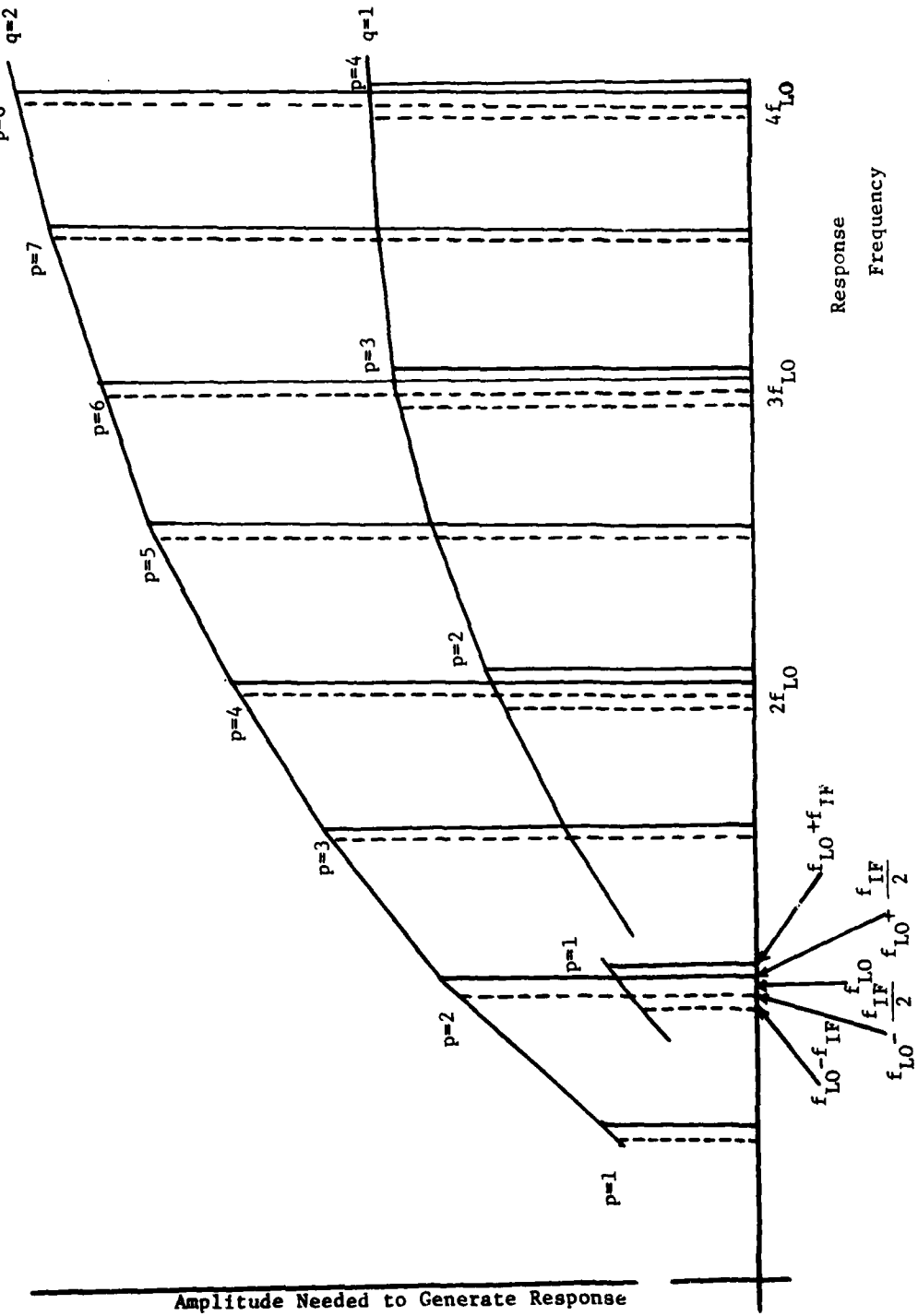


Figure 4-10 Amplitude needed to generate response vs. response frequency

Equation 4.147 will hold only in the non-adjacent channel region. In the adjacent channel region, the response will be of the form:

$$P_{SR} \text{ dBm} = I \log \frac{f}{f_0} + J \quad (4.148)$$

The spurious response powers in equations 3.147 and 3.148 may be related to the interference margin by noting that the interference margin is just the actual interfering signal level minus  $P_{SR}$ .

The piecewise linear equations which quantize the response as a function of  $p$  for  $q = 1$  are of the form given in equation 3.148. Analogous results for other values of  $q$  will also have a piecewise linear relationship. In general, however, the constants  $I$  and  $J$  will be quite different from those for the  $q=1$  responses, and must be determined for each receiver from experimental data.

As a rule of thumb, experimental data has shown that the  $q = 2$  responses will be approximately 15 dB below the  $q = 1$  responses, and the  $q = 3, 4$  responses will be on the order of 20 dB below the  $q = 1$  responses. These values will be utilized as default values in NONLIN in the absence of more complete user specifications.

The piecewise linear model described above has been validated completely and is discussed in detail in references 2 and 13. This model may be used to formulate default equations for spurious responses based on the CS04 limits of MIL-STD-461 (see Figure 4-4). The defaults will be formulated by assuming that the response,  $P_{SR}$ , will be a signal of the form seen in Figure 4-4. This assumption will then be utilized to solve for  $I$  and  $J$  in the various regions of interest. If this is done, the defaults in Table 4-10 will result. The equations in Table 4-10 describe the response if  $q=1$ . As stated previously,  $P_{SR}$  (in the region outside the 80 dB bandwidth) will be 15 dB lower if  $q=2$  and 20 dB lower if  $q = 3$  or 4. Inside the 80 dB bandwidth region, the default equations for higher values of  $q$  will be the same as the  $q=1$  equation in Table 4-10.

Table 4-10 Default Models for Spurious Responses

For Interfering signals within the receiver 80 dB bandwidth

$$f_o - \frac{W}{2} \leq f_{INT} \leq f_o + \frac{W}{2}$$

$$P_{SR} \text{dBm} = P_R \text{dBm} + \frac{160}{W} [f - f_o]$$

For interfering signals outside the receiver 80 dB bandwidth but within the overall tuning range of the receiver

$$f_L \leq f_{INT} \leq f_o - \frac{W}{2} \quad \text{or} \quad f_o + \frac{W}{2} \leq f_{INT} \leq f_H$$

$$P_{SR} \text{dBm} = P_R \text{dBm} + 80 \text{ dB}$$

For interfering signals outside the tuning range of the receiver

$$f_{INT} < f_L \quad \text{or} \quad f_{INT} > f_H$$

$$P_{SR} \text{dBm} = 0 \text{ dBm}$$

where

$f_o$  = receiver tuned frequency

$W$  = receiver 80 dB bandwidth

$P_R$  = receiver sensitivity

#### 4.7 References

1. "Intrasytem Electromagnetic Compatibility Analysis Program, Volumes I-IV," RADC-TR-74-342, December 1974.
2. Interference Notebook, RADC-TR-66-1, Contract AF 30(602)-3118; AD 484-485, June 1966.
3. "Adjacent Channel Interference Analysis," RADC-TR-68-595, Contract F30602-68-C-0061, March 1969.
4. Spina, John F. and Donald D. Weiner, Sinusoidal Analysis and Modeling of Weakly Nonlinear Circuits, Van Nostrand Reinhold Co., N.Y., 1980.
5. "Voice Communications Degradation Studies," Jansky & Bailey Engineering Dept., A Division of Atlantic Research Corp., RADC-TR-67-546, Contract No. AF 30(602)-4023.
6. Volterra, Vito, Theory of Functionals and of Integral and Integro-Differential Equations, Blackie and Sons Ltd., London, 1930.
7. Wiener, N., "Response of a Non-Linear Device to Noise," M.I.T. Radiation Laboratory Report V-16S, April 1942.
8. Nonlinear System Modeling and Analysis with Applications to Communications Receivers, RADC-TR-73-178, June 1978
9. Duff, W. G., "EMC Figure of Merit for Receivers," 1969 IEEE EMC Symposium Proceedings, Asbury Park, NJ, 1969.
10. 3rd Order Intermodulation Study, RADC-TR-67-344, IIT Research Institute, July 1967.
11. Wass, C. A., "A Table of Intermodulation Products," Journal of the Institute of Electrical Engineers, (London) Part III, p. 31; 1948.
12. Capraro, Gerard T., "Spurious Response Identification and Generation," Technical Memorandum No. EMC-TM-67-15, Rome Air Development Center, December 1967.
13. "Interference Analysis Study," RADC-TR-63-27, June 1963.
14. Myers, Glenford J., Software Reliability, Wiley Interscience, NY, 1976.
15. McMahon, J. H., "Interference and Propagation Formulas and Tables Used in the FCC Spectrum Management Task Force Land Mobile Frequency Assignment Model," IEEE Transactions on Vehicular Technology, Vol. VT-23, Nov., 1974.

## 5.0 NEW MODEL FOR PORT SPECTRA

The new port spectra model consists of a newly designed algorithm to replace the current "quantization" method in IEMCAP for modeling a port's spectra. The following features are incorporated in the new model:

- Generate Equipment Frequency Table
- User Specified Frequency Range for Analysis (C to 50 GHz and greater)
- User defined port spectra of up to 90 frequency - amplitude points for required and/or nonrequired frequency ranges
- Generate frequencies and amplitudes for prestored emitter and receptor models required by User's inputs currently required by IEMCAP
- Generate frequencies and amplitudes for harmonic signals as directed by User inputs currently required by IEMCAP
- Generate frequencies and amplitudes for any port's nonrequired spectra using prestored MIL-STDS (461A, 6181D and 704) and the corresponding system displacement factors.

Each of these features are discussed with regard to the present IEMCAP capability and then the developed replacement technique and models are described.

The equipment frequency table is generated by IEMCAP based on input data cards associated with keywords "FREQ" and "FQTBL." The FREQ card provides the lower ( $f_l$ ) and upper ( $f_u$ ) frequency limits, number of frequencies per octave and the maximum number of frequencies ( $n_{max}$ ) for the equipment. The FQTBL card(s) contains user specified frequencies (in ascending order) for the equipment. Using these data, the IEMCAP determines the total number of frequencies (up to  $n_{max}$ ) that are to be generated by the program for the equipment. The program geometrically spaces the program generated frequencies over the total frequency range ( $f_l$  to  $f_u$ ). The equipment frequency table is then

determined beginning with  $f_1$ . The next frequency is the lesser of the first program generated frequency or the first user specified frequency on the FQTBL card(s). This process is repeated up to and including the upper frequency limit ( $f_u$ ) of the equipment. The subroutine FTGEN generates the equipment frequency table.

FTGEN with subroutine FTSRCH establishes the appropriate table frequencies to be used on each port of the equipment. The port frequency range is presently based upon the MIL-STDS. For example, an RF emitter port under MIL-STD-461 has a frequency range of 14 kHz to 18 GHz. FTGEN selects the appropriate table frequencies to encompass this range.

The specified frequency range for IEMCAP is 30 Hz to 18 GHz. These frequency limits are based on the frequency limits associated with the MIL-STDS. Each of the different port types (i.e., RF, Signal/control, etc.) has an assigned receptor and emitter frequency range. A user may specify a frequency range less than the above, e.g., 30 Hz to 10 GHz, 14 kHz - 1 GHz, etc. and the port frequency ranges will be adjusted accordingly. A user may not specify a frequency range greater than the above, i.e., frequencies <30 Hz or greater than 18 GHz are not permitted.

IEMCAP has an option for user defined port spectra. This option allows a user to specify the required frequency range portion of a port's spectra. Up to ten amplitude-frequency pairs may be specified at the input level. These spectra will be used in place of a prestored model to represent the required frequency region of a port. When specifying a port spectra, an emitter's spectra are input in broadband units and a receptor's spectra is defined in terms of narrowband units.

To generate frequencies and amplitudes for prestored emitter and receptor models, the IEMCAP requires certain user inputs. The user inputs may consist of both time and frequency domain parameters. With the user specified data, the program determines the appropriate spectra via the spectra model routine. The spectra model routine consists of several subroutines which provide both emitter and receptor spectra in both the required and nonrequired frequency ranges. The required frequency range models are frequency domain, asymptotic expressions of the modulation envelope of a signal process. The non-required frequency range models consist of the various MIL-STDS that are pre-programmed in the IEMCAP.

A user is free to choose the frequency representation of a port in several ways as discussed above. However, the IEMCAP uses a "Quantizing technique" which may provide a distorted representation of a given prestored model or a user input spectrum (SPECT) on a port if the frequencies are not chosen in a judicious manner. Quantizing consists of choosing the maximum (emitters) or minimum (receptors) values within the frequency intervals established by the program for the equipment. Thus, the peaks and nulls associated with the quantized spectra will be shifted in frequency from the original spectra. The user must choose his frequency representation with care for an accurate representation. An acceptable procedure for determining the frequency representation of a model is presented in RADC-TR-78-140 (Paul).<sup>(1)</sup> This procedure is quite adequate for the present IEMCAP to implement but it requires considerable effort on the part of the user. A user must determine the frequencies required to represent a given model and then enter these frequencies via the FQTBL card(s) discussed above. This procedure must be performed for each port of an equipment. Similar techniques are used for the nonrequired frequency range modeling.

### 5.1 Generation of Equipment Frequency Table

To generate the equipment frequency table each port of an equipment will be examined for fundamental, tone and harmonic frequencies where applicable. Using these frequencies and the prestored model data the remainder of the port frequencies will be generated. Included in the port frequencies will be transition frequencies between required frequency range models and nonrequired frequency range models and the upper and lower frequency limits of the required frequency range. The new procedure for generating the equipment frequency table will be based upon the following.

- Prestored Model (Required)
  - Fundamental Frequency ( $f_c$ )
  - Tone Frequencies ( $f_t$ )
  - Frequencies of the intersect points of asymptotic expressions of model ( $f_I$ )
  - Fundamental frequency plus one-half the bandwidth of the channel ( $f_c + \frac{BWC}{2}$ )
  - Fundamental frequency minus one-half the bandwidth of the channel ( $f_c - \frac{BWC}{2}$ )

- MIL-STDS (Nonrequired)
  - Lowest port frequency ( $f_1$ )
  - Frequencies at intersection points of model (change in slope) ( $f_I$ )
  - $f_c - \frac{BWC}{2} - 0.001$  ( $f_-$ )
  - $f_c + \frac{BWC}{2} + 0.001$  ( $f_+$ )
  - Highest port frequency ( $f_h$ )
- Harmonic Frequencies\*
  - Harmonic Frequency ( $nf_c$ )
  - $n(f_c + \frac{BWC}{2})$
  - $n(f_c - \frac{BWC}{2})$
  - $n(f_c + \frac{BWC}{2}) + 0.001$
  - $n(f_c - \frac{BWC}{2}) - 0.001$
- User Specified Frequencies

The above procedure has been applied to each of the prestored models in IEMCAP, and the number of frequencies needed to define each model is shown in Table 5-1. The following example of RF emitter radar model with a rectangular pulse will desmonstrate how the numbers in Table 5-1 were derived.

---

\* For CW  $BWC = 1$  and only three frequencies

Table 5-1 Number of Model Frequencies

Prestored Model			No. Harmonic Frequencies For 9 Harmonics	Total Pre-stored and Harmonic	MIL-STDS	
Port Type	Name	Number Frequencies			461-A	6181D
RF Emitter	CW	1	27	28	4	4
	PDM	5				
	NRZPCM	5				
	BPPCM	5				
	PPM	4				
	TELEG $f_t=0$	7				
	TELEG $f_t \neq 0$	8				
	FSK	4				
	PAMFM	3				
	RADAR-TPZD	6				
	RECTPL	5				
	COSOD	4				
	GAUSS	3				
	CHIRP	9				
	AM-VOICE	6				
	CVOICE	7				
	NONVCE	5				
	DSBSC-V	5				
	DSBSC-CV	6				
	DSBSC-NV	4				
	LSSB-V	5				
	LSSB CV	6				
	LSSB-NV	4				
	USSB-V	5				
	USSB-CV	6				
	USSB-NV	4				
	FM	5				
	LOLKG	2				
SIGNAL CONTROL Emitter	PDM	3	N/A	3	5	4
	NRZPCM	3				
	RPPCM	3				
	PPM	4				
	TELEG $f_t=0$	3				
	TELEG $f_t \neq 0$	3				
	PAM	5				
	ESPIKE	3				
	RECTPL	3				
	TPZD	3				
	TRIANG	3				
	SAWTH	4				
	DMPSIN	5				
	VOICE	5				
RECEPTOR	CVOICE	6				
	EED	NONE	NONE	NONE	NONE	NONE
	CASE	NONE				
RECEPTOR	POWER	1				
	TRIANG	3	N/A	3	RF-2	RF-2
	TPZD	4				
RECEPTOR					S/C-2	S/C-2
			4	4	CASE-6	CASE-6
					POWER 4	POWER-4

The radar rectangular pulse representation in IEMCAP is the following:

$$P_{BB}(f) = P_r^2 f_B \quad ; |\Delta f| \leq \Delta f_M$$

$$P_{BB}(f) = P_r^2 f_B \left( \frac{\Delta f_M}{\Delta f} \right)^2 \quad ; \Delta f_M < |\Delta f| \leq \Delta f$$

where

$\tau$  = pulse duration

$f_B$  = bit rate

$$\text{bandwidth} = \frac{2}{\tau}$$

$$\Delta f_M = \frac{1}{\pi \tau}$$

$$\Delta f = f - f_c$$

$P$  = peak power

Figure 5-1 shows the frequency domain representation of the above

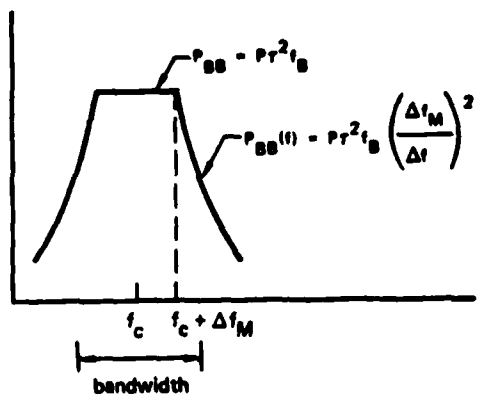


Figure 5-1 Radar Rectangular Pulse

From Figure 5-1 and recognizing that the required range is BWC (bandwidth of channel) wide, the prestored model (required) frequencies are

$$f_c, (f_c + \Delta f_m), (f_c + \frac{BWC}{2})$$

Thus, a total of 5 frequencies are used for the Radar Rect pulse in the required frequency range. To determine the nonrequired frequencies, the MIL-STDs are used. The nonrequired frequencies are:

$$f_{lo}, (f_c + \frac{BWC}{2} \pm 0.001), f_{hs}$$

Only four frequencies are used for the MIL-STD for this example because the specification for the radar pulse (RF) is a constant over the total frequency range (excluding the harmonics). The harmonic frequencies are specified by the following:

$$nf_c, (n(f_c + \frac{BWC}{2}), [n(f_c + \frac{BWC}{2}) \pm 0.001]$$

Five frequencies are used per harmonic and a total of 45 frequencies will be required if 9 harmonics are to be specified (the maximum number allowed by IEMCAP).

#### 5.1.1 Frequency Table Generation Routine (FTGEN)

The above procedure for generating the equipment frequency table can be integrated into the IEMCAP by replacing the present FTGEN routine. The new FTGEN routine will utilize the equipment port data to generate the equipment frequency table. The frequencies will be determined from prestored models, harmonics, user specification, military standards and/or combinations of any or all of these models. For prestored models (including Military Specifications) this routine generates frequencies at the interaction points (changes in shape for straight lines) in the model. The lower and upper frequency limits for the required frequency range model will be determined by the bandwidth of the channel as specified on the input data. The lower and upper frequency limits for Military Specifications are specified in the particular standard. Transition frequencies between the various models will be determined by the routine. Once the set of frequencies (<90) has been determined they are ordered in ascending order as required by the IEMCAP.

### 5.1.2 Frequency Range for Analysis

The specified frequency range of analysis is determined by prestored table values for each port type. The frequency limits are established according to the model capability limits programmed into the IEMCAP. The prestored table values are contained in arrays FMIN and FMAX of the FTGEN subroutine. The values assigned to FMIN are the lower frequency limit for each port type. The FMAX values are the upper frequency limit assigned to each port type. The absolute values assigned to these arrays are established via the "DATA FMIN/, FMAX/ STATEMENT" in subroutine FTGEN.

A lower frequency limit for a port should be greater than 0 Hz. The preferable lower frequency limit is 1 HZ. However, values close to zero may be used (e.g., 0.5, 0.75, etc.). The upper frequency limit of a port should be set to the maximum allowable value which is consistent with the IEMCAP modeling.

### 5.2 Generation of Port Spectra Amplitudes

The port spectra amplitudes are computed from prestored emitter and receptor models, harmonics, user specified data and prestored MILITARY STANDARDS models. Various combinations of these models may be used in determining the spectrum of a given port. The new SPECT option provides the following capability for representing a port's spectra:

- Specification of total spectra (both narrowband and broadband) with up to 90 frequency-amplitude pairs
- Specification of required spectra with up to 90 frequency-amplitude pairs
- Specification of nonrequired spectra with up to 90 frequency-amplitude pairs
- Specification of a portion of the total spectra contiguous in frequency (Required spectra may not be split between SPEC and prestored models, i.e., if it is desired that any part of required spectra be input, then all required spectra must be specified for this option)

Thus, with the New SPECT option the user has considerably more flexibility for representing the port spectra. The options available for an RF emitter port are shown in Figure 5-2. Figure 5-2 shows the RF emitter port representation for both a required model (MODSIG  $\neq$  SPECT) and a user specified model (MODSIG=SPECT) option. For both of these options the nonrequired models and harmonics are utilized as shown in Figure 5-2

The signal and control emitter port types are similar to the RF emitter port representation with the exception that there are no harmonics to be considered. Therefore, Figure 5-2 is representative of the signal and control emitter ports exclusive of the harmonic designations.

The emitter power port representation is similar to the RF emitter port except the required frequency range model is only a single frequency, i.e., the frequency of the power signal.

Both the emitter and receptor case port spectra may be represented as shown in Figure 5-1. A user may specify all or a portion of the case port spectra and the remainder will be represented by a MIL-STD. A case port has only a nonrequired frequency range.

The options for an RF receptor port are shown in Figure 5-4. As shown in this figure, there are several options available for combining pre-stored models (both required and nonrequired) and user specified data. Other receptor port types (signal, control, case and power) may be represented in a similar manner.

The EED port type is unchanged from the present capability provided by IEMCAP.

#### 5.2.1 Calculation of Port Spectra Levels

In order to determine the level for a given port frequency of an equipment, the various user options discussed above have been incorporated in the spectra level calculation. Each port of an equipment is examined for pre-stored model selection and/or user specified data.

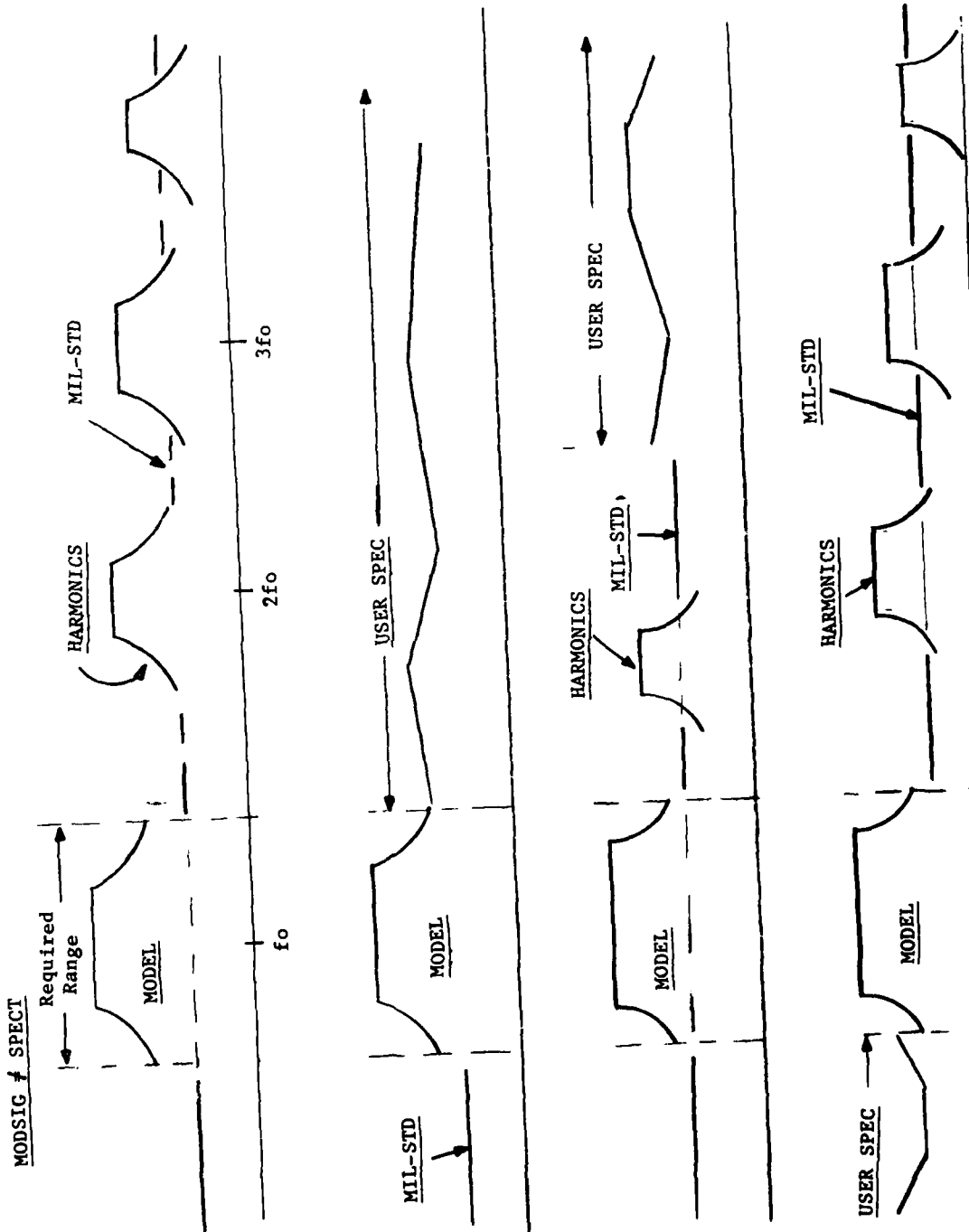


Figure 5-2 RF EMTR Port Spectra

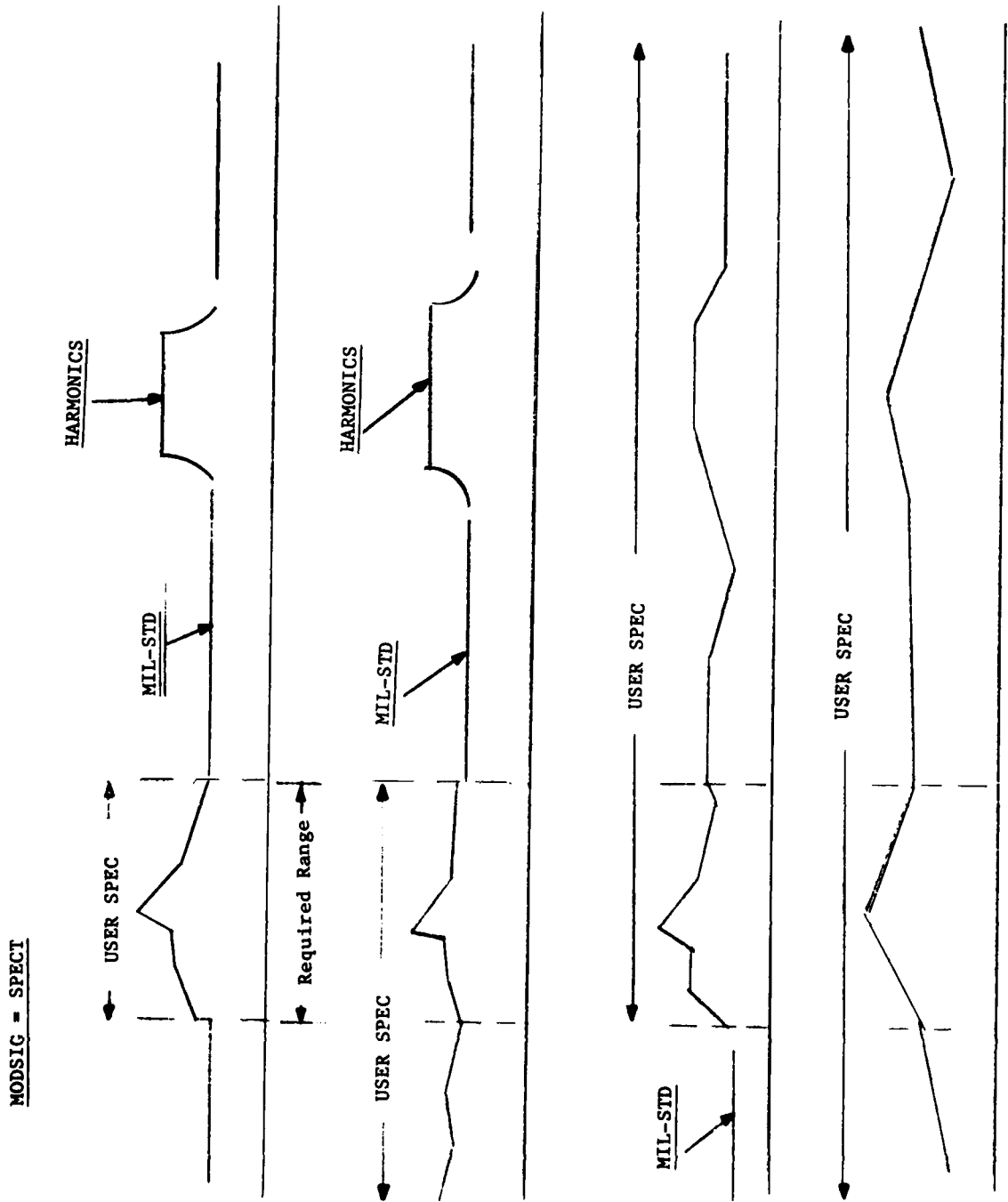


Figure 5-2 (Continued)

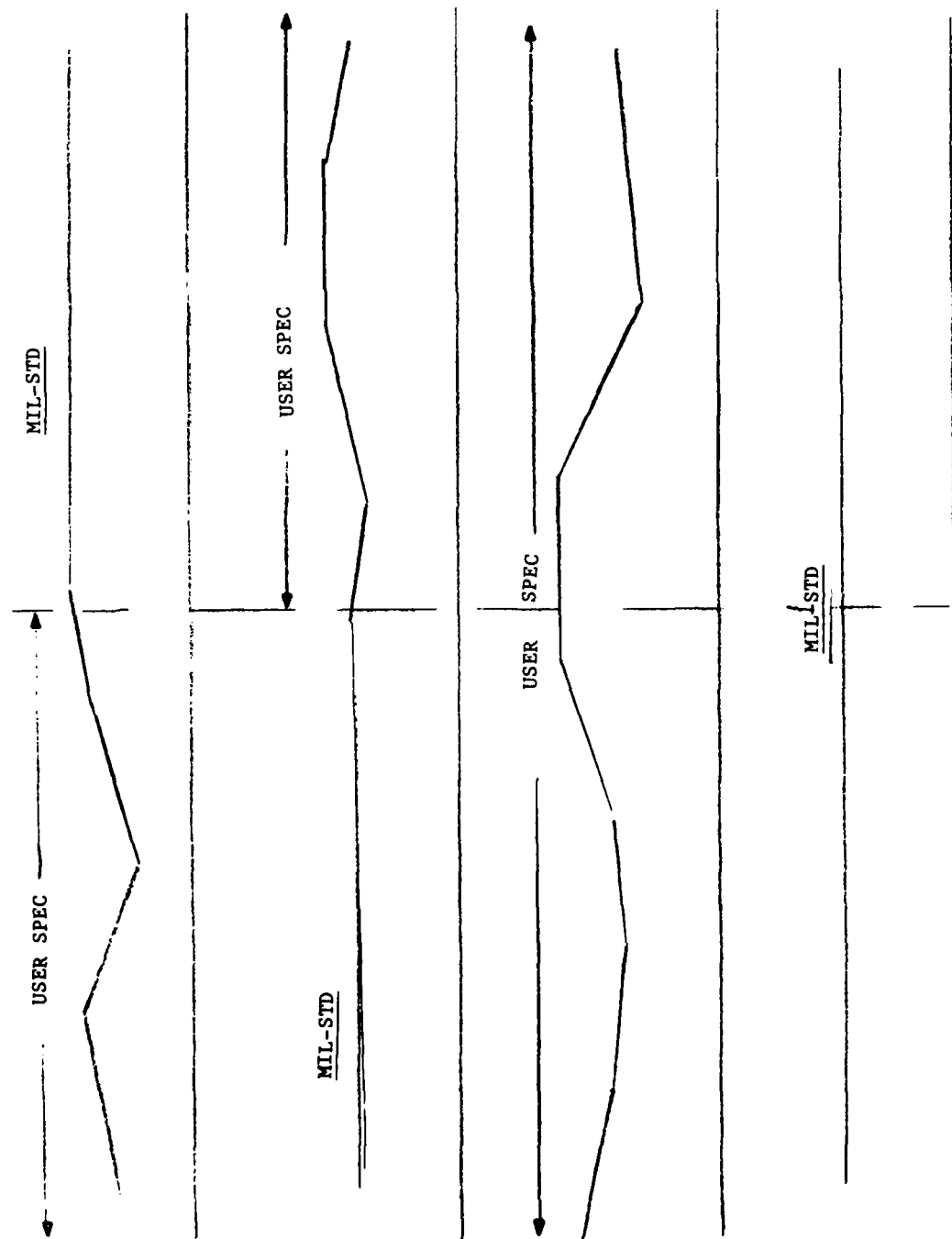


Figure 5-3 Case Port Spectra

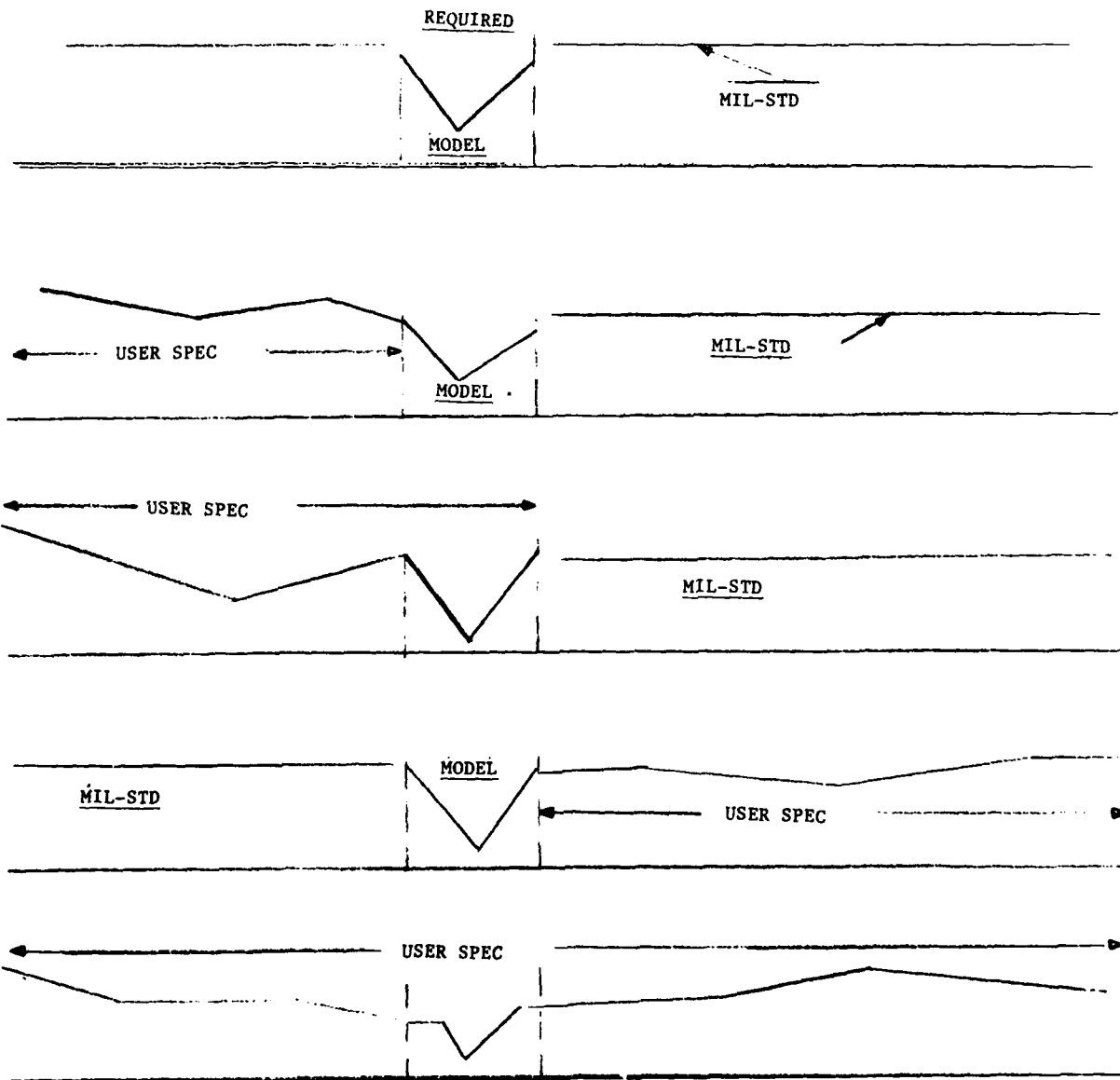


Figure 5-4 RF RCPT Port Spectra

5.3

References

1. Paul, Dr. Clayton R. and Weiner, Dr. Donald D., "A Summary of Required Input Parameters for Emitter Models In IEMCAP," RADC-TR-78-140, Final Technical Report, June 1978.
2. Intrasystem Electromagnetic Compatibility Analysis Program, Volume II - User's Manual Usage Section; RADC-TR-74-342, Final Report, December 1974.
3. Intrasystem Electromagnetic Compatibility Analysis Program, Volume I - User's Manual Engineering Section; RADC-TR-74-342, Final Report, December 1974, (A008526).

## 6.0

## INTEGRATION OF THE FOUR TASKS WITH THE IEMCAP

The objective of the subject contract was to increase the prediction capability of the IEMCAP. The increased capability was to be derived from the following four tasks:

- (1) Antenna Out-of-Band Radiation Characteristics Models
- (2) Nonaverage Power Sensitive Receptor Models
- (3) Nonlinear Effects Modeling
- (4) Port Spectra Representation Modeling

A detailed discussion of the modeling effect for each of these tasks is presented in prior sections of this report. The following subsections present the methods and locations of the interface with the IEMCAP.

## 6.1

Modifications to IEMCAP Logic Flow

The IEMCAP is divided into four sections as shown in Figure 6-1. As shown in the figure the four sections are: 1) Initial Processing Routine, 2) Wire MAP Routine, Specification Generation and Comparative EMI Analysis Routine and 4) NONLIN Routine. These sections are executed independently (i.e., separate programs) with various intermediate data storage files (disk or tape) as previously defined and used by IEMCAP. The program sections can be run in succession or executed in tandem. For systems with no wire, the second section can be omitted. This four section approach provides considerable flexibility in executing the new IEMCAP. As before, the first and second sections (for systems with wire bundles) can be run independently until data errors have been eliminated before running the analysis sections (TART and NONLIN).

A brief description of the functions performed by each program section is given below. The overall philosophy of the IEMCAP has been maintained and emphasis placed on segmenting program sections to keep down computer main memory requirements.

The first section of IEMCAP remains the IDIPR with the same purpose as before except the wire map routine has been removed. The input decode routine reads and decodes the tree-field input data from punched cards and checks the data for errors. All processing remains the same as that performed before the modifications to the program.

With the input cards properly processed, the initial processing routine performs data management, interfaces with the spectrum models and generates the working files. All prior functions performed by the initial processing routine are maintained.

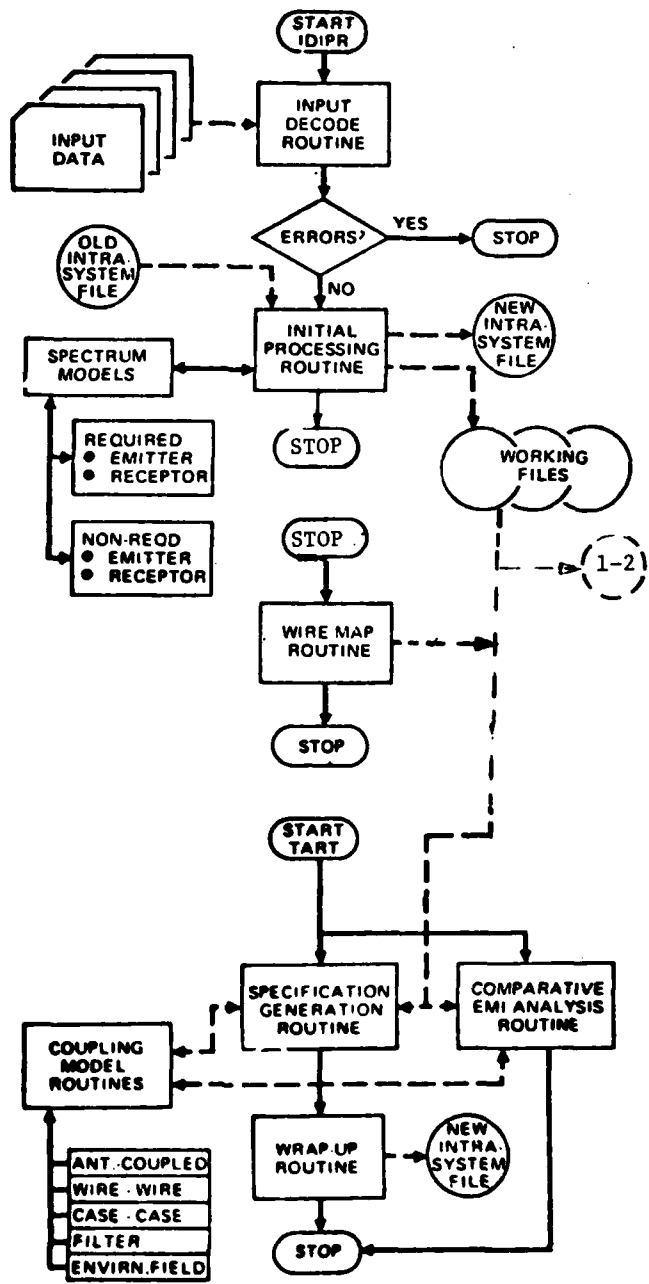


Figure 6-1 IEMCAP Functional Flow

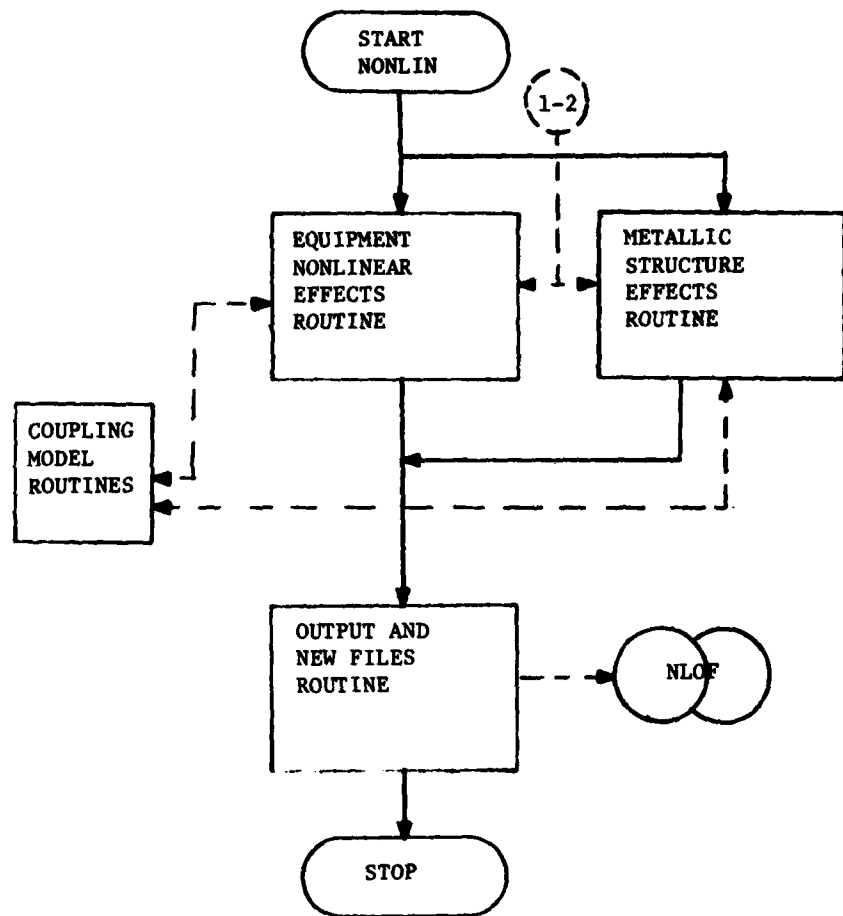


Figure 6-1 (Continued)

The second section of IEMCAP, called the Wire MAP Routine (WMR), is the same as the WMR of the previous IDIPR routine. WMR generates cross reference map arrays for use by the wire coupling models of TART. The WMR was set up as a separate program for two reasons. First, removal of WMR from the IDIPR reduces the computer main memory requirements (approximately 20K words) for IDIPR. Thus, allowing some flexibility in the memory requirement of the new IDIPR with modifications for the above tasks. Secondly, removal of WMR from the IDIPR provides more flexibility for analyzing non-wire systems. The second section is only required if the system under analysis contains wire bundles.

The third section of IEMCAP, TART, performs the same functions as that performed before the modifications to the program. The four tasks performed by TART are:

- Specification Generation
- Baseline System EMC Survey
- Trade-off Analysis
- Waiver Analysis

These tasks remain the same as defined in the IEMCAP documentation.

TART is composed of two basic routines (Figure 6-1). The Specification Generation Routine (SGR) performs the first task above and the comparative EMI analysis routine (CEAR) performs the other tasks. Both routines interface with the coupling models to compute transfer ratios between emitter and receptor ports.

The fourth section of IEMCAP, called the Nonlinear Effects Modeling Analysis Routine (NONLIN), uses the data compiled by IDIPR to perform the desired analysis task. The tasks performed by NONLIN are 1) nonlinear effects due to equipment nonlinearities and 2) nonlinear effects due to structurally generated intermods.

If only structurally generated intermods are to be examined, the SGENIM Routine is utilized. SGENIM interfaces with the coupling routine to generate system degradation due to nonlinear metallic junctions.

For nonlinear effects associated with electronic equipment, the program proceeds into the NOSGIM routine. The NOSGIM routine uses the nonlinear analysis data from IDIPR (working files) to determine which nonlinear effects models are appropriate in the analysis. NOSGIM interfaces with the coupling model routine to compute the transfer ratios between emitter and receptor ports.

A discussion of the new IEMCAP organization and overall logic flow was presented in Section 6.0. In this section, the major routines are identified and discussed to show the modifications to IDIPR and TART.

The WMR and NONLIN sections are not discussed in this section. The WMR remains the same as presented in prior IEMCAP documentation. Therefore, no further discussion of WMR is warranted. For NONLIN, the major routines are identified and discussed in the program documentation report.

#### 6.1.1 Modifications to IDIPR

The IDIPR consists of three basic programs. Figure 6-2 shows the overall logic flow through them and identifies the basic functions and data files used by each. The three subprograms are the Input Decode Routine (IPDCOD), Initial Processing Routine (IPR) and the Spectrum Model Routine (SPCMDL). The basic operation of these routines remains unchanged and will not be presented here. The remainder of this section discusses the modifications to these routines. The actual coding modifications are presented in the program documentation report of the various tasks with IEMCAP.

##### 6.1.1.1 Input Decode Routines

The Input Decode Routine (IPDCOD) performs the functions defined in Figure 6.2. Modifications to IPDCOD consisted of changes to read new input cards, increased arrays for storing the new data, modifying read and write statements, and elimination of the capability for handling wire bundles.

The specific routines involved are presented in the appropriate sections discussing the interface of the tasks with IEMCAP in the program documentation.

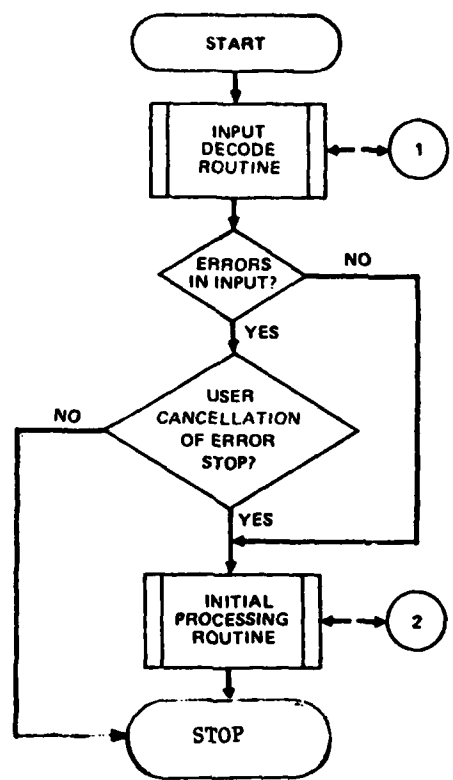


Figure 6-2 IDIPR Section of IEMCAP Top Level Functional Flow

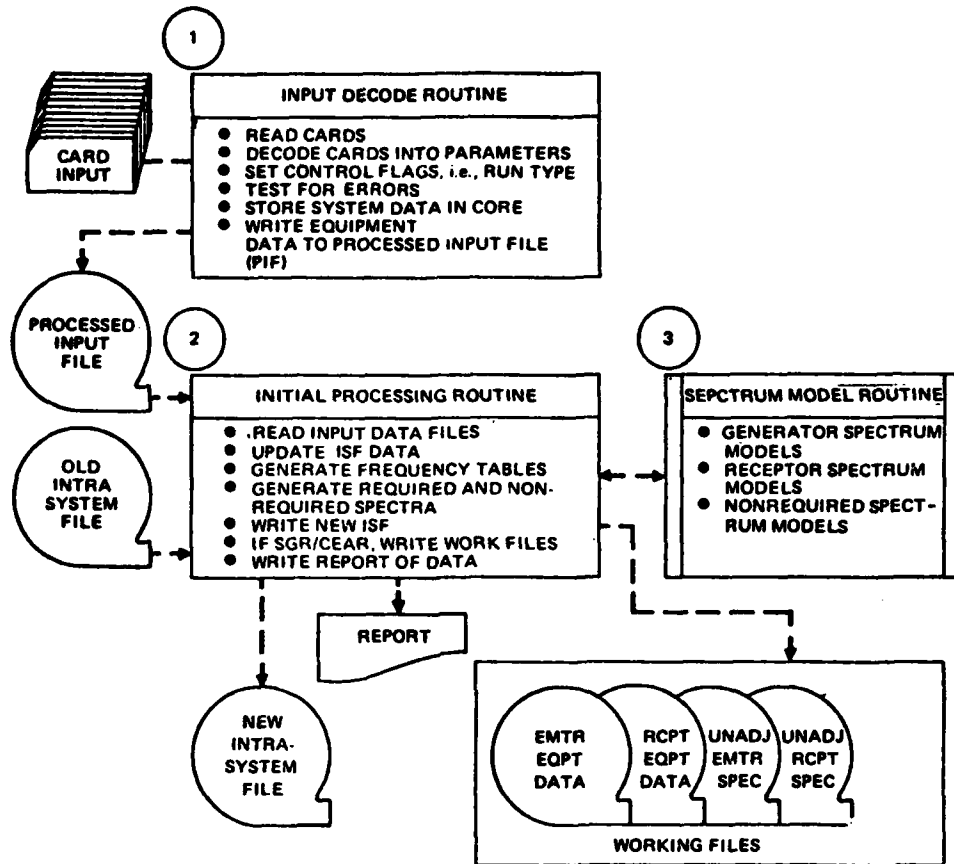


Figure 6-2 (Continued)

0P74-0267-110

#### 6.1.1.2 Initial Processing Routine

The IPR functions are as specified in Figure 6-2. No new functions were added to the IPR but essentially all of the functions were modified. The formatting for reading input data files was modified to accommodate the new input data required by the tasks on this effort. A new frequency generation subroutine was added to IPR to generate the equipment frequency table. The SPECT option on input data was modified and a new procedure was developed for generating the required and nonrequired port spectra.

#### 6.1.1.3 Spectrum Model Routine

The SPCMDL routine functions are as shown in Figure 6-2. These routines compute required and non-required spectra for emitters and receptors using mathematical models. The techniques used to obtain these spectra by the present IEMCAP is referred to as the "Quantization of Port Spectra". This technique has been replaced with the new procedure described in Section 5.0. The routines associated with SPCMDL remain essentially the same in number and name or designation, but several routines were redesigned to eliminate the quantization technique and accommodate the new port spectra representation. The required and nonrequired port modeling philosophy was retained.

#### 6.1.2 Modifications to TART

The TART consists of two basic programs. Figure 6-3 shows the overall logic flow through them and identifies the basic functions and data files used by each. The basic subprograms are the Specification Generation Routine (SGR) and the Comparative EMI Analysis Routine (CEAR). The coupling Path Routine (CPR) and Analysis and Spectrrum Adjust Routines are support functions for the basic subprograms. The overall operation of these routines are unchanged and thus the basic philosophy will not be presented here. Rather, the remainder of this section is devoted to discussing the actual modifications that were made to incorporate the various tasks associated with this effort. The actual coding modifications are presented in the sections pertaining to the interface of the four tasks with IEMCAP in the program documentation.

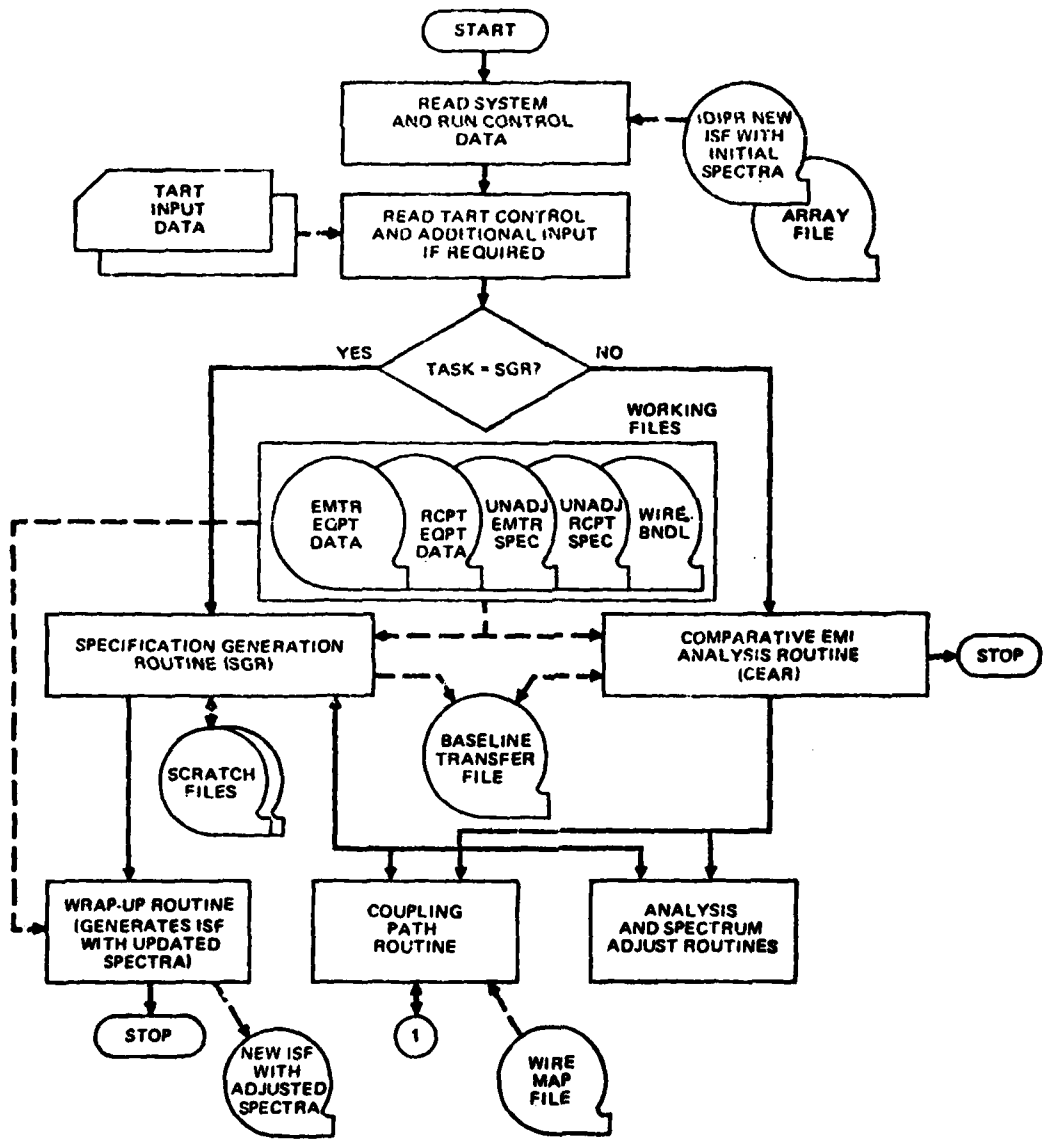


Figure 6-3 TART Section of IEMCAP Top Level Functional Flow

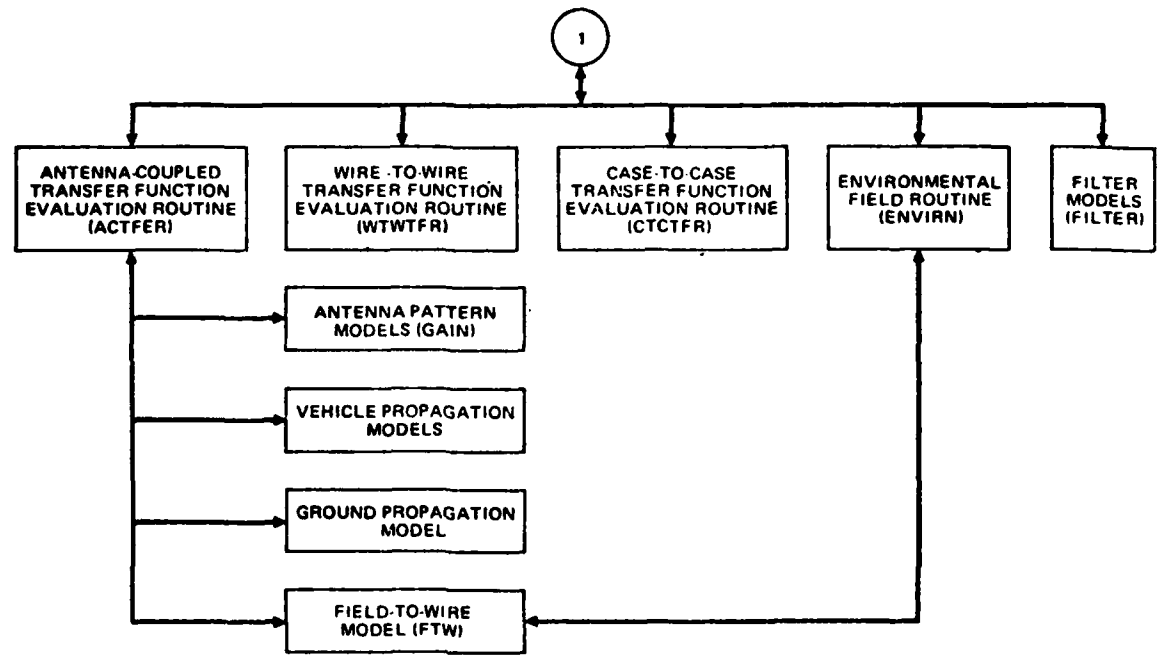


Figure 6-3 (Continued)

6.1.2.1 Specification Generation Routine

No modifications were made to the Specification Generation Routine SGR.

6.1.2.2 Comparative EMI Analysis Routine

CEAR performs the Baseline survey, Trade-off and Waiver analysis tasks of the IEMCAP. This routine was modified to handle the nonaverage power sensitive receptor models discussed in Section 3.0. CEAR was originally designed to perform the above tasks using average power as the criteria for determining EMI conditions. Hence, with the new requirements of the non-average power sensitive receptor task, CEAR must be able to handle interactions between various receptors with different susceptibility criteria.

6.1.2.3 Analysis and Spectrum Adjust Routines

The analysis and Spectrum Adjust routines are utilized by CEAR to perform the various functions required to obtain the EMI margins. The basic operation of these routines had to be modified to include the new susceptibility margins defined in Section 3.0. The models for total energy, peak current/voltage and bandwidth were added to these routines.

6.1.2.4 Coupling Path Routine

No modifications were made to the Coupling Path Routine CPR.

6.2 Interface of Antenna Out-of-Band Characteristics Models

The antenna out-of-band characteristics task was designed to provide an improved antenna model within the IEMCAP. Because of the complexity and large variations in parameters associated with an antenna type, it is not recommended that the antenna out-of-band characteristics modeling be implemented in IEMCAP at this time. Rather, it is recommended that additional effort be expended in this area to further refine the developed models.

6.2.1 Interface with IDIPR

None

6.2.2 Interface with TART

None

### 6.3

#### Interface of Nonaverage Power Sensitive Receptor Models

To implement the nonaverage power sensitive receptor modeling described in Section 3.0, several existing subroutines of the IEMCAP were modified. Both the IDIPR and TART Sections are affected by these modifications.

##### 6.3.1

###### Interface with IDIPR

The interface with IDIPR for the nonaverage power sensitive receptor models involves the input data requirements discussed in the User's Manual. The portion of the IDIPR affected by the input data includes the IDR, IPR and the SPCMDL. Subroutines modified in the IDR are

- CARDIN
- PIFRIT
- ALPSEL
- DUPCHK
- SSINIT
- STORE
- PARCHK

The modified IPR subroutines include:

- ISFRIT
- FTGEN
- SPCMDL
- SSINIT
- MERGE

Within SPCMDL the modified routines are:

- LOGLIN
- SCARFE

Flow diagrams of each of the above subroutines with the appropriate modifications are presented in the program documentation.

Several additional subroutines within IDIPR required some minor modifications. These modifications include items such as array dimensions, read and write statement formatting, elimination of frequency intervals, DO LOOP subscripts, etc. The routines effected by these minor changes are:

- READEQ
- REPORT

- WFRIT
- SCARFE
- SCARFR
- M461
- M6181
- M704

#### 6.3.2 Interface with TART

Since the TART section of IEMCAP performs the analyses, the subroutine interfaces will include additional data requirement and the new models for the nonaverage power sensitive receptors. The portion of the TART affected by the input data in the CEAR. Subroutines modified in CEAR are:

- CEAR
- EMCASA
- TORS
- EMTRD
- RCPTRD
- EMINTS

Flow diagrams of each of the above subroutines with the appropriate modifications are presented in the program documentation.

#### 6.4 Interface of the Nonlinear Effects Models

The nonlinear effects modeling has been designed to utilize the IDIPR section of the IEMCAP to input the necessary data required by the NONLIN section. That is, the IDIPR performs the necessary processing of the data requirements for NONLIN in the same manner as the data requirements for the linear (TART) section of the IEMCAP. Thus, it is a requirement that IDIPR be run before a NONLIN analysis is to be performed on a system.

#### 6.4.1 Interface with IDIPR

To obtain the input data described in Section 4 of this report, the data must be read off cards, decoded, and stored in arrays and working files. The same basic technique is used for inputting data for NONLIN as presently exists in IDIPR. Thus, several of the routines described in Section 6.2 are applicable for the NONLIN input data requirements. The IDIPR routines involved are repeated here for convenience.

Subroutines modified in the IDR are:

- CARDIN
- PIFRIT
- ALPSEL
- DUPCHK
- SSINIT
- STORE
- PARCHK

The modified IPR subroutines include:

- ISFRIT
- SSINIT
- MERGE

Flow diagrams of each of the above subroutines with the appropriate modifications are presented in the program documentation report.

#### 6.4.2 Interface with TART

There is no interface with TART for NONLIN.

#### 6.5 Interface of Port Spectra Representation

The interface of the port spectra representation modeling is involved with 1) removal of the port spectra quantization technique, 2) generation of the equipment frequency table, 3) establishing new frequency limits for the defined ports and 4) incorporating a replacement algorithm for the quantization technique. To incorporate these changes into IEMCAP required several modifications to existing subroutines in the IEMCAP.

#### 6.5.1 Interface with IDIPR

The interface with IDIPR for the port spectra representation model involves the input data requirements discussed in the User's Manual. The portion of the IDIPR affected by the input data includes the IDR, IPR and the SPCMDL. Subroutines modified in the IDR are:

- CARDIN
- PIFRIT
- ALPSEL
- DUPCHK
- SSINIT

- STORE
- PARCHK

The modified IPR subroutines include:

- ISFRIT
- FTGEN
- SPCMDL
- SSINIT

Within SPCMDL the modified routines are:

- LOGLIN
- SCARFE

Flow diagrams of each of the above subroutines with the appropriate modifications are presented in the program documentation report.

Several additional subroutines within IDIPR will require some minor modifications. These modifications include items such as array dimensions, read and write statement formatting, elimination of frequency intervals, DO LOOP, subscripts, etc. The routines affected by these minor changes are:

- READEQ
- REPORT
- WFRIT
- SCARFE
- SCARFR
- M461
- M6181
- M704

#### 6.5.2 Interface with TART

As a result of the change in the SPECT option associated with the port Spectra representation, a change in the integrated margin calculation was needed. Since a user may now specify the narrowband spectra for an emitter, it follows that the integrated margin calculation should include only those spectra specified by the user, that is, the IEMCAP method of integrating over bandwidth would provide an extremely "worst case" result. Thus, several routines within TART were modified to provide an integrated margin for narrowband specified spectra. For narrowband spectra, the integrated margin is

computed by summing the average levels (delta functions) over the specified frequency range. Subroutines modified in TART to provide this capability are:

- EMINTS
- TORS.

Flow diagrams of each of the above subroutines with the appropriate modification are presented in the program documentation report.



